2010

Functionalization of gold and nanocrystalline diamond atomic force microscope tips for single molecule force spectroscopy

Michael E. Drew
University of Pennsylvania

Functionalization of gold and nanocrystalline diamond atomic force microscope tips for single molecule force spectroscopy

Abstract

The atomic force microscope (AFM) has fueled interest in nanotechnology because of its ability to image surfaces at the nanometer level and act as a molecular force sensor. Functionalization of the surface of an AFM tip surface in a stable, controlled manner expands the capabilities of the AFM and enables additional applications in the fields of single molecule force spectroscopy and nanolithography. Two AFM tip functionalizations are described: the assembly of tripodal molecular tips onto gold AFM tips and the photochemical attachment of terminal alkenes to nanocrystalline diamond (NCD) AFM tips.

Two separate tripodal molecules with different linker lengths and a monopodal molecule terminated with biotin were synthesized to attach to a gold AFM tip for single molecule force spectroscopy. The immobilization of these molecules was examined by contact angle measurements, spectroscopic ellipsometry, infrared, and near edge x-ray absorption fine structure (NEXAFS) spectroscopy. All three molecules displayed rupture forces that agreed with previously reported values for the biotin–avidin rupture. The tripodal molecular tip displayed narrower distribution in their force histograms than the monopodal molecular tip. The performance of the tripodal molecular tip was compared to the monopodal molecular tip in single molecule force spectroscopy studies. Over repeated measurements, the distribution of forces for the monopodal molecular tip shifted to lower forces, whereas the distribution for the tripodal molecular tip remained constant throughout. Loading rate dependence and control experiments further indicated that the rupture forces of the tripod molecular tips were specific to the biotin–NeutrAvidin interaction.

The second functionalization method used the photochemical attachment of undecylenic acid to NCD AFM tips. The photochemical attachment of undecylenic acid to hydrogen-terminated NCD wafer surfaces was investigated by contact angle measurements, x-ray photoelectron, infrared, and NEXAFS spectroscopy. The same photochemical method was used to attach molecules to NCD AFM tips. Selective fluorescent labeling and adhesion measurements indicated that the functionalization of undecylenic acid was successful. Studies towards applying NCD AFM tips for nanolithography on a polymer surface are also described.

Degree Type

Dissertation

Degree Name

Doctor of Philosophy (PhD)

Graduate Group

Chemistry

First Advisor

Yoko Yamakoshi

Subject Categories

Chemistry

FUNCTIONALIZATION OF GOLD AND NANOCRYSTALLINE DIAMOND ATOMIC FORCE MICROSCOPE TIPS FOR SINGLE MOLECULE FORCE SPECTROSCOPY

Michael E. Drew

A DISSERTATION

in

Chemistry

Presented to the Faculties of the University of Pennsylvania

in

Partial Fulfillment of the Requirements for the

Degree of Doctor of Philosophy

2010

Yoko Yamakoshi, Assistant Professor of Radiology
Supervisor of Dissertation

Gary Molander, Hirschmann-Makineni Professor of Chemistry
Graduate Group Chair

Dissertation Committee:

Tobias Baumgart, Assistant Professor of Chemistry
Jeffrey Winkler, Merriam Professor of Chemistry
Donna Huryn, Adjunct Professor of Chemistry
Robert Carpick, Professor of Mechanical Engineering and Applied Mechanics

Dedicated to Emily Kong and the sun

Acknowledgments:

First and foremost, I thank Prof. Yoko Yamakoshi for giving me the opportunity to work in her laboratory and the chance to work with other excellent researchers in other departments. I learned diverse techniques to probe the chemical world in her lab and was able to freely pursue my interests. I am thankful to Prof. Jeff Bode for on the synthesis of molecules and teaching me about organic chemistry in his group meetings. I thank Professors Jeff Winkler, Donna Huryn, Tobias Baumgart, and Robert Carpick for being members of my committee. I greatly appreciate their help and guidance.

I acknowledge the help, assistance, and life lessons from our collaborators in the physics department at UC Santa Barbara. Without their help, I would be unable to operate an AFM. I thank Prof. Helen Hansma for the generous access and use of her AFM. I thank Dr. Emin Oroudjev for all the help with the AFM and troublesome Igor software. I thank Dr. Matthias Lauer for showing me the suggestive lewdness of gold terraces. I thank Dr. Arkadiusz Chworos for help and making me feel uncomfortable all the time by staring over my shoulder making sure I am taking force curves.

I acknowledge the assistance of Prof. Carpick and his lab members in the department of Mechanical Engineering and Applied Mechanics at Penn. I thank Rob Carpick for being an enthusiastic collaborator. Meetings and discussions with him led to new ideas and approaches that helped me finish my graduate studies. Within the Carpick research lab, I thank Dr. Papot Jaroenapibal for teaching me the HFCVD chamber and for TEM images. I thank Tevis Jacobs for taking TEM images of AFM tips for this project. I thank Graham Isapimp Wabiszewski for his help with sputtering and suggestions. Additionally, his impressions of Harry Caray always made me laugh.

Andy Konicek for taking NEXAFS spectra of my NCD surfaces. Also, I thank him for slowly discussing and explaining NEXAFS spectroscopy to me many times and assistance in analyzing the data. I thank Dr. Qunyang Li for suggestions for gold surfaces and AFM assistance. I thank Dr. Jason Bares for assistance with Matlab for analyzing batches force–distance curves and commiserating with me on the horrors of the instrument known as the PicoPlus. I thank Sina Ghassemi and Sammy Saber for the assistance with SEM images. I thank Dr. David Grierson for XPS spectra.

In the Materials Science and Engineering department, I thank Prof. Russ Composto for access to his lab and instruments and helpful suggestions. I acknowledge Marla McConnell for the synthesis of some of the polymers used in the nanolithography experiments. I thank Carme Ferrer for help with spin coating and her encouragement. I also thank Prof. Shu Yang for taking time to discuss my research.

I thank Prof. Cherie Kagan in the Electrical Engineering department for help with surface analysis. The use of her FTIR–ATR was critical to my research in the past year. Within the Kagan lab, I thank Dr. Paul Frail for his assistance with the FTIR–ATR instrument. I also thank Marjan Subotkin for her assistance in acquiring Raman spectroscopy studies on the NCD surfaces.

I thank all my chemistry teachers, especially Prof. Little and Prof. Geoffrey Strouse at UCSB for telling me I had to go to graduate school. I also thank Dave Bird at the College of the Sequoias for sparking my interest in chemistry.

In the Yamakoshi lab, I thank Yuko Iwamoto for taking the time to train me and tolerating the dissonant music I subjected her to in the lab. I thank Dimitar Vasilev for his joyful demeanor. I thank Dr. Betty Paulose for the encouragement. I thank Dr. Ye

Cai for teaching me all about Canada, I hope you are doing well with your family. I thank Dr. Andrew Lowell for the encouragement to finish my work and move on with my life. To the newest members of the Yamakoshi lab: Benjamin Delamare and Safwan Aroua I wish you the best in all your endeavors. I thank Benjamin Delamare for his help analyzing force–distance curves during the end of my graduate career. I thank all the undergraduates that have worked with me to be patient and for teaching me how to teach others: Brenee King, Natalie Spritzer, Adam Olinger, Seana Oriana, José Espinoza, Ben Rancatore, Zach Cassidy-Norris, Marika Harada, and Christie Langlois. A special thanks to Ben Rancatore for the help in the synthesis of the tripodal molecules and AFM analysis.

I would like to thank my fellow graduate students from UCSB for their support: Jake Cha, Sean Bonness, Alex Lippert, Nancy Carrillo and Justin Struble, Melissa Flores. Their friendship comforted me in troubling times. At Penn, I thank Shelly Zhang and Roshan Karunamuni for their friendship in the Radiology department and life affirming talks in the lunch room.

I thank my parents, Stephen and Kathleen, for their love and support. I thank them for all the character building they forced me to do by working long hours on the farm in the hot sun as a child. To my brothers and sister: Patrick, I thank you for opening the world of science to me. I thank Elizabeth for inspiring me to learn as a child. I thank Gregory for showing me the mechanical nature of all machines and tolerating me laughing at you injure yourself numerous times. I thank Philip for teaching me to bear with things and Vincent for all the laughter during our camping trips.

I thank my friends David Godshall and Shade Remelin and all the other Post-Maximalist Winners for all the love and support reminding me that the world is a stage for our dreams and fantasies. I thank Tiffany Leung, Keith Ellis, Rebecca Greenberg-Ellis, and Natalie Silverstein for their love and support.

To Ms. Emily Kong: Thank you for reminding me that all you need is love. Thank you for moving across the country to live with a picky eater with a bad taste in music.

ABSTRACT

FUNCTIONALIZATION OF GOLD AND NANOCRYSTALLINE DIAMOND ATOMIC FORCE MICRSCOPE TIPS FOR SINGLE MOLECULE FORCE SPECTROSCOPY

Michael E. Drew

Professor Yoko Yamakoshi

The atomic force microscope (AFM) has fueled interest in nanotechnology because of its ability to image surfaces at the nanometer level and act as a molecular force sensor. Functionalization of the surface of an AFM tip surface in a stable, controlled manner expands the capabilities of the AFM and enables additional applications in the fields of single molecule force spectroscopy and nanolithography. Two AFM tip functionalizations are described: the assembly of tripodal molecular tips onto gold AFM tips and the photochemical attachment of terminal alkenes to nanocrystalline diamond (NCD) AFM tips.

Two separate tripodal molecules with different linker lengths and a monopodal molecule terminated with biotin were synthesized to attach to a gold AFM tip for single molecule force spectroscopy. The immobilization of these molecules was examined by contact angle measurements, spectroscopic ellipsometry, infrared, and near edge x-ray absorption fine structure (NEXAFS) spectroscopy. All three molecules displayed rupture forces that agreed with previously reported values for the biotin–avidin rupture. The tripodal molecular tip displayed narrower distribution in their force histograms than the monopodal molecular tip. The performance of the tripodal molecular tip was

compared to the monopodal molecular tip in single molecule force spectroscopy studies. Over repeated measurements, the distribution of forces for the monopodal molecular tip shifted to lower forces, whereas the distribution for the tripodal molecular tip remained constant throughout. Loading rate dependence and control experiments further indicated that the rupture forces of the tripod molecular tips were specific to the biotin–NeutrAvidin interaction.

The second functionalization method used the photochemical attachment of undecylenic acid to NCD AFM tips. The photochemical attachment of undecylenic acid to hydrogen-terminated NCD wafer surfaces was investigated by contact angle measurements, x-ray photoelectron, infrared, and NEXAFS spectroscopy. The same photochemical method was used to attach molecules to NCD AFM tips. Selective fluorescent labeling and adhesion measurements indicated that the functionalization of undecylenic acid was successful. Studies towards applying NCD AFM tips for nanolithography on a polymer surface are also described.

Table of Contents

Title Page.....i

Dedication.....ii

Acknowledgements.....iii

Abstract.....vii

Table of Contents.....ix

List of Abbreviations.....xv

List of Figures.....xix

List of Schemes.....xxx

List of Tables.....xxxii

CHAPTER 1 BACKGROUND AND INTRODUCTION.....**1**

1.1 SCANNING PROBE MICROSCOPY AND ATOMIC FORCE MICROSCOPY BACKGROUND

.....1

1.1.1 Introduction to Scanning Probe Microscopy and Atomic Force Microscopy....1

1.1.2 Applications of AFM and Modified Tips.....3

1.2. CHEMICAL MODIFICATIONS OF AFM TIPS 4

1.2.1 Methods to Modify Atomic Force Microscope Tips.....4

1.3. APPLICATIONS OF CHEMICALLY MODIFIED AFM TIPS.....11

1.3.1. Single Molecule Force Spectroscopy......11

1.3.2 Nanolithography with AFM Tips......14

CHAPTER 2 SYNTHETIC MOLECULES TO MODIFY AFM TIPS FOR FORCE SPECTROSCOPY **34**

2.1. BACKGROUND 34

2.2 SYNTHESIS OF TRIPODAL MOLECULE 36

2.2.1 Synthetic Route for a Tripodal Molecular Tip 36

2.2.2 Synthesis of Tetrasubstituted Adamantane Core 38

2.2.3 Synthesis of Leg 39

2.2.4 Synthesis of Tripod Scaffolding 39

2.2.5 Synthesis of Biotinylated Linker 40

2.2.6 Coupling of Biotinylated Linker to Tripod Scaffolding 41

2.2.7 Synthesis of Monopodal Molecular Tip 42

2.2.8 Synthesis of a Molecular Tip with a Longer PEG Linker 43

2.3. MODIFICATION OF GOLD SURFACES WITH MOLECULAR TIPS 45

2.3.1 Background of Gold Surface Modification and Analysis. 45

2.3.2 Preparation of Gold Surfaces and Immobilization of Molecules. 45

2.3.3 Spectroscopic Ellipsometry Analysis of Modified Gold Surfaces 46

2.3.4 Sessile Drop Water Contact Angle Measurements 52

2.3.5 FTIR–ATR Analysis of Chemically Modified Gold Surfaces 52

2.3.6 Near Edge X-Ray Absorption Fine Structure Spectroscopy Analysis 58

2.3.7 Summary of Analysis of Modified Gold Surfaces 62

2.4. SINGLE MOLECULE FORCE SPECTROSCOPY EXPERIMENTS 64

2.4.1 Background and Introduction to Ligand–Receptor Binding 64

2.4.2. Immobilization of Molecular Tips on AFM Tips 67

2.4.3 Avidin Receptor Substrates 68

2.4.4 Force Spectroscopy Studies with Biotinylated Tripod A 69

2.4.5 Force Spectroscopy Studies with Biotinylated Monopod B 72

2.4.6 Stability Test with Monopod B and Tripod A 73

2.4.7 Force Spectroscopy Studies with Biotinylated Tripod C 76

2.4.8 Force Spectroscopy Control Experiments 78

2.4.9 Dynamic Force Spectroscopy 80

2.4.10 Summary of Force Spectroscopy Experiments 83

CHAPTER 3 FUNCTIONALIZATION OF NANOCRYSTALLINE DIAMOND AFM TIPS AND THEIR APPLICATION TOWARD NANOLITHOGRAPHY..... 96

3.1. BACKGROUND AND INTRODUCTION 96

3.1.1 Structure and Properties of Nanocrystalline Diamond 96

3.1.2 Chemical Modifications of Diamond Surfaces 103

3.1.3 NCD AFM Tip Functionalization and Its Application Toward Nanolithography 106

3.2 SYNTHESIS OF MOLECULES FOR NCD SURFACE MODIFICATION 108

3.2.1 Molecules for the Photochemical Functionalization of Diamond Surfaces ... 108

3.3 DEPOSITION AND FUNCTIONALIZATION OF NCD ON SILICON ON WAFER SURFACES 111

3.3.1 Preparation of NCD Films on Si Wafer Substrate 111

3.3.2 Functionalization of NCD with Undecylenic Acid 112

3.4 ANALYSIS OF FUNCTIONALIZED NCD SURFACES 113

3.4.1 FTIR–ATR Spectroscopy 113

3.4.2 Raman Spectroscopy Studies of Single Crystal and Nanocrystalline Diamond Films 116

3.4.3 Sessile Drop Water Contact Angle Measurements of H-NCD and UA-NCD Surfaces 117

3.4.4 XPS analysis of H-NCD and UA-NCD Surfaces 118

3.4.5 Near Edge X-Ray Absorption Fine Structure (NEXAFS) Spectroscopy 120

3.5 FUNCTIONALIZATION AND CHARACTERIZATION OF NCD-COATED AFM TIPS 121

3.5.1 Preparation of NCD-Coated AFM Tips 121

3.5.2 Transmission Electron Microscopy Observations of NCD Coated AFM Tips 123

3.5.3 Functionalization of NCD AFM Tips with Undecylenic Acid 125

3.5.4 Fluorescent Labeling of UA-NCD AFM Tips 126

3.5.5 Adhesion Measurements with NCD AFM Tips 129

.3.6 LITHOGRAPHY ON POLYMER SURFACES WITH UA-NCD AFM TIP 131

3.6.1 Thermal Deprotection of Polymer Surfaces 131

3.6.2 Chemical Lithography of Polymer Surfaces Using Contact Mode AFM 136

3.6.3 Imaging of Patterned Polymer Surfaces by Intermittent contact AFM 138

3.6.4 Fluorescent Labeling of Polymers after Nanolithography 143

3.6.5 Summary of Lithography Experiments Using UA-NCD AFM Tips 145

CHAPTER 4. CONCLUSION AND FUTURE DIRECTIONS 159

4.1 TRIPODAL MOLECULAR TIPS 159

4.1.1 Conclusion 159

4.1.2 Future Directions 160

4.2 FUNCTIONALIZATION OF NANOCRYSTALLINE DIAMOND AFM TIPS 162

4.2.1 Conclusion 162

4.2.2 Future Directions 163

CHAPTER 5 EXPERIMENTAL SECTION 168

5.1 SYNTHETIC PROCEDURES 168

5.1.1 General Procedures 168

5.1.2 Synthetic Procedure for Biotinylated Monopod and Tripodal Molecules 169

5.1.3 Synthetic Procedure for Molecules to Attach to Diamond Surfaces 193

5.2 GOLD SURFACE PREPARATION 201

5.2.1 Hydrogen Flame Annealing of Gold Surfaces 201

5.2.2 Surface Modifications of Gold Surfaces 202

5.3 SPECTROSCOPIC ANALYSIS OF GOLD AND NANOCRYSTALLINE DIAMOND SURFACES 202

5.3.1 Sessile Drop Contact Angle Measurements 202

5.3.2 Raman Spectroscopy 203

5.3.3 Spectroscopic Ellipsometry 203

5.3.4 Near Edge X-Ray Absorption Fine Structure (NEXAFS) Spectroscopy 203

5.3.5 Fourier Transform Infrared–Attenuated Total Reflectance (FTIR–ATR) Spectroscopy 204

5.3.6 X-Ray Photoelectron Spectroscopy. 205

5.4 FORCE SPECTROSCOPY 205

5.4.1 Functionalization of Gold AFM Tips 205

5.4.2 AFM Force Curve Measurements 206

5.4.3 Force Histograms for Loading Rate Experiments 207

5.5 NANOCRYSTALLINE DIAMOND DEPOSITION AND FUNCTIONALIZATION 210

5.5.1 Hot Filament Chemical Vapor Deposition 210

5.5.2 Functionalization of NCD with Undecylenic Acid (UA) 216

5.5.3 Au/Pd Sputtering on NCD AFM Tips 217

5.5.4 Additional NEXAFS Spectra 217

5.5.5 Fluorescent Labeling of Polymer Surfaces and AFM Cantilevers 221

5.6 LITHOGRAPHY WITH UA-NCD AFM TIPS ON POLYMER SURFACES 222

5.6.1 Spin Coating of Polymer Surfaces 222

5.6.2 FTIR–ATR Spectra of Polymer Surfaces 224

5.6.3 Atomic Force Microscopy 230

5.6.4 Adhesion Measurements 232

CHAPTER 6 SPECTRAL DATA 237

BIBLIOGRAPHY: 312

List of Abbreviations

Ac – acetyl

AcOH – acetic acid

AFM – atomic force microscope, atomic force microscopy

APTES – 3-aminopropyltriethoxysilane

ATP – adenosine triphosphate

CFM – chemical force microscopy

CI – chemical ionization

CVD – chemical vapor deposition

DCM – dichloromethane

DDT – dodecane thiol

DDT-Au – self-assembled monolayer of dodecane thiol on a gold surface

DIPEA – *N*,*N*-diisopropylethylamine

DMF – *N*,*N*-dimethylformamide

DMSO – dimethylsulfoxide

DNA – deoxyribonucleic acid

DPN – dip-pen nanolithography

EDC – 1-ethyl-3-(3′-dimethylaminopropyl)carbodiimide hydrochloride

EELS – electron energy loss spectroscopy

EI – electron impact

ESI – electrospray ionization mass spectrometry

ESR – electron spin resonance

EtOH – ethanol

FAB – fast atom bombardment

FTIR–ATR – Fourier transform infrared–attenuated total reflection

HBTU – *O*-benzotriazol-1-yl-*N*, *N*, *N'*, *N'*-tetramethyluronium hexafluorophosphate

HFCVD – hot filament chemical vapor deposition

HMDS – hexamethyldisilazane

H-NCD – hydrogen-terminated nanocrystalline diamond

IR – infrared

MALDI-TOF – matrix assisted laser desorption/ionization-time of flight

MeOH – methanol

Ms – methanesulfonyl-

MUA – 11-mercaptoundecanoic acid

MUA-Au – self-assembled monolayer of 11-mercaptoundecanoic acid on a gold surface

NCD – nanocrystalline diamond

NEXAFS – near edge x-ray absorption fine structure

NHS – *N*-hydroxysuccinimide

NMR – nuclear magnetic resonance

nN – nanonewton (10^{-9} N)

OEG – oligo(ethylene glycol)

OTS – octadecyltrichlorosilane

$P2X_2$ – purinoreceptor protein subunit 2

PAA – poly(acrylic acid)

PBS – phosphate buffered saline

PEG – poly(ethylene glycol)

PMMA – poly(methylmethacrylate)

pN – piconewton (10^{-12} N)

PS-*b*-PTBA – diblock copolymer of poly(styrene) and poly(*tert*-butyl acryate)

PS-*ran*-PTBA – random copolymer of poly(styrene) and poly(*tert*-butyl acrylate)

PTBA – poly(*tert*-butyl acrylate)

R_f – retention factor

RMS – root mean square

RNA – ribonucleic acid

SAM – self-assembled monolayer

SEM – scanning electron microscope

SMFS – single molecule force spectroscopy

SPM – scanning probe microscopy

STM – scanning tunneling microscopy

TBAF – tetra-*n*-butylammonium fluoride

TEM – transmission electron microscope

TFA – trifluoroacetic acid

TFAAD – trifluoroacetyl protected aminoundec-10-ene

THF – tetrahydrofuran

TIPS – triisopropylsilyl

TLC – thin layer chromatography

TMS – trimethylsilyl

TOF-SIMS – time of flight-secondary ion mass spectrometry

TREC – topography and recognition imaging

Tr – trityl, triphenylmethane

Ts – tosyl, 4-methylphenylsulfonyl

UA – undecylenic acid

UA-NCD – undecylenic acid-modified nanocrystalline diamond

UNCD – ultrananocrystalline diamond

UV – ultraviolet light

Vis – visible light

XPS – x-ray photoelectron spectroscopy

List of Figures

Figure 1-1. Schematic illustration of an atomic force microscope. 1

Figure 1-2. Schematic illustration of AFM probe chip.. 3

Figure 1-3. Physisorption modification of AFM tip with biotinylated bovine serum albumen (BSA)..... 6

Figure 1-4. Functionalization of silicon nitride and silcon AFM tips with ethanolamine hydrochloride. 7

Figure 1-5. Functionalization of silicon oxide with APTES.. 8

Figure 1-6. Self-assembly of monolayers of thiols onto a gold surface..... 9

Figure 1-7. Stepwise functionalization of AFM tips..... 9

Figure 1-8. Two examples of molecules synthesized and self-assembled onto gold AFM tips 9

Figure 1-9. Schematic diagram of AFM-based force spectroscopy experiment. 12

Figure 1-10. Schematic illustration of dip-pen nanolithography using alkyl thiols as the molecular ink, the AFM tip as a pen, and the Au substrate as paper.. 15

Figure 1-11. Schematic illustration of the Millipede device. 16

Figure 1-12. Thermolysis of *tert*-butyl ester by a heated AFM tip..... 16

Figure 2-1. Examples of molecular tips 35

Figure 2-2. Schematic illustration of AFM tip modification..... 37

Figure 2-3. Molecules adsorbed onto gold surfaces..... 47

Figure 2-4. Illustration of tilt angle. Schematic illustration of the tripod acetylene scaffolding approximated by a tetrahedron..... 48

Figure 2-5. Illustration of the biotinylated tripod on a gold surface with its PEG chain at a tilt angle of θ..... 50

Figure 2-6. FTIR–ATR spectra of biotinylated monopod B and tripod acetylene **2-11** immobilized on gold..... 54

Figure 2-7. FTIR–ATR spectra of tripod molecular tip A and tripod molecular tip C immobilized on gold..... 56

Figure 2-8. NEXAFS spectra of Biotinylated tripod A on a gold surface.. 59

Figure 2-9. Partial and total electron yield C K-edge spectra of tripod acetylene **2-11**. Partial and total electron yield C K-edge spectra of monopod molecular tip B. Tripod acetylene N K-edge spectra. O K-edge spectra of monopod B..... 61

Figure 2-10. Schematic illustration of force spectroscopy experiment with a ligand functionalized AFM tip and surface-bound receptor..... 65

Figure 2-11. Representative force–distance curves obtained on a NeutrAvidin-coated agarose bead and a streptavidin-coated glass slide..... 69

Figure 2-12. Representative force–distance curve with molecular tripod tip on NeutrAvidin-coated surface displaying a single rupture event and multimolecular events in one retraction. Histogram of all forces and only last forces..... 71

Figure 2-13. Histogram of rupture forces between the monopod molecular tip B and NeutrAvidin 73

Figure 2-14. Investigation of the robustness of molecular tips. Histograms of forces showing the rupture events of 600 continuous cycles using a single AFM tip functionalized with tripod or monopod. 74

Figure 2-15. Representative force–distance curve obtained with biotinylated tripod with a longer PEG linker. Histogram of all forces. Histogram of only last force. Histogram of forces at a distance between 10–20 nm only from each curve 77

Figure 2-16. Control experiments. Representative force–distance curve on an agarose bead without NeutrAvidin. Control experiment using unmodified gold AFM tip on NeutrAvidin beads. Biotinylated tripod A modified AFM tip on agarose beads without NeutrAvidin. Modified AFM tip on the NeutrAvidin beads in the presence of excess biotin. 79

Figure 2-17. The most probable rupture force for the biotin–NeutrAvidin pair as a function of loading rate. 82

Figure 3-1. Chemistry of hot filament CVD 98

Figure 3-2. Hot filament chemical vapor deposition 101

Figure 3-3. Structure of two tripodal molecules for NCD surface functionalization. 108

Figure 3-4. SEM images of NCD deposited on Si by HFCVD 111

Figure 3-5. Noncontact AFM image of NCD film. Topography and phase image 112

Figure 3-6. FTIR–ATR spectrum of UA-NCD surface with H-NCD as a background. Transmission FTIR spectrum of thin film of UA on NaCl plate 114

Figure 3-7. Raman spectra collected at 488 nm for boron-doped single crystal diamond and nanocrystalline diamond film deposited on Si wafer 116

Figure 3-8. XPS spectra of hydrogen terminated (H-NCD) and undecylenic acid modified NCD (UA-NCD) 119

Figure 3-9. NEXAFS partial electron yield C K edge and O K edge spectra spectra of H-terminated nanocrystalline diamond (H-NCD) and undecylenic acid functionalized nanocrystalline diamond (UA-NCD)..... 120

Figure 3-10. Intermittent contact mode AFM images of backside of NCD-coated cantilever..... 122

Figure 3-11. Effect of Au/Pd sputtering on NCD-coated cantilevers and tips. TEM images of AFM tips NCD-coated Si tip. Au/Pd intentionally sputtered on tip side of Si tip. NCD-coated Si tip with Au/Pd sputtering on backside of cantilever..... 124

Figure 3-12. TEM images of NCD-coated Si tips grown..... 124

Figure 3-13. Schematic illustration of the functionalization of NCD AFM tip with UA. 126

Figure 3-14. Optical microscope images of AFM cantilevers. Bright field and fluorescent images of H-NCD cantilevers after fluorescent treatment. Bright field and fluorescent images of an UA-NCD cantilevers..... 128

Figure 3-15. Schematic illustration of AFM tips and SAM gold surfaces used for adhesion measurements 129

Figure 3-16. Histogram of 200 adhesion forces with the same AFM tip in ethanol (H-NCD and UA-NCD) on functionalized gold surfaces.. 130

Figure 3-17. Intermittent contact mode AFM images after soaking in PBS buffer of PS-b-PAA (1:1) after 2 h soaking and PS-*b*-PAA (2:1) after 16 h soaking. Intermittent contact mode AFM images of PS-*ran*-PTBA (50% PTBA) as spin cast on silicon oxide and after thermal deprotection. 135

Figure 3-18. Schematic illustration of lithography experiment with UA-NCD AFM tip on PTBA surface 137

Figure 3-19. Intermittent contact AFM images of edge of a 70 μm region patterned with a UA–NCD tip on PTBA using a load of 20nN. Topography image, phase image, and 3-D image of edge of the pattern. Images of 40 μm pattern made with UA–NCD tip on PTBA surface with an increase in applied force (40nN) halfway through scan 50 μm image and 4 μm image inside higher applied force pattern. .. 139

Figure 3-20. Intermittent contact mode images of PTBA film scanned with H–NCD AFM tip. Topography, phase image, three-dimensional projection of surface. ... 140

Figure 3-21. Intermittent contact mode AFM images of PS-*ran*-PTBA (50%) after scanning in contact mode while heated to 100 °C. Images taken after soaking surface in PBS buffer (pH=7.4) for 2 h. 2 μm region inside patterned area and 2 μm region outside patterned area 142

Figure 3-22. Optical microscope images of polymer surface. Image of PTBA delaminated from the Si wafer. Selective labeling of PS-*ran*-PAA (30 mol% PAA). Fluorescent labeling of patterned PTBA spin coated on a glass slide and Si wafer. 144

Figure 4-1. Click chemistry tripod acetylene functionalized gold AFM tip with a biomolecule. 161

Figure 4-2. Photoactivable aryl azides to modify NCD surfaces 164

Figure 5-1. Force histograms for loading rate dependency experiments with molecular tip A. Loading rates, r, are inset in each histogram. 208

Figure 5-2. Force histograms for loading rate dependency experiments with molecular tip A. Loading rates, r, are inset in each histogram. 209

Figure 5-3. NEXAFS C and O K edge partial electron yield spectra for NCD surfaces. 219

Figure 5-4. Plot of peak area versus hours of irradiation for UA–NCD and UA–Me for C 1s to π^* transition of carbonyl and C 1s to σ^* transition of C–O. 220

Figure 5-5. FTIR–ATR of PTBA surfaces as cast and after annealing at 160 °C for 16 h. 224

Figure 5-6. FTIR–ATR spectra of PS-*ran*-PTBA (30 mol% PTBA) as cast and annealed at 185 °C for 15 h. 225

Figure 5-7. FTIR–ATR spectra of PS-*ran*-PTBA (50 mol% PTBA) as cast and after annealing for 15 h at 185 °C. 226

Figure 5-8. FTIR–ATR spectra of PS-*b*-PTBA (1:1) as cast and after annealing at 185 °C for 16 h. 227

Figure 5-9. FTIR–ATR spectra of PS-*b*-PTBA (2:1) as cast and after annealing at 160 °C for 2 d. 228

Figure 5-10. FTIR–ATR spectrum of PS-*b*-PTBA (1:1) annealed at 185°C for 16h, then soak 2h in PBS buffer, pH=7.4. 229

Figure 6-1. The thin film IR spectrum of compound **2-3**. 238

Figure 6-2. The 400 MHz ^{1}H NMR spectrum of compound **2-3** in $CDCl_3$ 239

Figure 6-3. The 100 MHz ^{1}H decoupled ^{13}C NMR spectrum of compound **2-3** in $CDCl_3$. 240

Figure 6-4. The thin film IR spectrum of compound **2-5**. 241

Figure 6-5. The 400 MHz ^{1}H NMR spectrum of compound **2-5** in $CDCl_3$ 242

Figure 6-6. The 100 MHz ^{1}H decoupled ^{13}C NMR spectrum of compound **2-5** in $CDCl_3$ 243

Figure 6-7. The thin film IR spectrum of compound **2-10**. 244

Figure 6-8. The 400 MHz ^{1}H NMR spectrum of compound **2-10** in $CDCl_3$ 245

Figure 6-9. The 400 MHz ^{1}H NMR spectrum of compound **2-10** in $CDCl_3$ 246

Figure 6-10. The 100 MHz ^{1}H decoupled ^{13}C NMR spectrum of compound **2-10** in $CDCl_3$ 247

Figure 6-11. The 100 MHz ^{1}H decoupled ^{13}C NMR spectrum of compound **2-10** in $CDCl_3$ 248

Figure 6-12. The 100 MHz ^{1}H decoupled ^{13}C NMR spectrum of compound **2-10** in $CDCl_3$ 249

Figure 6-13. The thin film IR spectrum of compound **2-11**. 250

Figure 6-14. The 400 MHz ^{1}H NMR spectrum of compound **2-11** in $CDCl_3$ 251

Figure 6-15. The 400 MHz ^{1}H NMR spectrum of compound **2-11** in $CDCl_3$ 252

Figure 6-16. The 100 MHz ^{1}H decoupled ^{13}C NMR spectrum of compound **2-11** in $CDCl_3$ 253

Figure 6-17. The thin film IR spectrum of compound **2-15**. 254

Figure 6-18. The 500 MHz ^{1}H NMR spectrum of compound **2-15** in $CDCl_3$ 255

Figure 6-19. The 500 MHz ^{1}H NMR spectrum of compound **2-15** in $CDCl_3$ 256

Figure 6-20. The 100 MHz ^{1}H decoupled ^{13}C NMR spectrum of compound **2-15** in $CDCl_3$ 257

Figure 6-21. The KBr pellet IR spectrum of **Molecular tip A**.....258

Figure 6-22. The 400 MHz ^{1}H NMR spectrum of **Molecular tip A** in DMSO-d_6.....259

Figure 6-23. The 400 MHz ^{1}H NMR spectrum of **Molecular tip A** in DMSO-d_6.....260

Figure 6-24. The 400 MHz ^{1}H NMR spectrum of **Molecular tip A** in DMSO-d_6.....261

Figure 6-25. The 100 MHz ^{1}H decoupled ^{13}C NMR spectrum of **Molecular tip A** in DMSO-d_6. 262

Figure 6-26. The 100 MHz ^{1}H decoupled ^{13}C NMR spectrum of **Molecular tip A** in DMSO-d_6. 263

Figure 6-27. The thin film IR spectrum of **2-21**. 264

Figure 6-28. The 400 MHz ^{1}H NMR spectrum of **2-21** in $CDCl_3$. 265

Figure 6-29. The 100 MHz ^{1}H decoupled ^{13}C NMR spectrum of **2-21** in $CDCl_3$. 266

Figure 6-30. The thin film IR spectrum of **Molecular tip B**.....267

Figure 6-31. The 400 MHz ^{1}H NMR spectrum of **Molecular tip B** in $CDCl_3$. 268

Figure 6-32. The 400 MHz ^{1}H NMR spectrum of **Molecular tip B** in $CDCl_3$. 269

Figure 6-33. The 100 MHz ^{1}H decoupled ^{13}C NMR spectrum of **Molecular tip B** in $CDCl_3$.....270

Figure 6-34. The 100 MHz ^{1}H decoupled ^{13}C NMR spectrum of **Molecular tip B** in $CDCl_3$.....271

Figure 6-35. The thin film IR spectrum of compound **2-22**. 272

Figure 6-36. The 500 MHz ^{1}H NMR spectrum of compound **2-22** in $CDCl_3$.....273

Figure 6-37. The 500 MHz ^{1}H NMR spectrum of compound **2-22** in $CDCl_3$.....274

Figure 6-38. The 125 MHz ^{1}H decoupled ^{13}C NMR spectrum of compound **2-22** in $CDCl_3$.....275

Figure 6-39. The 125 MHz ^{1}H decoupled ^{13}C NMR spectrum of compound **2-22** in $CDCl_3$ 276

Figure 6-40. The thin film IR spectrum of **Molecular tip C**. 277

Figure 6-41. The 500 MHz ^{1}H NMR spectrum of **Molecular tip C** in $CDCl_3$. 278

Figure 6-42. The 500 MHz ^{1}H NMR spectrum of **Molecular tip C** in $CDCl_3$. 279

Figure 6-43. The 500 MHz ^{1}H NMR spectrum of **Molecular tip C** in $CDCl_3$. 280

Figure 6-44. The 500 MHz ^{1}H NMR spectrum of **Molecular tip C** in $CDCl_3$. 281

Figure 6-45. The 125 MHz ^{1}H decoupled ^{13}C NMR spectrum of **Molecular tip C** in $CDCl_3$ 282

Figure 6-46. The 125 MHz ^{1}H decoupled ^{13}C NMR spectrum of **Molecular tip C** in $CDCl_3$ 283

Figure 6-47. The 125 MHz ^{1}H decoupled ^{13}C NMR spectrum of **Molecular tip C** in $CDCl_3$ 284

Figure 6-48. The 125 MHz ^{1}H decoupled ^{13}C NMR spectrum of **Molecular tip C** in $CDCl_3$ 285

Figure 6-49. The 125 MHz ^{1}H decoupled ^{13}C NMR spectrum of **Molecular tip C** in $CDCl_3$ 286

Figure 6-50. The thin film IR spectrum of compound **3-1**. 287

Figure 6-51. The 500 MHz ^{1}H NMR spectrum of compound **3-1** in $CDCl_3$ 288

Figure 6-52. The 125 MHz ^{1}H decoupled ^{13}C NMR spectrum of compound **3-1** in acetone-d_6 289

Figure 6-53. The thin film IR spectrum of compound **3-2**. 290

Figure 6-54. The 500 MHz ^{1}H NMR spectrum of compound **3-2** in $CDCl_3$ 291

Figure 6-55. The 125 MHz ^{1}H decoupled ^{13}C NMR spectrum of compound **3-2** in $CDCl_3$ 292

Figure 6-56. The thin film IR spectrum of compound **3-3**. 293

Figure 6-57. The 500 MHz ^{1}H NMR spectrum of compound **3-3** in $CDCl_3$ 294

Figure 6-58. The 125 MHz ^{1}H decoupled ^{13}C NMR spectrum of compound **3-3** in $CDCl_3$ 295

Figure 6-59. The thin film IR spectrum of compound **3-4**. 296

Figure 6-60. The 500 MHz ^{1}H NMR of compound **3-4** in $CDCl_3$ 297

Figure 6-61. The 125 MHz ^{1}H decoupled ^{13}C NMR spectrum of compound **3-4** in $CDCl_3$ 298

Figure 6-62. The thin film IR spectrum of compound **3-5**. 299

Figure 6-63. The 500 MHz ^{1}H NMR spectrum of compound **3-5** in $CDCl_3$ 300

Figure 6-64. The 125 MHz ^{1}H decoupled ^{13}C NMR spectrum of compound **3-5** in acetone-d_6 301

Figure 6-65. The thin film IR spectrum of compound **3-6**. 302

Figure 6-66. The 500 MHz ^{1}H NMR spectrum of compound **3-6** in $CDCl_3$ 303

Figure 6-67. The 125 MHz ^{1}H decoupled ^{13}C NMR spectrum of compound **3-6** in $CDCl_3$ 304

Figure 6-68. The thin film IR spectrum of compound **3-7**. 305

Figure 6-69. The 500 MHz ^{1}H NMR spectrum of compound **3-7** in $CDCl_3$ 306

Figure 6-70. The 125 MHz ^{1}H decoupled ^{13}C NMR spectrum of compound **3-7** in $CDCl_3$ 307

Figure 6-71. The thin film IR spectrum of compound **3-8**. 308

Figure 6-72. The 500 MHz ^{1}H NMR spectrum of compound **3-8** in $CDCl_3$.....309

Figure 6-73. The 500 MHz ^{1}H NMR spectrum of compound **3-8** in $CDCl_3$.....310

Figure 6-74. The 125 MHz ^{1}H decoupled ^{13}C NMR spectrum of compound **3-8** in $CDCl_3$.....311

List of Schemes

Scheme 2-1. Synthesis of 1,3,5,7-tetrasubstituted adamantane core of the tripod molecular tip.....38

Scheme 2-2. Synthesis of leg portion of the tripod molecular tip.....39

Scheme 2-3. Preparation of the tripodal scaffolding.....40

Scheme 2-4. Synthesis of biotinylated PEG-azide.....41

Scheme 2-5. Synthesis of biotinylated tripod, **molecular tip A**.....42

Scheme 2-6. Synthesis of biotinylated monopod, **molecular tip B**. 43

Scheme 2-7. Synthetic scheme for the preparation of biotinylated tripod with a longer PEG linker, **molecular tip C**. 44

Scheme 3-1. Chemical modifications of diamond surfaces. Fluorination of diamond powder allows substitution reactions to occur. Radicals generated by benzoyl peroxide enable acetic acid to bond to the surface of nanodiamond powder. Carbenes generated in situ insert into the C–H of a hydrogen terminated diamond surface.....103

Scheme 3-2. Chemical modifications of diamond surfaces. Glucose oxidase (GOx) was immobilized onto an UNCD surface by electrochemical reduction of an aryldiazonium. Reduction of aryldiazonium created a platform for further functionalization by Suzuki coupling. Photochemical reactions of NCD with the alkenes trifluoroacetyl-protected 10-aminoundec-1-ene (TFAAD) and undecylenic acid.....105

Scheme 3-3. Preparation of a terminal alkene leg **3-3**. 109

Scheme 3-4. Preparation of a terminal alkene leg **3-7** with an electron withdrawing group. 109

Scheme 3-5. Synthesis of tripodal molecule for photochemical attachment to diamond surface. 110

Scheme 3-6. Synthesis of TFAAD. 110

Scheme 3-7. Functionalization of NCD surface with UA. 113

Scheme 3-8. Schematic illustration of the fluorescent labeling of UA–NCD surfaces. 127

Scheme 3-9. Thermal annealing of *t*-butyl polymers on a silicon oxide surface 132

List of Tables

Table 2-1 Monolayer Thickness and Sessile Drop Contact Angle Measurements..... 51

Table 2-2. Assignment of peaks in FTIR–ATR and transmission spectra on NaCl. 53

Table 3-1. Types of diamond materials produced by CVD..... 102

Table 3-2. Assignment of peaks from FTIR–ATR spectra of spin cast and annealed polymer films on silicon oxide..... 133

Table 3-3. Adhesion measurements on PS-*b*-PTBA (33 mol % PTBA) surface at different temperatures..... 142

Chapter 1 Background and Introduction

1.1 Scanning Probe Microscopy and Atomic Force Microscopy Background

1.1.1 Introduction to Scanning Probe Microscopy and Atomic Force Microscopy

Since the atomic force microscope (AFM) was invented in 1986 by Binnig *et al.*,[1] AFM has fueled the nanotechnology revolution. AFM is part of the general class of scanning probe microscopy (SPM) that also includes scanning tunneling microscopy (STM). Both AFM and STM use the interaction of nanometer-sized probes to gain topographical images, mechanical properties, and electronic information of a substrate. The capability of AFM to characterize substrates in vacuum, air, and aqueous environments has had a profound effect on physics, chemistry, materials science, biology, and nanoscience as a whole.

In an AFM, a laser is reflected off the backside of a cantilever and focused into a

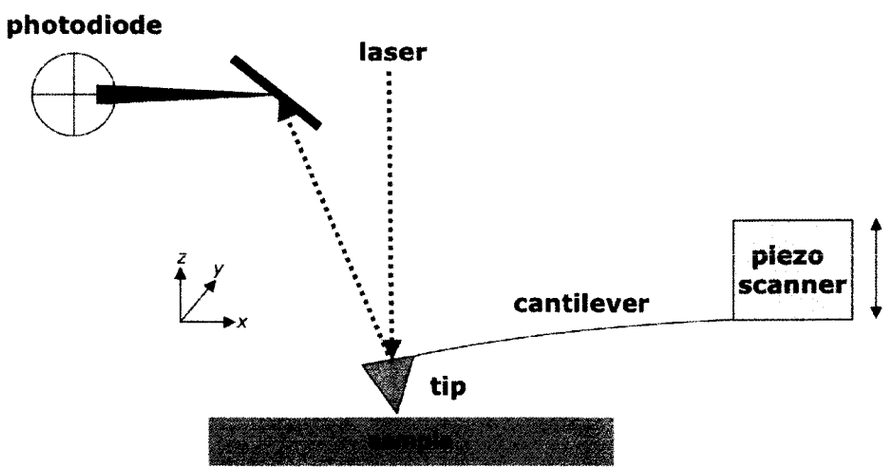

Figure 1-1. Schematic illustration of an atomic force microscope.

photodiode detector (Figure 1-1). The AFM can be used in various modes and spectroscopic studies. The most common imaging modes are contact and non-contact mode. Contact mode has the AFM tip in physical contact with the surface to give a topographical image of the surface. In non-contact mode, the tip oscillates near the sample and the amplitude is modified to provide a topography of the surface.[2] The AFM tip interacts with the surface of the sample and determines the lateral resolution of the image. The lateral resolution of an image is determined by the sharpness of the tip[3] and the height resolution is generally less than 1 nm. Both non-contact[4] and contact[5,6] modes have achieved atomic resolution of surfaces.

In addition to imaging, the AFM can also act as a molecular force sensor in force spectroscopy experiments to measure the adhesion force between the tip and the surface. The force resolution of an AFM is about 10^{-12} N (or 1 piconewton, pN) in fluid, approximately the amount of force necessary to rupture a single hydrogen bond.[7] In vacuum, the force resolution is on the order of 10^{-15} N.[8] The spring constant of the cantilever contributes to the force resolution of AFM.

The resonant frequency and the spring constant of the cantilever—as well as the geometry of the tip—are crucial elements in AFM experiments. AFM cantilevers are commercially available and primarily made from silicon or silicon nitride (SiN_x). Longer AFM cantilevers (300–400 μm long, 30–40 μm wide) are suitable for contact mode imaging and force spectroscopy applications because the lower spring constant and resonant frequency enable the detection of smaller forces (Figure 1-2). Stiffer and shorter cantilevers (e.g. 200–300 μm long, 30–40 μm wide) are more suited for non-

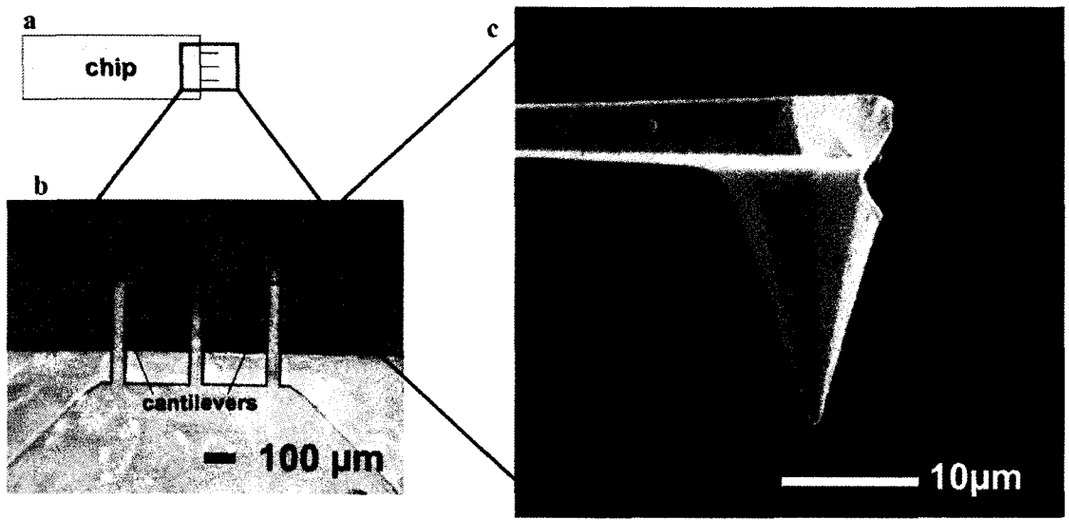

Figure 1-2. (a) Schematic illustration of AFM probe chip. (b) An expanded view of AFM chip to show the cantilevers and tips. The tips are facing the reader and are visible at the end of each cantilever. (c) A scanning electron microscope image of a conical AFM tip coated with nanocrystalline diamond.

contact imaging. The tip apex radius of curvature of the AFM tip interacts with the surface of the sample and thus determines the lateral resolution of the image. The shape of the tip is typically conical or pyramidal and a higher aspect ratio at the tip apex increases the lateral resolution of an image.[9]

1.1.2 Applications of AFM and Modified Tips

AFM has been applied to a multitude of surface characterization studies of organic monolayer films,[10] lipid bilayers,[11] transmembranal proteins,[12,13] and DNA.[14] It has also been used to study the mechanical properties of biomaterials,[15] monitor the kinetics of self-assembly[16] and protein folding,[17] and to quantify adhesion and friction.[18–20] Chemical modifications of AFM tips expand the capability of the AFM to explore a

larger variety of molecular interactions. Modified AFM tips have also allowed the visualization of individual pentacene molecules.[21] AFM tips modified with a host–guest component can be used to simultaneously obtain topography and its complementary molecular recognition component in topography and recognition imaging (TREC). This technique has the capability to map living cell surfaces through antibody–antigen interactions[22] and to probe the mechanical properties of the cell.[23] Moreover, AFM has been used as a molecular force sensor, a "pen" to pattern surfaces for lithography,[24] a manufacturing tool,[25,26] and to manipulate the structure of surfaces.[27,28]

1.2. Chemical Modifications of AFM tips

1.2.1 Methods to Modify Atomic Force Microscope Tips

Because modified AFM tips have a multitude of applications, there have been many reports on different methods to functionalize AFM tips. Methods to attach molecules to the tip vary according to the AFM tip surface. Silicon, silicon nitride, and gold-coated tips are commercially available, which makes them all accessible to chemical modification. Physisorption and chemisorption have both been used as methods to functionalize AFM tips.[29] These functionalization methods rely on common surface modification techniques to provide covalent modification of the tip.

Techniques such as infrared (attenuated total reflectance and reflection-absorption) spectroscopy, x-ray photoelectron spectroscopy (XPS), time of flight-secondary ion mass spectrometry (TOF-SIMS), fluorescent labeling, contact angle measurements, and ellipsometry are commonly used to characterize molecules

immobilized on a surface. The sensitivity of each method is generally suitable for a densely packed monolayer that has a maximum density of 10^{14}–10^{15} molecules/cm^2 (about 1 nanomole/cm^2). Surfaces with lower concentrations can be difficult to analyze. TOF–SIMS[30] has a detection limit of about 10^{13} molecules/cm^2 and FTIR has difficulty detecting molecules at concentrations lower than 10^{12} molecules/cm^2.[31] Fluorescent labeling has the ability to detect on the order of 10^9 molecules/cm^2.[31] Static time-of-flight secondary-ion mass spectrometry has identified organic and inorganic contaminants on AFM cantilevers,[32] but still cannot distinguish between the AFM tip and the cantilever. However, none of these methods have been developed to analyze a sample with a surface area as small as an AFM tip. Thus, it is difficult identify functional groups on the AFM tip surface by these current techniques and it remains a challenge to analyze AFM tip chemistry.

For the reasons listed above, AFM tip functionalization methods are first characterized on flat surfaces before applying the same methodology to the AFM tip surface. Because the ease of contaminating AFM tips and the difficulty in distinguishing between clean and contaminated surfaces is a challenge, a thorough cleaning by UV/ozone or other strong oxidizing reagent such as oxygen plasma or piranha solution (a mixture of H_2SO_4/H_2O_2) provides a clean surface for modification. However, in many cases it is not clear the tip is damaged, contaminated, or insufficiently functionalized until the desired experiment with the functionalized AFM tip is performed.

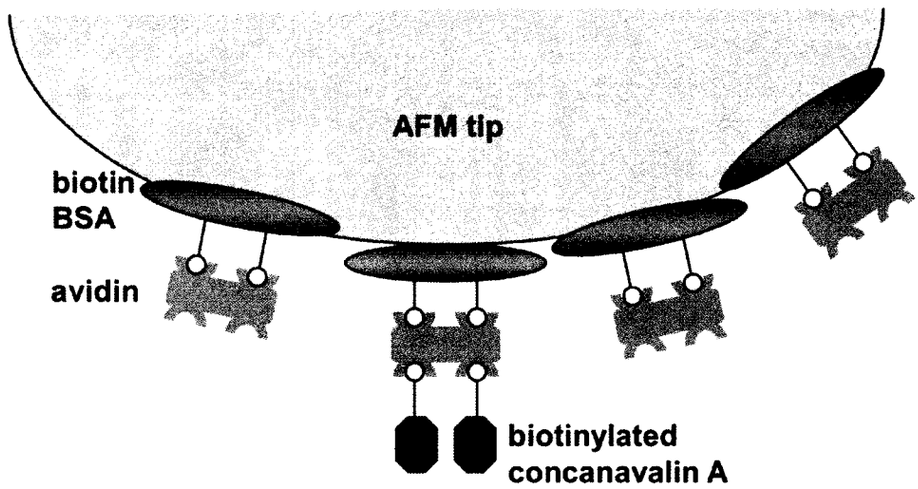

Figure 1-3. Physisorbing biotinylated bovine serum albumen (BSA) onto an AFM tip. Adopted from reference 35.

Protein physisorption onto AFM tips was the first technique that provided modified tips. Biotinylated bovine serum albumen has been physisorbed to the oxide layer on silicon nitride tips for measuring biotin–avidin interactions.[33,34] The biotin–avidin interaction has also been used to anchor biotinylated concanavalin A (Figure 1-3),[35] P-selectin,[36] or single stranded DNA[37] to the AFM tip. The nitrilotriacetic acid functionality bound to Ni^{2+} has been used to complex histidine tagged antibodies[38] to adsorb molecules onto the AFM tip surface. These physisorption and noncovalent linking methods were used in early AFM tip functionalizations and are now less commonly reported.

Currently, chemisorption is more commonly employed in AFM tip functionalizations because the strength of covalent bonds can withstand the mechanical stress necessary to break molecular complexes better than physisorbed molecules.[39]

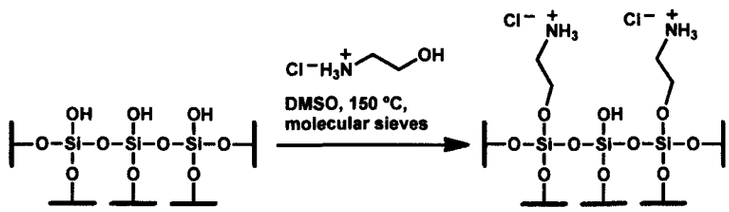

Figure 1-4. Functionalization of silicon nitride and silcon AFM tips with ethanolamine hydrochloride from reference 42.

Other modifications of AFM tips with organic molecules have included carbon nanotubes[40] from Lieber's group, which provide excellent tips for imaging, but remain technically difficult to attach to AFM tips. The two most commonly used materials for AFM tips are silicon and gold. Silicon AFM tips have a thin layer of silicon oxide on their surface due to oxidation that has been used to attach siloxy groups to its surface.[41] Treatments usually begin with oxidation to provide uniformly oxidized silicon surfaces. Ethanolamine hydrochloride and 3-aminopropyltriethoxysilane (APTES) are two reagents commonly used to create amine-terminated surfaces on silicon AFM tips.

Ethanolamine hydrochloride creates an amine-terminated surface on silicon nitride AFM tips.[42] Several reports of functionalization of silica surfaces by 1-hexadecanol[43] at 200 °C or 1-dodecanol[44] at 250 °C encouraged Hinterdorfer *et al.* to use ethanolamine hydrochloride (Figure 1-4) to create amine-terminated AFM tip surfaces. The disadvantages of ethanolamine hydrochloride are that it creates uneven surfaces of undetermined thickness and the mechanism of binding to silica is unknown.[29]

Amine-terminated surfaces on silicon oxide and mica have been created with 3-aminopropyltriethoxysilane (APTES). From infrared spectroscopic studies, APTES functionalization of silicon dioxide has several mechanistic steps. At low

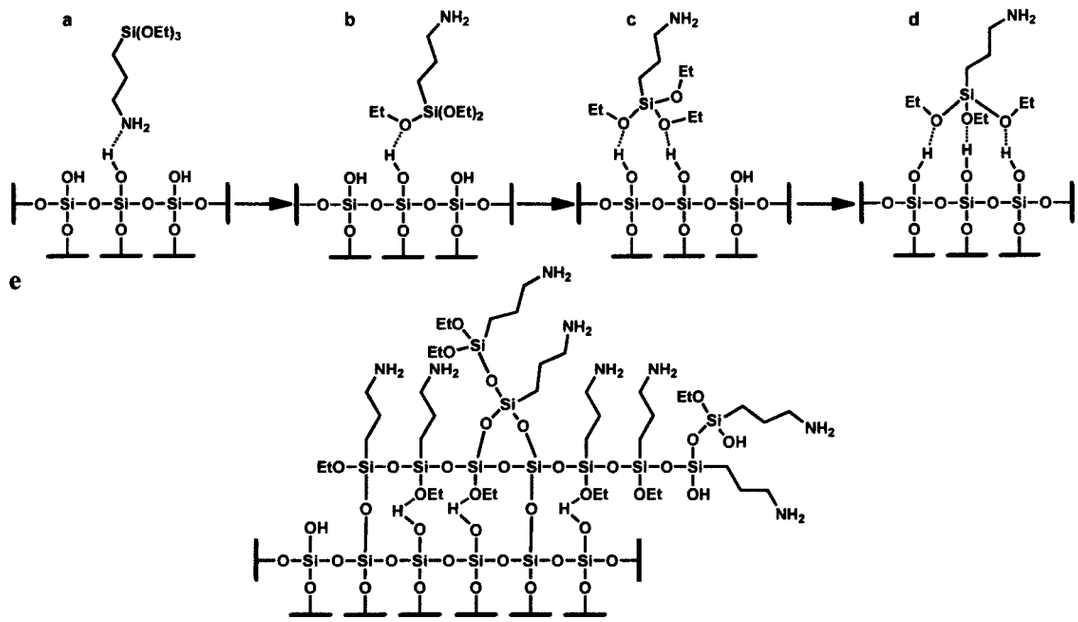

Figure 1-5. Functionalization of silicon oxide with APTES. (a) Hydrogen bonding of amino group to silanol. (b)–(d) APTES orients its ethoxy groups to hydrogen bond at three sites on the silicon dioxide surface. (e) After annealing a layer of APTES forms either covalent siloxane bonds or a network of hydrogen bonding. Adopted from reference 29.

concentrations, the amine of APTES forms hydrogen bonds with the silanol groups (Figure 1-5).[45] APTES then flips enabling its alkoxy groups to form hydrogen bonds to the silanols. The concentration of silanol groups on the surface is sufficient to bind to APTES through multiple sites.[46] Upon annealing, APTES condenses and forms covalent siloxane bridges.[47] The siloxy groups form less organized monolayers on the silicon oxide layer than SAM on gold. The method used to apply APTES to the surface is important to the formation of a stable, uniform monolayer ready for subsequent functionalization steps.[29] There are also issues with polycondensation and physisorption of APTES (Figure 1-5e)[48–50] and the APTES linkage degrades in the presence of amines and in basic solution.[51]

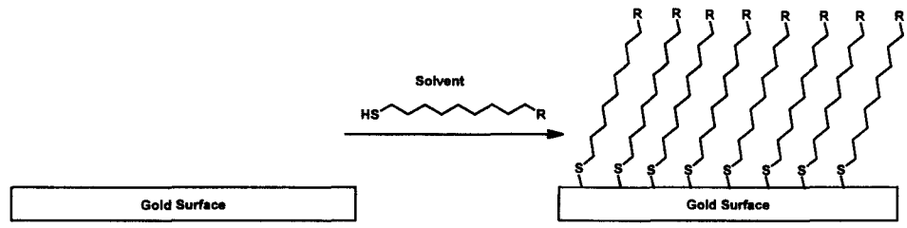

Figure 1-6. A self assembled monolayer of thiols on a gold surface.

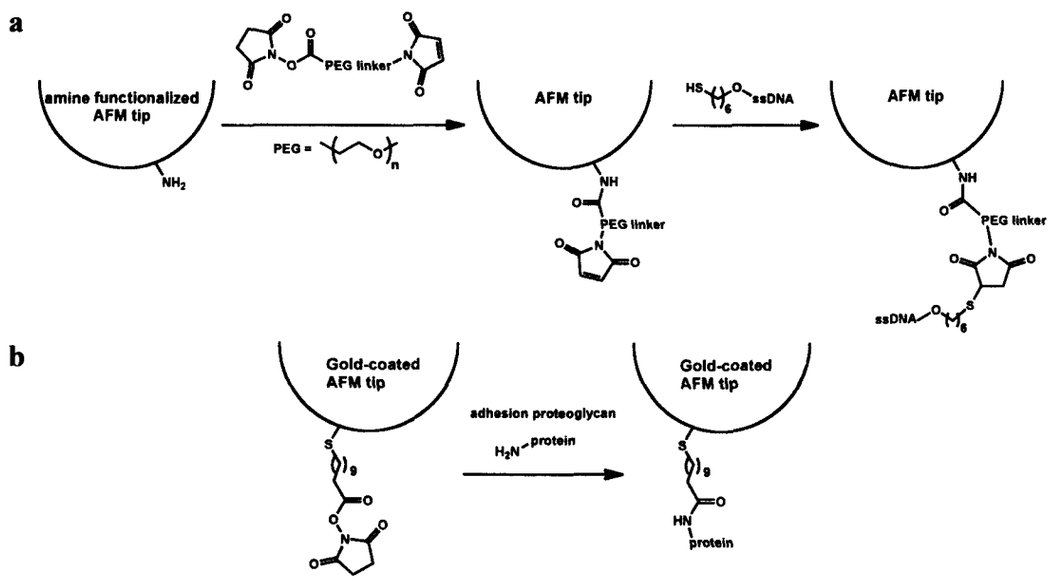

Figure 1-7. Stepwise functionalization of AFM tips. (a) Stepwise functionalization of a silicon nitride tip. Adopted from reference 57. (b) Stepwise functionalization of a gold-coated AFM tip. Adopted from reference 58.

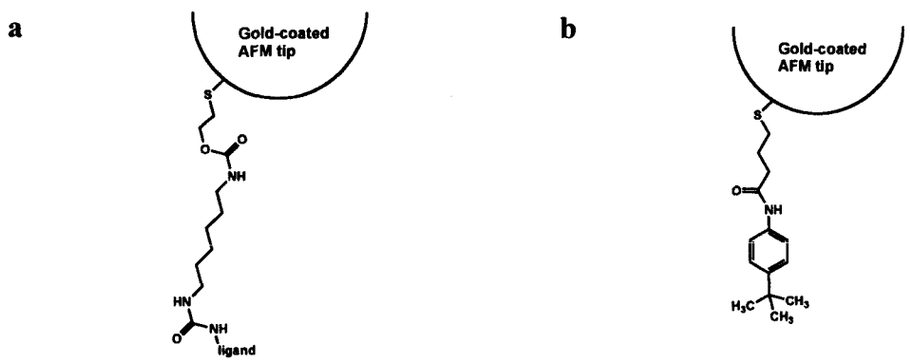

Figure 1-8. Two examples of molecules synthesized and self-assembled onto gold AFM tips. (a) A linker for force spectroscopy with hydrogen bonded supramolecular polymers. Adopted from reference 60. (b) A molecule that complexes to β-cyclodextrin was synthesized and immobilized on AFM tip. Adopted from reference 53.

Another common AFM tip functionalization technique is the formation of self-assembled monolayers (SAM)[52] of thiols on gold tips.[53] A SAM on a gold surface forms spontaneously, driven by the covalent bond formed between a sulfur and a gold atom on the surface (Figure 1-6). Gold is the standard material for making monolayers for the following reasons: gold is easily obtained as a flat, single crystal film by evaporation or sputtering. Gold is compatible with cells and nontoxic,[54] whereas other metals that form SAM, such as silver and copper, are either easily oxidized in ambient air or cytotoxic.[55] Gold is inert, tolerant to oxidation, and unreactive towards most chemicals, except for binding strongly to thiols.[56] It is easy to incorporate studies of monolayers on gold with current instrumentation because gold is commonly used in infrared and surface plasmon resonance spectroscopy, ellipsometry, and quartz crystal microbalances.

Functionalizations of AFM tips occur over three general steps: surface functionalization, attachment of a linker, and immobilization of the ligand. These three steps can be performed sequentially on the surface of silicon AFM tips (Figure 1-7).[57,58] The AFM tip can be functionalized and then connected to the linker-ligand conjugate. Gold-coated tips have also been used in stepwise functionalization of AFM tips.[59] Unlike silicon AFM tips, gold-coated AFM tips can be functionalized in a single step. The entire molecule to be immobilized can be synthesized, followed by its self-assembly onto the AFM tip (Figure 1-8).[53,60] Although there have been functionalizations of hydrogen-terminated silicon tips with terminal alkenes,[61] there have not been any reports for the modification of diamond AFM tips even though the chemistry for functionalization is similar to hydrogen-terminated silicon.[62]

1.3. Applications of Chemically Modified AFM Tips

1.3.1. Single Molecule Force Spectroscopy.

Interactions of different strengths and complexity between biological molecules provide a range of cellular processes to perform cell functions. Single molecule spectroscopy has found particular interest in the biological sciences because of its ability to reveal properties of molecules that can be masked by ensemble averaging.[63] For example, in ensemble methods, observing a sequence of events can often lead to events happening out of phase with other molecules. This may lead to the complex behavior and loss of detail of individual events. Because different states are mixed by ensemble averaging, the use of single molecule measurements avoids complications caused by molecules that are out of phase.[64] Numerous observations of single molecule behavior are collected and analyzed using statistics. Single molecule studies are often compared to values obtained in bulk studies.

Force spectroscopy has rapidly developed as a vital biophysical and single molecule technique. A variety of methods operating over a range of forces has been used in recent years.[65] These methods include: optical traps (range of forces: 0.1-150 pN), magnetic tweezers (0.01-100 pN), biomembrane force probes (0.5-1000 pN) and atomic force microscopes (greater than 1 pN). Because the AFM dynamically detects forces over several orders of magnitude it makes an excellent intra- and intermolecular force sensor. In a force experiment with an AFM (Figure 1-9), the laser reflection off the backside of a cantilever is focused into a photodiode detector to monitor its change in

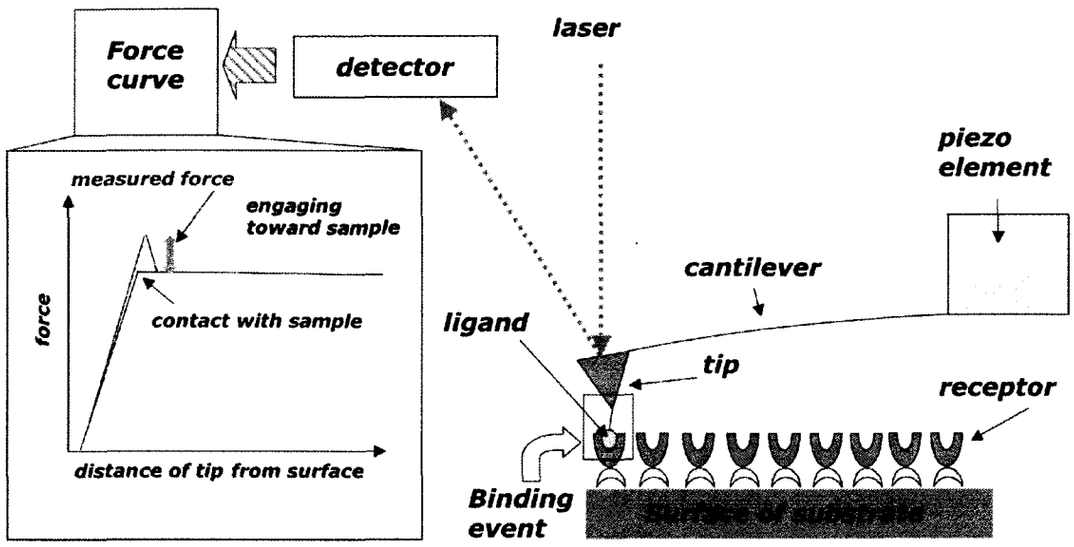

Figure 1-9. Schematic diagram of AFM-based force spectroscopy experiment.

position. From Hooke's law, the detected force is equal to the spring constant of the cantilever, *k*, multiplied by the displacement of the cantilever, z. The force is plotted versus the displacement, or distance from the surface, to obtain what is called a force–distance curve. Analysis of the magnitude of adhesion forces, also called rupture events, from force curves provides the necessary spectroscopic data. For example, in our studies we are interested in ligand–receptor interactions, thus the measured force of adhesion is the force necessary to rupture the noncovalent ligand–receptor complex.

Some examples of molecular recognition elements used in single molecule force spectroscopy experiments include: RNA,[66] DNA,[67] polysaccharides,[68] receptor–ligand complexes,[69] antigen–antibody interactions,[70] protein folding and unfolding,[17] and motor proteins.[71] Single molecule force spectroscopy has also been used to study the mechanical strength of a covalent bond,[39] the adhesion effects in chiral molecules,[72] and the energetics of a molecular motor.[73] Recently, single molecule force spectroscopy has

been able to achieve angstrom resolution to examine biological processes. In an impressive achievement of using force as a biological probe, Block and co-workers have used an optical trap to track the real-time base pair stepping of RNA polymerase during transcription,[74] as well as accurately determine DNA sequences[75] using a single molecule of RNA polymerase. Furthermore, Fernandez and co-workers were able to observe sub-angstrom conformational transitions in their studies of polysaccharides.[76]

An important area of intermolecular interactions is the binding of a small molecule ligand to its receptor, generally a large molecule such as a protein. The focus of the research in our group is the $P2X_2$ receptor, a transmembrane protein that binds to adenosine triphosphate (ATP). The $P2X_2$ receptors are members of the ion channel P2X family, a group of proteins from $P2X_1$ to $P2X_7$. "P" represents its function as a purinoreceptor because it is activated by the purine, ATP. It is a ligand-gated cation channel containing 472 amino acids with both its C and N terminus inside the cell. The large extracellular loop is the binding site of ATP. Recent work indicates that the function of $P2X_2$ plays a vital role in pain signaling and chronic pain.[77] The three dimensional structure of the protein is unknown, but AFM imaging suggests that there exists two transmembrane domains.[78] For $P2X_2$, these domains likely exist in trimeric form within the cell membrane and result in a pore in the center of the protein[78c] that possibly forms a permeation pathway.

In order to perform force spectroscopy experiments, it is necessary to immobilize the biomolecule of interest on the surface of the AFM tip. We are interested in making a molecular platform that is easily modified to use with a variety of ligands to probe structure and function of $P2X_2$. This molecular platform will be a tripodal molecule that

binds to the AFM tip through multiple attachments to create a stable modification of AFM tips for single molecule force spectroscopy. Our efforts toward this goal are detailed in Chapter 2.

1.3.2 Nanolithography with AFM Tips.

Because creating patterns on the nanoscale impacts information technology, researchers are investigating new lithographic techniques that create smaller features. Lithographic techniques such as UV and deep UV lithography can create features down to 80 nm.[79] Particle-, ion-, and electron-beam techniques are available down to 50 nm, but costs rise prohibitively under these conditions and the addressable size decreases at this scale. The size limit of these techniques has likely met the end of economically feasible progress.[80] AFM is a candidate to create ordered features at a scale smaller than these techniques. Progress continues to be made in scanning probe-based lithography with dip-pen nanolithography, thermal AFM probes, and using the AFM tip as a catalyst.

Dip-pen nanolithography (DPN) was reported as a method that uses the capillary forces between an AFM tip and alkyl thiols to pattern gold surfaces.[24] It is a direct write scanning probe based lithographic tool using an AFM tip to deliver chemical agents to desired regions of the target substrate. Early studies used alkyl thiols on gold that allowed writing lines with widths less than 100 nm (Figure 1-10). The DPN process has also been used in arrays with up to 55,000 AFM tips in attempts to apply the technique to larger areas.[81] A variety of "inks" has been used: small organic molecules, organic

a

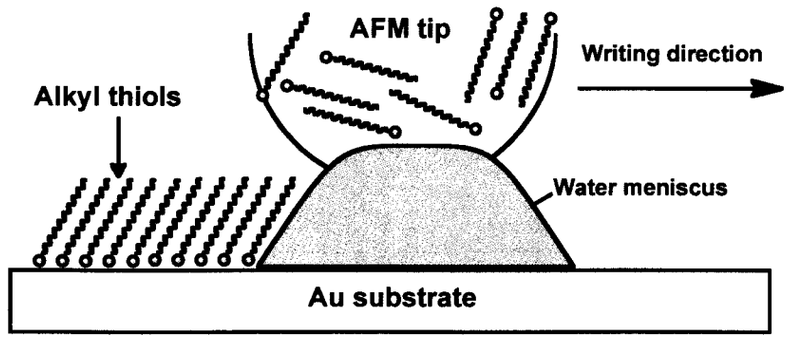

Figure 1-10. Schematic illustration of dip-pen nanolithography using alkyl thiols as the molecular ink, the AFM tip as a pen, and the Au substrate as paper. Adopted from reference 24.

and biological polymers, colloids, and metal ions.[82] DPN has found uses in patterning biomolecular arrays,[83] tailoring surfaces for molecular recognition of cells and single molecules,[84] creating templates for orthogonal assembly on surfaces,[85] and generation of hard nanostructures.[86] A combination of contact printing and dip-pen nanolithography used an array of 11 million "polymer pens" to pattern 16-mercaptohexadecanoic acid onto a gold surface.[87] This method used tips made from a polymeric material and manipulated the contact time and applied force to make 90 nm to hundreds of microns in less than an hour. In comparison, dip-pen nanolithography takes about 30 minutes to make a 10 by 10 μm feature of thiols on a gold substrate. An example of DPN with ultrananocrystalline diamond (UNCD) probes to make features as small as 80 nm in width has been demonstrated. Because of its exceptional resistance to wear, chemical inertness, and a relatively low friction coefficient compared to conventional tips,[88] UNCD is an ideal choice for probe material.

Using the AFM tip as a tool in lithography and manufacturing has been developed to hundreds of probes in parallel in such projects as the IBM Millipede

device.[89] The Millipede device uses an array of doped AFM tips that can be heated individually by an applied current. The tips are heated to 400 °C and placed against a poly(methylmethacrylate) (PMMA) surface that softens upon contact to create indentations on the polymer surface. The indentations on the polymer are in the shape of the AFM tip and are used as bits in data storage. The PMMA surface is "erased" when it is heated to 150 °C.

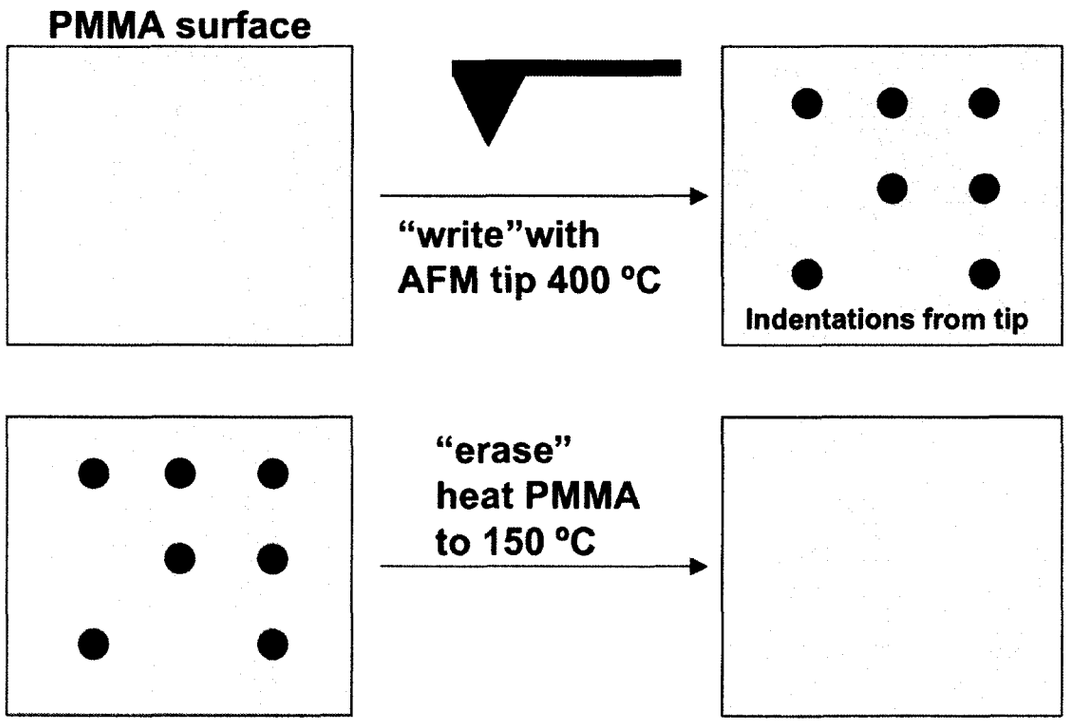

Figure 1-11. Schematic illustration of the Millipede device.

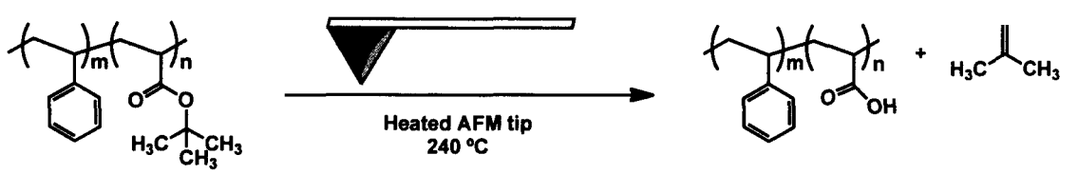

Figure 1-12. Thermolysis of a *tert*-butyl ester by a heated AFM tip.

Heated AFM probes have also been used to cause chemical reactions on polymer surfaces. Duvigneau *et al.* recently reported the thermal deprotection of the block copolymer poly(styrene-*b*-*tert*-butyl acrylate) (PS-*b*-PTBA) using thermal scanning probe lithography (Figure 1-12).[90] The thermal deprotection of the *tert*-butyl esters with heated AFM probe tips allowed the nascent carboxylic acids to be activated by EDC/NHS and coupled to either a fluorescent label or a poly(ethylene glycol) (PEG) in an area as small as 370 nm by 580 nm. A copper-coated AFM tip was used to catalyze a 1,3-dipolar cycloaddition in an alkyne solution with an azide-functionalized silicon surface to create patterns.

Similar to the Cu-coated AFM tip, we wish to catalyze a reaction with an AFM tip. Also, our group has been interested in the stability of surface functionalizations for biological applications and is particularly interested in diamond AFM tips as nanometer probes. Our aim is to modify a diamond AFM tip to catalyze the hydrolysis reaction of a polyester polymer surface. Such a system will be able to pattern and manipulate material down to nanometer levels. Our goal is to convert areas of a polymer surface with an undecylenic acid functionalized tip. The carboxylic acid moieties attached to the AFM tip will be used to catalyze the hydrolysis of the esters side chains of the polymer. Previous work by the Composto group demonstrated the global thermal deprotection of a thin film of the block copolymer poly(styrene-*b*-*tert*-butyl acrylate) yielded cylindrical domains of poly(acrylic acid) (PAA) that swelled into mushroom-shaped features in buffered solution.[91] The hydrolysis produces a change in the topography of the polymer surface that can be monitored by AFM imaging. Our efforts toward this goal are described in Chapter 3.

References:

(1) Binnig, G.; Rohrer, H.; Gerber, C.; Weibel, E. "Atomic Force Microscope" *Phys. Rev. Lett.* **1986**, *56*, 930–933.

(2) García, R.; San Paulo, A. "Attractive and Repulsive Tip-Sample Interaction Regimes in Tapping-Mode Atomic Force Microscopy" *Phys. Rev. B* **1999**, *60*, 4961–4967.

(3) Smith, R. L.; Rohrer, G. S. The Preparation of Tip and Sample Surfaces for Scanning Probe Experiments. In *Scanning Probe Microscopy and Spectroscopy Theory, Techniques, and Applications*, 2nd edition; Bonnell, D. Ed.; Wiley: New York, 2001; 170–178.

(4) Giessibl, F. J. "Atomic Resolution of the Silicon (111)-(7x7) Surface by Atomic Force Microscopy" *Science* **1995**, *267*, 68–71

(5) Giessibl, F. J.; Binnig, G. "Investigation of the (001) Cleavage Plane of Potassium Bromide with an Atomic Force Microscope at 4.2 K in Ultra-High Vacuum" *Ultramicroscopy* **1992**, *42*, 281–289.

(6) Ohnesorge, F.; Binnig, G. "True Atomic Resolution by Atomic Force Microscopy Through Repulsive and Attractive Forces" *Science* **1993**, *260*, 1451–1456.

(7) Hoh, J. H.; Cleveland, J. P.; Prater, C. B.; Revel, J.-R.; Hansma, P. K. "Quantized Adhesion Detected with the Atomic Force Microscope" *J. Am. Chem. Soc.* **1992**, *114*, 4917–4918.

(8) Smith, D. P. E. "Limits of Force Microscopy" *Rev. Sci. Instrum.* **1995**, *66*, 3191–3195.

(9) Hafner, J. H.; Cheung, C.-L.; Woolley, A. T.; Lieber, C. M. "Structural and Functional Imaging with Carbon Nanotube AFM Probes" *Prog. Biophys. Mol. Biol.* **2001**, *77*, 73–110.

(10) Burnham, N. A.; Dominguez, D. D.; Mowery, R. L.; Colton, R. J. "Probing the Surface Forces of Monolayer Films with an Atomic-Force Microscope" *Phys. Rev. Lett.* **1990**, *64*, 1931–1934.

(11) Naumann, R.; Schiller, S. M.; Giess, F.; Grohe, B.; Hartman, K. B.; Kärcher, I.; Köper, I.; Lübben, J.; Vasilev, K.; Knoll, W. "Tethered Lipid Bilayers on Ultraflat Gold Surfaces" *Langmuir*, **2003**, *19*, 5435–5443.

(12) Kedrov, A.; Ziegler, C.; Janovjak, H.; Kühlbrandt, W.; Müller, D. J. "Controlled Unfolding and Refolding of a Single Sodium-Proton Antiporter Using Atomic Force Microscopy" *J. Mol. Biol.* **2004**, *340*, 1143–1152.

(13) Cisneros, D. A.; Muller, D. J.; Daud, S. M.; Lakey, J. H. "An Approach to Prepare Membrane Proteins for Single-Molecule Imaging" *Angew. Chem. Int. Ed.* **2006**, *45*, 3252–3256.

(14) Hansma, H. G.; Hoh, J. H. "Biomolecular Imaging with the Atomic Force Microscope" *Annu. Rev. Biophys. Biomol. Struct.* **1994**, *23*, 115–139.

(15) Choudhuri, O.; Parekh, S. H.; Fletcher, D. A. "Reversible Stress Softening of Actin Networks" *Nature* **2007**, *445*, 295–298.

(16) Balgar, T.; Bautista, R.; Hartmann, N.; Hasselbrink, E. "An AFM study of the Growth Kinetics of the Self-Assembled Octadecylsiloxane Monolayer on Oxidized Silicon" *Surf. Sci.* **2003**, *532*, 963–969.

(17) (a) Rief, M.; Gautel, M.; Oesterhelt, F. Fernandez, J. M.; Gaub, H. E. "Reversible Unfolding of Individual Titin Immunoglobulin Domains by AFM" *Science* **1997**, *276*, 1109–1112. (b) Schlierf, M.; Li, H.; Fernandez, J. M. "The Unfolding Kinetics of Ubiquitin Captured with Single-Molecule Force-Clamp Techniques" *Proc. Nat. Acad. Sci.* **2004**, *101*, 7299–7304. (c) Cecconi, C.; Shank, E. A.; Bustamante, C.; Marqusee, S. "Direct Observation of the Three-State Folding of a Single Protein Molecule" *Science* **2005**, *309*, 2057–2060.

(18) Noy, A.; Frisbie, C. D.; Rozsnyai, L. F.; Wrighton, M. S.; Lieber, C. M. "Chemical Force Microscopy: Exploiting Chemically-Modified Tips to Quantify Adhesion, Friction, and Functional Group Distributions in Molecular Assemblies" *J. Am. Chem. Soc.* **1995**, *117*, 7943–7951.

(19) Overney, R. M.; Meyer, E.; Frommer, J.; Brodbeck, D.; Lüthi, R.; Howald, L.; Güntherodt, H.-J.; Fujihira, M.; Takano, H.; Gotoh, Y. "Friction Measurements on Phase-Separated Thin Films with a Modified Atomic Force Microscope" *Nature* **1992**, *359*, 133–135.

(20) Sinniah, S. K.; Steel, A. B. Miller, C. J.; Reutt-Robey, J. E. "Solvent Exclusion and Chemical Contrast in Scanning Force Microscopy" *J. Am. Chem. Soc.* **1996**, *118*, 8925–8931.

(21) Gross, L.; Mohn, F.; Moll, N.; Liljeroth, P.; Meyer, G. "The Chemical Structure of a Molecule Resolved by Atomic Force Microscopy" *Science* **2009**, *325*, 1110–1114.

(22) Dupres, V.; Menozzi, F. D.; Locht, C.; Clare, B. H.; Abbott, N. L.; Cuenot, S.; Bompard, C.; Raze, D.; Dufrêne, Y. F. "Nanoscale Mapping and Functional Analysis of Individual Adhesins on Living Bacteria" *Nat. Methods* **2005,** *2*, 515–520.

(23) Hinterdorfer, P.; Dufrêne, Y. F. "Detection and Localization of Single Molecular Recognition Events Using Atomic Force Microscopy" *Nat. Methods* **2006**, *3*, 347–355.

(24) Piner, R. D.; Zhu, J.; Xu, F.; Hong, S.; Mirkin, C. A. "'Dip–Pen' Nanolithography" *Science* **1999**, *283*, 661–663.

(25) Kufer, S. K.; Puchner, E. M.; Gumpp, H.; Liedl, T.; Gaub, H. E. "Single-Molecule Cut-and-Paste Surface Assembly" *Science* **2008**, *319*, 594–596.

(26) Hsiao, S. C.; Crow, A. K.; Lam, W. A.; Bertozzi, C. R.; Fletcher, D. A.; Francis, M. B. "DNA-Coated AFM Cantilevers for the Investigation of Cell Adhesion and the Patterning of Live Cells" *Angew. Chem. Int. Ed.* **2008**, *47*, 8473–8477.

(27) Knoll, A.; Bächtold, P.; Bonan, J.; Cherubini, G.; Despont, M.; Dreschsler, U.; Dürig, U.; Gotsmann, B.; Häberle, W.; Hagleitner, C.; Jubin, D.; Lantz, M. A.; Pantazi, A.; Pozidis, H.; Rothuizen, H.; Sebastian, A.; Stutze, R.; Vettiger, P.; Wiesmann, D.; Eleftherious, E. S. "Integrating Nanotechnology into a Working Storage Device" *Microelectron. Eng.* **2006**, *83*, 1692–1697.

(28) IBM The Millipede Project: A Nanomechanical AFM-based Data Storage System. http://www.zurich.ibm.com/st/storage/concept.html (accessed Dec 9, 2009).

(29) Ebner, A.; Wildling, L.; Zhu, R.; Rankl, C.; Haselgrübler, T.; Hinterdorfer, P.; Gruber, H. J. "Functionalization of Probe Tips and Supports for Single-Molecule Recognition Force Microscopy" *Top. Curr. Chem.* **2008**, *285*, 29–76.

(30) (a) Medard, N.; Aouinti, M.; Poncin-Epiallard, F.; Bertrand, P. "TOF-SIMS Ability to Quantify Surface Chemical Groups: Correlation with XPS Analysis and Spectrochemical Titration" *Surf. Interface Anal.* **2001**, *31*, 1042–1047. (b) Kim, J.; Shon, H. K.; Jung, D.; Moon, D. W.; Han, S. Y.; Lee, T. G. "Quantitative Chemical Derivatization Technique in Time-Of-Flight Secondary Ion Mass Spectrometry for Surface Amine Groups on Plasma-Polymerized Ethylenediamine Film. *Anal. Chem.* **2005**, *77*, 4137–4141. (c) Ivanov, V. B.; Behnisch, J.; Hollander, A.; Mehdorn, F.; Zimmermann, H. "Determination of Functional Groups on Polymer Surfaces Using Fluorescence Labeling" *Surf. Interface Anal.* **1996**, *24*, 257–262.

(31) Xing, Y.; Borguet, E. "Specificity and Sensitivity of Fluorescence Labeling of Surface Species" *Langmuir*, **2007**, *23*, 684–688.

(32) Lo, Y.-S.; Heufner, N. D.; Chan, W. S.; Dryden, P.; Hagenhoff, B.; Beebe, T. P. "Organic and Inorganic Contamination on Commercial AFM Cantilevers" *Langmuir*, **1999**, *15*, 6522–6526.

(33) Florin, E.-L.; Moy, V. T.; Gaub, H. E. "Adhesion Forces Between Individual Ligand-Receptor Pairs" *Science*, **1994**, *264*, 415–417.

(34) Yuan, C.; Chen, A.; Kolb, P.; Moy, V. T. "Energy Landscape of Steptavidin-Biotin Complexes Measured by Atomic Force Microscopy" *Biochemistry* **2000**, *39*, 10219–10223.

(35) Chen, A.; Moy, M. T. "Cross-Linking of Cell Surface Receptors Enhances Cooperativity of Molecular Adhesion" *Biophys. J.* **2000**, *78*, 2814–2820.

(36) Fritz, J.; Katopodis, A. G.; Kolbinger, F.; Ansemetti, D. "Force-Mediated Kinetics of Single P-Selectin/Ligand Complexes Observed by Atomic Force Microscopy" *Proc. Nat. Acad. Sci.* **1998**, *95*, 12283–12288.

(37) Jin, Y.; Wang, K.; Tan, W.; Wu, P.; Wang, Q.; Huang, H.; Huang, S.; Tang, Z.; Guo, Q. "Monitoring Molecular Beacon/DNA Interactions Using Atomic Force Microscopy" *Anal. Chem.* **2004**, *76*, 5721–5725.

(38) Riener, C. K.; Kienberger, F.; Hahn, C. D.; Buchinger, G. M.; Egwim, I. O. C.; Haselgrübler, T.; Ebner, A.; Romanin, C.; Klampfl, C.; Lackner, B.; Prinz, H.; Blaas, D.; Hinterdorfer, P.; Gruber, H. J. "Heterobifunctional Crosslinkers for Tethering Single Ligand Molecules to Scanning Probes" *Anal. Chim. Acta*, **2003**, *497*, 101–114.

(39) Grandbois, M.; Beyer, M.; Rief, M.; Clausen-Schaumann, H.; Gaub, H. E. "How Strong Is a Covalent Bond?" *Science*, **1999**, *283*, 1727–1730.

(40) (a) Woolley, A. T.; Cheung, C. L.; Hafner, J. H.; Lieber, C. M. "Structural Biology with Carbon Nanotube AFM Probes" *Chem. Biol.* **2000**, *7*, R193–R204. (b) Hafner, J. H.; Cheung, C. L.; Woolley, A. T.; Lieber, C. M. "Structural and Functional Imaging with Carbon Nanotube AFM Probes" *Prog. Biophys. Mol. Biol.* **2001**, *77*, 73–110.

(41) Riener, C. K.; Stroh, C. M.; Ebner, A.; Klampfl, C.; Gall, A. A.; Romanin, C.; Lyubchenko, Y.; Hinterdorfer, P.; Gruber, H. J. "Simple Test System for Single Molecule Recognition Force Microscopy" *Anal. Chim. Acta* **2003**, *479*, 59–75.

(42) Hinterdorfer, P.; Baumgartner, W.; Gruber, H. J.; Schilcher, K.; Schindler, H. "Detection and Localization of Individual Antibody-Antigen Recognition Events by Atomic Force Microscopy" *Proc. Nat. Acad. Sci.* **1996**, *93*, 3477–3481.

(43) Zaborski, M.; Vidal, A.; Ligner, G.; Balard, H.; Papirer, E. "Comparative Study of the Surface Hydroxyl Groups of Fumed and Precipitated Silicas. 1. Grafting and Chemical Characterization" *Langmuir* **1989**, *5*, 447–451.

(44) Trau, M.; Murray, B. S.; Grant, K.; Grieser, F. "An Ellipsometric Study of Thin Films on Silica Plates Formed by Alkylchlorosilylation Reagents" *J. Colloid Interface Sci.* **1992**, *148*, 182–189.

(45) Piers, A. S.; Rochester, C. H. "Infrared Study of the Adsorption of 1-Aminopropyltrialkoxysilanes on Silica at the Solid/Liquid Interface" *J. Coll. Interface Sci.* **1995**, *174*, 97–103.

(46) V. Y. Davydov, Kiselev, A. V.; Zhuravlex, L. T. "Study of the Surface and Bulk Hydroxyl Groups of Silica by Infra-Red Spectra and D_2O-Exchange" *Trans. Faraday Soc.* **1964**, *60*, 2054–2264.

(47) Waddell, T. G.; Leyden, D. E.; DeBello, M. T. "The Nature of Organosilane to Silica-Surface Bonding" *J. Am. Chem. Soc.* **1981**, *103*, 5303–5307.

(48) Tian, R.; Seitz, O.; Li, M.; Hu, W.; Chabal, Y. J.; Gao, J. "Infrared Characterization of Interfacial Si–O Bond Formation on Silanized Flat SiO2/Si Surfaces" *Langmuir* **2010** ASAP. DOI: 10.1021/la904597c accessed February 25, 2010.

(49) Brandriss, S.; Margel, S. "Synthesis and Characterization of Self-Assembled Hydrophobic Monolayer Coatings on Silica Colloids" *Langmuir* **1993**, *9*, 1232–1240.

(50) Parikh, A.; Liedberg, B.; Atre, S. V.; Ho, M.; Allara, D. L. "Correlation of Molecular Organization and Substrate Wettability in the Self-Assembly of *n*-Alkylsiloxane Monolayers" *J. Phys. Chem.* **1995**, *99*, 9996–10008.

(51) Yang, W.; Auciello, O.; Butler, J. E.; Cai, W.; Carlisle, J. A.; Gerbi, J. E.; Gruen, D. M.; Knickerbocker, T.; Lasseter, T. L.; Russell, Jr., J. N.; Smith, L. M.; Hamers, R. J. "DNA-Modified Nanocrystalline Diamond Thin-Films as Stable, Biologically Active Substrates" *Nature Mat.* **2002**, *1*, 253–257.

(52) Bain, C. D.; Troughton, E. B.; Tao, Y.-T.; Evall, J.; Whitesides, G. M.; Nuzzo, R. G. "Formation of Monolayer Films by the Spontaneous Assembly of Organic Thiols from Solution onto Gold" *J. Am. Chem. Soc.* **1989**, *111*, 321–325.

(53) Auletta, R.; de Jong, M. R.; Mulder, A.; van Veggel, F. C. J. M.; Huskens, J.; Reinhoudt, D. N.; Zou, S.; Zapotoczny, S.; Schonherr, H.; Vancso, G. J.; Kuipers, L. "ß-Cyclodextrin Host-Guest Complexes Probed under Thermodynamic Equilibrium: Thermodynamics and AFM Force Spectroscopy" *J. Am. Chem. Soc.* **2004**, *126*, 1577–1584.

(54) Love, J. C.; Estroff, L. A.; Kriebel, J. K.; Nuzzo, R. G.; Whitesides, G. M. "Self-Assembled Monolayers of Thiolates on Metals as a Form of Nanotechnology" *Chem. Rev.* **2005**, *105*, 1103–1169.

(55) Laibinis, P. E.; Whitesides, G. M.; Allara, D. L.; Tao, Y.-T.; Parikh, A. N.; Nuzzo, R. G. "Comparison of the Stuctures and Wetting Properties of Self-Assembled Monolayers of *n*-Alkanethiols on the Coinage Metal Surfaces, Cu, Ag, Au" *J. Am. Chem. Soc.* **1991**, *113*, 7152–7167.

(56) Nuzzo, R. G.; Allara, D. L. "Adsorption of Bifunctional Organic Disulfides on Gold Surfaces" *J. Am. Chem. Soc.* **1983**, *105*, 4481–4483.

(57) Lin, L.; Wang, H.; Liu, Y.; Yan, H.; Lindsay, S. "Recognition Imaging with a DNA Aptamer" *Biophys. J.* **2006**, *90*, 4236–4238.

(58) Strunz, T.; Oroszlan, K.; Schäfer, R.; Güntherodt, H.-J. "Dynamic Force Spectroscopy of Single DNA Molecules" *Proc. Nat. Acad. Sci.* **1999**, *96*, 11277–11282.

(59) Dammer, U.; Popescu, O.; Wagner, P.; Anselmetti, D.; Guntherodt, H.-J., Misevic, G. N. "Binding Strength Between Cell Adhesion Proteoglycans Measured by Atomic Force Microscopy" *Science* **1995**, *267*, 1173–1175.

(60) Zou, S.; Schonherr, H.; Vancso, G. J. "Stretching and Rupturing Individual Supramolecular Polymer Chains by AFM" *Angew. Chem. Int. Ed.* **2005**, *44*, 956–959.

(61) Yam, C.-M.; Xiao, Z.; Gu, J.; Boutet, S.; Cai, C. "Modification of Silicon AFM Cantilever Tips with an Oligo(ethylene glycol) Derivative for Resisting Proteins and Maintaining a Small Tip Size for High-Resolution Imaging" **2003**, *125*, 7498–7499.

(62) Strother, T.; Knickerbocker, T.; Russell, J. N.; Butler, J. E.; Smith, L. M.; Hamers, R. J. "Photochemical Functionalization of Diamond Films" *Langmuir* **2002**, *18*, 968–971.

(63) (a) Weiss, S. "Measuring Conformational Dynamics of Biomolecules by Single Molecule Fluorescence Spectroscopy" *Nature Struct. Biol.* **2000**, *7*, 724–729. (b) Ishijima, A.; Yanagida, T. "Single Molecule Nanobioscience" *Trends Biochem. Sci.* **2001**, *26*, 438–444. (c) Xie, S. Single-Molecule Approach to Enzymology *Single Mol.* **2001**, *2*, 229–236. (d) Joachim, C.; Gimzewski, J. K. "Nanoscience of Single Molecules Using Local Probes" *Science* **1999**, *283*, 1683–1688.

(64) Bustamante, C. "*In Singulo* Biochemistry: When Less Is More" *Annu. Rev. Biochem.* **2008**, *77*, 45–50.

(65) Clausen-Schaumann, H; Seitz, M.; Krautbauer, R.; Gaub, H. E. "Force Spectroscopy with Single Bio-Molecules" *Curr. Opin. Chem. Biol.* **2000**, *4*, 524–530.

(66) (a) Liphardt, J.; Onoa, B.; Smith, S. B.; Tinoco, Jr., I.; Bustamante, C. "Reversible Unfolding of Single RNA Molecules by Mechanical Force" *Science* **2001**, *292*, 733–736. (b) Onoa, B.; Dumont, S.; Liphardt, J.; Smith, S. B.; Tinoco, Jr., I.; Bustamante, C. "Identifying Kinetic Barriers to Mechanical Unfolding of the *T. thermophila* Ribozyme" *Science* **2003**, *299*, 1892–1895.

(67) (a) Strick, T. R.; Bensimon, D.; Croquette, V. "Micro-Mechanical Measurement of the Torsional Modulus of DNA" *Genetica* **1999**, *106*, 57–62. (b) Charvin, G.; Allemand, J.-F.; Strick, T. R.; Bensimon, D.; Croquette, V. "Twisting DNA: Single Molecule Studies" *Contemp. Physics* **2004**, *45*, 393–403. (c) Bryant, Z.; Stone, M. D.; Gore, J.; Smith, S. B.; Cozzarelli, N. R.; Bustamante, C. "Structural Transitions and Elasticity from Torque Measurements on DNA" *Nature* **2003**, *424,* 338–341.

(68) (a) Marszalek, P. E.; Li, H.; Fernandez, J. M. "Fingerprinting polysaccharides with Single-Molecule Atomic Force Microscopy" *Nat. Biotech.* **2001**, *19*, 258–262. (b) Zhang, Q.; Lu, Z.; Hu, H.; Yang, W.; Marszalek, P. E. "Direct Detection of the Formation of V-Amylose Helix by Single Molecule Force Spectroscopy" *J. Am. Chem. Soc.* **2006**, *128*, 9387–9393.

(69) (a) Florin, E.-L.; Moy, V. T.; Gaub, H. E. "Adhesion Forces Between Individual Ligand–Receptor Pairs" *Science* **1994**, *264*, 415–417. (b) Moy, V. T.; Florin, E.-L.; Gaub, H. E. "Intermolecular Forces and Energies Between Ligands and Receptors" *Science* **1994**, *266*, 25—259. (c) Merkel, R.; Nassoy, P.; Leung, A.; Ritchie, K.; Evans, E. "Energy Landscapes of Receptor–Ligand Bonds Explored with Dynamic Force Spectroscopy" *Nature* **1999**, *397*, 50–53.

(70) (a) Ros, R.; Schwesinger, F.; Anselmetti, D.; Kubon, M.; Schafer, R.; Pluckthun, A.; Tiefenauer, L. "Antigen Binding Forces of Individually Addressed Single-chain Fv Antibody Molecules" *Proc. Natl. Acad. Sci.* **1998**, *95*, 7402–7405. (b) Albrecht, C.; Blank, K.; Lalic-Multhaler, M.; Hirler, S.; Mai, T.; Gilbert, I.; Schiffmann, S.; Bayer, T.; Clausen-Schaumann, H.; Gaub, H. E. "DNA: A Programmable Force Sensor" *Science* **2003**, *301*, 367–370. (c) Berquand, A.; Xia, N. Castner, D. G.; Clare, B. H.; Abbott, N. L.; Dupres, V.; Adriaensen, Y.; Dufrene, Y. F. "Antigen Binding Forces of Single Antilysozyme Fv Fragments Explored by Atomic Force Microscopy" *Langmuir* **2005**, *21,* 5517–5523.

(71) Schnitzer, M. J.; Visscher, K.; Block, S. M. "Force Production by Single Kinesin Motors" *Nat. Cell Biol.* **2000**, *2*, 718–723.

(72) McKendry, R., Theoclitou, M.-E.; Rayment, T.; Abell, C. "Chiral Discrimination by Chemical Force Microscopy" *Nature* **1998**, *391*, 566–568.

(73) Bough, B.; Northrop, B. H.; Schmidt, J. J.; Tseng, H.-R.; Houk, K. N.; Stoddart, J. F.; Ho, C.-M. "Evaluation of Synthetic Linear Motor-Molecule Actuation Energetics" *Proc. Nat. Acad. Sci.* **2006**, *103*, 8583–8588.

(74) Abbondanzieri, E. A.; Greenleaf, W. J.; Shaevitz, J. W.; Landick, R.; Block, S. M. "Direct Observation of Base-pair Stepping by RNA Polymerase" *Nature* **2005**, *438*, 460–465.

(75) Greenleaf, W. J.; Block, S. M. "Single-Molecule, Motion-Based DNA Sequencing Using RNA Polymerase" *Science*, **2006**, *313*, 801.

(76) Walther, K. A.; Brujic, J.; Li, H.; Fernandez, J. M. "Sub-Angstrom Conformational Changes of a Single Molecule Captured by AFM Variance Analysis" *Biophys. J.* **2006**, *90*, 3806–3812.

(77) (a) Reviews of P2X family of proteins: Ralevic, V.; Burnstock, G. "Receptors for Purines and Pyrimidines" *Pharm. Rev.* **1998**, *50*, 415–492. (b) Khakh, B. S. "Molecular Physiology of P2X Receptors and ATP Signalling at Synapses" *Nat. Rev. Neurosci.* **2001**, *2*, 165–174. (c) North, R. A. "Molecular Physiology of P2X Receptors" *Physiol. Rev.* **2002**, *82*, 1013–1067. (d) Khakh, B. S.; North, R. A. "P2X Receptors as Cell-Surface ATP Sensors in Health and Disease" *Nature Rev.* **2006**, *442*, 527–532.

(78) (a) Mio, K.; Kubo, Y.; Ogura, T.; Yamamoto, T.; Sato, C. "Visualization of the Trimeric P2X2 Receptor with a Crown-capped Extracellular Domain" *Biochem. Biophys. Res. Commun.* **2005**, *337*, 998–1005. (b) Barrera, N. P.; Ormond, S. J.; Henderson, R. M.; Murrell-Lagnado, R. D.; Edwardson, J. M. "AFM Imaging Demonstrates That P2X2 Receptors Are Trimers, But That P2X6 Receptor Subunits Do Not Oligomerize" *J. Biol. Chem.* **2005**, *180*, 10759–10765. (c) Nakazawa, K.; Yamakoshi, Y.; Tsuchiya, T.; Ohno, Y. "Purification and Aqueous Phase Atomic Force Microscopic Observation of Recombinant P2X2 Receptor" *Eur. J. Pharm.* **2005**, *518*, 107–110.

(79) Service, R. F. "Optical Lithography Goes To Extremes—And Beyond" *Science* **2001**, *293*, 785–786.

(80) Wouters, D.; Schubert, U. S. "Nanolithography and Nanochemistry: Probe-Related Patterning Techniques and Chemical Modification for Nanometer-Sized Devices" *Angew. Chem. Int. Ed.* **2004**, *43*, 2480–2495.

(81) Salaita, K.; Wang, Y.; Fragala, J.; Vega, R. A.; Liu, C.; Mirkin, C. A. "Massively Parallel Dip–Pen Nanolithography with 55 000-Pen Two-Dimensional Arrays" *Angew. Chem. Int. Ed.* **2006**, *45*, 7220–7223.

(82) Ginger, D. S.; Zhang, H.; Mirkin, C. A. "The Evolution of Dip-Pen Nanolithography" *Angew. Chem. Int. Ed.* **2004**, *43*, 30–45.

(83) Wilson, D. L.; Martin, R.; Hong, S.; Cronin-Golomb, M.; Mirkin, C. A.; Kaplan, D. L. "Surface Organization and Nanopatterning of Collagen by Dip-Pen Nanolithography" *Proc. Natl. Acad. Sci.* **2001**, *98*, 13660–13664.

(84) Lee, K.-B.; Park, S.-J.; Mirkin, C. A.; Smith, J. C.; Mrksich, M. "Protein Nanoarrays Generated By Dip-Pen Nanolithography" *Science* **2002**, *295*, 1702–1705.

(85) Ivanisevic, A.; Im, J.-H.; Lee, K.-B.; Park, S.-J.; Demers, L. M.; Watson, K. J.; Mirkin, C. A. "Redox-Controlled Orthogonal Assembly of Charged Nanostructures" *J. Am. Chem. Soc.* **2001**, *123*, 12424–12425.

(86) Ali, M. B.; Ondarçuhu, T.; Brust, M.; Joachim, C. "Atomic Force Microscope Tip Nanoprinting of Gold Nanoclusters" *Langmuir* **2002**, *18*, 872–876.

(87) Huo, F.; Zheng, Z.; Zheng, G.; Giam, L. R.; Zhang, H.; Mirkin, C. A. "Polymer Pen Lithography" *Science*, **2008**, *321*, 1658–1660.

(88) Kim, K.-H.; Moldovan, N.; Ke, C.; Espinosa, H. D.; Xiao, X.; Carlisle, J. A.; Auciello, O. "Novel Ultrananocrystalline Diamond for High-Resolution Low-Wear Nanolithographic Techniques" *Small* **2005**, *1*, 866–874.

(89) Dürig, U.; Cross, G.; Despont, M.; Drechsler, U.; Häberle, W.; Lutwyche, M. I.; Rothuizen, H.; Stutz, R.; Widmer, R.; Vettiger, P.; Binnig, G. K.; King, W. P.; Goodson, K. E. "'Millipede' – An AFM Data Storage System at the Frontier of Nanotribology" *Tribol. Lett.* **2000**, *9*, 25–32.

(90) Duvigneau, J.; Schönherr, H.; Vancso, G. J. "Atomic Force Microscopy Based Thermal Lithography of Poly(*tert*-butylacrylate) Block Copolymer Films for Bioconjugation" *Langmuir* **2008**, *24*, 10825–10832.

(91) Xu, C.; Fu, S.; Fryd, M.; Xu, S.; Wayland, B. B.; Winey, K. I.; Composto, R. J. "Reversible Stimuli-Responsive Nanostructures Assembled from Amphiphilic Block Copolymers" *Nano Lett.* **2006**, *6*, 282–287

Chapter 2 Synthetic Molecules to Modify AFM Tips for Force Spectroscopy

2.1. Background

The first chapter covered commonly used modifications of AFM tips by self-assembled monolayers (SAM) of thiols on gold-coated tips and silane groups on silicon. The molecular tripods[1] reported by Yao and Tour were the first attempt to modify AFM tips with synthetic molecules (Figure 2-1a). The tripods were based on tetrahedral silicon structures with sulfur groups at each terminus for binding to the gold-coated AFM tips. Building on this work, Keana and co-workers[2] synthesized several molecules for binding to gold-coated AFM tips with tower and tripod structures (Figure 2-1b–c). Keana and co-workers published several derivatives of a symmetrically substituted adamantane and tetraphenyl methane and established that these structures are sufficiently large and rigid to be imaged by a conventional AFM tip.[2] However, these groups did not report the use of their tripods for AFM tip modification. Our group has also previously reported the use of a photoswitching tripod molecular tip (Figure 2-1d) used in non-contact imaging.[3] In this chapter, the synthesis of tripod-shaped molecules for AFM tip modification and their application to single molecule ligand–receptor unbinding measurements will be described.

In single molecule experiments, it is necessary to functionalize the AFM tips with an optimum density of ligands. If there are not enough ligands bound to the tip surface, force spectroscopy results in too few ligand–receptor bindings, leading to an inadequate number of events for statistical analysis. On the other hand, with a high

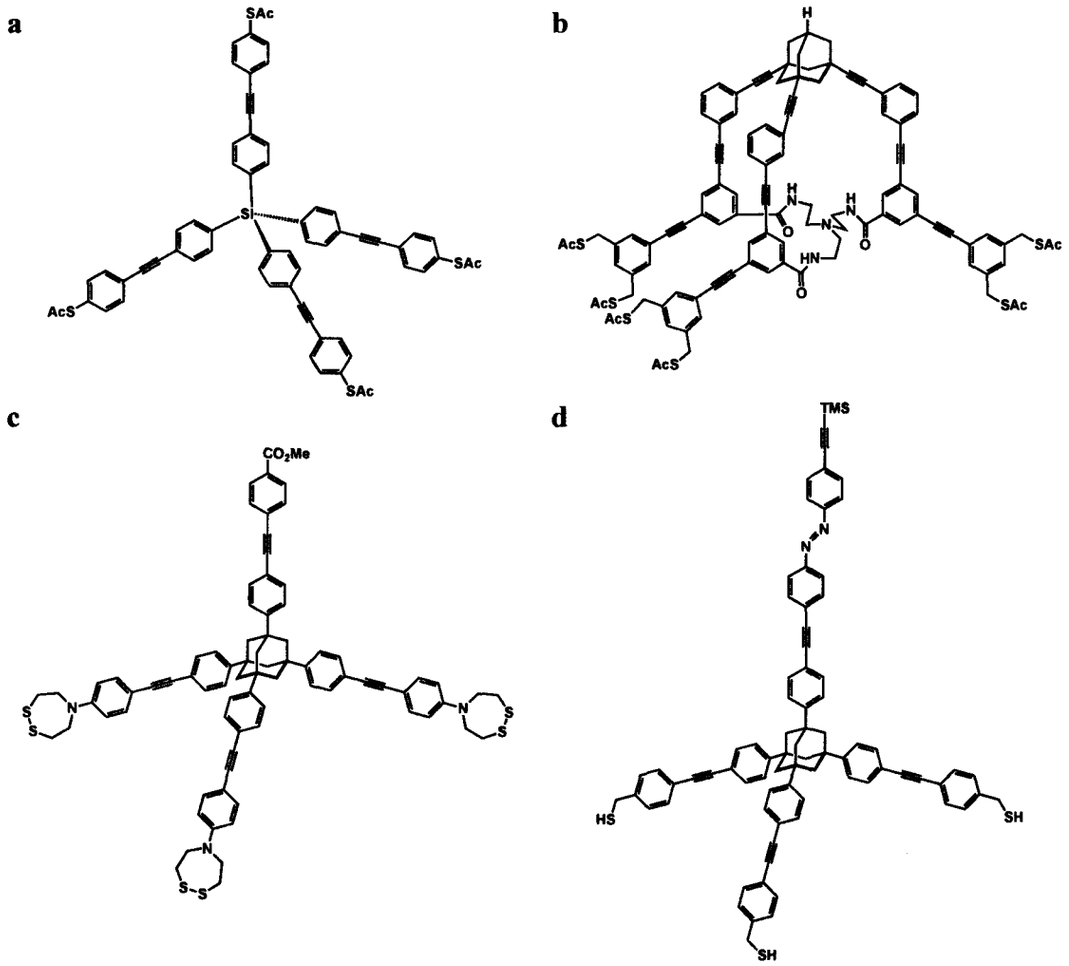

Figure 2-1. Examples of molecular tips. (a) Molecular tips derived from tetrahedral silicon were synthesized by Yao and Tour. (b) Tower-shaped molecular tips with an adamantane apex. (c) A 1,3,5,7-tetrahedral substituted adamantane synthesized by Keana and co-workers. (d) A tetrasubstituted adamantane from our group with an azo-photoswitching moiety.

density of ligands on the AFM tip, there can be multiple ligand–receptor bindings that create difficulties in obtaining single molecule resolution. Molecules that have larger scaffolds provide a lower density of molecules on a surface and should improve single molecule experiments. Because of their attractive qualities, sulfur terminated tripodal molecules were synthesized for attachment to a gold-coated AFM tip. Two different tripod molecules with different lengths of linkers were synthesized and used in single

molecule force spectroscopy (SMFS) experiments. For comparison, a monopodal molecule was synthesized and used in SMFS experiments.

2.2 Synthesis of Tripodal Molecule

2.2.1 Synthetic Route for a Tripodal Molecular Tip

Our focus was to develop a versatile synthetic organic method that can modify an AFM tip for use in single molecule force spectroscopy. This molecular tip must fulfill two requirements: the molecular tip requires a facile method to attach to the AFM tip and another moiety to covalently link to ligands. Many studies employ an organic thiol SAM approach as shown in Figure 2-2a, we wished to synthesize a molecule that has a wider base than a simple long chain alkyl thiol. A tripodal base, as shown in Figure 2-2b, would not only occupy more space and yield a lower density of ligands than a normal SAM, but it also provides a stronger point of attachment as well.

The core of our target molecule (Figure 2-2c) begins with a tetrahedral-substituted adamantane. The adamantane core is stable and can be easily functionalized. From the adamantane core, three phenylethynyl units provide conformationally rigid "legs" to attach to the AFM tip. Rigidity should reduce any stretching of bonds and thus any contribution of the legs to the force–distance curve measurements. The attachment to the AFM tip is via disulfide functionality in the 1,2,5-dithiazepane rings that are connected to the phenyl ring. The disulfide provides a facile route to formation of SAM for tip attachment. As a fourth substituent to the adamantane, a terminal alkyne was

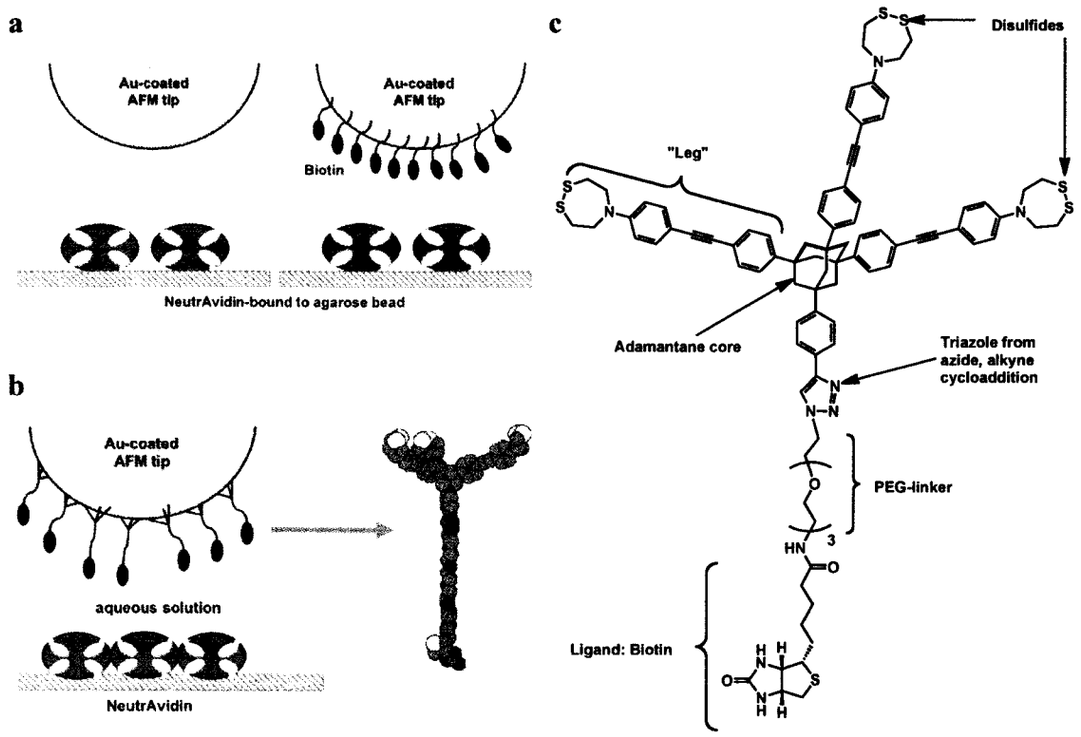

Figure 2-2. Schematic illustration of AFM tip modifications. (a) An unmodified AFM tip and a tip modified by a thiol SAM. (b) A tripodal molecule adsorbed on AFM tip with a space-filled model of the molecular tip (c) A tripodal molecular tip for single molecule force spectroscopy with its labeled components.

chosen. Using click chemistry[4] would allow a variety of ligands to attach to the terminal acetylene of the tripod scaffolding. Because the force experiments are carried out in aqueous solution, an oligoethylene glycol (OEG) chain serves to provide the necessary water solubility. As a model study, we decided to use biotin as a ligand and NeutrAvidin, a deglycosylated avidin with similar biotin binding properties and less nonspecific interactions,[5] as a receptor.

All newly synthesized compounds were characterized by ^{1}H and ^{13}C NMR spectroscopy, IR spectroscopy, and mass spectrometry. The experimental procedures for

the compounds are provided in the experimental section in Chapter 5 and the NMR and IR spectra are provided in Chapter 6.

2.2.2 Synthesis of Tetrasubstituted Adamantane Core

Our approach began from 1-bromoadamantane (Scheme 2-1). A Friedel-Crafts alkylation of benzene with 1-bromoadamantane, *t*-butyl bromide, and $AlCl_3$ in benzene afforded the insoluble 1,3,5,7-tetraphenyl adamantane **2-1** in good yields.[6] After purification of **2-1** by $CHCl_3$ extraction in a Soxhlet apparatus, subsequent iodination with [bis(trifluoroacetoxy)iodo]benzene and I_2 provided tetrakis-iodo product **2-2**. Sonogashira coupling of **2-2** with triisopropylsilylacetylene gave the protected alkyne **2-3** in low yields. At this point in the synthesis, the three aryl iodides were poised to couple with the terminal alkyne of the leg and the alkyne was in place for later deprotection.

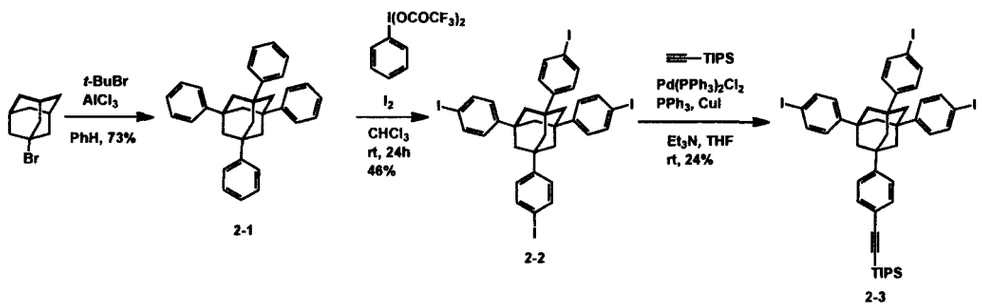

Scheme 2-1. Synthesis of 1,3,5,7-tetrasubstituted adamantane core of the tripod molecular tip.

2.2.3 Synthesis of Leg

The synthesis of the leg (Scheme 2-2) began with 4-iodoaniline, which was allowed to react with ethylene oxide to yield diol **2-4**. Compound **2-4** was then treated with *p*-toluenylsulfonyl chloride. The resulting tosylate **2-5** was displaced by KSCN in the presence of 18-crown-6 ether to give bis-thiocyanate **2-6** in good yield. Upon treatment with KOH in aqueous ethanol, the bis-thiocyanate yielded the ring-closed 1,2,5-dithiazepane **2-7**. Sonogashira coupling of iodide **2-7** with trimethylsilylacetylene and following deprotection in basic methanol, alkyne **2-9** was obtained.

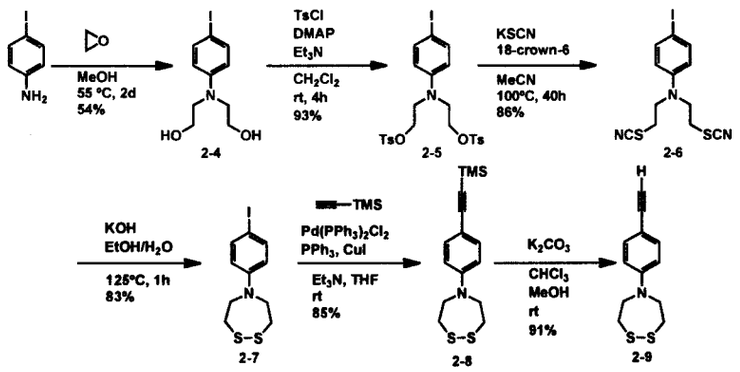

Scheme 2-2. Synthesis of leg portion of the tripod molecular tip.

2.2.4 Synthesis of Tripod Scaffolding

The leg portion **2-9** was connected to the core **2-3** by Sonogashira coupling (Scheme 2-3). Early reaction conditions used excess leg **2-9** (6 equivalents), but this produced the homocoupled alkyne that was difficult to separate from the product. When 3.05 equivalents of the terminal alkyne were used in the reaction, significantly less of the homocoupled impurity was present. The terminal alkyne **2-9** coupled with aryl iodide **2-**

3 provided the tripod molecule **2-10** in good yield. Deprotection of the triisopropylsilyl alkyne with TBAF afforded the terminal alkyne **2-11**. After the coupling of the legs to the adamantane core, the tripod scaffolding was intact. At this point in the synthesis, the tripod structure now had the functionality necessary to covalently link ligands to its scaffold and attach to the gold surface.

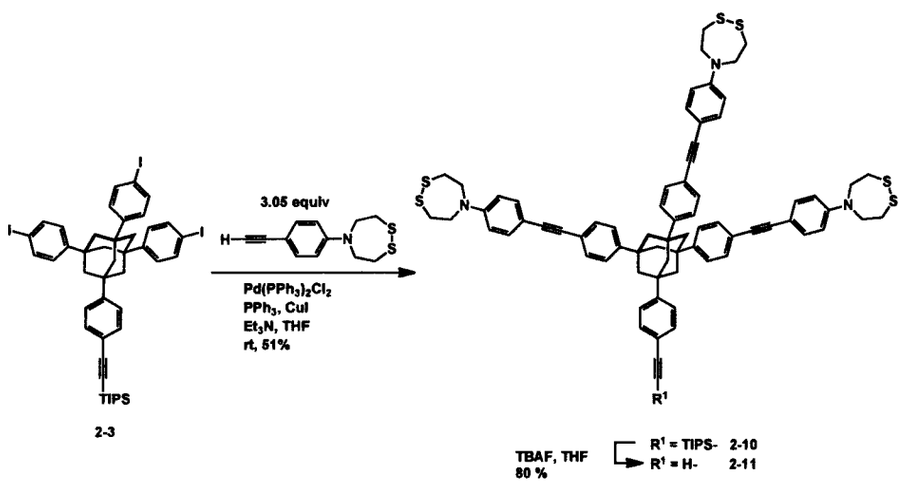

Scheme 2-3. Preparation of the tripodal scaffolding.

2.2.5 Synthesis of Biotinylated Linker

We envisioned a cycloaddition with the terminal alkyne and the azide via click chemistry would give the 1,4-triazole. Synthesis of the unsymmetric OEG linker (Scheme 2-4) began from tetraethylene glycol.[7] Treating tetraethylene glycol with methanesulfonyl chloride (MsCl) followed by the displacement of the mesylate by NaN_3 provided bis-azide **2-13**. Reduction of **2-13** in a biphasic mixture of PPh_3 in ether and aqueous H_3PO_4 gave the amine-OEG-azide **2-14** in good yield. Coupling of **2-14** to biotin with HBTU as an activating agent furnished biotinylated OEG-azide **2-15**.

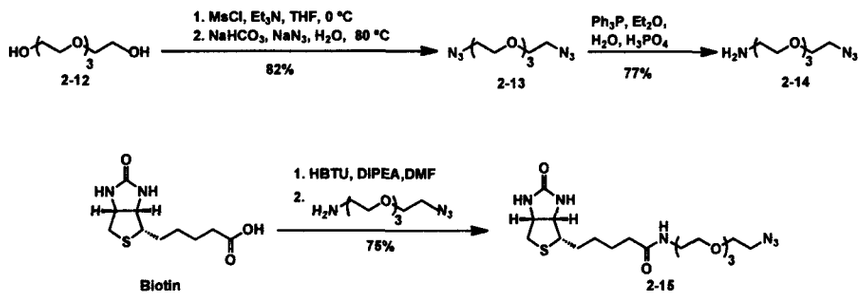

Scheme 2-4. Synthesis of biotinylated OEG-azide.

2.2.6 Coupling of Biotinylated Linker to Tripod Scaffolding

The final step of the synthesis connected the biotinylated OEG linker to the terminal alkyne of the tripod scaffolding. A preliminary trial with **2-15** and phenylacetylene using the click chemistry conditions reported by Sharpless and co-workers (1:1 *t*-BuOH/H_2O, 1% $CuSO_4$, and 10% ascorbic acid) afforded the desired 1,4-substituted triazole product in nearly quantitative yields at room temperature in two hours.[4a] However, similar conditions with **2-15** and the terminal alkyne tripod **2-11** gave no reaction or very low yields. This was thought to be caused by the low solubility of **2-11** in *t*-BuOH at room temperature. Thus, we tried alternative conditions using another source of copper under more dilute conditions. Following the procedure reported by Meldal and co-workers (Scheme 2-5),[4b] CuI in degassed THF with *N,N*-diisopropylethylamine (DIPEA) at 60 °C gave a sufficient yield. After trituration in dichloromethane to remove excess biotinylated linker and size exclusion chromatography, the biotinylated tripod molecular tip **A** was obtained.

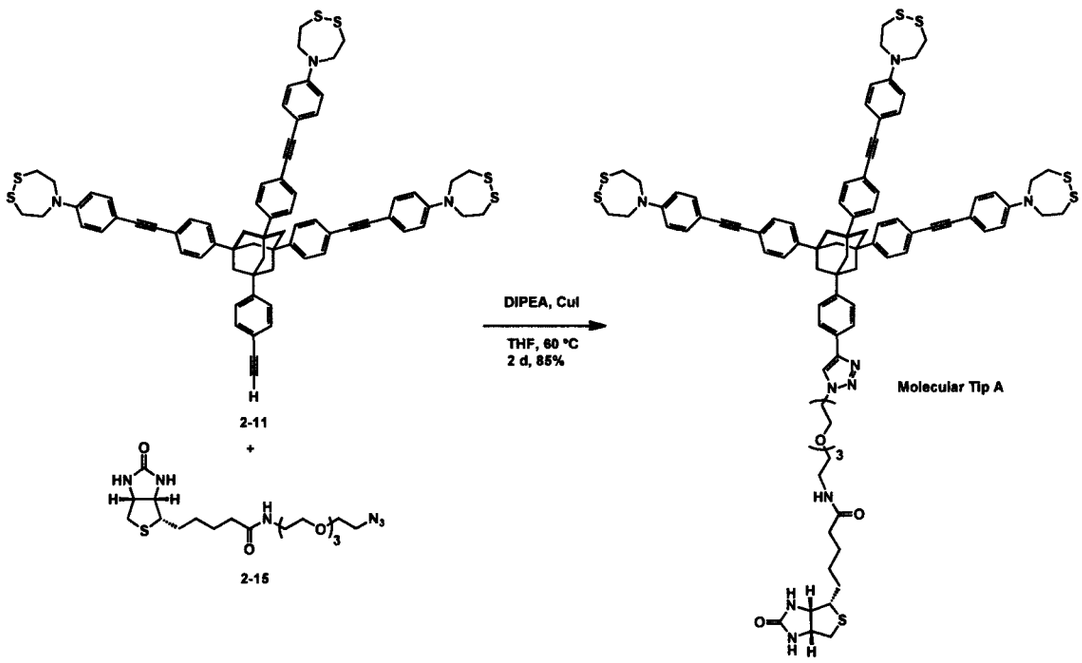

Scheme 2-5. Synthesis of the biotinylated tripod molecular tip **A**.

2.2.7 Synthesis of Monopodal Molecular Tip

After the completion of the synthesis of the tripodal molecular tip **A**, a biotinylated molecular tip with a single point of attachment, or a monopod, was synthesized. Molecular tip **B**, the biotinylated monopod (Scheme 2-6), is terminated on one end with a thiol for attachment to the gold surface and with biotin on the other for molecular recognition. The thiol has a ten carbon spacer to encourage efficient packing of the alkyl chains on the gold surface[8] and the tetraethylene glycol spacer provides water solubility and flexibility for biotin. Our synthetic scheme followed the procedure of Nelson *et al.* with minor variations.[9,10] Biotin was coupled to 2,3,5,6-tetrafluorphenol with diisopropylcarbodiimide and the activated biotin ester **2-17** was isolated in good yield. The tetrafluorophenol ester was added slowly to the OEG diamine (note the extra

methylene group between the OEG and the amines) to give the amide **2-18**. The 11-mercaptoundecanoic acid **2-19** was treated with triphenylmethane chloride (TrCl) to give the trityl-protected thiol **2-20**. The biotinylated amine linker **2-18** was then coupled to the trityl-protected carboxylic acid to give **2-21**. The trityl group was deprotected in a 1:1 mixture of TFA/DCM with 5% triethylsilane to give the molecular monopod tip **B**.

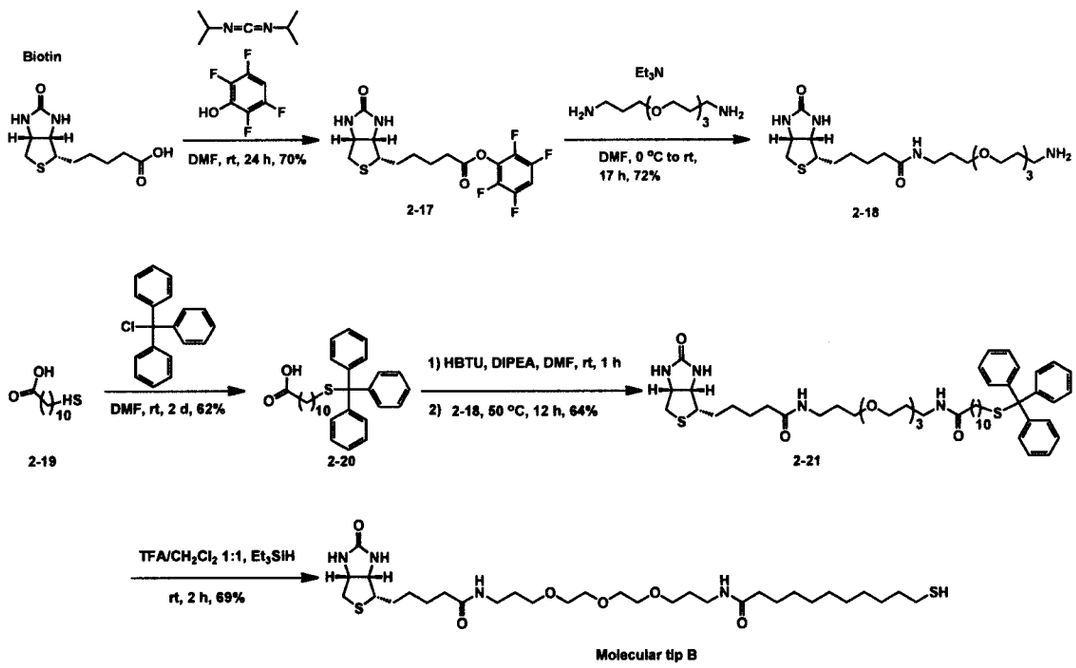

Scheme 2-6. Synthesis of the biotinylated monopod molecular tip **B**.

2.2.8 Synthesis of a Molecular Tip with a Longer PEG Linker

According to the previous studies on single molecule force spectroscopy studies, the length of the linker between the AFM tip and the ligand (or other molecular recognition element) was suggested to be a factor in force spectroscopy experiments.[11] PEG is the most commonly used linker and has been used with molecular weights from

800[12] to 5000, [13] which corresponds to lengths of 5 nm and 32 nm, respectively. Because the longer linker can help provide the spatial resolution necessary to distinguish between the nonspecific and specific rupture forces, a longer biotinylated linker connected to the tripod scaffolding was prepared. A commercially available heterobifunctional PEG linker with an azide and an amine (MW=2000 and a polydispersity index of 1.05) was used as a starting material. The activated ester of biotin **2-17** (Scheme 2-7) was used because the tetrafluorophenol byproduct displaced after amide bond formation with the amine-terminated PEG is soluble in diethyl ether. PEG is soluble in most organic solvents, but can be precipitated in cold diethyl ether. After several precipitations, the biotinylated PEG azide **2-22** was coupled to the terminal alkyne tripod scaffolding **2-11** by click chemistry. After precipitation of the excess

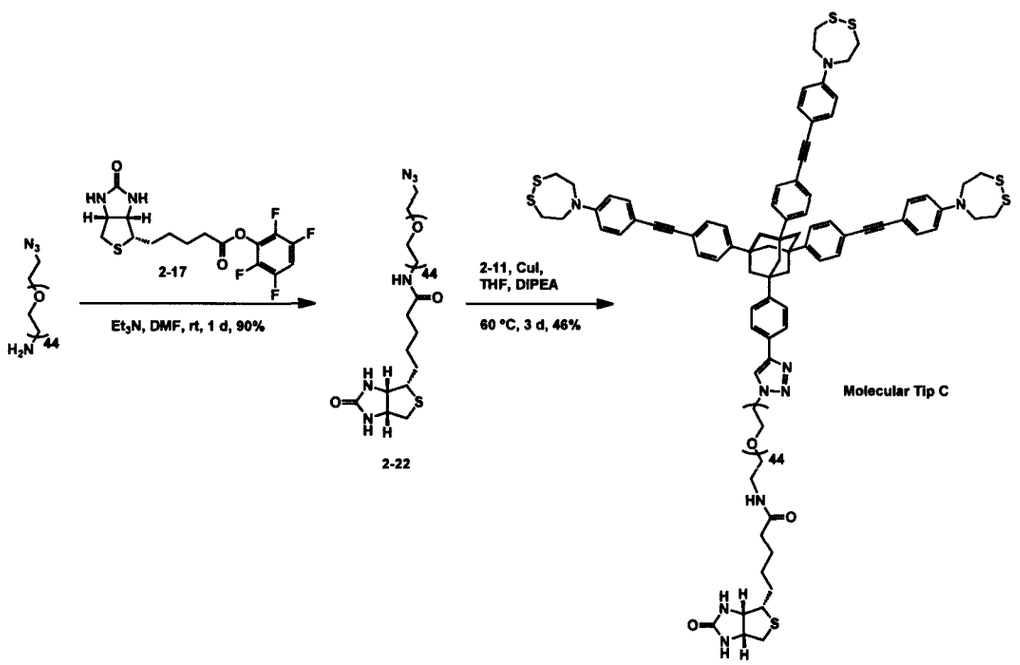

Scheme 2-7. Synthetic scheme for the preparation of biotinylated tripod with a longer PEG linker, molecular tip **C**.

excess tripod scaffolding, size exclusion and preparative thin layer chromatography, the molecular tip **C** with the longer PEG biotinylated linker was obtained in 46% yield.

2.3. Modification of Gold Surfaces with Molecular Tips

2.3.1 Background of Gold Surface Modification and Analysis.

After the synthesis, purification, and characterization of the two tripodal molecules and one monopodal molecule, they all were adsorbed onto gold surfaces and investigated. Molecular tips **A**–**C** and the acetylene-terminated tripod **2-11** (Figure 2-3) were characterized after immobilization on gold surfaces by sessile drop water contact measurements, spectroscopic ellipsometry, Fourier transform infrared–attenuated total reflectance (FTIR–ATR) spectroscopy, and near edge x-ray absorption fine structure (NEXAFS) spectroscopy. These surface analysis techniques not only demonstrate the successful immobilization of the molecular tips on a gold surface, but also give insight into the conformation and packing of the molecules on the surface.

2.3.2 Preparation of Gold Surfaces and Immobilization of Molecules.

Freshly prepared gold surfaces were vital to obtain reproducible results for the following experiments. Because gold is easily contaminated by ambient contaminants,[14] the films of gold used were cleaned before use in all experiments. Hydrogen flame annealing was found to be a simple, effective method.[15,16] The surfaces were hydrogen

flame annealed for one minute at approximately 800 °C (when an orange flare begins to show on the surface).[17] The flame can reach a temperature of 1150 °C, which is above the melting point of gold at 1064 °C and care must be taken to prevent the formation of bubbles on the surface. After annealing, the surfaces were immediately placed in a solution of the molecule of interest at a concentration of 0.1–1.0 mM. After removal from the solution, the gold surfaces were washed exhaustively to remove physisorbed molecules and then dried under a stream of nitrogen. The samples were then used immediately or stored in nitrogen-filled containers while being transported for analysis.

2.3.3 Spectroscopic Ellipsometry Analysis of Modified Gold Surfaces

Spectroscopic ellipsometry measures the polarization change of elliptically polarized visible and infrared light after it is reflected off the surface of a sample. The change in the amplitude ratio and phase of the reflected light is measured.[18] If the refractive index (n) and extinction coefficient (k) of all layers in a sample is known, then a film thickness can be obtained from the change in the polarization. It was necessary to measure the n and k of each individual gold surface after annealing to give accurate film thickness because the n and k of gold varies with the thickness of the gold film. After annealing, the n and k of gold were measured and the gold was immediately soaked in a solution of the molecule of interest. In modeling an organic film on top of the gold film, the k is assumed to be zero and the refractive index is estimated.[19] The refractive index of simple alkyl thiols on gold is generally estimated between 1.45 and 1.50. A value of

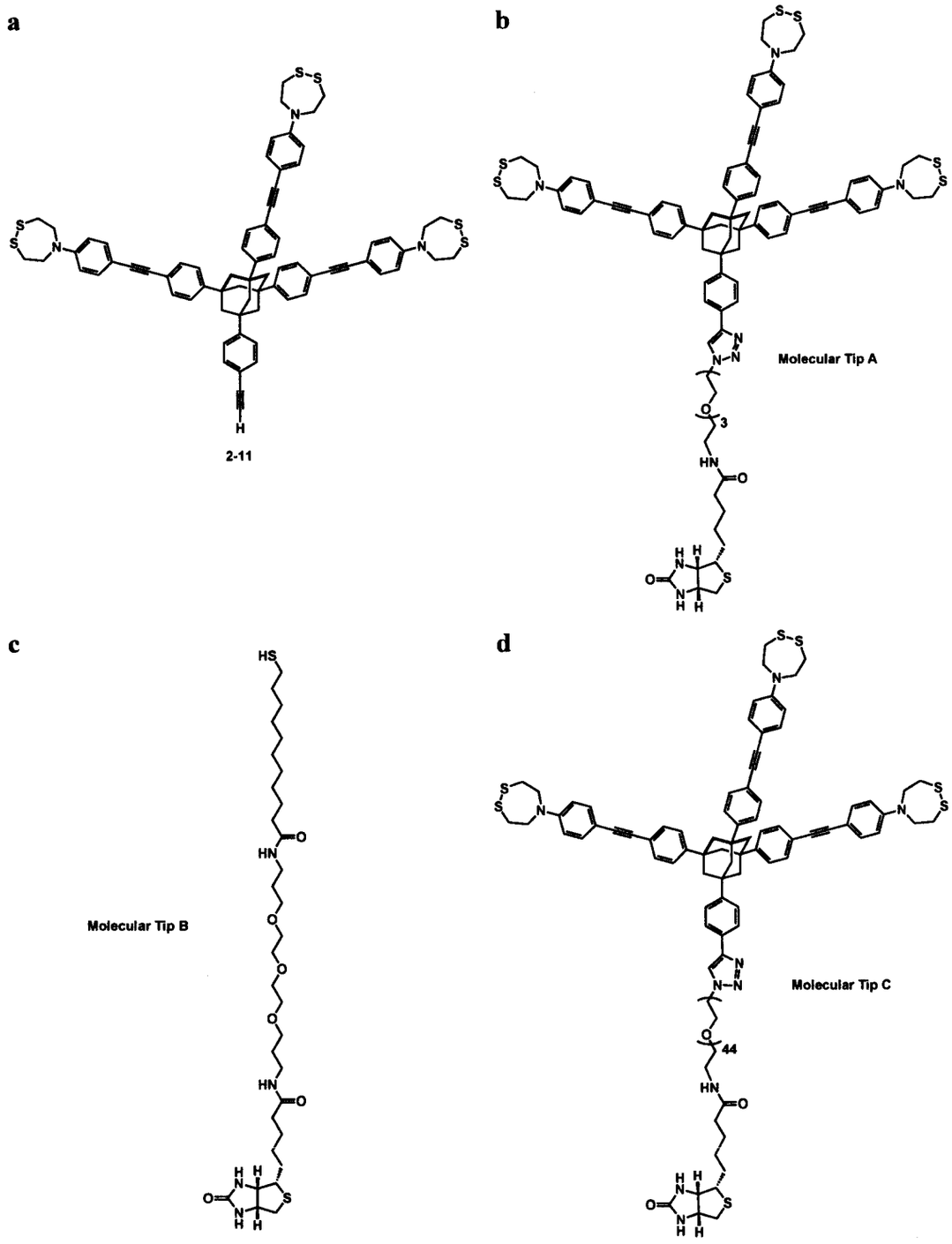

Figure 2-3. Molecules adsorbed onto gold surfaces. (a) Tripod acetylene **2-11**. (b) Tripod molecular tip **A**. (c) Monopod molecular tip **B**. (d) Tripod molecular tip **C** with long linker.

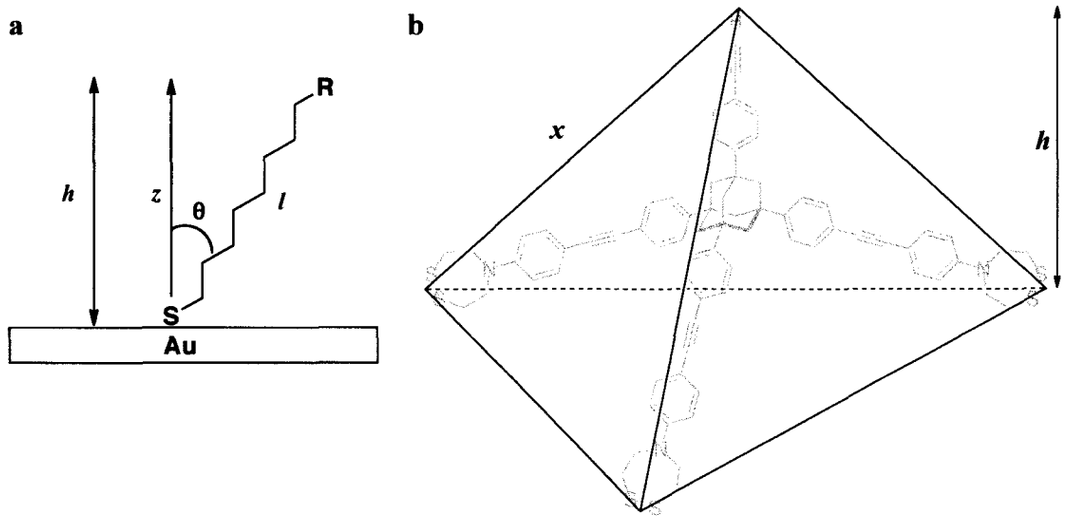

Figure 2-4. (a) Illustration of tilt angle, θ, with an alkyl thiol on a Au surface with height, *h*, and length, *l*, of the molecule. (b) Schematic illustration of the tripod acetylene scaffolding approximated by a tetrahedron with edge length, *l*, and height, *x*.

1.475 was chosen as a refractive index for the biotinylated monopod **B**. Molecules similar to the tripodal molecules with phenylethynylene or biphenyl groups[20–23] were reported to have refractive indices between 1.46 and 1.55. In this study, a refractive index of 1.50 was chosen for the tripodal acetylene **2-11** and for biotinylated tripods **A** and **C**.

Gold surfaces immersed in a solution of monopod molecular tip **B** gave a film thickness of 3.54 nm. After molecular modeling energy minimization, the length of the monopod **B** was calculated to be 4.06 nm.[24] The smaller measured thickness was hypothesized to the tilt angle the monolayer makes with the surface or with bent OEG chains. Self-assembled monolayers on gold are not usually perpendicular to the surface; they have a tilt angle dependent on their composition and the packing of their chains. The tilt angle, θ, is defined as the angle the axis of the methylene chain makes to the surface normal direction *z* (Figure 2-4a). Based on the calculated length,[25] the chains of

the biotinylated monopod monolayer have a tilt angle of 29.3° that is in good agreement with previous reports of alkyl monolayers on gold that have reported tilt angles of 30°.[26,27] The other possibility is that the monopod has well-ordered alkyl regions and the PEG component lacks a definite conformation. It is unlikely that the molecule has *gauche* conformations within the alkyl chain as previous spectroscopic evidence suggests that the methylene groups in SAM adopt an antiperiplanar conformation.[27,28]

Calculated thicknesses of the tripod acetylene were obtained by minimizing the tripod acetylene. For comparison, the leg portion of the molecule was compared to a crystal structure of the same moiety. The distance measured from the crystal structure[29] from the sulfur atoms to the end of the phenyl ring was 1.33 nm. The average calculated length of the three legs was 1.31 nm, which is in good agreement with the distance observed in the crystal structure. Because the legs are all of the same length, the height of the tripod acetylene was calculated by assuming that the tripod can be approximated by a tetrahedron (Figure 2-4b).[30] The calculated distance between the sulfur atoms of the legs to the terminal acetylene was averaged and taken to be one edge of the tetrahedron. The height, h, of a regular tetrahedron[31] with an edge of length x is:

$$h = \frac{1}{3}\sqrt{6}x$$

For the tripod acetylene, the average distance from the disulfides to the acetylene was 2.20 nm. A tetrahedron with an edge length of 2.20 nm has a height of 1.80 nm. When a value n = 1.50 is used, the monolayer thickness of the tripod acetylene is 1.74 nm, close to the predicted height of the tripod acetylene. The difference between the heights

measured by ellipsometry is likely because of the estimation of the refractive index of the film.

Modified gold surfaces with the tripodal molecules had a film thickness of 3.67 nm (Table 1). The length of the biotinylated linker was calculated to be 2.38 nm. The tilt angle θ can be calculated by subtracting the measured film thickness of the tripod acetylene from the measured film thickness of the biotinylated tripod (Figure 2-5). This difference and the calculated length of the linker can be used to calculate the tilt angle of the linker. Tilt angle can be calculated for a well-packed SAM like the monopod **B**, but it is unknown how to interpret the tilt angle for a flexible linker bound to a rigid support. Because the base of the tripod is large enough to preclude van der Waals interactions between linker chains, the biotinylated linker possibly contains *gauche* conformations

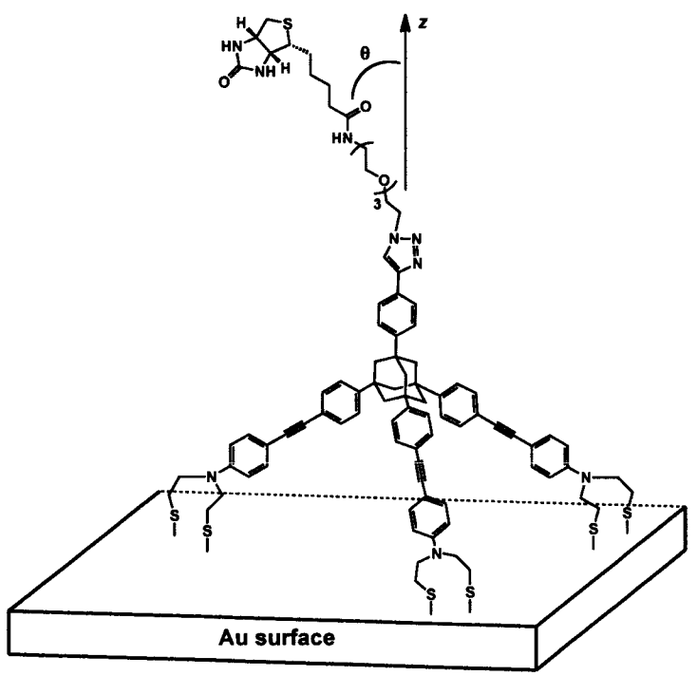

Figure 2-5. Illustration of the biotinylated tripod on a gold surface with its OEG chain at a tilt angle of θ.

Table 2-1 Monolayer Thickness and Sessile Drop Contact Angle Measurements[a]

Entry	Thickness of Monolayer (nm)[b]	Contact Angle
Tripod **A**	3.67 ± 0.11	48.1 ± 2.5°
Monopod **B**	3.54 ± 0.12	40.8 ± 5.4°
Tripod **C**	1.71 ± 0.16	33.8 ± 1.1°
Tripod acetylene **2-11**	1.74 ± 0.16	48.9 ± 2.6°

[a] Values are reported as mean ± standard deviation from three independently prepared samples with 10 different areas measured on each sample. [b] Determined by spectroscopic ellipsometry.

that lead to bends in the linker OEG chain. If the tripod is bound by the three disulfides to the surface, the measured thickness of the biotinylated tripod puts the linker at a tilt angle of 35.8° from the surface normal.

The biotinylated tripod **C** with the longer PEG linker had a film thickness of 1.71 nm on gold. Because the longer PEG linker is not likely to protrude completely away from the surface for the entirety of its 10–15 nm length, the PEG chain can block the adsorption of molecules onto the Au surface. Although PEGs with helical structures have been observed,[32] a PEG of similar length on gold surfaces was found to be more randomly oriented and amorphous in character.[33] The steric bulk of the PEG chain can block the further adsorption of molecules to produce a film thickness lower than the length of its PEG chain.

2.3.4 Sessile Drop Water Contact Angle Measurements

Sessile drop contact angle is a method for gauging the relative polarity of a surface. A more hydrophilic surface will have a smaller water contact angle than a more hydrophobic one. The results of the contact angle measurements are summarized in Table 2-1. The monopod **B** monolayer yields a more hydrophilic surface than the either the tripod **A** or tripod acetylene **2-11** with a contact angle of 40.8°. The biotinylated monopod forms a more densely packed monolayer on the surface to expose the hydrophilic ethylene glycol and biotin moieties to the surface interface. Although the biotinylated tripod **A** has the same biotin moiety, its large size precludes packing at a similar density as the monopod and most of the occupied space contains the hydrophobic aromatic groups of the tripod scaffold and tripod **A** has a contact angle of 48.1°. The tripod acetylene has no hydrophilic moieties and would therefore be expected to give a more hydrophobic surface with a higher contact angle than tripod **A**. However, these two tripods show little difference in contact angle measurements; the acetylene-terminated tripod **2-11** has a contact angle of 48.9°. The biotinylated tripod with the longer PEG linker displayed the most hydrophilic character of the four molecules. The long, hydrophilic PEG chain covers the surface after deposition, creating a more easily wetted surface.

2.3.5 FTIR–ATR Analysis of Chemically Modified Gold Surfaces

FTIR–ATR spectroscopy uses an infrared laser reflected through a polished germanium crystal to measure IR spectra of surfaces and other materials. The peaks observed in FTIR allow identification of specific functional groups present on the

surface and can give insight into the conformation of monolayers. It is critical in FTIR–ATR of monolayers to have a clean, fresh background sample to use before taking each sample. For gold, a freshly hydrogen flame annealed sample was used as a background. The tripod acetylene **2-11**, biotinylated tripod **A**, monopod **B**, and the longer linker tripod **C** were immobilized on gold surfaces and examined by FTIR.

The packing of a monolayer of the surface can be described as crystalline in a well-packed monolayer of alkyl thiols.[8] On the other hand, a system with less defined

Table 2-2. Assignment of peaks in FTIR–ATR and transmission spectra.

	Biotinylated Tripod **A**		Biotinylated Monopod **B**		Biotinylated Tripod **C**		Terminal Acetylene tripod	
	ATR	KBr	ATR	NaCl	ATR	NaCl	ATR	NaCl
N–H	3388	3414	3261	3290	3433	3521	–	–
sp C–H	–	–	–	–	–	–	3329	3287
sp^2 C–H	3082 3041	3079 3040	–	–	–	3082 3042	3086 3037	3080 3035
$–CH_2–$ stretch	2929[a] 2857[b]	2922[a] 2853[b]	2923[a] 2854[b]	2927[a] 2858[b]	2930[a] 2870[b]	2897[a] 2870[b]	2928[a] 2855[b]	2925[a] 2851[b]
C≡C	2207	2205	–	–	2206	2207	2206 2111	2204 2106
C=O	1708	1700	1697	1689	1700	1702	–	–
	1653	–	1653	1647	1653	1656	–	–
aryl C=C	1604	1603	–	–	1603	1603	1604	1604
C–O–C	1133	1138	1127	1126	1114	1107	–	–

Values reported in cm^{-1}. [a]Antisymmetric methylene stretch and [b]symmetric methylene stretch. Transmission spectra were obtained by KBr pellet or a thin film on NaCl plate.

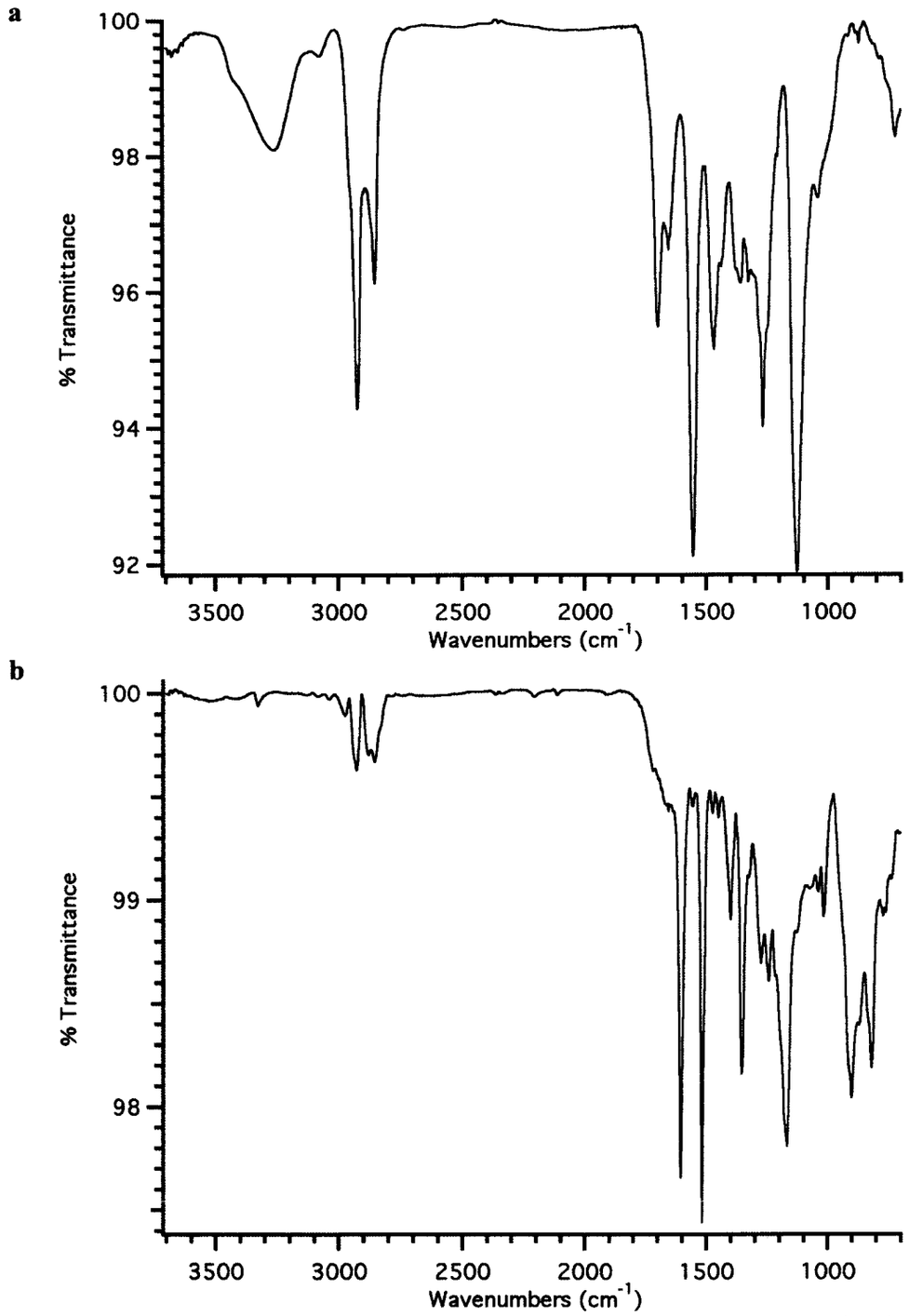

Figure 2-6. FTIR–ATR spectra of (a) biotinylated monopod **B** and (b) tripod acetylene scaffolding **2-11** immobilized on gold.

packing and more disordered alkyl chains are described as liquid at the surface interface. The asymmetric and symmetric stretches of the methylene group of alkyl chains shift in the FTIR spectrum depending on the order in the system.[8] In an ordered, crystalline system, the asymmetric and symmetric bands appear close to 2920 and 2850 cm^{-1}, whereas in the more loosely packed liquid system the bands appear at higher energy near 2928 and 2856 cm^{-1}, respectively.

A description of the observed peaks and a comparison of the IR spectra on the Au surface and the transmissions IR spectra are detailed in Table 2-2. Overall, the IR stretches occurred at similar wavenumbers except for the N–H stretches, which vary widely between the ATR and transmission spectra. The FTIR spectrum of the monopod **B** on gold is shown in Figure 2-6a. There is a broad N–H peak at 3261 cm^{-1} that is indicative of hydrogen bonding within the monolayer and there are also sp^3 C–H stretches at 2850–2950 cm^{-1}. In the monopod **B**, the symmetric and asymmetric peaks occurred at 2854 cm^{-1} and 2923 cm^{-1}, respectively. The alkyl chain of the monopod is somewhat well-packed on the surface with the tetraethylene glycol portion of the molecule more freely sampling space at the interface to give rise to separate peaks for the two distinct regions of the molecule.[9] The crystalline methylene groups of the alkyl chains absorb at higher wavenumbers, whereas the liquid-like methylene groups of the ethylene glycol portion of the molecule absorb at lower wavenumbers. The FTIR spectrum further confirms the presence of the amide carbonyl groups and the intense C–O stretch at 1127 cm^{-1}.

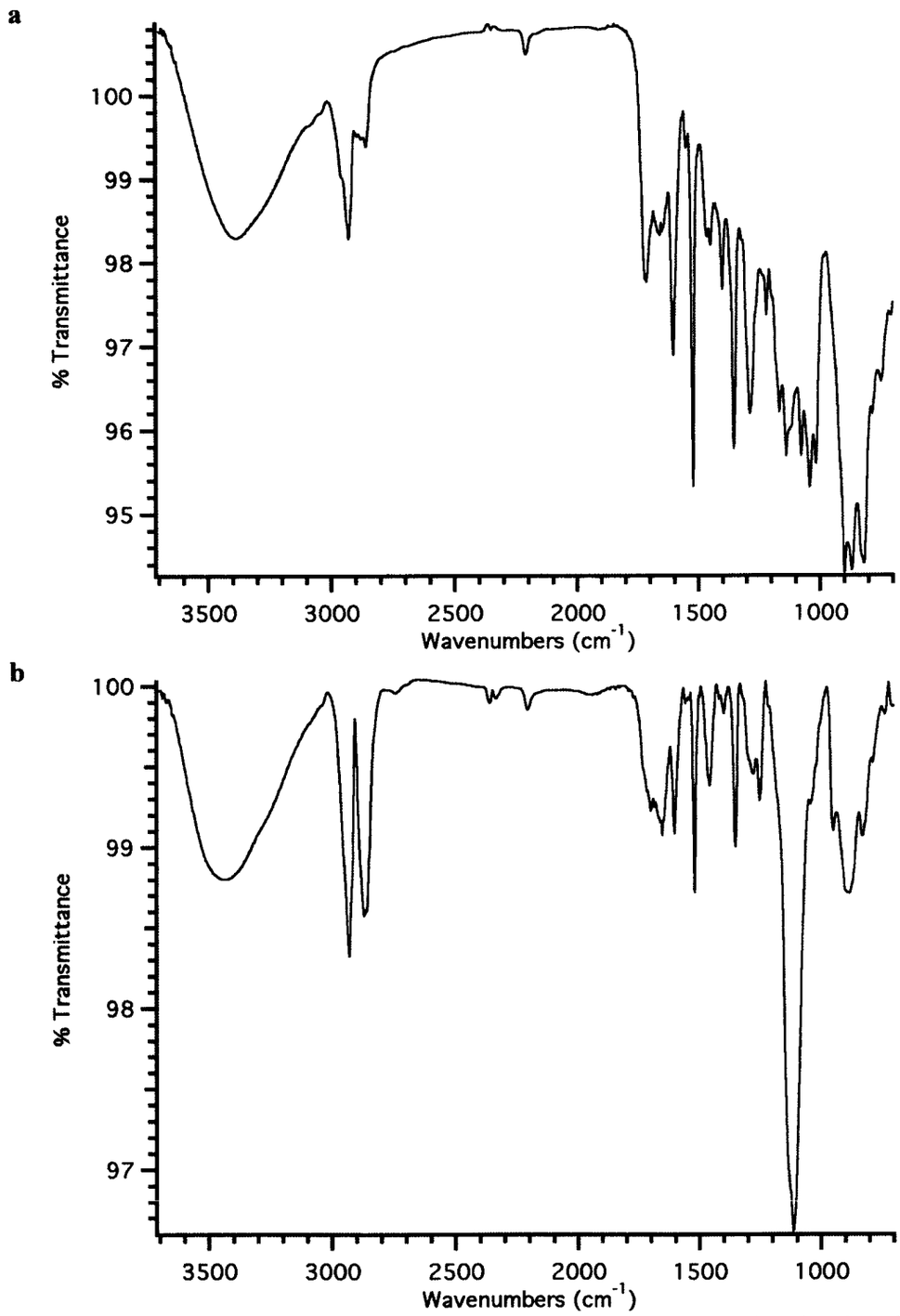

Figure 2-7. FTIR–ATR spectra of (a) tripod molecular tip **A** and (b) tripod molecular tip **C**.

In the spectra of the tripod acetylene (Figure 2-6b) the sp^3 and sp^2 C–H stretches are present. There is also an sp C–H stretch present at 3229 cm^{-1}. Towards the middle of the spectrum there are also two weak alkyne peaks, one that corresponds to the internal alkyne of the legs of the tripod at 2206 cm^{-1} and another that corresponds to the terminal alkyne at 2111 cm^{-1}. There is also the aromatic C=C stretch present in the spectrum at 1604 cm^{-1}.

In the spectrum of the tripod **A** (Figure 2-7a), there are several distinguishable IR peaks. There is a broad amide N–H stretch present at 3388 cm^{-1}. The C–H sp^2 peaks are weak and appear in the same region as in the transmission spectrum of tripod **A**. On the gold surface, the methylene antisymmetric and symmetric stretches appear at 2929 cm^{-1} and 2857 cm^{-1}, whereas these stretches appear at 2922 cm^{-1} and 2853 cm^{-1} in the KBr transmission spectrum of tripod **C**. There are two carbonyl peaks, the ureido carbonyl of biotin and the amide bands of the carbonyl connecting biotin to the OEG linker at 1708 cm^{-1}, and 1653 cm^{-1}. The aromatic C=C stretches and internal alkynes of the legs also appear in the FTIR–ATR spectrum in similar positions as the transmission spectrum.

The FTIR spectrum of the longer PEG linker tripod **C** is shown in Figure 2-7b. There is a broad amide N–H stretch present at 3433 cm^{-1}. The intensity of this peak is large and likely contains additional intensity because of the water O–H stretch from the hygroscopic PEG linker. The sp^2 C–H peaks are likely overlapped by the strong N–H and O–H peak. On the gold surface, the methylene antisymmetric and symmetric stretches are broad and appear at 2930 cm^{-1} and 2870 cm^{-1}. The internal alkynes of the tripod legs occur at 2206 cm^{-1} in the FTIR spectrum. There are two amide carbonyl stretches present at 1700 cm^{-1} and 1653 cm^{-1}. The aromatic C=C stretches also arise at

1603 cm^{-1} in both of the spectra. The strongest peak in the spectrum is the intense C–O stretch that appears at 1114 cm^{-1}.

2.3.6 Near Edge X-Ray Absorption Fine Structure Spectroscopy Analysis

NEXAFS spectroscopy uses polarized x-ray to excite inner core (1s, K shell) electrons into the σ^* and π^* orbitals of low *Z* atoms. Upon relaxation to the ground state, photons are emitted through an Auger process.[34] From these photons, the oxidation state of atoms can be probed by NEXAFS spectroscopy. It can identify carbon, nitrogen, and oxygen on a surface, but unfortunately the beamline used was unable to measure sulfur absorption spectra. NEXAFS spectroscopy has the ability to measure at multiple angles to investigate the angle dependence of the absorption spectra of molecules on a surface. If the molecules on the surface are well packed and oriented regularly then there should be a dependence on the angle observed in the spectra.

The C K-edge spectra of molecular tip **A** shown in Figure 2-8 have an absorption in the π-bonded carbon region with a maximum at 285.2 eV. There is a shoulder near the carbon edge at 287.6 eV that corresponds to C–H σ^* transitions.[35] There is a second π^* transition that corresponds to the C=C π^* transition in the aromatic groups at 288.8 eV.[23] The peak at 289.6 eV is assigned to the methylene groups in the PEG linker.[36] There are also C–C σ^* transitions at 293.2 eV and at approximately 303 eV. The N K-edge spectrum has a small shoulder at about 399.0 eV that corresponds to the N 1s to aromatic π^* transition of the aniline groups on the legs of the tripod.[37] The peak at 402.2

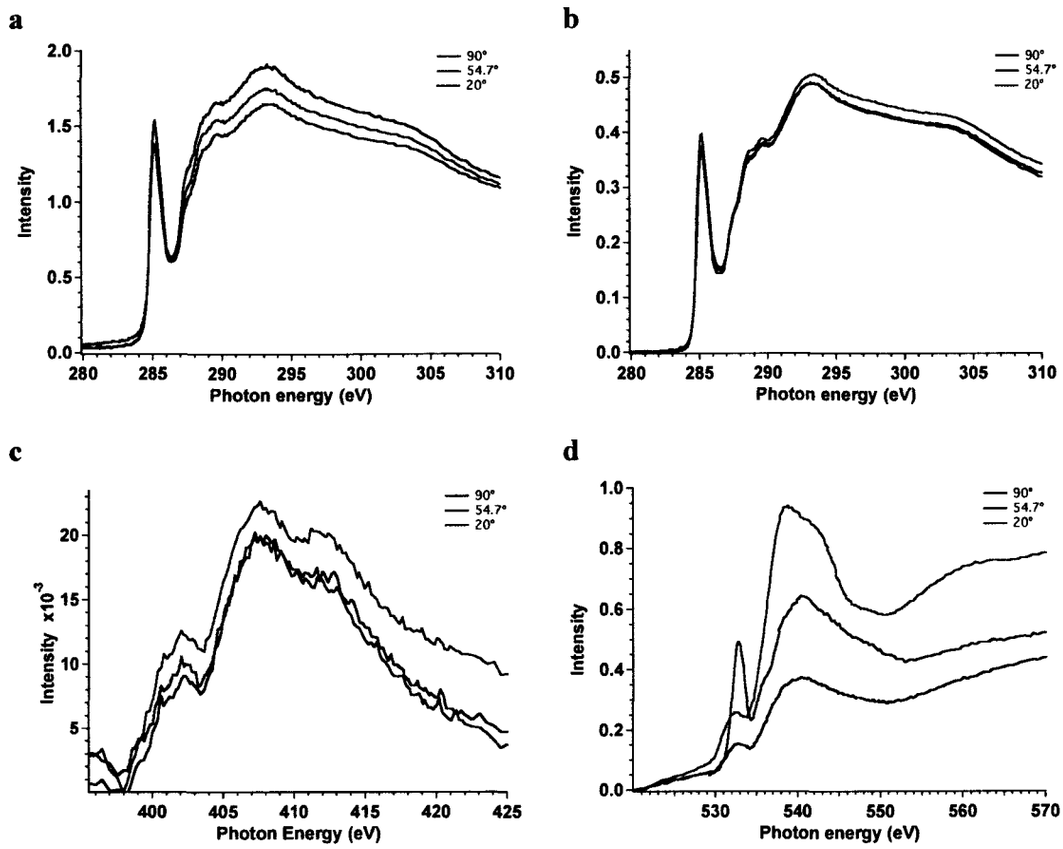

Figure 2-8. NEXAFS spectra of biotinylated tripod **A** on a gold surface. (a) Partial and (b) total electron yield of C K-edge spectra (c) Total electron yield of N K-edge spectrum and (d) Partial electron yield of O K-edge spectrum.

eV corresponds to the N 1s to π^* transition in the amide and ureido groups[38] and possibly overlaps the N=N π^* transitions of the 1,2,3-triazole.[39,40] The broad peaks at 407.6 eV and 412.0 eV correspond to N 1s to N–C and N–H σ^* transitions.[41] In the O K-edge spectrum of molecular tip **A**, there is π^* signal at 532.8 eV corresponding to the carbonyls. There is also a broad, asymmetric σ^* signal from 535–550 eV corresponding to the oxygens in the OEG chain.

The C K-edge spectra of the acetylene tripod scaffold **2-11** is similar to the molecular tip **A** except for the absence of the transition associated with the OEG chains

(Figure 2-9a–b). The two π^* transitions occurs at the same position as in molecular tip **A** at 285.2 and 288.8 eV. The N K-edge spectrum (Figure 2-9e) has a small shoulder at about 399.0 eV that corresponds to the N 1s to aromatic π^* transition. The peak at 401.8 eV cannot be an amide resonance; it is much sharper than the broad peaks in the molecular tip **A.** The broad peak at 407.7 eV correspond to N–C σ^* transitions.

Figure 2-9 also displays the NEXAFS spectra of molecular tip **B**. The C 1s to C–H σ^* transition of the methylene groups of the alkyl and OEG chain occurs at 288.5 and 287.7 eV, respectively. There are broad absorptions for the C 1s to C–C σ^* transition at 292.2 eV and at approximately 303 eV. The π-bonded carbon present in the monopod NEXAFS spectra (285.0 eV) resulted from either contamination[34] or x-ray damage of the thiol monolayer.[42] Monopod **B** showed the most angle dependence in the C 1s spectra. The 20° angle of incidence led to an almost doubling in the intensity in the intensities of the spectra. However, the shape of the C K-edge spectra obtained at 54.70 and 90° has an anomalous shape that makes a comparison of angle dependence unreliable. In the O K-edge spectra (Figure 2-9f), the peak at 532.6 eV and the broad peak at 540.3 eV correspond to the O 1s to C=O π^* and C–O σ^* transitions, respectively. Again, the 20° spectra is much more intense than the other two angles. The monopod **B** exhibited weak absorption in the nitrogen K shell spectrum (spectra not shown).

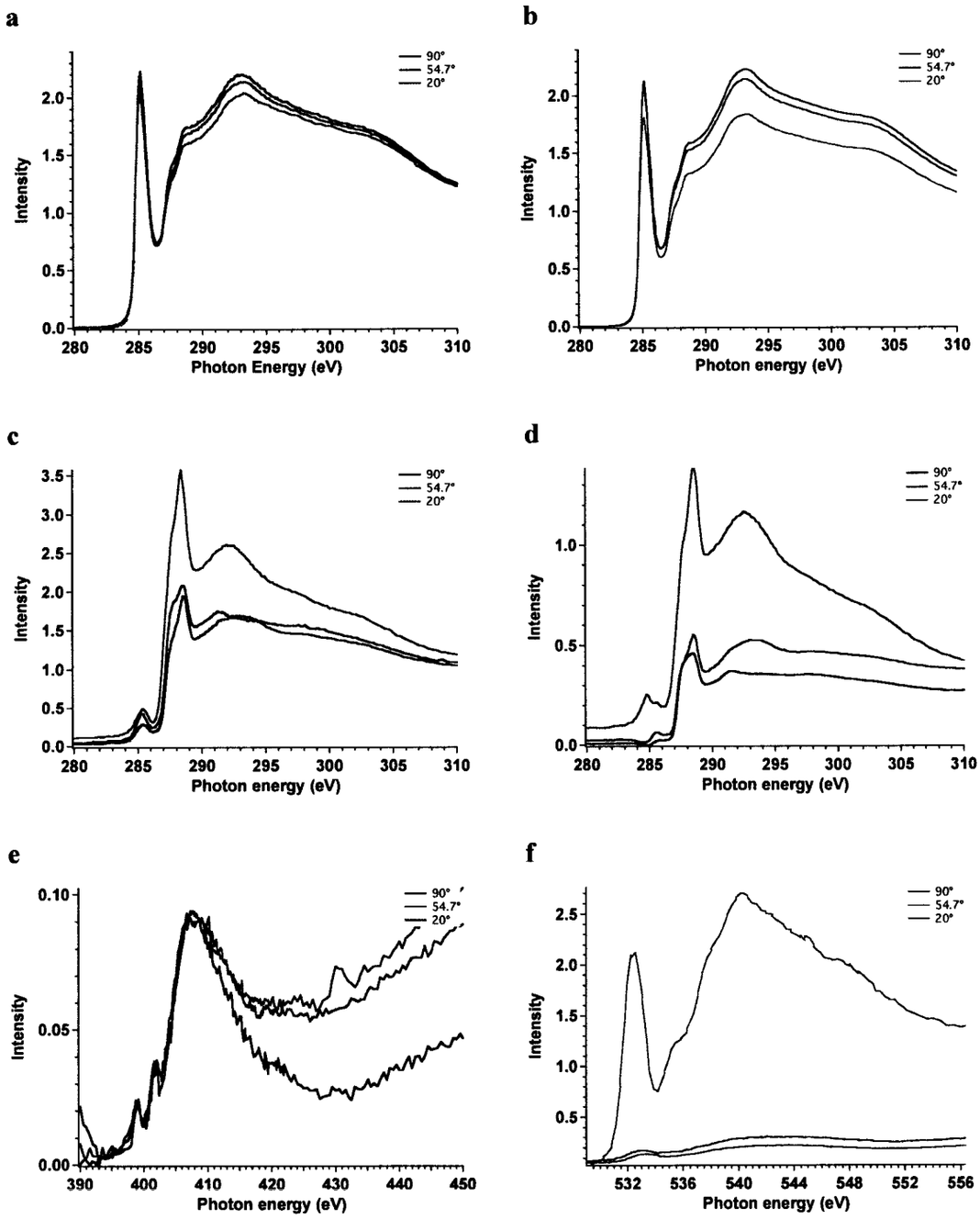

Figure 2-9. NEXAFS spectra. (a) Partial and (b) total electron yield C K-edge spectra of tripod acetylene **2-11** (c) Partial and (d) total electron yield C K-edge spectra of monopod molecular tip **B**. (e) tripod acetylene **2-11** N K-edge spectra. (f) O K-edge spectra of monopod **B**.

2.3.7 Summary of Analysis of Modified Gold Surfaces

Molecular tips **A–C** and **2-11** were immobilized on gold surfaces and analyzed by contact angle measurements, FTIR–ATR, ellipsometry, and NEXAFS spectroscopy. Each surface analysis technique added some information to the arrangement of the molecules on the surface and the combined information to give insight into the properties of the molecules adsorbed onto the surface. The analysis of the monolayers was performed to investigate the immobilized molecules and to enable the future designs of molecules that bind to surfaces with the desired orientation and function.

Contact angle measurements for the biotinylated tripod **A** and tripod acetylene **2-11** did not shed much light on the characteristics of the monolayers. The biotinylated tripod produced a surface more hydrophobic than that of the biotinylated monopod **B** as predicted.[43] Spectroscopic ellipsometry measured a thickness of 3.67 nm, about the same thickness as monopod **B**. Unlike the biotinylated monopod, the packing of the tripod on the surface is not easily discerned from the FTIR data, but all the major functional group absorptions could be assigned to peaks with similar values as in the transmission IR spectra. NEXAFS spectra showed strong signals for σ- and π-bonded carbon and less intense signals for oxygen and nitrogen on the surface. Because the tripod does not form an oriented surface with any of its bonds, no angle dependence is observed in any of the spectra. The lack of angle dependence in the spectra indicated random orientation of the tripod molecules on the surface.

The biotinylated monopod **B** produced a film that was measured by ellipsometry to be 3.54 nm thick, which was hypothesized to be caused by the molecules tilting at an angle of 29.3°. The biotinylated monopod **B** only produced slightly more hydrophilic

surfaces than that of biotinylated tripods **A** and **C** by water contact angle measurements. The well-ordered, crystalline packing was also confirmed by FTIR experiments. Monopod **B** is forming a rather ordered monolayer with some crystalline character as indicated by the position of the methylene symmetric and antisymmetric absorption in the FTIR spectra. NEXAFS spectroscopy for monopod **B** did not display an angle dependence, which indicates that the monolayer is disordered, but unlike the FTIR–ATR spectra, the NEXAFS measurements were not taken on freshly prepared substrates.

The biotinylated tripod **C** displayed the most hydrophilic surface of all the measured samples. FTIR–ATR spectrum of tripod PEG 2000 biotin immobilized on the gold surface displayed the expected peaks for all functional groups in the molecule. The thickness of tripod **C** measured by ellipsometry was approximately the same as the tripod acetylene, 1.71 nm. The measured film thickness could be attributed to the longer PEG chains collapsing on the gold surface and the chains sterically preventing any further chemisorption of the tripodal molecules onto the gold surface. Thus, a lower thickness would be measured.

The relatively low values for the contact angle measurements of the tripod acetylene scaffolding **2-11** can be due to the slow adsorption of the molecule onto the gold surface. It was necessary to make a ten-fold less concentrated solution of the tripod acetylene because of its poor solubility. An incompletely modified surface might leave some areas of the hydrophilic gold surface[44] exposed that could lead to a lower contact angle. Spectroscopic ellipsometry shows the films of the tripod acetylene **2-11** to have a thickness of 1.74 nm that agrees well with the calculated height of 1.80 nm. FTIR–ATR spectra confirm the presence of the functional groups of the tripod on the gold surface in

similar positions as the transmission spectrum. The σ- and π-bonded C appear in the C K-edge NEXAFS spectra but no angle dependence was observed.

2.4. Single Molecule Force Spectroscopy Experiments

2.4.1 Background and Introduction to Ligand–Receptor Binding

Ligand–receptor force spectroscopy investigates the force necessary to rupture a ligand–receptor complex. The initial studies in ligand–receptor unbinding by AFM were performed by Gaub and co-workers who studied the biotin–NeutrAvidin complex.[45] Their studies measured the unbinding of a NeutrAvidin-coated AFM tip from a biotinylated agarose bead. The techniques and statistical analysis in their study remains the template for receptor–ligand studies.

An illustration of a force–distance curve that corresponds to a single molecular recognition event is shown in Figure 2-10. During the approach of the AFM tip, the tip detects no force and the curve is flat (Figure 2-10a). The cantilever deflects upon contact with the surface and there is a sharp change in the curve (Figure 2-10b). When the tip is in contact with the surface and if the ligand is in proximity to the receptor, the pair binds to form a complex (Figure 2-10c). As the tip is retracted from the surface, the ligand–receptor complex is ruptured and the cantilever is deflected a magnitude proportional to the force necessary to remove the ligand from its binding site (Figure 2-10d). Multiple rupture forces are then compiled into a histogram to find the most probable force of rupture.

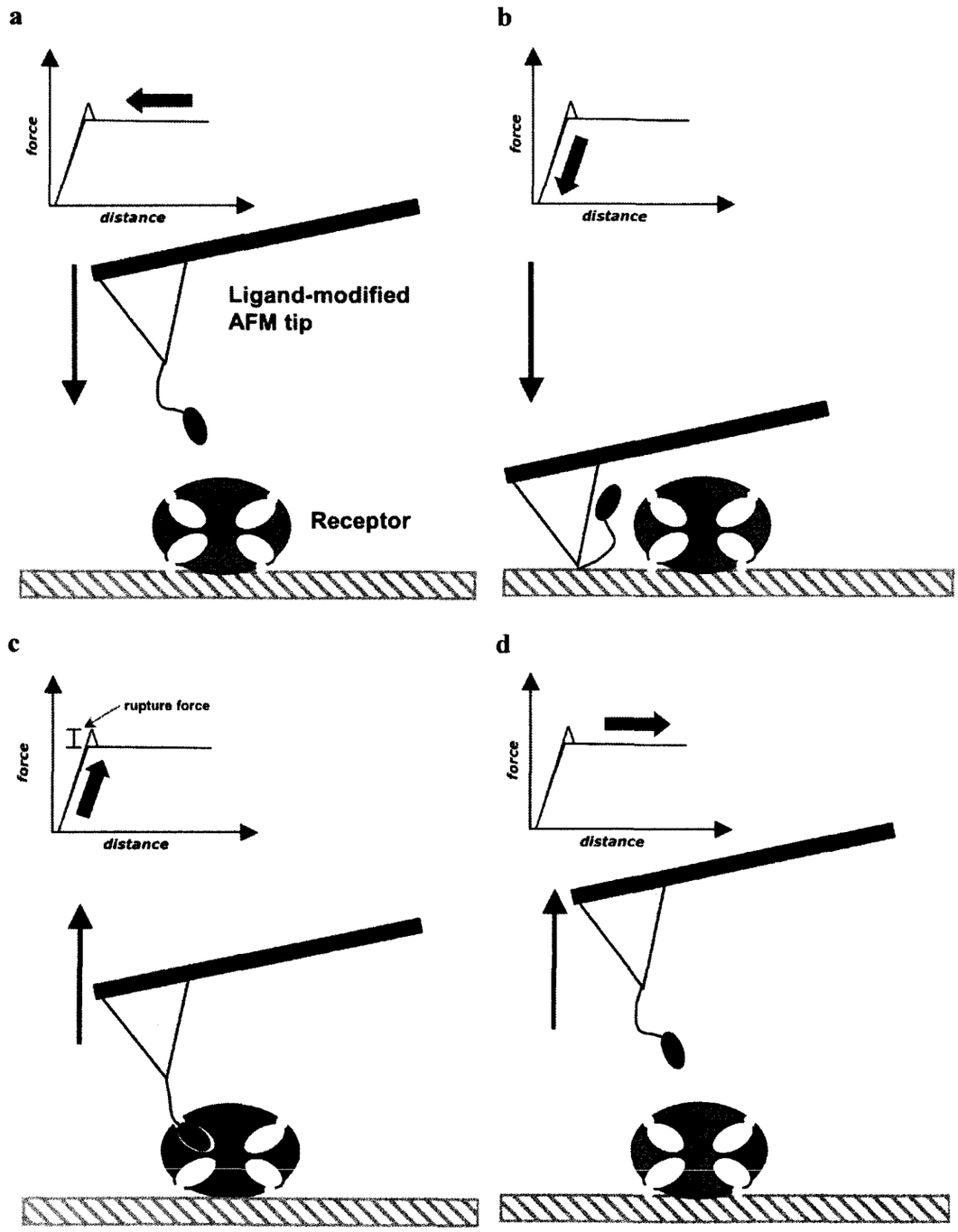

Figure 2-10. Schematic illustration of force–distance curve with a ligand functionalized AFM tip and a surface-bound receptor. The inset on each figure corresponds to the position of the cantilever on the force–distance curve. (a) The approach of the AFM tip to the surface. (b) The AFM tip contacts the surface. (c) If the ligand is close enough to the binding area of the receptor, a complex forms and the ligand–receptor rupture force is measured. (d) The AFM tip retracts from the surface.

Gaub and co-workers noticed that when the AFM tip was removed from the surface of the bead, two distinct forces were observed. The first observed force, the interaction nearest the surface, was a much larger magnitude force. A second, smaller rupture force followed. The analysis of their force–distance curves assigned the initial large adhesive force to the desorption and removal of the tip from the surface. A *nonspecific* interaction refers to an interaction from any other intermolecular interaction present between the AFM tip and the surface. The type of nonspecific interaction depends on the nature of the surfaces: it can be a hydrophobic interaction, van der Waals, or electrostatic in nature. The second, smaller force was detected furthest from the surface and was the *specific* interaction of the biotinylated AFM tip surface on the NeutrAvidin bead. A *specific* rupture event refers to the force measured from the rupture of a biotin–NeutrAvidin complex that has formed. When the smaller, second forces were plotted in a histogram, a periodic pattern became apparent at multiples of 160 pN. The 160 pN periodicity corresponded to the recognition of multiple biotin–NeutrAvidin complexes because the magnitude of multiple simultaneous ruptures are additive.

AFM force spectroscopy studies of molecular recognition components have been performed on a variety of biomolecules. In this study, the force spectroscopy experiments focused specifically on ligand–receptor complexes because of their importance in the expression of biological activity. Our interest in single molecule force spectroscopy stems from the ability of the AFM to operate under physiological conditions using picomolar concentrations of protein to analyze binding of molecules. The ability to measure the binding of a receptor provides insight into the strength of the

ligand–receptor interaction. In our model study with the molecular tips, we used the biotin–avidin complex because of its binding strength and many previous reports in force spectroscopy experiments.[45,46]

2.4.2. Immobilization of Molecular Tips on AFM Tips

Several considerations of AFM tip preparation are noteworthy. First, AFM tip surfaces, especially gold-coated tips, have organic and inorganic contaminations present on their surface as purchased. These contaminations include polydimethylsilane (PDMS) and other organic materials from the packaging of the manufacturer and the ambient atmosphere.[47,48] Although some researchers obtained single molecule resolution without cleaning AFM tip surfaces,[49] we found it necessary to remove these contaminants before immobilization of the molecular tips. Because flame annealing is not practical with such a small sample, gold-coated AFM tips were cleaned by UV/ozone treatment.[50,51]

Adsorbing adventitious material from the ambient atmosphere contaminates gold surfaces. To prevent any organic contamination from the ambient air, after UV/ozone treatment, the tips were immediately immersed in a freshly prepared solution of the desired molecular tip. Freshly prepared solutions of the molecular tips **A**–**C** (0.10 mM in DMSO) were necessary to obtain reproducible results. After 20–24 h of immersion, the tips were washed exhaustively to remove physisorbed material and mounted in the AFM for the force spectroscopy experiments. Modified and washed AFM tips were stored in DMSO for a maximum of one day.

2.4.3 Avidin Receptor Substrates

Immobilization of proteins on substrates remains an important aspect in AFM force spectroscopy experiments. Mica is a common surface for protein immobilization because it is compatible with biomolecules in aqueous solution. Also, it has near atomic smoothness and it has a negatively charged surface to adsorb proteins. Proteins for AFM studies are commonly immobilized on the negatively charged surface of mica by ionic interaction and van der Waals forces. Other options of immobilization are to covalently attach the proteins to glass,[52] silicon,[53] mica,[54] or gold[55] substrates.

Because avidin proteins are commercially available as solids or immobilized on surfaces, there was a choice to either physisorb or covalently modify the surface. Several different avidin substrates were used: streptavidin on mica, streptavidin on glass slides, and NeutrAvidin on agarose beads. Using streptavidin on mica or glass slides gave irreproducible results. This was hypothesized to be caused by the rigid surfaces that yielded sharp adhesion forces that did not allow distinction between specific and nonspecific rupture forces. To alleviate this problem, NeutrAvidin bound to agarose beads was chosen as the receptor substrate. NeutrAvidin is a deglycosylated avidin with low nonspecific binding.[5] The agarose beads were approximately 20–150 μm in diameter and were large enough to be viewed in the camera of the AFM. The size of the bead was sufficiently large to maneuver the AFM tip onto the bead. Figure 2-11 displays force–distance curves obtained with a gold-coated AFM tips modified with molecular tip **A** on a protein covered glass and bead substrate. In these force curves there are no

rupture forces upon retraction of the AFM tip, but the curves demonstrate the different stiffness of each surface. The agarose bead is hypothesized to be more compressible, which caused a broader, less defined desorption of the tip from the surface, whereas the glass surface has a sharp desorption. The compressible, rounded bead made it difficult to discern the absolute distance of the tip from the surface during retraction.

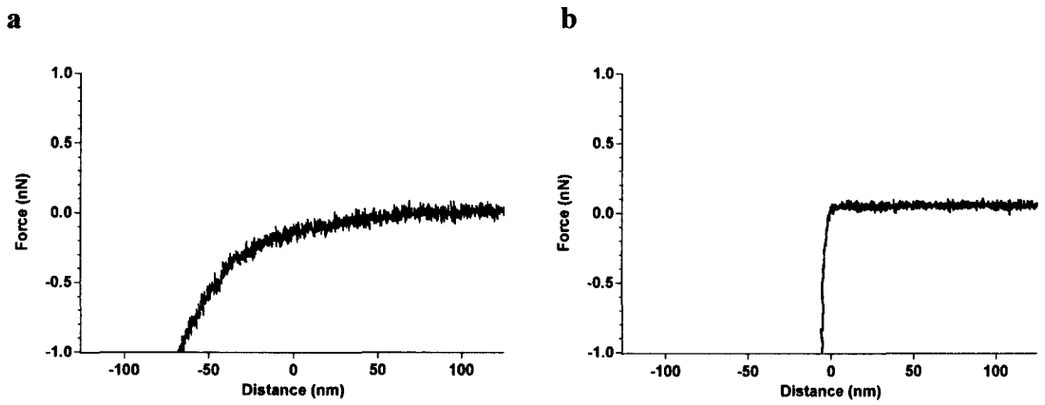

Figure 2-11. Representative force–distance curves obtained on (a) a NeutrAvidin-coated agarose bead and (b) a streptavidin-coated glass slide.

2.4.4 Force Spectroscopy Studies with Biotinylated Tripod A

Example force–distance curves are displayed in Figure 2-12a–b. From the force–distance curves, the distance from the surface and the magnitude of the rupture force is obtained. Numerous curves are collected and the rupture events are plotted in histograms to analyze the frequency of each event. For the rupture forces of the tripod molecular tip **A**, there is a sharp decrease in the frequency of events after 20 nm. With a linker length of about 2 nm, it is unlikely that there are rupture events occurring after this distance. But because the agarose beads are a compressible surface, the point that the tip

leaves the surface is difficult to discern. For stiffer surfaces, the distance that the tip is removed from the surface is more clearly defined by the sharp change in the curve.

Because of its wider base, the biotinylated tripod is expected to yield a lower density of ligand molecules on the surface compared to the biotinylated monopod. The binding of the tripod was examined by collecting force–distance curves until 200 were collected with multimolecular events. This was 500–600 cycles for each experiment. For the force–distance curves, 29% of the examined curves had detectable rupture forces. In Figure 2-12a–b, representative force–distance curves obtained with the molecular tip **A** are displayed that correspond to a single and a multiple rupture event. The average number of forces observe in the biotinylated tripod force spectroscopy experiments was 1.7. Two separate experiments are shown in Figure 2-12c and e. On each histogram, there are Gaussian fits overlaid to fit the most frequent events. The maxima of the distributions for the biotinylated tripod **A**, or the most probable rupture force, were at 176 pN and 137 pN. There is a second Gaussian fit overlaid at slightly more than twice the most probable rupture force at 288 pN for the second experiment. This broader second peak corresponded to the rupture of two biotin–NeutrAvidin complexes. Because there was no distribution lower than the 176 pN, this distribution corresponds to the rupture of a single biotin–NeutrAvidin complex. Furthermore, the most probable force was close to the 160 pN reported value for a single biotin–avidin complex to rupture.[56] The most probable force of rupture varied slightly in these two experiments because of error in calibrating the spring constant of the cantilever,[57] differences in temperature and pH, and loading rate (See Section 4.5.1).

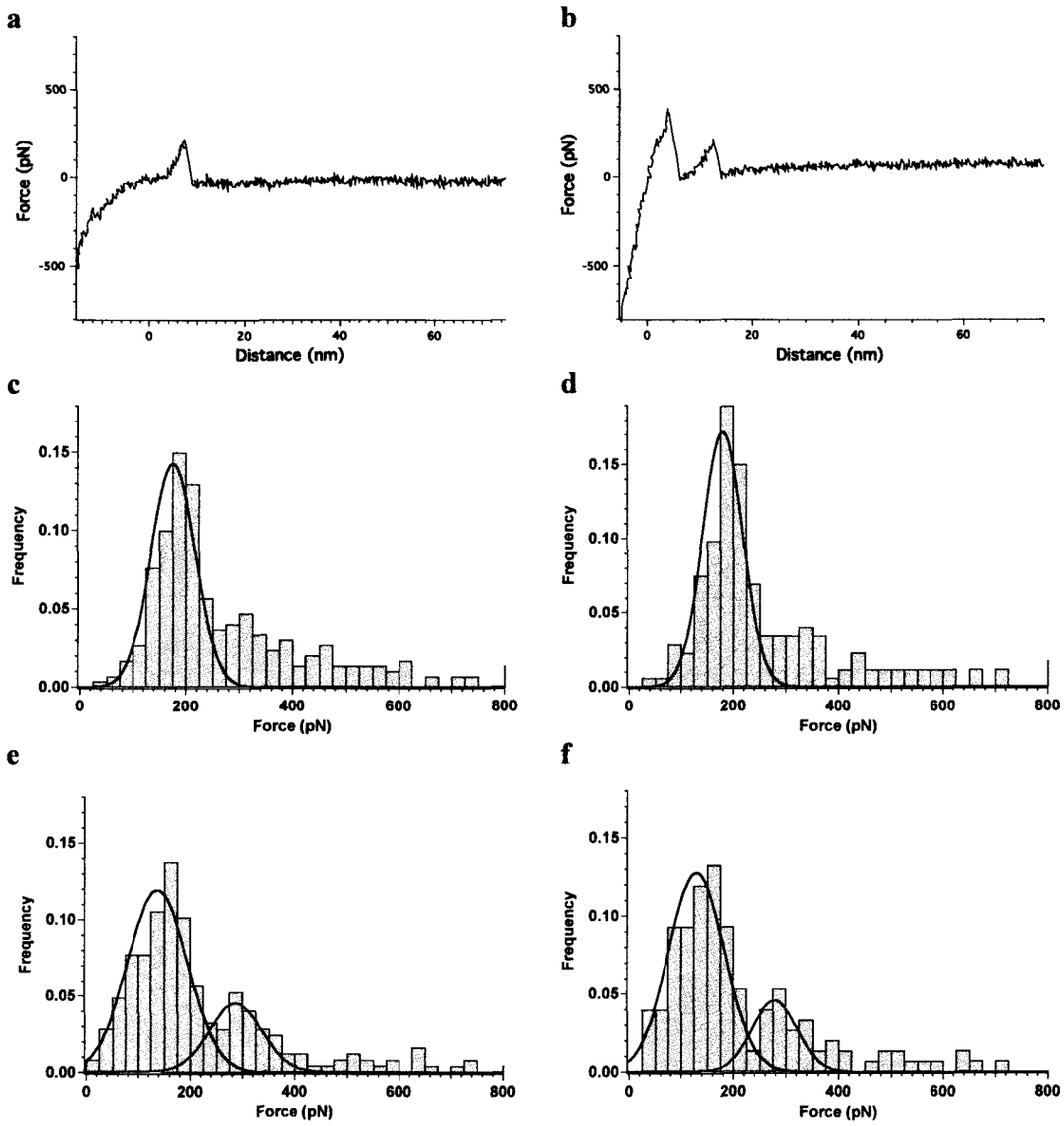

Figure 2-12. Representative force–distance curves with molecular tripod tip on NeutrAvidin-coated surface displaying (a) a single rupture event and (b) multimolecular events in one retraction. Histogram of (c) all forces and (d) only last forces. The most probable force of rupture for all the forces and in the only last forces is 176 pN and 180 pN, respectively. Another experiment with molecular tripod tip on NeutrAvidin with (e) a histogram of all forces having a most probable force of 137 pN (black line) and 288 pN (red line, respectively. (f) A histogram of only last forces detected showed a bimodal distribution centered at 140 and 293 pN. Loading rates for (c) and (e) were 1.0×10^5 and 8.0×10^4 pN/s, respectively.

In many force–distance curves, a large desorption force followed by multimolecular rupture events were observed before the last rupture event, which has a relatively small rupture force. As the AFM tip is retracted from the surface, the last detected interaction is most likely corresponded to the unbinding of biotin and the NeutrAvidin.[58] Therefore, we also extracted the rupture forces from only the last detected rupture events of each measurement. In Figure 2-12d, only the last force of each force–distance curve are plotted in the histogram. In the last force only histograms, the distribution is narrower because they correspond to single molecule interactions.

2.4.5 Force Spectroscopy Studies with Biotinylated Monopod B

Force spectroscopy experiments with molecular tip **B** with NeutrAvidin on agarose beads were performed in the same manner as those of the biotinylated tripod **A**. Force–distance curves were collected until 200 curves with minimal multimolecular events were obtained (between 500–600 cycles). Of the force–distance curves obtained, 38% had detectable rupture events. There is almost a 10% increase in rupture events compared to the biotinylated tripod **A** because of the increased density of ligands on the surface. A histogram of the rupture forces is shown in Figure 2-13b and the most probable rupture force for the biotinylated monopod **B** was 142 pN. The distribution of forces for the biotinylated monopod **B** is wider than that of the biotinylated tripod **A**. The second Gaussian fit is centered at 303 pN, twice the value of the single molecular rupture events. The broader distribution appears because there are more rupture events observed with the biotinylated monopod **B** below 100 pN. Similar to the analysis of the

biotinylated tripod **A** force spectroscopy data, a histogram of only the last rupture force is displayed in Figure 2-13. For molecular tip **B**, the histogram of only the last forces removes some nonspecific interactions, but does not clearly resolve a single molecule interaction as in the analysis of forces for molecular tip **A**.

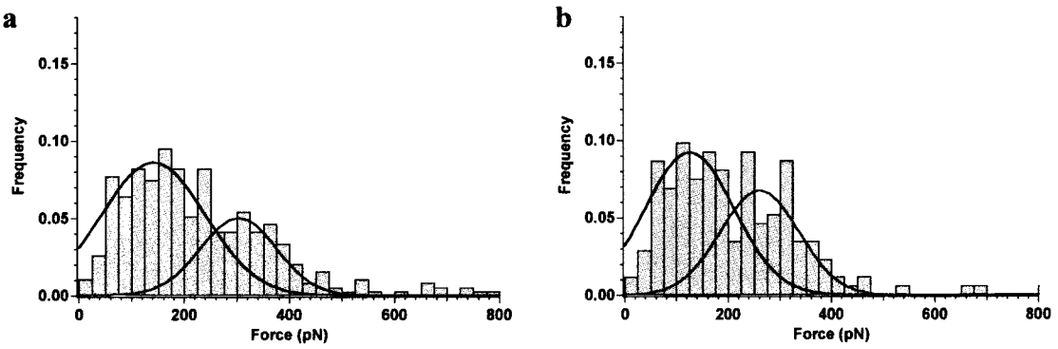

Figure 2-13. Histogram of rupture forces between the monopod molecular tip **B** and NeutrAvidin. Histogram of (a) all forces and (b) only last force. For (a), the most probable forces of rupture are 142 and 304 pN. For (b), the most probable forces of rupture are 125 and 262 pN. The loading rate was 8.0 x 10^4 pN/s.

2.4.6 Stability Test with Monopod B and Tripod A

Because hundreds of cycles are needed to provide the necessary statistical data for conclusive results in force spectroscopy experiments, it is expected that damage to the chemically modified AFM tip can occur during repeated measurements. Possibilities of damage include: mechanical wear,[59] oxidative cleavage of S–Au bond,[60] and exchange of the monolayer on the gold surface.[61] Thus, the robustness of the chemically modified AFM tip becomes essential to obtain reproducible results in force spectroscopy experiments. As described above, we hypothesized that the tripod tip **A**, which is bound

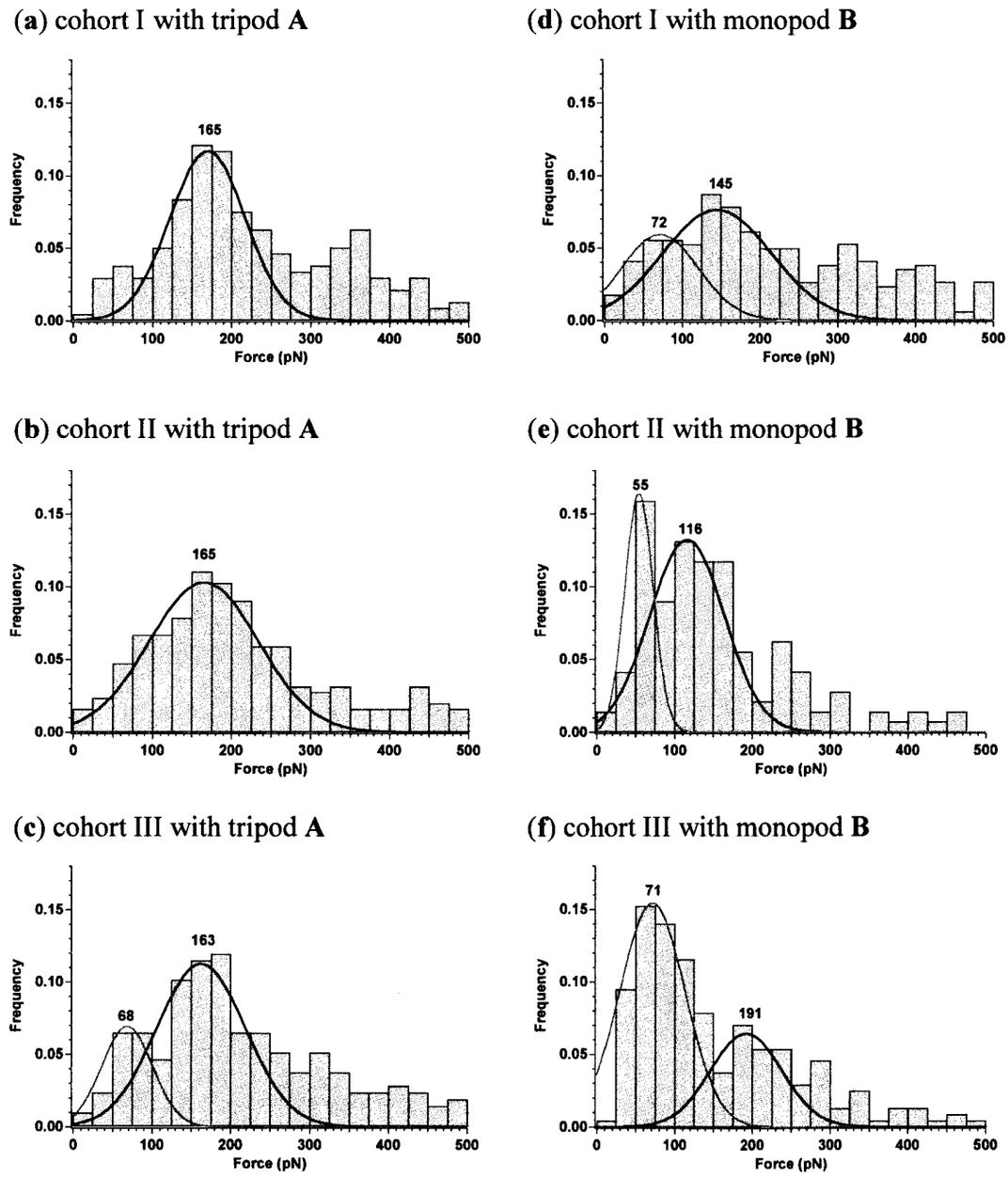

Figure 2-14. Investigation of the robustness of molecular tips. Histograms of forces showing the rupture events of 600 continuous cycles using a single AFM tip functionalized with tripod (a–c) or monopod (d–f). The 600 cycles were divided into three cohorts: cycles 1–200 (cohort I), cycles 201–401 (cohort II), cycles 401–600 (cohort III). The numbers at the center of each distribution are the most probable rupture force from the Gaussian fits to the data corresponding to the single molecule rupture events (black line) and the observed nonspecific rupture forces (green lines). The loading rates for **A** and **B** were 1.0×10^5 and 6.4×10^4 pN/s, respectively.

to the AFM tip through multiple points, could better withstand these stresses. This hypothesis was tested by comparing the robustness of the tripod **A** and the monopod **B** molecular tips. In each experiment, 600 continuous cycles were taken with molecular tripod and monopod tips and the measurements were divided into three cohorts (I–III). Cohort I included cycles 1–200; cohort II, 201–400; and cohort III, 401–600. The resulting rupture forces in each cohort were plotted in force histograms for the tripod **A** (Figure 2-14a–c) and monopod **B** (Figure 2-14d–f). The force measurements with an AFM tip functionalized with tripod **A** had a most probable force of rupture of 165 pN for all three cohorts. Only in cohort III did a small peak of lower force become apparent at 68 pN, which is indicative of nonspecific forces from a damaged monolayer or tip. In contrast, the histogram of forces with the monopod **B** shows significant variations in the most probable rupture force in the histograms. New forces occur prominently at lower rupture forces (50–80 pN), especially in cohort II and III. The appearance of these lower forces and their predominance in the force histograms can be attributed to a change in the surface properties of the tip. The shift toward smaller rupture forces is indicative of nonspecific forces that are unrelated to ligand–receptor rupture. A van der Waals or hydrophobic attraction between the partially damaged layer of organic molecules on the surface of the AFM tip and the NeutrAvidin-coated surface could cause this interaction. The tripod force histograms remain constant throughout the duration of the experiment because of the increased stability of tripod **A** on the gold surface.

2.4.7 Force Spectroscopy Studies with Biotinylated Tripod C

The longer PEG chain tripod **C** was used to examine the distance dependence of specific and nonspecific rupture events. The longer PEG chain should separate the nonspecific and specific forces better than both molecular tips **A** and **B**. The segment length of polyethylene glycol is 0.28–0.29 nm in water.[62,63] For the average PEG 2000 there are 44 repeat ethylene glycol units that give an extended PEG chain length of approximately 12 nm. The purchased PEG linker has a narrow weight distribution (PDI=1.05), which corresponds to a length distribution of 3.9 nm. In addition to investigating the magnitude of the rupture forces for molecular tip **C**, the distances where the rupture forces occurred were also analyzed. Using the pliant agarose beads, it remained difficult to discern the distance from the surface, but nonetheless the distance the rupture events occurred from the surface were examined. When the biotinylated molecular tripod **A** and monopod **B** were used in force spectroscopy experiments, there was an exponential decrease in the number of forces as the distance between the tip and the surface was increased. With the biotinylated PEG 2000 tripod there is a similar distribution, however the region between 0–10 nm can be eliminated from the rupture force analysis. The 0–10 nm region contains only nonspecific forces because if biotin has complexed with the NeutrAvidin, the linker has not reached full extension yet and the complex cannot have been ruptured at this distance. Being able to rule out forces by their position in the force–distance curve is a distinct advantage of using longer PEG linkers.

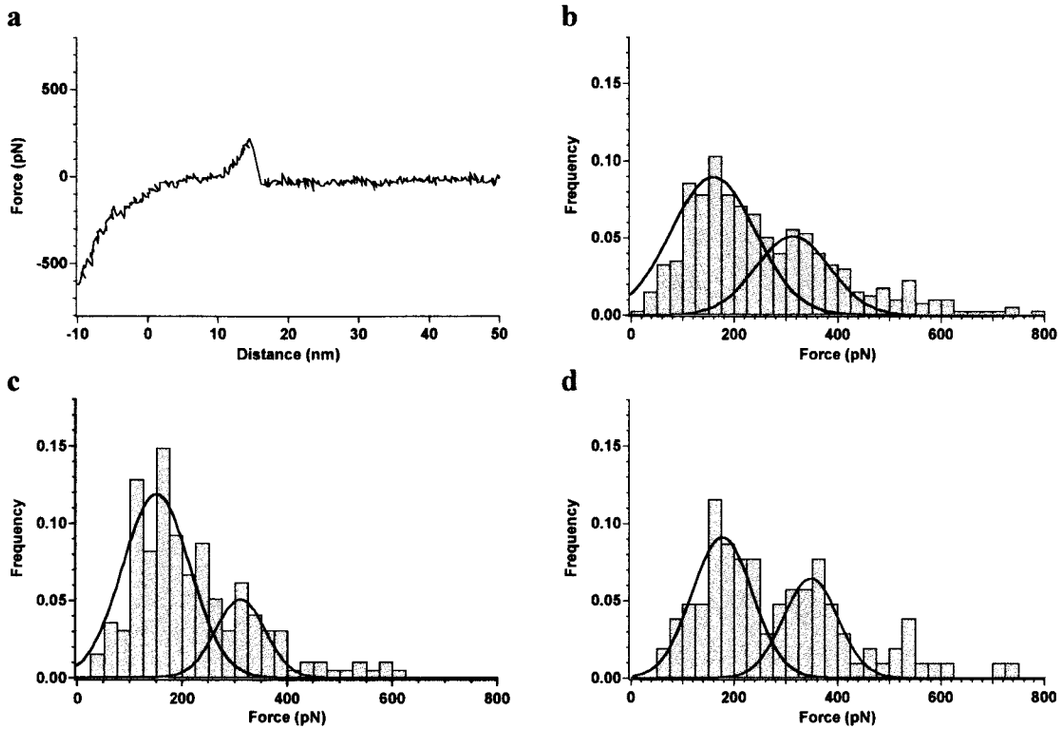

Figure 2-15. (a) Representative force–distance curve obtained with biotinylated tripod with a longer PEG linker. (b) Histogram of all forces. Most probable forces of rupture from the Gaussian fit of the first and second distribution are 160 pN and 314 pN. (c) Histogram of only last force with the most probable forces of rupture for the distributions at 150 and 312 pN. Because of the 12 nm length of the PEG linker, the distance 0–10 nm is unlikely to be from specific rupture events of the biotin–NeutrAvidin complex. (d) Histogram of forces at a distance between 10–20 nm only from each curve. Most probable forces of rupture from the Gaussian fit of the first and second distribution are 178 pN and 349 pN. The loading rate was 9.9 x 10^4 pN/s.

In Figure 2-15a, a representative single molecule force rupture event is shown with a rupture event 12 nm from the surface. A histogram of all forces is shown in Figure 2-15b for molecular tip **C** that has a most probable force at 160 and 314 pN for the single and double rupture events. When only the last forces are considered, the most probable forces are at 150 and 312 pN (Figure 2-15c). The histogram of last forces only appears similar to the histogram of all forces because of the reduced number of nonspecific ruptures produced by the longer PEG. With the longer linker, only rupture

forces between 10 and 20 nm were examined, and the resulting histogram of forces is plotted in Figure 2-15d. This histogram has a shifted distribution because it removes the some of lower magnitude, nonspecific forces and there is less overlap between the two Gaussian fits. It has most probable force of rupture values of 178 and 349 pN that correspond well with single and double rupture events.

2.4.8 Force Spectroscopy Control Experiments

To confirm that the observed force distribution peaks in the experiments with molecular tip **A** corresponds to the specific rupture of the biotin–NeutrAvidin complex, three control experiments were performed: (1) using an unfunctionalized AFM tip on a NeutrAvidin-coated surface, (2) using a functionalized AFM tip on agarose beads without NeutrAvidin, and (3) using a functionalized AFM tip with NeutrAvidin in the presence of excess free biotin.

The histograms of forces for the three control experiments are shown in Figure 2-16. There is no significant force maximum in any range of forces in all of the control experiments. There are few forces in control 1, and the measured rupture forces are spread evenly between 0–800 pN (Figure 2-16b). Although there are some rupture forces in the range of 50–250 pN in control experiment 2, the distribution was broad and there were relatively few rupture forces when compared to the experiment using a NeutrAvidin surface (Figure 2-16c). No rupture forces were detected in 80% of the measurements in control experiment 2, which corresponded to an average of 0.5 rupture

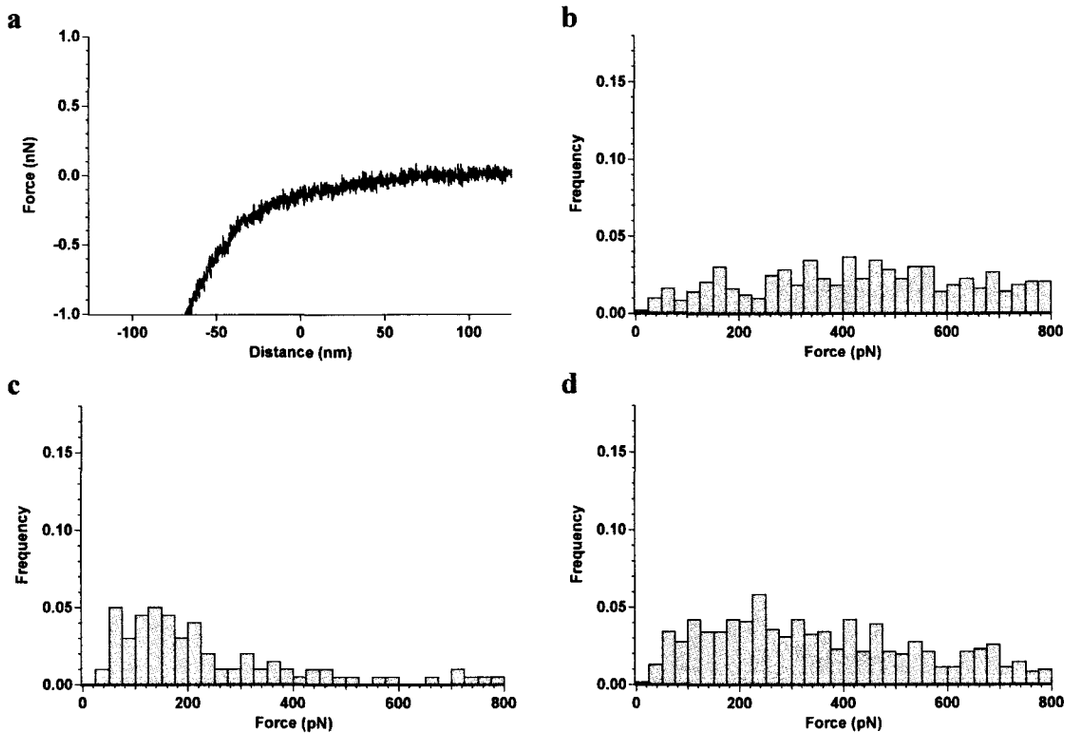

Figure 2-16. Control experiments. (a) Representative force–distance curve on an agarose bead without NeutrAvidin (b) control experiment using unmodified gold AFM tip on NeutrAvidin beads. (c) Biotinylated tripod **A** modified AFM tip on agarose beads without NeutrAvidin. (d) Modified AFM tip on the NeutrAvidin beads in the presence of excess biotin.

forces per measurement. For the third control, excess biotin was added to the buffer solution to quench any binding between the biotinylated AFM tip and the NeutrAvidin substrate (Figure 2-16d). In these experiments, there were multiple ruptures (3.2 per measurement on average) in each measurement, indicating there were many interactions between the modified AFM tip and the protein. Even though there were many forces in this control, the forces were spread evenly between 50–500 pN because the interactions were not specific to a molecular recognition event. These control experiments confirm that the distinct distribution of forces centered at 165 pN in the experiments with molecular tips **A**–**C** are specific to the rupture of a single biotin–NeutrAvidin complex.

2.4.9 Dynamic Force Spectroscopy

Early ligand–receptor systems were generally probed by single molecule force spectroscopy at a single loading rate, or the rate at which the force was applied.[45] Later studies used multiple loading rates—hence the term dynamic force spectroscopy—to probe the energy landscape of the ligand–receptor binding.[56,64] For example, dynamic force spectroscopy was used to estimate the equilibrium dissociation constants K_D of vancomycin and D-Ala-D-Ala.[65] The dissociation kinetic rate constant (k_{off}) were obtained by measuring the trend in the most probable force of rupture at different loading rates and extrapolating to zero force. The association kinetic rate constant (k_{on}) of the complexation was obtained by examining the probability of complex formation as a function of time. By varying the time the AFM tip was in contact with the surface, the time needed for half-maximal probability of binding was used to calculate a half-life of bond formation. The value for the equilibrium dissociation constant ($K_D = k_{off}/k_{on}$) was calculated to be three orders of magnitude higher in the AFM force spectroscopy studies than the constant measured either on a surface or in solution.[66] The enthalpic contribution to the ligand–receptor dissociation[46] is directly proportional to the most probable rupture force for the biotin–avidin system. However, the free energy of dissociation, ΔG, does not correlate well because the entropic term is different in force spectroscopy experiments than in bulk solution methods. Because the ligand is generally tethered to the AFM tip and the receptor is immobilized to a generally planar surface, there is a difference in the entropic term of binding and dissociation. Another contribution to the inaccurate K_D is the steric interactions introduced by the short linker.

The most probable rupture force of a ligand–receptor complex depends on several factors including pH, temperature, and loading rate. To probe the energy landscape of the system, an easily modified variable is the loading rate, or the rate at which force is applied, (measured in pN/s). In AFM force spectroscopy, the loading rate is obtained by multiplying the spring constant of the modified cantilever by the velocity of the tip.[65] The dependence on the loading rate can be measured by varying the speed of the AFM tip by several orders of magnitude.

Based on the Bell model of surface adhesion, the dissociation constant k:[67]

$$k(f) = k_d \exp\left(\frac{f x_\beta}{k_B T}\right)$$

where f is the applied external force, x_β is the distance between the bound intermediate and the transition state barrier, r is loading rate, k_B is the Boltzmann constant, T is absolute temperature, k_d is the thermal dissociation rate with no applied force. From the above equation it can be been derived that:[68]

$$F^* = \frac{k_B T}{x_\beta} \ln\left(\frac{r x_\beta}{k_d k_B T}\right)$$

This equation implies that for a ligand–receptor system the most probable force of rupture will be dependent on the logarithm of the loading rate.

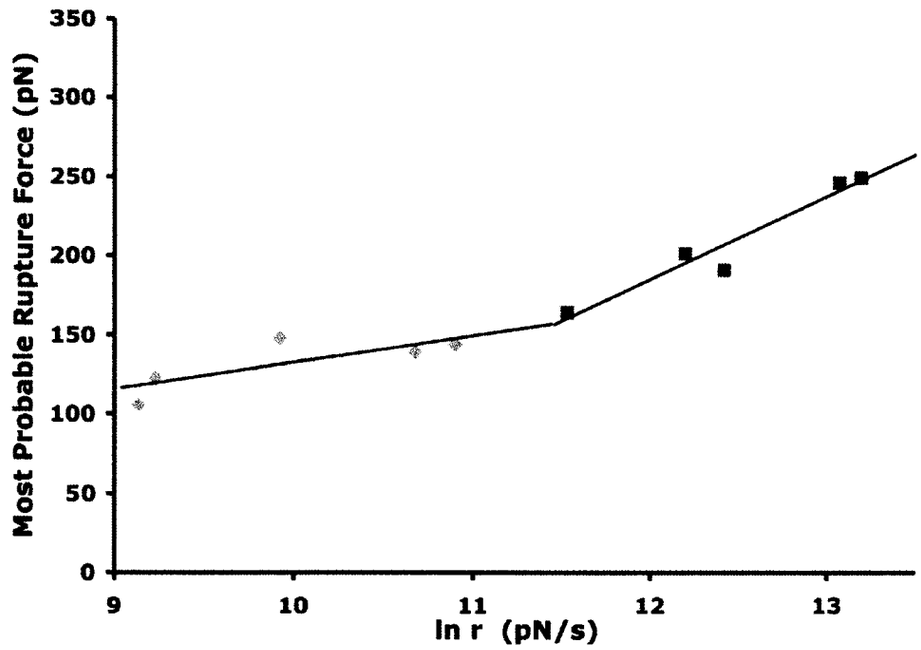

Figure 2-17. The most probable rupture force for the biotin–NeutrAvidin pair as a function of loading rate.

A plot of the F* versus the natural logarithm of the loading rate gave two regimes, one at lower rates 10^4–10^5 pN/s and one above 10^5 pN/s (Figure 2-17). The two separate regimes are attributed to two different barriers in the unbinding of the biotin–NeutrAvidin pair.[69] Previous studies on the loading rate of the biotin–avidin pair system also showed two regimes when the loading rate was varied.[56,64] The trend in F* obtained for the different loading rates was similar to the previous reports for avidin and streptavidin, two slightly different proteins than the NeutrAvidin used in the experiments. The loading rate dependence of the most probable rupture force further demonstrates that the observed forces are specific to the rupture of the biotin–NeutrAvidin complex.

2.4.10 Summary of Force Spectroscopy Experiments

Molecular tips **A**–**C** were immobilized onto gold AFM tips for single molecule force spectroscopy measurements. The biotinylated tips **A**–**C** had most probable rupture forces of 176, 142, and 160 pN, respectively. The distribution in the histogram of forces for monopod **B** was wider than both molecular tips **A** and **C**. Tripod **A** and monopod **B** were examined for deterioration of the specific interaction through multiple observations. Over 600 measurements, monopod **B** had shifts of forces towards lower, nonspecific interactions. However, the distribution of forces for the tripod molecular tip **A** maintained constant throughout all 600 measurements, which indicates that molecular tip **A** provides a robust modification for gold AFM tips. With tripod molecular tip **C**, the rupture forces were also analyzed by the distance they occurred from the surface. This analysis led to easier identification of specific rupture events. By varying the AFM tip velocity, the dependence of the most probable force of rupture with loading rate was studied. Increasing the loading rate resulted in an increase in the most probable force of rupture, which agrees with previous reports. Moreover, control experiments indicate that the rupture forces between 160–180 pN are specific to the rupture of biotin–NeutrAvidin complex.

References:

(1) Yao, Y.; Tour, J. M.; "Facile Route to Molecular Caltrops" *J. Org. Chem.* **1999**, *64*, 1968–1971.

(2) (a) Li, Q.; Rukavishnikov, A. V.; Petukhov, P. A.; Zaikova, T. O.; Keana, J. F. W. "Nanoscale 1,3,5,7-Tetrasubstituted Adamantanes and *p*-Substituted Tetraphenyl-Methanes for AFM Applications" *Org. Lett.* **2002**, *4*, 3631–3634. (b) Li, Q.; Rukavishnikov, A. V.; Petukhov, P. A.; Zaikova, T. O.; Jin, C.; Keana, J. F. W. "Nanoscale Tripodal 1,3,5,7-Tetrasubstituted Adamantanes for AFM Applications" *J. Org. Chem.* **2003**, *68*, 4862–4869. (c) Li, Q.; Jin, C.; Petukhov, P. A.; Rukavishnikov, A. V.; Zaikova, T. O.; Phadke, A.; LaMunyon, D. H.; Lee, M. D.; Keana, J. F. W. "Synthesis of Well-Defined Tower-Shaped 1,3,5-Trisubstituted Adamantanes Incorporating a Macrocyclic Trilactam Ring System" *J. Org. Chem.* **2004**, *69,* 1010–1019.

(3) Takamatsu, D.; Yamakoshi, Y.; Fukui, K. "Photoswitching Behavior of a Novel Single Molecular Tip for Noncontact Atomic Force Microscopy Designed for Chemical Identification" *J. Phys. Chem. B* **2006**, *110*, 1968–1970.

(4) (a) Rostovtsev, V. V.; Green, L. G.; Fokin, V. V.; Sharpless, K. B. "A Stepwise Huisgen Cycloaddition Process: Copper (I)-Catalyzed Regioselective Ligation of Azides and Terminal Alkynes" *Angew. Chem. Int. Ed.* **2002**, *114*, 2708–2711. (b) Tornoe, C. W.; Christensen, C.; Meldal, M. "Peptidotriazoles on solid phase: [1, 2,3]-Triazoles by Regiospecific Copper (I)-Catalyzed 1,3-Dipolar Cycloadditions of Terminal Alkynes to Azides" *J. Org. Chem.* **2002**, *67*, 3057–3064.

(5) Hiller, Y.; Gershoni, J. M.; Bayer, E. A.; Wilchek, M. "Biotin Binding to Avidin. Oligosaccharide Side Chain Not Required for Ligand Association" *Biochem. J.* **1987**, *248*, 167–171.

(6) Reichert, V. R.; Mathias, L. J. "Expanded Tetrahedral Molecules from 1,3,5,7-Tetraphenyladamantane" *Macromolecules* **1994**, *27*, 7015–7023.

(7) Schwabacher, A. W.; Lane, J. W.; Schiesher, M. W.; Leigh, K. M.; Johnson, C. W. "Desymmetrization Reactions: Efficient Preparation of Unsymmetrically Substituted Linker Molecules" *J. Org. Chem.* **1998**, *63*, 1727–1729.

(8) Porter, M. D.; Bright, T. B.; Allara, D. L.; Chidsey, C. E. D. "Spontaneously Organized Molecular Assemblies. 4. Structural Characterization of *n*-Alkyl Thiol Monolayers on Gold by Optical Ellipsometry, Infrared Spectroscopy, and Electrochemistry" *J. Am. Chem. Soc.* **1987**, *109*, 3559–3568.

(9) Nelson, K. E.; Gamble, L.; Jung, L. S.; Boeckl, M. S.; Naeemi, E.; Golledge, S. L.; Sasaki, T.; Castner, D. G.; Campbell, C. T.; Stayton, P. S. "Surface Characterization of Mixed Self-Assembled Monolayers Designed for Streptavidin Immobilization" *Langmuir* **2001**, 2807–2816.

(10) Shumaker-Perry, J. S.; Zareie, M. H.; Aebersold, R.; Campbell, C. T. "Microspotting Streptavidin and Double-Stranded DNA Arrays on Gold for High-Throughput Studies of Protein–DNA Interactions by Surface Plasmon Resonance Microscopy" *Anal. Chem.* **2004**, *76*, 918–929.

(11) Riener, C. K.; Kienberger, F.; Hahn, C. D.; Buchinger, G. M.; Egwim, I. O. C.; Haselgrübler, T.; Ebner, A.; Romanin, C.; Klampfl, C.; Lackner, B.; Prinz, H.; Blaas, D.; Hinterdorfer, P.; Gruber, H. J. "Heterobifunctional Crosslinkers for Tethering Single Ligand Molecules to Scanning Probes" *Anal. Chim. Acta* **2003**, *497*, 101–114.

(12) (a) Hinterdorfer, P.; Baumgartner, W.; Gruber, H. J.; Schilcher, K.; Schindler, H. "Detection and Localization of Individual Antibody–Antigen Recognition Events by Atomic Force Microscopy" *Proc. Natl. Acad. Sci.* **1996**, *93*, 3477–3481. (b) Haselgrübler, T.; Amerstorfer, A.; Schindler, H.; Gruber, H. J. "Synthesis and Applications of a New Poly(ethylene glycol) Derivative for the Crosslinking of Amines with Thiols" *Bioconj. Chem.* **1995**, *6*, 242–248.

(13) Ros, R.; Schwesinger, F.; Anselmetti, D.; Kubon, M.; Schäfer, R.; Plückthun, A.; Tiefennauer, L. "Antigen Binding Forces of Individually Addressed Single-Chain Fv Antibody Molecules" *Proc. Natl. Acad. Sci.* **1998**, *95*, 7402–7405.

(14) Ron, H.; Matlis, S.; Rubinstein, I. "Self-Assembled Monolayers on Oxidized Metals. 2. Gold Surface Oxidative Pretreatment, Monolayer Properties, and Depression Formation" *Langmuir*, **1998**, *14*, 1116–1121.

(15) Kolb, D. M. "Reconstruction Phenomena at Metal-Electrolyte Interfaces" *Prog. Surf. Sci.* **1996**, *51*, 109–173.

(16) Agilent Technologies (Santa Clara, CA). "Hydogen Flame-Annealing"

(17) Lauer, M. E.; Jungmann, R.; Kindt, J. H.; Magonov, S.; Fuhrhop, J.-H.; Oroudjev, E.; Hansma, H. G. "Formation and Healing of Micrometer-Sized Channel Networks on Highly Mobile Au(111) Surfaces" *Langmuir* **2007**, *23*, 5459–5465.

(18) Humlícek, J. Polarized Light and Ellipsometry. In *Handbook of Ellipsometry*. Tompkins, H. G.; Irene, E. A., Eds. William Andrew Publishing/Noyes: Norwich, New York, 2005; 1–19.

(19) Casson, B. D.; Bain, C. D. "Determination of the Optical Properties of Monolayers on Water" *Langmuir* **1997**, *13*, 5465–5469.

(20) de Boer, B.; Meng, H.; Perepichka, D. F.; Zheng, J.; Frank, M. M.; Chabal, Y. J.; Bao, Z. "Synthesis and Characterization of Conjugated Mono- and Dithiol Oligomers and Characterization of Their Self-Assembled Monolyars" *Langmuir* **2003**, *19*, 4272–4284.

(21) Kang, J. F.; Ulman, A.; Liao, S.; Jordan, R.; Yang, G.; Liu, G. "4'-Substituted-4-Mercaptobiphenyls on Gold and Silver Surfaces" *Langmuir* **2001**, *17*, 95–106.

(22) Hacker, C. A.; Batteas, J. D.; Garno, J. C.; Marquez, M.; Richter, C. A.; Richter, L. J.; van Zee, R. D.; Zangmeister, C. D. "Sturctural and Chemical Characterization of Monofluoro-Substituted Oligo(phenylene–ethynylene) Thiolate Self-Assembled Monolayers on Gold" *Langmuir* **2004**, *20*, 6195–6205.

(23) Nilsson, D.; Watcharinyanon, S.; Eng, M.; Li, L.; Moons, E.; Johansson, L. S. O.; Zharnikov, M.; Shaporenko, A.; Albinsson, B.; Mårtensson, J. "Characterization of Self-Assembled Monolayers of Oligo(phenyleneethynylene) Derivatives of Varying Shapes on Gold: Effect of Laterally Extended π-Systems" *Langmuir* **2007**, *23*, 6170–6181.

(24) Molecular tips **A**–**C** and the alkyne-terminated tripod were minimized using the Amber* calculation in Macromodel.

(25) Bradford, D. C.; Hutter, E.; Fendler, J. H.; Roy, D. "Surface-Enhanced Infrared Ellipsometry of Self-Assembled Undecane Thiol and Dodecanethiol Monolayers on Disordered Gold Nanoisland Substrates" *J. Phys. Chem. B* **2005**, *109*, 20914–20922.

(26) Laibinis, P. E.; Whitesides, G. M.; Allara, D. L.; Tao, Y.-T.; Parikh, A. N.; Nuzzo, R.G. "Comparison of the Structures and Wetting Properties of Self-Assembled Monolayers of *n*-Alkanethiols on the Coinage Metal Surfaces, Cu, Ag, Au" *J. Am. Chem. Soc.* **1991**, *113*, 7152–7167.

(27) Nishi, N.; Hobara, D.; Yamamoto, M.; Kakiuchi, T. "Chain-Length-Dependent Change in the Structure of Self-Assembled Monolayers of *n*-Alkanethiols on Au(111) Probed by Broad-Bandwidth Sum Frequency Generation Spectroscopy" *J. Chem. Phys.* **2003**, *118*, 1904–1911.

(28) Harris, A. L.; Chidsey, C. E. D.; Levinos, N. J.; Loiacono, D. N. "Monolayer Vibrational Spectroscopy by Infrared-Visible Sum Generation at Metal and Semiconductor Surfaces" *Chem. Phys. Lett.* **1987**, *141*, 350–356.

(29) Bertin, P. A.; Georganopoulou, D.; Liang, T.; Eckermann, A. L.; Wunder, M.; Ahrens, M. J.; Blackburn, G. F.; Meade, T. J. "Electroactive Self-Assembled Monolayers on Gold via Bipodal Dithiazepane Anchoring Groups" *Langmuir* **2008**, *24*, 9096–9101.

(30) Nikitin, K.; Lestini, E.; Lazzari, M.; Altobello, S.; Fitzmaurice, D. "A Tripodal [2]Rotaxane on the Surface of Gold" *Langmuir* **2007**, *23*, 12147–12153.

(31) Jackson, F.; Weisstein, E. W. "Tetrahedron" From MathWorld—A Wolfram Web Resource: http://mathworld.wolfram.com/Tetrahedron.html. (accessed Dec 9, 2009).

(32) Takahashi, Y.; Tadokoro, H. "Structural Studies of Polyethers, (–(CH_2)*m*–O–)*n* Crystal Structure of Poly(ethylene oxide)" *Macromolecules* **1973**, *6*, 672–675.

(33) Zwahlen, M.; Herrwerth, S.; Eck, W.; Grunze, M.; Hähner, G. "Conformational Order in Oligo(ethylene glycol)-Terminated Self-Assembled Monolayers on Gold Determined by Soft X-Ray Absorption" *Langmuir* **2003**, *19*, 9305–9310.

(34) Stöhr, J. *NEXAFS Spectroscopy*; Gomer, R., Ed.; Springer Series in Surface Sciences Vol. 25; Springer-Verlag: New York, 1992.

(35) Bagus, P.; Weiss, K.; Schertel, A.; Wöll, C.; Braun, W.; Hellwig, C.; Jung, C. "Identification of Transitions into Rydberg States in the X-ray Absorption Spectra of Condensed Long-Chain Alkanes" *Chem. Phys. Lett.* **1996**, *248*, 129–135.

(36) Urquhart, S. G.; Hitchcock, A. P.; Priester, R. D.; Rightor, E. G. "Analysis of Polyurethanes Using Core Excitation Spectroscopy. Part II: Inner Shell Spectra of Ether, Urea, and Carbamate Model Compounds" *J. Polym. Sci., Part B: Polym. Phys.* **1995**, *33*, 1603–1620.

(37) Guay, D.; Stewart-Ornstein, J.; Zhang, X.; Hitchcock, A. P. "In Situ Spatial and Time-Resolved Studies of Electrochemical Reactions by Scanning Transmission X-ray Microscopy" *Anal. Chem.* **2005**, *77*, 3479–3487.

(38) Gordon, M. L.; Cooper, G.; Morin, C.; Araki, T.; Turci, C. C.; Kaznatcheev, K.; Hitchcock, A. P. "Inner-Shell Excitation Spectroscopy of the Peptide Bond: Comparison of the C 1s, N 1s, and O 1s Spectra of Glycine, Glycyl-Glycine, and Glycyl-Glycyl-Glycine" *J. Phys. Chem. A* **2003**, *107*, 6144–6159.

(39) Walsh, J. F.; Dhariwal, H. S.; Gutiérrez-Sosa, A.; Finetti, P.; Muryn, C. A.; Brookes, N. B.; Oldman, R. J.; Thornton, G. "Probing Molecular Orientation in Corrosion Inhibition via a NEXAFS Study of Benzotriazole and Related Molecules on Cu (100)" *Surf. Sci.* **1998**, *415*, 423–432.

(40) Stöhr, J.; Jaeger, R. "Absorption-Edge Resonances, Core-Hole Screening, and Orientation of Chemisorbed Molecules: CO, NO, and N_2 on Ni (100) *Phys. Rev. B* **1982**, *26*, 4111–4131.

(41) Liu, X.; Jang, C.-H.; Zheng, F.; Jürgensen, A.; Denlinger, J. D.; Dickson, K. A.; Raines, R. T.; Abbot, N. L.; Himpsel, F. J. "Characterization of Protein Immobilization at Silver Surfaces by Near Edge X-ray Absorption Fine Spectroscopy" *Langmuir* **2006**, *22*, 7719–7725.

(42) Heister, K.; Zharnikov, M.; Grunze, M. "Characterization of X-ray Induced Damage in Alkanethiolate Monolayers by High-Resolution Photoelectron Spectroscopy" *Langmuir* **2001**, *17*, 8–11.

(43) Sakata, T.; Maruyama, S.; Ueda, A.; Otsuka, H.; Miyahara, Y. "Stable Immobilization of an Oligonucleotide Probe on a Gold Substrate Using Tripodal Thiol Derivatives" *Langmuir* **2007**, *23*, 2269–2272.

(44) Smith, T. "The Hydrophilic Nature of a Clean Gold Surface" *J. Colloid Interface Sci.* **1980**, *75*, 51–55.

(45) Florin, E.-L., Moy, V. T.; Gaub, H. E. "Adhesion Forces Between Individual Ligand–Receptor Pairs" *Science* **1994**, *264*, 415–417

(46) Moy, V. T.; Florin, E.-L.; Gaub, H. E. "Intermolecular Forces and Energies Between Ligands and Receptors" *Science* **1994**, *266*, 257–259.

(47) Lo, Y.-S.; Huefner, N. D.; Chan, W. S.; Dryden, P.; Hagenhoff, B.; Beebe, Jr., T. P. "Organic and Inorganic Contamination on Commercial AFM Cantilevers" *Langmuir*, **1999**, *15*, 6522–6526.

(48) Bonaccurso, E.; Gillies, G. "Revealing Contamination on AFM Cantilevers by Microdrops and Microbubbles" *Langmuir* **2004**, *20*, 11824–11827.

(49) Ebner, A.; Wildling, L.; Zhu, R.; Rankl, C.; Haselgrübler, T.; Hinterdorfer, P. Gruber, H. J. "Functionalization of Probe Tips and Supports for Single-Molecule Recognition Force Microscopy" *Top. Curr. Chem.* **2008**, *285*, 29–76.

(50) Fujijira, M.; Okabe, Y.; Tani, Y.; Furugori, M.; Akiba, U. "A Novel Cleaning Method of Gold-Coated Atomic Force Microscope Tips for Their Chemical Modification" *Ultramicroscopy* **2000**, *82*, 181–191.

(51) (a) Tang, J.; Ebner, A.; Badelt-Lichtblau, H.; Völlenkle, C.; Rankl, C.; Kraxberger, B.; Leitner, M.; Wildling, L.; Gruber, H. J.; Sleytr, U. B.; Hinterdorfer, P. "Recognition Imaging and Highly Ordered Molecular Templating of Bacterial S-Layer Nanoarrays Containing Affinity-Tags" *Nano Lett.* **2008**, *8*, 4312–4319. (b) Touhami, A.; Hoffmann, B.; Vasella, A.; Denis, F.; Dufrêne, Y. F. "Aggregation of Yeast Cells: Direct Measurement of Discrete Lectin–Carbohydrate Interactions" *Microbiology* **2003**, *149*, 2873–2878.

(52) Brogan, K. L.; Shin, J. H.; Schoenfisch, M. H. "Influence of Surfactants, and Antibody Immobilization Strategy on Reducing Nonspecific Protein Interactions for Molecular Recognition Force Microscopy" *Langmuir* **2004**, *20*, 9729–9735.

(53) Allen, S.; Chen, X.; Davies, J.; Davies, M. C.; Dawkes, A. C.; Edwards, J. C.; Roberts, C. J.; Sefton, J.; Tendler, S. J.; Williams, P. M. "Detection of Antigen–Antibody Binding Events with the Atomic Force Microscope" *Biochemistry* **1997**, *36*, 7457–7463.

(54) Stroh, C.; Wang, H.; Bash, R.; Ashcroft, B.; Nelson, J.; Gruber, H.; Lohr, D.; Lindsay, S. M.; Hinterdorfer, P. "Single-Molecule Recognition Imaging Microscopy" *Proc. Nat. Acad. Sci.* **2004**, *101*, 12503–12507.

(55) Yadavalli, V. K.; Forbes, J. G.; Wang, K. "Functionalized Self-Assembled Monolayers on Ultraflat Gold as Platforms for Single Molecule Force Spectroscopy and Imaging" *Langmuir* **2006**, *22*, 6969–6976.

(56) Merkel, R.; Nassoy, P.; Leung, A.; Ritchie, K.; Evans, E. "Energy Landscapes of Receptor–Ligand Bonds Explored with Dynamic Force Spectroscopy" *Nature* **1999**, *397*, 50–53.

(57) Hutter, J. L.; Bechhoefer, J. "Calibration of Atomic Force Microscope Tips" *Rev. Sci. Instr.* **1993**, *64,* 1868–1873.

(58) Fantner, G.E.; Oroudjev, E.; Schitter, G.; Golde, L. S.; Thurner, P.; Finch, M. M.; Turner, P.; Gutsmann, T.; Morse, D. E.; Hansma, H.; Hansma, P. K. "Sacrificial Bonds and Hidden Length: Unraveling Molecular Mesostructures in Tough Materials" *Biophys. J.* **2006**, *90*, 1411–1418.

(59) Peng, L.; Lee, H.; Teizer, W.; Liang, H. "Nanowear of Gold and Silver Against Silicon" *Wear* **2009**, *267*, 1177–1180.

(60) Schoenfisch, M. H.; Pemberton, J. E. "Air Stability of Alkane thiol Self-Assembled Monolayers on Silver and Gold Surfaces" *J. Am. Chem. Soc.* **1998**, *120*, 4502–4513.

(61) Schlenoff, J. B.; Li, M.; Ly, H. "Stability and Self-Exchange in Alkane Thiol Monolayers" *J. Am. Chem. Soc.* **1995**, *117*, 12528–12536.

(62) Zdyrko, B.; Varshney, S. K.; Luzinov, I. "Effect of Molecular Weight on Synthesis and Surface Morphology of High-Density Poly(ethylene glycol) Grafted Layers" *Langmuir*, **2004**, *20*, 6727–6735.

(63) Oesterhelt, F.; Rief, M.; Gaub, H. E. "Single Molecule Force Spectroscopy by AFM Indicates Helical Structure of Poly(ethylene-glycol) in Water" *New J. Phys.* **1999**, *1*, 6.1–6.11.

(64) Lo, Y.-S.; Zhu, Y.-J.; Beebe Jr., T. P. "Loading-Rate Dependence of Individual Ligand-Receptor Forces Studied by Atomic Force Microscopy" *Langmuir* **2001**, *17*, 3741–3748.

(65) Gilbert, Y.; Deghorain, M.; Wang, L.; Xu, B.; Polheimer, P. D.; Gruber, H. J.; Errington, J.; Hallet, B.; Haulot, X.; Verbelen, C.; Hols, P.; Dufrêne, Y. F. "Single-Molecule Force Spectroscopy and Imaging of the Vancomycin/D-Ala-D-Ala Interaction" *Nano Lett.***2007**, *7*, 796–801.

(66) Lahiri, J.; Isaacs, L.; Tien, J.; Whitesides, G. M. "A Strategy for the Generation of Surfaces Presenting Ligands for Studies of Binding Based on an Active Ester as a Common Reactive Intermediate: A Surface Plasmon Resonance Study" *Anal. Chem.* **1999**, *71*, 777–790.

(67) Bell, G. I. "Models for the Specific Adhesion of Cells to Cells" *Science* **1978**, *200*, 618–627.

(68) Strunz, T. Oroszlan, K., Schumakovitch, I., Güntherodt, H.-J., Hegner, M. "Model Energy Landscapes for the Force-Induced Dissociation of Ligand-Receptor Bonds" *Biophys. J.* **2000**, *79*, 1206–1212.

(69) Yuan, C.; Chen, A.; Kolb, P.; Moy, V. T. "Energy Landscape of Streptavidin–Biotin Complexes Measured by Atomic Force Microscopy" *Biochemistry* **2000**, *39*, 10219–10223.

Chapter 3 Functionalization of Nanocrystalline Diamond AFM Tips and Their Application Toward Nanolithography

3.1. Background and Introduction

3.1.1 Structure and Properties of Nanocrystalline Diamond

Diamond has long been a material of interest to scientists. Based on its refractive index, Isaac Newton proposed that diamond is an organic material.[1] In 1772, Antoine Lavoisier found the combustion product of diamond was carbon dioxide.[2] Smithson Tennant later found that coal, graphite, and diamond produced the same gaseous byproduct.[3] Diamond was first discovered to be a covalent crystal of carbon in 1813 by Humphrey Davy[4] and the x-ray experiments by William Henry and William Lawrence Bragg confirmed the face centered cubic unit cell of diamond.[5]

The strong C–C bonds that give diamond its chemical structure also give diamond extraordinary physical properties. Diamond has an extremely high Young's modulus (1050–1200 GPa) and has the highest hardness and thermal conductivity of known materials. It has a hole mobility that is higher than Si and is only surpassed by germanium and indium antimonide, which both have poor dielectric strength.[6] In addition, it has a low coefficient of friction. These properties combine to give diamond high desirability for a variety of applications including biosensing electrodes to coatings for microelectronicmechanical sensors (MEMS) and nanometer probes.

Because of diamond's amazing properties listed above, it has long been regarded as a material of synthetic interest. But only since the middle of the 20th century has it

been possible to synthesize diamond. Two distinct methods have been created to prepare diamond: a high pressure–high temperature method and a low pressure–high temperature methods through chemical vapor deposition (CVD). The high pressure–high temperature method uses the characteristic phase properties of carbon to convert from the thermodynamically stable graphite to diamond. The main difficulty in achieving diamond by this method was to create pressure and temperature at a high enough magnitude. Howard Tracy Hall and the high pressure diamond research group at General Electric were the first to grow synthetic diamonds from graphite in 1954 using an apparatus that could simultaneously reach three million pounds per square inch and 5000 °C.[7] Soon thereafter, DeCarli and Jamieson produced diamond particles that were 1–50 μm in diameter by a shock-wave method at DuPont.[8]

The low pressure–high temperature techniques such as CVD generally produce films of diamond on a solid substrate. CVD has several fundamental steps: (1) the transport of reactive gaseous species to the surface, (2) the adsorption of reactant species to the surface, (3) the heterogeneous surface reaction catalyzed by the surface, (4) the surface diffusion of species to growth sites, (5) the nucleation and growth of the film, and (6) the desorption of gaseous reaction products away from the surface.[9] Changing the parameters such as temperature, pressure, and gas composition controls the grain size of the diamond. Pressures used are generally between 10–100 Torr with an atmosphere of 95–99% H_2. The remaining composition of the mixture includes inert gases (N_2 or Ar) and a carbon carrier (generally CH_4). Diamond is easily deposited by homoepitaxial growth, the growth on diamond surfaces. In contrast, heteroepitaxial growth, the growth on a different substrate, is too slow for practical use without seeding the substrate. By

seeding substrates, diamond has been deposited on variety of non-diamond substrates that include metals, semiconductors, and insulators. Examples of substrates include: Mo, W, WC, Ta, Cr, Co, Cu, Al, Au, Pt, Ni, Fe, stainless steel, Si, SiC, Si_3N_4, Ti, TiC, TiN, silica, MgO, Al_2O_3, and $YZrO_2$.[10] Among these materials, Si is the most commonly used substrate in diamond CVD.

There are three parts of diamond film preparation: pretreatment of the substrate, diamond growth, and hydrogen-termination (H-termination). Pretreatment of the substrate surface enables a practical rate of diamond growth. The pretreatment methods include scratching, chemical etching, electrical biasing, and seeding with diamond particles. For instance, sonication in the presence of a suspension of diamond particles encourages diamond growth by creating nucleation sites on the surface. The seed layer reduces the incubation period, the time required before diamond growth begins. The density of the seed layer affects the thickness, crystallite size, homogeneity, morphology, adhesion, and surface roughness of the diamond film.[11]

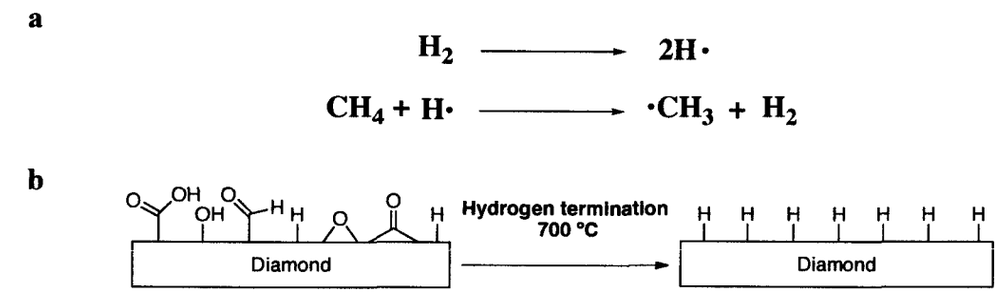

Figure 3-1. The chemistry of hot filament CVD. (a) Dissociation of molecular hydrogen leads to hydrogen atom abstraction from methane to produce the methyl radical that is responsible for diamond growth. (b) Hydrogen termination of a diamond surface effectively removes oxygen species and creates C–H bonds at the interface.

Hot filament CVD (HFCVD) is a common method for growing thin diamond films. Matsumoto *et al.* initially reported the deposition of microcrystalline diamond on silicon and molybdenum substrates using HFCVD.[12] HFCVD has the advantages of low cost, simplicity, ease of scaling, and the capability of forming quality, uniform films over large areas. Films can be grown at a rate of 0.3–40 μm/h on areas as large as 100–400 cm^2.[13] Two disadvantages in this technique are the long-term stability of the metal filament and the possibility of the deposition of metal contaminants.[14] For the choice of metal filament used, the chemical and mechanical stability of the metal and the possible incorporation of the metal into the growing diamond film must be considered.[15] Tungsten filaments form a stable carbide layer after a carburization treatment to prevent metal contamination. Straight filaments tend to break unless given space to expand and contract, whereas coiled filaments allow for expansion during the heating and cooling process.

Diamond growth begins with the formation of amorphous carbon clusters on the surface that are a mixture of hybridizations. The continuous molecular rain of activated carbon species and atomic hydrogen on the substrate provide a path to convert the amorphous carbon material to sp^3 carbons. Although there have been reports on the spectroscopic observation of acetylene[16] and C_2 radical species[17] as carbon carriers in some CVD processes, the most important intermediate in HFCVD is the methyl radical.[18] The high temperature of the filament (1800–2000 °C) stimulates the dissociation of molecular hydrogen to atomic hydrogen (Scheme 1a). This atomic hydrogen abstracts a hydrogen atom from methane to form methyl radicals. Atomic hydrogen also removes hydrogen atoms from the substrates to introduce surface radicals,

also called dangling bonds, and the methyl radical attaches to the growing layer (Figure 3-1).[19] After the addition of a methyl radical to the surface, hydrogen atoms on the growing surface are abstracted by atomic hydrogen to introduce more dangling bonds on the surface that can react further with methyl radicals. This mechanism represents a stepwise addition of carbon atoms to the growing diamond surface.[20]

The atomic hydrogen plays an important role in the growth process. It not only helps form methyl radicals and dangling bonds on the surface, but also the preferred formation of diamond possible. During the growth process in CVD other forms of carbon, such as graphite, can also be formed, especially in the initial stage of the deposition. But atomic hydrogen etches and removes graphite at a rate more than 450 times faster than diamond.[21] At the end of the growth period, there generally is a treatment of the diamond surface with solely atomic hydrogen, called hydrogen-termination. The H-termination process effectively removes defects, etches other carbon material, and removes oxidized bonds that include carboxylic acids, alcohols, and epoxides. After an effective H-termination, the diamond surface is terminated with C–H bonds to give diamond a negative electron affinity and create a hydrophobic surface (Figure 3-1b).[22-23]

Nanocrystalline diamond (NCD) and ultrananocrystalline diamond (UNCD) are polycrystalline films of diamond that have similar characteristics as diamond including extreme hardness, low coefficient of friction, high thermal conductivity, and resistance to wear. NCD and UNCD are forms of *nanocarbon*, carbon materials produced with control of either size or structure at the nanometer scale.[24] UNCD film growth was first

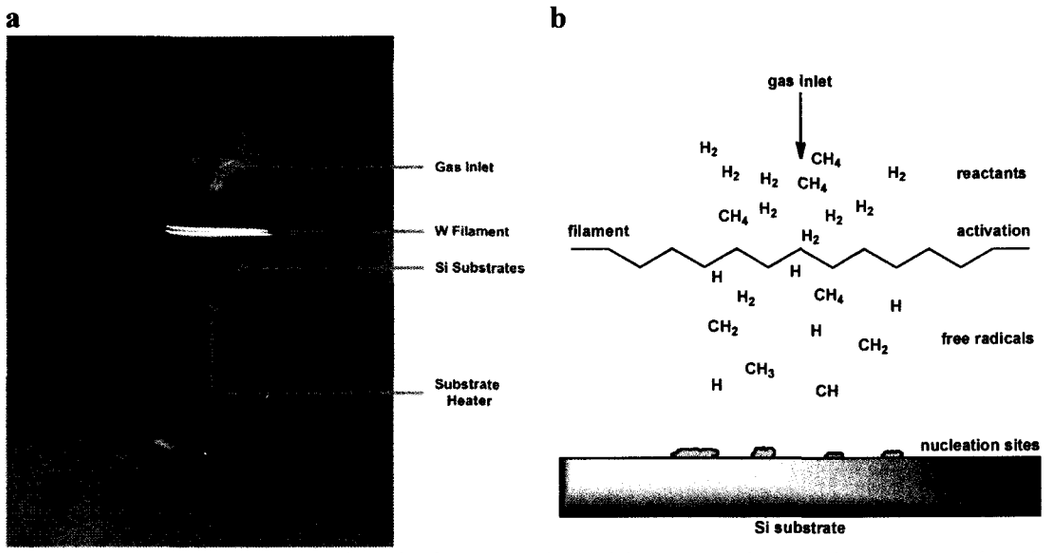

Figure 3-2. Hot filament chemical vapor deposition. (a) Photo of HFCVD chamber used in diamond deposition for this study. (b) A simplified view of the chemistry involved during HFCVD. Adopted from reference 19.

achieved at Argonne National lab by CVD methods in the 1990's.[25,26] NCD and UNCD have nanometer-sized grains of diamond with sp^2 carbon in the grain boundaries. They are distinct from diamond-like carbon and microcrystalline diamond (Table 3-1). Thin films of NCD have grains 50–100 nm in size containing a mixture of sp^2 and sp^3 hybridized carbon within the grain boundaries. Both NCD and UNCD can be deposited onto a variety of substrates by microwave plasma assisted CVD or HFCVD. NCD is a desirable material because of its chemical inertness, biocompatibility, hardness, and electrical properties upon doping.[27] It is an insulating material in its undoped state and belongs to the class of wide band gap semiconductors. Doping gives NCD and UNCD semiconductor properties.[28] The electrical properties can be tuned by doping,[29] providing it properties desirable for electronic and biosensing devices.[30] The doping of both NCD and UNCD films is carried out by the addition of diborane or nitrogen gas to the

Table 3-1. Types of diamond materials produced by CVD. Data was adopted from reference 26.

	Microcrystalline diamond (MCD)	Nanocrystalline Diamond (NCD)	Ultra-Nanocrystalline Diamond (UNCD)	Diamond-like carbon	
				Tetrahedral Amorphous Carbon	Hydrogenated Tetrahedral Amorphous Carbon
Growth species	CH_3*	CH_3*	C_2	C	C
Crystallinity	Columnar	Mixed diamond and non-diamond	Equiaxed diamond	Mixed diamond and amorphous	Amorphous
Grain size	~0.5–10 μm	50–100 nm	2–5 nm	Variable	—
Surface roughness	400 nm– 1 μm	50–100 nm	20–40 nm	5–100 nm	1–30 nm
Electronic bonding character	sp^3	Up to 50% sp^2 (secondary phase)	2–5% sp^2 (grain boundaries)	up to 80% sp^3	up to 40% sp^3
Hydrogen content	< 1%	< 1%	< 1%	< 1%	15–60%

diamond growth mixture in the CVD chamber. When diborane is introduced in the diamond deposition process, boron is substituted into the crystal lattice of diamond. Boron doping enhances the *p*-type conductivity of NCD films.[31] When the concentration of nitrogen gas is high in the deposition process, nitrogen is incorporated into the grain boundaries and increases the size of the boundaries themselves. As a result of the addition of nitrogen, the fraction of sp^2 carbon in the grain boundaries is also increased, improving the electrical conductivity through the increased π-bonding character. Diamond surfaces are characterized by a variety of methods: infrared and Raman spectroscopy, nuclear magnetic resonance (NMR), and electron spin resonance (ESR), secondary ion mass spectrometry, x-ray photoelectron spectroscopy (XPS), near edge x-ray absorption fine structure spectroscopy (NEXAFS), Auger electron spectroscopy, electron energy loss spectroscopy (EELS), UV photoelectron spectroscopy, scanning

electron microscopy (SEM), transmission electron microscopy (TEM), AFM, and x-ray diffraction, electron diffraction, and low energy electron diffraction.

3.1.2 Chemical Modifications of Diamond Surfaces

There have been numerous reports of covalent bonds formed with single crystal and polycrystalline diamond surfaces as well as diamond nanoparticles. The type of diamond surface used—whether UNCD, NCD, microcrystalline diamond, or diamond nanoparticles—was not considered for the method of chemical functionalization.

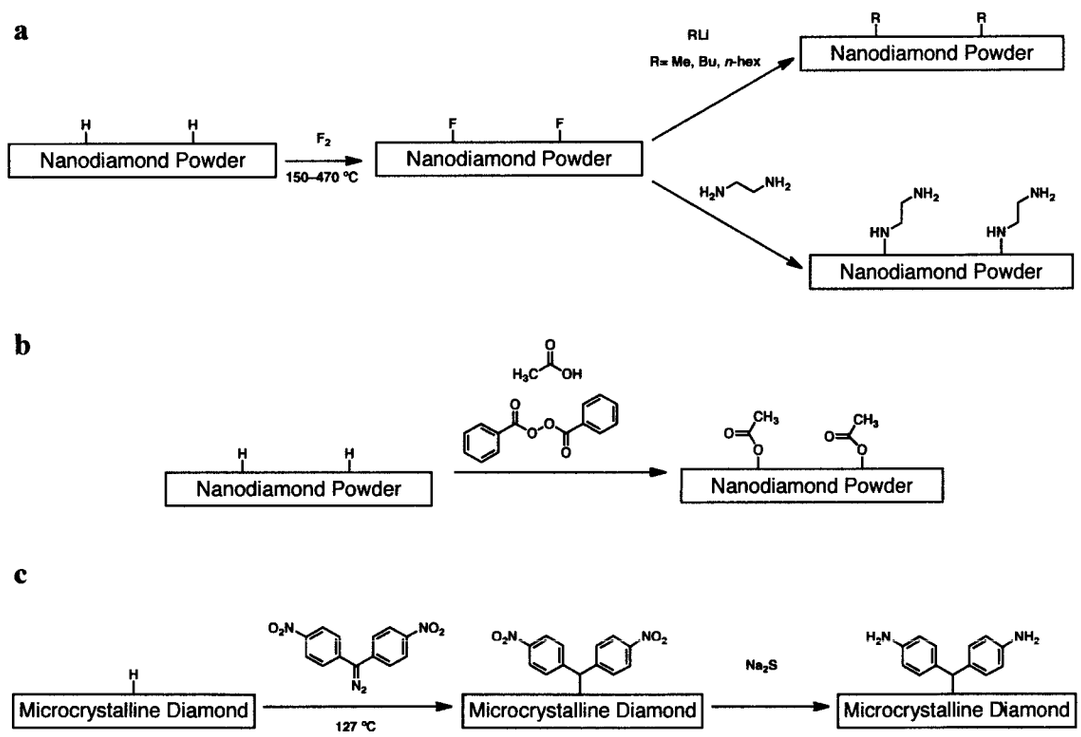

Scheme 3-1. Chemical modifications of diamond surfaces. (a) Fluorination of diamond powder allows substitution reactions to occur. (b) Radicals generated by benzoyl peroxide enable acetic acid to bond to the surface of nanodiamond powder. (c) Carbenes generated *in situ* insert into the C–H of a hydrogen terminated diamond surface.

Reports generally first include a H-termination step to ensure uniformly clean surfaces without oxidized defects and graphitic impurities from the deposition process. H-termination also produces a diamond surface, whether single-crystal or polycrystalline, that exhibits a negative electron affinity.[23,32]

Diamond nanoparticles, also called nanoscale diamond powder, have been fluorinated at elevated temperature (Scheme 3-1a) to give fluorinated surfaces that could be functionalized by alkyl lithiums or amines.[33] Another study reported the attachment of carboxylic acids to diamond using benzoyl peroxide[34] to generate surface radicals (Scheme 3-1b). Recently, Foord and co-workers[35] used a thermally generated diarylcarbene (Scheme 3-1c) to insert into the C–H bonds of the H-terminated diamond surface. In their report, Na_2S reduced the aryl nitro groups on the surface to amines that could be used for further functionalizations, such as the attachment of the amine to a fluorophore. The use of electrochemical deposition (Scheme 3-2a) of 4-nitro-aryldiazoniums followed by electrochemical reduction of the nitro group to the amine provided a method to link glucose oxidase onto a NCD surface.[36] Using this same electrochemical technique, 4-bromo-aryldiazonium (Scheme 3-2b) was grafted to a diamond surface and a subsequent Suzuki coupling modified nanodiamond powder[37] with pyrene, a fluorescent tag. Suzuki coupling also provided fullerene modified NCD films[38] as a platform for molecular electronics. Furthermore, several reports have used this electro-grafting technique to make polymers of poly(ethylene glycol)methacrylate,[39] poly(methyl methacrylate), and polystyrene[40] by atom transfer radical polymerization on diamond surfaces.

Photochemical grafting of terminal alkenes in the presence of ultraviolet (UV) light is a common method to attach molecules to diamond (Scheme 3-2c–d). UV light

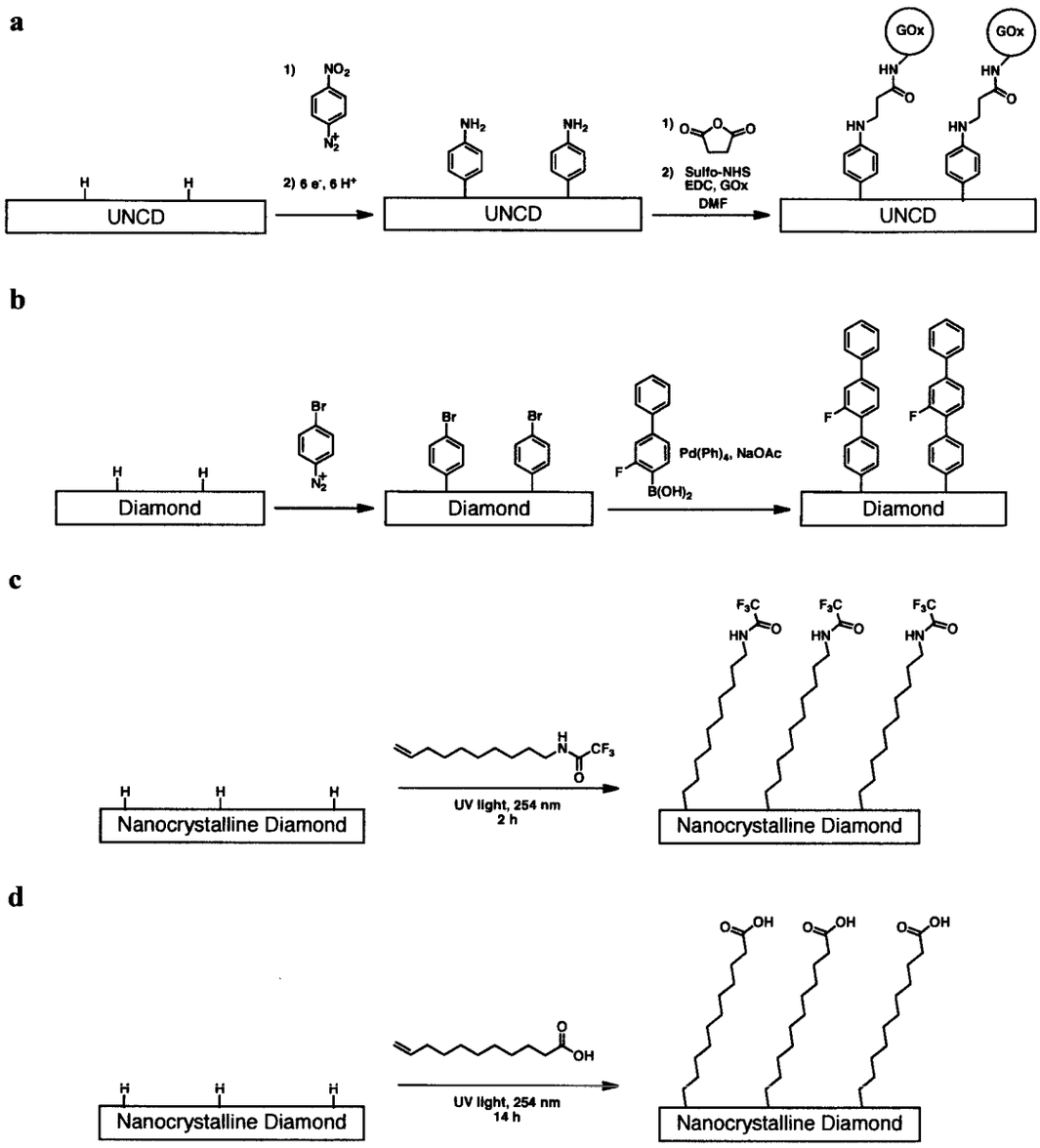

Scheme 3-2. Chemical modifications of diamond surfaces. (a) Glucose oxidase (GOx) was immobilized onto an UNCD surface by electrochemical reduction of an aryldiazonium. (b) Reduction of the aryldiazonium created a platform for further functionalization by Suzuki coupling. Photochemical reactions of NCD with alkenes: (c) trifluoroacetyl-protected 10-aminoundec-1-ene (TFAAD) and (d) undecylenic acid.

(254 nm) ejects an electron from the diamond into the surface-liquid alkene interface to facilitate the formation of a C–C bond.[41] This mechanism parallels the thermal and photochemical functionalization of H-terminated Si surfaces with terminal alkenes.[42] Recent results indicate that the presence of an electron-accepting group in the alkene increases the photochemical reaction rate.[43] After the treatment of diamond surfaces with trifluoroacetyl-protected 10-aminoundec-1-ene (TFAAD) with UV light (Scheme 3-2c), the trifluoroacetyl group was removed by acid or base to liberate the nucleophilic primary amine to immobilize DNA[44] and proteins.[45] Zhong *et al.*[46] used microcrystalline and sub-microcrystalline diamond surfaces to attach undecylenic acid (UA) in the presence of UV light (Scheme 3-2d). XPS, conductivity measurements, and attachment of fluorophores verified the presence of a carboxylic acid on the surface. Wenmackers *et al.*[47] applied the same photochemical reaction to NCD and UNCD substrates to create carboxylic acid-terminated diamond surfaces that were used to attach DNA to study the conformation of DNA by ellipsometry. The same photochemical methodology was used to functionalize NCD-coated AFM tips in the study detailed in this chapter.

3.1.3 NCD AFM Tip Functionalization and Its Application Toward Nanolithography

AFM tips are prone to wear while engaging tips to a surface and while scanning a surface.[48] The lifetime of a probe is dependent on the handling, mechanical operation, wear, and contamination from scanning samples. Wear is more likely to occur in contact mode and scanning probe lithographic techniques such as dip-pen nanolithography[49] and

thermomechanical data storage.[50] Besides affecting image quality and resolution, this mechanical wear also challenges the integrity of chemical modification of tip surfaces. Silicon, the most common tip material, does not possess sufficient mechanical stability to further advancements in some applications of scanning probe lithography. The lack of durability of AFM tips has led researchers to search for materials that are more robust. Because of its exceptional resistance to wear, chemical inertness, and a relatively low coefficient of friction compared to other conventional tips, UNCD is regarded as an ideal choice for probe material. AFM probes have been made entirely of UNCD with a tip radius of curvature of 30 nm.

Our group is interested in the stability of surface functionalizations for biological applications and is particularly interested in AFM tips as nanometer probes. Because of the ideal properties of NCD for AFM tip applications, we tried to functionalize NCD tips with UA in order to convert specific areas of a polymer surface. The carboxylic acid moieties of UA attached onto the AFM tip surface serve to catalyze the hydrolysis of the esters groups of poly(*tert*-butyl acrylate). Such a system will be able to pattern and manipulate material down to the radius of the AFM tip at the nanometer level.

There have not been previous reports on the chemical functionalization of diamond AFM tips.[51] Because it is challenging to characterized the surface of an AFM tip, the NCD films deposited on silicon wafers were first characterized by water contact angle measurements, XPS, FTIR–ATR spectroscopy, and NEXAFS spectroscopy to ensure the functionalization of the NCD surface by UA. After the functionalization was deemed successful by these analytical techniques, the photochemical UA modification was applied to NCD-coated AFM tips. Fluorescent labeling and adhesion measurements

verified the AFM tip was terminated with carboxylic acids. We attempted to use the acid-functionalized NCD AFM tips to catalyze the hydrolysis of a film of poly(*tert*-butyl acrylate), or a random or block copolymer with poly(styrene). After using the functionalized tip to catalyzed the reaction, we examined the progress of the reaction by intermittent contact AFM imaging, adhesion measurements, and fluorescent labeling.

3.2 Synthesis of Molecules for NCD Surface Modification

3.2.1 Molecules for the Photochemical Functionalization of Diamond Surfaces

For the diamond surface modification, we synthesized several molecules with terminal alkenes. Our design of molecules to modify diamond surfaces used the same tripodal approach described and applied in Chapter 2 on gold surfaces. The tripodal molecule designed to attach to the NCD surface possessed the same adamantane core with three legs terminated with alkenes for the attachment to the diamond surface

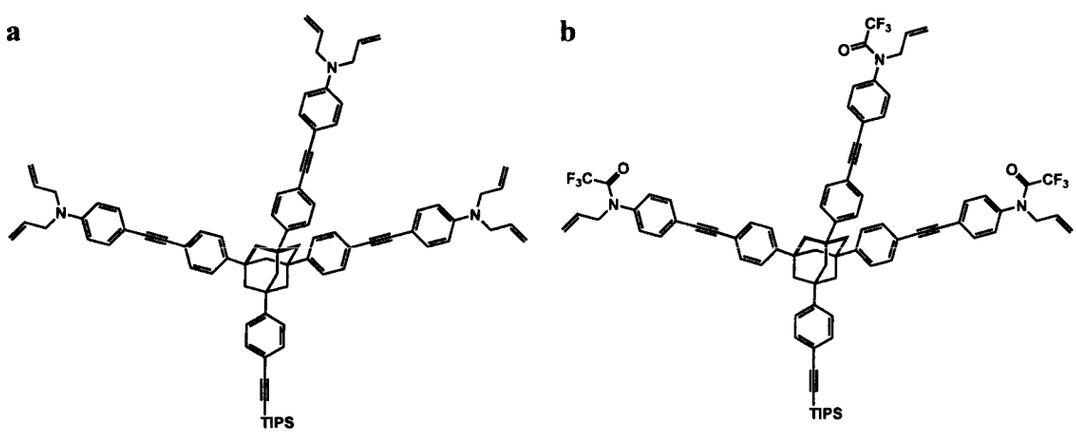

Figure 3-3. The structure of two tripodal molecules for NCD surface functionalization.

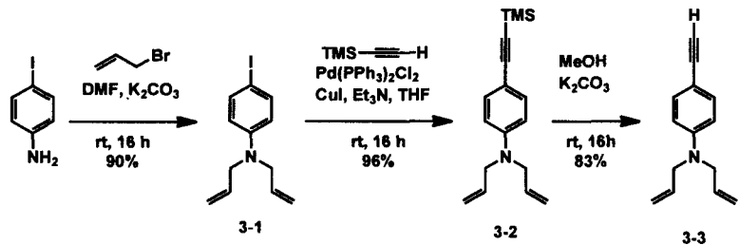

Scheme 3-3. Preparation of a terminal alkene leg **3-3**.

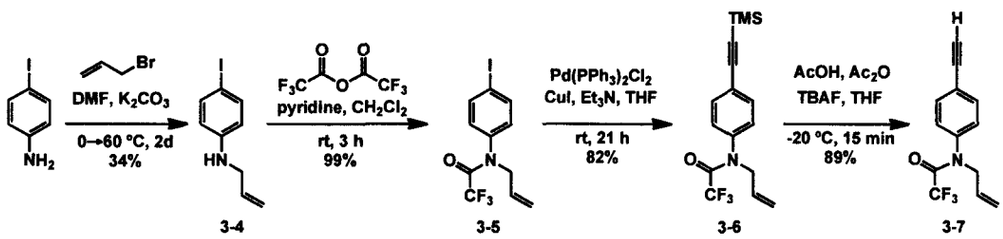

Scheme 3-4. Preparation of a terminal alkene leg **3-7** with an electron withdrawing group.

(Figure 3-3). Two different legs were synthesized, one with two terminal alkenes (Figure 3-3a) and another with a trifluoroacetamide group (Figure 3-3b), an electron withdrawing group to enhance grafting. TFAAD was also synthesized for the initial photochemical studies. We began the synthesis of the leg portion of the tripod with 4-iodoaniline, which was treated with allyl bromide to produce the bis-allyl aniline **3-1** (Scheme 3-3). Sonogashira coupling of *N*,*N*-diallyl-4-iodoaniline with TMS-acetylene gave the protected alkyne **3-2**. Treatment of the TMS-alkyne **3-2** with basic methanol yielded the terminal alkyne **3-3** that was ready to couple with the adamantane core.

Our second synthetic target for a leg of the tripod was a terminal alkene with an electron withdrawing group. Allylation of 4-iodoaniline provided the *N*-allylaniline **3-4** (Scheme 3-4) in low yield. **3-4** was treated with trifluoroacetic anhydride and pyridine

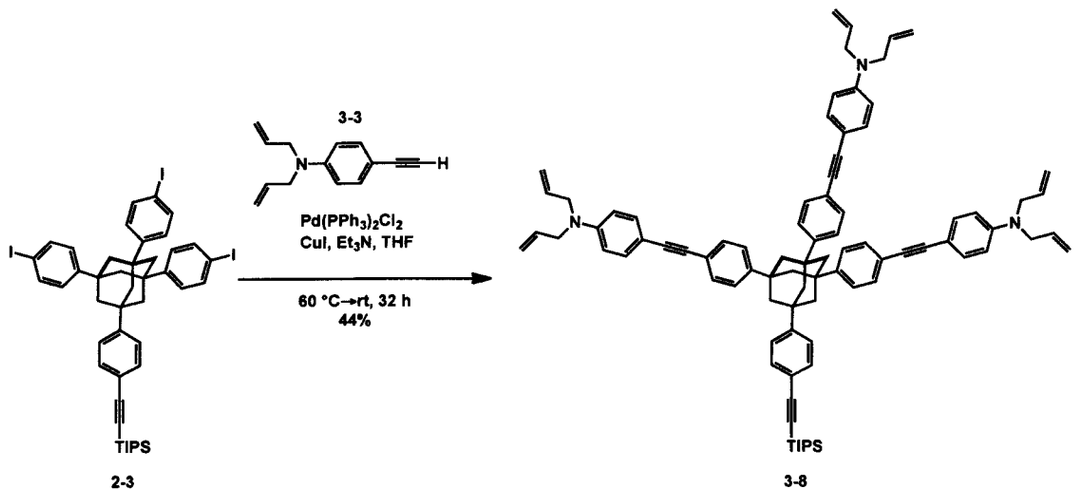

2-3 3-8

Scheme 3-5. Synthesis of tripodal molecule for photochemical attachment to diamond surface.

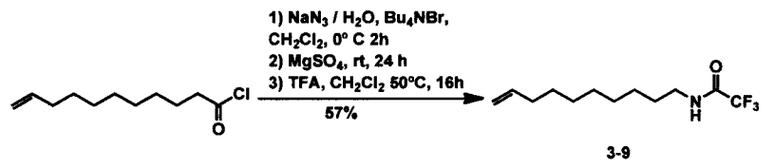

3-9

Scheme 3-6. Synthesis of TFAAD.

to give compound **3-5** in excellent yield. Sonogashira coupling of TMS-acetylene with **3-5** yielded the protected alkyne **3-6**. Because the trifluoroacetamide group is base sensitive, deprotection could not be performed with K_2CO_3 in methanol. Deprotection of the TMS alkyne by tetra-*n*-butylammonium fluoride (TBAF) in acetate buffered THF followed by sublimation gave the terminal alkyne **3-7** in good yield,[52] which is ready to couple with the adamantane core **2-3**.

Sonogashira coupling of terminal alkyne **3-3** with the tetrahedral adamantane derivative **2-3** afforded the TIPS-alkyne tripodal structure after purification by silica gel and size exclusion chromatography (Scheme 3-5). TFAAD was synthesized to compare to previous grafting experiments. TFAAD was synthesized by a Curtius rearrangement

starting from 10-undecenoyl chloride (Scheme 3-6).[53] TFAAD was used in early studies, but was not pursued because it did not provide the desired functional group without further synthetic steps after immobilization onto the diamond surface. UA was purchased and used without further purification.

3.3 Deposition and Functionalization of NCD on Silicon on Wafer Surfaces

3.3.1 Preparation of NCD Films on Si Wafer Substrate

NCD was deposited onto Si wafers by HFCVD. The diamond growth on flat surfaces was initiated to monitor the photochemical reaction with UA before applying to the AFM tip. The diamond was grown at 700 °C with a H_2/CH_4 ratio of 96:4 for one

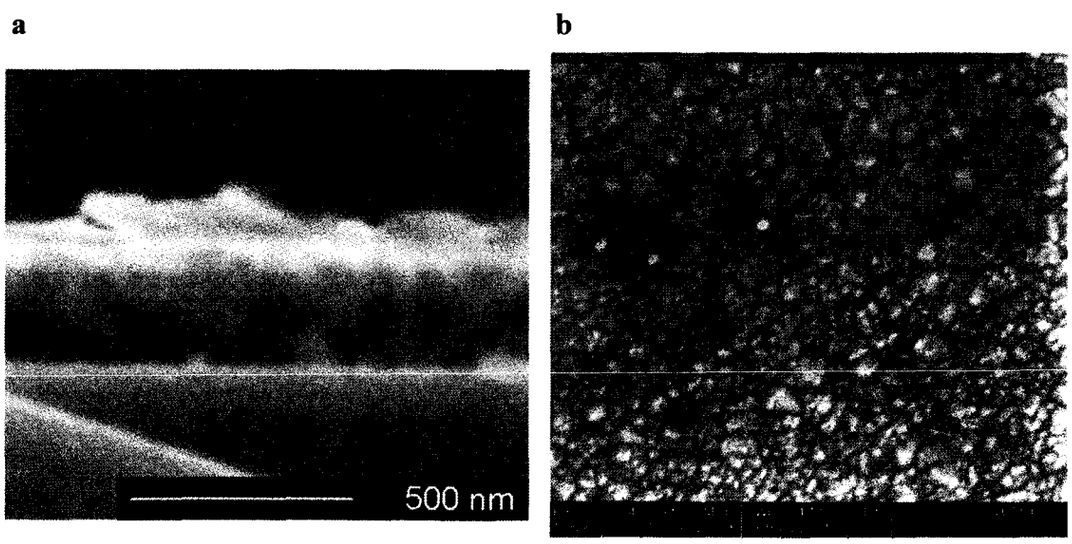

Figure 3-4. SEM images of NCD deposited on Si by HFCVD. (a) Cross sectional view of a fractured NCD film on Si wafer shows the film to be approximately 280 nm thick. (b) Image of a NCD surface reveals diamond grains on surface.

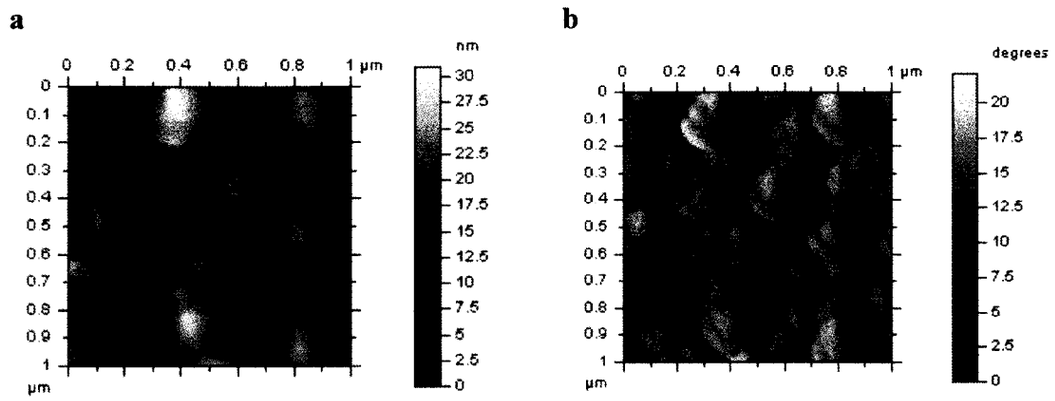

Figure 3-5. Intermittent contact AFM image of NCD film. (a) topography and (b) phase image.

hour. Following the deposition, the surfaces were treated with H_2 for 20 minutes (20 Torr, 700 °C). To ensure the successful creation of H-terminated surfaces, the hydrogen flow was kept at 20 Torr until the substrate had cooled below 400 °C.[41] SEM images assert that the NCD film deposited on Si wafers has a thickness of about 280 nm (Figure 3-4a). The deposition parameters created a NCD surface with root mean square (RMS) height of 12 nm in a scan size of 1 μm^2 (Figure 3-5).

3.3.2 Functionalization of NCD with Undecylenic Acid

Based on previous photochemical modifications of diamond surfaces,[46,47] we tried the functionalization of H-terminated NCD (H-NCD) surfaces with UA (Scheme 3-7.). UA-modified NCD surfaces (UA-NCD) were prepared immediately after H-termination to prevent oxidation and contamination of the NCD surface. UA was

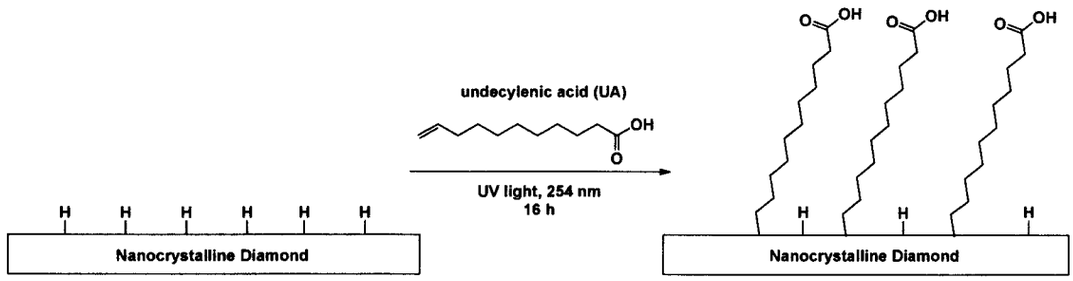

Scheme 3-7. Functionalization of NCD surface with UA.

degassed before use and was placed in a nitrogen flushed sealed quartz vessel for UV irradiation. The NCD surfaces were immersed in UA neat liquid and irradiated for 16 h. After irradiation, the surfaces were washed and sonicated in dichloromethane and methanol before drying with nitrogen. In earlier attempts, NCD surfaces were washed with acetic acid and water in efforts to remove hydrogen bonded dimers, but it was found not to be necessary by FTIR–ATR analysis. Thus, the obtained UA-NCD surfaces were analyzed by the surface characterization methods described in the following sections.

3.4 Analysis of Functionalized NCD Surfaces

3.4.1 FTIR–ATR Spectroscopy

FTIR–ATR spectroscopy provided evidence of the NCD surface modification with UA. Our early FTIR studies of UA-NCD did not clearly display the IR stretches that correspond to the structure of UA. In the hydrocarbon region, there was a weak signal for the alkyl chain and strong water peaks masked the carbonyl peak. The quality

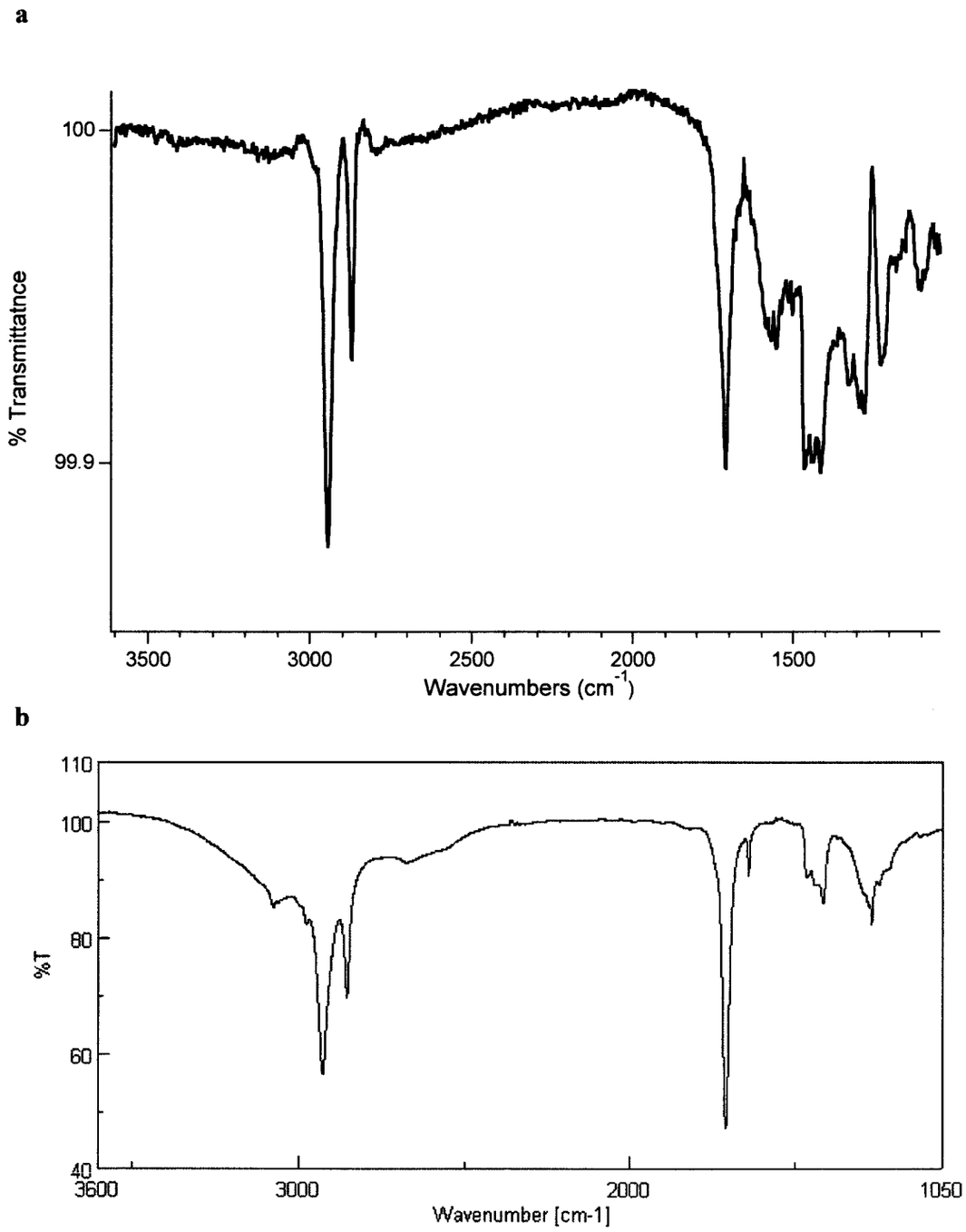

Figure 3-6. (a) FTIR–ATR spectrum of UA-NCD surface with H-NCD as a background. (b) Transmission FTIR spectrum of thin film of UA on NaCl plate.

of the background scan was essential to obtaining a good IR spectrum. Freshly prepared H-NCD surfaces were found to be necessary for the background spectrum. The H-NCD was stored under dry nitrogen until ready for use and allowed to adsorb water from the ambient air. Using oven-dried (100 °C) H-NCD as a background produced water peaks that overlapped carbonyl peaks for the UA–NCD sample. Because of the hydrophilic carboxylic acid moieties, UA-NCD surface likely has a water layer that increases the intensity of the water signal and overwhelms the relatively smaller amount of water adsorbed on an oven-dried NCD surface. When the same H-NCD surface adsorbed water from the ambient atmosphere and then used as a background, the carbonyl peak was evident.

Figure 3-6a shows the FTIR–ATR spectrum of a prepared UA-NCD surface. The symmetric and antisymmetric methylene stretches appear at 2853 cm^{-1} and 2927 cm^{-1}, respectively. The carbonyl stretch appears at 1709 cm^{-1}, which is consistent with the FTIR transmission spectra (Figure 3-6b) of undecylenic acid and previously reported IR spectra of UA on silicon surfaces.[54] Because there is no shift in the carbonyl stretch, it is unlikely the undecylenic acid is attaching to the NCD through the oxygen in the carboxylic acid. The carbonyl absorption of a deprotonated carboxylic acid occurs at approximately 1450 cm^{-1}.[55] There is a peak in this region, but it is observed in the transmission spectrum of undecylenic acid and is associated with the antisymmetric stretch of the methylene group adjacent to the carbonyl.[56] Thus, FTIR measurements suggest that the carboxylic acid is in the protonated form and capable of donating its acidic proton.

3.4.2 Raman Spectroscopy Studies of Single Crystal and Nanocrystalline Diamond Films

Raman spectroscopy uses the inelastic scattering of photons from a laser to probe a surface. The incident beam couples to molecular vibrations to scatter photons, about 1 in every 10^7, at a different energy than the incident beam. Raman spectroscopy does not involve transitions between energy levels directly, but it suggests virtual states that exist between the ground and excited states.[57] Graphite, amorphous carbon, glassy carbon, diamond-like carbon, and diamond materials all exhibit distinct spectra.[58] Even within the types of diamond, single crystal and polycrystalline also display distinct differences in their observed bands. Birrell *et al.* studied the effect of decreasing grain size from microcrystalline diamond to UNCD on the shape of the peaks in Raman spectroscopy.[59] Furthermore, they studied the sensitivity of polycrystalline diamond samples to the excitation wavelength. Because of its distinct peak at 1331 cm^{-1}, Raman is commonly used to identify diamond surfaces.

In this study, we compared boron-doped single crystal diamond and H-NCD

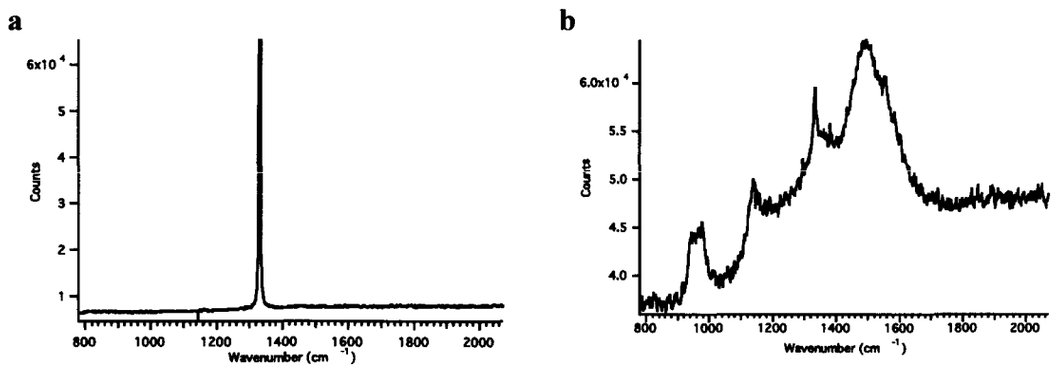

Figure 3-7. Raman spectra collected at 488 nm for (a) boron-doped single crystal diamond (b) nanocrystalline diamond film deposited on Si wafer.

surfaces by Raman spectroscopy. In the boron-doped single crystal diamond sample (Figure 3-7a), there is a single sharp, intense peak centered at 1331 cm^{-1}. The nanocrystalline diamond sample has a spectrum similar to previously reported spectra (Figure 3-7b). The D-band 1332 cm^{-1} was observed in all samples with varied sharpness. The G-band at 1555 cm^{-1} is observed in materials like NCD that have disordered sp^2-bonded carbon regions. There are also peaks at 1494 and 1130 cm^{-1} that are attributed to C–H bonds in the grain boundaries.[59] The broad signal at 976 cm^{-1} was attributed to the Si wafer beneath the NCD film. The Raman spectra confirmed the presence of the polycrystalline diamond film on the surface.

3.4.3 Sessile Drop Water Contact Angle Measurements of H-NCD and UA-NCD Surfaces

We focused on the formation of monolayers with UA on NCD surfaces. The H-NCD surfaces deposited by hot HFCVD had sessile drop water contact angle values between 85 ± 1°, similar to previously reported H-NCD surfaces.[60] UA-NCD surfaces showed contact angles of 50 ± 3°. UA-NCD surfaces were more easily wetted than H-NCD films because of the carboxylic acid-terminated surface. However, the UA-NCD surface is not as easily wetted as a carboxylic acid-terminated self-assembled monolayer of thiols on a gold surface presumably because the density of carboxylic acids is lower on the UA-NCD.[61,62] Also, the roughness of the NCD surface can be expected to contribute to a higher contact angle value.[63]

3.4.4 XPS analysis of H-NCD and UA-NCD Surfaces

XPS survey spectra of H-NCD and UA-NCD surfaces are shown in Figure 3-8a. Based on the peak areas, the relative percentage of carbon decreased from 89% to 86% after UA treatment. The oxygen content increased from 11% to 14% from the H-NCD to the UA-NCD sample. The C 1s signal is more asymmetric and additional peaks are observed at 286.7 eV and 289.1 eV. The increase in the concentration of oxygen on the surface and the additional peaks in the C 1s region are consistent with the presence of the carboxylic acid functional group (Figure 3-8b). In the expanded spectra shown in Figure 3-8c, the O 1s peak is more asymmetric and increases in intensity.

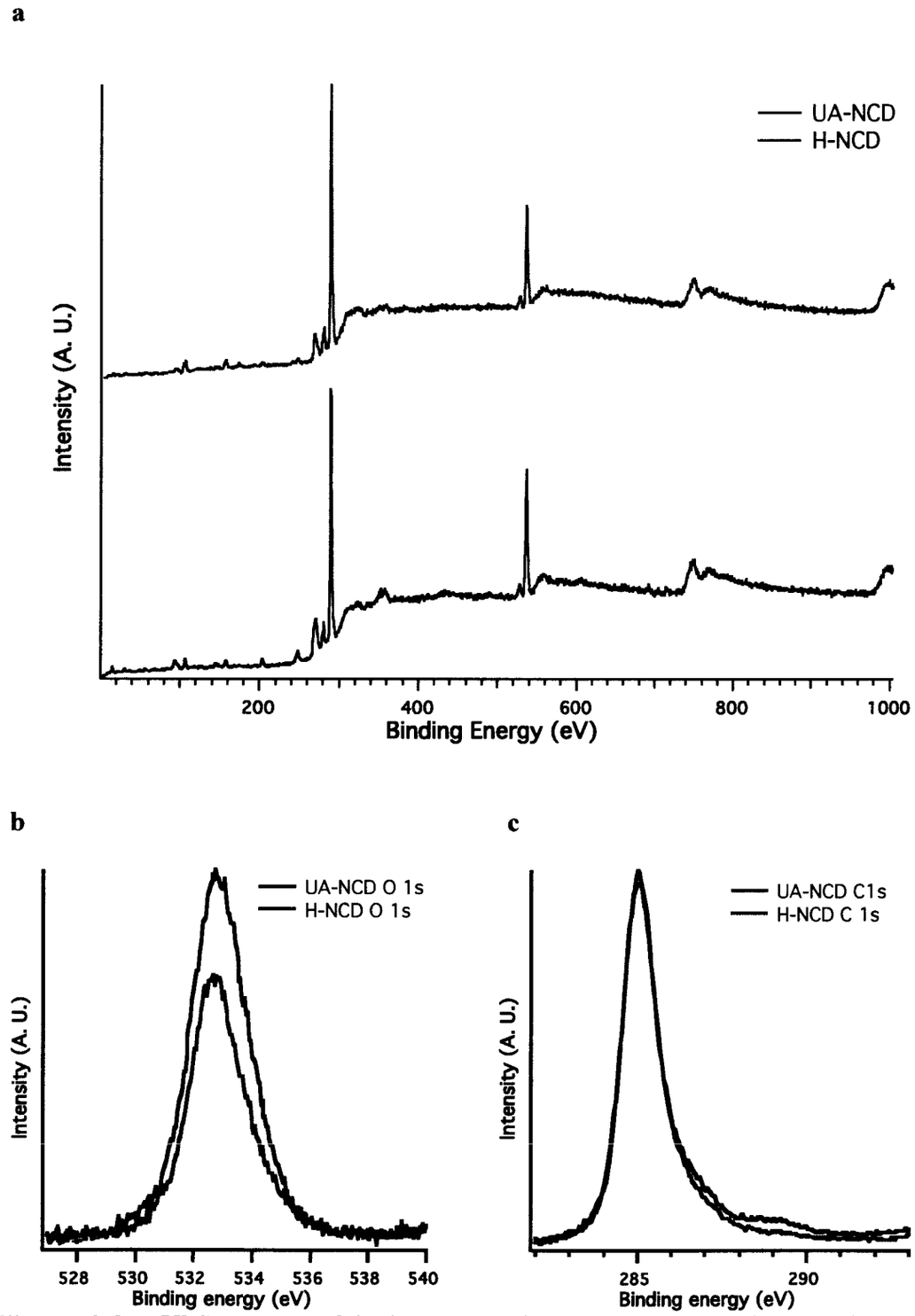

Figure 3-8. XPS spectra of hydrogen terminated (H-NCD) and undecylenic acid modified NCD (UA-NCD). (a) Survey spectra. (b) C 1s spectra (c) O 1s spectra.

3.4.5 Near Edge X-Ray Absorption Fine Structure (NEXAFS) Spectroscopy

H-NCD and UA-NCD surfaces were further analyzed by NEXAFS spectroscopy (Figure 3-9). Spectra were also taken at intermediate exposure times and we found that the peaks varied in a non-monotonic manner (shown in experimental section). We do not fully understand this but it is possibly caused by contaminants and byproducts of incomplete modification. However, the H-NCD and UA-NCD spectra are in agreement with quality diamond surfaces. The C K-edge spectra of H-NCD and UA-NCD are similar with a weak absorption at 285.0 eV indicative of minimal sp^2 hybridized carbon content.[64] At 289.0 eV there is the edge jump and a bandgap at 302.0 eV within the broad 1s to σ^* transition absorption between 290 and 315 eV that are indicative of quality diamond films.[65] The samples differ most in the region between 286 and 289 eV where C–H (287.5 eV),[66] C–O (288.5 eV), C=O (286.4 eV) absorptions occur. There is an increase in the C–O, C–H, and C=O absorptions in the spectra which agrees with the

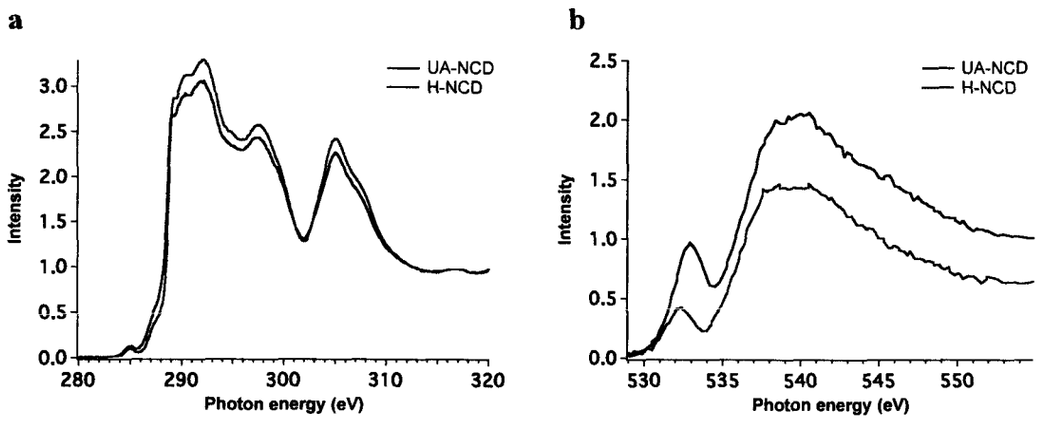

Figure 3-9. NEXAFS partial electron yield spectra of H-terminated nanocrystalline diamond (H-NCD) and undecylenic acid functionalized nanocrystalline diamond (UA-NCD). (a) C K-edge spectra and (b) O K-edge spectra.

addition of an alkyl carboxylic acid to the surface. Compared to the H-NCD sample, the O K-edge spectrum of UA-NCD has a more intense absorption in both the O 1s to π^* and σ^* transitions at 532.9 eV and 539.7 eV, respectively. Moreover, the increase in σ- and π-bonded oxygen in the O K-edge spectra confirms the UA-NCD attaches to the NCD film. The results from the characterization of the UA-NCD surfaces encouraged us to pursue the same modification on a NCD-coated AFM tip.

3.5 Functionalization and Characterization of NCD-Coated AFM Tips

3.5.1 Preparation of NCD-Coated AFM Tips

The deposition of NCD onto silicon wafers and functionalization of NCD with UA led us to try the same technique to coat Si AFM tips with NCD and subsequently functionalize the NCD tips with UA. Seeding, diamond growth, and H-termination were performed on AFM tips under the same conditions in the HFCVD chamber as on the Si wafer surface as described in section 3.3.1. The AFM cantilevers were placed with the tips facing towards the filament during the deposition and NCD growth occurred on both the tip side and the backside of the cantilever. The low reflectivity of NCD on the backside of the cantilevers was detrimental to obtaining a sufficient total signal in AFM experiments.

The difference between poor total signal of the cantilevers and those from the early diamond depositions was hypothesized to be the seeding method. In early procedures, the tips were immersed in the seed solution by exposing the entire AFM chip to the seed solution. To simplify the seeding procedure, the chips were held in a Teflon

cantilever holder that exposed only half of the chip to the seed solution. When the Si cantilevers were seeded by both methods and grown again, both displayed total signals sufficient for imaging. It generally was possible to see the NCD coating by eye, but the cantilevers grown under these conditions had NCD that was only visible by using an optical microscope. The AFM probe chips placed further from the filament during NCD deposition tended to have higher total signals. Thus, the thickness of the coatings of NCD on the backside of the cantilever led to poor total signal. The seeding of the substrates was not as much of a factor in the thickness of the deposited film as the position of the tip relative to the filament in the HFCVD chamber.

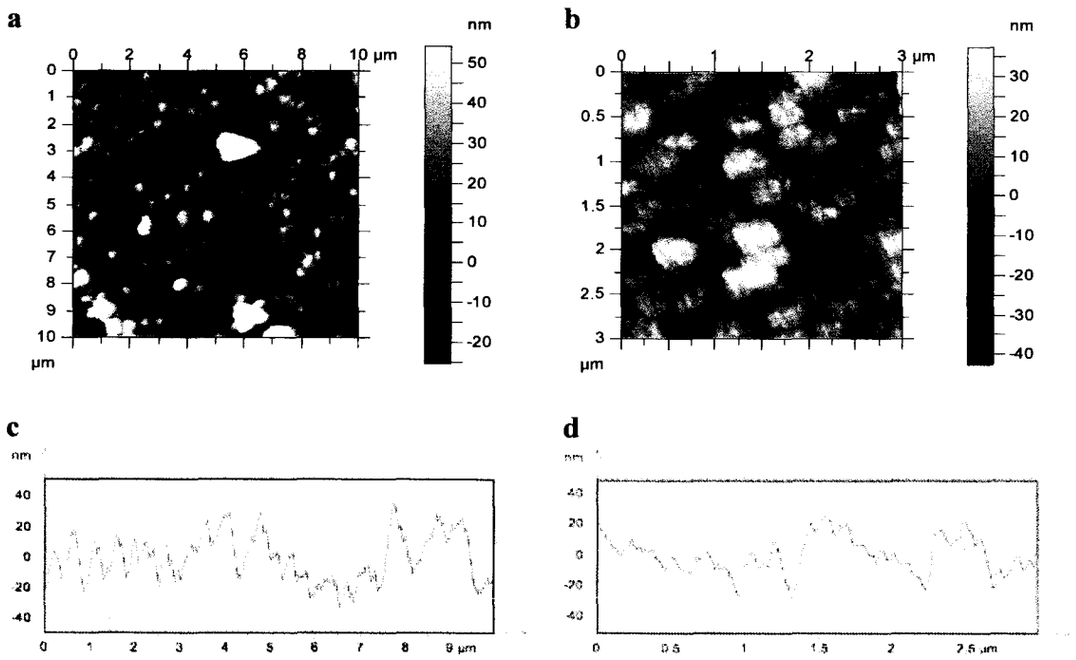

Figure 3-10. Intermittent contact mode AFM images of backside of NCD-coated cantilever (a) 10 µm scan and (b) 3 µm scan. The RMS heights of (a) and (b) are 32 nm and 19 nm, respectively. (c) Line scan of (a). (d) Line scan of (b).

The backside of an NCD coated cantilever with poor reflectivity was imaged by intermittent contact AFM (Figure 3-10). The root mean square (RMS) height of the NCD coating of the cantilever (16–32 nm) was slightly higher than the NCD surface deposited on a Si wafer (12 nm). The coating appears rougher than that of NCD on Si wafer. There were several large features on the backside of the cantilever (Figure 3-10a) that likely contributed to the poor total signal. SEM and AFM could not resolve the grain size of the NCD on the AFM tip. We turned to TEM images to further investigate the NCD-coated tip characteristics.

3.5.2 Transmission Electron Microscopy Observations of NCD Coated AFM Tips

TEM was used to investigate the deposition of NCD onto the Si tips. Some difficulties were encountered in depositing films of NCD on the commercial Si AFM tip surface. The backside of the cantilever reflected the laser of the AFM poorly making the total signal too low to use the tips in the AFM (section 3.5.1). After three consecutive diamond depositions with this low reflectivity problem, Pd/Au was sputtered on the backside of the cantilever to improve reflectivity and the total signal. The sputtering significantly improved the total signal. However, TEM images revealed that the sputtering contaminated the tip even though the sputtering was done solely on the backside of the cantilever (Figure 3-11). A typical NCD tip is shown in Figure 3-11a. A Si AFM tip intentionally sputtered on the tip side is shown in Figure 3-11b. In Figure 3-11c, the sputtering of Au/Pd on the backside of a cantilever displays a dark material

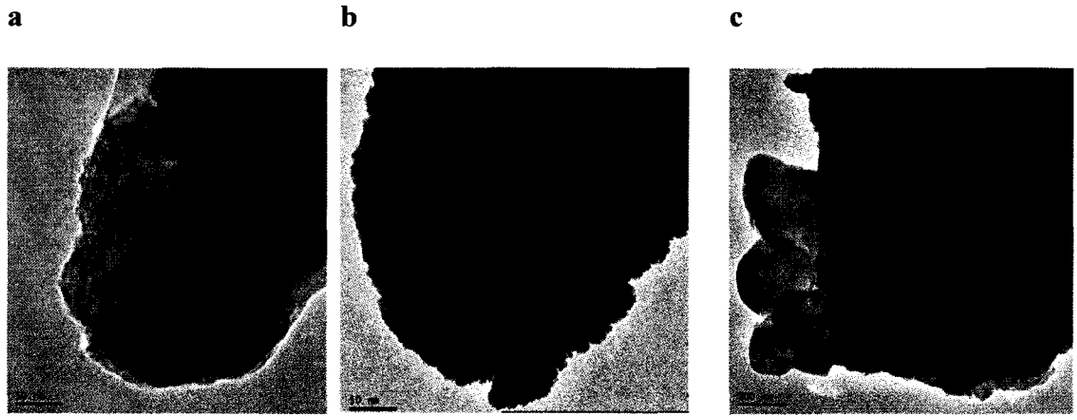

Figure 3-11. Effect of Au/Pd sputtering on NCD-coated cantilevers and tips. TEM images of AFM tips (a) NCD-coated Si tip (b) Au/Pd intentionally sputtered on tip side of Si tip (c) NCD-coated Si tip with Au/Pd sputtering on backside of cantilever. All images were taken by Tevis Jacobs of the Carpick group.

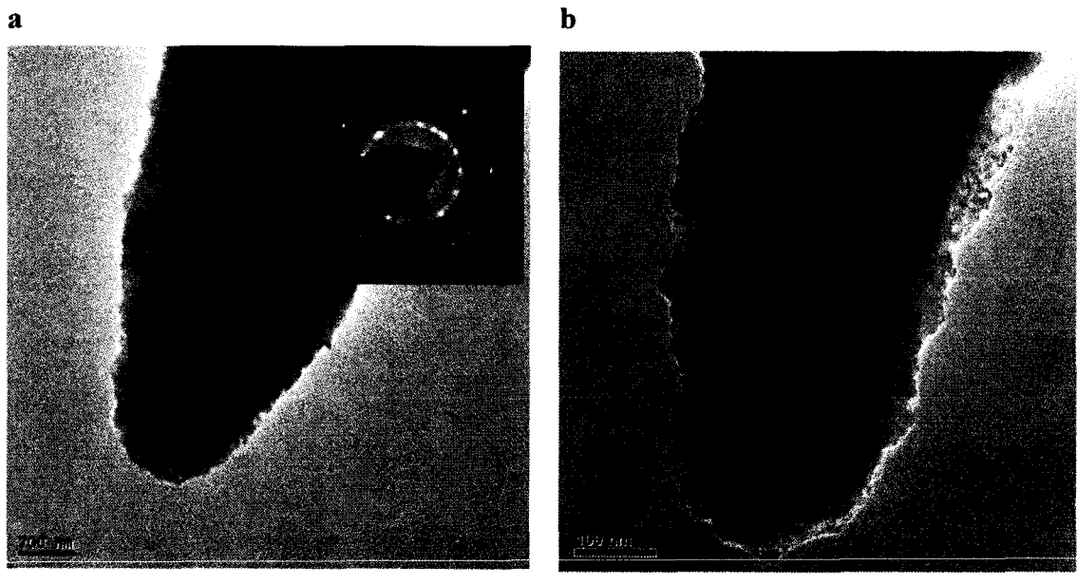

Figure 3-12. TEM images of NCD-coated Si tips grown. (a) NCD tips grown and imaged by Dr. Papot Jaroenapibal with inset electron diffraction spectrum of the tip. (b) NCD deposited on Si tips May 2009. Image taken by Tevis Jacobs of the Carpick group.

similar to the material in Figure 3-11b on the tip, which is indicative of a metallic material. This contamination agrees with previous reports in which AFM tips that were only gold coated on the backside of the cantilever were found to have gold contamination on the tip side.[67]

A TEM image of a HFCVD treated Si tip is shown in Figure 3-12. From the TEM image, there is a polycrystalline coating present on the AFM tip with grain sizes approximately 10–20 nm with a film thickness of approximately 100 nm. Moreover, the electron diffraction pattern (inset in Figure 3-12a) is consistent with NCD.[68,69] The NCD-coated tip has a relatively large radius of curvature (about 150 nm), but remains a suitable substrate for modification studies. The TEM images confirmed the presence of the NCD on the tip and showed that the tip was poised for photochemical functionalization.

3.5.3 Functionalization of NCD AFM Tips with Undecylenic Acid

The functionalization of NCD-coated AFM tips with UA was performed in the same manner as on the NCD films on silicon wafers (Figure 3-13). NCD tips were stored under nitrogen and were used as soon as possible after H-termination to prevent the adsorption of adventitious material. UA was degassed thoroughly and the tips were placed in a quartz reaction vessel flushed with nitrogen for UV illumination. After 16 hours of illumination, the tips were washed exhaustively and treated by sonication in dichloromethane and methanol separately before drying. Functionalized tips were used immediately after washing when possible or stored under nitrogen until ready for use.

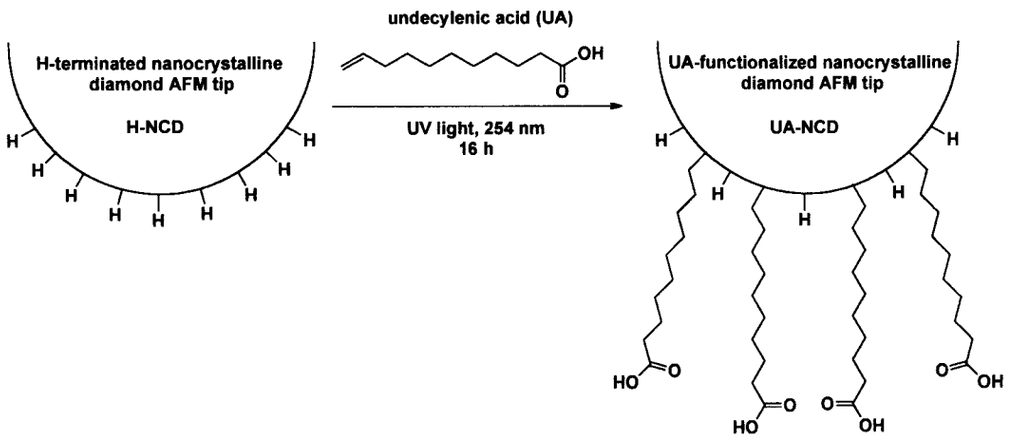

Figure 3-13. Schematic illustration of the functionalization of a NCD AFM tip with UA.

3.5.4 Fluorescent Labeling of UA-NCD AFM Tips

The photochemical functionalization technique of NCD-coated wafer surfaces with UA was extended to NCD-coated Si AFM tips. The NCD-coated tips were functionalized in the same manner as wafer surfaces with UA to yield a carboxylic acid terminated-surface. The UA-NCD AFM cantilevers obtained were treated with 1-ethyl-3-(3-dimethylaminopropyl) carbodiimide/*N*-hydroxysuccinimide (EDC/NHS) and subsequently were treated with fluorescein cadaverine (Scheme 3-8). As a control, H-terminated NCD AFM cantilevers were treated under the same conditions. Both sets of cantilevers were imaged by fluorescent microscopy. The control images (Figure 3-14b) showed no fluorescence on the cantilever portion of the chip with minimal fluorescence on the chip, whereas the UA-NCD cantilevers showed a significantly higher intensity of fluorescence (Figure 3-14d). Because the AFM tips are about 20 μm in height, the tip

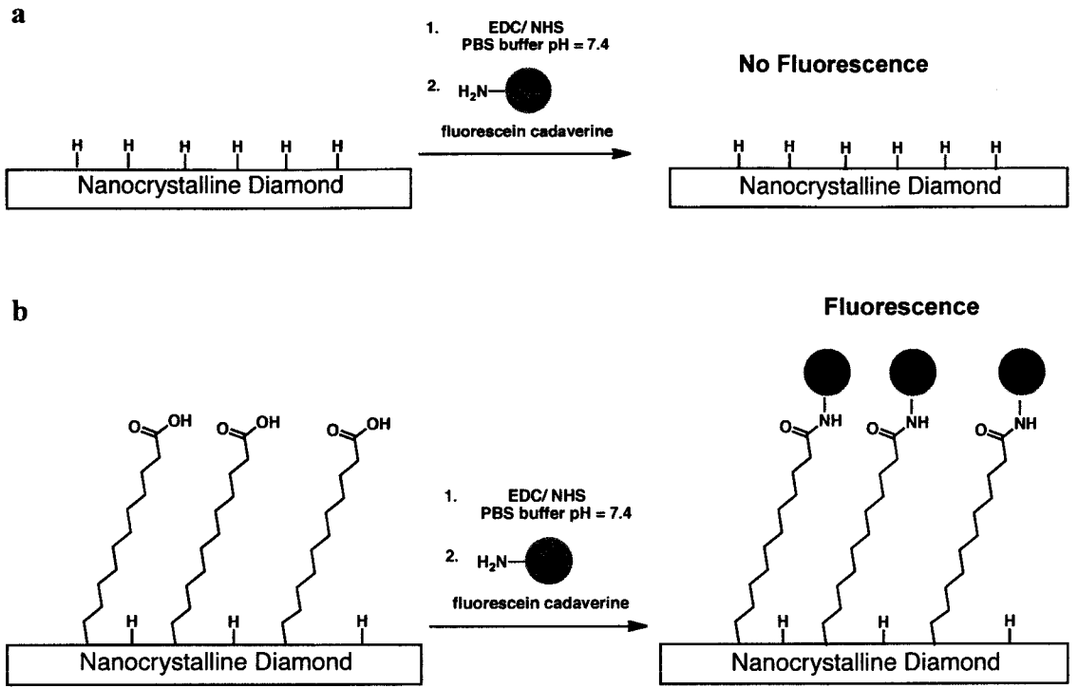

Scheme 3-8. Schematic illustration of the fluorescent labeling of UA–NCD surfaces. (a) The H-NCD surface was hypothesized to exhibit less fluorescence than (b) an UA-NCD surface.

itself is out of focus in Figure 3-14a–e. In Figure 3-14e, the tip is the blurred green spot at the end of the cantilever. In Figure 3-14f, the microscope was focused on the tip itself and the conical shape of the tip is evident. If the microscope focused further above the plane of the cantilever, fluorescence is observed down to about the limits of the microscope, about 1 μm. This fluorescence labeling result gives further evidence of the effectiveness of the functionalization on the AFM cantilevers and tips. Moreover, it demonstrates that the carboxylic acids of UA can be activated and modified with amine molecules.

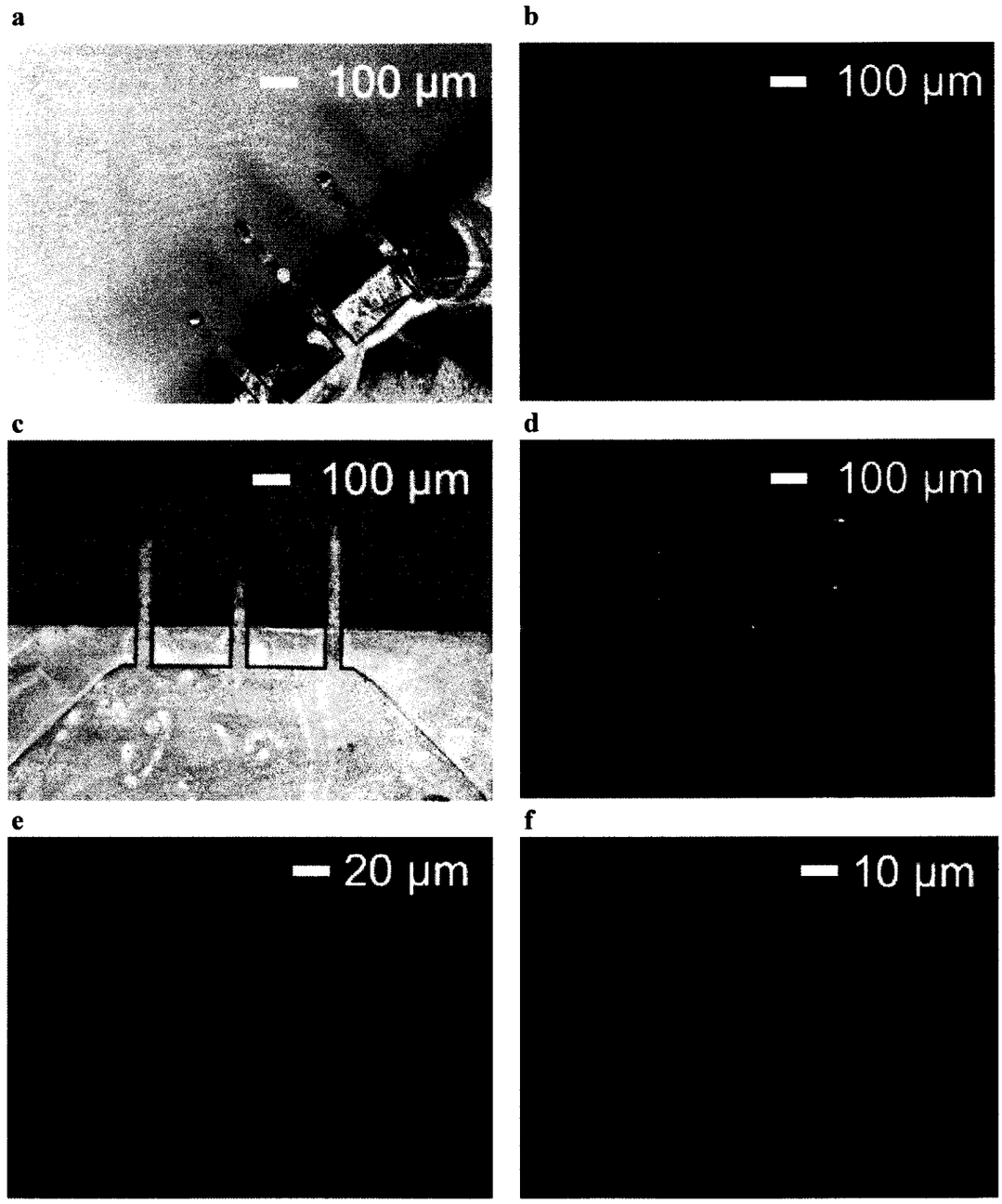

Figure 3-14. Optical microscope images of AFM cantilevers. (a) Bright field and (b) Fluorescent images of H-terminated NCD cantilevers after fluorescent treatment. (c) Bright field and (d–f) fluorescent images of an UA-NCD cantilevers. (e) A UA-modified cantilever focusing on the plane of the cantilever. (f) A UA modified cantilever focusing on the tip slightly above the plane of the cantilever. (b) and (d) have the same exposure time of 1 s, (e) and (f) have an exposure time of 4 s.

3.5.5 Adhesion Measurements with NCD AFM Tips

The adhesion forces of H-NCD and UA-NCD tips were compared on a SAM adsorbed onto a gold surface coated with 11-mercaptoundecanoic acid (MUA-Au) or dodecane thiol (DDT-Au) (Figure 3-15). All measurements were performed in ethanol to remove uncertainties from capillary forces and the same tip was used before and after functionalization to limit the variation of adhesion force from the different tip sizes. The histograms of the adhesive forces from 200 adhesion measurements are shown in Figure 3-16 for H-NCD and UA-NCD tips on both surfaces. The H-NCD tip had adhesion forces of (mean ± standard deviation) 0.36 ± 0.13 nN and 0.21 ± 0.11 nN on the DDT-Au and MUA-Au surfaces, respectively. The adhesion of the UA-NCD tip on the DDT-Au and MUA-Au surfaces was 0.35 ± 0.27 nN and 1.27 ± 0.48 nN. The H-NCD

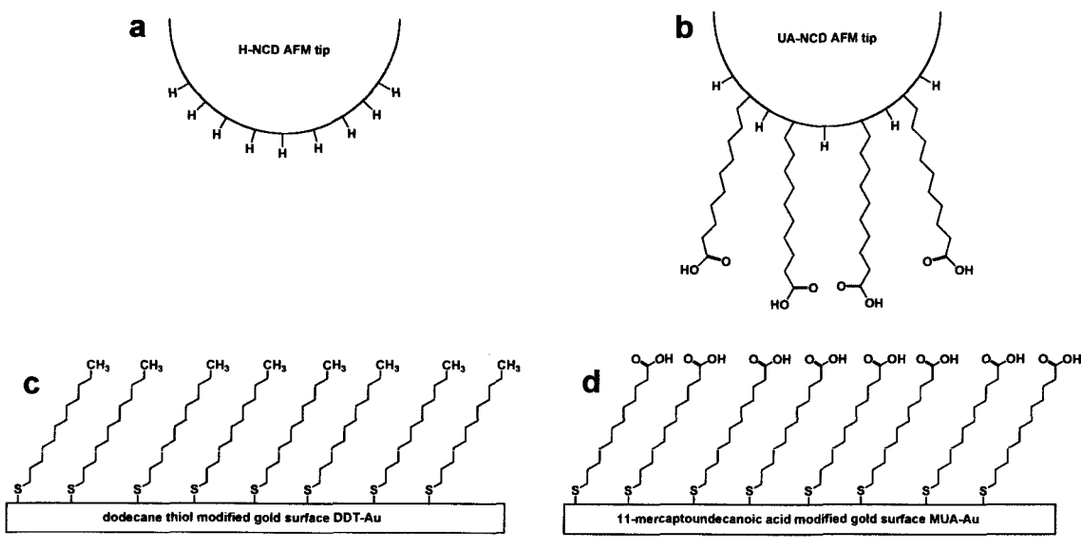

Figure 3-15. Schematic illustration of AFM tips (a and b) and SAM gold surfaces (c and d) used for adhesion measurements. (a) H-NCD AFM tip. (b) UA-NCD AFM tip. (c) SAM of DDT-Au. (d) SAM of MUA-Au.

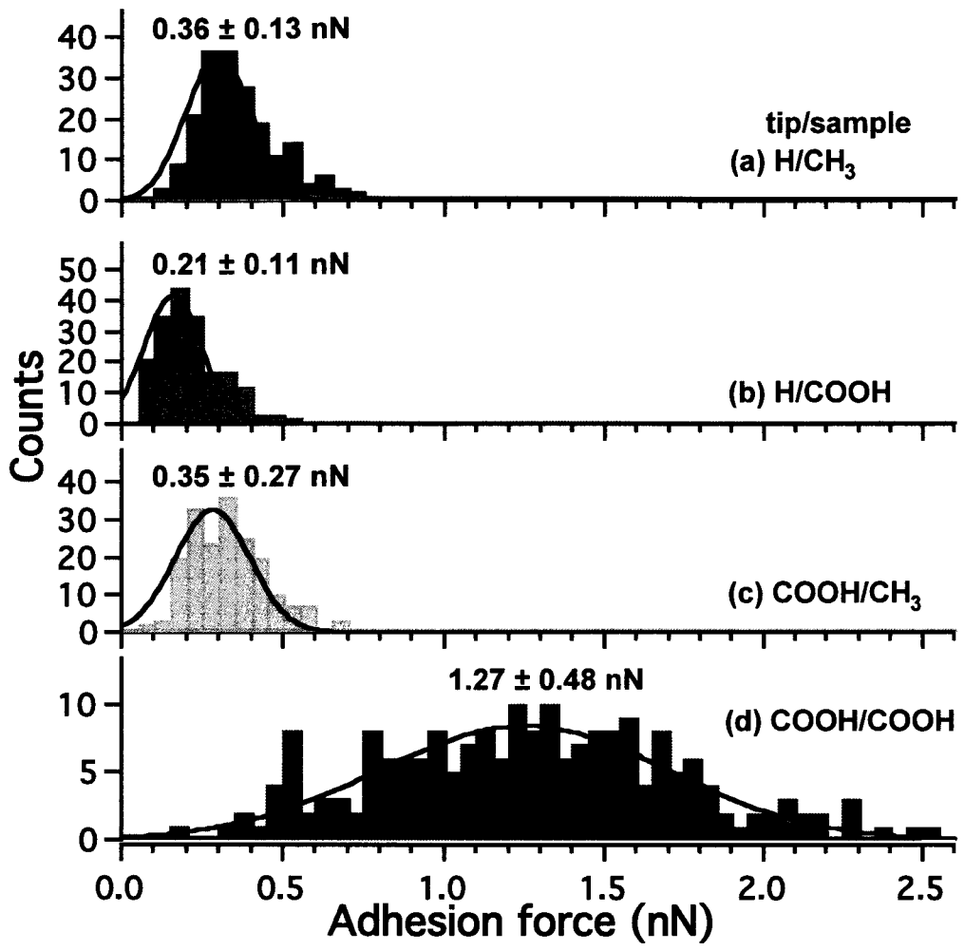

Figure 3-16. Histogram of 200 adhesion forces with the same AFM tip in ethanol (H-NCD and UA-NCD) on functionalized gold surfaces. The numbers above the Gaussian fits are the mean ± standard deviation for each measurement. (a) H-NCD tip on DDT-Au surface (b) H-NCD tip on MUA-Au surface. (c) UA-NCD tip on DDT-Au surface. (d) UA-NCD tip on MUA-Au surface. The tip velocity was 100 nm/s over a distance of 200 nm. The loading rate was 4.9 x 10^4 pN/s.

tip presumably only has van der Waals forces attracting it to each surface; these forces are additive and slightly greater on the hydrophobic surface. The largest adhesion occurs between the UA-NCD tip and the MUA gold surface because the carboxylic acids of the tip can form hydrogen bonds with the acids on the SAM surface in addition to the van der Waals forces.

.3.6 Lithography on Polymer Surfaces with UA-NCD AFM Tip

Because the modification of NCD AFM tip was confirmed in the previous section, we became interested in the applications of UA-NCD AFM tip. One potential application of the functionalized AFM tip could be the acid catalyzed reaction on a polymer surface. We thought that the local chemical reaction can be catalyzed by the chemically modified AFM tip to provide tailored chemical surfaces. Patterned areas on such a small scale could be useful for nanolithography applications. Before describing the lithography experiments, initial studies on the chemistry of the polymer reaction will be detailed.

3.6.1 Thermal Deprotection of Polymer Surfaces

For nanolithography experiments, it is difficult to identify the chemical species patterned on the polymer surface in micron size areas. The global, thermal deprotection of an entire polymer surface was pursued as a standard for comparison. Composto and co-workers have reported the thermal deprotection of *t*-butyl esters on oxidized Si wafers in block and random copolymers of poly(styrene)-*b*-poly(*t*-butyl acrylate).[70] The silanol groups of the oxidized silicon surface act as an acid catalyst at the elevated temperatures to deprotect the esters (Scheme 3-9). We anticipated a similar transformation would occur with PTBA to form poly(acrylic acid) (PAA). However,

a

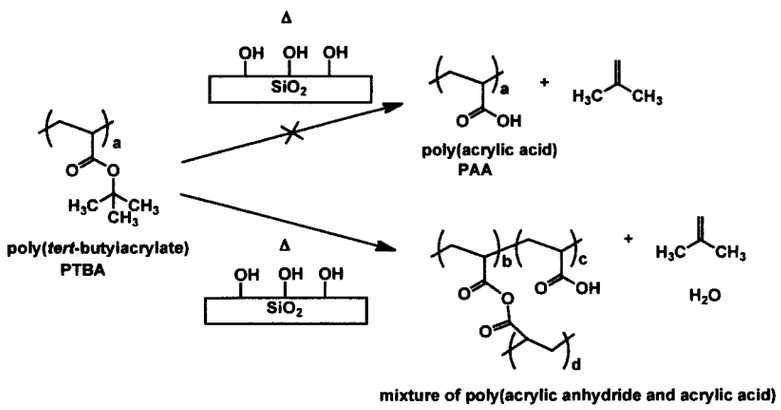

b

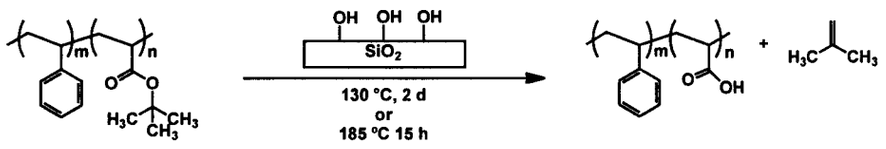

poly(styrene)-*block*-poly(*tert*-butylacrylate)
and
poly(styrene)-*random*-poly(*tert*-butylacrylate)
PS-*b*-PTBA and PS-*ran*-PTBA

poly(styrene)-*block*-poly(acrylic acid)
and
poly(styrene)-*random*-poly(acrylic acid)
PS-*b*-PAA and PS-*ran*-PAA

Scheme 3-9. Thermal annealing of *t*-butyl polymers on a silicon oxide surface. (a) Annealing of poly(*tert*-butyl acrylate) PTBA yielded a mixture containing mostly the poly(acrylic anhydride) with a minor component of poly(acrylic acid). (b) Annealing the poly(styrene-*random*- and *block*-*t*-butyl acrylate) polymer yields the deprotected side chain, the carboxylic acids.

FTIR–ATR analysis of annealed PTBA surfaces in a vacuum oven produced the starting material, the acid anhydride, or a mixture of acid anhydride and carboxylic acid. The progress of the deprotection was monitored by the shift of the carbonyl stretch of the *t*-butyl ester at 1729 cm^{-1} and the methyl bending bands of the *t*-butyl group at 1391 and 1367 cm^{-1} (Table 3-2).[71] The acid anhydride was identified by the presence of the intense symmetric and asymmetric carbonyl stretches respectively at 1760 and 1803 cm^{-1} and the disappearance of the *t*-butyl group bands. (All FTIR–ATR spectra of polymer films

Table 3-2. Assignment of peaks from FTIR–ATR spectra of spin cast and annealed polymer films on silicon oxide.

	FTIR–ATR bands (cm^{-1})		
	Carbonyl stretches		CH_3– bends of *tert*-butyl
polymers	As cast	Annealed	As cast
Poly(*t*-butyl acrylate)	1729	1760 1803	1367 1391
Poly(styrene-*b*-*t*-butyl acrylate), 50 mol% PTBA	1730	1720	1368 1393
Poly(styrene-*b*-*t*-butyl acrylate), 33 mol % PTBA	1728	1717	1368 1393
Poly(styrene-*ran*-*t*-butyl acrylate), 50 mol% PTBA	1724	1721	1367 1391
Poly(styrene-*ran*-*t*-butyl acrylate), 30 mol % PTBA	1725	1704	1367[a] 1391[a]

Values reported in cm^{-1}. [a] Weak bands remained after annealing. Spectra are provided in the experimental section.

are shown in the experimental section 5.6.2.) Attempts to hydrolyze the acid anhydride to the carboxylic acid in water or with water vapor dissolved the polymer and resulted in the removal of the polymer from the surface. Previous studies have reported an acceleration of the rate of deprotection reaction of PTBA surfaces after an initial induction period because of the increased concentration of carboxylic acids in the polymer.[72] We were unable to find an optimum temperature and length to produce the desired carboxylic acids from PTBA. The identification of a specific topography by AFM of the deprotected surface was needed to corroborate the AFM topography images after exposure to the UA-NCD AFM tip. The formation of the anhydride by annealing PTBA surfaces led us to examine other polymers for the nanolithography application.

Random copolymers of poly(styrene) and poly(*t*-butyl acrylate) were graciously provided by the Composto group[73,74] and examined as candidate materials for nanolithography applications. Random copolymers with 30 mol% and 50 mol% PTBA were used in the thermal deprotection on oxidized Si wafers at 185 °C for 16 h. The reaction was monitored by FTIR based on the shift and broadening of the carbonyl stretch as the identifying feature of the deprotected side chains of the polymer and the formation of carboxylic acids. In the 30 mol% PTBA sample, the deprotection did not proceed to completion as the IR results indicate that there are still weak bands associated with the *t*-butyl groups at 1391 and 1367 cm^{-1} (Table 3-2). In the 50 mol% PTBA random copolymer, the reaction went to completion. There were no *t*-butyl bands after 15 h at 185 °C in the vacuum oven, yet the shift in the carbonyl band is not as pronounced. The carbonyl stretch shifts from 1724 cm^{-1} to 1721 cm^{-1} and broadens. The increased concentration of acrylic acid in the 50 mol% PTBA polymer relative to the 30 mol% PTBA random copolymer helps to accelerate the reaction to completion under the same reaction conditions because the presence of acid side chains presumably accelerates the deprotection.

The same thermal deprotection was applied to two different ratios of the block copolymer of poly(styrene) (PS) and PTBA (PS/PTBA 1:1 and 2:1). The 1:1 block copolymer shows both a shift of its carbonyl stretch from 1730 cm^{-1} to 1720 cm^{-1} and a broadening of the peak. There is also the complete disappearance of the *t*-butyl peaks and a weak O–H stretch. After annealing at 185 °C for 16 h, a 1:1 copolymer of the PS-*b*-PTBA was soaked in PBS buffer (pH=7.4) for 2 h to examine the effects of swelling after the deprotection. After swelling, the polymer displayed a prominent O–H stretch.

The carbonyl peak broadens and shifts from 1720 cm^{-1} to 1693 cm^{-1}, which indicates an increase in hydrogen bonding of the carbonyl. Similarly, after heating at 160 °C for 2 d, the 2:1 PS-*b*-PTBA has no *t*-butyl groups and the carbonyl peak broadened and shifted from 1728 cm^{-1} to 1717 cm^{-1} (Table 3-2).

Annealed polymer surfaces were examined by intermittent contact AFM imaging. The block copolymer was imaged before and after annealing to monitor any change that occurred from the thermal deprotection. The cylindrical features were

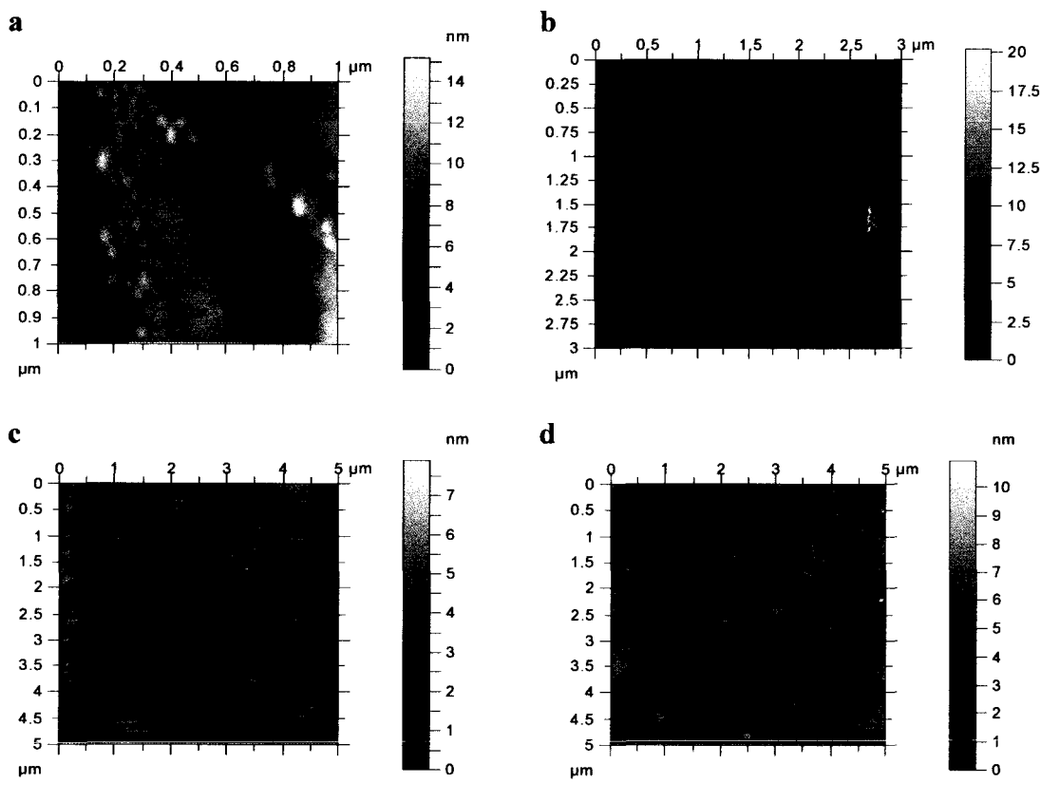

Figure 3-17. Intermittent contact mode AFM images after soaking in PBS buffer of (a) PS-*b*-PAA (1:1) after 2 h soaking and (b) PS-b-PAA (2:1) after 16 h soaking. Intermittent contact mode AFM images of PS-*ran*-PTBA (50% PTBA) (c) as spin cast on silicon oxide and (d) after thermal deprotection.

observed after soaking for two hours in buffer and were similar (Figure 3-17a) to the reported images by the Composto group. Upon longer soaking, these features formed a layer of PAA on the surface that flattened as the PAA domains swelled to cover the entire surface (Figure 3-17b). The thermally deprotected random copolymers showed a minor change in topography in intermittent contact AFM imaging. Before annealing, the random copolymer surface is more pliant (Figure 3-17c) and changes to have sharper features after annealing (Figure 3-17d). After soaking the deprotected random copolymers in PBS buffer, there was no further effect on the topography of the polymer.

3.6.2 Chemical Lithography of Polymer Surfaces Using Contact Mode AFM

Contact mode scanning of the homopolymer PTBA with a UA–NCD AFM tip was performed to hydrolyze the *t*-butyl ester to give the carboxylic acid (Figure 3-18). The amount of applied force could be changed during scanning by simply adjusting the setpoint. When the setpoint was increased in the scan, the features on the surface increased in height. Although the change of height in the features indicates the topographical change is mechanical in nature, it was difficult to confirm that the increased force also induces the chemical change. After scanning with the UA–NCD tip, intermittent contact imaging was used to monitor the change in the topography of the PTBA surface. The chemical species present on the scanned PTBA surface were further examined by fluorescent labeling and adhesion measurements.

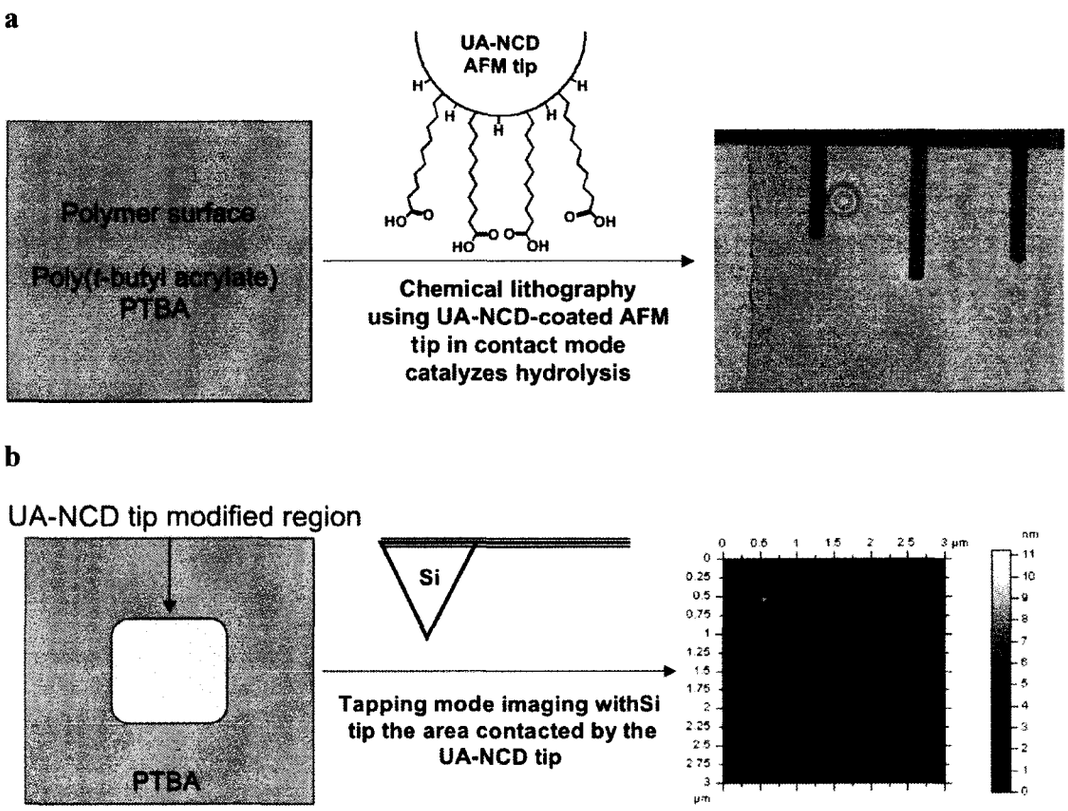

Figure 3-18. Schematic illustration of lithography experiment with UA-NCD AFM tip on PTBA surface. (a) Contact mode scanning with a UA-NCD tip. (b) Intermittent contact mode AFM imaging patterned region with silicon tip.

Several parameters can affect the pattern formation during contact mode AFM of the polymer: the applied load, the scanning rate, the scan (or pattern) size, and the number of line scans. Dr. Papot Jaroenapibal of the Carpick group previously acquired promising results with UA-NCD tips on a PTBA surface but it is unknown what force was applied during the contact mode scanning in these AFM experiments. Larger patterns (50 x 50 μm) were necessary to try to provide an area that is large enough to visualize the labeling of the carboxylic acid groups by fluorescent microscopy. The same number of lines was used but the scan rate had to be increased to complete the scan

in a reasonable amount of time. The slowest rate allowed by the AFM software was 0.1 lines/s. The applied load (20 nN) was chosen based on preliminary lithography experiments.

3.6.3 Imaging of Patterned Polymer Surfaces by Intermittent Contact AFM

The features on the edge and within the area contacted by UA–NCD tip on PTBA are shown in Figure 3-19. The features within the pattern are conical and about 150–200 nm in diameter and fairly uniform height (4 nm). These features can be compared to the uncontacted regions of PTBA in the images taken at the edge of the pattern. The unmodified area of PTBA is smoother with a RMS height of 0.22 nm. Using a similar load, the H–NCD tip gave a feature height of 2–4 nm and the features within the pattern have diameters of 100–150 nm. If the UA–NCD tip was catalyzing the hydrolysis of PTBA to poly(acrylic acid) (PAA) on the polymer surface, the PAA would be expected to swell by absorbing ambient moisture. After swelling the PAA would then have a larger height and diameter. Because this reaction is expected to occur only on the PTBA film and not through the entire PTBA layer, which was observed in the thermal annealing experiments by the Composto group, the change can be predicted to be smaller.

It was hypothesized that the features made by the contact of the H–NCD tip should cause some change in the topography image because the hard diamond tip may plow into the soft polymer surface while in contact mode. Indeed, the change in the

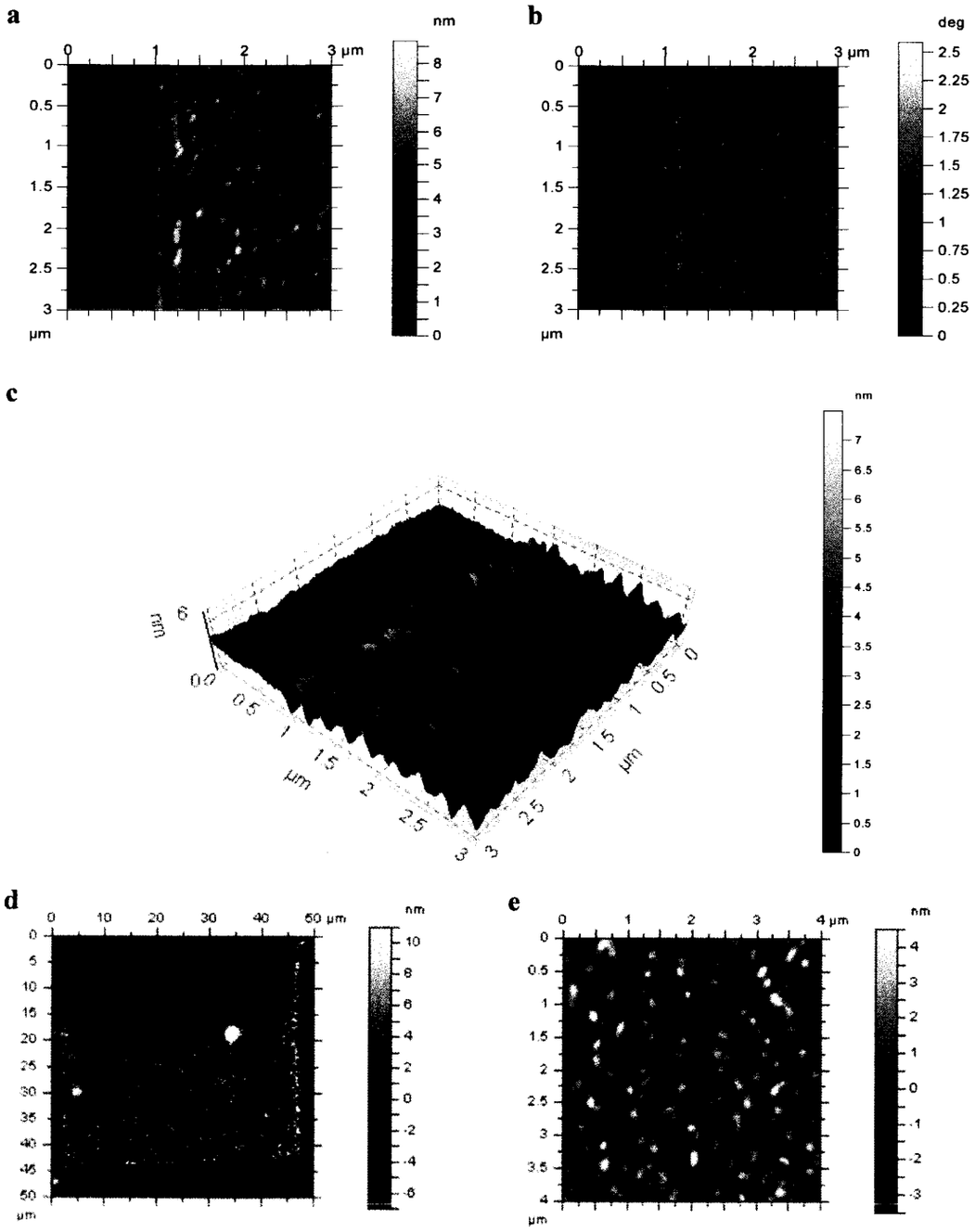

Figure 3-19. Intermittent contact AFM images of edge of a 70 μm region patterned with a UA–NCD tip on PTBA using a load of 20nN. (a) Topography image (b) phase image and (c) 3-D image of edge of the pattern. The rougher region is inside the patterned area. Images of 40 μm pattern made with UA–NCD tip on PTBA surface with an increase in applied force (40nN) halfway through scan (d) 50 μm image and (e) 4 μm image inside higher applied force pattern.

height (2–4 nm) change in height of PTBA in the regions contacted by H–NCD tip shown in the topography images appeared different from the patterns obtained with the UA-NCD tip (Figure 3-20). The phase images of both the H–NCD and UA–NCD appear similar.

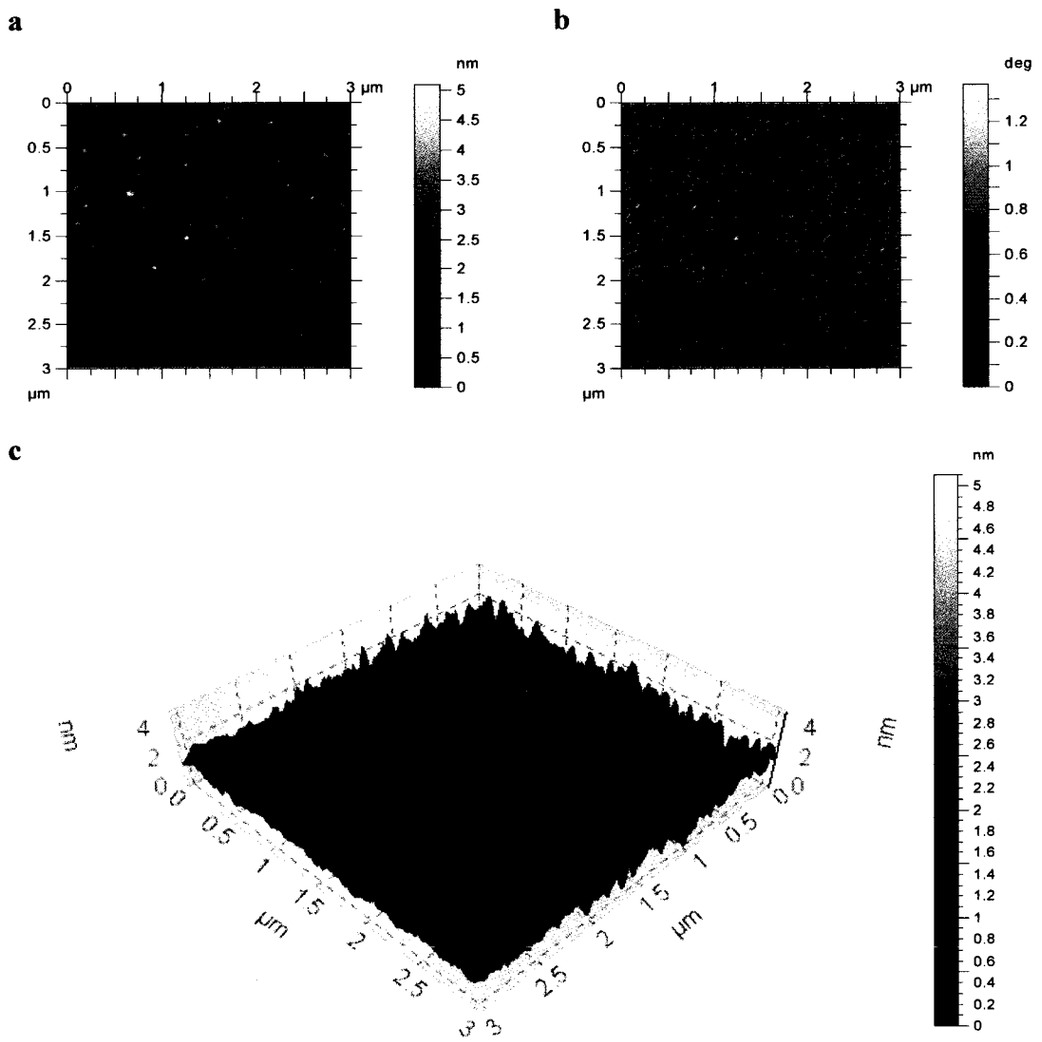

Figure 3-20. Intermittent contact mode images of PTBA film scanned with H–NCD AFM tip. (a) Topography and (b) phase image (3 µm scan). (c) Three-dimensional projection of surface.

Because the hydrolysis of the ester can be accelerated at higher temperature, it was possible the reaction with the UA-NCD tip would be more probable to occur while heating the polymer substrate. Several experiments were performed using the heating stage on the AFM to promote the hydrolysis of PTBA. The heating stage was set at 100 °C on the PS-*ran*-PTBA and PS-*b*-PTBA (1:1). The PS-*b*-PTBA surface was rough; there were ridges 20 nm or more in height throughout the sample present from the spin coating. Thus, it was difficult to identify the region that had been scanned by the UA–NCD tip. Usually there was a shape of the square pattern made in the contact mode scan that can be located during intermittent contact imaging, but in the case of the PS-*b*-PTBA (1:1) it was not possible to locate the patterned region. It was possible to find the region made with a UA–NCD tip on PS-*ran*-PTBA (Figure 3-21). Two separate regions were imaged: a region inside and a region outside the pattern made by the UA–NCD tip. Both images have similar features and roughness; there was no clear difference between the two regions.

Because it was not possible to see the change in surface topography in both the PS-*b*-PTBA (1:1) and PS-*ran*-PTBA films, further heating experiments were performed using PS-*b*-PTBA (2:1). The PS-*b*-PTBA (2:1) films had minimal roughness (RMS height = 0.65 nm) and were able to give phase separated regions of PS and PAA domains after deprotection. A UA–NCD tip scanning on PS-*b*-PTBA (2:1) were carried out at room temperature, 50, 100, and 150 °C. There was no observed significant difference in adhesion between inside and outside the patterned regions were observed under any conditions (Table 3-3). Additionally, the patterned regions could not be located by subsequent intermittent contact AFM imaging. The force–distance curves

have broad desorption peaks above 100 °C because the polymer softens and melts. Poly(*t*-butyl acrylate) and poly(styrene) have glass transition temperatures of 32 °C and 100 °C, respectively.[75] Heating experiments did not show the deprotection by AFM imaging. After the contact of UA-NCD tip and PS-*b*-PTBA (2:1), the patterns were not able to be located, likely because the polymer melted or softened during heating to erase any pattern made by the AFM tip.

Table 3-3. Adhesion measurements on PS-*b*-PTBA (33 mol % PTBA) surface at different temperatures. Values all reported in nN as mean ± standard deviation of five measurements.

Temperature	Before patterning	Inside Pattern	After Pattern
20 °C	84.45 ± 0.63	59.72 ± 0.44	59.49 ± 0.83
50 °C	54.67 ± 0.66	51.54 ± 0.68	49.19 ± 0.97
100 °C	34.39 ± 1.97	37.67 ± 0.22	37.34 ± 0.31
150 °C	66.99 ± 2.18	60.19 ± 0.26	58.25 ± 1.35

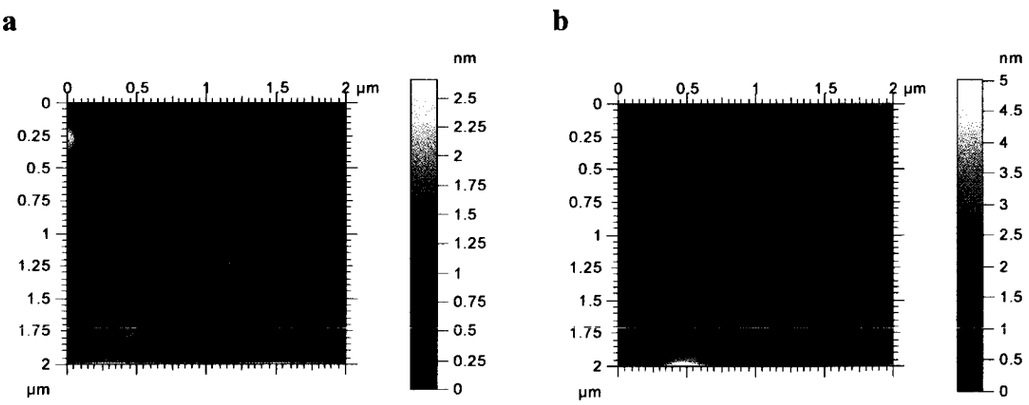

Figure 3-21. Intermittent contact mode AFM images of PS-*ran*-PTBA (50%) after scanning in contact mode while heated to 100 °C. Images were taken after soaking surface in PBS buffer (pH=7.4) for 2 h. (a) 2 µm region inside patterned area (b) 2 µm region outside patterned area. RMS height: (a) 0.23 nm (b) 0.29 nm.

Adhesion forces were acquired with the UA–NCD tip before scanning PTBA, after scanning inside the patterned region, and after scanning outside the patterned region. Because the UA–NCD tip contains the hydrophilic carboxylic acid, it was predicted that if the transformation to PAA occurred in the scanned region, the patterned region should have a greater adhesion force than the unscanned region outside the pattern where only PTBA was present. However, the adhesion measurements for the region patterned by UA-NCD were (mean ± standard deviation) 60.85 ± 23.38 nN and on the region outside the patterned region to be 61.51 ± 22.62 nN. In most cases the adhesion on PTBA was similar to the patterned region. In an experiment using an unmodified H–NCD tip on PTBA, a similar trend was observed. The adhesion outside the patterned region (58.74 ± 10.81 nN) was slightly greater than the adhesion inside the pattern (55.56 ± 5.69 nN). The adhesion measurements were ambiguous, thus fluorescent labeling was attempted to selectively label the putative carboxylic acids of the patterned region.

3.6.4 Fluorescent Labeling of Polymers after Nanolithography

In addition to AFM imaging and adhesion measurements, fluorescent labeling of the polymer surface was attempted to verify the chemistry of the polymer surface. The surface was first patterned with the UA–NCD tip and then subjected to labeling conditions. If the PTBA was converted to PAA by the UA–NCD tip, there would be carboxylic acids on the surface of the polymer that could be confirmed by fluorescent labeling methods with EDC/NHS activation and subsequent treatment with fluorescein

cadaverine. During the EDC/NHS activation step, the PTBA was removed from the Si surface; the delamination of PTBA was visible by eye, as well as by optical microscopy. Although most of the surface remained intact, there was no way to distinguish if the scanned area was damaged or removed during the soaking (Figure 3-22a). In earlier studies, the Si wafer was oxidized to form a uniform SiO_2 surface before spin-coating the polymer. The random copolymer of PS-*ran*-PAA (PS-*ran*-PTBA after thermal

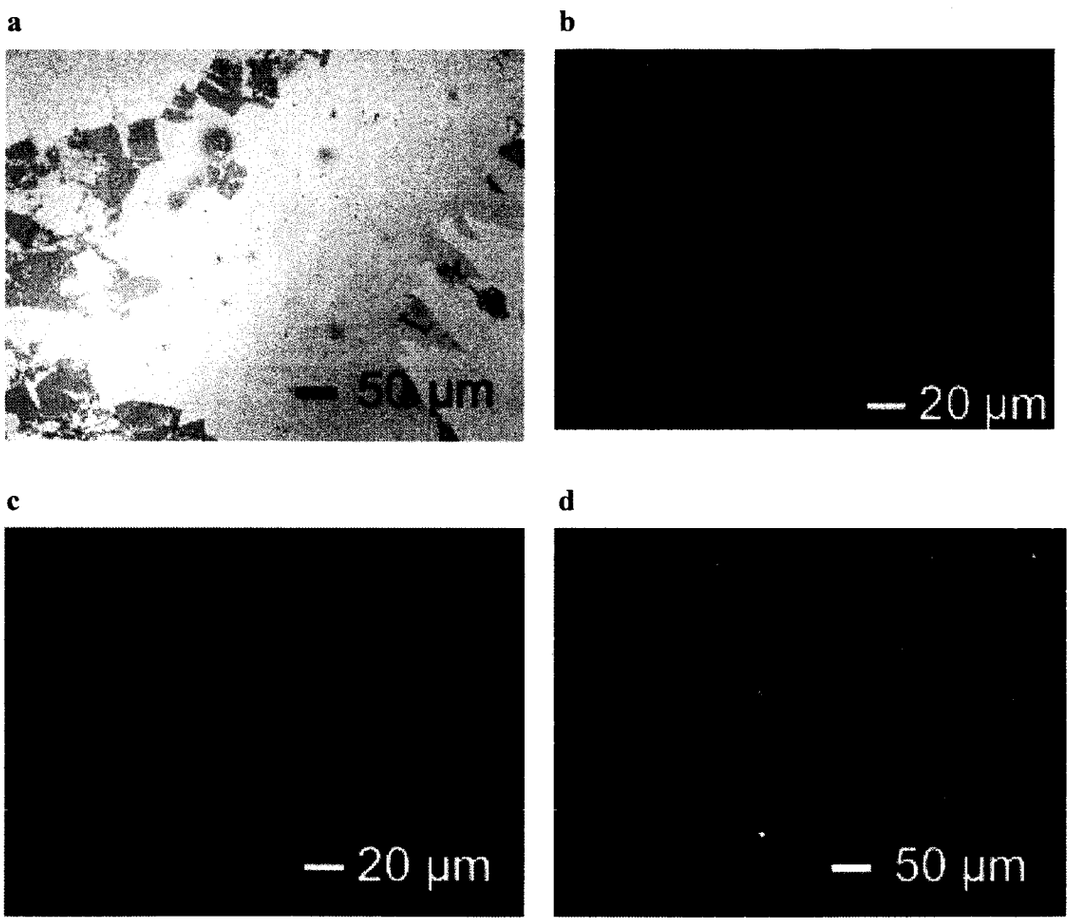

Figure 3-22. Optical microscope images of polymer surface (a) Image of PTBA delaminated from the Si wafer. (b) Selective labeling of PS-*ran*-PAA (30 mol% PAA). (c) Fluorescent labeling of patterned PTBA spin coated on a glass slide and (d) Si wafer.

deprotection) was also labeled under the same conditions, but it showed selective labeling and was stable to the labeling conditions (Figure 3-22b).

PTBA spin coated on glass displayed no contrast between the area contacted by the UA–NCD tip and the unmodified PTBA; the surface appeared saturated with dye even under short dye exposure times (30 min). PTBA spin coated on Si wafers was also attempted, with no success (Figure 3-22d). To increase polymer adhesion to the Si wafer, the Si wafers were treated with hexamethyldisilazane (HMDS) and octadecyltrichlorosilane (OTS) to increase the hydrophobicity of the Si wafer and encourage the polymer to adhere to the surface during the aqueous treatment. The hydrophobic Si wafers were able to adhere to the polymers better in aqueous solution, but the hydrophobic surface prevented spin coating the polymer at the necessary one nanometer roughness. Without a smooth enough surface, it was not possible to find the patterned polymer region of the surface. The fluorescent labeling experiments could not establish the transformation to PAA.

3.6.5 Summary of Lithography Experiments Using UA-NCD AFM Tips

The annealing of PTBA, PS-*ran*-PTBA, and PS-*b*-PTBA surfaces was examined by FTIR–ATR spectroscopy. The FTIR results showed that for PTBA a mixture of *tert*-butyl ester, carboxylic acid, and acid anhydride were formed under the conditions used. The PS-*ran*-PTBA and PS-*b*-PTBA samples were determined by FTIR–ATR analysis to be successfully deprotected. The UA-NCD AFM tips were scanned on PTBA surfaces in contact mode in an attempt to locally catalyze the hydrolysis of the *tert*-butyl groups

on the polymer surface. As a control, H-NCD tips were scanned on PTBA surfaces. After contacting the surface, the areas scanned by the UA-NCD and H-NCD tips were imaged by intermittent contact AFM. Although the areas scanned by both the UA-NCD and H-NCD had similar feature height (2–4 nm), the features were broader with the UA-NCD AFM tip. Alternatively, we attempted scanning the PS-*b*-PTBA and PS-*ran*-PTBA surfaces while heating but intermittent contact AFM images and adhesion measurements did not indicate that PAA was formed. Fluorescent labeling was also unable to confirm the formation of the PAA domains on the PTBA surface scanned with the UA-NCD tip.

References:

(1) Little, R. B.; Roache, J. "Treatise on the Resolution of the Diamond Problem After 200 Years" *Prog. Solid State Chem.* **2008**, *36*, 223–251.

(2) Lavoisier, A. L. "Resultat de quelques experiences faites sur le diamant, par MM. Macquer, Cadet and Lavoisier, lu à la séance publique de l'Académie Royale des Sciences le 29 Avril 1772" Referenced in Siegfried, R. "Lavoisier's View of the Gaseous State and Its Early Application to Pneumatic Chemistry" *Isis*, **1972**, *63*, 59–78.

(3) Tennant, S. "On the Nature of the Diamond" *Phil. Trans. R. Soc. Lond.* **1797**, *87*, 123–127. Referenced in May, P. W. "Diamond Thin Films: a 21st-Century Material" *Phil. Trans. R. Soc. Lond.* A **2000**, *358*, 473–495.

(4) Davy, H. *Elements of Chemical Philosophy* Stuart and Murray: London, 1840; pp. 221–232.

(5) Bragg, W. H.; Bragg, W. L. "The Structure of the Diamond" *Proc. R. Soc. Lond. A* **1913**, *89*, 277–291.

(6) Yoder, M. N. Diamond Properties and Applications. In *Diamond Films and Coatings*; Davis, R. F., Ed.; Noyes Publications: Park Ridge, New Jersey, 1993: pp. 1–15.

(7) Nassau, K. Synthesis of Bulk Diamond: History and Present Status. In *Diamond Films and Coatings*; Davis, R. F., Ed.; Noyes Publications: Park Ridge, New Jersey, 1993: pp. 40–49.

(8) De Carli, P. S.; Jamieson, J. C. "Formation of Diamond by Explosive Shock" *Science* **1961**, *133*, 1821–1822.

(9) Jensen, K. F. Fundamental of Chemical Vapor Deposition. In *Chemical Vapor Deposition Principles and Applications*; Hitchman, M. L, Jensen, K. F., Eds.; Academic Press: San Diego, CA, 1993; 31–66.

(10) Liu, H.; Dandy, D. S. *Diamond Chemical Vapor Deposition*, Noyes Publications: Park Ridge, New Jersey, 1995; p. 39.

(11) Liu, H.; Dandy, D. S. *Diamond Chemical Vapor Deposition*, Noyes Publications: Park Ridge, New Jersey, 1995; pp. 46–78.

(12) Matsumoto, S.; Sato, Y.; Kamo, M.; Setaka, N. "Vapor Deposition of Diamond Particles from Methane" *Jpn. J. Appl. Phys.* **1982**, *21*, L183–L185.

(13) Liu, H.; Dandy, D. S. *Diamond Chemical Vapor Deposition*, Noyes Publications: Park Ridge, New Jersey, 1995; pp.14–45.

(14) Haubner, R.; Lux, B. "Diamond Growth by Hot-Filament Chemical Vapor Deposition: State of the Art" *Diamond Relat. Mater.* **1993**, *2*, 1277–1294.

(15) Argoitia, A.; Kovach, C. S.; Angus, J. C. Hot-Filament CVD Methods. In *Handbook of Industrial Diamonds and Diamond Films*; Prelas, M. A., Popovici, G., Bigelow, L. K., Eds.; Marcel Dekker Inc.: New York, 1998; pp. 797–816.

(16) Skokov, S.; Weiner, B.; Frenklach, M. "Elementary Reaction Mechanism of Diamond Growth from Acetylene" *J. Phys. Chem.* **1994**, *98*, 8–11.

(17) Zhou, D.; McCauley, T. G.; Qin, L. C.; Krauss, A. R.; Gruen, D. M. "Synthesis of Nanocrystalline Diamond Thin Films from an Ar–CH_4 Microwave Plasma" *J. Appl. Phys.* **1998**, *83*, 540–543.

(18) May, P. W.; Ashfold, M. N. R.; Mankelevich, Y. A. "Microcrystalline, Nanocrystalline, and Ultrananocrystalline Diamond, Chemical Vapor Deposition: Experiment and Modeling of the Factors Controlling Growth Rate, Nucleation, and Crystal Size" *J. Appl. Phys.* **2007**, *101*, 053115-1–053115-9.

(19) May, P. W. "Diamond Thin Films: a 21st-Century Material" *Phil. Trans. R. Soc. Lond.* A **2000**, *358*, 473–495.

(20) Goodwin, D. G.; Butler, J. E. Theory of Diamond Chemical Vapor Deposition In *Handbook of Industrial Diamonds and Diamond Films*; Prelas, M. A., Popovici, G., Bigelow, L. K., Eds.; Marcel Dekker Inc.: New York, 1998; pp. 546–586.

(21) Angus, J. C.; Will, H. A.; Stanko, W. S. "Growth of Diamond Seed Crystals by Vapor Deposition" *J. Appl. Phys.* **1968**, *39*, 2915–2922.

(22) Diederich, L.; Küttel, O. M.; Aebi, P.; Maillard-Schaller, E.; Fasel, R.; Schlapbach, L. "Photoelectron Emission from the Negative Electron Affinity Caesiated Natural Diamond (100) Surface" *Diamond Rel. Mater.* **1998**, *7*, 660–665.

(23) Himpsel, F. J.; Knapp, J. A.; Van Vechten, J. A.; Eastman, D. E. "Quantum Photoyield of Diamond (111)—A Stable Negative-Affinity Emitter" *Phys. Rev. B* **1979**, *20*, 624–627.

(24) Inagaki, M.; Kaneko, K.; Nishizawa, T. "Nanocarbons – Recent Research in Japan" *Carbon,* **2004**, *42*, 1401.

(25) Shenderova, O. A.; Barnard, A. S.; Gruen, D. M. Carbon Family at the Nanoscale. In *Ultrananocrystalline Diamond Synthesis, Properties, and Applications;* Shenderova, O. A., Gruen, D. M.; William Andrew Publishing: Norwich, New York, 2006; pp. 3–12.

(26) Krauss, A. R.; Auciello, O.; Gruen, D. M.; Jayatissa, A.; Sumant, A.; Tucek, J.; Mancini, D. C.; Moldovan, N.; Erdemir, A.; Ersoy, D.; Gardos, M. N.; Busmann, H. G.; Meyer, E. M.; Ding, M. Q. "Ultrananocrystalline Diamond Thin Films for MEMS and Moving Mechanical Assembly Devices" *Diamond Relat. Mater.* **2001**, *10*, 1952–1961.

(27) Kulish, W.; Popov, C.; Bliznakov, S.; Ceccone, G.; Gilliland, D.; Sirghi, L.; Rossi, F. "Surface Bioproperties of Nanocrystalline Diamond/Amorphous Carbon Nanocomposite Films" *Thin Solid Films* **2007**, *515*, 8407–8411.

(28) Szunerits, S.; Boukherroub, R. "Different Strategies for Functionalization of Diamond Surfaces" *J. Solid State Electrochem.* **2008**, *12*, 1205–1218.

(29) Nebel, C. E.; Rezek, B.; Shin, D.; Uetsuda, H.; Yang, N. "Diamond for Bio-Sensor Applications" *J. Phys. D: Appl. Phys.* **2007**, *40*, 6443–6466.

(30) Wang, J.; Carlisle "Covalent Immobilization of Glucose Oxidase on Conducting Ultrananocrystalline Diamond Thin Films" *Diamond Relat. Mater.* **2006**, *15*, 279–284.

(31) Tjong, S. C. Properties of Chemical Vapor Deposited Nanocrystalline Diamond and Nanodiamond/Amorphous Carbon Composite Films. In *Nanocomposite Thin Films and Coatings: Processing Properties and Performance*; Zhang, S.; Ali, N. Eds; Imperial College Press: London, 2007; pp 167–206.

(32) Maier, F.; Ristein, J.; Ley, L. "Electron Affinity of Plasma-Hydrogenated and Chemically Oxidized Diamond (100) Surfaces" *Phys. Rev. B* **2001**, *64*, 165411-1–165411-7.

(33) Liu, Y.; Gu, Z.; Margrave, J. L.; Khabashesku, V. N. "Functionalization of Nanoscale Diamond Powder: Fluoro-, Alkyl-, Amino-, and Amino Acid-Nanodiamond Derivatives" *Chem. Mater.* **2004**, *16*, 3924–3930.

(34) Tsubota, T.; Tanii, S.; Ida, S.; Nagata, M.; Matsumoto, Y. "Chemical Modification of Diamond Surface with $CH_3(CH_2)_nCOOH$ Using Benzoyl Peroxide" *Phys. Chem. Chem. Phys.* **2003**, *5*, 1474–1480.

(35) Wang, H.; Griffiths, J.-P.; Egdell, R. G.; Moloney, M. G.; Foord, J. S. "Chemical Functionalization of Diamond Surfaces by Reaction with Diaryl Carbenes" *Langmuir* **2008**, *24*, 862–868.

(36) Yang, W.; Baker, S. E.; Butler, J. E.; Lee, C.-S.; Russell, Jr., J. N.; Shang, L.; Sun, B.; Hamers, R. J. "Electrically Addressable Biomolecular Functionalization of Conductive Nanocrystalline Diamond Thin Films" *Chem. Mater.* **2005**, *17*, 938–940.

(37) Yeap, W. W.; Chen, S.; Loh, K. P. "Detonation Nanodiamond: An Organic Platform for the Suzuki Coupling of Organic Molecules" *Langmuir*, **2009**, *25*, 185–191.

(38) (a) Zhong, Y. L.; Loh, K. P.; Midya, A.; Chen, Z.-C. "Suzuki Coupling of Aryl Organics on Diamond" *Chem. Mater.* **2008**, *20*, 3137–3144. (b) Zhong, Y. L.; Midya, A.; Ng, Z.; Chen, Z.-C.; Daenen, M.; Nesladek, M.; Loh, K. P. "Diamond-Based Molecular Platform for Photoelectrochemistry" *J. Am. Chem. Soc.* **2008**, *130*, 17218–17219.

(39) Kulisch, W.; Popov, C.; Gilliland, D.; Ceccone, G.; Sirghi, L.; Ruiz, A.; Rossi, F. "Surface Properties of Differently Prepared Ultrananocrystalline Diamond Surfaces" *Diamond Rel. Mater.* **2009**, *18*, 745–749.

(40) Matrab, T.; Chehimi, M. M.; Boudou, J. P.; Benedic, F.; Wang, J.; Naguib, N. N.; Carlisle, J. A. "Surface Functionalization of Ultrananocrystalline Diamond Using Atom Transfer Radical Polymerization (ATRP) Initiated by Electro-Grafted Aryldiazonium Salts" *Diamond Rel. Mater.* **2006**, *15*, 639–644.

(41) Nichols, B. M.; Butler, J. E.; Russell, Jr., J. N.; Hamers, R. J. "Photochemical Functionalization of Hydrogen-Terminated Diamond Surfaces: A Structural and Mechanistic Study" *J. Phys. Chem. B* **2005**, *109*, 20938–20947.

(42) (a) Cicero, R. L.; Chidsey, C. E. D.; Lopinski, G. P.; Wayner, D. D. M.; Wolkow, R. A. "Olefin Additions of H–Si(111): Evidence for a Surface Chain Reaction Initiated at Isolated Dangling Bonds" *Langmuir* **2002**, *18*, 305–307. (b) Yang, N.; Uetsuka, H.; Watanabe, H.; Nakamura, R.; Nebel, C. E. "Photochemical Amine Layer Formation on H-Terminated Single-Crystalline CVD Diamond" *Chem. Mater.* **2007**, *19*, 2852–2859

(43) Colvita, P. E.; Streifer, J. A.; Sun, B.; Wang, X.; Warf, P.; Hamers, R. J. "Enhancement of Photochemical Grafting of Terminal Alkenes at Surfaces via Molecular Mediators: The Role of Surface-Bound Electron Acceptors" *J. Phys. Chem. C* **2008**, *112*, 5102–5112.

(44) Yang, W.; Auciello, O.; Butler, J.E.; Cai, W.; Carlisle, J. A.; Gerbi, J. E.; Gruen, D. M.; Knickerbocker, T.; Lasseter, T. L.; Russell, Jr., J. N.; Smith, L. M.; Hamers, R. J. "DNA-Modified Nanocrystalline Diamond Thin-Films as Stable, Biologically Active Substrates: *Nature Mat.* **2002**, *1*, 253–257.

(45) Härtl, A.; Schmich, E.; Garrido, J. A.; Hernando, J.; Catharino S. C. R.; Walter, S.; Feulner, P.; Kromka, A.; Steinmüller, D.; Stutzmann, M. "Protein-Modified Nanocrystalline Diamond Thin Films for Biosensor Applications" *Nature Mat.* **2004**, *3*, 736–742.

(46) Zhong, Y. L.; Chong, K. F.; May, P. W.; Che, Z.-K.; Loh, K. P. "Optimizing Biosensing Properties on Undecylenic Acid-Functionalized Diamond" *Langmuir* **2007**, *23*, 5824–5830.

(47) Wenmackers, S.; Pop, S. D.; Roodenko, K.; Vermeeren, V.; Williams, O. A.; Daenen, M.; Douhéret, O.; D'Haen, J.; Hardy, A.; Van Bael, M. K.; Hinrichs, K.; Cobet, C.; van de Ven, M.; Ameloot, M.; Haenen, K.; Michiels, L.; Esser, N.; Wagner, P. "Structural and Optical Properties of DNA Layers Covalently Attached to Diamond Surfaces" *Langmuir* **2008**, *24*, 7269–7277.

(48) Su, C.; Huang, L.; Kjoller, K.; Babcock, K. "Studies of Tip Wear Processes in Tapping Mode Atomic Force Microscopy" *Ultramicroscopy*, **2003**, *97*, 135–144.

(49) Piner, R. D.; Zhu, J.; Xu, F.; Hong, S.; Mirkin, C. A. "'Dip–Pen' Nanolithography" *Science* **1999**, *283*, 661–663.

(50) Binnig, G.; Despont, M.; Drechsler, U.; Häberle, W.; Lutwyche, M.; Vettiger, P.; Mamin, H. J.; Chui, B. W.; Kenny, T. W. "Ultrahigh-Density Atomic Force Microscopy Data Storage with Erase Capability" *Appl. Phys. Lett.* **1999**, *74*, 1329–1331.

(51) Ebner, A.; Wildling, L.; Zhu, R.; Rankl, C.; Haselgrübler, T.; Hinterdorfer, P.; Gruber, H. J. "Functionalization of Probe Tips and Supports for Single-Molecule Recognition Force Microscopy" *Top. Curr. Chem.* **200**, *285*, 29–76.

(52) Gryko, D. T.; Clausen, C.; Roth, K. M.; Dontha, N.; Bocian, D. F.; Kuhr, W. G.; Lindsey, J. S. "Synthesis of 'Porphyrin-Linker-Thiol' Molecules with Diverse Linkers for Studies of Molecular-Based Information Storage" *J. Org. Chem.* **2000**, *65*, 7345–7355.

(53) Pfister, J. R.; Wymann, W. E. "A Useful Variant of the Curtius Reaction" *Synthesis* **1983**, 38–40.

(54) Voicu, R.; Boukherroub, R.; Bartzoka, V.; Ward, T.; Wojtyk, J. T. C.; Wayner, D. D. M. "Formation, Characterization, and Chemistry of Undecanoic Acid-Terminated Silicon Surfaces: Patterning and Immobilization of DNA" *Langmuir* **2004**, *20*, 11713–11720.

(55) Arnold, R.; Azzam, W.; Terfort, A.; Wöll, C. "Preparation, Modification, and Crystallinity of Aliphatic and Aromatic Carboxylic Acid Terminated Self-Assembled Monolayers" *Langmuir* **2002**, *18*, 3980–3992.

(56) Mayo, D. W.; Pike, R. M.; Trumper, P. K. Introduction to Infrared Spectroscopy. In *Microscale Techniques for the Organic Laboratory*, 2nd edition; John Wiley and Sons: New York, 2001, pp 151–161.

(57) Grasselli, J. G.; Snavely, M. K.; Bulkin, B. J. The Raman Effect. In *Chemical Applications of Raman Spectroscopy* Wiley New York 1981: 1–11.

(58) Knight, D. S.; White, W. B. "Characterization of Diamond Films by Raman Spectroscopy" *J. Mater. Res.* **1989**, *4*, 385–393

(59) Birrell, J.; Gerbi, J.E.; Auciello, O.; Gibson, J. M.; Johnson, J.; Carlisle, J. A. "Interpretation of the Raman Spectra of Ultrananocrystalline Diamond" *Diam. Relat. Mater.* **2005**, *14*, 86–92.

(60) Garguilo, J. M.; Davis, B.A.; Buddie, M.; Köck, F. A. M.; Nemanich, R. J. "Fibrinogen Adsorption onto Microwave Plasma Chemical Vapor Deposited Diamond Films" *Diam. Rel. Mat.* **2004**, *13*, 595–599.

(61) Chidsey, C. E. D.; Loiacono, D. N. "Chemical Functionality in Self-Assembled Monolayers: Structural and Electrochemical Properties" *Langmuir* **1990**, *6*, 682–691.

(62) Yang, Z.; Engquist, I. Wirde, M.; Kauffmann, J.-M.; Gelius, U.; Liedberg, B. "Preparation and Characterization of Mixed Monolayer Assemblies Composed of Thiol Analogues of Cholesterol and Fatty Acid" *Langmuir* **1997**, *13*, 3210–3218.

(63) Quéré, D. "Rough Ideas on Wetting" *Physica A* **2002**, *313*, 32–46.

(64) Stöhr, J. *NEXAFS Spectroscopy*; Gomer, R., Ed.; Springer Series in Surface Sciences Vol. 25; Springer-Verlag: New York, 1992.

(65) Konicek, A. R.; Grierson, D. S.; Gilbert, P. U. P. A.; Sawyer, W. G.; Sumant, A. V.; Carpick, R. W. "Origin of Ultralow Friction and Wear in Ultrananocrystalline Diamond" *Phys. Rev. Lett.* **2008**, *100*, 235502-1–234402-4.

(66) Bagus, P.; Weiss, K.; Schertel, A.; Wöll, C.; Braun, W.; Hellwig, C.; Jung, C. "Identification of Transitions into Rydberg States in the X-Ray Absorption Spectra of Condensed Long-Chain Alkanes" *Chem. Phys. Lett.* **1996**, *248*, 129–135.

(67) Lo, Y.-S.; Huefner, N. D.; Chan, W. S.; Dryden, P.; Hagenhoff, B.; Beebe, T. P. "Organic and Inorganic Contamination on Commercial AFM Cantilevers" *Langmuir*, **1999**, *15*, 6522–6526.

(68) Lin, T.;Yu, C. Y.; Wee, A. T. S.; Shen, Z. X.; Loh, K. P. "Compositional Mapping of the Argon–Methane–Hydrogen System for Polycrystalline to Nanocrystalline Diamond Film Growth in a Hot-Filament Chemical Vapor Deposition System" *Appl. Phys. Lett.* **2000**, *77*, 2692–2694.

(69) Nistor, L. C.; Van Landuyt, J.; Ralchenko, V. G.; Obraztsova, E. D.; Smolin, A. A. "Nanocrystalline Diamond Films: Transmission Electron Microscopy and Raman Spectroscopy Characterization" *Diamond Relat. Mater.* **1997**, *6*, 159–168.

(70) Xu, C.; Fu, S.; Fryd, M.; Xu, S.; Wayland, B. B.; Winey, K. I.; Composto, R. J. "Reversible Stimuli-Responsive Nanostructures Assembled from Amphiphilic Block Copolymers" *Nano Lett.* **2006**, *6*, 282–287.

(71) La, Y.-H.; Edwards, E. W.; Park, S.-M.; Nealey, P. F. "Directed Assembly of Cylinder-Forming Block Copolymer Films and Thermochemically Induced Cylinder to Sphere Transition: A Hierarchical Route to Linear Arrays of Nanodots" *Nano. Lett.* **2005**, *5*, 1379–1384.

(72) Wallraff, G.; Hutchinson, J.; Hinsberg, W.; Houle, F.; Seidel, P.; Johnson, R.; Oldham, W. "Thermal and Acid-Catalyzed Deprotection Kinetics in Candidate Deep Ultraviolet Resist Materials" *J. Vac. Sci. Technol. B* **1994**, *12*, 3857–3862.

(73) McConnell, M. D.; Bassani, A. W.; Yang, S.; Composto, R. J. "Tunable Wetting of Nanoparticle-Decorated Polymer Films" *Langmuir* **2009**, *25*, 11014–11020.

(74) McConnell, M. D.; Yang, S.; Composto, R. J. "Covalent Nanoparticle Assembly onto Random Copolymer Films" *Macromolecules* **2009**, *42*, 517–523.

(75) Obtained from the distributor, Polymer Source, Inc. (Montreal, Canada).

Chapter 4 Conclusion and Future Directions

4.1 Tripodal Molecular Tips

4.1.1 Conclusion

Three biotinylated molecular tips (**A**–**C**) were synthesized for the chemical modification of AFM tips for SMFS measurements. The molecular tripod tips have three rigid phenylethynyl legs that diverge from a tetrasubstituted adamantane core with a terminal alkyne as the fourth substituent. Biotinylated tripod molecular tips **A** and **C** with different linker lengths were prepared. For comparison, molecular monopod **B** with an alkyl thiol scaffold and ethylene glycol linker terminated with biotin was also synthesized. These three biotinylated molecular tips **A**, **B**, and **C** were adsorbed onto gold surfaces of AFM tips and successfully employed in force–distance curve measurements with a NeutrAvidin substrate. The single molecule rupture events were observed in the experiments with molecular tripod tips (**A** and **C**), with significantly sharper force distributions than molecular monopod tip **B**, indicating that the rigid tripod scaffold is advantageous for SMFS. The rupture force values obtained in this study are in good agreement with previously reported results. The length of the linker in molecular tripod tips did not significantly affect the distribution of rupture forces, but the longer linker in molecular tip **C** simplified the identification of specific rupture forces.

Also, the robustness of the tripod and monopod tips for SMFS was compared by continuously repeated measurements. As observations were accumulated during the repeated approach/retract cycles, the distribution of the rupture forces for the monopod system was rapidly altered toward nonspecific interactions, whereas tripod **A** provided

consistent results throughout the experiments. We hypothesize this reproducibility results from the strong connection of the molecular tripod tip onto the gold surface through six covalent S–Au bonds in the tripod legs. The loading rate dependence of the rupture of the biotin–NeutrAvidin complex followed a similar trend as previously reported. Complementary results of the control experiments demonstrated that the majority of the observed rupture force distribution peaks in molecular tripod tips **A** and **C** corresponded to the specific unbinding force of biotin and NeutrAvidin.

4.1.2 Future Directions

The molecular tripod tips have potential uses in AFM tip modifications. The terminal acetylene of the tripod gives the molecule the capability to link to any azide-containing molecule *via* click chemistry. The terminal alkyne group of the tripod scaffold can be attached to various ligands by click chemistry for SMFS studies. Also, the tripod scaffolding with the terminal acetylene can be immobilized on the AFM tip followed by an *in situ* click reaction with various ligands (Figure 4-1). The ability to attach molecules in a high yielding manner to AFM tips can be applied toward the development of screening drug candidates by SMFS. SMFS requires only a small amount of protein for analysis. Transmembrane receptors like $P2X_2$[1] are desirable targets because of the difficulty in obtaining significant amounts of pure protein and their importance in pain signaling in the body.

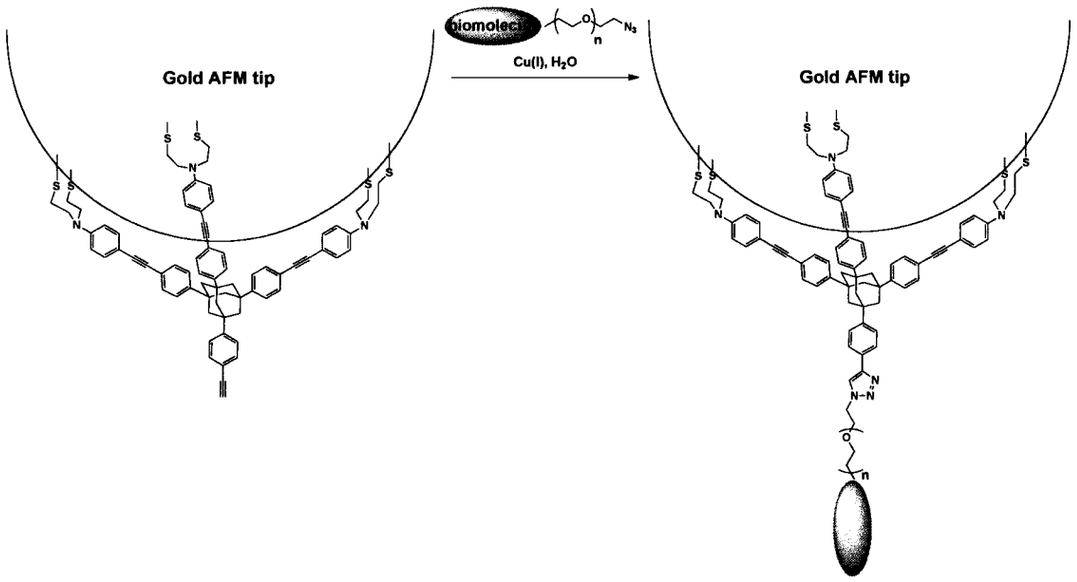

Figure 4-1. The tripod acetylene functionalized gold AFM tip can react through click chemistry with a biomolecule.

The mechanism of the damage of thiols on gold AFM tips in the force spectroscopy studies was not thoroughly investigated. The damage could have been caused by oxidation followed by desorption of the thiols or by the delamination of the gold layer that effectively removes the molecules adsorbed on the gold layer. To investigate the method of detachment, force spectroscopy measurements can be performed in degassed solvents under an inert atmosphere. If the damage to the monolayer is from oxidation of the sulfur groups, the damage should be decreased under inert conditions, whereas if the monolayer damage is from delamination, the inert atmosphere experiments will have a minimal effect on the stability of the monolayer.

4.2 Functionalization of Nanocrystalline Diamond AFM Tips

4.2.1 Conclusion

NCD films and NCD-coated AFM tips were prepared by HFCVD. The deposited films were composed of quality diamond as determined by Raman and NEXAFS spectroscopy. SEM and AFM images of NCD films on Si wafers showed that the polycrystalline diamond surface had grains 20-100 nm in diameter. SEM and AFM images of the backside of NCD cantilevers revealed a similar polycrystalline coating. TEM images of the AFM tips showed grains 10–20 nm in diameter whose electron diffraction patterns were consistent with NCD. The H-NCD and UA-NCD surfaces were compared with water contact angle measurements, FTIR–ATR, XPS, and NEXAFS spectroscopy. These surface analysis techniques verified the success of the UA treatment and encouraged us to functionalize NCD AFM tips. Compared to the H-NCD AFM tips, the UA-NCD AFM tips showed enhanced fluorescence when subjected to carboxylic acid selective labeling conditions. Also, UA-NCD AFM tips displayed greater adhesion with a carboxylic acid-terminated surface. Thus, we document the first successful functionalization of NCD AFM tips. The modification of NCD tips is expected to find use in scanning probe based lithography, biological applications, or other applications that require stable linkages to a durable, wear-resistant AFM tip.

UA and H-NCD tips were used in contact mode scanning to pattern a PTBA surface. After patterning, intermittent contact AFM images showed a distinct difference between the patterns made by the two separate tips that indicated the chemical modification of NCD tips was successful. However, the chemical transformation from

PTBA to the carboxylic acid could not be determined definitively on such a small scale in our studies. Annealed polymer surfaces created acid anhydride groups that were not easily hydrolyzed to the carboxylic acid. Random and block copolymers were also examined, but it remained difficult to analyze the chemical transformation. Adhesion measurements and intermittent contact images of polymer surfaces heated while scanned with the UA-NCD tip showed no change in the patterned region.

4.2.2 Future Directions

Chemical modifications of AFM tips are currently performed on silicon and gold tips. The UA-NCD AFM tips can be used to examine the durability of each of the AFM tip functionalizations. Durability tests can be performed with functionalized silicon, gold, and NCD tips on modified gold surfaces to examine if there are shifts in forces over repeated force–distance curves. We hypothesize that the NCD AFM tips will degrade at a slower rate than the silicon and gold AFM tips. A durability study would be useful to determine the most robust functionalization of AFM tips.

Future work could also include a new chemical modification of NCD surfaces. Another proposal is the modification of a H-terminated diamond surface with aryl azides to crosslink molecules to NCD surfaces (Figure 4-2).[2] Aryl nitrenes can be generated photochemically from aryl azides[3] and perfluorinated aryl azides.[4,5] Previous reports of this insertion into C–H bonds of polymer surfaces reached completion after less than a minute of treatment.[7] A short reaction time is an advantage to the long treatments (16

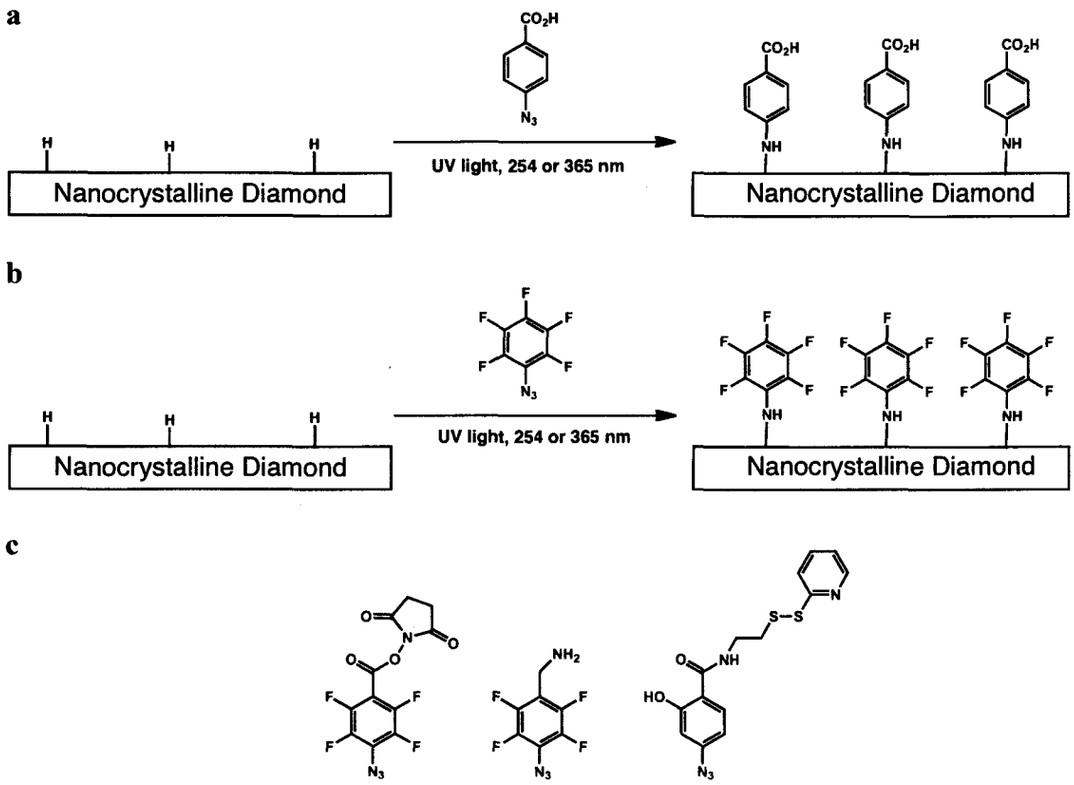

Figure 4-2. Photoactivable aryl azides to modify NCD surfaces. (a) UV treatment of 4-azidobenzoic acid on H-NCD could yield a carboxylic acid terminated surface. (b) Perfluorinated aryl azide for modification of a NCD surface. (c) Some examples of commercially available aryl azides to crosslink biomolecules with NCD surfaces.

hours) necessary to treat NCD surfaces with undecylenic acid. The modified surfaces would be initially studied by various spectroscopic methods (XPS, FTIR–ATR spectroscopy, contact angle) to examine the insertion of the nitrene into the C–H bonds of the NCD surface. There are many commercially available aryl azides to act as linkers between polymer surfaces and biomolecules.[6,7] Commercially available aryl azides have NHS-ester, amine, and disulfide (Figure 4-2c) functional groups that can be used to attach various molecules after immobilization onto the diamond surface. This

functionalization method could be used for NCD films and on NCD AFM tips for immobilization of biomolecules for SMFS and other biological applications.

References:

(1) Nakazawa, K.; Yamakoshi, Y.; Tsuchiya, T.; Ohno, Y. "Purification and Aqueous Phase Atomic Force Microscopic Observation of Recombinant P2X2 Receptor" *Eur. J. of Pharmacol.* **2005**, *518*, 107–110.

(2) Gross, A. J.; Yu, S. S. C.; Downard, A. J. "Two-Component Mixed and Patterned Films on Carbon Surfaces Through the Photografting of Arylazides" *Langmuir* **2010** *ASAP*, DOI: 10.1021/la904442u.

(3) Brunner, J. "New Photolabeling and Crosslinking Methods" *Annu. Rev. Biochem.* **1993**, *62*, 483–514.

(4) Keana, J. F. W.; Cai, S. X. "New Reagents for Photoaffinity Labeling: Synthesis and Photolysis of Functionalized Perfluorophenyl Azides" *J. Org. Chem.* **1990**, *55*, 3640–3647.

(5) Haugland, R. P. Chapter 5 Crosslinking and Photoactivatable Reagents. In *The Handbook: A Guide to Fluorescent Probes and Labeling Technologies*, 10th edition; Spence, M. T. Z.; Invitrogen Corp: USA, 2005, pp. 170–171.

(6) (a) Yan, M.; Cai, S. X.; Wybourne, M. N.; Keana, J. F. W. "Photochemical Functionalization of Polymer Surfaces and the Production of Biomolecule-Carrying Micrometer-Scale Structures by Deep-UV Lithography Using 4-Substituted Perfluorophenyl Azides" *J. Am. Chem. Soc.* **1993**, *115*, 814–816. (b) Yan, M.; Cai, S. X.; Wybourne, M. N.; Keana, J. F. W. "*N*-Hydroxysuccinimide Ester Functionalized Perfluorophenyl Azides as Novel Photoactive Heterobifunctional Cross-Linking Reagents. The Covalent Immobilization of Biomolecule to Polymer Surfaces" *Bioconj. Chem.* **1994**, *5*, 151–157.

(7) Sugawara, T.; Matsuda, T. "Photochemical Protein Fixation on Polymer Surfaces via Derivatized Phenyl Azido Group" *Langmuir*, **1995**, *11*, 2272–2276.

Chapter 5 Experimental Section

5.1 Synthetic Procedures

5.1.1 General Procedures

The melting points were measured with MELTEMP (Laboratory Devices, Holliston, MA) and are uncorrected. ^{1}H- and ^{13}C-NMR spectra were recorded on a Varian 400 MHz NMR spectrometer (Varian Inc., Palo Alto, CA USA) at 400 and 100 MHz or on a Bruker 500 MHz NMR spectrometer (Bruker, Newark, DE USA) at 500 MHz and 125 MHz. Mass spectrometry was performed on the VG70 double-focusing mass spectrometer (VG Analytical, Manchester, UK) for the ionization methods of electron impact (EI), chemical ionization (CI), and fast atom bombardment (FAB). Electrospray ionization (ESI) MS was performed on the PE Sciex Qstar (Applied Biosystems, Foster City, CA) and matrix assisted laser-desorbed ionization–time of flight (MALDI–TOF) MS was performed on MALDI–TOF DYNAMO system (Thermo Bioanalysis, Santa Fe, NM or on a Bruker MALDI-TOF-TOF). IR spectra were recorded on a FT/IR-430 (JASCO, Tokyo, JPN). All the reagents were purchased from the corresponding commercially available sources and purified as described when needed. All solvents were purchased from EMD Chemicals Inc. (Gibbston, NJ USA) unless described. THF, acetonitrile, and methanol were passed over activated alumina under an Ar atmosphere and DMF was passed over molecular sieves under an Ar atmosphere by a solvent system (Innovative Technology Inc., Newburyport, MA). Benzene and dichloromethane were distilled over calcium hydride. Column chromatography, analytical TLC, and preparative TLC were performed on Silica Gel

(Merck Silica gel 60 F254 (Art 5715) 0.25 mm, EMD Science silica gel 60 PF254, and E. Merck Silica gel 60 (230-400 mesh), respectively). TLC plates were visualized by UV light, a phosphomolybdic acid stain, or a $KMnO_4$ stain.

5.1.2 Synthetic Procedure for Biotinylated Monopod and Tripodal Molecules

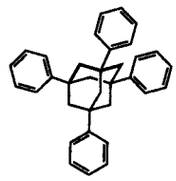

2-1

1,3,5,7-Tetraphenyladamantane (2-1).[1] To a solution of 1-bromoadamantane (Alfa Aesar, 9.00 g, 41.7 mmol) in 80 mL of benzene (distilled over CaH_2), *t*-butyl bromide (Alfa Aesar, 14.3 mL, 125 mmol) and $AlCl_3$ (Alfa Aesar, 0.560 g, 0.417 mmol) were added and the reaction mixture was refluxed for 4 hours. A colorless solid precipitated formed and the reaction mixture was cooled to room temperature and filtered. The grayish precipitate was washed with benzene (50 mL), H_2O (50 mL), and $CHCl_3$ (75 mL). The residue was dried in a vacuum oven overnight and then purified in a Soxhlet apparatus using refluxing $CHCl_3$. The gray solid was dried in a vacuum oven to give colorless powder that was insoluble in organic solvents **2-1** (13.4 g, 30.4 mmol, 73%): MS (EI): $[M^+]$ calcd for $C_{34}H_{32}$ 440.3, found 440.0.

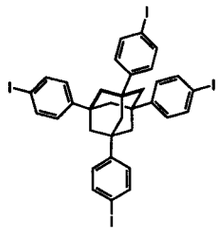

2-2

1,3,5,7-Tetrakis-(4-iodophenyl)adamantane) (2-2).[1] To a suspension of **2-1** (2.00 g, 4.54 mmol) in $CHCl_3$ (50 mL), I_2 (EMD, 2.30 g, 9.06 mmol) that was crushed with a mortar and pestil was added and stirred until the I_2 was fully dissolved. Subsequently, [bis-(trifluoroacetoxy)iodo]benzene (Alfa Aesar, 3.90 g, 9.08 mmol) was added to the purple reaction mixture and stirred under N_2 atmosphere for two hours. Then two more equivalents of I_2 (2.30 g, 9.06 mmol) were added into the solution and stirred for 30 min. Two more equivalents of [bis-(trifluoroacetoxy)iodo]benzene (3.90 g, 9.08 mmol) were added and the solution was stirred overnight. The solution was filtered and the solid was washed three times with $CHCl_3$ (10 mL). The $CHCl_3$ filtrate was washed with a 5% $NaHSO_3$ solution (75 mL) and the purple $CHCl_3$ solution became yellow. The $CHCl_3$ layer was then washed with water (75 mL), brine (75 mL), and was dried over Na_2SO_4. The crude mixture was purified by flash chromatography (5:1 hexanes/$CHCl_3$) to give colorless crystals **2-2** (2.79 g, 2.96 mmol, 65%): ^1H NMR (400 MHz, $CDCl_3$) δ 7.68 (d, J = 8.8 Hz, 8H), 7.19 (d, J = 8.8 Hz, 8H), 2.06 (s, 12H); MS (FAB): [M^+] calcd for $C_{34}H_{28}I_4$ 943.8, found 944.0.

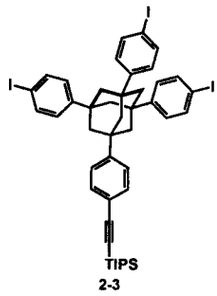

2-3

Triisopropyl[4-[3,5,7-tris-(4-iodophenyl)adamantan-1-yl]phenylethynyl]silane (2-3). In a solution of **2-2** (1.28 g, 1.36 mmol) in THF (10 mL), $Pd(PPh_3)_2Cl_2$ (48 mg, 0.068 mmol), CuI (5 mg, 0.03 mmol), PPh_3 (8 mg, 0.03 mmol), and Et_3N (5 mL) were added in a Schlenck tube and the mixture was degassed 4 times by freeze/pump/thaw. Triisopropylsilylacetylene (Fluka, 0.152 mL, 0.678 mmol) was added through the septum and the reaction mixture was degassed three times more. A balloon filled with Ar was added and the reaction was stirred at room temperature overnight. The reaction mixture was concentrated *in vacuo* and the crude mixture was purified by flash chromatography twice (5:1 hexanes/$CHCl_3$) to give colorless crystals **2-3** (0.250 g, 0.250 mmol, 18%): mp 182–185 °C; IR (thin film): 3087, 3046, 2938, 2897, 2862, 2154, 1898, 1504, 1487, 1462, 1449, 1391, 1357, 1263, 1068, 1189, 1003, 883, 835, 818, 779, 739, 705, 679, 662 cm^{-1}; ^1H NMR (400 MHz, $CDCl_3$) δ 7.68 (d, J = 8.4 Hz, 6H, Ar***H*** *ortho* to iodine), 7.48 (d, J = 8.4 Hz, 2H, Ar***H*** *ortho* to –TIPS alkyne), 7.37 (d, J= 8.3 Hz, 2H, Ar***H*** *meta* to TIPS alkyne), 7.21 (d, J = 8.6 Hz, 6H, Ar***H*** *meta* to iodine), 2.08 (s, 12H, adamantane), 1.14 (s, 21H, –TIPS group); ^{13}C NMR (100 MHz, $CDCl_3$) δ 149.10, 148.68, 137.69, 132.35, 127.35, 125.01, 121.82, 106.99, 91.91, 90.70, 46.90, 46.85, 39.38, 39.24, 18.87, 11.49; MS (FAB): $[M^+]$ calcd for $C_{45}H_{49}I_3Si$, 998 found 998 and $[M–C_3H_7]^+$ 955.

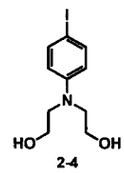

2-4

***N,N*-Bis(2-hydroxyethyl)-4-iodoaniline (2-4).**[1] Ethylene oxide (TOXIC GAS! Praxair Technology Inc., Danbury, CT, 10.6 g, 0.240 mol, 12.0 mL) was condensed by attaching the lecture bottle to a thick-walled reaction tube (Schlenk tube) cooled in a dry ice/acetone bath. A solution of 4-iodoaniline (Alfa Aesar, Ward Hill, MA, 7.00 g, 32.0 mmol) in MeOH (12 mL) cooled to 0 °C was added to the reaction tube. The reaction tube was sealed and stirred at 0°C for 30 min. Then it was slowly warmed up to 60 °C and stirred overnight. The reaction mixture was opened and vented in the hood for several minutes before transferring to a flask for rotary evaporation. The crude mixture was purified by flash chromatography (9:1 to 4:1 CH_2Cl_2/MeOH) to give colorless crystals of **2-4** (7.26 g, 23.6 mmol, 74%): ^{1}H NMR (400 MHz, $CDCl_3$) δ 7.45 (d, J = 9.0 Hz, 2H), 6.47 (d, J = 9.0 Hz, 2H), 3.80 (t, J = 4.9 Hz, 4H), 3.53 (t, J = 4.9 Hz, 4H); MS (EI): [M^+] calcd for $C_{10}H_{14}INO_2$ 307.0, found 307.1.

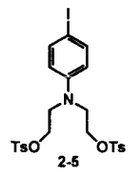

2-5

***N,N*-Bis(2-tosyloxy)-4-iodoaniline (2-5).** A solution of **2-4** (2.00 g, 6.51 mmol) in distilled CH_2Cl_2 (50 mL) in a 200 mL round bottom flask was cooled to 0 °C and (in

order) Et_3N (EMD Chemicals Inc., Gibbstown, NJ, 5.50 mL, 39.1 mmol), DMAP (Sigma-Aldrich Co., Milwaukee, WI, 0.160 g, 1.31 mmol) and TsCl (Sigma-Aldrich, 3.72 g, 19.5 mmol) were added. After the reaction was stirred for 30 minutes at 0 °C, the ice bath was removed and the reaction was subsequently stirred for three hours at room temperature under N_2 atmosphere. When the reaction was deemed complete by TLC, the mixture was diluted with CH_2Cl_2 (50 mL). The organic layer was washed three times with brine (100 mL), dried over Na_2SO_4, and concentrated *in vacuo*. The crude mixture was purified by flash chromatography (4:1 to 1:1 hexanes/EtOAc) to give colorless crystals **2-5** (3.71 g, 6.03 mmol, 93%): R_f = 0.67 (1:1 hexanes/EtOAc); mp 96–98 °C; IR (thin film) 3061, 2956, 2925, 1587, 1496, 1361, 1266, 1189, 1176, 1096, 972, 894, 813, 769, 738, 703, 664, 553 cm^{-1}; ^1H NMR (400 MHz, $CDCl_3$) δ 7.68 (d, J = 8.2 Hz, 4H, Ar***H*** *ortho* to sulfone), 7.35 (d, J = 8.4 Hz, 2H, Ar***H*** *meta* to amine), 7.26 (d, J = 8.6 Hz, 4H, Ar***H*** *meta* to sulfone), 6.18 (d, J = 8.5 Hz, 2H, Ar***H*** *ortho* to amine), 4.07 (t, J = 5.8 Hz, 4H, –$CH_2C\boldsymbol{H_2}OTs$), 3.53 (t, J = 5.8 Hz, 4H, –$C\boldsymbol{H_2}CH_2OTs$), 2.44 (s, 6H, –PhC$\boldsymbol{H_3}$); ^{13}C NMR (100 MHz, $CDCl_3$) δ 145.31, 145.20, 137.82, 132.23, 129.93, 127.78, 114.20, 78.43, 66.38, 49.93, 21.76; HRMS (ESI): $[M+H]^+$calcd for $C_{24}H_{27}INO_6S_2$ 616.0324, found 616.0303.

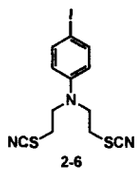

2-6

***N,N*-Bis(2-thiocyanatoethyl)-4-iodoaniline (2-6).**[1] To a solution of 18-crown-6 (Alfa Aesar, 1.28 g, 4.83 mmol) and **2-5** (3.71 g, 6.03 mmol) in dry CH_3CN (60 mL), excess KSCN (Alfa Aesar, 11.7 g, 121 mmol) was added slowly while the solution was stirred vigorously. The reaction was refluxed for 2 days under N_2 atmosphere and was monitored by NMR analysis. When the reaction was complete by NMR, the reaction mixture was cooled to room temperature and diluted with water (150 mL). The solution was then extracted three times with CH_2Cl_2 (100 mL) and the combined organic layers were dried over Na_2SO_4 and concentrated to dryness. The crude mixture was purified by flash chromatography (4:1 hexanes/EtOAc) to give yellowish crystals **2-6** (2.03 g, 5.08 mmol, 84%): ^{1}H NMR (400 MHz, $CDCl_3$) δ 7.56 (d, J = 9.1 Hz, 2H), 6.57 (d, J = 9.1 Hz, 2H), 3.83 (t, J = 6.8 Hz, 4H), 3.12 (t, J = 7.0 Hz, 4H); MS (EI): [M^+] calcd for $C_{12}H_{12}IN_3S_2$ 389.0, found 388.9.

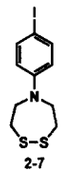

2-7

5-(4-Iodoethyl)-[1,2,5]dithiazepane (2-7).[1] A solution of **2-6** (2.02 g, 5.19 mmol) in 9:1 EtOH/H_2O (156 mL) with potassium hydroxide (EMD, 0.577 g, 10.3 mmol) was refluxed for 1 h when no starting material remained when checked by TLC (4:1

hexanes/EtOAc). The reaction was cooled and concentrated to remove the solvent and water (75 mL) was added. The aqueous layer was extracted with $CHCl_3$ (3 x 75 mL) and the combined organic extracts were washed with brine (2 x 50 mL), dried over Na_2SO_4, and concentrated *in vacuo* to give colorless crystals. The crystals were purified by flash chromatography (2:1 hexanes/CH_2Cl_2) to give colorless crystals **2-7** (1.45 g, 4.30 mmol, 83%): R_f = 0.74 (4:1 hexanes/EtOAc); ^{1}H NMR (400 MHz, $CDCl_3$) δ 7.47 (d, J = 9.1 Hz, 2H), 6.42 (d, J = 9.1Hz, 2H), 3.94 (t, J = 5.5 Hz, 4H), 3.07 (t, J = 5.7 Hz, 4H); MS (EI): [M^+] calcd for $C_{10}H_{12}INS_2$ 337.0, found 337.0.

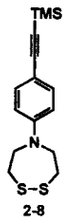

2-8

5-(4-Trimethylsilanylethynyl)-[1,2,5]dithiazepane (2-8).[1] To a solution of **2-7** (1.28 g, 3.80 mmocl) in THF (5 mL), $Pd(PPh_3)_2Cl_2$ (Sigma-Aldrich, 0.267 g, 0.380 mmol), PPh_3 (Alfa Aesar, 0.050 g, 0.19 mmol), Et_3N (EMD, 5 mL) and trimethylsilylacetylene (Alfa Aesar, 2.7 mL, 19 mmol) were added in a Schlenk tube and degassed three times by freeze/pump/thaw. Next, CuI (Alfa Aesar, 12 mg, 0.11 mmol) was added through the septum and the freeze/pump/thaw was repeated twice more. An Ar balloon was added and the reaction was stirred at room temperature for 2 days. The orange solution was then concentrated *in vacuo* and extracted with CH_2Cl_2 (100 mL), washed with water (3 x 25 mL) and dried over Na_2SO_4. The dried extracts were filtered and concentrated *in vacuo* to give a yellow oil that was purified by flash chromatography

(8:1 hexanes/$CHCl_3$). The oil crystallized overnight under vacuum to give yellow crystals **2-8** (1.00 g, 3.25 mmol, 86%): R_f = 0.62 (1:1 hexanes/toluene); ^{1}H NMR (400 MHz, $CDCl_3$) δ 7.35 (d, J = 9.1 Hz, 2H), 6.54 (d, J = 8.9 Hz, 2H), 3.97 (t, J = 5.6 Hz, 4 H), 3.08 (t, J = 5.6 Hz, 4H), 0.23 (s, 9H); MS (EI): [M^+] calcd for $C_{15}H_{21}NS_2Si$ 307.1, found 307.1.

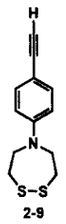

2-9

5-(4-Ethynylphenyl)-[1,2,5]dithiazepane (2-9).[1] To a solution of **2-8** (0.990 g, 3.22 mmol) in $CHCl_3$ (4 mL), K_2CO_3 (EMD, 0.750 g, 5.43mmol) in MeOH (8 mL) was added under a N_2 atmosphere. The reaction was stirred overnight at room temperature and worked up when no starting material remained by TLC (hexanes/toluene (1 : 1)). The reaction mixture was concentrated *in vacuo* to dryness and then dissolved in CH_2Cl_2 (75 mL). The organic layer was washed with H_2O (25 mL) and with brine (2 x 25 mL), dried over Na_2SO_4, and concentrated *in vacuo*. The crude yellowish crystals were purified by flash chromatography (1:1 hexanes/CH_2Cl_2) to give colorless crystals **2-9** (0.692 g, 2.94 mmol, 91%): R_f = 0.50 (1:1 hexanes/toluene); ^{1}H NMR (400 MHz, $CDCl_3$) δ 7.37 (d, J = 9.1 Hz, 2H), 6.57 (d, J = 9.1 Hz, 2H), 3.98 (t, J = 5.5 Hz, 4H), 3.09 (t, J = 5.8 Hz, 4H), 2.98 (s, 1H); MS (EI): [M^+] calcd for $C_{12}H_{13}NS_2$ 235.0, found 235.0.

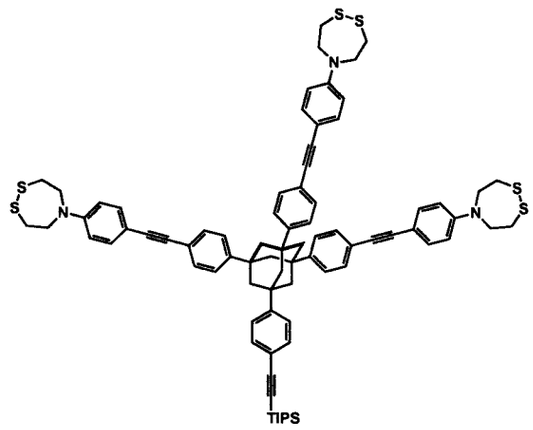

2-10

Triisopropyl[4-[3,5,7-tris-[4-[4-(1,2,5-dithiazepan-5-yl)phenylethynyl]phenyl]adamantan-1-yl]phenylethynyl]silane (2-10). **2-3** (0.486 g, 0.487 mmol), compound **2-9** (0.400 g, 1.70 mmol), THF (15 mL), $Pd(PPh_3)_2Cl_2$ (24 mg, 0.034 mmol), PPh_3 (13 mg, 0.050 mmol), and Et_3N (5 mL) were added to a thick walled sealed Schlenk tube. The mixture was thoroughly degassed by freeze/pump/thaw before CuI (20 mg, 0.11 mmol) was added. The reaction mixture was stirred at room temperature for 2 days and then heated to 60 °C for 4 h. The reaction was cooled and then concentrated *in vacuo* to dryness. The crude was dissolved in CH_2Cl_2 (100 mL) and washed with 1 M HCl (50 mL) and 9:1 NH_4OH/NH_4Cl (2 x 50 mL) to remove any remaining copper. The reaction was purified by column chromatography to give a powdery brown solid **2-10** (325 mg, 0.246 mmol, 51%): R_f = 0.48 (5:1 toluene/hexanes); mp 210 °C (dec); IR (thin film) 3081, 3039, 2924, 2861, 2209, 2153, 1602, 1521, 1468 1398, 1352, 1285, 1216, 1167, 1138, 1014, 900, 815 cm^{-1}; ^1H NMR (400 MHz, $CDCl_3$) δ 7.53–7.39 (m, 22 H, Ar***H***), 6.60 (d, J = 9.1 Hz, 6H, Ar***H*** *ortho* to

amine), 3.99 (t, J = 5.4 Hz, 12H, –NCH_2CH_2SS–), 3.10 (t, J = 5.5 Hz, 12 H, –NCH_2CH_2SS–), 2.16 (s, 6H, adamantane), 2.14 (s, 6H, adamantane), 1.14 (s, 21H, –TIPS group); ^{13}C NMR (100 MHz, $CDCl_3$) δ 148.73, 146.47, 137.70, 133.39, 132.31, 131.56, 127.33, 125.21, 125.16, 122.11, 111.34, 110.77, 91.93, 90.47, 90.25, 87.59, 52.64, 47.06, 39.45, 36.95, 18.89, 11.52; MS (FAB): $[M+H]^+$ calcd for $C_{81}H_{85}N_3S_6Si$ 1320, found 1320.

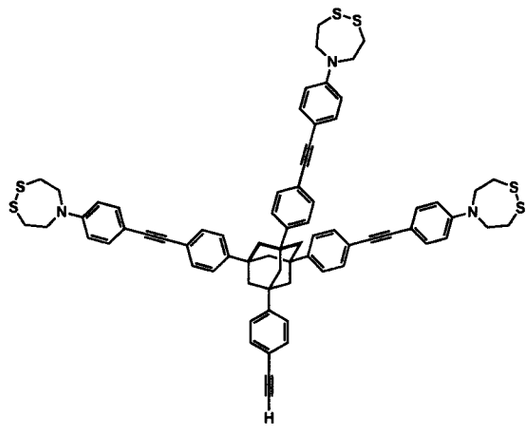

2-11

5,5',5''-(((((1*s*,3*s*,5*s*)-7-(4-ethynylphenyl)adamantane-1,3,5-triyl)tris(benzene-4,1-diyl))tris(ethyne-2,1-diyl))tris(benzene-4,1-diyl))tris(1,2,5-dithiazepane) (2-11). A solution of **2-10** (0.200 g, 0.152 mmol) in THF (5 mL) was sonicated until all solids dissolved. A 1.0 M solution of TBAF (Sigma-Aldrich, 0.160 mL, 0.160 mmol) in THF was added at room temperature. When no starting material was detected by TLC, the solution was concentrated *in vacuo*. The solid was dissolved in CH_2Cl_2 (50 mL) and NH_4Cl (15 mL) was added. The organic layer was separated, dried over Na_2SO_4 and filtered through a plug of silica. The filtrate was then concentrated *in vacuo* to give a

yellowish solid. Et_2O (20 mL) was added to the solid and sonicated for 10 min. The supernatant liquid was removed by pipette and disposed. This process was repeated two more times to give a yellowish powder **2-11** (160 mg, 0.137 mmol, 90%): mp >260°C (dec); IR (thin film): 3287, 3080, 3035, 2925, 2851, 2204, 1604, 1520, 1398, 1352, 1216, 1180, 1166, 1138, 1012, 900, 814, 645, 555, 526 cm^{-1}; ^1H NMR (400 MHz, $CDCl_3$) δ 7.53–7.38 (m, 22H, Ar***H***), 6.60 (d, J = 9.1 Hz, 6H, Ar***H*** *ortho* to amine), 3.99 (t, J = 5.4 Hz, 12 H, –$NCH_2C\boldsymbol{H_2}SS$–), 3.10 (t, J = 5.5 Hz, 12H, –$NC\boldsymbol{H_2}CH_2SS$–), 3.07 (s, 1H, terminal alkyne), 2.16 (s, 12H, adamantane); ^{13}C NMR (100 MHz, $CDCl_3$) δ 148.67, 146.46, 133.39, 132.42, 131.57, 131.46, 128.59, 125.34, 125.21, 122.13, 111.32, 110.74, 90.25, 87.56, 83.79, 76.12, 52.65, 47.04, 39.45, 36.94; MS (FAB): $[M+H]^+$ calcd for $C_{72}H_{66}N_3S_6$ 1164, found 1164.

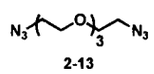

2-13

1,11-Diazido-3,6,9-trioxaundecane (2-13).[2] Tetraethylene glycol **2-12** (Tokyo Chemical Industry Co. Ltd., Tokyo, Japan, 9.0 mL, 52 mmol) was added to a flask with toluene (5 mL) and concentrated by rotary evaporator to dryness. This process was repeated two more times. The residue was then transferred to a flask and dissolved in THF (40 mL) and placed on an ice bath. MsCl (Alfa Aesar, 9.00 mL, 106 mmol) was added and a solution of Et_3N in THF (16.2 mL/20 mL) solution was added over 45 minutes by a dropping funnel. The reaction was stirred at 0 °C for 30 minutes under N_2 atmosphere and then at room temperature for 6 hrs. The reaction was then placed in an ice bath and a yellow solid precipitated. Water (40 mL) and $NaHCO_3$ (4.3 g) were

added to adjust the pH ≥ 8 and the pH was checked by pH paper to ensure a basic solution. **EXPLOSIVE, TOXIC, HN_3** can form under acidic conditions! NaN_3 (Sigma-Aldrich, 6.98 g, 105 mmol) was added slowly, the reaction mixture was allowed to warm to room temperature, then refluxed overnight. The reaction mixture was cooled to room temperature and extracted five times with Et_2O (25 mL) and each layer was washed with brine (30 mL). The combined organic layers were dried over Na_2SO_4, filtered, and concentrated *in vacuo*. The crude oil was purified by flash chromatography (2:1 hexanes/EtOAc) to yield a colorless oil **2-13** (10.45g, 42.8 mmol, 82%): R_f = 0.58 (1:1 hexanes/EtOAc), TLC spots were visualized by $KMnO_4$/acetone; ^1H NMR (400 MHz, $CDCl_3$) δ 3.66 (m, 12H), 3.37 (t, J = 5.3 Hz, 4H); MS (CI): $[M+H]^+$ calcd for $C_8H_{17}N_6O_3$ 245, found 245.

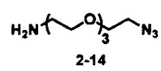

2-14

1-amino-11-azido-3,6,9-trioxaundecane (2-14).[2] **2-13** (4.27 g, 17.5 mmol) was added to a two-neck roundbottom flask equipped with a stir bar. A solution of H_3PO_4 (EMD, 1.77 mL of 85% H_3PO_4 in 40 mL of H_2O) was added and the reaction was put under N_2. PPh_3 (3.99 g, 15.2 mmol) was dissolved in Et_2O (30 mL) and added by dropping funnel over the course of an hour. The reaction was stirred vigorously overnight and a colorless solid precipitated (PPh_3O). The reaction mixture was filtered and the filtrate was placed in a separatory funnel. The Et_2O layer was removed and the aqueous layer was washed three times with Et_2O (15 mL) and KOH (3.3 g) was added to the aqueous layer. The aqueous mixture was refrigerated for 4 h, filtered and washed three times

with water. KOH (9.2 g) was added and the filtrate was extracted 16 times with CH_2Cl_2 (30 mL). The combined organic layers were dried over Na_2SO_4, filtered, and concentrated *in vacuo* to give an amber oil. The oil was purified by flash chromatography (10:1 MeOH/NH_4OH) to give an amber oil **2-14** (2.9 g, 13 mmol, 76%): R_f = 0.35 (10:1 MeOH/NH_4OH), TLC spots were visualized by $KMnO_4$/acetone; ^1H NMR (400 MHz, $CDCl_3$) 3.68 (m, 10H), 3.52 (t, J = 5.3 Hz, 2H), 3.40 (t, J = 5.2 Hz, 2H), 2.88 (t, J = 5.2 Hz, 2H); MS (ESI): $[M+H]^+$ calcd for $C_8H_{19}N_4O_3$ 219.1, found 219.3.

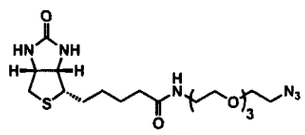

2-15

Biotinylated tetraethyleneglycol linker (2-15). To a solution of D-biotin (Sigma-Aldrich, 390 mg, 1.59 mmol) and HBTU (664 mg, 1.75 mmol) in DMF (6 mL), DIPEA (Lancaster, 0.6 mL) was added slowly and the milky white reaction mixture turned orange. Next, linker **2-14** (347 mg, 1.59 mmol) in DMF (0.5 mL) was added. The reaction was stirred overnight under nitrogen atmosphere at room temperature. The reaction mixture was extracted with CH_2Cl_2 (75 mL), washed with H_2O (25 mL), NH_4Cl (25 mL), and dried over Na_2SO_4. The dried organic extracts were then filtered and concentrated *in vacuo* to give an orange oil. The crude was purified by flash chromatography (10:1 CH_2Cl_2/MeOH to 10:1:0.05 CH_2Cl_2/MeOH/Et_3N) to yield a yellow, sticky solid **2-15** (0.536 g, 1.21 mmol, 76%): R_f = 0.50 (10:1 $CHCl_3$/MeOH), TLC spots were visualized by a phosphmolybdate stain; mp 91–93°C; IR (thin film):

3392, 2927, 2871, 2111, 1690, 1648, 1554, 1462, 1347, 1267, 1119, 938 cm^{-1}; ^1H NMR (400 MHz, $CDCl_3$) δ 6.90 (t, *J* = 5.4Hz, amide N***H***), 6.82 (s, 1H, biotin ureido N***H***), 5.94 (s, 1H, biotin ureido N***H***), 4.48 (m, 1H, biotin –$SCH_2CHNHCONH$–), 4.28 (m, 1H, biotin –$SCH(CH_2$–)$CHNHCONH$–), 3.68–3.58 (m, 10H, PEG –OCH_2CH_2O–), 3.55 (t, *J* = 5.1 Hz, 2H, PEG –OCH_2CH_2NHCO–), 3.41 (m, 2H, PEG –OCH_2CH_2NHCO–), 3.38 (m, 2H, PEG –$OCH_2CH_2N_3$), 3.12 (m, 1H, biotin –$SCH(CH_2$–)$CHNH$–), 2.87 (dd, *J* = 12.3 Hz, 5.0 Hz, 1H, biotin –$SCH(H)CHNH$–), 2.73 (d, *J* = 12.8 Hz, 1H, biotin –$SCH(H)CHNH$–), 2.21 (t, *J* = 7.8Hz, 2H, biotin –CH_2CONH–), 1.79–1.59 and 1.46–1.36 (m, 6H, biotin –$CH_2CH_2CH_2CH_2CONH$–); ^{13}C NMR (100 MHz, $CDCl_3$) δ 173.63, 164.48, 70.76, 70.58, 70.18, 70.15, 70.11, 61.90, 60.37, 55.90, 50.78, 40.68, 39.25, 36.14, 28.44, 28.24, 25.82; HRMS (ESI): $[M+Na]^+$ calcd for $C_{18}H_{32}N_6O_5SNa$ 467.2053, found 467.2038.

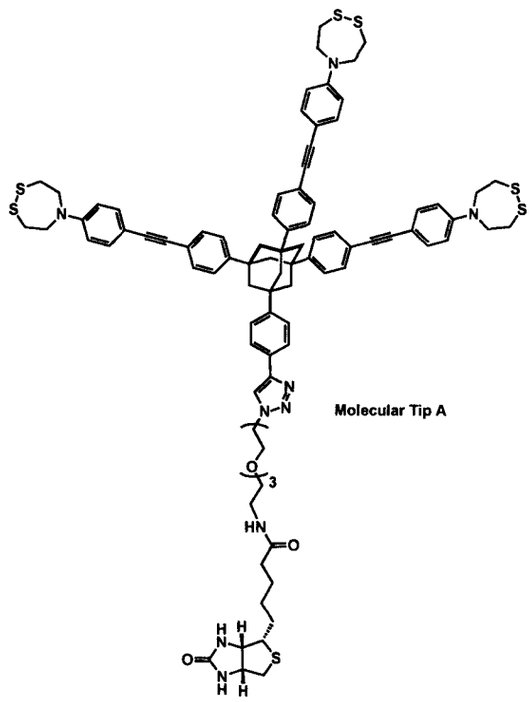

Molecular tip A. The biotinylated linker **2-15** (0.102 g, 0.230 mmol) and tripod scaffold molecule **2-11** (0.250 g, 0.215 mmol) were added to THF with *N, N*-diisopropyl ethylamine and degassed by freeze/pump/thaw. CuI was added and reaction mixture was heated to 60 °C and stirred for 2 days. The reaction mixture was concentrated *in vacuo*. The crude was then dissolved in CH_2Cl_2 (60 mL) and then washed with a mixture of NH_4OH/NH_4Cl (9:1, 2 x 20 mL) twice to remove any remaining copper. The organic layer was dried over Na_2SO_4 and concentrated *in vacuo* to give a yellowish solid. This solid was triturated three times with CH_2Cl_2 (5 mL) to remove excess of azide **2-15** to give a brownish, powdery solid **Molecular tip A** (0.294 g, 0.183 mmol, 85%): mp >260 (dec); IR (KBr): 3414, 3079, 3040, 2922, 2853, 2205, 1700, 1603, 1521, 1466, 1399, 1353, 1286, 1217, 1180, 1167, 1138, 1012, 900, 817,

533 cm^{-1}; ^1H NMR (400 MHz, DMSO-d_6) δ 8.50 (s, 1H, triazole), 7.90–7.30 (overlapping, 4H, Ar***H***), 7.62 (d, 6H, J = 8.7 Hz, Ar***H***), 7.46 (d, 6H, J = 8.7 Hz, Ar***H***), 7.33 (d, 6H, J = 8.7 Hz, Ar***H***), 6.73 (d, 6H, J = 8.7 Hz, Ar***H*** *ortho* to amine), 6.70 (overlapping, 1H, amide N***H***), 6.38 (s, 1H, biotin ureido N***H***), 6.32 (s, 1H, biotin ureido N***H***), 4.56 (t, 2H, J = 4.4 Hz, triazole–C***H***$_2$CH$_2$O–), 4.26 (m, 1H, biotin –SCH$_2$C***H***NHCONH–), 4.09 (m, 1H, biotin –SCH(CH$_2$–)C***H***NHCONH–), 3.95 (br t, 12H, –NCH$_2$C***H***$_2$SS–), 3.87 (t, J = 4.9 Hz, 2H, triazole–CH$_2$C***H***$_2$O–), 3.60–3.30 (m, 12H, PEG –OC***H***$_2$C***H***$_2$O–), 3.14 (m, 1H, biotin –SC***H***(CH$_2$–)CHNH–), 3.08 (br s, 12H, –NC***H***$_2$CH$_2$SS–), 2.78 (dd, J = 12.3 Hz, 5.0 Hz, 1H, –SC***H***(H)CHNH–), 2.55 (d, J = 11.9 Hz, 1H, biotin –SC***H***(H)CHNH–), 2.12 (br s, 12H, adamantane), 2.03 (t, 2H, J = 7.0 Hz, biotin –C***H***$_2$CONH–), 1.63–1.35 (m, 6H, biotin –C***H***$_2$C***H***$_2$C***H***$_2$CH$_2$CONH–); ^{13}C NMR (100 MHz, DMSO-d_6) δ 172.07, 162.66, 149.34, 146.69, 133.70, 132.72, 130.77, 128.52, 125.75, 125.59, 124.99, 121.51, 120.79, 111.41, 108.74, 90.31, 87.27, 69.78–68.64, 61.00, 59.16, 57.51, 55.40, 52.03, 49.97, 49.56, 38.40, 36.21, 35.07, 28.17, 28.01, 25.24; MS (MALDI-TOF): $[M+Na]^+$ calcd for $C_{90}H_{97}N_9O_5S_7Na$ 1630.6, found 1630.6.

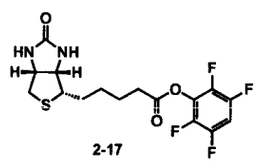

2-17

2,3,5,6-Tetrafluorophenol ester of Biotin (2-17).[3,4] Biotin (0.976 g, 4.00 mmol) and 2,3,5,6-tetrafluorophenol (Sigma-Aldrich, 0.797g, 4.80 mmol) were added to DMF (16 mL) and heated gently until the two solids dissolved. The mixture was allowed to cool

to room temperature and 1,3-diisopropyl carbodiimide (VWR, 0.689 mL, 4.40 mmol) was added. The reaction mixture was stirred overnight under Ar at room temperature with occasional heating to redissolve the solids that precipitated. DMF was removed to give a colorless solid. The crude solid was dissolved in $CHCl_3$ (100 mL) and the organic layer was washed with water (50 mL) and brine (50 mL). The organic layer was dried over Na_2SO_4 and concentrated to dryness. The crude was purified by flash chromatography (10:1 CH_2Cl_2/MeOH) to yield a sticky, orange solid **2–17** (1.10 g, 2.79 mmol, 70%): R_f = 0.39 (20:1 $CHCl_3$/MeOH); ^{1}H NMR (400 MHz, $CDCl_3$) δ 7.05 (m, 1H, -OC_6F_4***H***), 5.49 (br s, 1H, -N***H***), 4.98 (br s, 1H, –N***H***), 4.54 (m, 1H, biotin –SCH_2C***H***NH–), 4.35 (m, 1H, biotin –SCH(alkyl)C***H***NH-), 3.20 (m, 1H, biotin, –SC***H***(alkyl)CH–), 2.95 (dd, J = 12.8 Hz, 4.9 Hz, 1H, biotin –SC(***H)***HCHNH–), 2.75 (overlapping d, J = 10.7 Hz, biotin –SC(***H)***HCHNH–), 2.72 (overlapping t, J = 7.5 Hz, 2H, –OC(O)C***H***$_2CH_2$–), 1.89–1.68 and 1.62–1.40 (m, 6H, alkyl chain); MS (ESI): $[M+H]^+$ calcd for $C_{16}F_4H_{17}N_2O_3S$ 393.1, found 393.1.

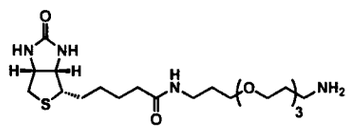

2-18

***N*-(3-(2-(2-(3-aminopropoxy)ethoxy)ethoxy)propyl)-5-((3a*S*,4*S*,6a*R*)-2-oxohexahydro-1*H*-thieno[3,4-*d*]imidazol-4-yl)pentanamide, biotin tetraethylene glycol amine (2-18).**[4] 4,7,10-trioxa-1,13-tridecane diamine (Acros, 4.96 mL, 18.8 mmol), triethylamine (0.8 mL), and DMF (15.0 mL) were stirred at 0 °C under Ar. The tetrafluorophenol ester of biotin (0.840 g, 2.14 mmol) in DMF (20 mL) was then added

over 12 h to the reaction mixture by syringe pump. The reaction was stirred for 5 h at room temperature and then rotovapped to give a yellow oil. The crude mixture was then precipitated by addition of cold diethyl ether. The solid was then purified by flash chromatography (MeOH to 20:1 to 10:1 MeOH/NH_4OH) to yield a sticky, orange solid **2-18** (0.686 g, 1.53 mmol, 72%): R_f= 0.38 (10:1 MeOH/NH_4OH); ^{1}H NMR (400 MHz, DMSO-d_6) δ 7.86 (br s, 1H, J = Hz), 6.51 (br s, 1H, biotin –N***H***), 6.41 (br s, 1H, biotin –N***H***), 4.30 (m, 1H, biotin –SCH_2C***H***NH–), 4.13 (m, 1H, biotin –SCH(alkyl)C***H***NH–), 3.60–3.35 (m, 12H, –C***H₂***O(C***H₂CH₂***O)$_2$C***H₂***–), 3.13–3.00 (overlapping m, 3H, –C***H₂***NHCO– and –SC***H***(alkyl)CH–), 2.82 (dd, J = 12.4 Hz, 5.1 Hz, 1H, biotin –SC(***H***)HCHNH–), 2.74 (t, J = 7.0 Hz, 2H, H_2NC***H₂***CH_2–), 2.58 (d, J = 12.4 Hz, 1H, biotin –SCH(***H***)CHNH–), 2.05 (t, J = 7.3 Hz, 2H, –NHCOC***H₂***CH_2–), 1.76–1.41 and 1.34–1.23 (m, 10H, alkyl); MS (ESI): $[M+H]^+$ calcd for $C_{20}H_{38}N_4O_5S$ 447.3, found 447.3.

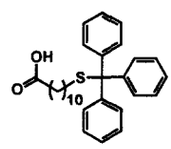

2-20

11-(tritylthio)undecanoic acid (2-20).[5] Trityl chloride (Sigma-Aldrich, 0.371 g, 13.3 mmol) and 11-mercaptoundecanoic acid (Sigma-Aldrich, 2.64 g, 12.1 mmol) were stirred in DMF (5.0 mL) under Ar at room temperature for 2 days. The solvent was removed and the crude mixture was purified by flash chromatography (10:1 hexanes/EtOAc) to yield a colorless solid **2-20** (3.46 g, 7.52 mmol, 62%): mp 47–50 °C

R_f = 0.61 (1:1 hexanes/EtOAc); IR (thin film): 3080, 3057, 3030, 2926, 2853, 1708, 1595, 1489, 1444, 1280, 1184, 1082, 1034, 1001, 934, 852, 765, 700 cm^{-1}; ^1H NMR (400 MHz, $CDCl_3$) δ 7.43-7.17 (m, 15 H, aromatic), 2.33 (t, J = 7.5 Hz, 2H, TrSC***H***$_2$$(CH_2)_9CO_2H$), 2.13 (t, J = 7.4 Hz, 2H, –C***H***$_2$$CO_2H$), 1.61 (m, 2H, $TrSCH_2C$***H***$_2$$(CH_2)_8CO_2H$), 1.42–1.07 (m, 14H, alkyl); ^{13}C NMR (100 MHz, $CDCl_3$) δ 180.45, 145.27, 129.79, 127.98, 126.88, 126.68, 66.54, 34.28, 32.19, 29.51, 29.37, 29.31, 29.21, 29.17, 28.76, 24.85; HRMS (ESI): $[M+Na]^+$ calcd for $C_{30}H_{36}O_2SNa$ 483.2328, found 483.2331.

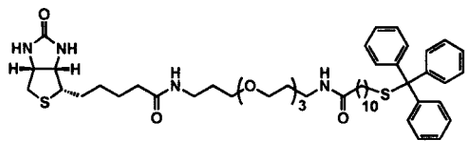

2-21

N*-(15-oxo-19-((3a*S*,4*S*,6a*R*)-2-oxohexahydro-1*H*-thieno[3,4-*d*]imidazol-4-yl)-4,7,10-trioxa-14-azanonadecyl)-11-(tritylthio)undecanamide (2-21).** **2-20** (0.080g, 0.17 mmol) was stirred in DMF (5 mL) with HBTU (0.073g, 0.19 mmol) and DIPEA (0.14 mL, 0.80 mmol) under Ar for an hour before **2-18** (0.092g, 0.26 mmol) was added as a solution in DMF (0.2 mL). The mixture was heated to 50 °C overnight under Ar. Evaporation of the solvent followed by purification by flash chromatography twice in (10:1 to 5:1 $CHCl_3$/MeOH) gave a sticky, colorless solid **2-21** (0.099 g, 0.11 mmol, 64%): R_f = 0.28 (10:1 $CHCl_3$/MeOH); mp 91–92 °C; IR (thin film): 3293, 2925, 2854, 1702,1644, 1548, 1444, 1263, 1119, 743, 700 cm^{-1}; ^1H NMR (400 MHz, $CDCl_3$) δ 7.43–7.17 (m, 15 H, aromatic), 6.76 (br s, 1H, amide NH***), 6.62 (br s, 1H, amide N***H***),

6.40 (br s, 1H, biotin –N***H***), 5.81 (br s, 1H, biotin –N***H***), 4.49 (m, 1H, biotin –SCH_2C***H***NH–), 4.30 (m, 1H, biotin –SCH(alkyl)C***H***NH–), 3.64–3.53 (m, 12 H, –C***H***$_2O(C$***H***$_2C$***H***$_2O)_2C$***H***$_2$–), 3.33 (m, 4H, –OCH_2C***H***$_2NHC(O)$-), 3.13, (m, 1H, biotin –SC***H***(alkyl)CH–), 2.88 (dd, 1H, J = 12.8 Hz, 4.9 Hz, 1H, biotin –SC(***H***)HCHNH–), 2.74 (d, J =10.7 Hz, 1H, biotin –SC(***H***)HCHNH–), 2.22–2.11 (m, 4H, –C***H***$_2C(O)NH$–), 1.78–1.10 (m, 26H, alkyl H); ^{13}C NMR (100 MHz, $CDCl_3$) δ 173.46, 173.38, 164.15, 145.21, 129.74, 127.95, 126.65, 70.58, 70.17, 70.11, 70.01, 66.50, 61.97, 60.34, 55.87, 40.69, 37.72, 36.95, 36.14, 32.17, 29.56, 29.53, 29.43, 29.33, 29.30, 29.15, 28.74,28.40, 28.25, 25.98, 25.86; MS (ESI): $[M+Na]^+$ calcd for $C_{50}H_{72}N_4O_6S_2Na$ 911.4785, found 911.4798.

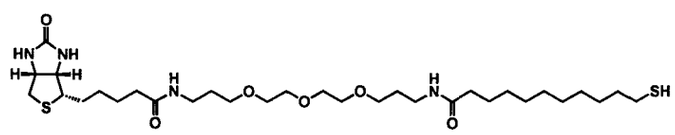

Molecular Tip B

Molecular tip B.[4] **2-21** (0.020g, 0.023 mmol) was dissolved in degassed dichloromethane (0.050 mL) and placed under an Ar atmosphere. Degassed TFA (0.050 mL) was added dropwise and the reaction was allowed to stir for 30 minutes. Addition of degassed triethylsilane (0.036 mL, 0.23 mmol) turned the yellow reaction mixture colorless. After stirring for two more hours the reaction mixture was diluted with degassed CH_2Cl_2 (1 mL) and degassed water (1 mL) was added. After three extractions with degassed CH_2Cl_2 (1 mL each) the combined organic layers were evaporated to dryness and purified by plug of silica (CH_2Cl_2 to 10:1 CH_2Cl_2/MeOH) gave a sticky, colorless solid **Molecular tip B** (0.010g, 0.015 mmol, 69%): R_f = 0.54

(5:1 CH_2Cl_2/MeOH); mp 74–78 °C; IR (thin film): 3290, 3089, 2927, 2858, 1689, 1647, 1550, 1458, 1354, 1257, 1200, 1126, 798, 717 cm^{-1}; ^1H NMR (400 MHz, $CDCl_3$) δ 6.58 (br s, 1H, amide –N***H***), 6.32 (br s, 1H, amide N***H***), 5.95 (br s, 1H, biotin –N***H***), 5.11 (br s, 1H, biotin –N***H***), 4.52 (m, 1H, biotin –SCH_2CHNH–), 4.33 (m, 1H, biotin –SCH(R)C***H***NH–), 3.67–3.55 (m, 12H, –$CH_2OCH_2CH_2OCH_2$–), 3.37–3.33 (m, 4H, –$CONHCH_2$–), 3.18–3.14 (m, 1H, biotin –SC***H***(alkyl)CH–), 2.95–2.89 (m, 1H, –SC(***H***)HCHNH–), 2.74 (d, J = 10.7 Hz, 1H, biotin –SC(***H***)HCHNH–), 2.52 (t, J = 7.3 Hz, 2H, $HSCH_2(CH_2)_9$–), 2.21 (t, 2H, J = 7.4 Hz, –$CH_2C(O)NH$–) 2.15 (t, 2H, J = 7.7 Hz, –$CH_2C(O)NH$–) 1.82–1.20 (m, 26H, alkyl chain); ^{13}C NMR (100 MHz, $CDCl_3$) δ 173.54, 173.19, 163.57, 70.65, 70.37, 70.24, 70.09, 62.03, 60.31, 55.67, 40.78, 38.14, 37.82, 37.04, 36.11, 35.00, 30.80, 30.06, 29.71, 29.67, 29.61, 29.59, 29.47, 29.35, 29.29, 29.14, 28.27, 28.29, 26.04, 25.79, 23.68; HRMS (ESI): $[M+Na]^+$ calcd for $C_{31}H_{58}N_4O_6S_2Na$ 669.3690, found 669.3678.

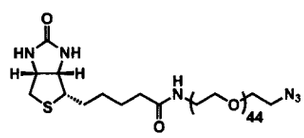

2-22

Biotinylated PEG azide linker 2-22. **2-17** (0.020 g, 0.051 mmol) was stirred in DMF (0.4 mL) with amine and azide functionalized PEG (Intezyne Technologies, Tampa Bay, FL USA, 0.10 g, 0.051 mmol) and gently heated until all reagents were fully dissolved. Triethylamine (10 μL, 0.071 mmol) was added and the reaction was stirred under Ar at room temperature overnight. The reaction mixture was dried *in vacuo* to remove DMF and triethylamine. After the crude was fully dried, a small amount of

$CHCl_3$ was added to dissolve the solids and the PEG was precipitated by cold diethyl ether (0 °C). The solids were centrifuged and the ether layer removed. The precipitation process was carried out three times total to yield **2-22** (0.110 g, 0.048 mmol, 96%): mp 37–39 °C; IR: (thin film) 3304, 2883, 2106, 1702, 1650, 1467, 1148, 1114 cm^{-1}; ^1H NMR (500 MHz, $CDCl_3$) δ 6.78 (br s, 1H), 6.46 (br s, 1H), 5.66 (br s, 1H), 4.42 (s, 1H), 4.23 (s, 1H), 3.69–3.31 (m, PEG chain 176 H), 3.06 (br s, 1H), 2.82 (d, J = 7.5 Hz, 1H), 2.67 (d, J = 12.0 Hz, 1H), 2.15 (br t, 2H), 1.75–1.30 (m, 6H); ^{13}C NMR (125 MHz, $CDCl_3$) δ 173.30, 163.96, 72.55, 70.87–69.92 multiple PEG peaks, 61.74, 61.63, 60.19, 55.59, 50.67, 45.79, 40.50, 39.14, 35.90, 28.21, 28.11, 25.58; MS (MALDI-TOF): $[M+K]^+$ calcd for $C_{94}H_{184}N_6O_{43}SK$ 2156.2 (41 PEG units), found 2156.6 with a distribution separated by 44 Da for each PEG unit between each peak.

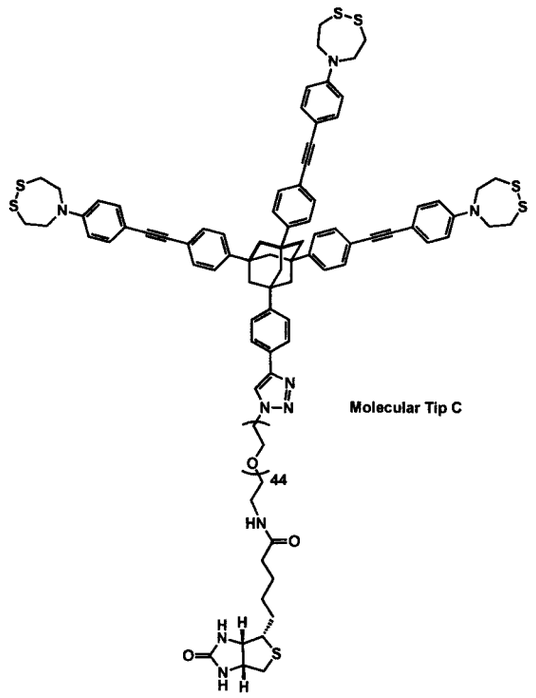

Molecular tip C. **2-11** (10 mg, 8.6 μmol), **2-22** (13 mg, 5.7 μmol), CuI (5.5 mg, 0.029 mmol), diisopropylethylamine (10 μL, 5.7 μmol), and THF (1.0 mL) were added to a Schlenck tube. The mixture was degassed three times by freeze/pump/thaw, and filled with Ar. The reaction was stirred at 60 °C for three days and then evaporated to dryness. The crude solids were dissolved in $CHCl_3$ (150 mL) and washed with 10:1 NH_4Cl/NH_4OH (3 x 100 mL). The organic layer was washed with water (100 mL) and brine (100 mL) and then dried over Na_2SO_4. The dried organic layer was filtered and evaporated to dryness. The crude was purified by size exclusion chromatography (Sephadex LH-20 swollen and eluted with THF). The fractions were analyzed by NMR and those containing the product were further purified by preparative thin layer chromatography (5:1 $CHCl_3$/MeOH). The largest band was removed and the silica was washed with (5:1 $CHCl_3$/MeOH) and evaporated. The solid was dissolved in a small

amount of $CHCl_3$, precipitated with cold hexanes, and centrifuged. The hexanes layer was removed to give **Molecular tip C** (8.4 mg, 2.6 μmol, 46%): R_f = 0.44 (5:1 $CHCl_3$/MeOH); mp 85–88 °C; IR (thin film): 3521, 3360, 3082, 3042, 2897, 2870, 2207, 1702, 1656, 1603, 1522, 1455, 1400, 1352, 1323, 1290, 1250, 1218, 1182, 1135, 1107, 1039, 1015 cm^{-1}; ^1H NMR (500 MHz, $CDCl_3$) δ 7.99 (s, 1H), 7.83 (d, 2H, J = 7.9 Hz), 7.55–7.39 (m, 18H), 7.22 (t, J = 8.1 Hz, 2H), 6.88 (t, J = 7.4 Hz, 2H), 6.83 (t, J = 8.0 Hz, 2H), 6.77 (br s, 1H), 6.59 (d, J = 8.8 Hz, 6H), 5.51 (br s, 1H), 4.88 (br s, 1H), 4.59 (t, J = 4.9 Hz, 2H), 4.5 (m, 1H), 4.32 (m, 1H), 3.98 (t, J = 5.2 Hz, 12H), 3.91 (t, J = 4.9 Hz, 2H), 3.75–3.54 (m, PEG chain 176H), 3.49 (t, J = 5.0 Hz, 1H), 3.44 (q, J = 4.9 Hz, 1H), 3.15 (m, 1H), 3.09 (t, J = 5.4 Hz, 12H), 2.90 (dd, J = 12.8 Hz, 5.0 Hz, 1H), 2.72 (d, J = 12.7 Hz, 1H), 2.31 (t, J = 7.7 Hz, 2H), 2.24–2.14 (m, 12H), 1.88–1.25 (m, 6H); ^{13}C NMR (125 MHz, $CDCl_3$) δ 173.28, 156.23, 148.76, 146.40, 133.44, 133.31, 131.48, 129.68, 129.00, 125.88, 125.63, 125.16, 122.10, 122.03, 121.08, 120.37, 115.49, 111.25, 110.72, 90.15, 87.53, 70.66, 68.11, 61.87, 60.18, 55.37, 52.58, 50.49, 47.05, 41.10, 40.67, 39.43, 39.36, 39.25, 36.88, 35.77, 32.05, 29.83, 29.79, 29.61, 29.49, 29.43, 29.27, 28.14, 25.74, 25.55, 22.83; MS (MALDI-TOF): $[M+Na]^+$ calcd for $C_{166}H_{249}N_9O_{43}S_7Na$ (41 PEG units) 3303.5, found 3302.9 with a distribution separated by 44 Da for each PEG unit between each peak.

5.1.3 Synthetic Procedure for Molecules to Attach to Diamond Surfaces

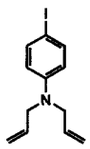

3-1

***N,N*-diallyl-4-iodoaniline (3-1).** 4-iodoaniline (1.00 g 4.57 mmol), allyl bromide (1.58 mL, 18.3 mmol), and K_2CO_3 (2.62 g, 18.3 mmol) were stirred at room temperature for 16 h under N_2 and then filtered. The solid was washed with CH_2Cl_2 and $CHCl_3$ to give a purple oil. The oil was rotovapped to dryness and the crude was purified by flash chromatography (40:1 to 20:1 hexanes/EtOAc) to give a dark oil **3-1** (1.22 g, 4.08 mmol, 90%): R_f = 0.57 (10:1 hexanes/EtOAc); IR (thin film): 3054, 2986, 2685, 2411, 2305, 1588, 1496, 1421, 1265, 909, 896, 740, 706 cm^{-1}; ^1H NMR (500 MHz, $CDCl_3$) δ 7.45 (d, J = 8.7 Hz, 2H), 6.47 (d, J = 8.7 Hz, 2H), 5.82 (m, 2H), 5.15 (m, 4H) 3.89 (br s, 4H); ^{13}C NMR (125 MHz, acetone-d_6) δ 149.81, 138.93, 135.33, 117.00, 116.31, 77.70, 54.01; HRMS (ESI): $[M+H]^+$ calcd for $C_{12}H_{15}IN$ 300.0249, found 300.0113.

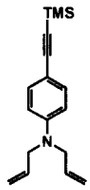

3-2

***N,N*-diallyl-4-((trimethylsilyl)ethynyl)aniline (3-2).** **3-1** (1.20 g, 4.02 mmol), TMS acetylene (5.7 mL, 40 mmol), $Pd(PPh_3)_2Cl_2$ (0.141 g, 0.201 mmol), triethylamine (6 mL), and THF (6 mL) degassed three times by freeze/pump/thaw. CuI (8 mg, 0.04 mmol) was added and the mixture was degassed 2 times more. The reaction was warmed to room temperature and the yellowish mixture was stirred for 16 h. Rotary evaporation gave a black crude that was purified by flash chromatography twice (1^{st} column: 20:1 hexanes/EtOAc; 2^{nd} column: hexanes to 10:1 hexanes/EtOAc) to give a yellow oil **3-2** (1.04 g, 3.88 mmol, 96%): R_f = 0.52 (10:1 hexanes/EtOAc); IR (thin film): 2958, 2898, 2150, 1677, 1606, 1515, 1402, 1249, 1178, 864, 841, 760 cm^{-1}; ^1H NMR (500 MHz, $CDCl_3$) δ 7.31 (d, J = 8.6 Hz, 2H), 6.58 (d, J = 8.7 Hz, 2H), 5.82 (m, 2H), 5.15 (m, 4H), 3.92 (d, J = 4.1Hz, 4H), 0.24 (s, 9H); ^{13}C NMR (125 MHz, $CDCl_3$) δ 148.77, 133.46, 133.31, 116.41, 111.87, 110.17, 106.69, 91.302, 52.764, 0.42; HRMS (CI): $[M^+]$ calcd for $C_{17}H_{23}NSi$ 269.1600, found 269.1588.

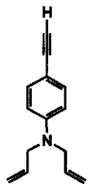

3-3

***N,N*-diallyl-4-ethynylaniline (3-3).** **3-2** (1.04 g, 3.87 mmol) and K_2CO_3 (1.07 g, 7.74 mmol) was stirred in MeOH (6.5 mL) at room temperature overnight under N_2. When the TLC showed no starting material, the reaction was filtered, washed with CH_2Cl_2, and concentrated to dryness. The crude mixture was purified by flash chromatography (50:1 hexanes/EtOAc) to give a brown oil **3-3** (0.633 g, 3.21 mmol, 83%): R_f = 0.58 (10:1 hexanes/EtOAc); IR (thin film): 3302, 3054, 2986, 2305, 1607, 1517, 1421, 1265, 1180, 896, 738, 706 cm^{-1}; ^1H NMR (500 MHz, $CDCl_3$) δ 7.32 (d, J = 8.7 Hz, 2H), 6.60 (d, J = 8.7 Hz, 2H), 5.82 (m, 2H), 5.15 (m, 4H), 3.92 (d, J = 4.5 Hz, 4H), 2.96 (s, 1H); ^{13}C NMR (125 MHz, $CDCl_3$) δ 148.85, 133.38, 133.33, 116.33, 111.86, 108.97, 84.93, 74.93, 52.72; HRMS (CI): [M^+] calcd for $C_{14}H_{15}N$ 197.1204, found 197.1207.

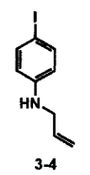

3-4

***N*-allyl-4-iodoaniline (3-4).** 4-iodoaniline (11.0 g, 50.2 mmol) and K_2CO_3 (5.18 g, 37.5 mmol) were dissolved in DMF (380 mL) and placed at 0 °C under N_2. Allyl bromide (3.30 mL, 3.75 mmol) was added by syringe pump at a rate of 0.2 mL/hr. The solution was slowly warmed to ambient temperature and then heated to 60 °C for 2

days. The reaction was separated into two flasks which were both diluted with water (500 mL) and extracted with ether (4 x 125 mL). The organic extracts were washed with brine (150 mL), dried over Na_2SO_4, filtered, and evaporated to dryness. The crude oil was purified by flash chromatography (20:1 to 10:1 hexanes/EtOAc) to give an orange oil **3-4** (4.40 g, 16.9 mmol, 34%): R_f = 0.43 (10:1 hexanes/EtOAc); IR (thin film): 3418, 3085, 3060, 3011, 2977, 2917, 2845, 1591, 1495, 1395, 1316, 1294, 1264, 1182, 1060, 995, 909, 810, 732 cm^{-1}; ^1H NMR (500 MHz, $CDCl_3$) δ 7.42 (d, J =8.8 Hz, 2H), 6.40 (d, J = 8.8 Hz, 2H), 5.92 (m, 1H), 5.27 (d, J = 17.2 Hz, 1H), 5.17 (d, J = 10.3 Hz, 1H), 3.83 (br s, 1H), 3.74 (br s, 2H); ^{13}C NMR (125 MHz, $CDCl_3$) δ 147.79, 137.96, 135.03, 116.70, 115.37, 78.246, 46.49; HRMS (ESI): $[M+H]^+$ calcd for $C_9H_{11}IN$ 259.9936, found 259.9948.

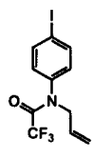

3-5

***N*-allyl-2,2,2-trifluoro-*N*-(4-iodophenyl)acetamide (3-5).** **3-4** (0.500 g, 1.97 mmol), and pyridine (0.31 mL, 3.9 mmol) were stirred in CH_2Cl_2 (5 mL) under nitrogen at 0 °C. Trifluoroacetic anhydride (0.54 mL, 3.9 mmol) was added slowly over 15 min. After 3 h, the reaction was quenched with the addition of water (5 mL). The aqueous layer was extracted with CH_2Cl_2 (3 x 10 mL) and the organic extracts were dried over Na_2SO_4. The extracts were filtered and evaporated to dryness. The crude oil was purified by flash chromatography (10:1 to 8:1 hexanes/EtOAc) to give a reddish yellow oil **3-5** (0.698 g, 1.97 mmol, 99%): R_f = 0.40 (10:1 hex/EtOAc); IR (thin film): 3381, 3087,

3066, 3018, 2985, 2934, 2874, 2779, 1904, 1699, 1644, 1583, 1487, 1415, 1210, 1189, 1152, 1009, 977, 934, 866, 739 cm^{-1}; ^1H NMR (500 MHz, $CDCl_3$) δ 7.75 (d, J = 8.5 Hz, 2H), 6.94 (d, J = 8.3 Hz, 2H), 5.82 (m, 1H), 5.22 (d, J = 10.1 Hz, 1H), 5.13 (d, J = 17.1 Hz, 1H), 4.28 (d, J = 6.5 Hz, 2H); ^{13}C NMR (125 MHz, acetone-d_6) δ 156.97 (q, J = 35 Hz), 140.45, 139.98, 132.67, 132.27, 120.67, 117.91 (q, J = 288 Hz), 95.81, 55.50; HRMS (ESI): $[M+H]^+$ calcd for $C_{12}H_9F_3INO$ 355.9759, found 355.9734.

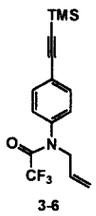

3-6

***N*-allyl-2,2,2-trifluoro-*N*-(4-((trimethylsilyl)ethynyl)phenyl)acetamide (3-6).** **3-5** (2.77 g, 7.81 mmol), $Pd(PPh_3)_2Cl_2$ (274 mg, 0.390 mmol), TMS acetylene (5.57 mL, 39.0 mmol), CuI (15 mg, 0.078 mmol), TEA (5.6 mL, 0.30 mmol), and THF (19 mL) were degassed by freeze/pump/thaw four times and then stirred at room temperature for 21 h. The reaction was then evaporated to dryness and purified by flash chromatography (50:1 to 10 :1 hexanes/EtOAc) to give a yellowish brown oil **3-6** (2.09 g, 6.42 mmol, 82%): R_f = 0.43 (10:1 hexanes/EtOAc); IR (thin film): 3087, 2961, 2901, 2161, 1704, 1645, 1603, 1503, 1415, 1252, 1212, 1189, 1175, 1155, 1077, 1025, 996, 978, 933, 865, 845, 760, cm^{-1}; ^1H NMR (500 MHz, $CDCl_3$) δ 7.49 (d, J = 8.5 Hz, 2H), 7.12 (d, J = 8.3 Hz, 2H), 5.82 (m, 1H), 5.20 (d, J = 10.1 Hz, 1H), 5.10 (d, J = 17.1 Hz, 1H), 4.28 (d, J = 6.4 Hz, 2H), 0.25 (s, 9H); ^{13}C NMR (125 MHz, $CDCl_3$) δ: 156.61 (q, J = 36 Hz), 138.89, 133.05, 130.69, 128.53, 124.41, 120.41, 116.45 (q, J = 288 Hz),

103.67, 96.62, 54.68, -0.02; HRMS (ESI): $[M+H]^+$ calcd for $C_{16}H_{19}F_3NOSi$ 326.1188, found 326.1221.

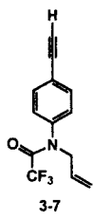

3-7

***N*-allyl-*N*-(4-ethynylphenyl)-2,2,2-trifluoroacetamide (3-7).**[6] TBAF (1.75 mL of 1 M solution in THF) was added dropwise to a solution of **3-6** (0.545 g, 1.67 mmol) in AcOH (32 μL, 0.55 mmol), Ac_2O (33 μL, 0.35 mmol), and THF (8.35 mL) at -20 °C. After 15 minutes, the reaction was filtered through a pad of silica and the silica was washed with ether. The eluent was then evaporated to give a sticky, colorless oil. The reaction was left under house vacuum overnight to remove ether and then sublimed with vacuum pump at 40 °C to give colorless crystals **3-7** (0.375 g, 1.48 mmol, 89%): mp 41–42°C; R_f = 0.33 (10:1 hexanes/EtOAc); IR (thin film): 3307, 3276, 3091, 3041, 3020, 2986, 2943, 2253, 1690, 1603, 1502, 1415, 1211, 1187, 1160, 1146, 1139, 940, 847 cm^{-1}; ^1H NMR (500 MHz, $CDCl_3$) δ 7.53 (d, J = 8.3 Hz, 2H), 7.16 (d, J = 8.1 Hz, 2H), 5.83 (m, 1H), 5.22 (d, J = 10.1 Hz, 1H), 5.13 (d, J = 17.0 Hz, 1H), 4.30 (d, J = 6.4 Hz, 1H), 3.16 (s, 1H); ^{13}C NMR (125 MHz, $CDCl_3$) δ 156.60 (q, J = 36 Hz), 139.30, 133.27, 130.68, 128.64, 123.44, 120.44, 116.44 (q, J = 288 Hz), 82.42, 79.23, 54.71; HRMS (ESI): $[M+H]^+$ calcd for $C_{13}H_{11}F_3NO$ 254.0793, found 254.0798.

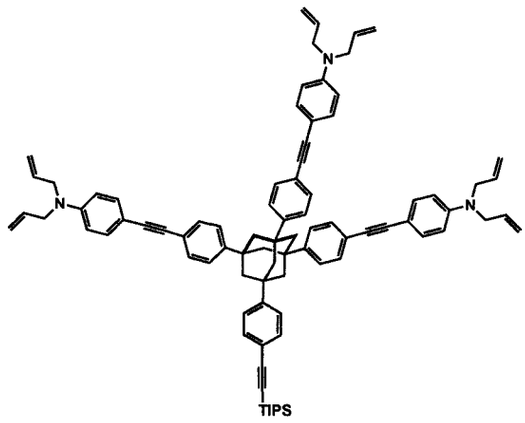

3-8

Tripodal Molecule (3-8). **2-3** (73 mg, 0.074 mmol), **3-3** (45 mg, 0.23 mmol), $Pd(PPh_3)_2Cl_2$ (4 mg, 5 μmol), CuI (1 mg, 7 μmol), triethylamine (0.50 mL) were added to THF (1.6 mL) to a sealed tube and degassed 5 times by freeze/pump/thaw. The mixture was heated to 60 °C for 2 h and at room temperature for 30 h. The reaction mixture was then transferred to a flask and rotovapped to remove THF. The crude was then dissolved in $CHCl_3$ (40 mL) and washed 4 times with 9:1 NH_4OH/NH_4Cl (15 mL) to remove Cu. The crude was washed with 1 M HCl (20 mL), brine (20 mL), dried over Na_2SO_4, filtered, and rotovapped to dryness. The crude solids were purified by flash chromatography (40:1 to 10:1 hexanes/EtOAc). The compound was further purified by size exclusion chromatography (lipophilic Sephadex, LH-20 swollen and eluted in THF) to give a yellow solid **3-8** (0.040 g, 0.033 mmol, 44%): mp 153–154°C; R_f = 0.45 (10:1 hexanes/EtOAc); IR (thin film): 3052, 2925, 2209, 2153, 1602, 1522, 1463, 1393, 1357, 1264, 1236, 1181, 1137, 1017, 922, 817 cm^{-1}; ^1H NMR (500 MHz, $CDCl_3$) δ 7.51–7.40 (m, 16H), 7.36 (d, J = 8.8 Hz, 6H), 6.63 (d, J = 8.8 Hz, 6H), 5.82 (m, 6H), 5.16 (m, 12H), 3.93 (d, J = 4.5 Hz, 12H), 2.13 (d, J = 9.5 Hz, 12H), 1.12 (s, 21H); ^{13}C

NMR (125 MHz, $CDCl_3$) δ 148.62, 133.56, 133.46, 133.06, 132.92, 132.31, 131.55, 131.11, 129.03, 125.17, 122.28, 116.45, 112.11, 110.44, 107.25, 90.53, 87.38, 52.83, 47.10, 39.56, 39.46, 39.42, 32.14; HRMS (ESI): $[M+H]^+$ calcd for $C_{87}H_{92}N_3Si$ 1206.7061, found 1206.6923.

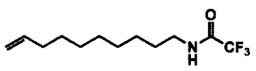

3-9

***N*-(dec-9-en-1-yl)-2,2,2-trifluoroacetamide (3-9).**[7] Undecylenic acid chloride (Acros, 2.02 g, 10.0 mmol) and tetra *n*-butylammonium bromide (Acros, 10 mg, 0.031 mmol) were dissolved in dichloromethane (distilled from CaH_2) at 0 °C. NaN_3 (800 mg, 12.2 mmol) in 3 mL H_2O was added slowly over 30 min and the reaction was allowed to stir for 2 h at 0 °C. The organic layer was separated and washed with H_2O (2 x 5 mL) and $MgSO_4$ was added. Small nitrogen bubbles evolved upon the addition of $MgSO_4$ and the mixtured was stirred for 24 h. The mixture was filtered and refluxed at 50 °C with trifluoroacetic acid (1 mL) for 16 h. The reaction mixture was cooled to room temperature, washed with a saturated solution of $NaHCO_3$ (2 x 10 mL), and dried over Na_2SO_4. After filtration and evaporation, the crude oil was purified by flash chromotography (10:1 hexanes/EtOAc) to yield a colorless oil **3-9** (1.42 g, 5.65 mmol, 57%): IR (thin film): 3307, 3105, 3080, 2976, 2929, 1704, 1641, 1560, 1665, 1443, 1209, 1185, 910 cm^{-1}; ^1H NMR (500 MHz, $CDCl_3$) δ 6.22 (br s, 1H), 5.80 (m, 1H), 5.01 (d, J = 17.0 Hz, 1H), 4.92 (d, J = 10.0 Hz, 1H), 3.36 (m, 2H), 2.04 (m, 2H), 1.57 (m, 2H), 1.36–1.28 (m, 10H); HRMS (ESI): $[M+H]^+$ calcd for $C_{12}H_{21}F_3NO$ 252.1564,

found 252.1561.

5.2 Gold Surface Preparation

5.2.1 Hydrogen Flame Annealing of Gold Surfaces

Gold on mica (Au 150 nm thickness on mica, 1.0 x 1.1 cm, Agilent, Santa Clara, CA USA) was hydrogen flame annealed before use. The sample was placed in the center of a cleaned quartz disk and the hydrogen flame was ignited in a dark room. The hydrogen flow was adjusted to give a flame 3–4 cm in length. The flame was used to gently warm the quartz around the sample for about 30 seconds. During this gentle heating, water droplets were briefly evident on the quartz disk before quickly evaporating. Then the flame was held at about 30° angle and moved back and forth across the sample moving closer and closer until a dim orange spot was visible on the gold. The flame was moved back and forth about once per second for 60 seconds. Overheating the Au film was possible and was evident when small bubbles appeared on the Au film. This affected the flatness of the gold film, but was not found to affect FTIR–ATR measurements. The sample was placed immediately in the solution of the molecule to be adsorbed. The vessel was then flushed with nitrogen. When used as a control, the gold film was flame annealed and used immediately afterward or stored under nitrogen until use.

5.2.2 Surface Modifications of Gold Surfaces

A 100 μmol/L solution of the terminal alkyne tripod scaffold (**2-11**) (0.5 mg, 4 μmol tripod acetylene in 4 mL $CHCl_3$, HPLC grade, Sigma-Aldrich) was made and sonicated for 15 min. It was then filtered (Millex PTFE syringe filter, 0.22 μm, Sigma-Aldrich) into a vial. After the gold film was hydrogen flame annealed, it was placed in the solution for 21 h. The sample was removed and washed extensively with $CHCl_3$ and used immediately.

Solutions of the **Molecular tip A** (3.2 mg in 2.0 mL DMSO, 1.0 mM), **Molecular tip B** (1.3 mg in 2.0 mL DMSO, 1.0 mM), and **Molecular tip C** (1.1 mg in 3.33 mL DMSO, 0.10 mM) were sonicated for 15 min to fully dissolve all solids. The solutions were syringe filtered into a vial and Au surfaces were immersed for 21 h in the respective solutions. The Au surfaces were washed excessively with DMSO, Millipore water, and ethanol. The substrates were then dried with a stream of N_2 and used immediately. The same preparation procedure was used for FTIR, ellipsometry, and NEXAFS samples.

5.3 Spectroscopic Analysis of Gold and Nanocrystalline Diamond Surfaces

5.3.1 Sessile Drop Contact Angle Measurements

A 3 μL drop of water (Millipore Milli-Q water, 18.2 MΩ, 0.2 μm filtered) was placed on a sample illuminated by a light source. The image of the sample was

captured by a CCD camera. The angle was then measured using the Scion Image program (Scion Corp. Frederick, MD).

5.3.2 Raman Spectroscopy

Raman measurements were taken on H-NCD samples with an Ar laser at 488 nm using a slit size of 0.15 mm and 25 s exposure by Marjan Subotkin in the lab of Professor Kagan.

5.3.3 Spectroscopic Ellipsometry

For monolayers on gold, an Alpha-SE J.A. Woollam spectroscopic ellipsometer (J. A. Woollam Co., Inc. Omaha, NE) was used with an angle of incidence of 70 ° using the wavelengths between 380 nm to 900 nm. The values of n and k are dependent on the thickness of the gold film and were measured for the Au films individually immediately after hydrogen flame annealing. The values of n chosen were 1.50^{8-11} for the **Molecular tips A**, **C**, and **2-11**. A value of $n = 1.475$ was chosen for **Molecular tip B**.

5.3.4 Near Edge X-Ray Absorption Fine Structure (NEXAFS) Spectroscopy

NEXAFS spectra were obtained on beamline U7A at the National Synchotron Light Source at Brookhaven National Laboratory (Upton, NY) by Andy Konicek of the Carpick group. The beamline uses a 600 line/mm grating with an exit slit set to 30 x 30 μm. Carbon K-edge spectra were obtained from 275–355 eV; nitrogen K-edge spectra

were obtained from 390–435 eV; and oxygen K-edge spectra were obtained from 515–580 eV. Partial electron yield was obtained at a bias of -50 V for the carbon and nitrogen spectra and at a bias of -300 V for oxygen spectra. The pre-edges of the spectra were normalized to the initial intensity of the beam that was measured by an 85% transmissive gold mesh. The normalization of the pre-edge was averaged for the first 5 eV of each spectra. A factor of one was subtracted to set the pre-edge to zero for only the carbon spectra. Also in the carbon spectra, the post-edge was averaged from 318 to 322 eV to align the spectra at approximately 320 eV. Spectra were obtained in partial electron yield, which is sensitive to only the 3–5 nm of a sample nearest the surface, and total electron yield, which measures the bulk surface. The incident beamline angle was varied: 90° (normal to surface), 54.7°, 35°, and 20°. A single crystal of freshly H-terminated boron doped diamond was used as a standard because it had minimal π-bonded carbon at 285 eV and an intense peak at 287 eV for the σ-bonded carbon in the sample. Peak fitting data software was performed with custom software from the Carpick group. To compare the spectra of several samples, the spectra were plotted in Igor Pro 6.01 (Lake Oswego, OR).

5.3.5 Fourier Transform Infrared–Attenuated Total Reflectance (FTIR–ATR) Spectroscopy

Fourier transform infrared attenuated total reflection (FTIR–ATR) spectroscopy was performed with a Nicolet 6700 (Thermo Scientific, Waltham, MA) spectrometer with a Harrick GATR (Pleasantville, NY) at an angle of incidence of 65° using a liquid

nitrogen cooled MCT/A detector. The Ge crystal was wiped clean with a methyl ethyl ketone soaked cotton swab and dried with a stream of nitrogen before and after each sample. 500 scans were taken for all monolayer films with a 4 cm^{-1} resolution.

5.3.6 X-Ray Photoelectron Spectroscopy.

XPS was performed by David Grierson at the University of Wisconsin on Perkin-Elmer 5400 ESCA spectrometer with a Mg Kα x-ray source. No monochromator was used and a 9° angle between x-ray source and sample normal was used. There was a 45° takeoff angle between sample and energy analyzer.

5.4 Force Spectroscopy

5.4.1 Functionalization of Gold AFM Tips

All solvents used in AFM modification were HPLC grade (Sigma-Aldrich, St. Louis, MO). Purchased gold-coated silicon nitride AFM cantilevers (NPG-20, f_0 = 12-24 kHz, with spring constants of 0.06 N/m, Veeco Instruments, Santa Barbara, CA) were cleaned before use by washing exhaustively with $CHCl_3$ and irradiating by UV light (222 nm) for one hour. After preliminary trials of soaking in solutions of $CHCl_3$ and THF, DMSO was selected as the solvent that provided enough solubility for all molecular tips **A**, **B**, and **C**. Shorter exposure times to the solutions (2 h) did not yield significant rupture forces for statistical analysis. For sufficient exposure time, overnight soaking was applied for **A**, **B**, and **C**. The cantilevers were soaked overnight

immediately after UV irradiation in filtered (Millex PTFE 0.2 μm filter, Millipore, Billerica, MA) 100 μM solutions of either molecular tip **A**, **B**, or **C** in DMSO overnight. Subsequently, the tips were washed with DMSO, then EtOH and H_2O five times each to remove any unbound molecule. Tips were mounted onto the AFM for the force spectroscopy measurements.

5.4.2 AFM Force Curve Measurements

Force curves measurements were carried out using MFP-1D AFM (Asylum Research, Santa Barbara, CA) equipped with gold-coated silicon nitride modified with molecular tip **A**, **B**, or **C**. Force curves were generated in Igor Pro 4.09 (WaveMatrics Inc., Lake Oswego, OR). Each cantilever was calibrated using the thermal noise method before and after modification in each measurement.[12]

An aliquot (1 μL) of NeutrAvidin-coated beads (Ultralink immobilized NeutrAvidin, 6% crosslinked beaded agarose covalently linked to NeutrAvidin with a biotin capacity of 20 μg/mL resin, Pierce, Rockford, IL) were mixed with filtered (0.2 μm PTFE filter, Millipore) 20 mM HEPES (pH=7.4) on a cleaned glass slide. NeutrAvidin is a modified avidin protein derivative that provides a biotin-binding property in exceptionally low nonspecific manner.[13] All the experiments were carried out in the same HEPES buffer. Force–distance curves were collected with a tip velocity of 500 nm/s and pull distance of 2.0 μm. Each measurement was generally repeated several hundred times depending on the measurements.

For a control experiment, force measurements were carried out in the presence of excess amount of free ligand molecule (saturated biotin solution in buffer about 0.22 mg/mL, which was estimated to be approximately 100 times excess of the total binding sites of the receptors).

Sepharose CL-6B (crosslinked 6% agarose) was used as a substrate for the other control experiment in the absence of NeutrAvidin. Sepharose CL-6B beads were soaked in the HPLC grade water and then centrifuged. The supernatant liquid was removed and discarded. This process was repeated five times to remove the ethanol on the beads and the resulting beads were stored in HEPES buffer overnight. The last control experiment using non-functionalized AFM tips were carried out using the same type of Au-coated AFM tip after cleaning by UV-irradiation and washing with the same solvents.

5.4.3 Force Histograms for Loading Rate Experiments

Loading rates were varied by changing the tip velocity within the software of the AFM. Loading rates (pN/s) were calculated by multiplying the calibrated spring constant (pN/nm) of the cantilever by the tip velocity (nm/s).

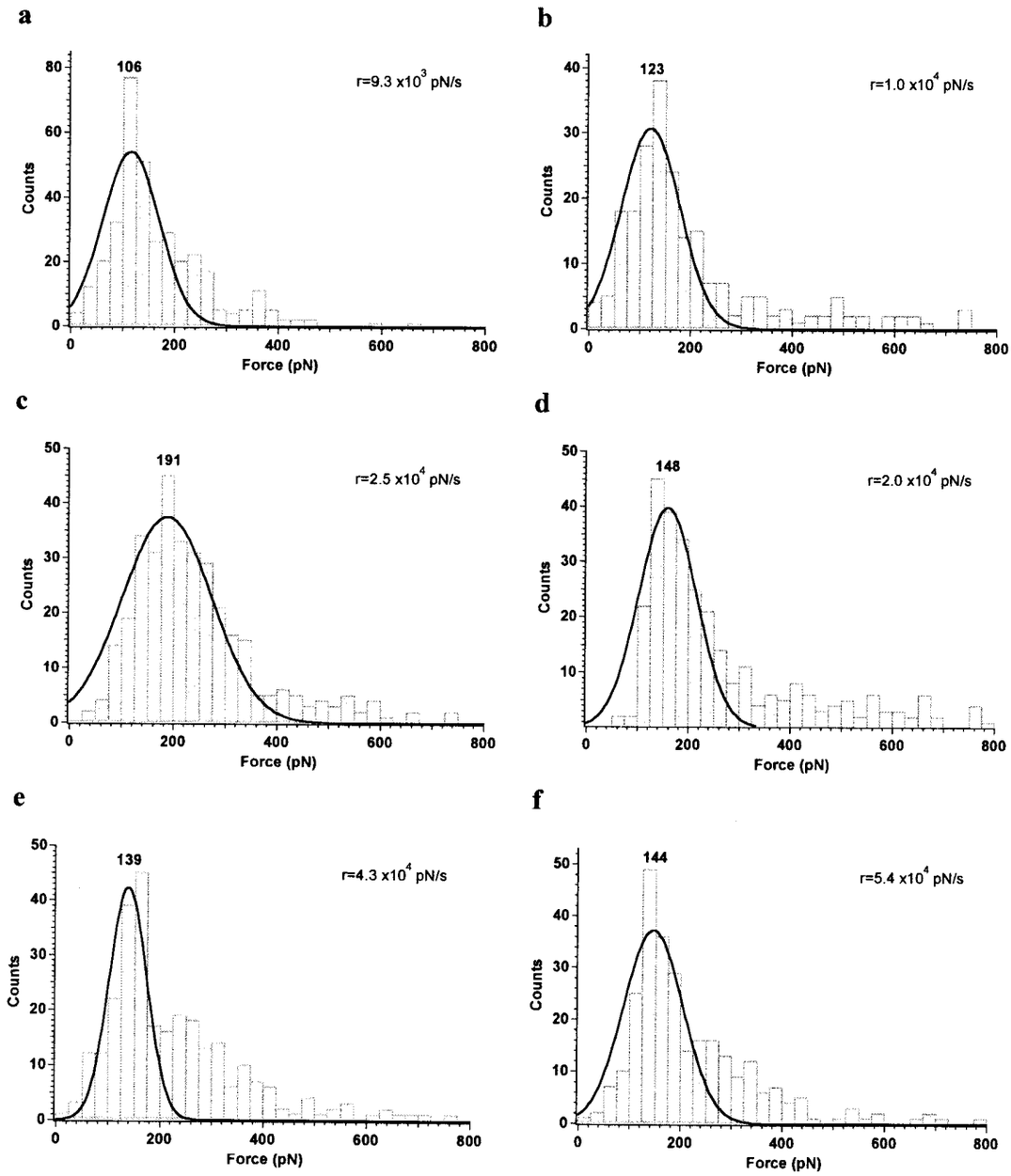

Figure 5-1. Force histograms for loading rate dependency experiments with molecular tip **A**. Loading rates, r, are inset in each histogram.

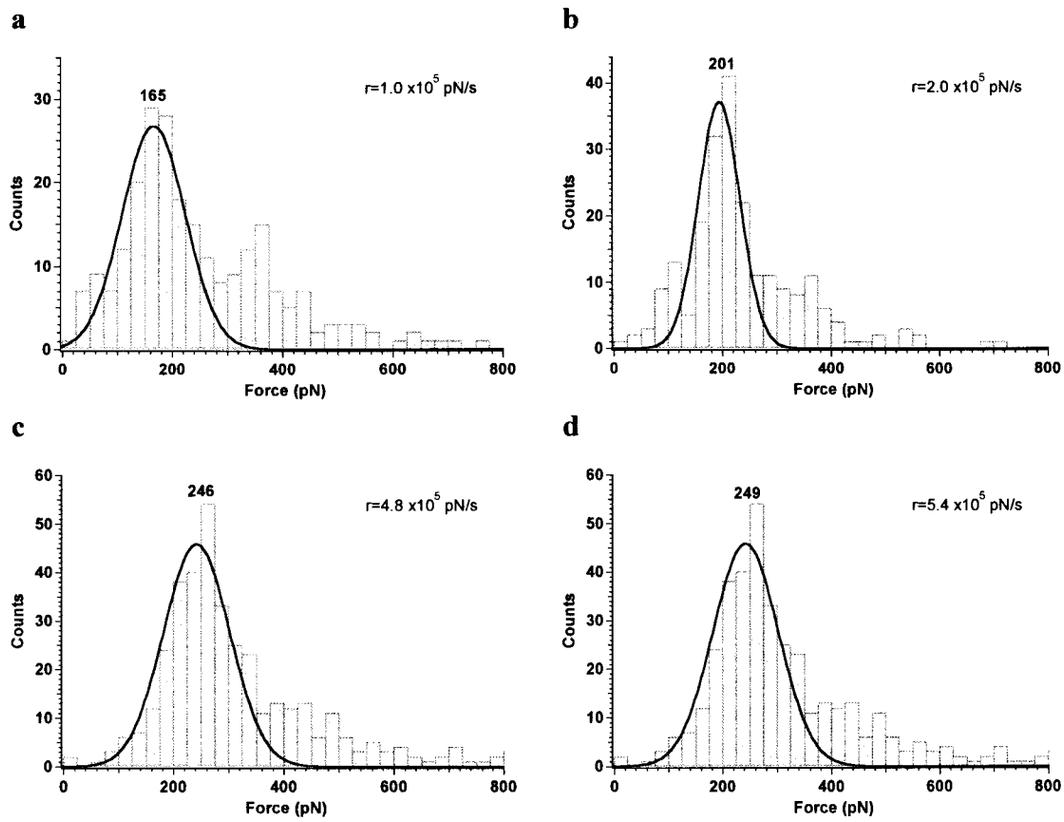

Figure 5-2. Force histograms for loading rate dependency experiments with molecular tip **A**. Loading rates, r, are inset in each histogram.

5.5 Nanocrystalline Diamond Deposition and Functionalization

5.5.1 Hot Filament Chemical Vapor Deposition

Diamond deposition was performed in a HFCVD 007 diamond reactor chamber (Blue Wave Semiconductors, Baltimore, MD USA) in the Carpick lab.

Venting the chamber: The pump power remained on all the time. Pump oil needed to be changed about every six months or when the pump was not reaching as low of vacuum. There are two knobs for adjusting the pressure in the chamber, the vacuum valve (coarse adjustment) and the needle valve (fine adjustment). The latch was unscrewed and opened on the chamber door. To vent, both valves, the vacuum and needle valve, were closed completely. Because there were no samples in the chamber at this point, the venting was done quickly with the vent valve. The vent valve line was connected to the nitrogen tank and the N_2 tank was opened. The vent valve was opened a full turn at first (more if necessary) so that the chamber vented quickly (within a couple of minutes). The chamber door was open slightly when the chamber reached atmospheric pressure. The pressure gauge on the chamber did not respond properly to the rapid pressure change. The vent valve was closed and the filament holder was removed at this point by unscrewing the four screws: two on top and one on either side of the holder. If they are unscrewed too far, the screws fell into the chamber and were difficult to recover.

Preparing tungsten wire: A piece of tungsten wire (99.95% W wire, 0.5 mm diameter, Goodfellow Cambridge Ltd., Huntingdon, England) was tightened onto the filament holder. It was necessary to carburize the wire before deposition to prevent the deposition of tungsten and its impurities onto the substrate surface. The wire was held down by a washer on either side and was tightened with a screwdriver. The screws holding the wire were not tightened too much, only as tight as one can tighten with the use of fingers. When tightening the wire under the second screw, the wire was held in the same position as the second screw was tightened to avoid introducing stress in the wire. It was important not to introduce stress into the wire at any time because tungsten carbide, a brittle material, can break easily during the cooling process after carburization or diamond growth. There are two ways to fashion the wire for the holder: one used the curve of the wire from the spindle to span the filament holder or, alternatively, the wire was curved into a "W-shape" by slowly bending the wire around a finger. Care was taken not to introduce kinks in the formation of the "W-shaped" wire. After a diamond growth cycle, the curved wire always fractured upon cooling. Because of its brittle and stressed position in the filament holder, a new curved wire was needed with each growth. With the "W-shaped" wire it was possible to do up to three diamond growths if care was taken when cooling the wire.

Pumping down the chamber: The filament holder was placed back into the chamber until it fitted into the slot and the four screws were tightened. The vacuum and needle valves were opened slowly until they were completely opened. The vacuum chamber was pumped down to about 4 $x10^{-3}$ Torr.

Seeding the substrates: While pumping down the chamber and during carburization, the diamond seed solution was prepared. Si wafers were cut with the diamond cutter with the polished side face down on a Kimwipe. The flat side of the wafer acted a guide for the cutting: pieces were cut either perpendicular or parallel to the flat side for the cleanest breaks. 1 mL of nanodiamond slurry in DMSO (>98% purity, cubic phase, 4-5 nm primary particle size, 30 nm average agglomerate size, International Technology Center, Research Triangle Park, NC USA) was suspended in 30 mL MeOH (HPLC grade, Fisher Scientific, Fair Lawn, NJ USA) and sonicated in a beaker covered with parafilm for 10 minutes. The silicon substrates (Si AFM tips, or Si wafer, etc.) were sonicated in the seed solution for 30 min in a beaker covered in parafilm. A maximum of two Si pieces (~1 cm^2 each) were sonicated in the diamond seed at a time to attain even seeding because uneven seeding can lead to unevenly coated diamond surfaces. AFM tips were either held with tweezers or in a Teflon AFM chip holder. The Teflon holder was easiest to use and provided the same results. Next, the substrate was removed from the diamond seed solution and cleaned by sonication in methanol for 10 minutes. Finally, the substrates were dried with a stream of N_2.

Carburizing the tungsten filament: Once pressure reached a minimum, the methane tank was opened to a pressure of 25 psi. The methane flow meter was turned on with the power switch, the toggle switch was moved to the middle position, and the valve was opened to the right of the flow meter. The knob was adjusted for the methane so that the flow rate was 9.00 sccm (standard cubic centimeters per minute).

The vacuum valve was closed almost all the way. The pressure increased slowly at first but increased quickly after closing almost all the way. The pressure was adjusted to about 20 Torr. The pressure was adjusted until it was stable enough to ensure that only fine adjustments to pressure were necessary during the carburization process. The needle valve was adjusted so there was room to make adjustments during the heating process as the pressure increased as the wire was heated. The circulation pump was turned on by the switch on the pillar next to the chamber. The filament power switch was turned on and the filament power knob slowly turned to 20 V over the course of about 3 minutes. The pressure was adjusted to 30 Torr and the chamber remained at this power and pressure for 20 minutes. The pressure was closely monitored and adjusted to 30 Torr as the power is increased. The filament power was slowly adjusted to 50 V over the course of 3 minutes and was left at 50 V for one minute. The filament was adjusted slowly to 80 V over the course of 3 minutes and left at 80 V for one minute. The filament power was turned down slowly because the brittle carburized tungsten (WC) filament was prone to fracture. Thus, cooling must be done slowly to prevent breaking the filament. The WC filament never broke while ramping up the filament power, the break always occurred while cooling. The rapid changes in temperature caused stress and fracture in the brittle filament. When it was first attempted, counting to five at every increment was a sufficiently slow enough rate, e.g. counting to five as the filament power was being turned from 80 V to 79 V and then counting to five again as the power was held at 79 V before counting to five as the power was turned to 78. The pressure in the chamber was not important as the filament power was decreased. After the filament power was at 0 V, the filament power was

turned off and the methane was turned off about 30 min after the filament power was off. The chamber door was unscrewed and unlatched. Then the vacuum and needle valve were closed completely. The N_2 was turned on and the vent valve opened about a quarter of a turn. Once the chamber door was open, the vent valve and N_2 was turned off. The filament had a dull gray appearance after carburization. The filament was cooled for a minimum of 1 hour before diamond deposition.

Diamond deposition: The seeded Si substrates were carefully placed on the stage in the chamber, while being mindful not to break the WC filament. The samples were placed directly underneath the filaments for the Si wafer surfaces for optimum thickness and slightly to the side (~1 cm) of the center of the filament for the Si AFM chips. The vacuum valve was opened slowly until the chamber pressure reached about 4×10^{-3} Torr by opening both vacuum valves fully. The hydrogen and methane gas cylinders were opened and the chamber was filled with H_2 (90 sccm) and CH_4 (3.80 sccm) to 20–25 Torr; this allowed for the increase in pressure as the chamber was heated.

The temperature controller was turned on and set for four sections.

Section 1: Target temperature was set to 700 °C. Ramp rate 50°C/min.

Section 2: Hold the temp for 80 min: 60 min for growth and 20 min for H-termination.

Section 3: Target temperature 30°C. Ramp rate 10°C/min.

Section 4: End.

The substrate heater enable was turned on and run was pressed on the temperature controller. After pressing run, the screen on the temperature controller flashes "RUN" as it ramped up the temperature. The temperature of the stage was set to

700 °C. The temperature of the WC filament was about 1200–1500 °C to cleave the bonds of H_2. As the stage was heating, the pressure was adjusted and stabilized at 20–25 Torr and the needle valve was positioned to have room to open and close to adjust the pressure during filament heating. The temperature was about 300 °C before the filament power was turned on. The circulation pump for the water was switched on before turning the filament power was turned on.

When the temperature was 300 °C or greater, the filament power was slowly increased to 87 V over the course of 10 minutes. The pressure was adjusted with the needle valve to 30 Torr. The deposition time for diamond was 60 minutes and the pressure was monitored and adjusted to 30 Torr during diamond growth. After 60 minutes, the methane was switched off with both switches and the valve. The pressure was then adjusted to 20 Torr for H-termination. After 20 minutes, the filament power was carefully turned down. The temperature controller automatically started decreasing the temperature as it was programmed to do. IMPORTANT: The hydrogen termination during cooling was important because hydrogen can desorb from the surface above this temperature. Leaving hydrogen on during cooling ensured an effectively H-terminated diamond surface. The hydrogen was kept on until the stage temperature was less than 400 °C. A rate of about 5 V/min was maintained until the power reached 20 V. The power remained at 20 V for 5 min and was then decreased to 15 V. After another 5 min at 15 V, the power was decreased to 12.5 V. Every 7 min, the power was decreased 2.5 V until the power reached 0 V. The filament usually fractured when the filament power was below 5 V. Giving the chamber and filament sufficient time to cool decreased the risk of filament fracture. It took 60–90 min to turn the filament power all

the way to 0 V. The filament power was turned off. The hydrogen switches were turned off and the chamber door was unlatched. The nitrogen (labeled Ar) was opened to 35 sccm. The vacuum and needle valves were closed completely. Substrate heater power and substrate heater enable were turned off. The gauge power was turned off when filling with nitrogen overnight to lengthen the lifespan of the digital gauge. The chamber was filled with nitrogen slowly over several hours to prevent the substrates from being broken or blown off the stage. The circulation pump was turned off.

Sample removal: After the chamber was vented, which usually took overnight, the door was open. The samples were carefully removed. After the samples were removed, the chamber door was closed and the vacuum valves both opened completely. The pump power was left on all the time. The gauge power and the main power switch were turned off and only the pump power was left on continuously.

5.5.2 Functionalization of NCD with Undecylenic Acid (UA)

The functionalization of NCD films on Si and on AFM tips was performed with undecylenic acid (UA) degassed by 3 cycles of freeze/pump/thaw. UA is a solid at room temperature (mp 22–25 °C), but after gently heating, it generally remained a liquid. A Teflon AFM cantilever holder was used to hold AFM chips for functionalization. The NCD substrates were immersed in neat UA in a nitrogen flushed quartz vessel in a photochemical reactor (Southern New England Ultraviolet Company, Middletown, CT USA) equipped with five low pressure Hg lamp 8 W bulbs with an

emission wavelength of 254 nm. After 16 h, the substrates were washed with dichloromethane and sonicated for 10 minutes in dichloromethane for two cycles. The substrates were washed, sonicated in methanol for 10 minutes, and then dried with a stream of nitrogen. AFM tips were used as soon as possible after functionalization.

5.5.3 Au/Pd Sputtering on NCD AFM Tips

Au/Pd alloy was sputtered on the backside of NCD-coated tips with a Cressington Sputter Coater 108 (Cressington Scientific Instruments, Watford, UK). The Ar tank was turned on and the AFM chips were placed in the sputtering chamber with the tip side down. The chamber was evacuated to below 0.10 mbar and then filled with Ar. This was repeated three times to decrease the pressure down to about 0.05 mbar. A small amount of Ar was allowed into the chamber to a pressure of 0.10 mbar. The tips were then sputtered for 40 s. The vacuum was closed after the sputtering. The chamber was vented to remove the sample and the Ar tank was turned off.

5.5.4 Additional NEXAFS Spectra

C K edge absorption peaks for C=C (285.0 eV), C=O (286.4 eV), C–H (287.5 eV), and C–O (288.6 eV) were examined for all the surfaces. The samples examined include: a single crystal, H-terminated B-doped diamond (1 xtal), H-terminated NCD (H-NCD, used as comparison throughout NEXAFS spectra), undecylenic acid (UA) treated NCD for varying amounts of time (UA–NCD 4 h, 8 h, 12 h, 16 h), a NCD surface treated with oxygen plasma for 10 min (O plasma), a methyl ester of UA (UA-

Me), and the deprotected methyl ester of UA (UA-Me deprot) (Figure 5-3). Spectra for each modified surface had the H-NCD surface data subtracted from the partial electron yield values (Figure 5-3c). Expanded spectra are shown (283 eV to 289.5 eV). The UA-NCD 16 h had the weakest signal in this area. The spectra for the UA-NCD samples overlapped well. Spectra were also divided by the H-NCD partial electron yield values (Figure 5-3d). The divided spectra maintained similar trends as the subtracted spectra.

In the C K-edge spectra there is overlap of several crucial peaks (C–O, C=O, C–H). Because of the close proximity to each other, peak fitting that considers overlapping peaks is needed. The Carpick lab uses a program to calculate the contribution of each peak to the area. From the peak fitting, normalized areas were calculated for the C–O and C=O peaks. In Figure 5-4, a plot of the peak fitting areas is shown for the beam perpendicular to the surface. The H-terminated NCD sample (H–NCD) was used for the 0 h sample. For the UA time treatment, C=O and C–O increases up to 12 h. After 12 h, there was no significant increase in these signals.

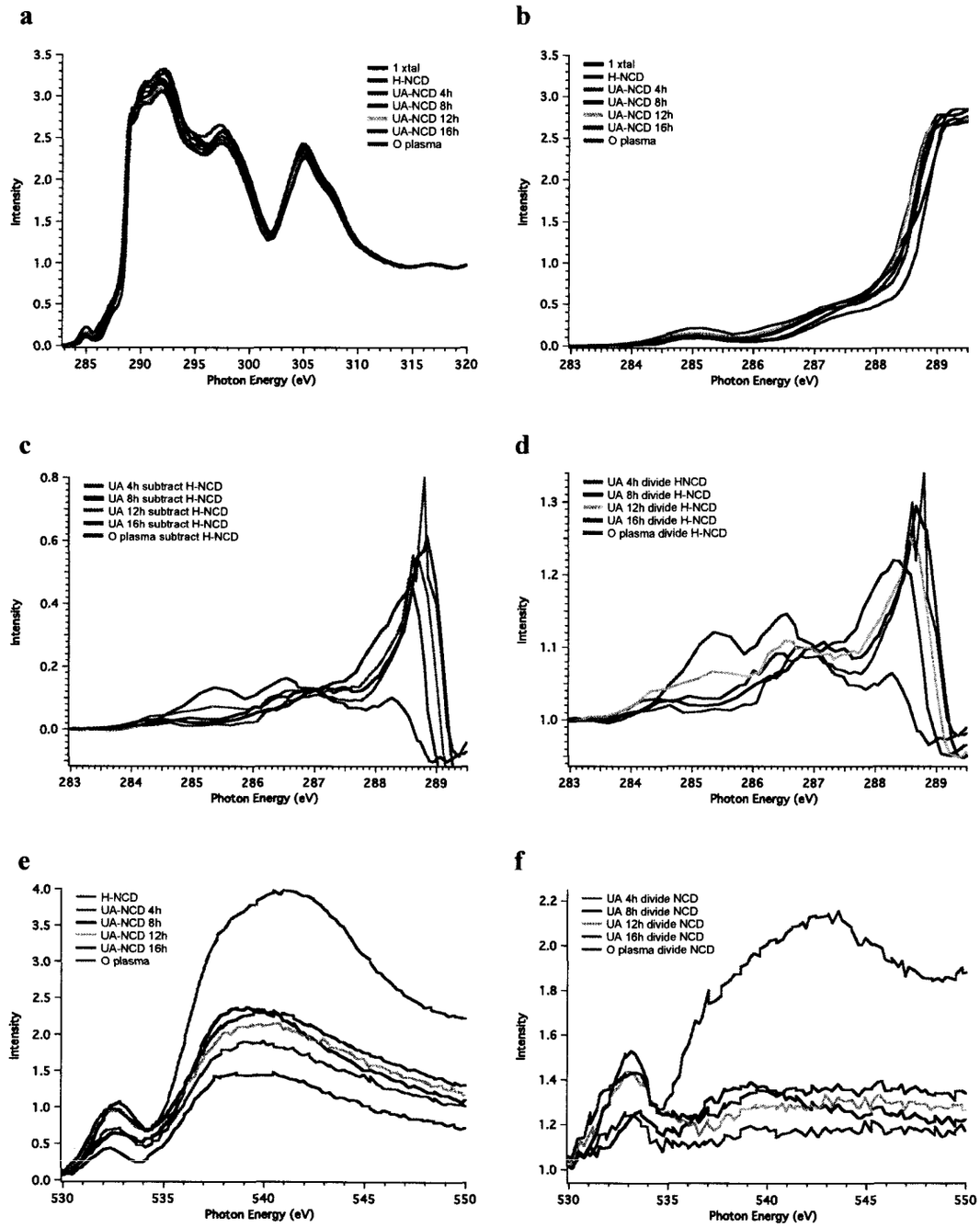

Figure 5-3. NEXAFS C and O K edge partial electron yield spectra for NCD surfaces. (a) Spectra of all samples. (b) Expanded region of C K-edge spectra. (c) Expanded region of C K-edge spectra subtracted by H-terminated NCD values. (d) Expanded region of spectra of C K-edge spectra divided by H-terminated NCD values. (e) O K-edge spectra of samples. (f) Expanded region of spectra of O K-edge spectra divided by H-terminated NCD values.

a

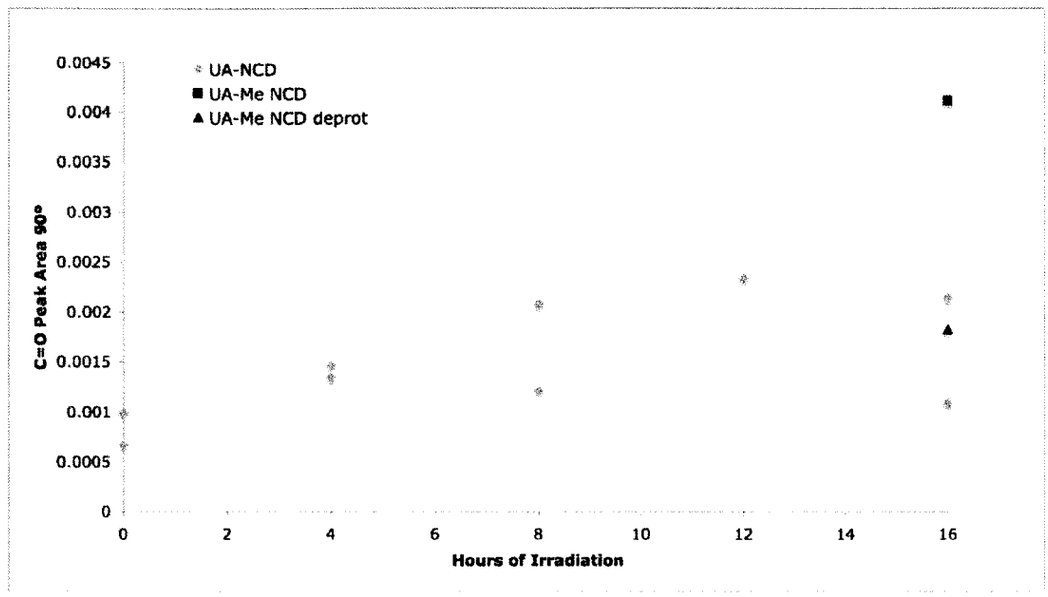

b

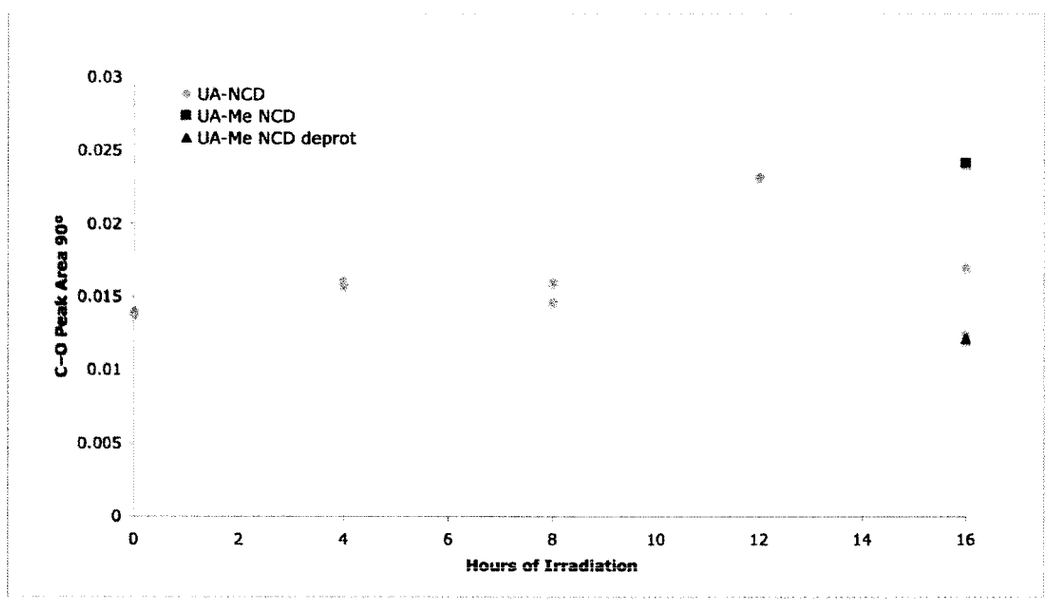

Figure 5-4. Plot of peak area versus hours of irradiation for UA–NCD and UA–Me for (a) C 1s to π^* transition of carbonyl and (b) C 1s to σ^* transition of C–O.

5.5.5 Fluorescent Labeling of Polymer Surfaces and AFM Cantilevers

PBS buffer refers to Phosphate Buffered Saline (pH = 7.4, Cellgrow Mediatch Inc., Manassas, VA USA). Solutions of EDC (144 mg in 5 mL PBS, 200 mM, Sigma-Aldrich) and N-hydroxysuccinimide (48 mg in 5 mL PBS, 250 mM, Sigma-Aldrich) were sonicated for 10 min and filtered through a 0.2 μm filter (PTFE syringe filter, Millex, Billerica, MA) before applying to the polymer surfaces. The surfaces were immersed in the EDC/NHS solution for 16 h before being washed exhaustively with PBS buffer and Millipore water. Fluorescein cadaverine (2.1 mg in 15 mL PBS, 20 mM, Biotium Inc., Hayward, CA, USA) was sonicated for 10 min and then filtered through a 0.2 μm filter. The polymer surfaces were then immersed in the fluorescein cadaverine solution for 1 h. The polymer surfaces were washed exhaustively with PBS buffer and Millipore water. The surfaces were immediately imaged with the fluorescent microscope (Olympus BX-51, Center Valley, PA with a 75 W xenon bulb using the 10X, 20X, 50X, and 100X objectives). Images were collected with an Olympus digital camera.

Undecylenic acid functionalized NCD tips (UA–NCD) and H-terminated NCD (H-NCD) tips were subjected to the same fluorescent labeling conditions. After functionalization, the UA–NCD tips were immersed in 200 mM EDC/250 mM NHS solution for 24 h. The tips were rinsed with PBS buffer and immersed in 1×10^{-4} M solution of fluorescein cadaverine in pH=7.4 PBS buffer for 1 h. The tips were washed with PBS buffer and then sonicated in Millipore water for 10 min and then washed and sonicated in acetone for 10 min. The tips were imaged with the fluorescent microscope.

5.6 Lithography with UA-NCD AFM Tips on Polymer Surfaces

5.6.1 Spin Coating of Polymer Surfaces

The PTBA purchased (Polymer Source Inc., Dorval, Quebec Canada) had different solubility than the PTBA synthesized by the Composto group. It would not dissolve in toluene, the solvent generally used in spin coating. The Si surfaces (*n*-type, P doped, Silicon Quest International, Santa Clara, CA) were treated with piranha solution (sulfuric acid/hydrogen peroxide 3:1 at 80 °C) and then washed ten times with Millipore water. The Si wafers were then treated with UV/ozone for ten minutes (UVO-Cleaner Model 42, Jelight Co., Inc. Irvine, CA) to ensure the even formation of a silicon oxide layer. The surfaces of the Si wafer contaminated quickly, immediately after cleaning there was visual evidence of dirt. There were also streaks on the coated surface that were indicative of a dirty Si surface. The thickness of the polymer films on the Si wafer were measured with a Rudolph Auto EL-II ellipsometer (Rudolph Instruments, Denville, NJ) using a 632.8 nm laser with a fixed angle of 70°.

Poly(*tert*-butyl acrylate) (PTBA, PDI=1.25, MW= 15kDa, 1 w/v% in toluene) was spin coated onto the cleaned Si wafers or photoetched glass slides (square cover slip photoetched , #2 thickness, 23 x 23 mm, Bellco, Vineland, NJ USA) at a thickness of about 30 nm. Thickness was measured on Si wafers by ellipsometry and assumed to be of similar thickness on glass slides under the same spin-coating conditions. Random copolymer (PS-*ran*-PTBA) with 30% and 50% of PTBA[14,15] were spin coated from 1 w/v% solutions in toluene at 2000 rpm for 60 sec to give films 40 nm and 50 nm thick,

respectively. Block copolymers (PS-b-PTBA) (M_n(PS) = 45kDa, M_n(PTBA) = 49kDa, PDI =1.09 and M_n(PS) = 66.2kDa, M_n(PTBA) = 32kDa, PDI = 1.05, Polymer Source, Inc. Dorval, Quebec, Canada) were also spin coated from 1 w/v% solutions in toluene to give surfaces about 40 nm thick films. The FTIR–ATR spectra of the as cast and annealed polymers are on the following pages in section 5.6.2.

5.6.2 FTIR–ATR Spectra of Polymer Surfaces

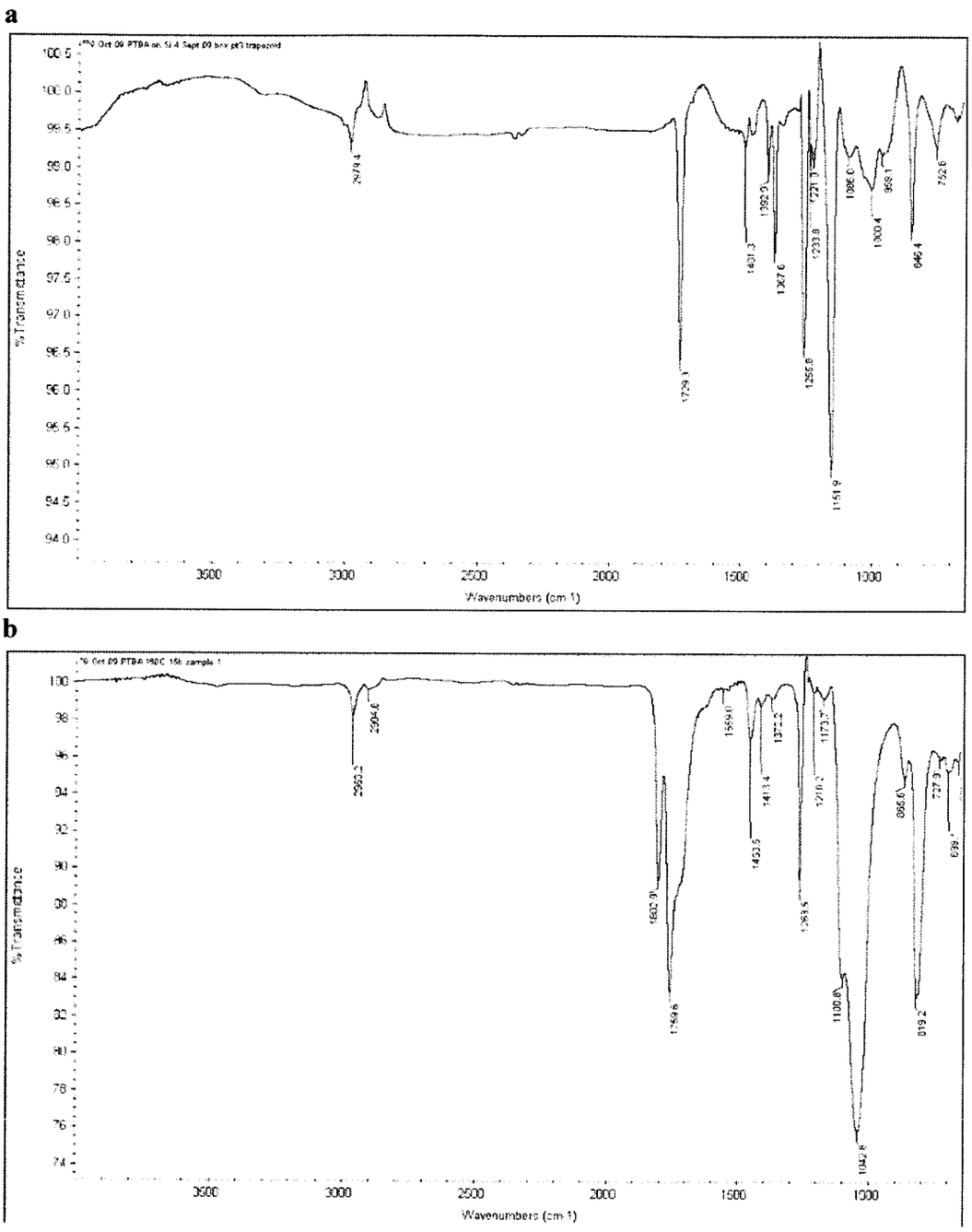

Figure 5-5. FTIR–ATR of PTBA surfaces. (a) As cast. (b) After annealing at 160 °C for 16 h.

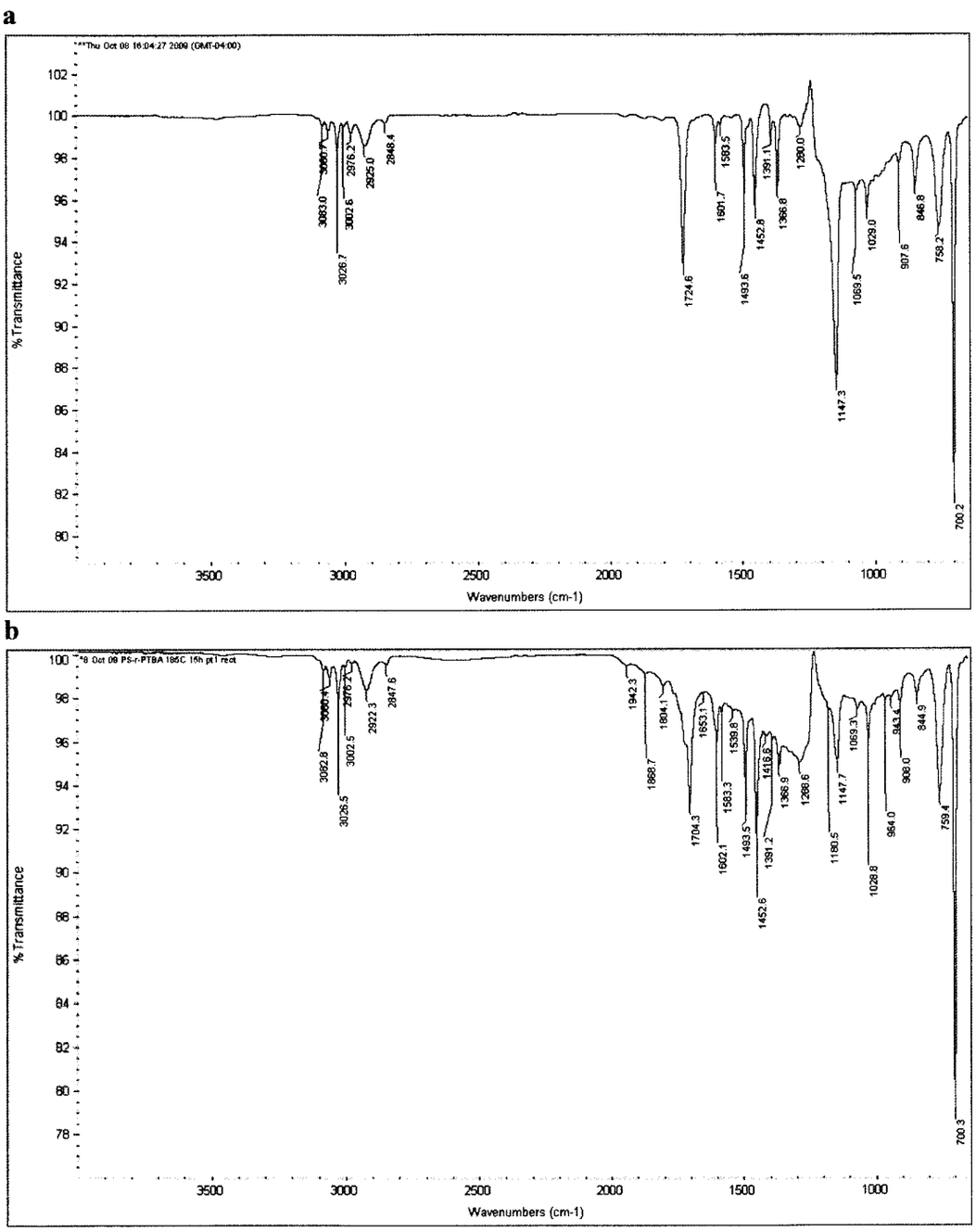

Figure 5-6. FTIR–ATR spectra of PS-*random*-PTBA (30 mol% PTBA). (a) As cast (b) Annealed at 185 °C for 15 h.

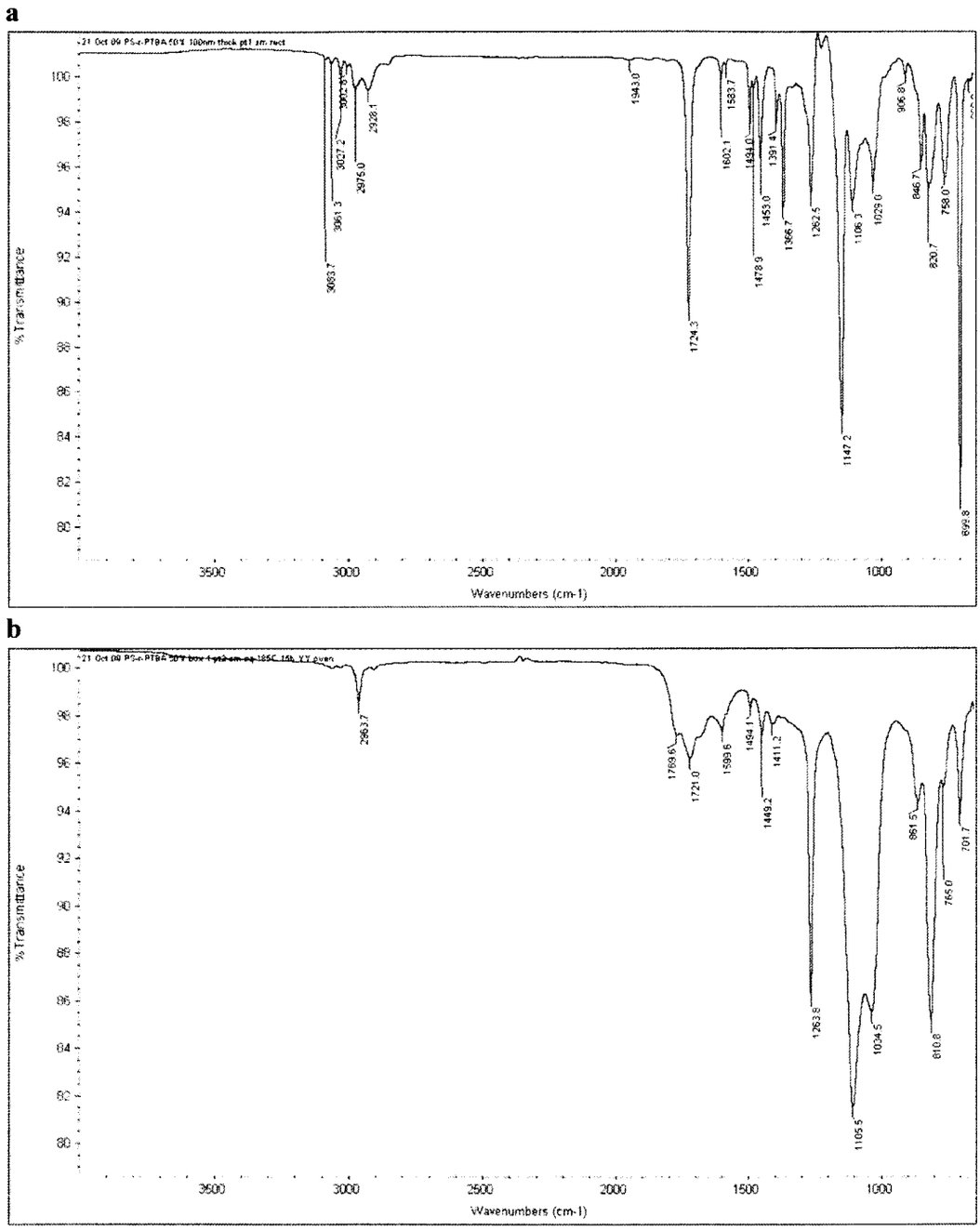

Figure 5-7. FTIR–ATR spectra of PS-*random*-PTBA (50 mol% PTBA). (a) As cast. (b) After annealing for 15 h at 185 °C.

a

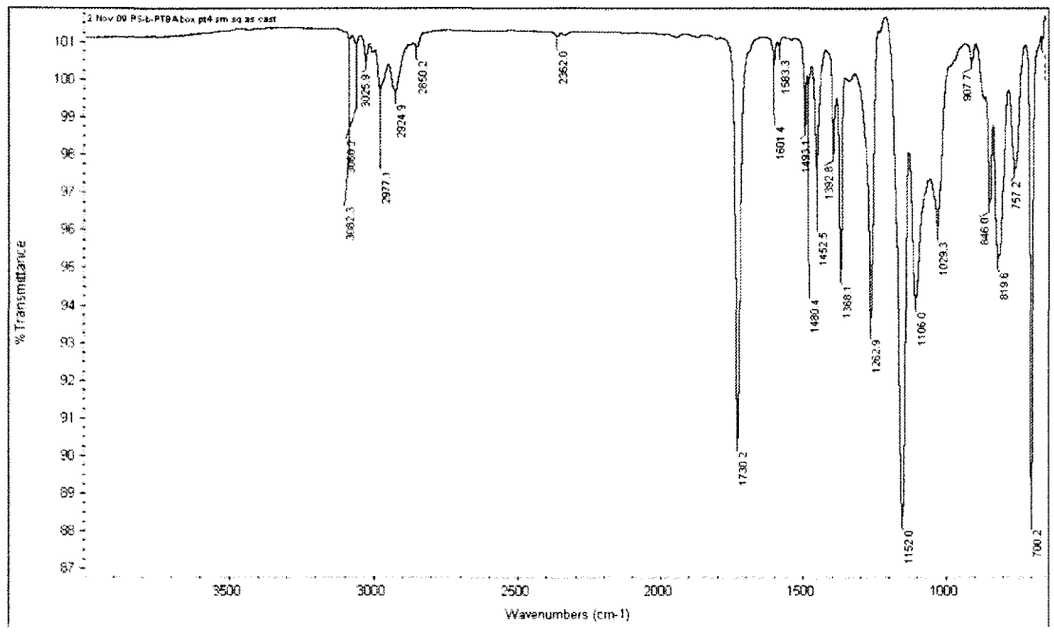

b

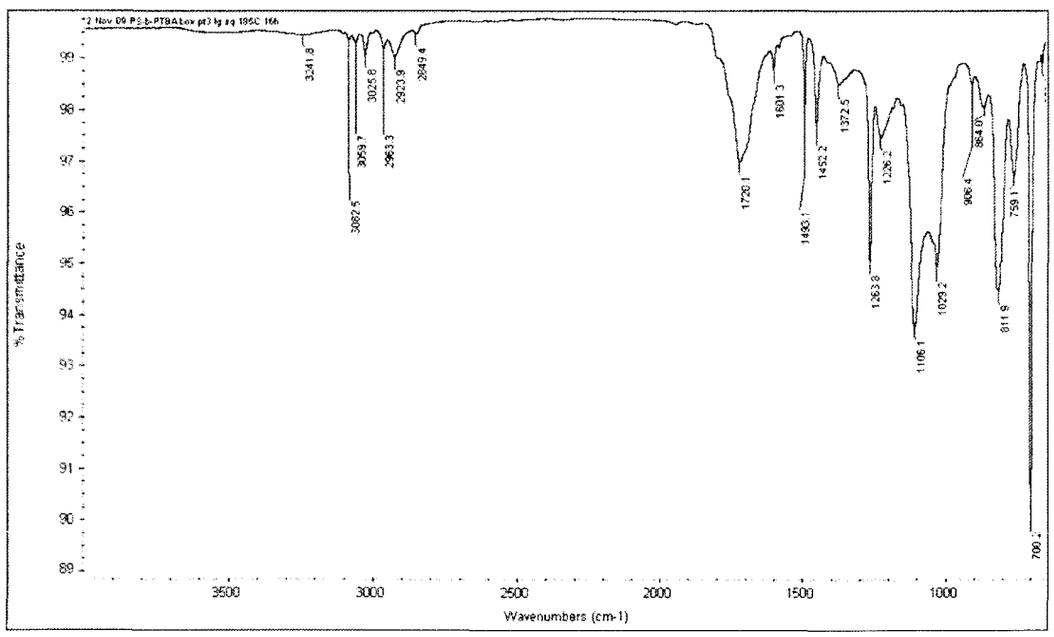

Figure 5-8. FTIR–ATR spectra of PS-*block*-PTBA (1:1). (a) As cast. (b) 1:1 After annealing at 185 °C for 16 h.

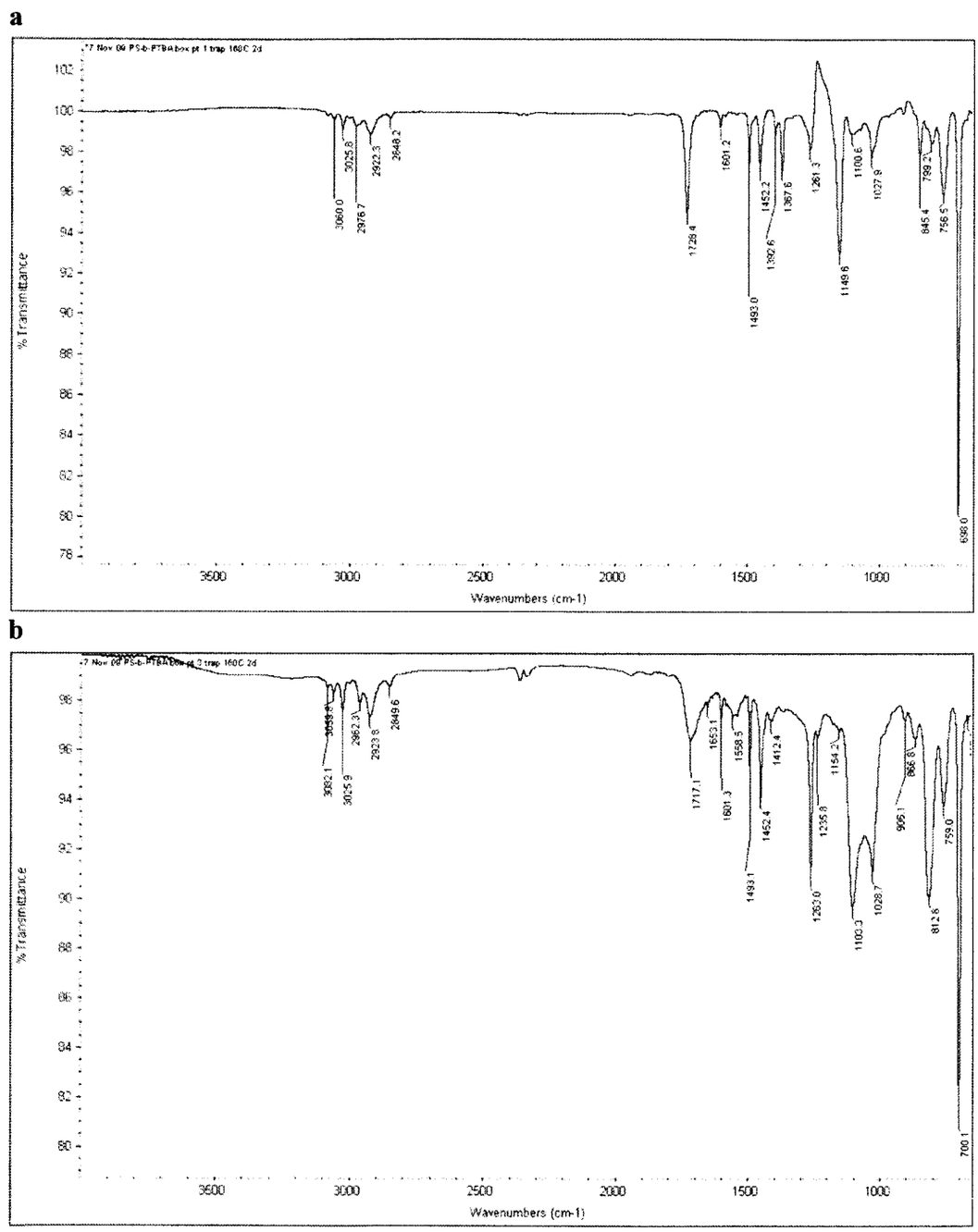

Figure 5-9. FTIR–ATR spectra of PS-*block*-PTBA (2:1). (a) As cast. (b) After annealing at 160 °C for 2 d.

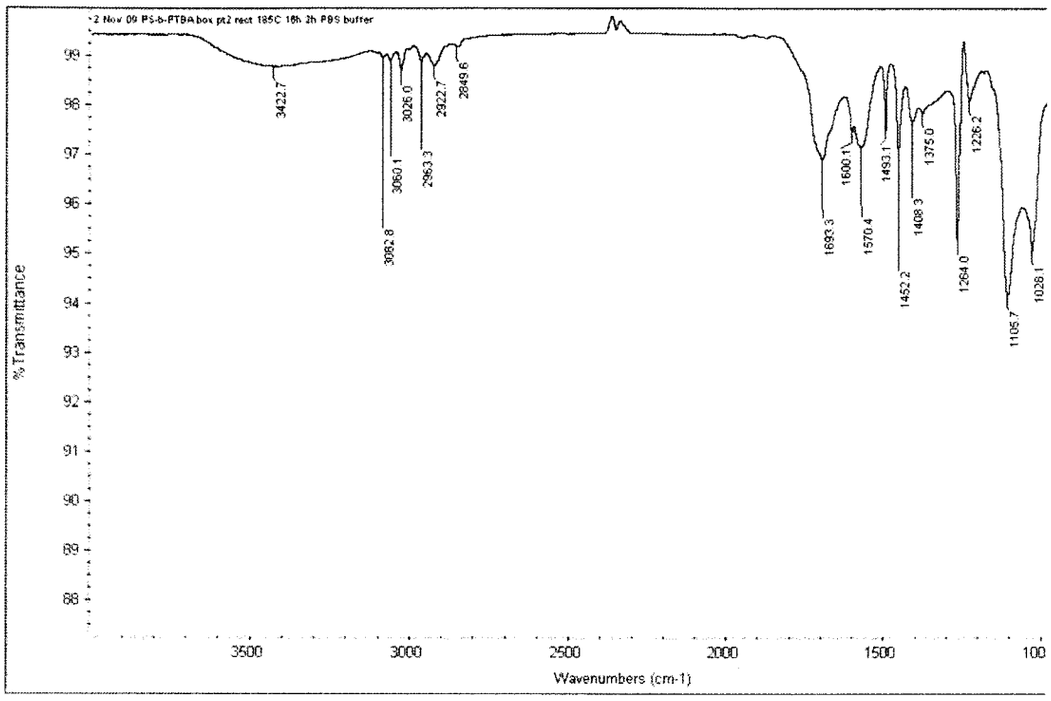

Figure 5-10. FTIR–ATR spectrum of PS-*b*-PTBA 1:1 annealed at 185°C for 16h, then soak 2h in PBS buffer, pH=7.4.

5.6.3 Atomic Force Microscopy

For AFM imaging of the polymer surfaces, a Pico Plus 5500 AFM (Molecular Imaging, now Agilent Technologies Santa Clara, CA USA) was used with a MAC/AAC controller. All images were collected with PicoScan 1.6.4 and processed using Pico Image. Samples were loaded on the sample stage and enclosed in the bell jar. The contact and acoustic alternating current (AAC, or intermittent contact mode) nose cones were used. The large scanner (100 μm range) was generally used in the polymer lithography experiments because of its range and ability to scan in closed loop. After calibration according to the description of the manufacturer, the closed loop scanning was engaged. Although the closed loop scanning decreased the piezo creep and drift during contact scans, when the tip was withdrawn from the surface to move to another point on the surface, the closed loop was disengaged. The closed loop was engaged again before each scan. Drift still occurred while scanning the larger patterns (70 μm). For the larger patterns, 50 μm or more, the scanning was performed in open loop. For smaller patterns, 5 to 10 μm, closed loop scanning was performed.

NCD coated contact mode Si tips (CSC 37 MikroMasch San Jose, CA USA, no Al back siding, resonant frequency, f_0 = 21 and 28 kHz, spring constant, k = 0.3 and 0.35 N/m for the longer and medium sized cantilevers, respectively) were used to scan the polymer surfaces in contact mode. After aligning the laser and engaging the surface, force curves were obtained on the polymer surface to guide in finding a setpoint for contact mode scanning. From the force curve, the flat region of the curve where the tip was removed from the surface was chosen as the setpoint to maintain

stable contact with the surface. Generally, the setpoint was set 0.30 V above this value, which corresponded to approximately 20 nN of applied force. General scanning parameters: 5 μm scan with 100 μm scanner with 1024 lines at a scan rate of 0.5 lines/s. For larger areas it was found to be too cumbersome to scan at such a rate. It was found that a 70 μm pattern could be scanned at this rate and still yield surfaces that appear consistent with the smaller patterns. During contact scanning, several images of the tip location were captured to give a general idea where the patterns were being made. These images helped find the patterned area after switching to intermittent contact tip. For contact mode, the longest cantilever of the three was used to scan the surface. Force–distance curves were collected with the functionalized NCD tip before, during, and after scanning to help find a suitable setpoint for contact mode scanning and for adhesion measurements. Force curves were collected inside the scanned area by withdrawing the tip from the surface after scanning and engaging to the surface again. After collecting five curves the tip was withdrawn again and the sample stage was moved to position the tips over an area that had not been scanned previously to obtain force curves outside the patterned region.

For AAC (intermittent contact) mode, the contact nose cone was used and intermittent contact mode tip was inserted (MikroMasch, NSC 16, f_0 = 170 kHz, spring constant, k = 40 N/m). After laser alignment, the tip was positioned near the patterns made in contact mode by the camera images captured during contact scanning or by the position of the pattern relative to the grids on the glass slide. Distinguishing blemishes on the surface also served as guides to locate the patterned regions. The surface was scanned at 2 Hz for scan 5 μm or less and at 1 Hz for scan sizes larger than 5 μm.

For heating experiments, the high temperature stage was used with a temperature controller (Lake Shore Cryotonics, Inc. Westerville, OH) and checked with a thermometer (Fluke 51 thermocouple K/J thermometer, Fluke Corporation, Everett, WA). The temperature controller was set at a ramp rate of 5 °C/min with proportional, integral, and differential gains set to 6, 6, and 100, respectively. The setpoint was set at 100 °C, and the "heater high" setting was used, which gave a heater percent of 20%. The microscope was set up as it normally was while the stage was heated. After the temperature reached its setpoint, the system was allowed to equilibrate for 1.5 h, which according to the manufacturer was enough time to minimize drift (Pico Plus manual).

Cantilevers were calibrated on the Pico Plus using the Sader method for rectangular cantilevers.[16,17] Resonant frequencies were obtained with the AAC nose cone and the Q factor was calculated in Matlab using custom software from the Carpick lab. The fluid density and viscosity of air at 20 °C was 1.204 kg/m^3 and 1.8369 x 10^{-5} kg/m/s, respectively.

5.6.4 Adhesion Measurements

Hydrogen flame annealed gold surfaces (gold on mica, Agilent Technologies, Santa Clara, CA) were immersed in 1.0 mM solutions of dodecane thiol (Sigma-Aldrich) or 11-mercaptoundecanoic acid (Sigma-Aldrich) in ethanol degassed by freeze/pump/thaw. After 18 h immersed in their respective solutions, the gold substrates were washed exhaustively with ethanol to remove physisorbed molecules. The surfaces were used immediately after washing.

Adhesion measurements were made on a Pico Plus 5500 AFM (Agilent Technologies) in ethanol in the fluid cell. Ethanol was filtered with a syringe filter (0.2 μm PTFE filter, Millipore Corp. Billerica, MA) before use. A crystallization dish with about 20 mL of ethanol was placed at the bottom of the bell jar to saturate the bell jar with ethanol vapor and slow the evaporation of ethanol from the fluid cell. Additionally, the ethanol needed to be refilled in the fluid cell every 30 min. Force–distance curves were obtained at a rate of 100 nm/s with the tip traveling a distance of 200 nm. The softest cantilever on the chip was used in all measurements, which was calibrated by the Sader method to be approximately 0.4 N/m. The loading rate was 4.9 x 10^4 pN/s. 200 measurements were collected on each surface (DDT-Au, MUA-Au) with the same tip before and after UA functionalization (H-NCD, UA-NCD AFM tip). 20 measurements were taken in one spot and then the tip was withdrawn and moved to a different area to exclude the possibility of damaging the monolayer on the surface.

References:

(1) Li, Q.; Rukavishnikov, A. V.; Petukhov, P. A.; Zaikova, T. O.; Keana, J. F. W. "Nanoscale 1,3,5,7-Tetrasubstituted Adamantanes and *p*-Substituted Tetraphenyl-methanes for AFM Applications" *Org. Lett.* **2002**, *21*, 3631-3634.

(2) Schwabacher, A. W.; Lane, J. W.; Schriesher, M. W.; Leigh, K. M.; Johnson, C. W. "Desymmetrization Reactions: Efficient Preparation of Unsymmetrically Substituted Linker Molecules" *J. Org. Chem.* **1998**, *63*, 1727-1729.

(3) Bottari, P.; Ruedi, A.; Turecek, F.; Gelb, M. H. "Design and Synthesis of Visible Isotope-Coded Affinity Tags for the Absolute Quantification of Specific Proteins in Complex Mixtures" *Bioconj. Chem.* **2004**, *15*, 380–388.

(4) Nelson, K. E.; Gamble, L.; Jung, L. S.; Boeckl, M. S.; Naeemi, E.; Golledge, S. L.; Sasaki, T.; Castner, D. G.; Campbell, C. T.; Stayton, P. S. "Surface Characterization of Mixed Self-Assembled Monolayers Designed for Streptavidin Immobilization" *Langmuir* **2001**, *17*, 2807–2816.

(5) Vutukuru, S.; Bethi, S. R.; Kane, R. S. "Protein Interactions with Self-Assembled Monolayers Presenting Multiple Ligands: A Surface Plasmon Resonance Study" *Langmuir* **2006**, *22*, 10152–10156.

(6) Gryko, D. T.; Clausen, C.; Roth, K. M.; Dontha, N.; Bocian, D. F.; Kuhr, W. G.; Lindsey, J. S. "Synthesis of 'Porphyrin-Linker-Thiol' Molecules with Diverse Linkers for Studies of Molecular-Based Information Storage" *J. Org. Chem.* **2000**, *65*, 7345–7355.

(7) Pfister, J. R.; Wymann, W. E. "A Useful Variant of the Curtius Reation" *Synthesis* **1983**, 38–40.

(8) de Boer, B.; Meng, H.; Perepichka, D. F.; Zheng, J.; Frank, M. M.; Chabal, Y. J.; Bao, Z. "Synthesis and Characterization of Conjugated Mono- and Dithiol Oligomers and Characterization of Their Self-Assembled Monolayers" *Langmuir* **2003**, *19*, 4272–4284.

(9) Kang, J. F.; Ulman, A.; Liao, S.; Jordan, R.; Yang, G.; Liu, G. "4'-Substituted-4-mercaptobiphenyls on Gold and Silver Surfaces" *Langmuir* **2001**, *17*, 95–106.

(10) Hacker, C. A.; Batteas, J. D.; Garno, J. C.; Marquez, M.; Richter, C. A.; Richter, L. J.; van Zee, R. D.; Zangmeister, C. D. "Sturctural and Chemical Characterization of Monofluoro-Substituted Oligo(phenylene–ethynylene) Thiolate Self-Assembled Monolayers on Gold" *Langmuir* **2004**, *20*, 6195–6205.

(11) Nilsson, D.; Watcharinyanon, S.; Eng, M.; Li, L.; Moons, E.; Johansson, L. S. O.; Zharnikov, M.; Shaporenko, A.; Albinsson, B.; Mårtensson, J. "Characterization of Self-Assembled Monolayers of Oligo(phenyleneethynylene) Derivatives of Varying Shapes on Gold: Effect of Laterally Extended π-Systems" *Langmuir* **2007**, *23*, 6170–6181.

(12) Hutter, J. L.; J. Bechhoefer, J. "Calibration of Atomic Force Microscope Tips" *Rev. Sci. Instr.* **1993**, *64*, 1868–1873.

(13) Hiller, Y.;Gershoni, J. M.; Bayer, E. A.; Wilchek, M. "Biotin Binding to Avidin Oligosaccharide Chain Not Required for Ligand Association" *Biochem. J.* **1987**, *248*, 167–171.

(14) McConnell, M. D.; Yang, S.; Composto, R. J. "Covalent Nanoparticle Assembly onto Random Copolymer Films" *Macromolecules* **2009**, *42*, 517–523.

(15) McConnell, M. D.; Bassani, A. W.; Yang, S.; Composto, R. J. "Tunable Wetting of Nanoparticle-Decorated Polymer Films" *Langmuir* **2009**, *25*, 11014–11020.

(16) Sader, J. E.; Chon, J. W. M.; Mulvaney, P. "Calibration of Rectangular Atomic Force Microscope Cantilevers" *Rev. Sci. Instrum.* **1999**, *70*, 3967–3969.

(17) Atomic Force Microscope Cantilevers (Calibration Method of Sader) http://www.ampc.ms.unimelb.edu.au/afm/calibration.html accessed June 5, 2009.

Chapter 6 Spectral Data

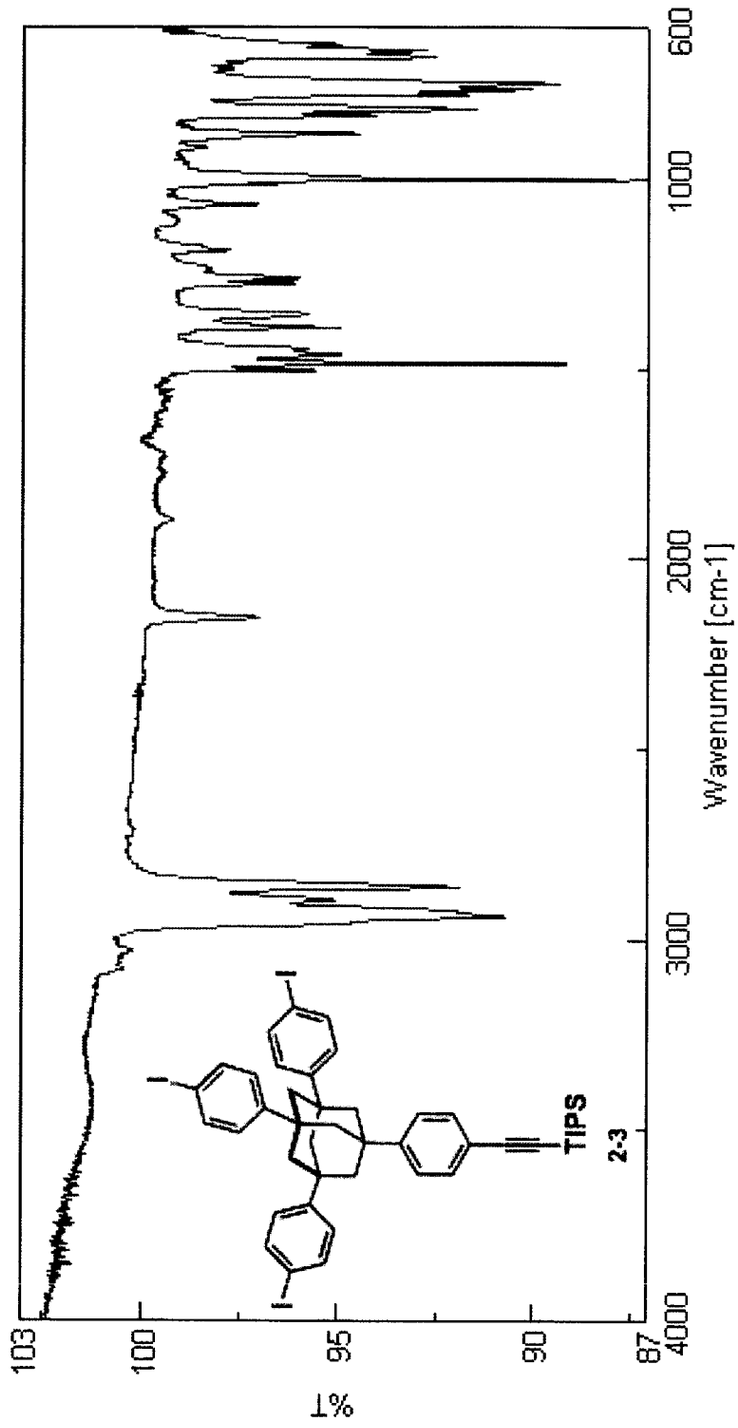

Figure 6-1. The thin film IR spectrum of compound **2-3**.

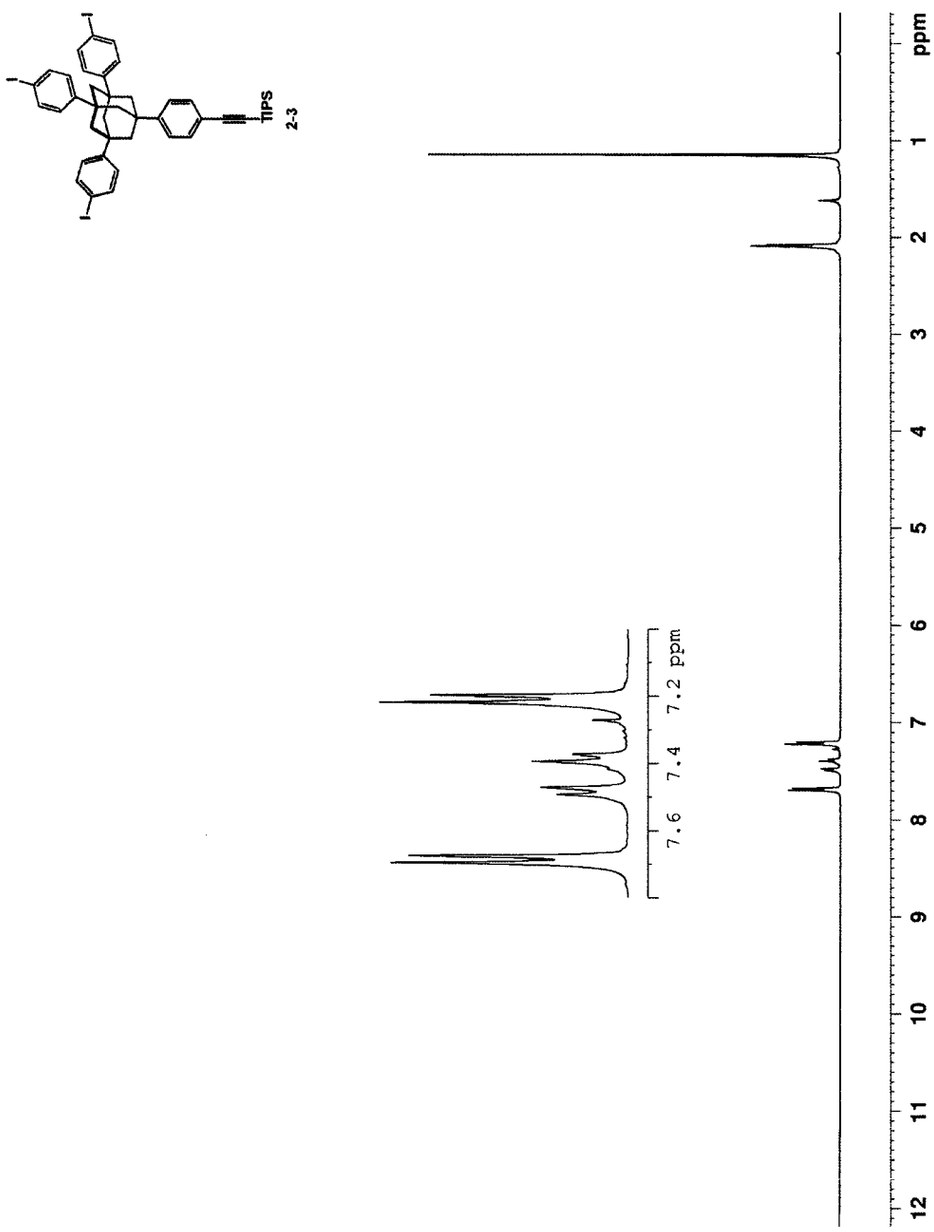

Figure 6-2. The 400 MHz ^{1}H NMR spectrum of compound **2-3** in $CDCl_3$.

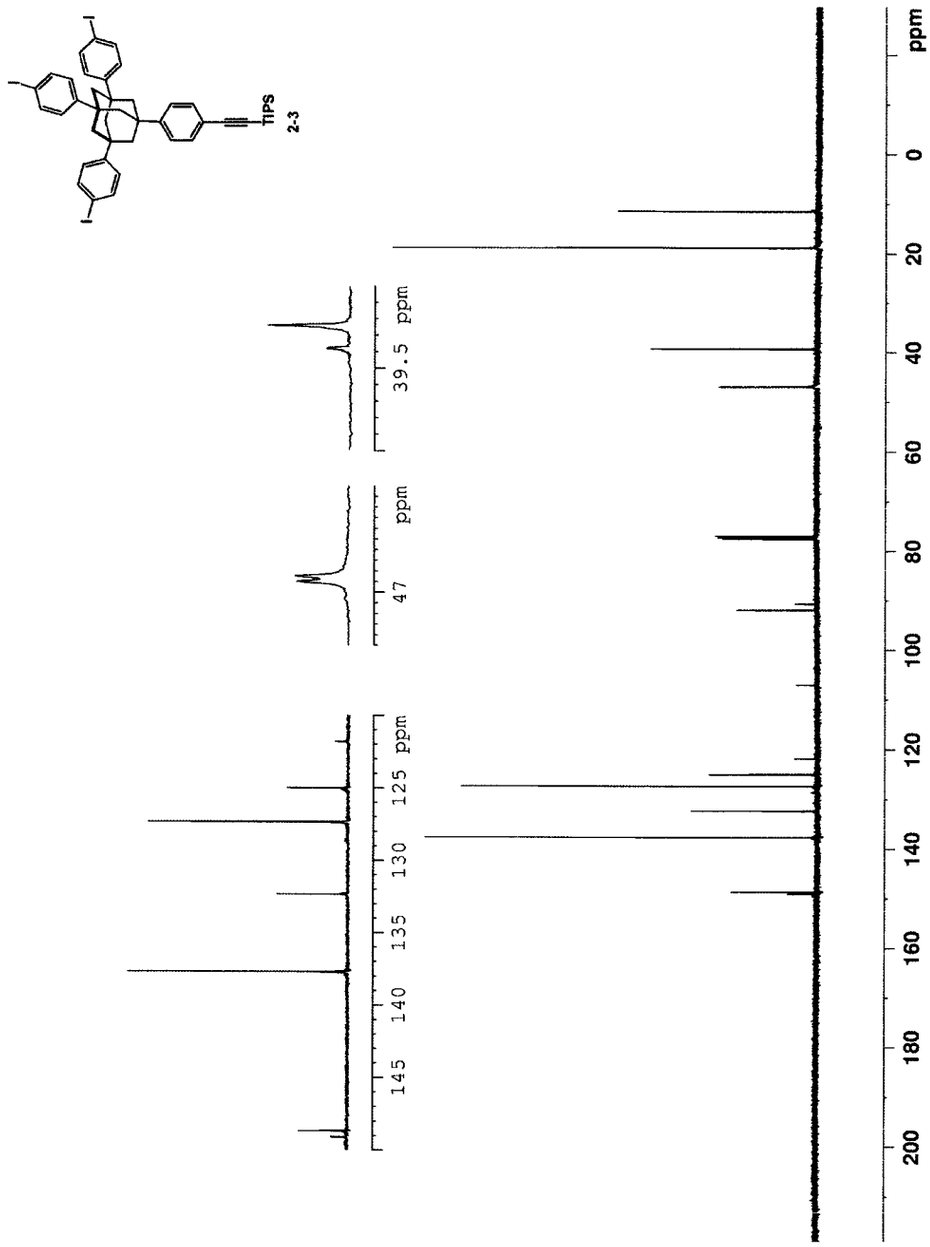

Figure 6-3. The 100 MHz ^{1}H decoupled ^{13}C NMR spectrum of compound **2-3** in $CDCl_3$.

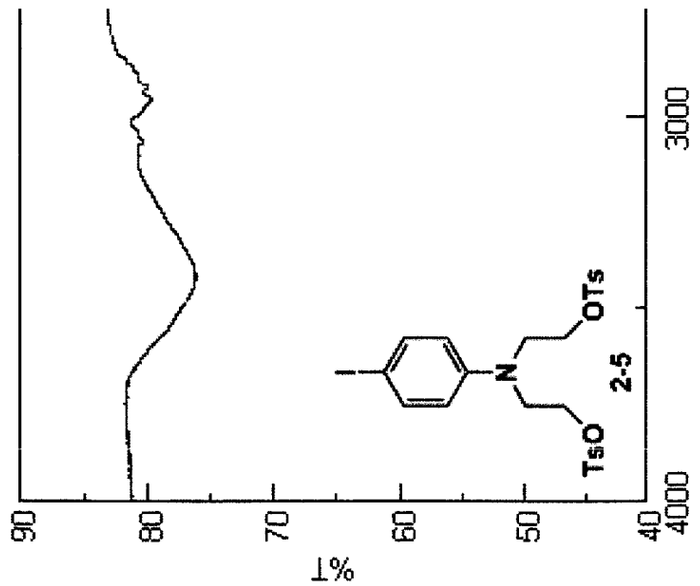

Figure 6-4. The thin film IR spectrum of compound **2-5**.

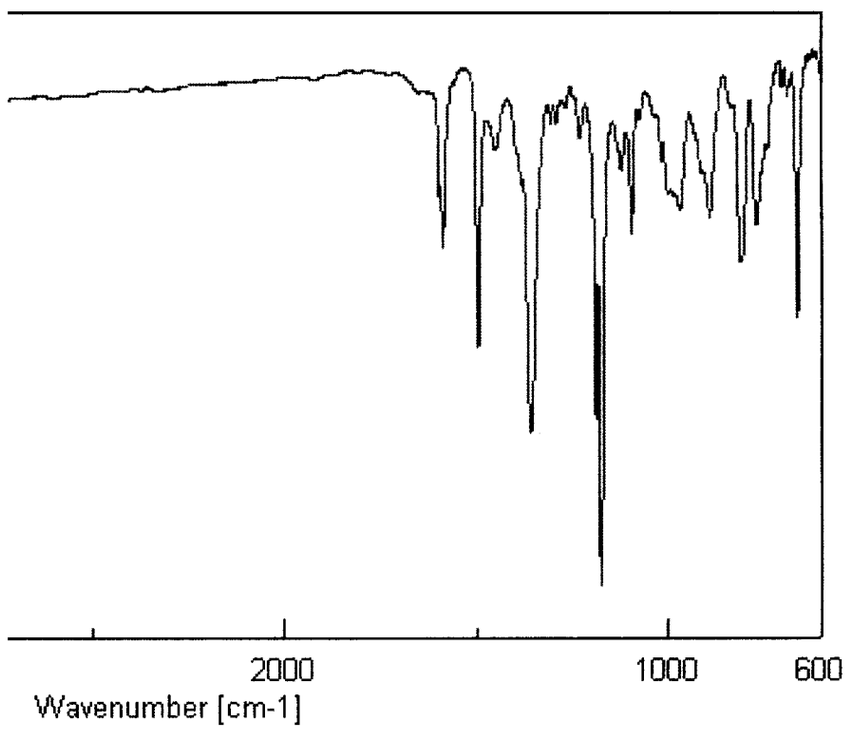
2000
1000
600
Wavenumber [cm-1]

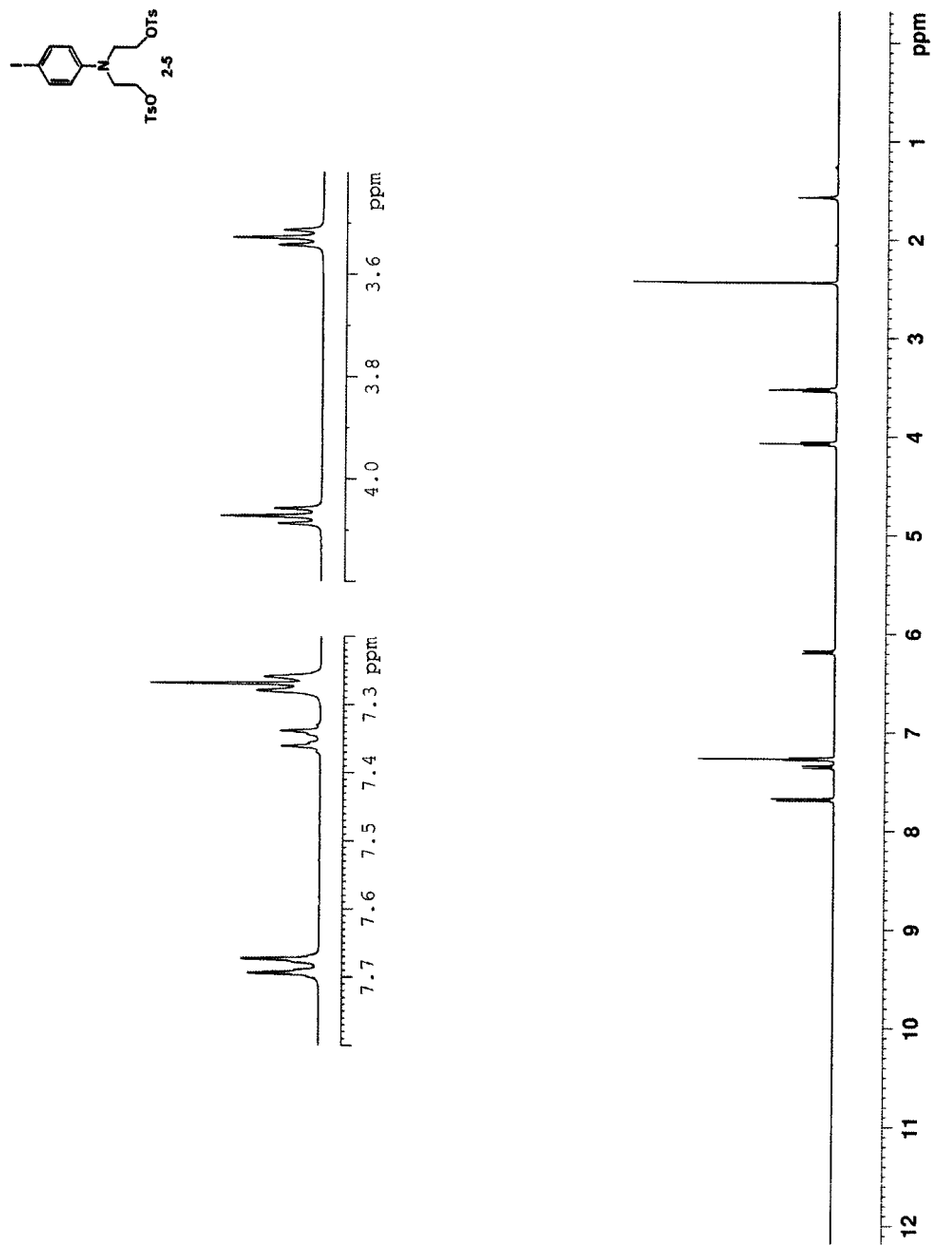

Figure 6-5. The 400 MHz ^{1}H NMR spectrum of compound **2-5** in $CDCl_3$.

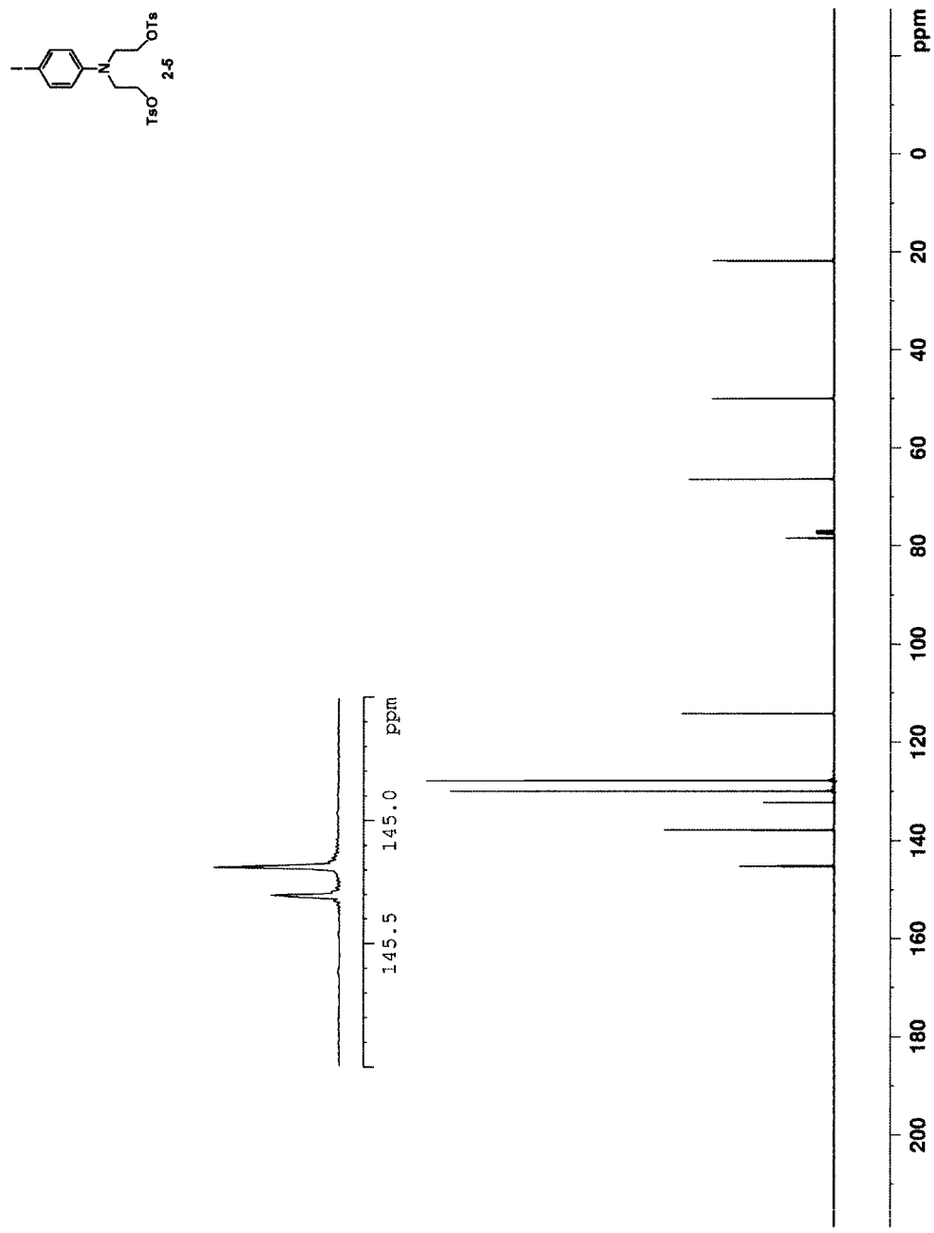

Figure 6-6. The 100 MHz ^{1}H decoupled ^{13}C NMR spectrum of compound **2-5** in $CDCl_3$.

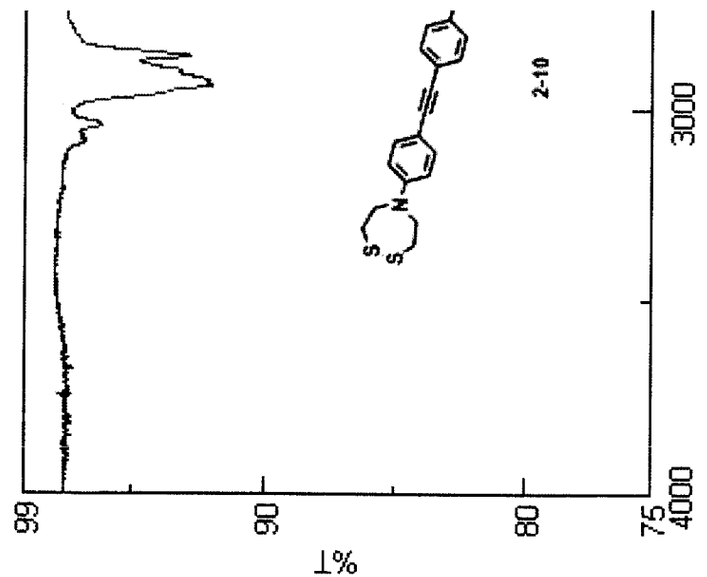

Figure 6-7. The thin film IR spectrum of compound **2-10**.

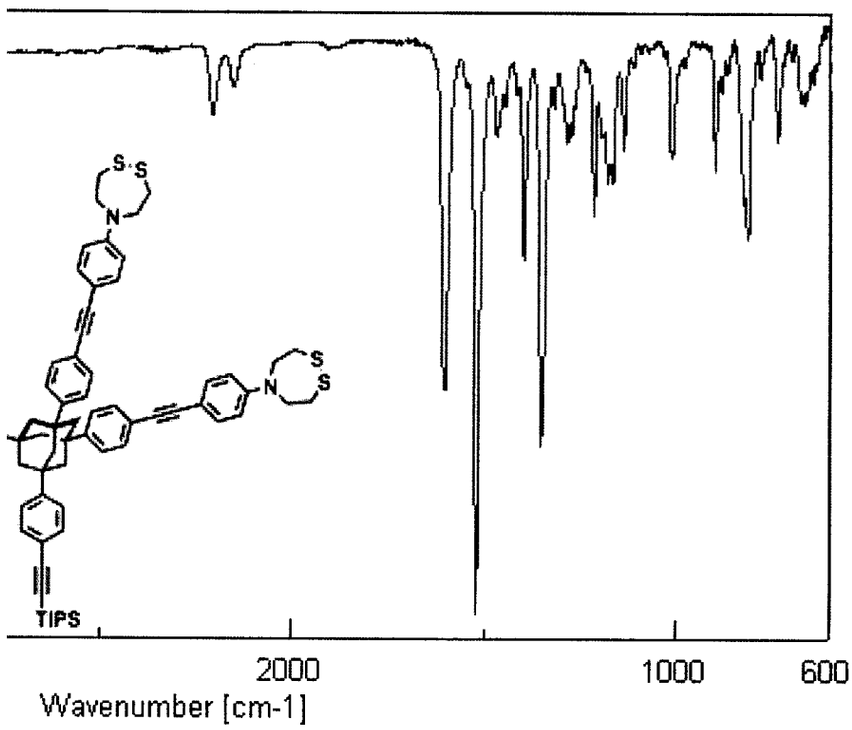
S
S
N
S
S
N
TIPS
2000
1000
600
Wavenumber [cm-1]

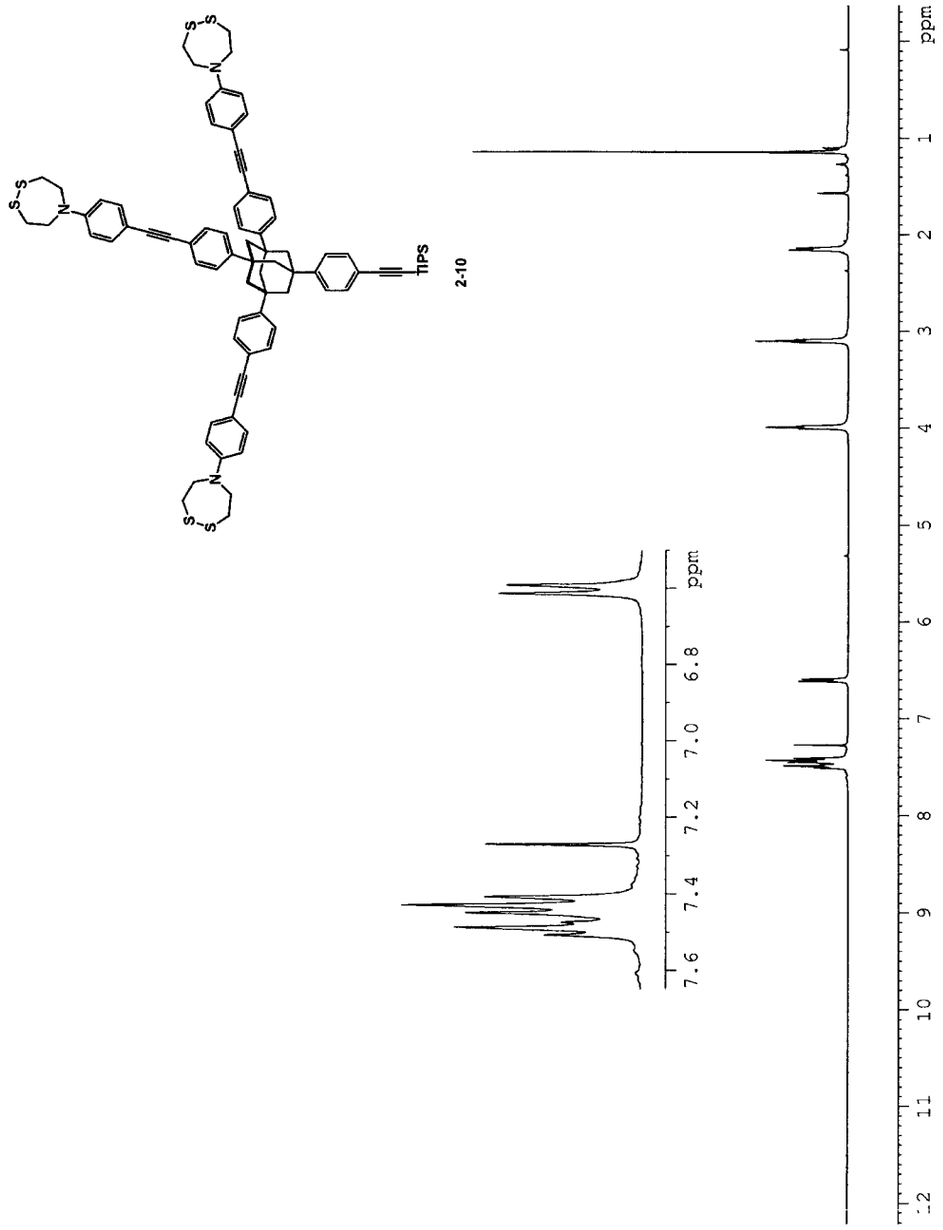

Figure 6-8. The 400 MHz ^{1}H NMR spectrum of compound **2-10** in $CDCl_3$.

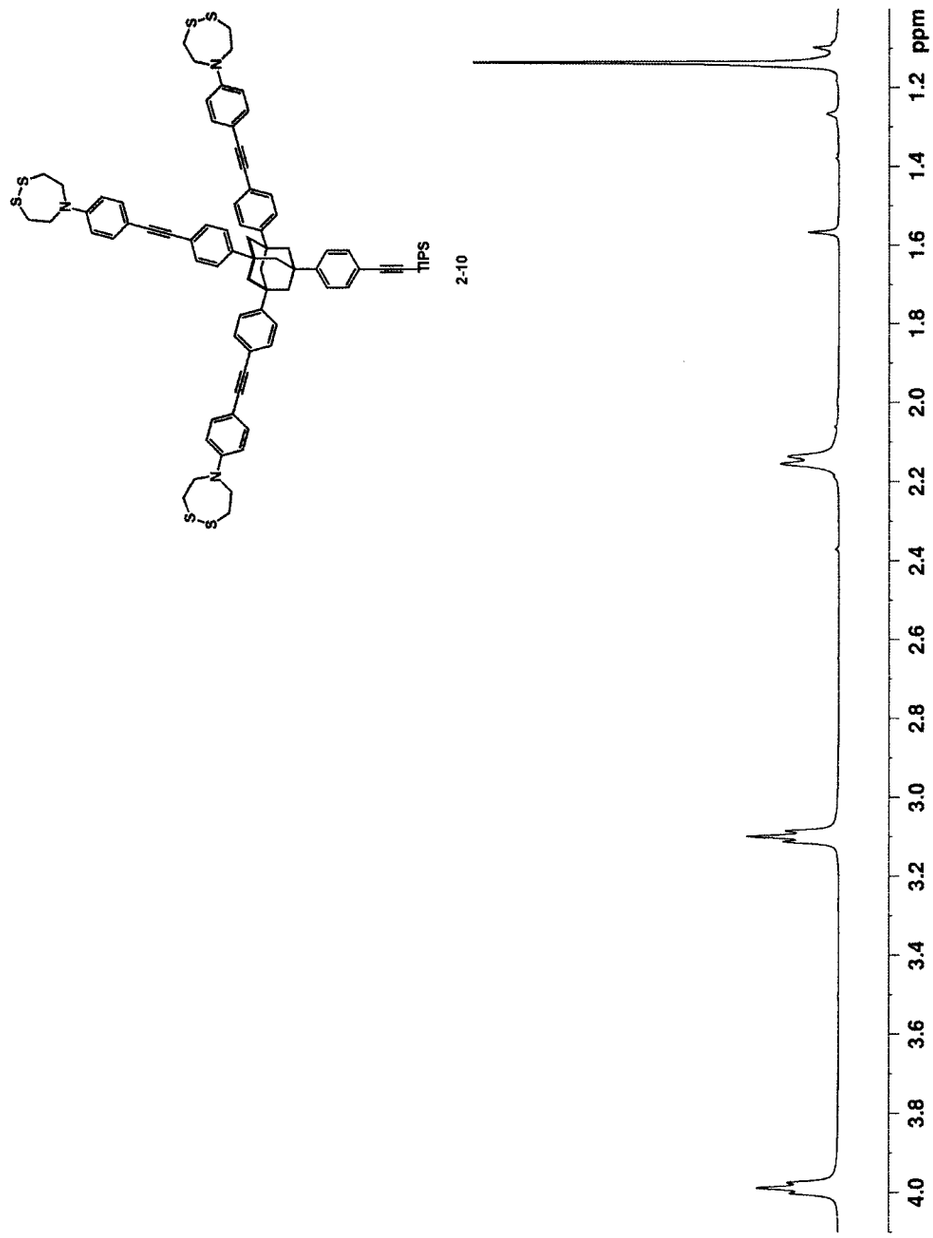

Figure 6-9. The 400 MHz ^{1}H NMR spectrum of compound **2-10** in $CDCl_3$.

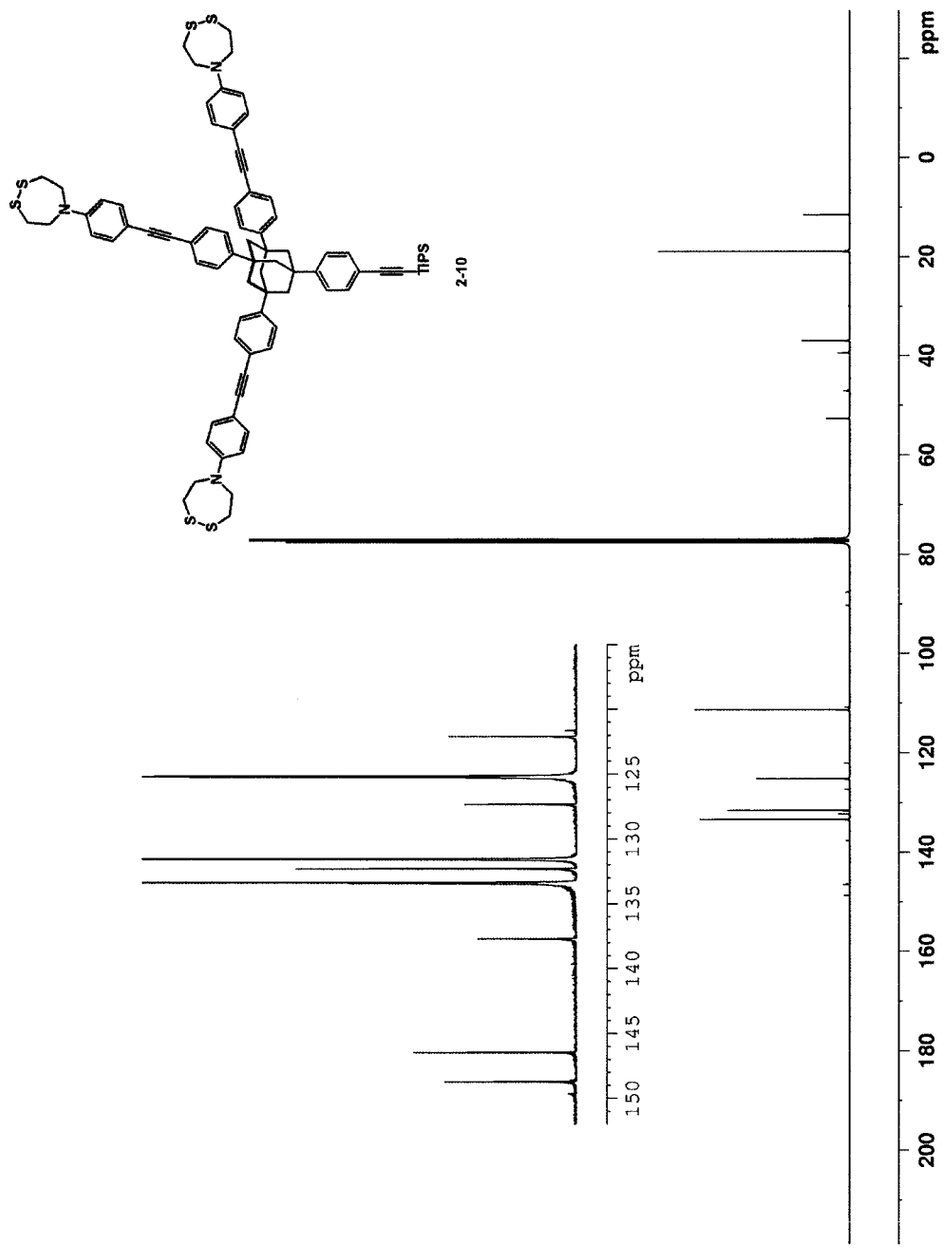

Figure 6-10. The 100 MHz ^{1}H decoupled ^{13}C NMR spectrum of compound **2-10** in $CDCl_3$.

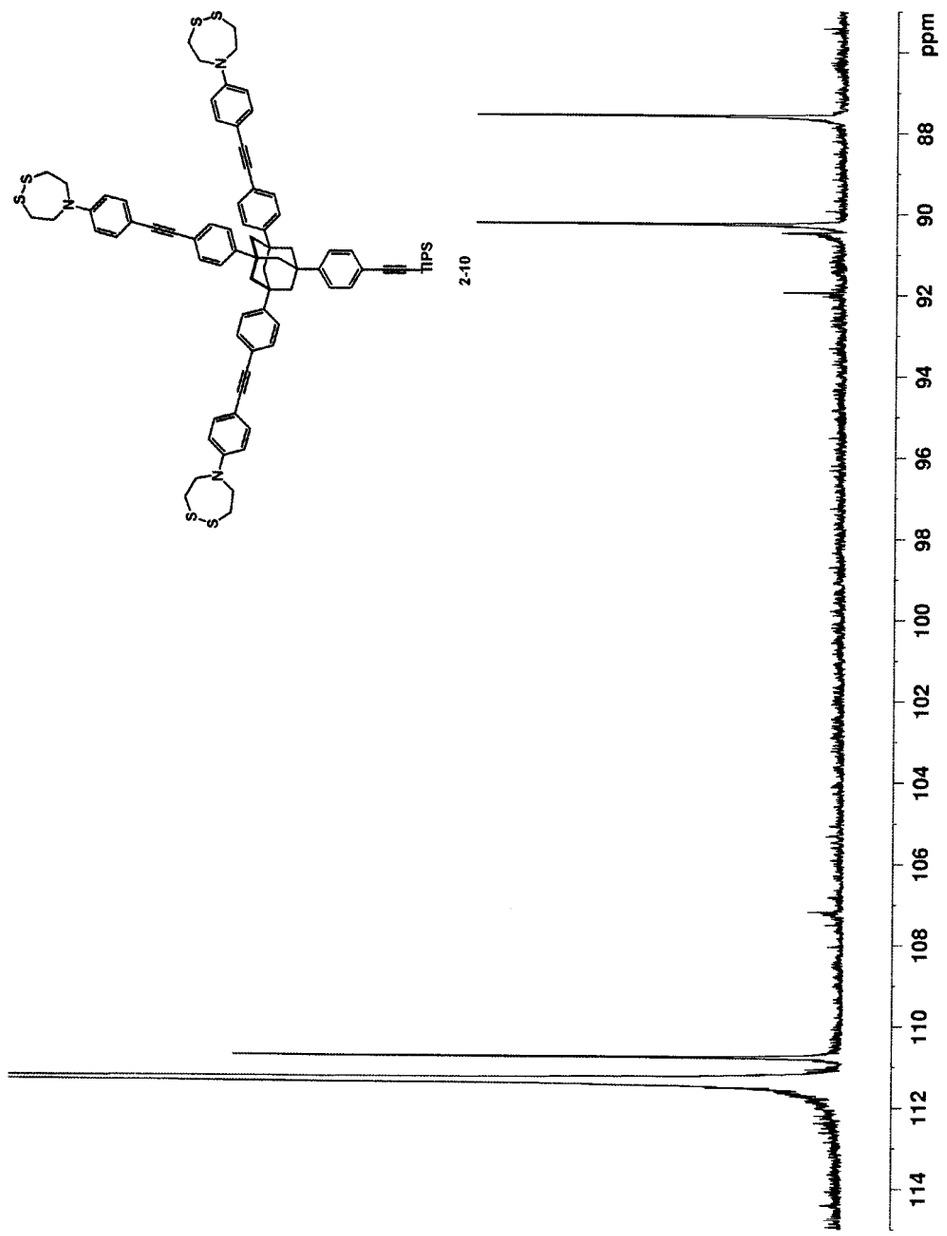

Figure 6-11. The 100 MHz ^{1}H decoupled ^{13}C NMR spectrum of compound **2-10** in $CDCl_3$.

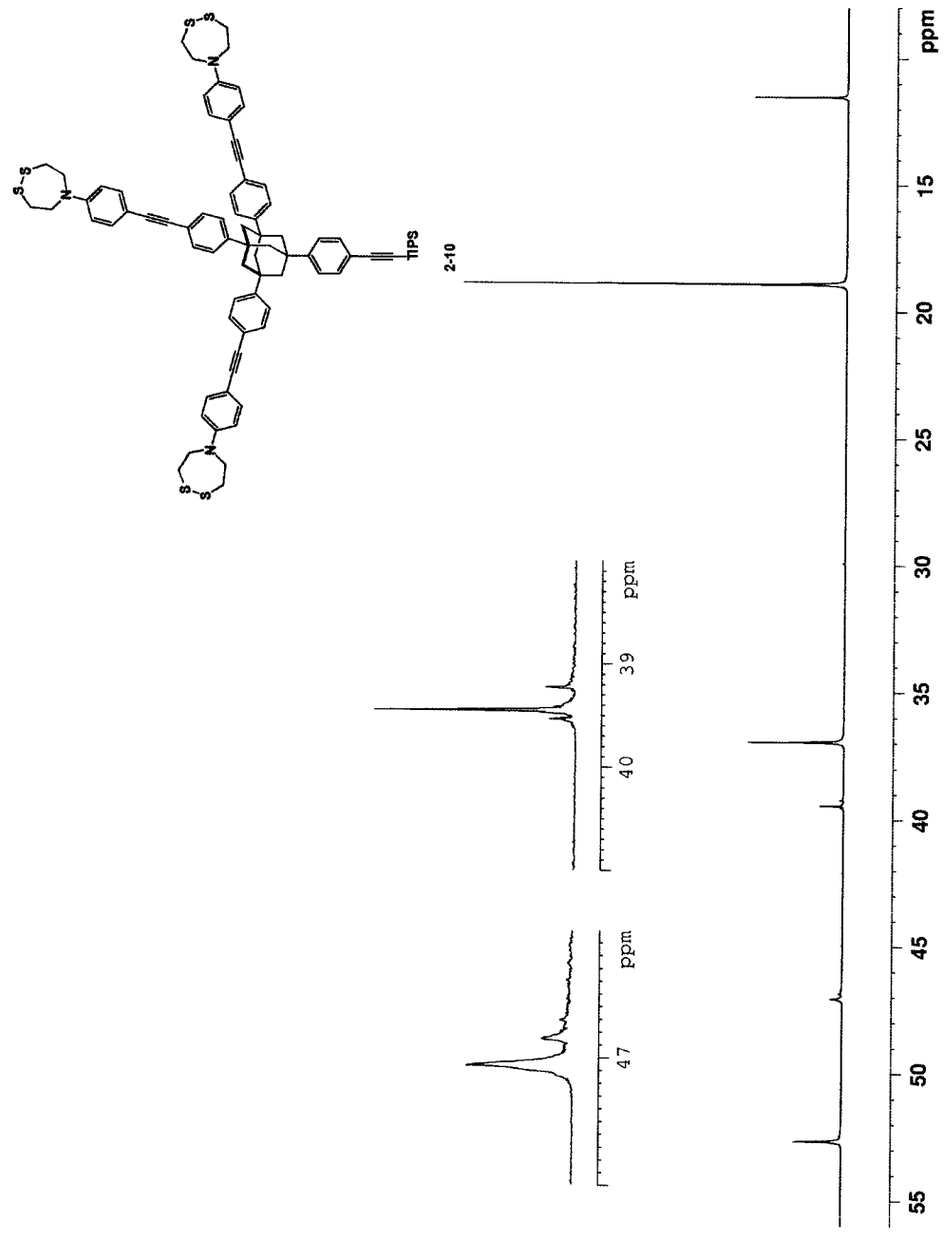

Figure 6-12. The 100 MHz ^{1}H decoupled ^{13}C NMR spectrum of compound **2-10** in $CDCl_3$.

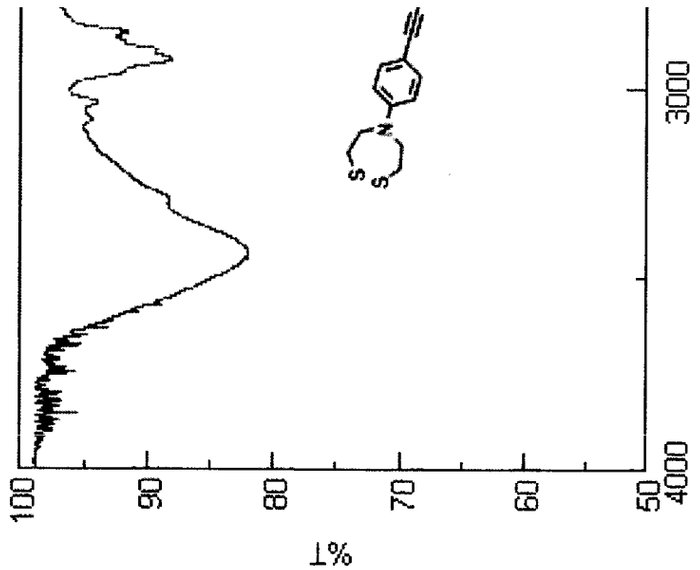

Figure 6-13. The thin film IR spectrum of compound **2-11**.

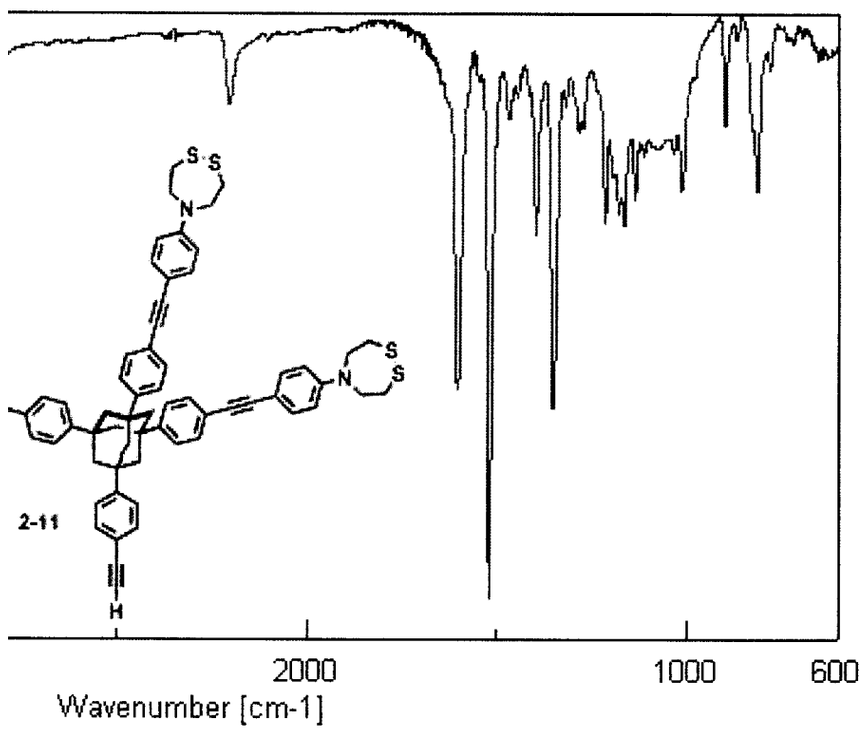
S
S
N
S
N
S
2-11
H
2000
1000
600
Wavenumber [cm-1]

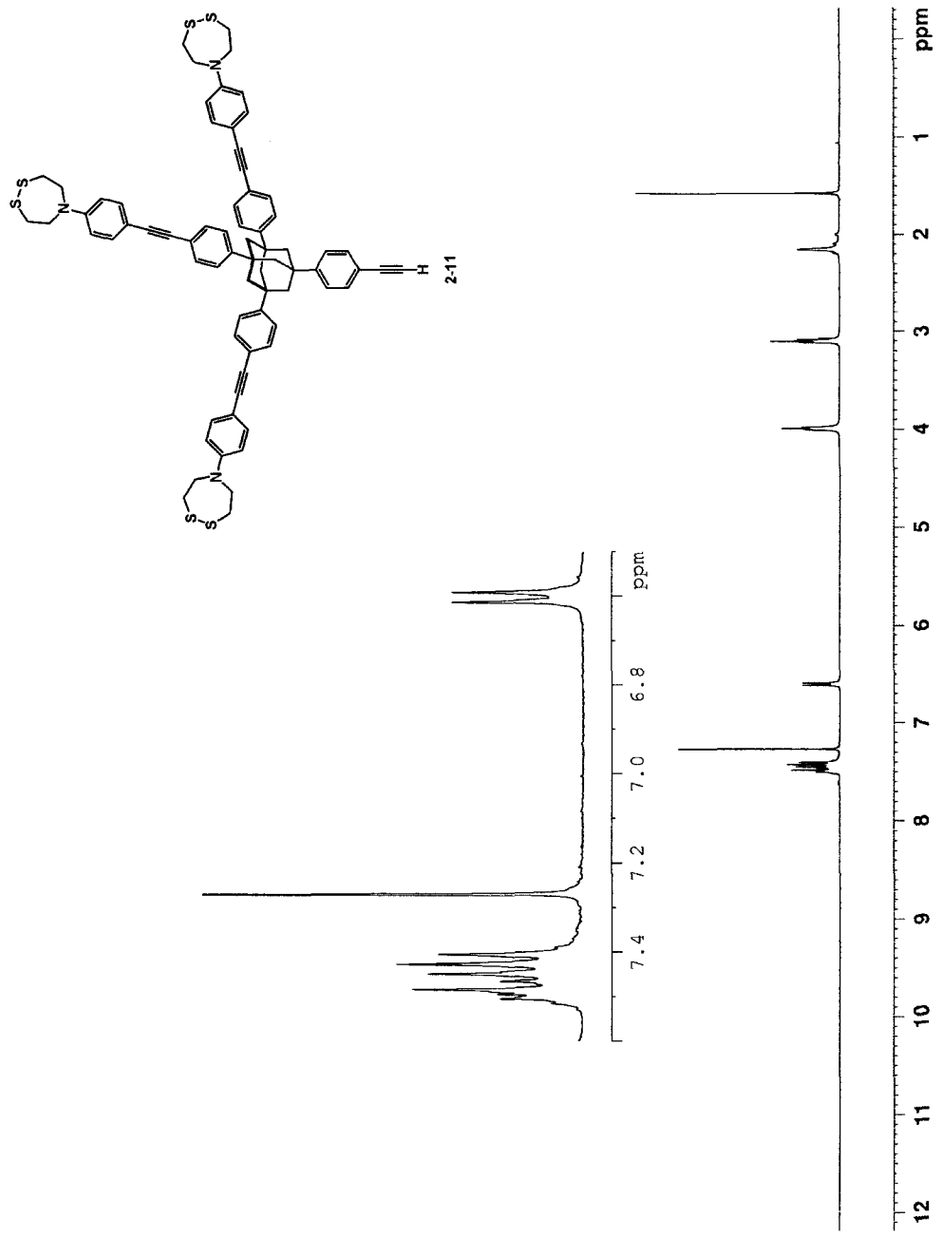

Figure 6-14. The 400 MHz ^{1}H NMR spectrum of compound **2-11** in $CDCl_3$.

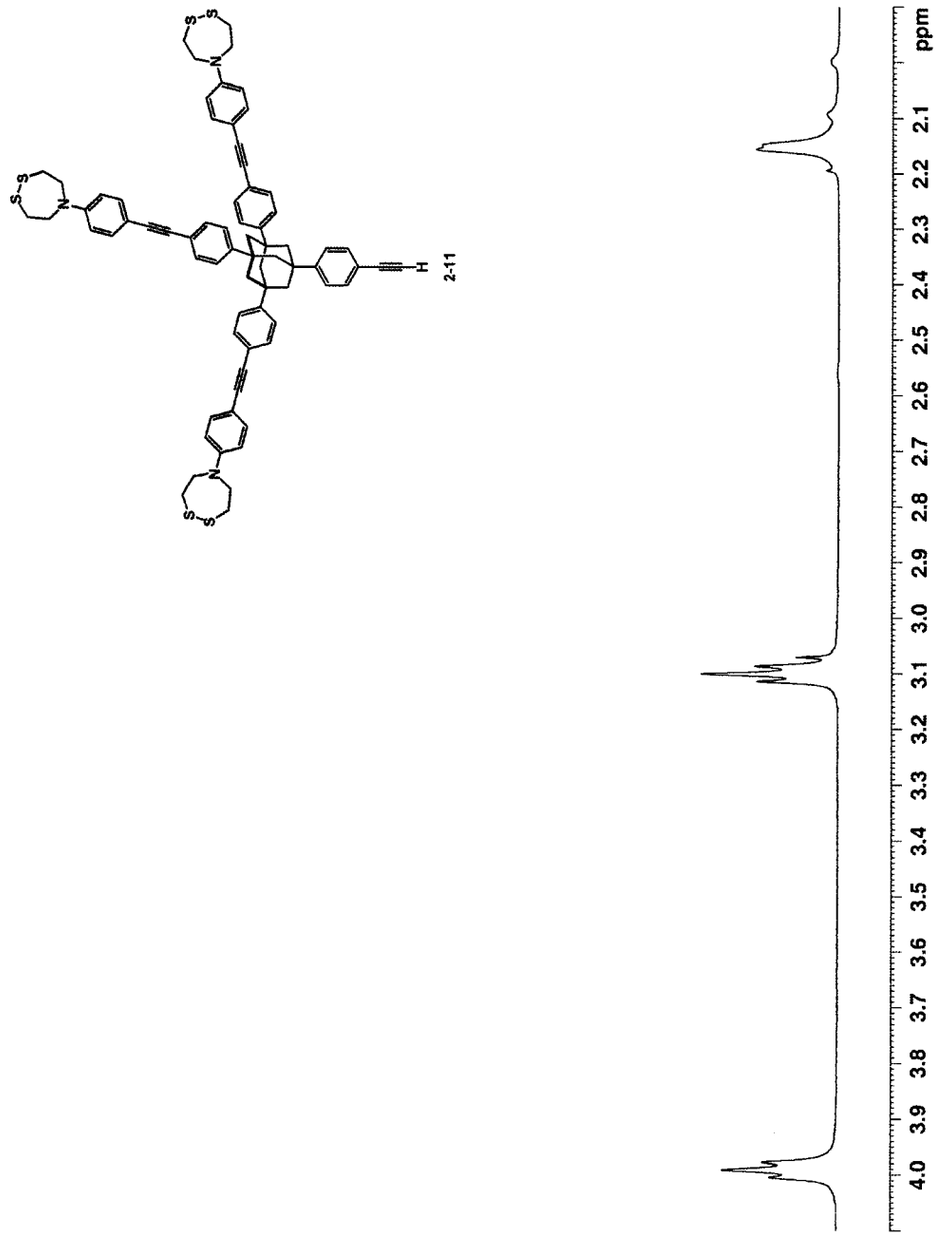

Figure 6-15. The 400 MHz ^{1}H NMR spectrum of compound **2-11** in $CDCl_3$.

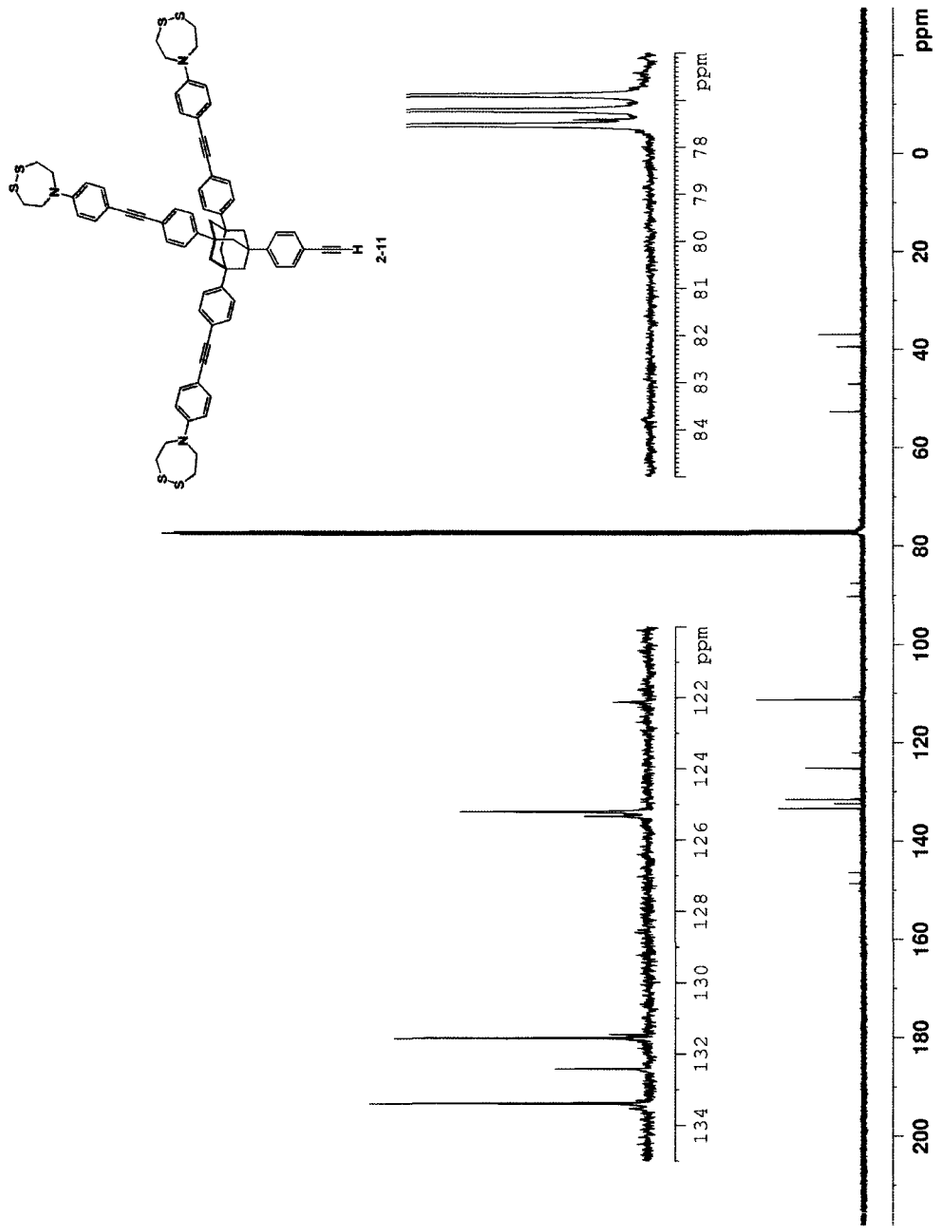

Figure 6-16. The 100 MHz ^{1}H decoupled ^{13}C NMR spectrum of compound **2-11** in $CDCl_3$.

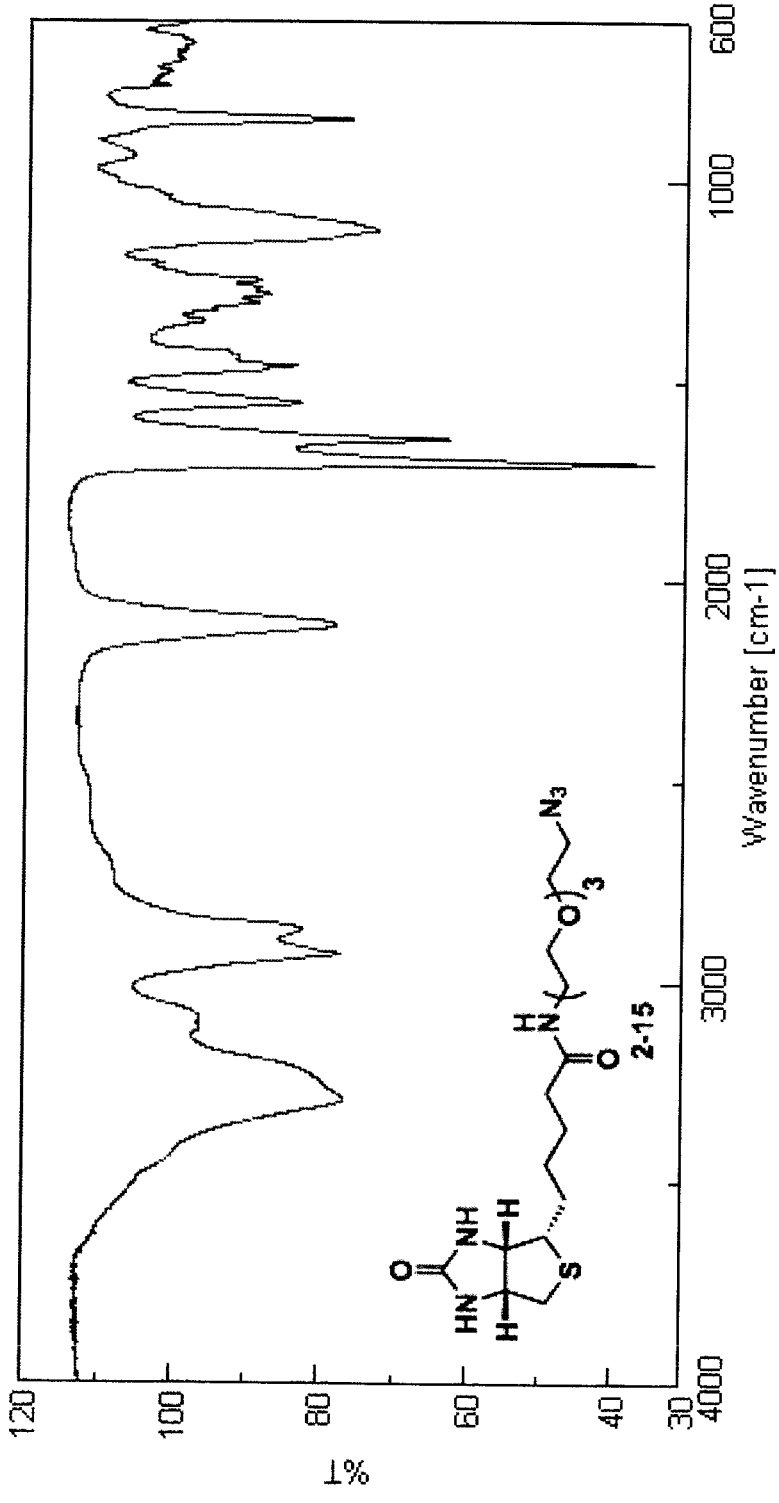

Figure 6-17. The thin film IR spectrum of compound **2-15**.

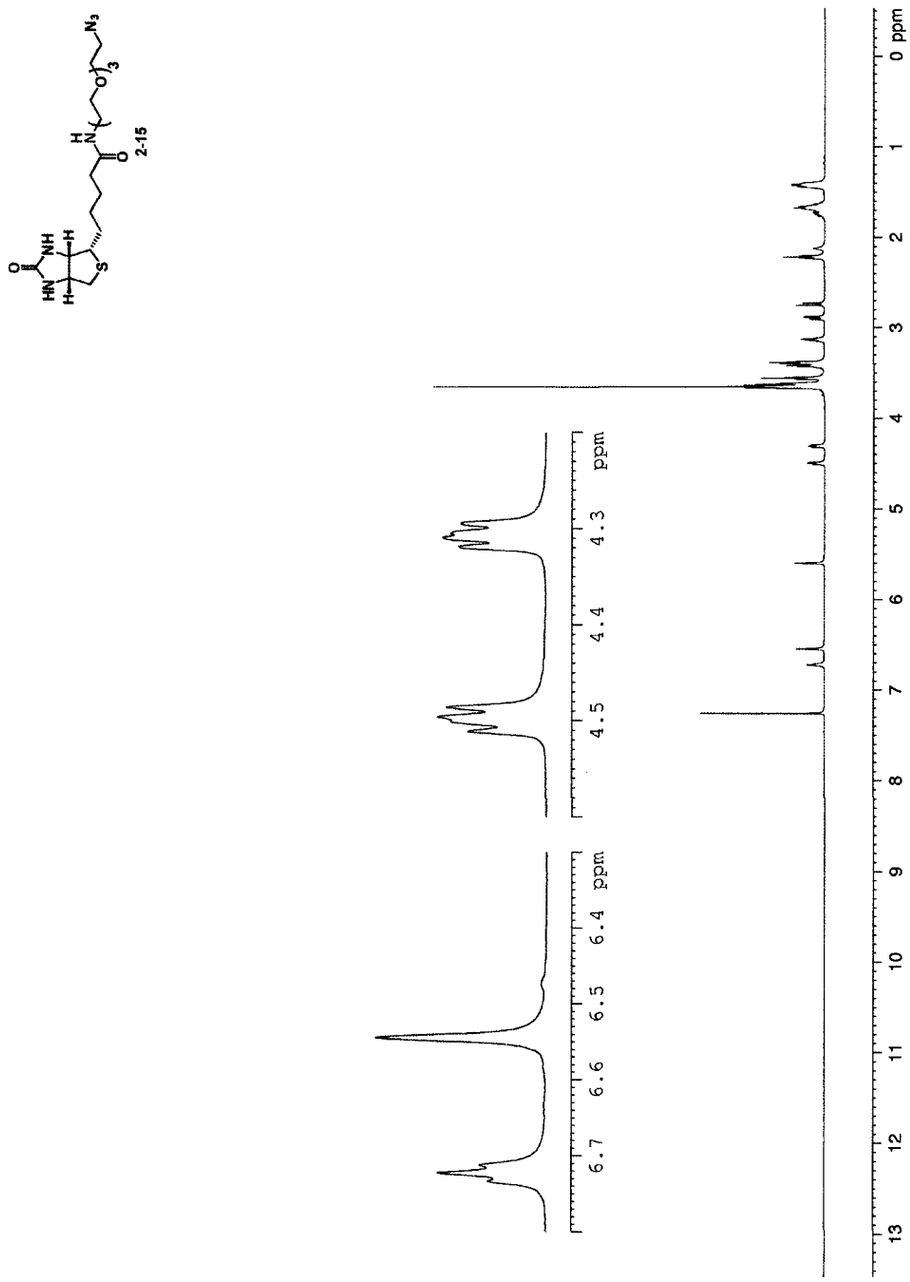

Figure 6-18. The 500 MHz ^{1}H NMR spectrum of compound **2-15** in $CDCl_3$.

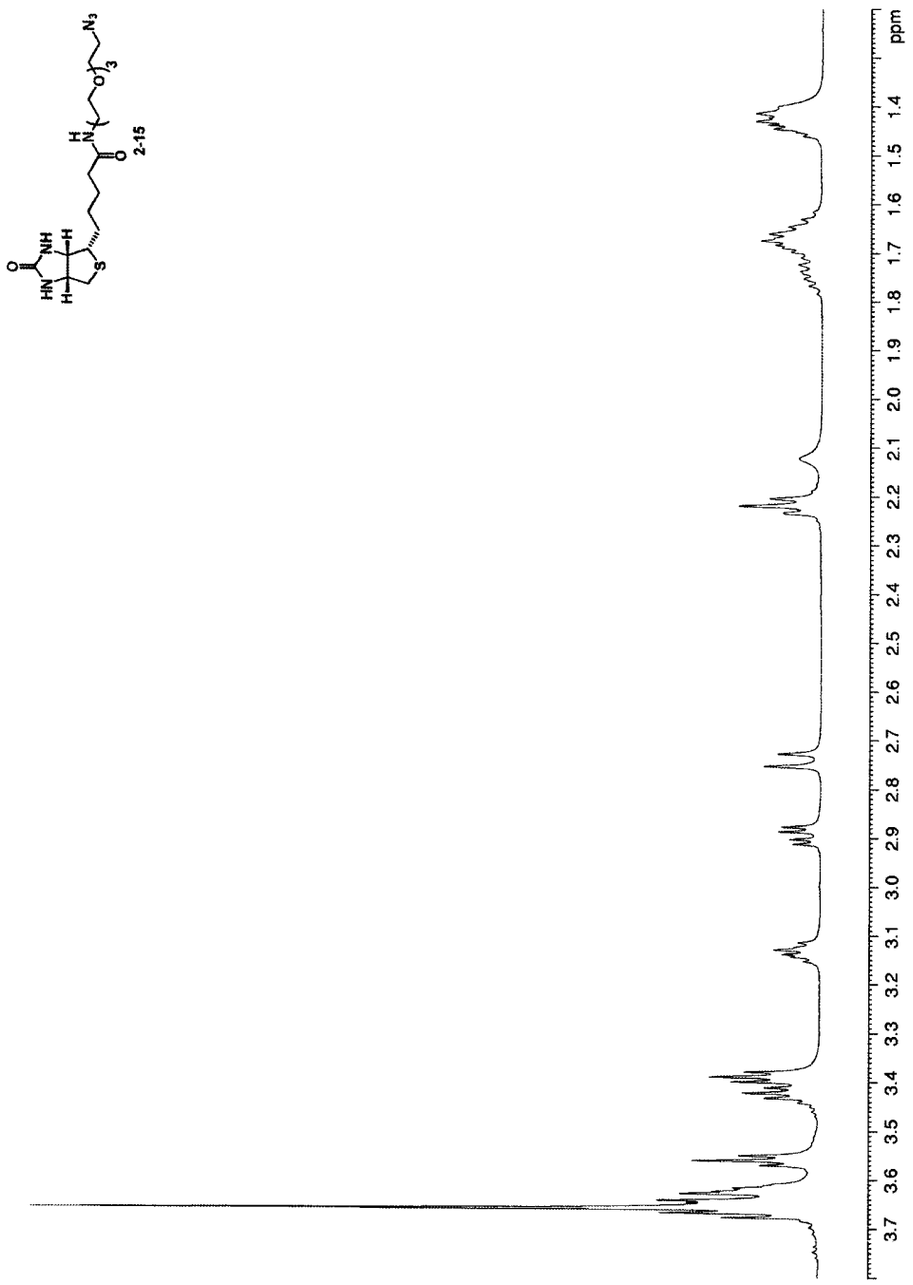

Figure 6-19. The 500 MHz ^{1}H NMR spectrum of compound **2-15** in $CDCl_3$.

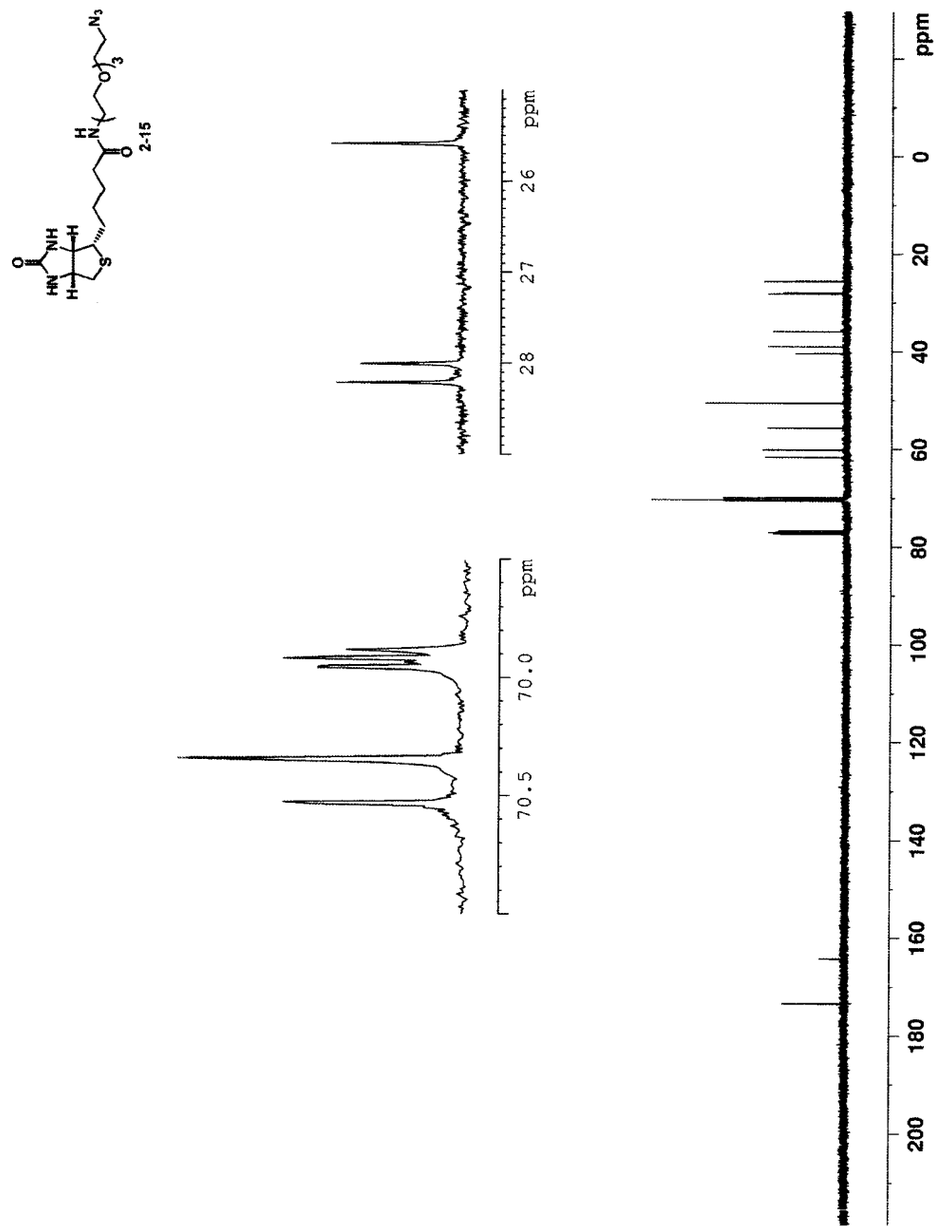

Figure 6-20. The 100 MHz ^{1}H decoupled ^{13}C NMR spectrum of compound **2-15** in $CDCl_3$.

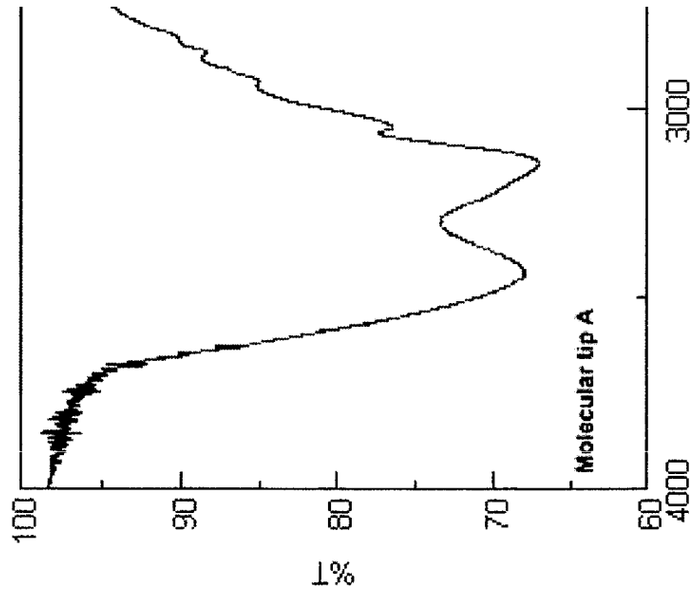

Figure 6-21. The KBr pellet IR spectrum of **Molecular tip A**.

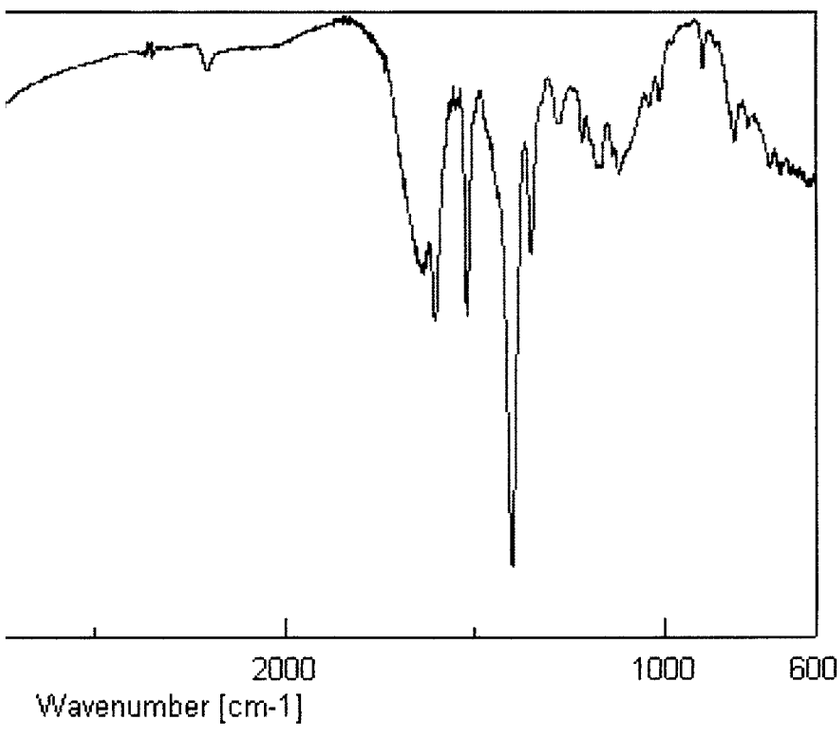
2000
1000
600
Wavenumber [cm-1]

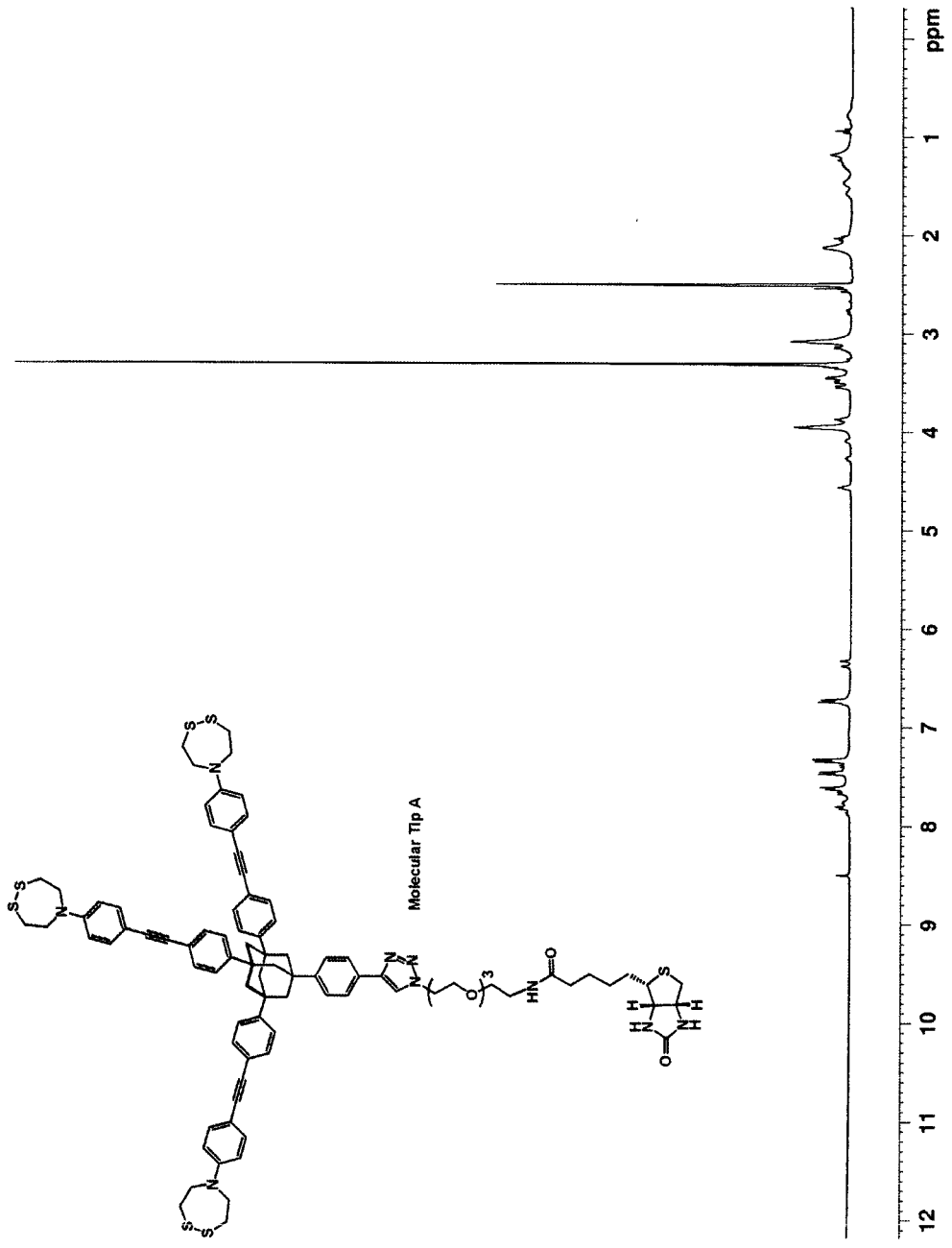

Figure 6-22. The 400 MHz ^{1}H NMR spectrum of **Molecular tip A** in DMSO-d_6.

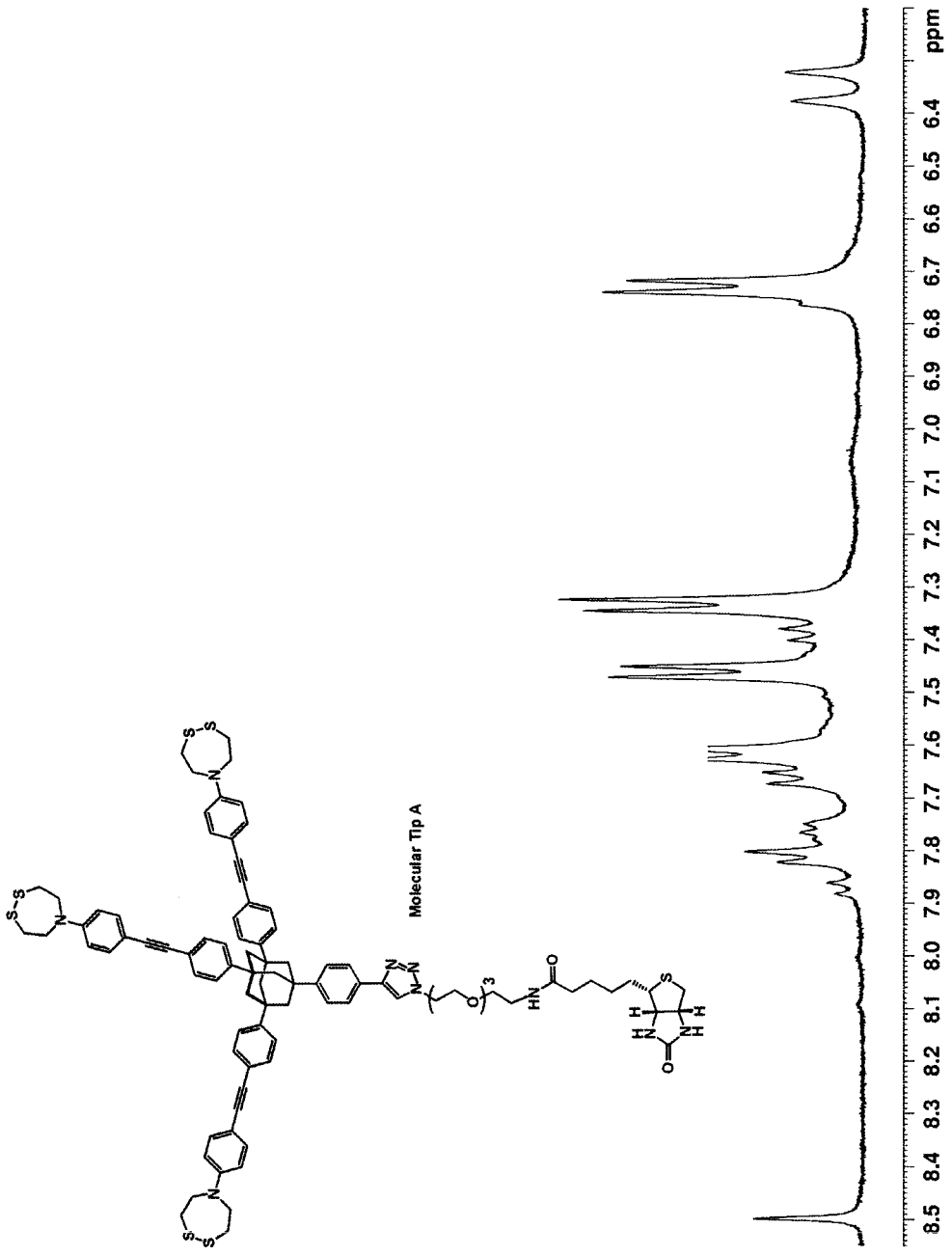

Figure 6-23. The 400 MHz ^{1}H NMR spectrum of **Molecular tip A** in DMSO-d_6.

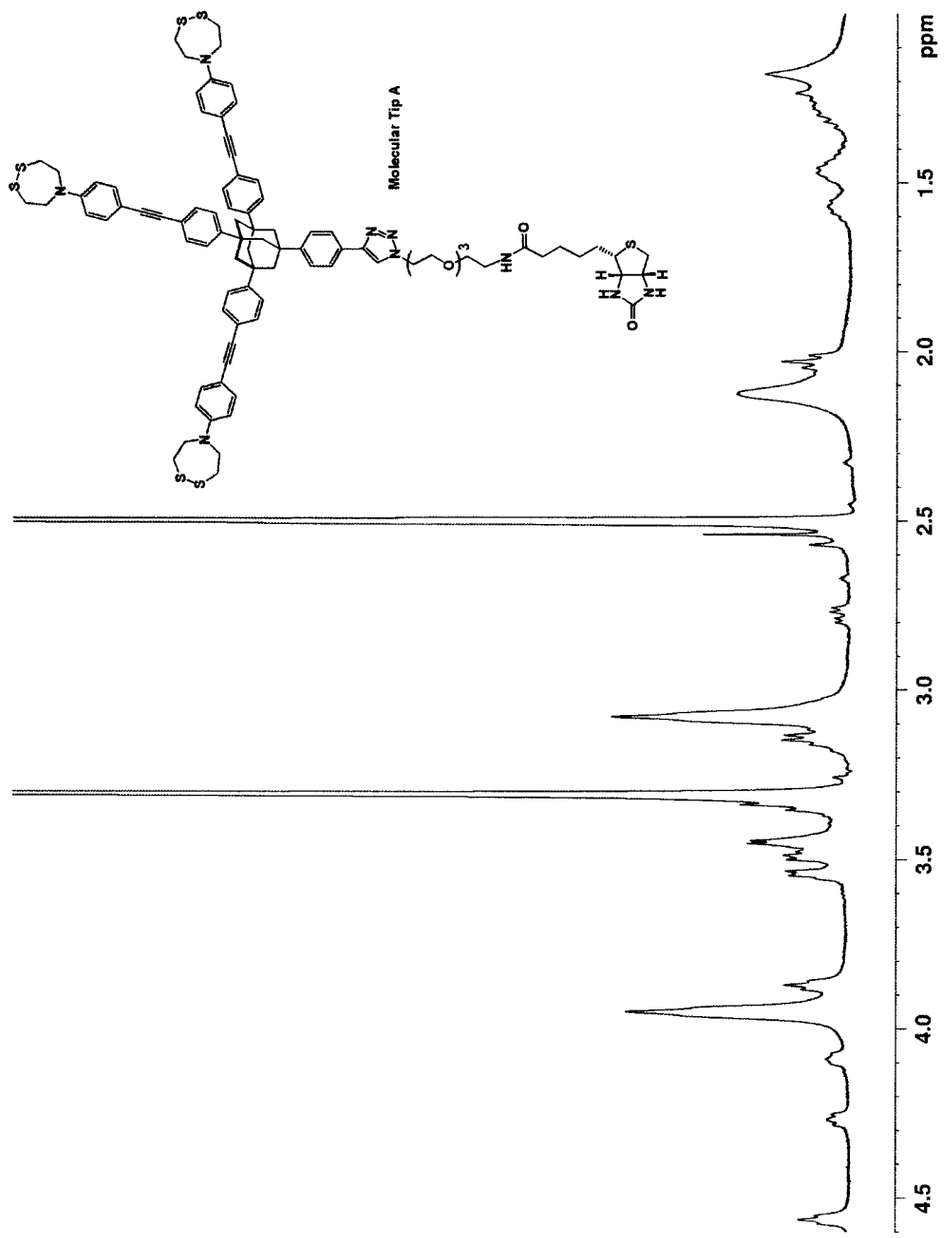

Figure 6-24. The 400 MHz ^{1}H NMR spectrum of **Molecular tip A** in DMSO-d_6.

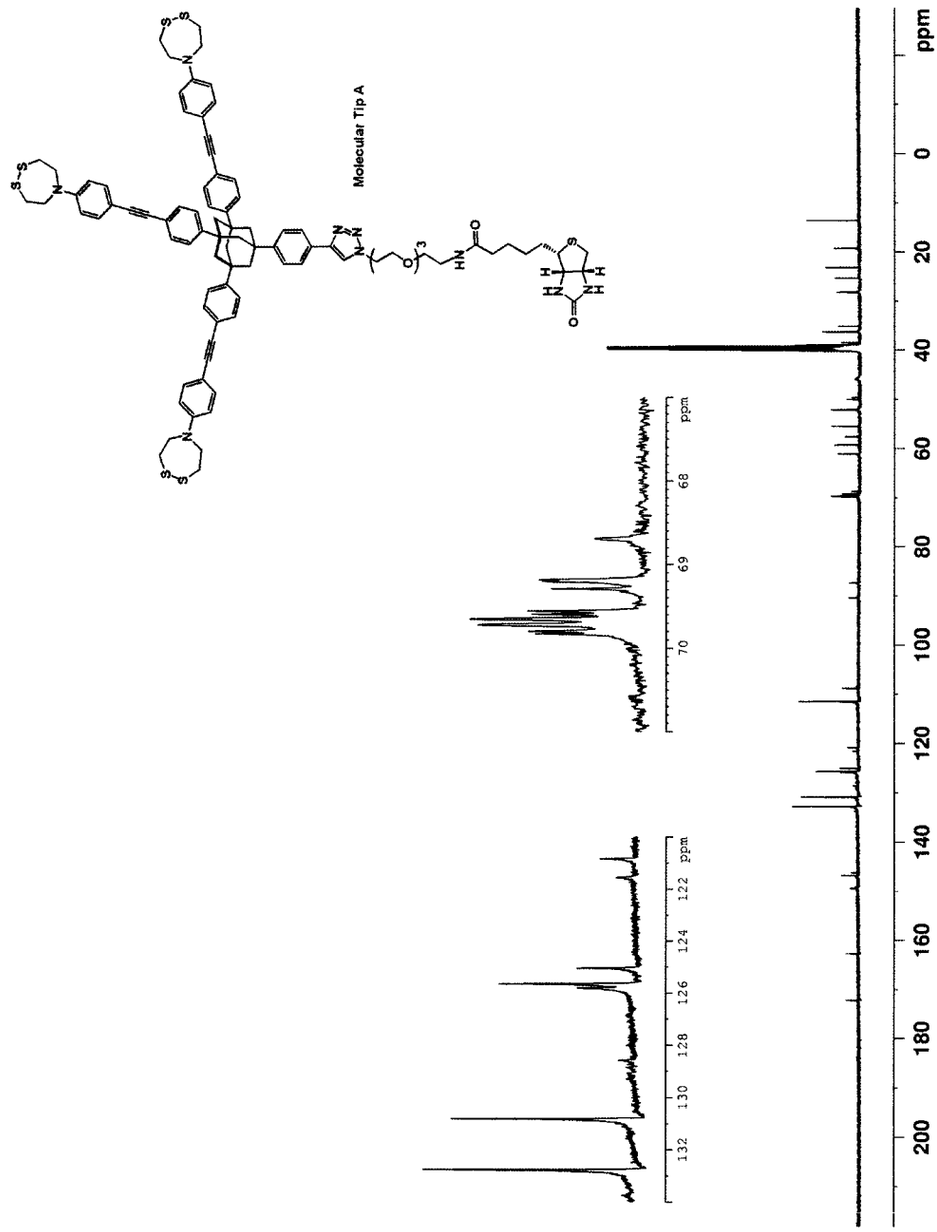

Figure 6-25. The 100 MHz ^{1}H decoupled ^{13}C NMR spectrum of **Molecular tip A** in DMSO-d_6.

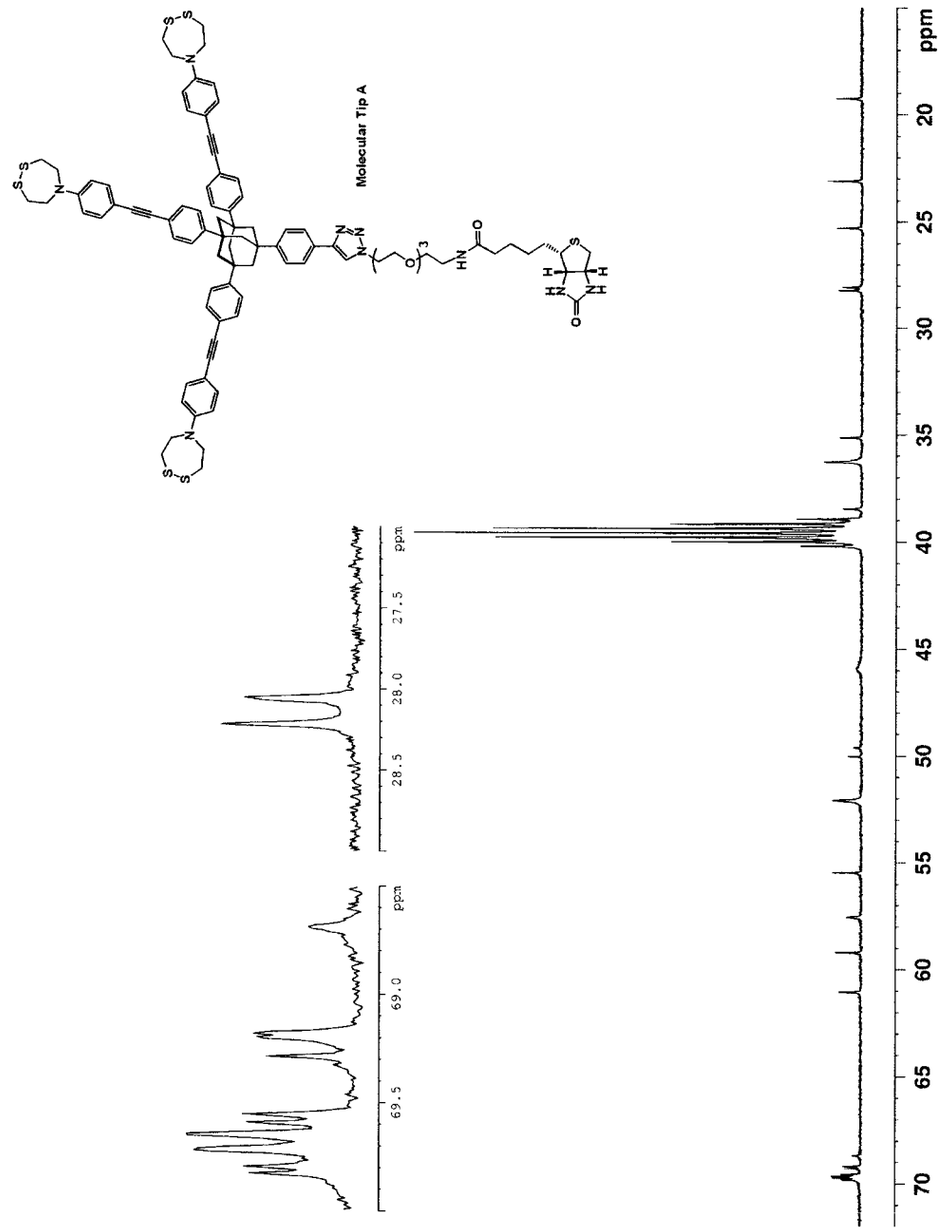

Figure 6-26. The 100 MHz ^{1}H decoupled ^{13}C NMR spectrum of **Molecular tip A** in DMSO-d_6.

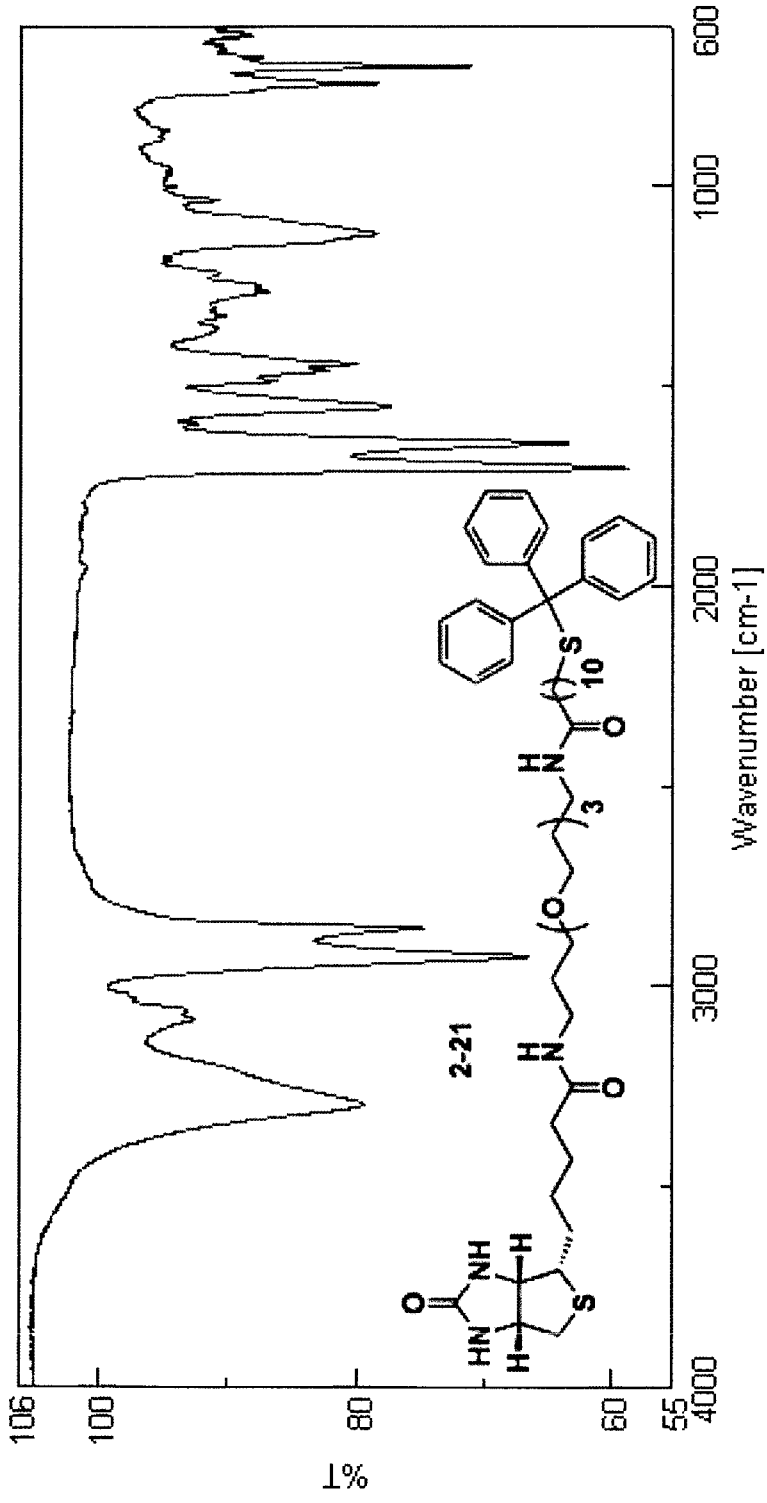

Figure 6-27. The thin film IR spectrum of **2-21**.

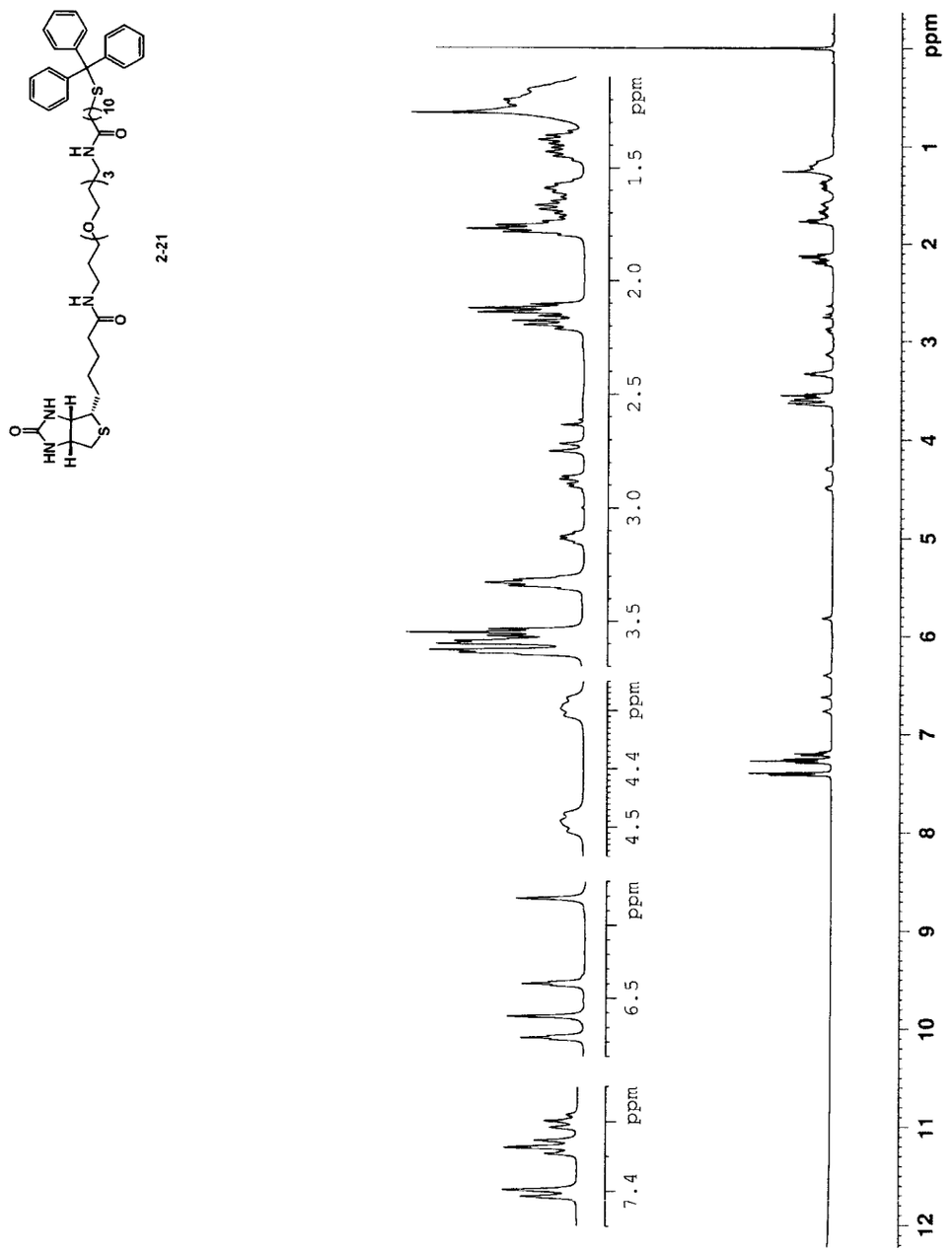

Figure 6-28. The 400 MHz ^{1}H NMR spectrum of **2-21** in $CDCl_3$.

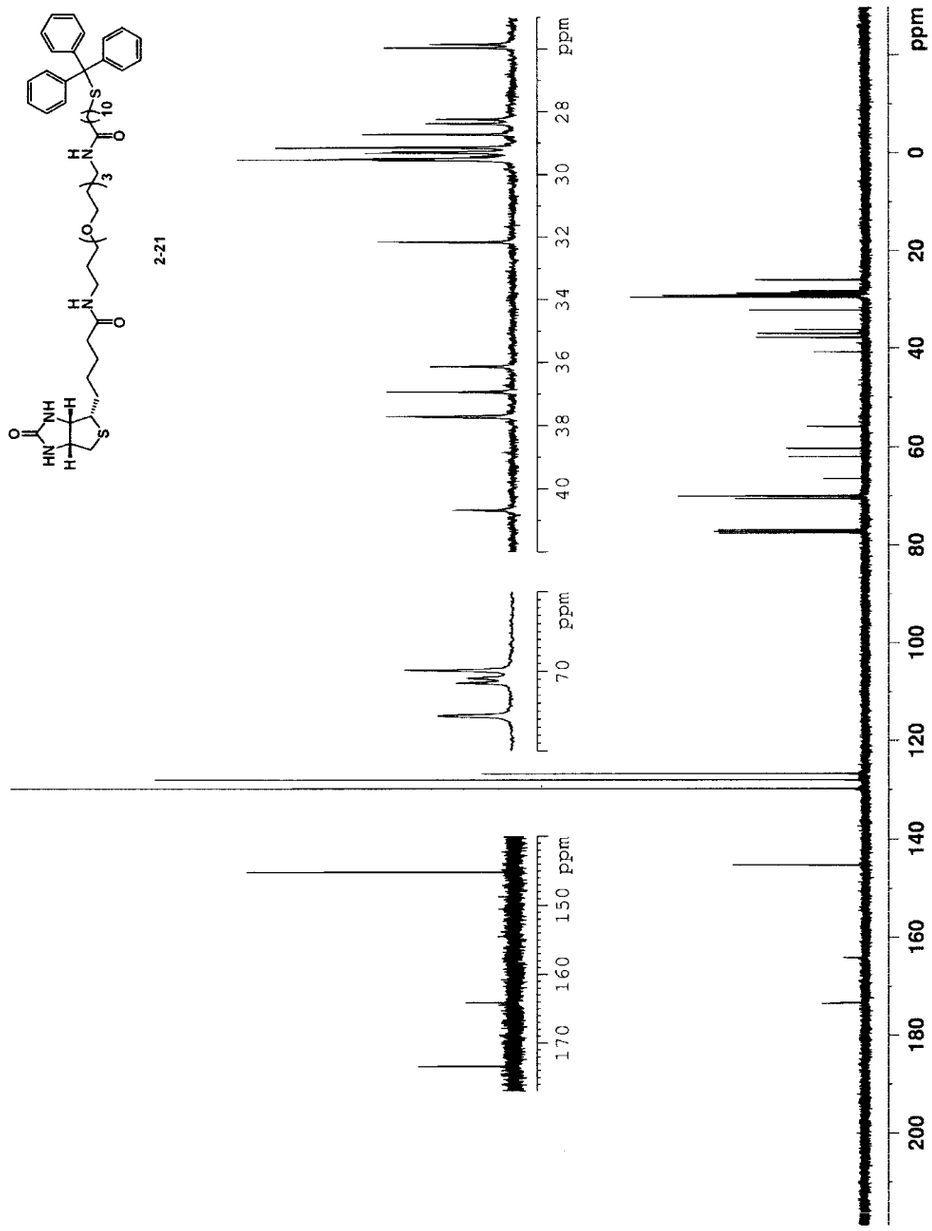

Figure 6-29. The 100 MHz ^{1}H decoupled ^{13}C NMR spectrum of **2-21** in $CDCl_3$.

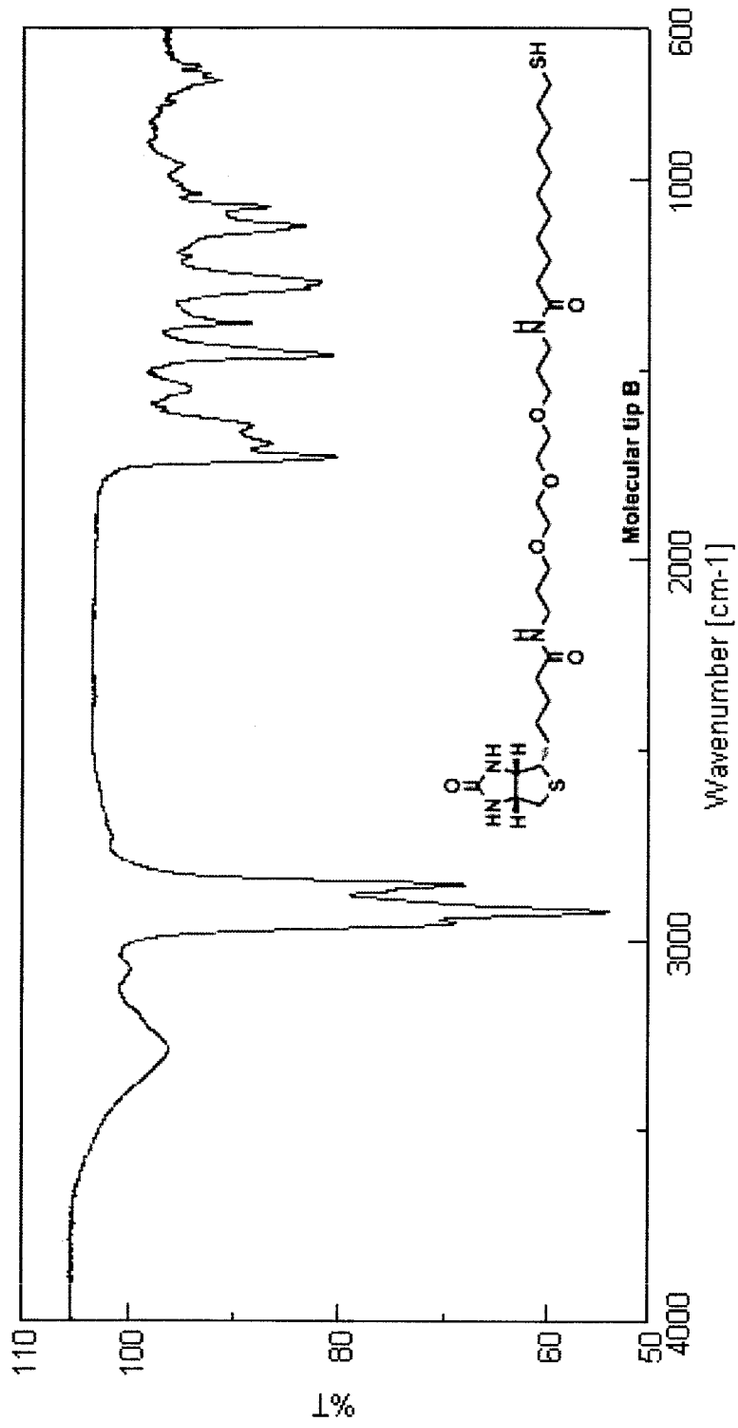

Figure 6-30. The thin film IR spectrum of **Molecular tip B**.

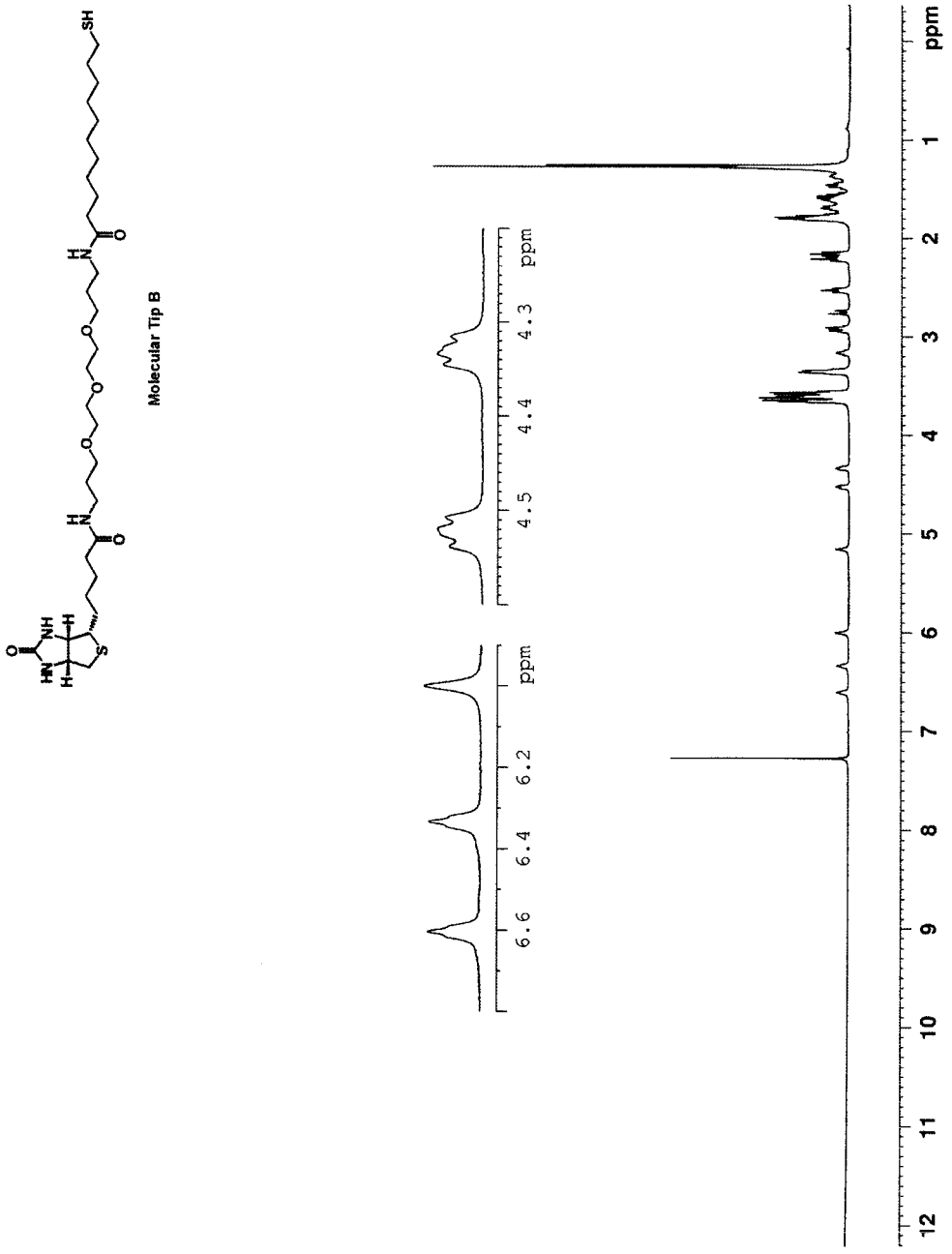

Figure 6-31. The 400 MHz ^{1}H NMR spectrum of **Molecular tip B** in $CDCl_3$.

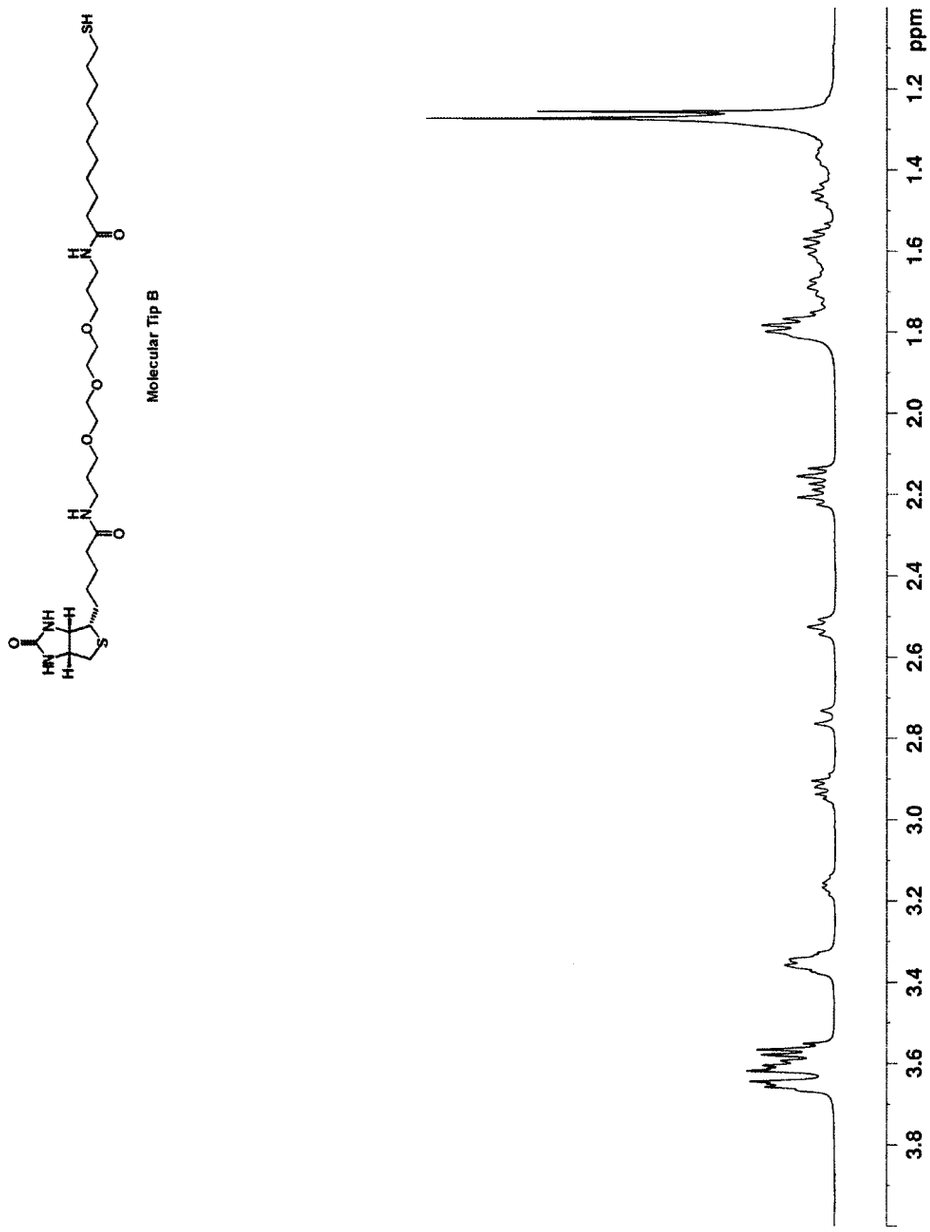

Figure 6-32. The 400 MHz ^{1}H NMR spectrum of **Molecular tip B** in $CDCl_3$.

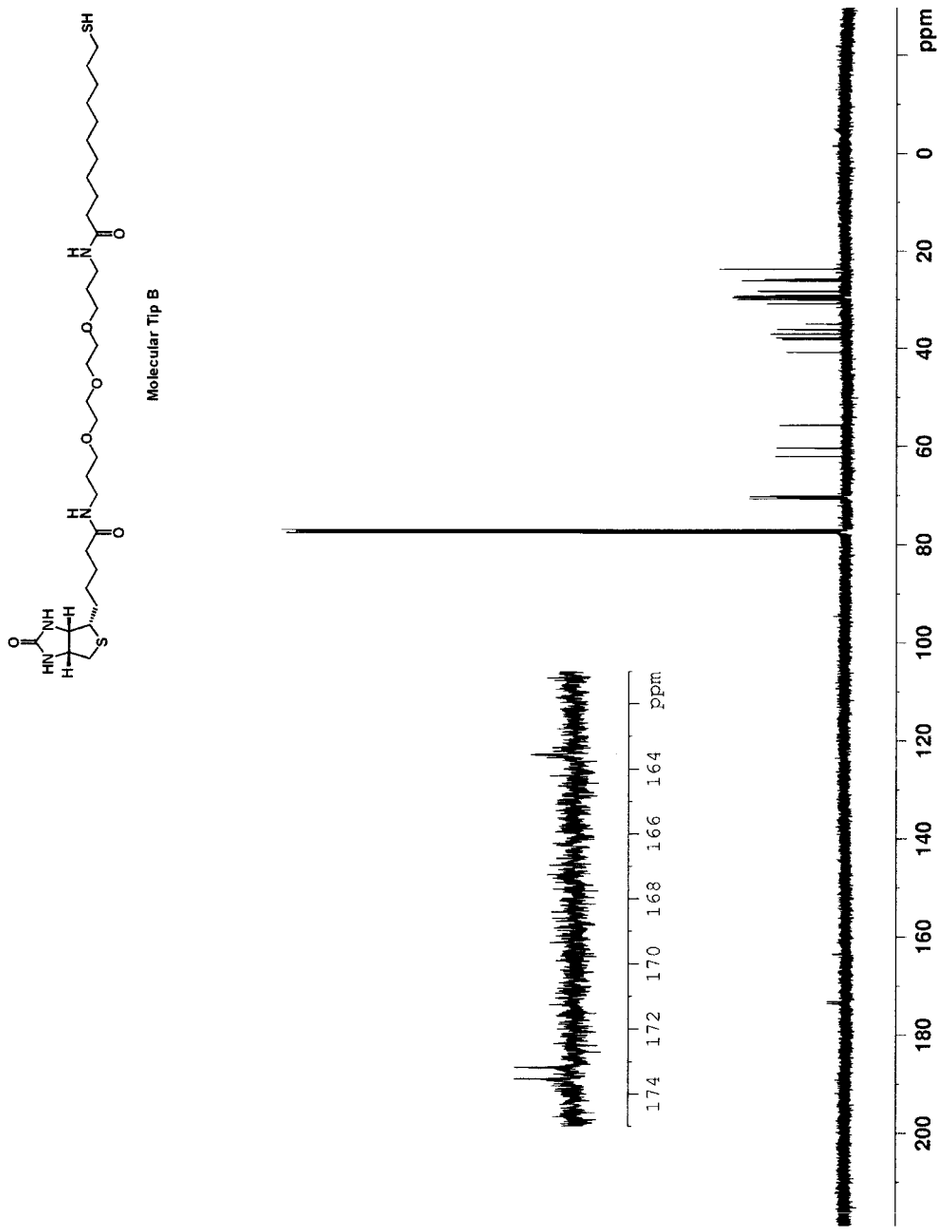

Figure 6-33. The 100 MHz ^{1}H decoupled ^{13}C NMR spectrum of **Molecular tip B** in $CDCl_3$.

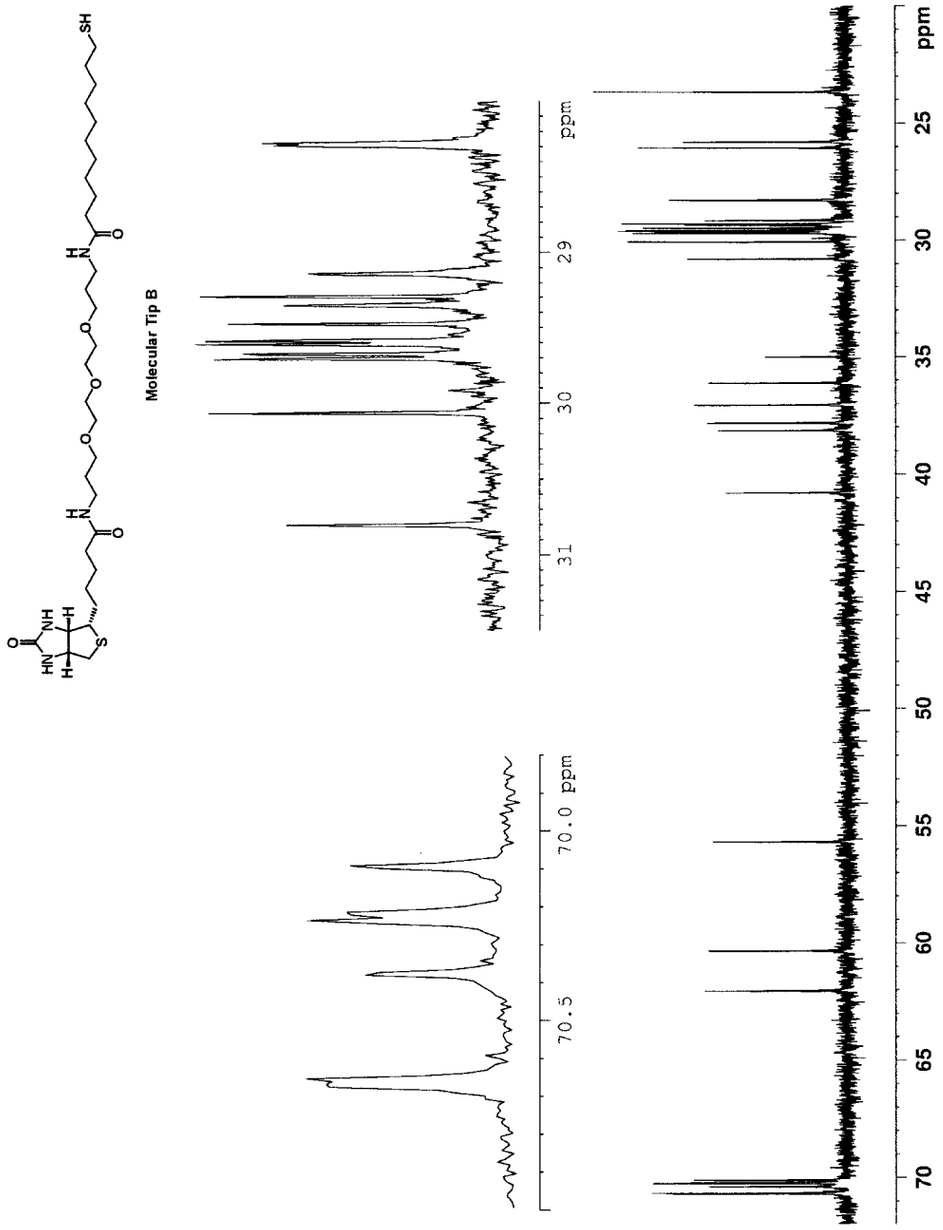

Figure 6-34. The 100 MHz ^{1}H decoupled ^{13}C NMR spectrum of **Molecular tip B** in $CDCl_3$.

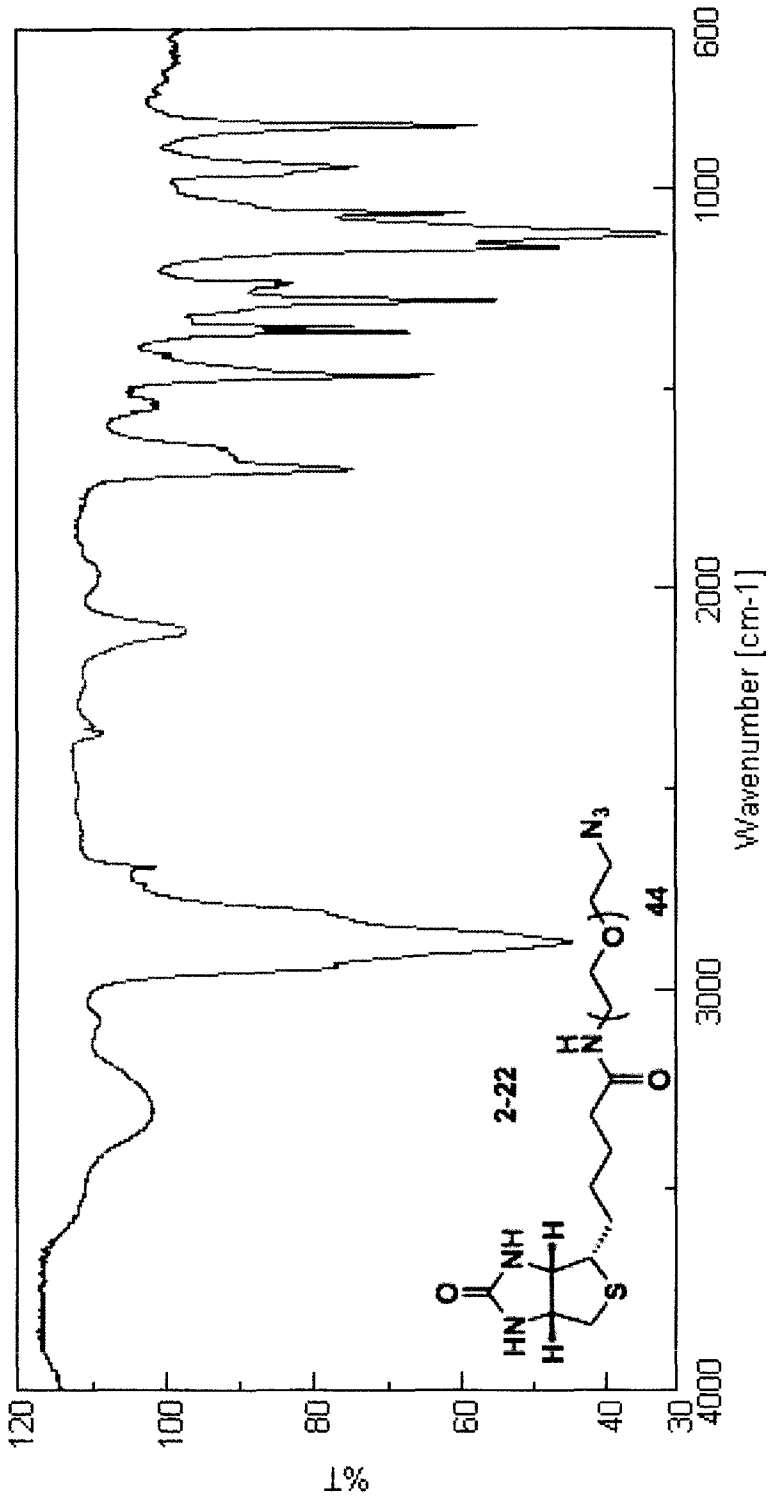

Figure 6-35. The thin film IR spectrum of compound **2-22**.

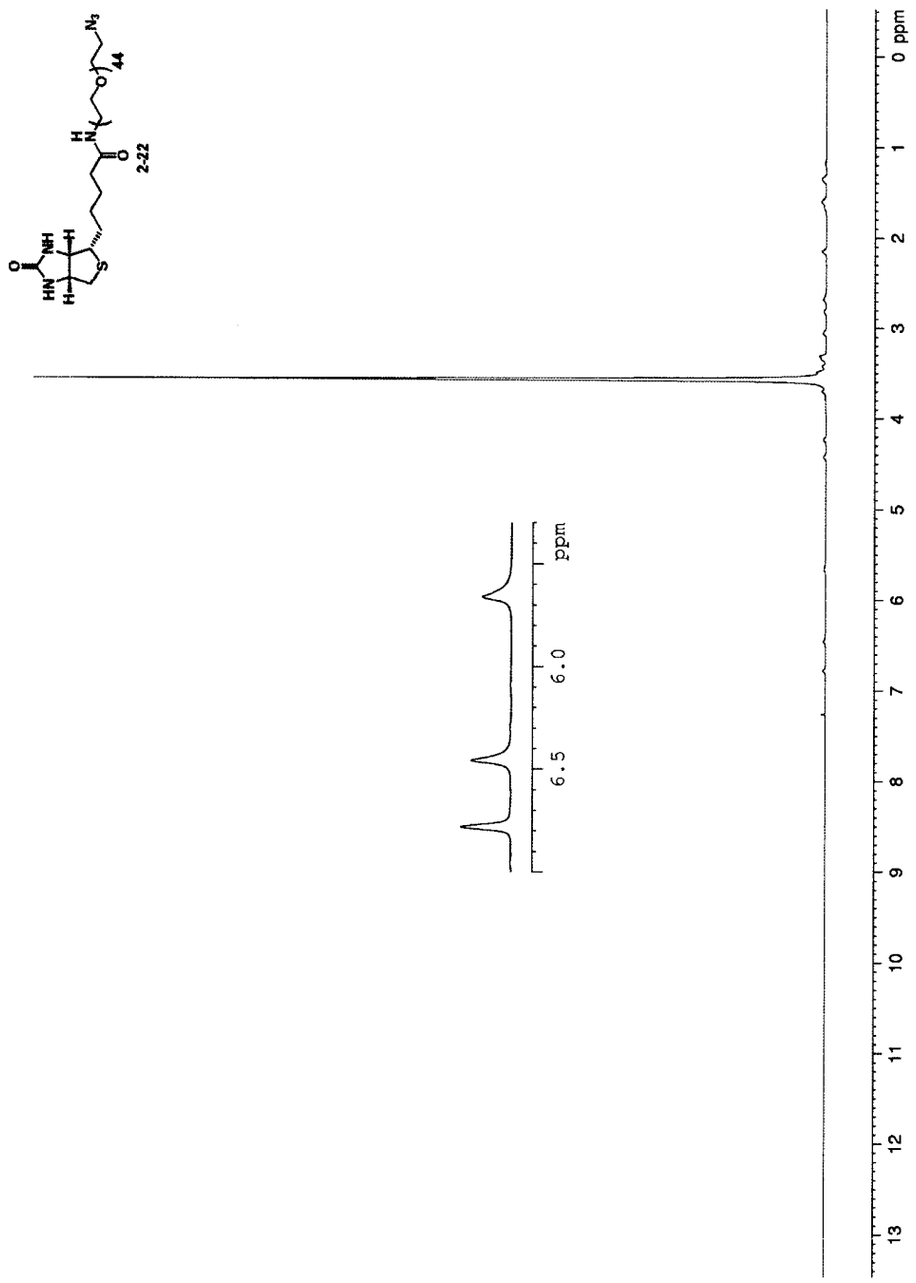

Figure 6-36. The 500 MHz ^{1}H NMR spectrum of compound **2-22** in $CDCl_3$.

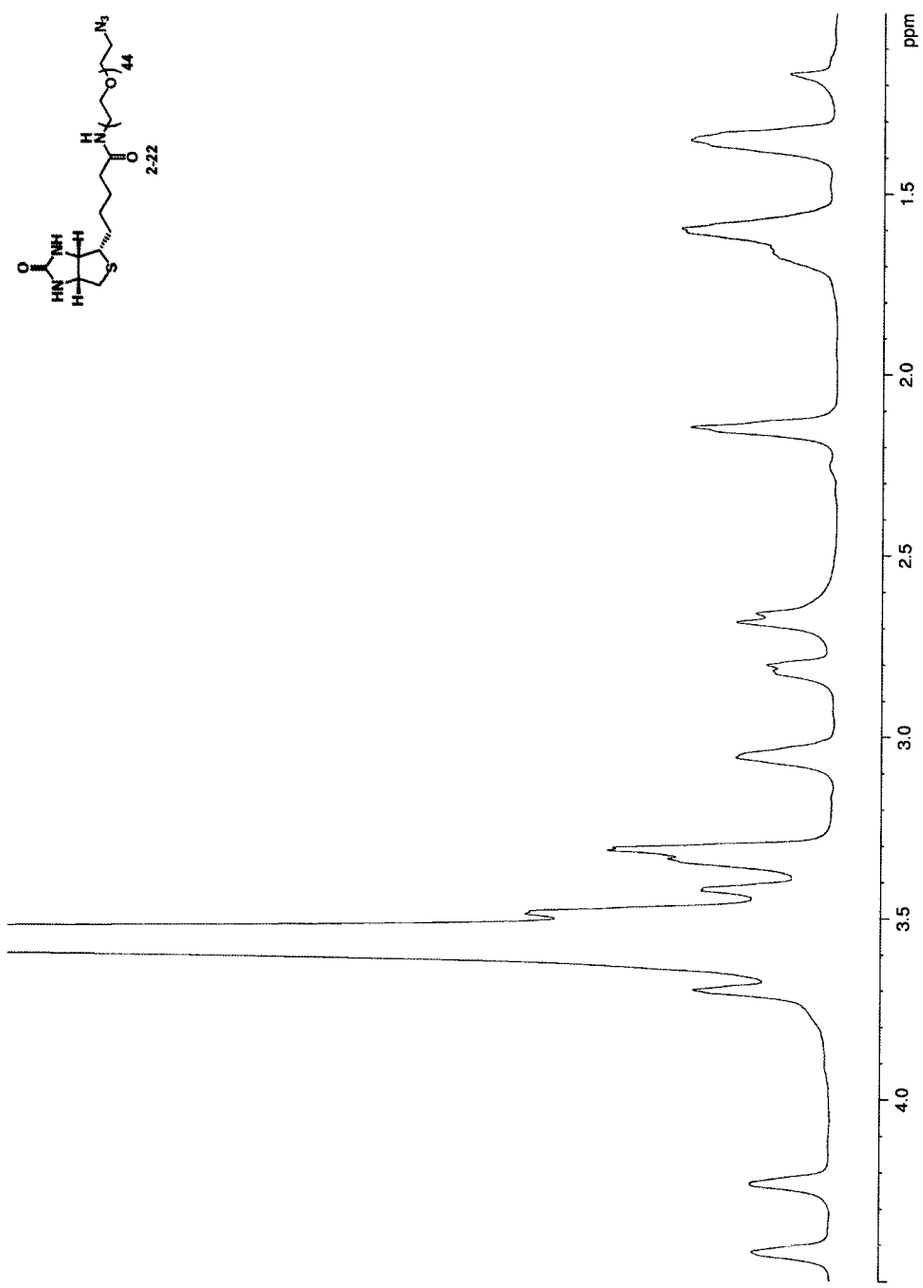

Figure 6-37. The 500 MHz ^{1}H NMR spectrum of compound **2-22** in $CDCl_3$.

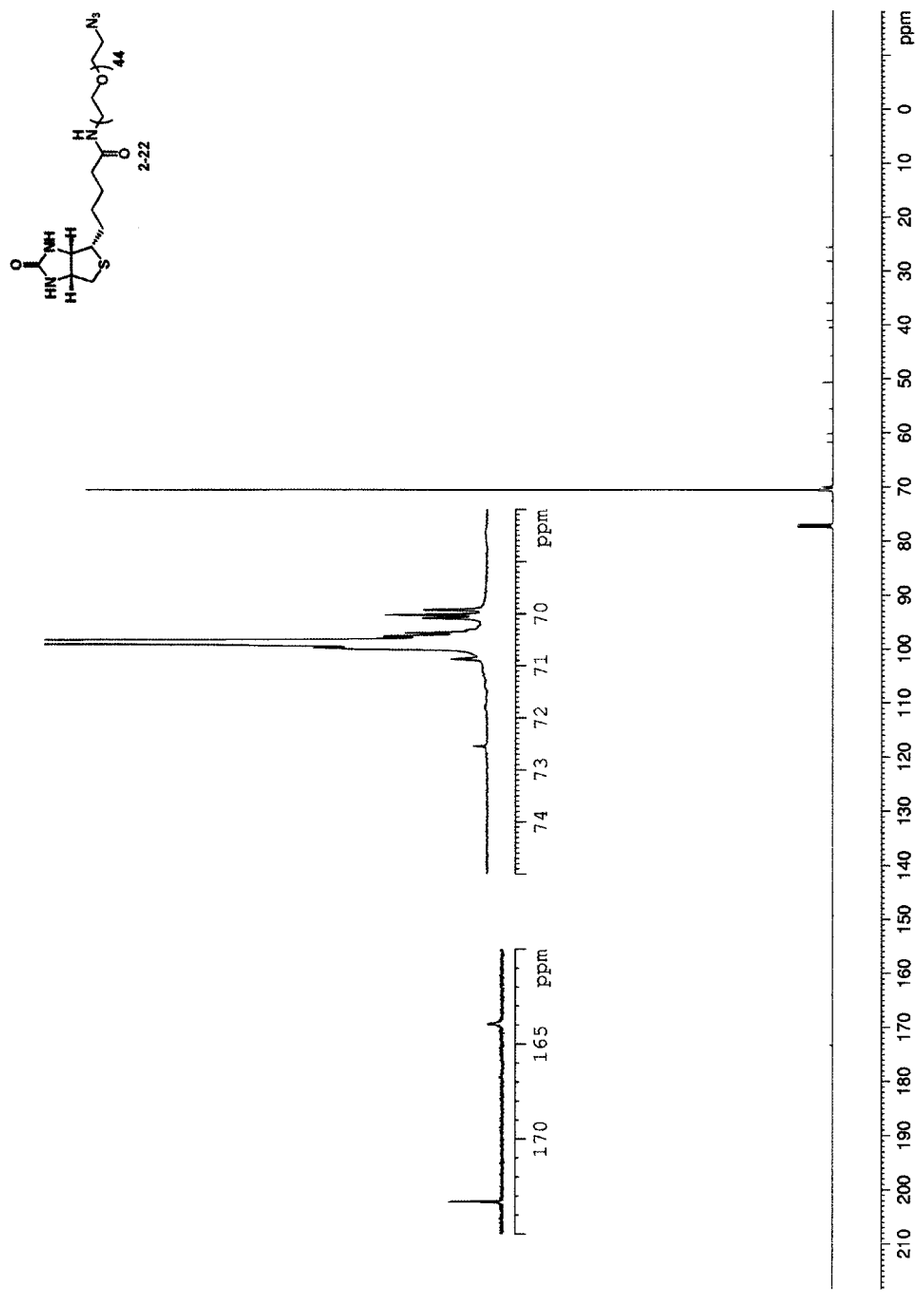

Figure 6-38. The 125 MHz ^{1}H decoupled ^{13}C NMR spectrum of compound **2-22** in $CDCl_3$.

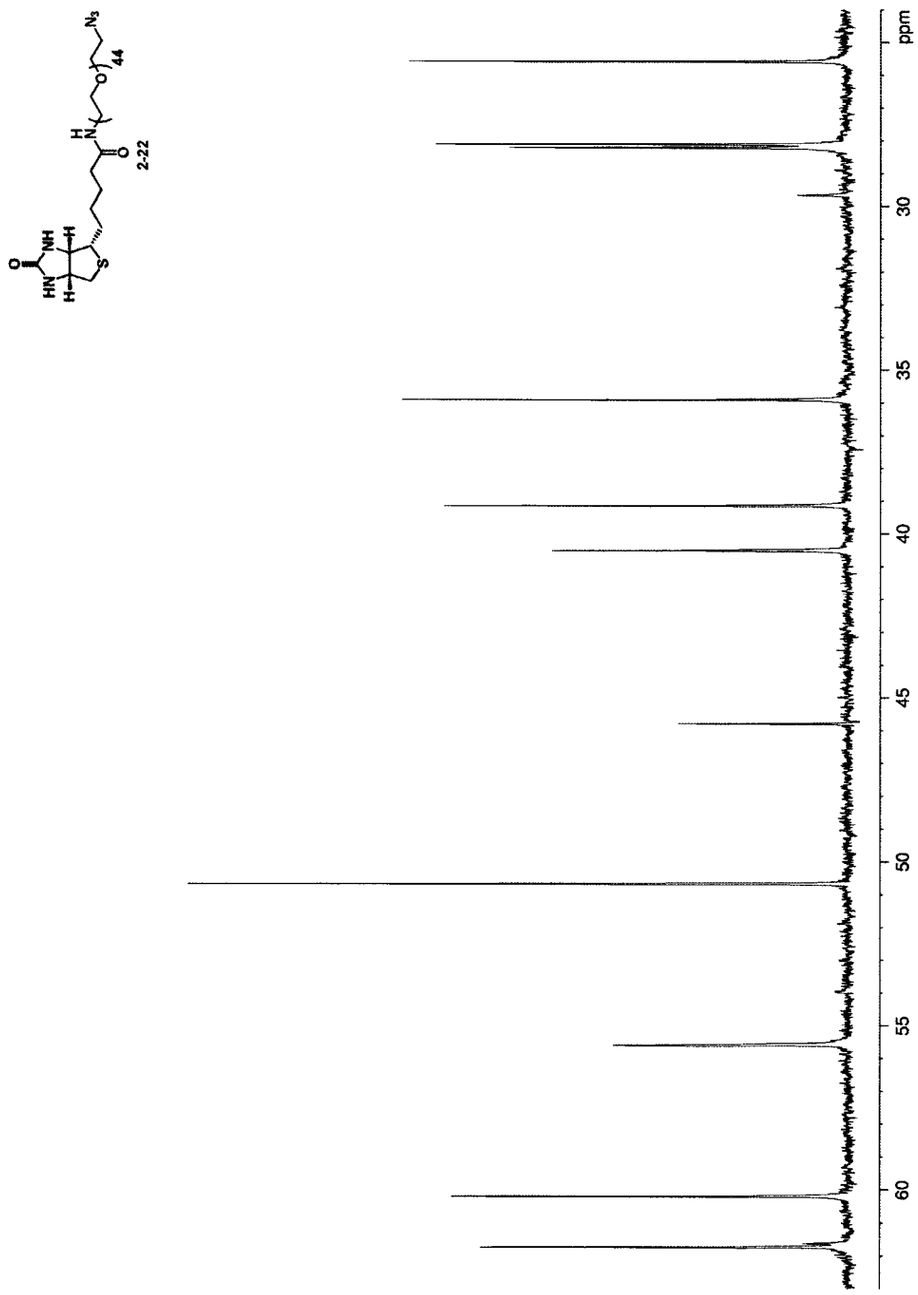

Figure 6-39. The 125 MHz ^{1}H decoupled ^{13}C NMR spectrum of compound **2-22** in $CDCl_3$.

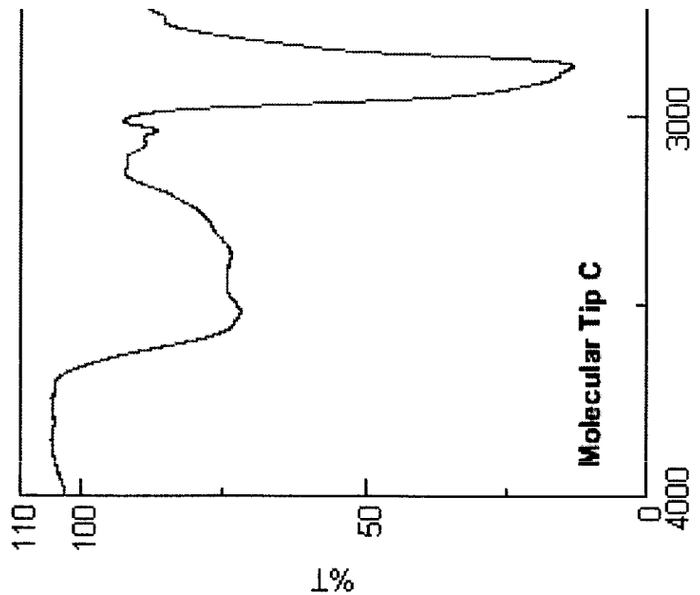

Figure 6-40. The thin film IR spectrum of **Molecular tip C**.

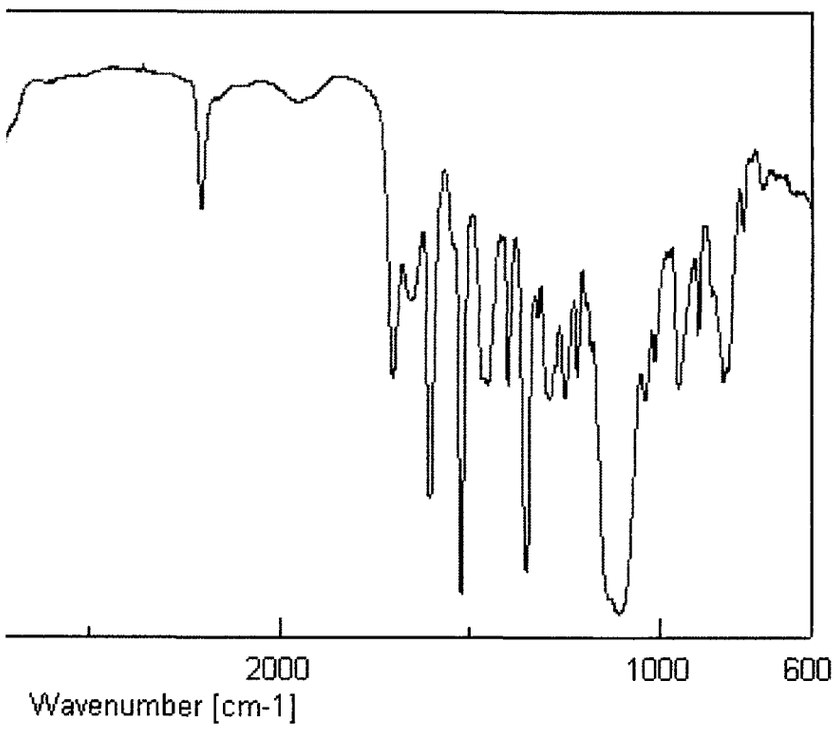
2000
1000
600
Wavenumber [cm-1]

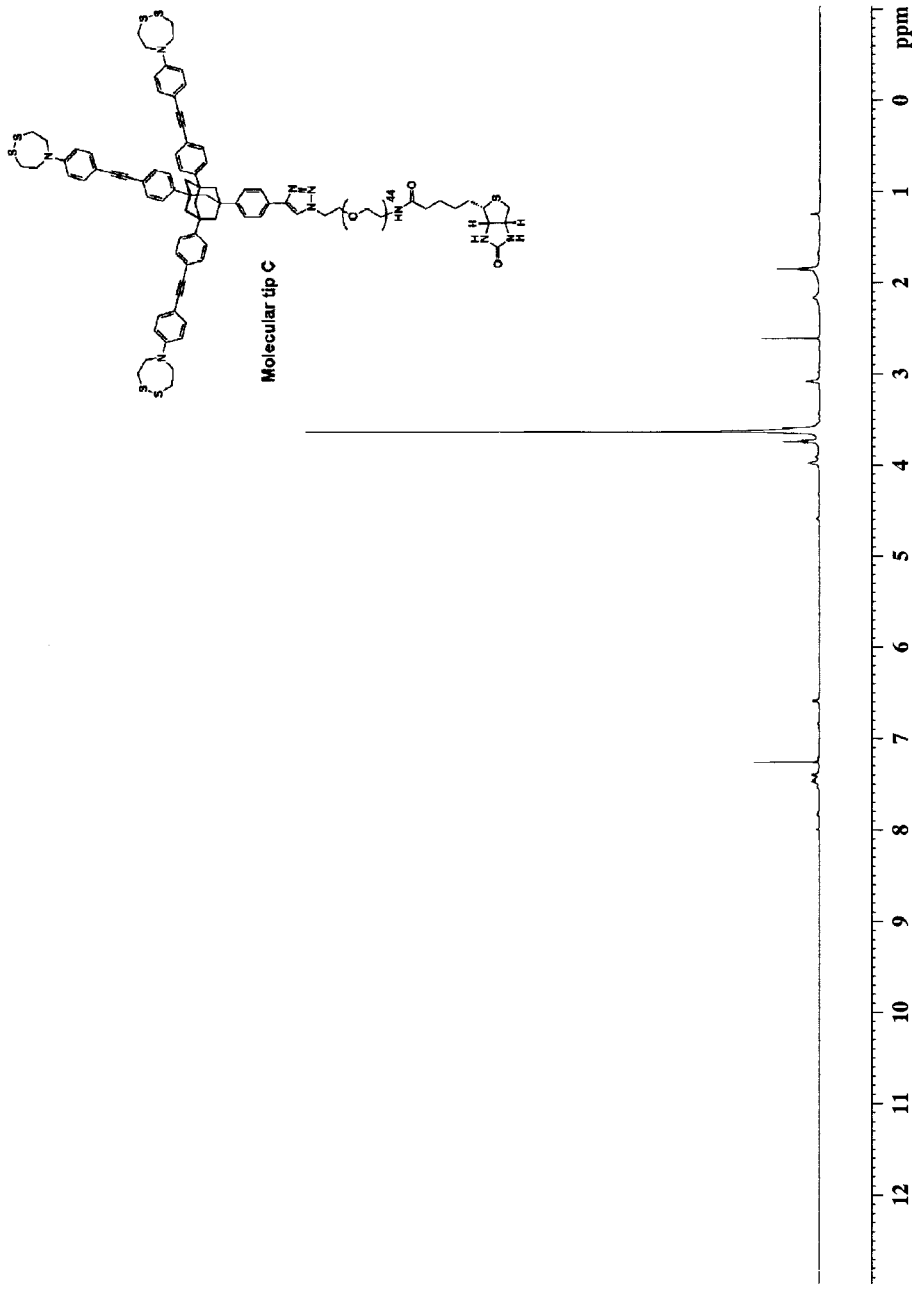

Figure 6-41. The 500 MHz ^{1}H NMR spectrum of **Molecular tip C** in $CDCl_3$.

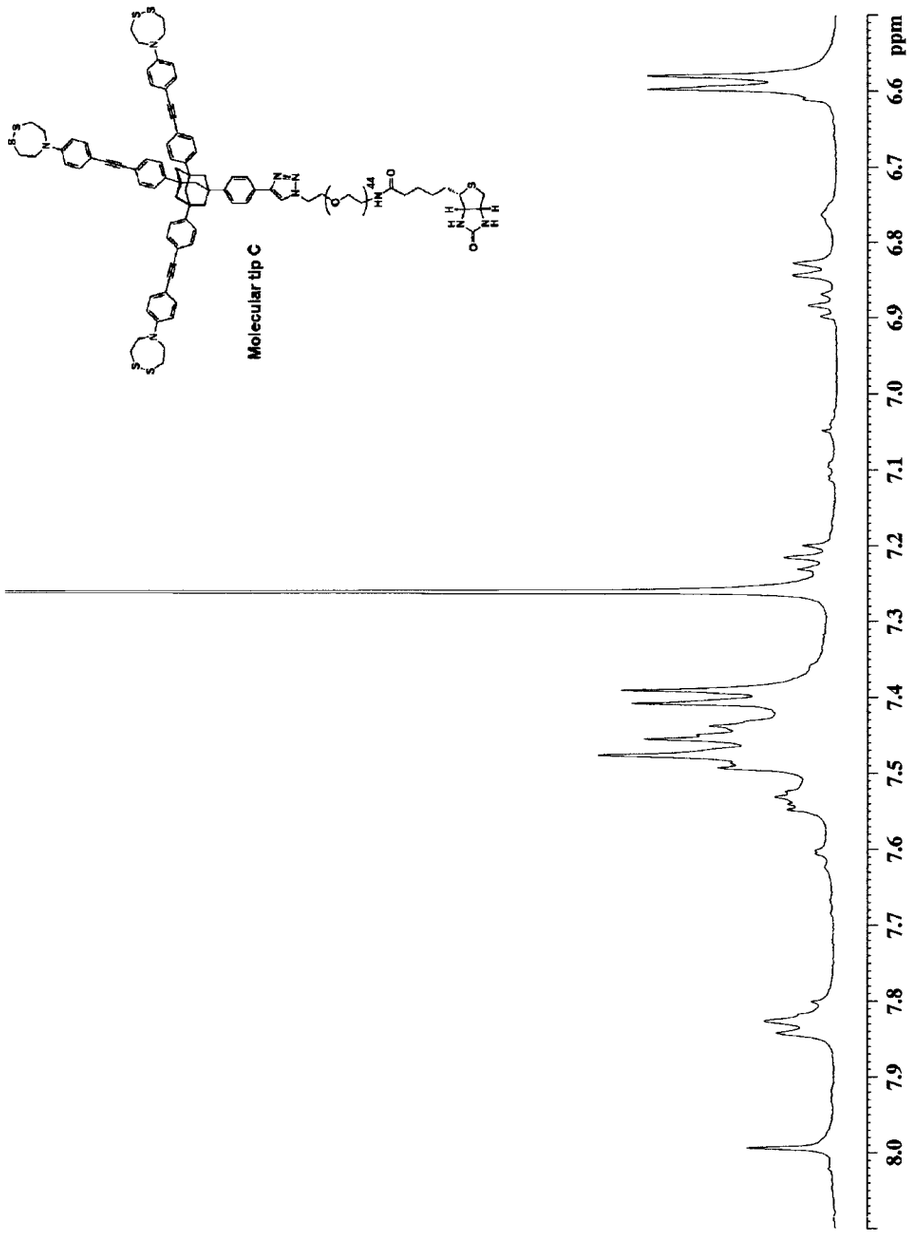

Figure 6-42. The 500 MHz ^{1}H NMR spectrum of **Molecular tip C** in $CDCl_3$.

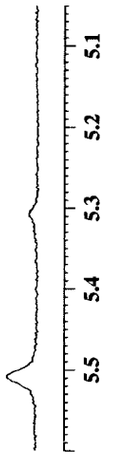

Figure 6-43. The 500 MHz ^{1}H NMR spectrum of **Molecular tip C** in $CDCl_3$.

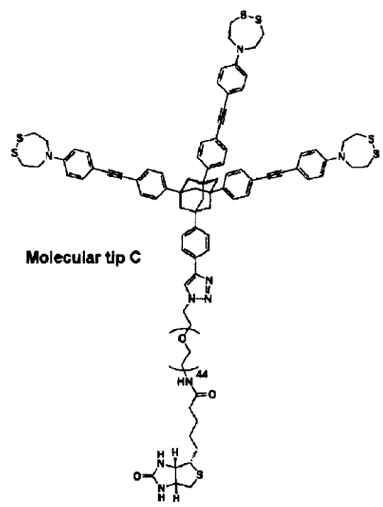
Molecular tip C

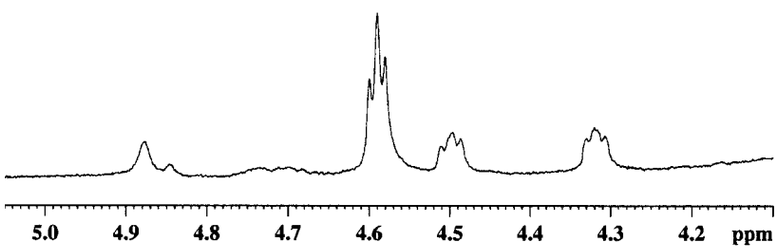
5.0
4.9
4.8
4.7
4.6
4.5
4.4
4.3
4.2
ppm

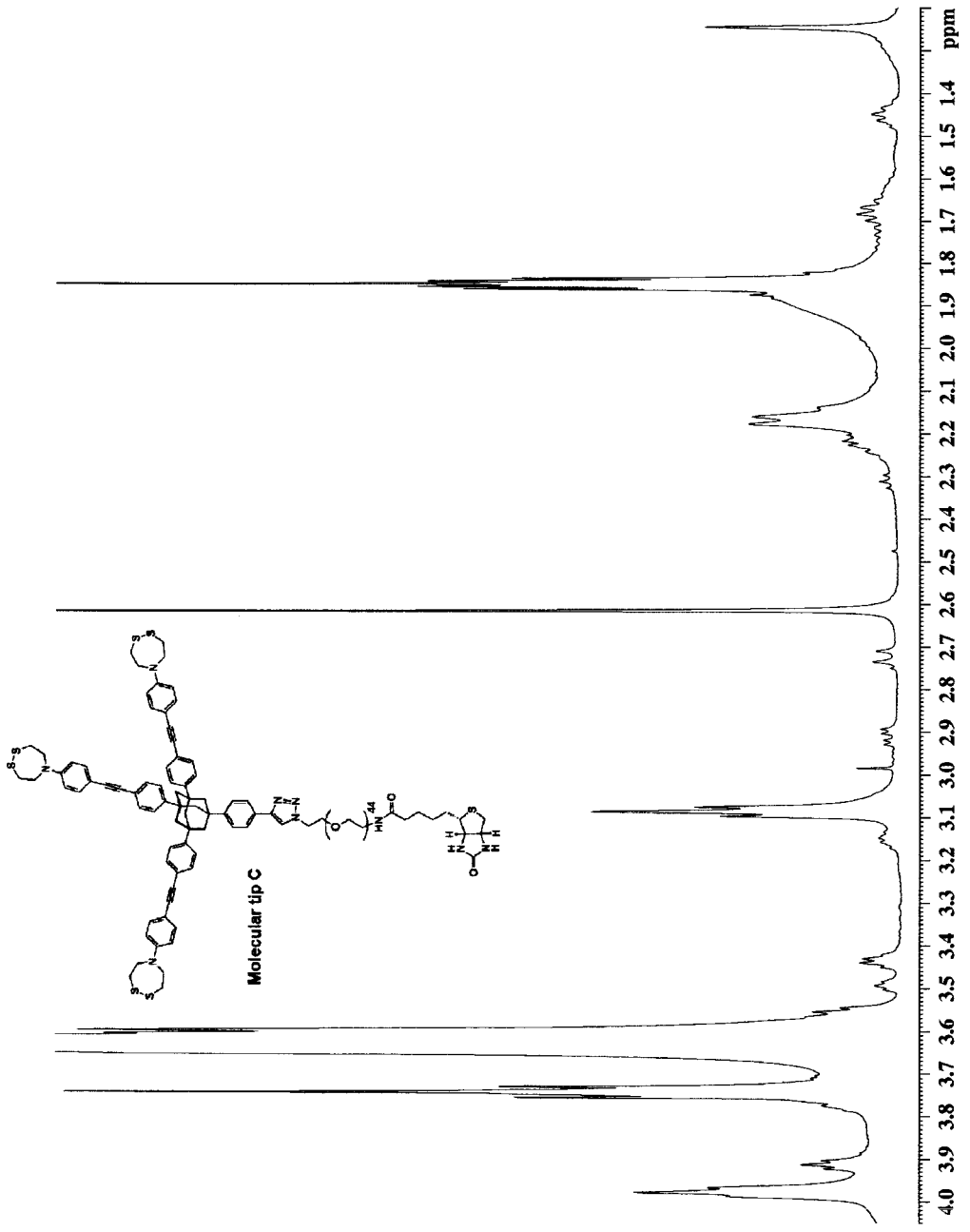

Figure 6-44. The 500 MHz ^{1}H NMR spectrum of **Molecular tip C** in $CDCl_3$.

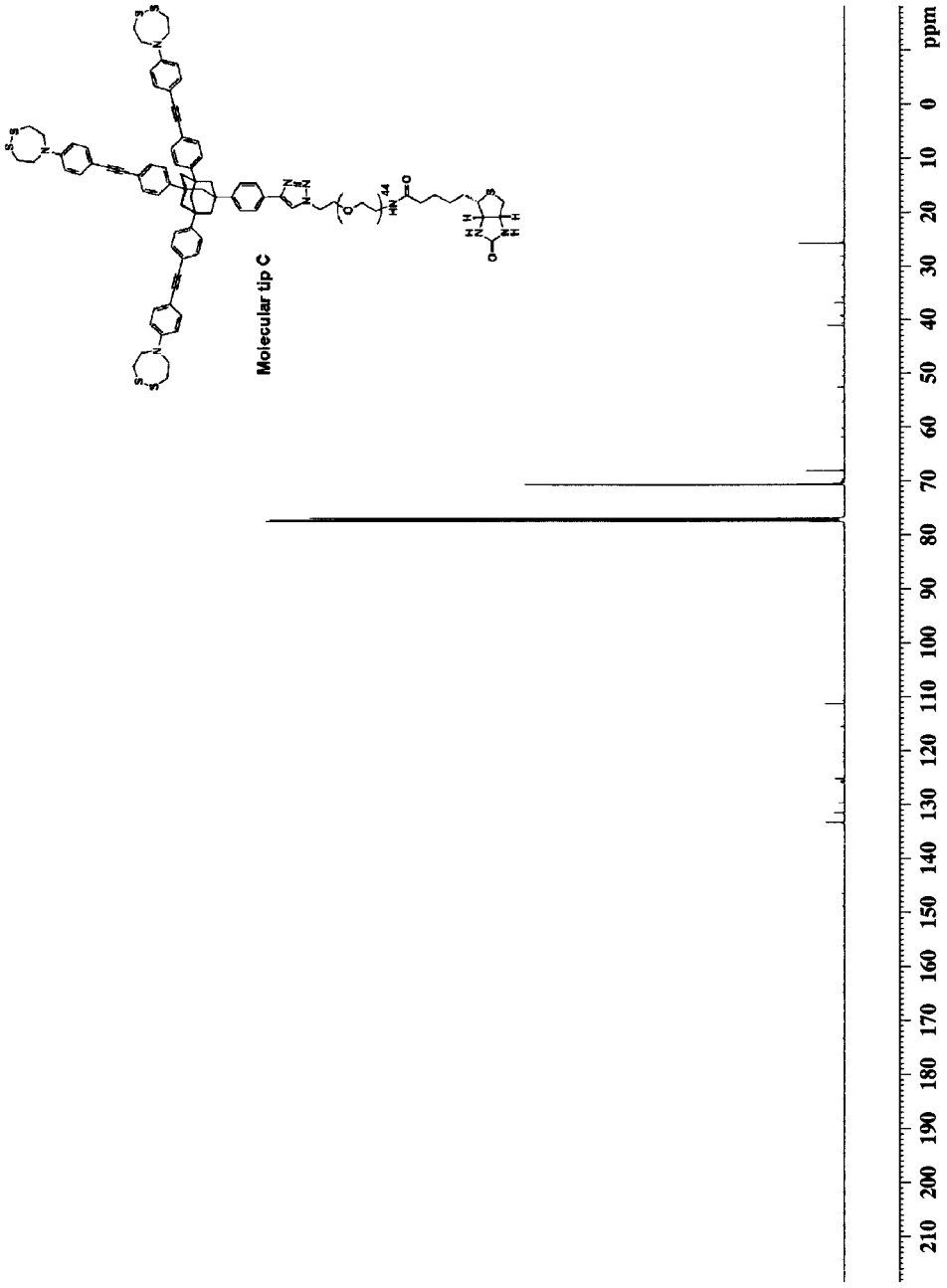

Figure 6-45. The 125 MHz ^{1}H decoupled ^{13}C NMR spectrum of **Molecular tip C** in $CDCl_3$.

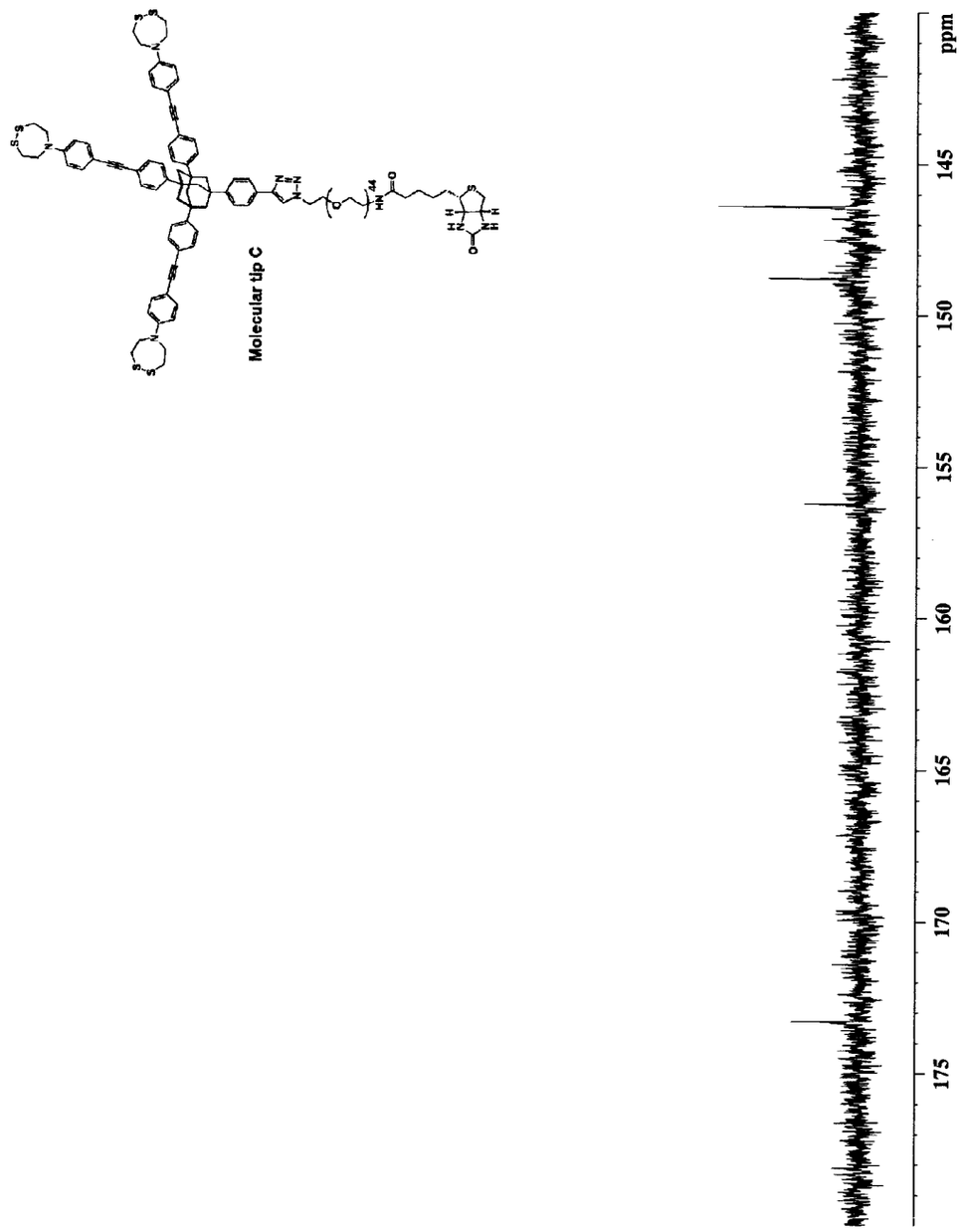

Figure 6-46. The 125 MHz ^{1}H decoupled ^{13}C NMR spectrum of **Molecular tip C** in $CDCl_3$.

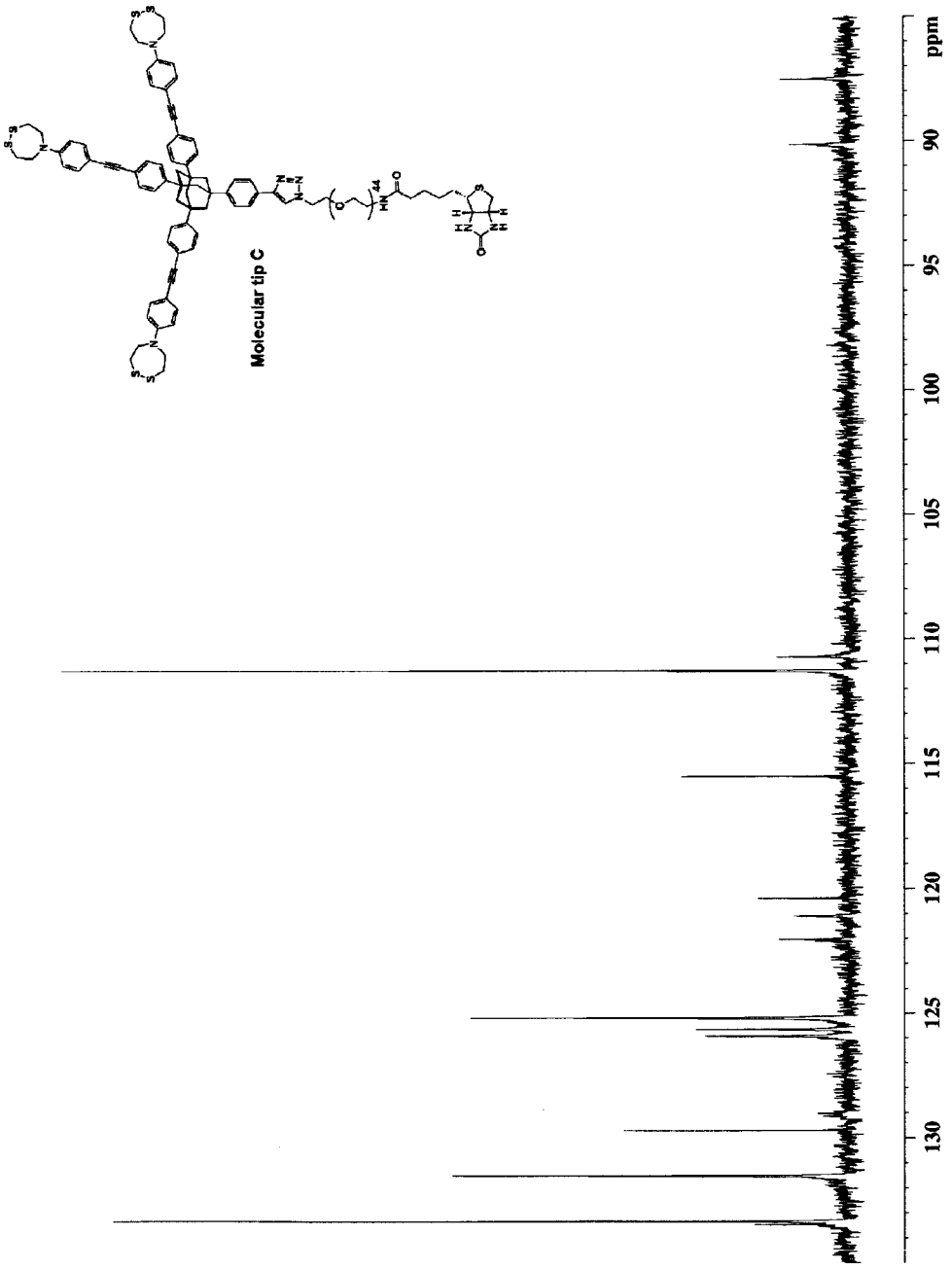

Figure 6-47. The 125 MHz ^{1}H decoupled ^{13}C NMR spectrum of **Molecular tip C** in $CDCl_3$.

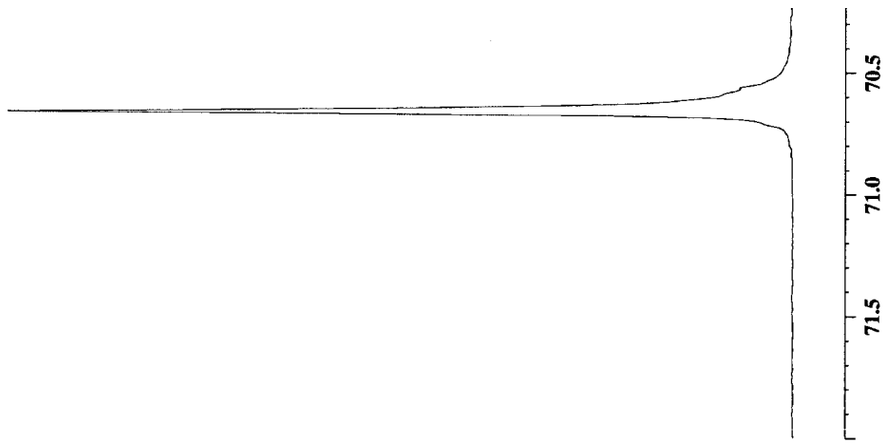

Figure 6-48. The 125 MHz ^{1}H decoupled ^{13}C NMR spectrum of **Molecular tip C** in $CDCl_3$.

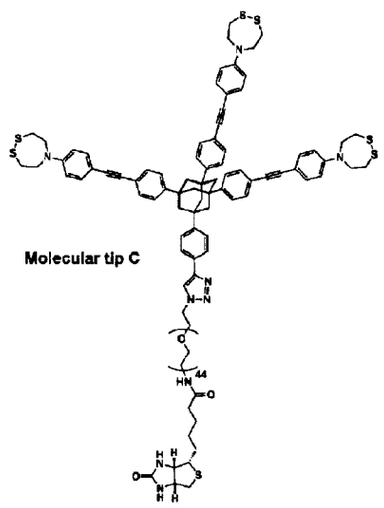

Molecular tip C

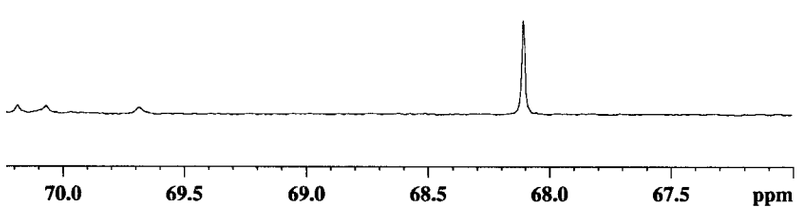

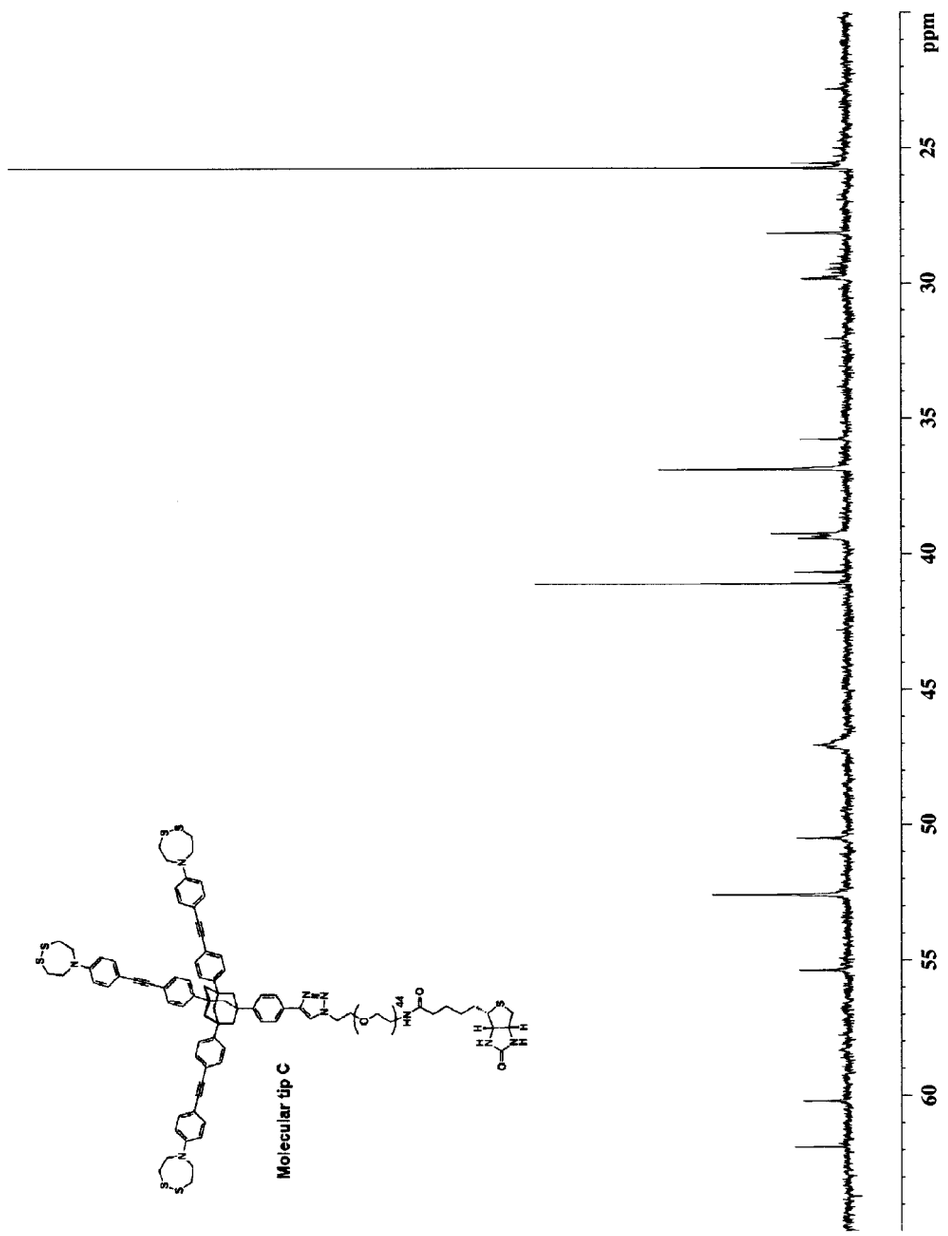

Figure 6-49. The 125 MHz ^{1}H decoupled ^{13}C NMR spectrum of **Molecular tip C** in $CDCl_3$.

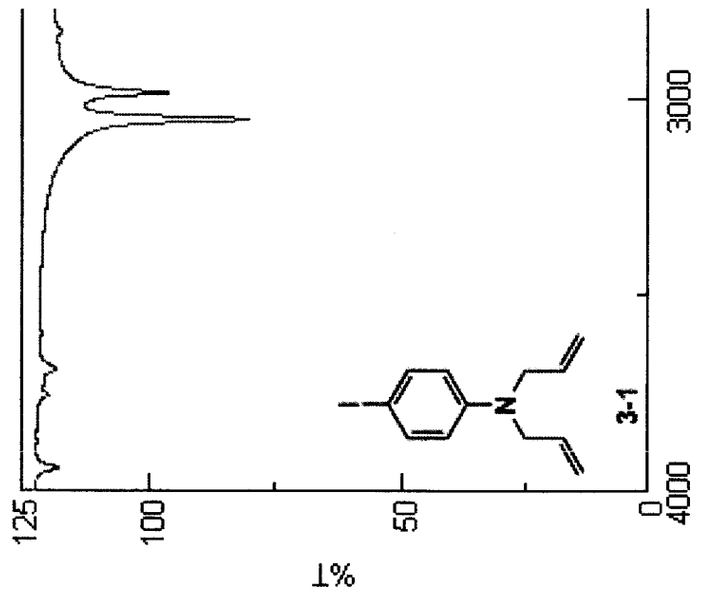

Figure 6-50. The thin film IR spectrum of compound **3-1**.

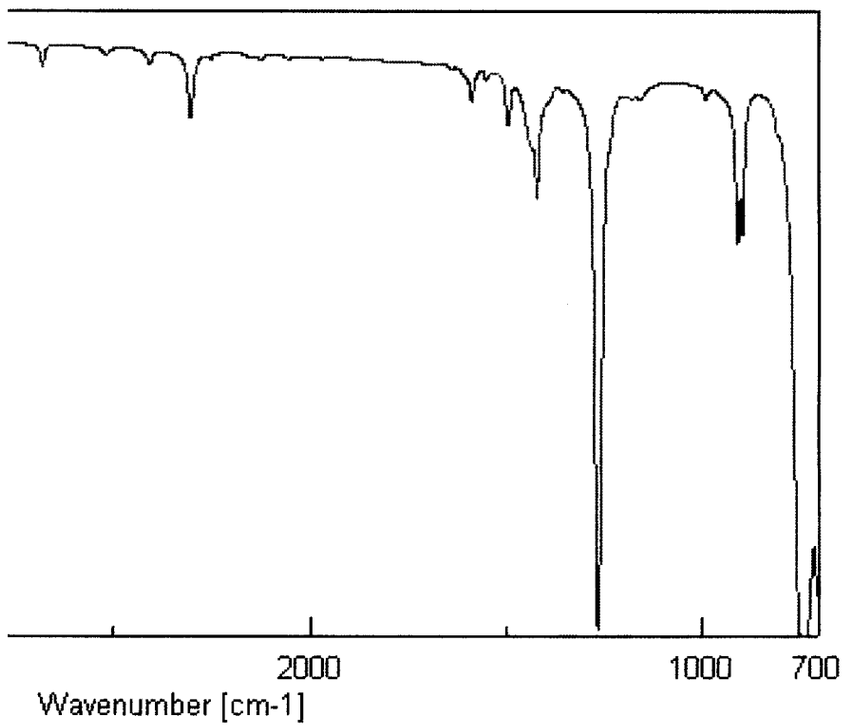
2000
1000
700
Wavenumber [cm-1]

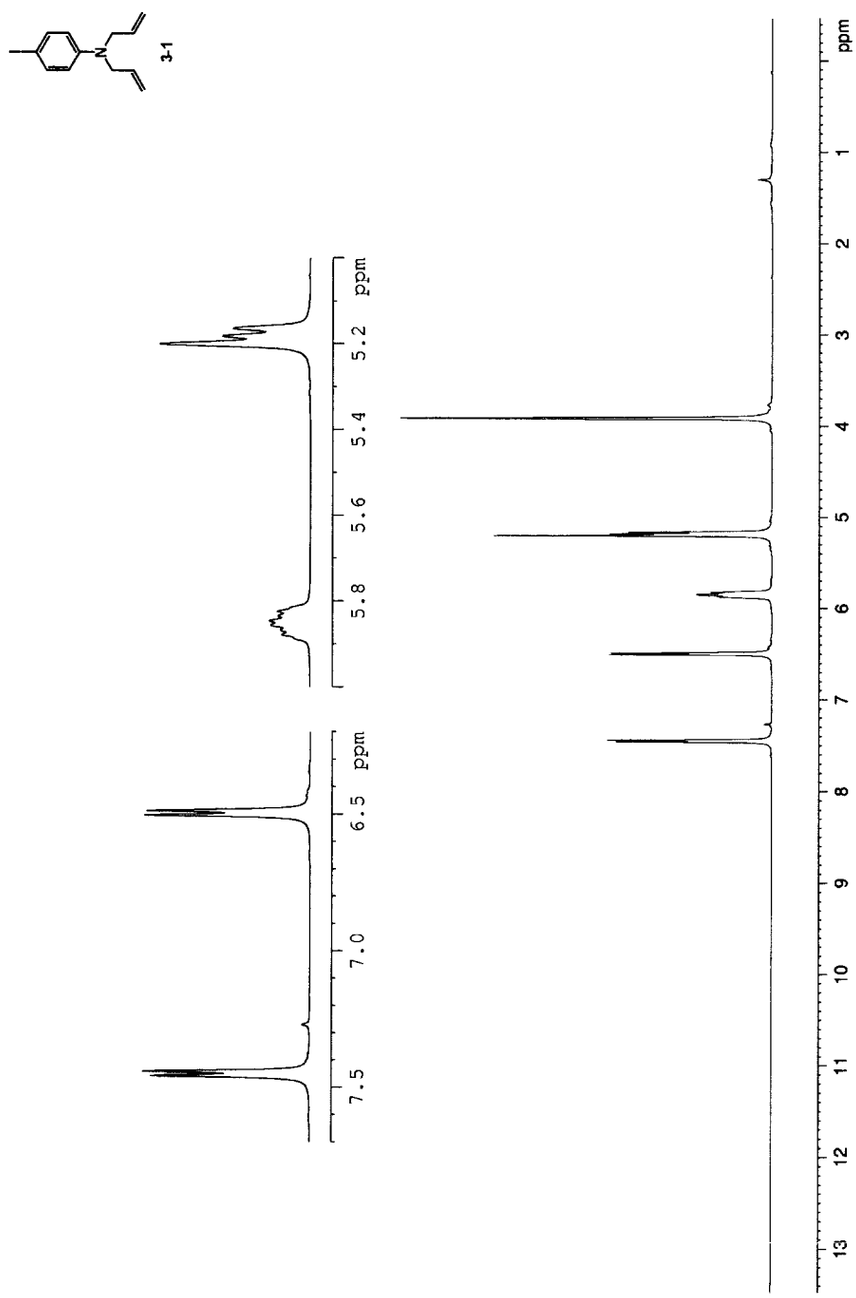

Figure 6-51. The 500 MHz ^{1}H NMR spectrum of compound **3-1** in $CDCl_3$.

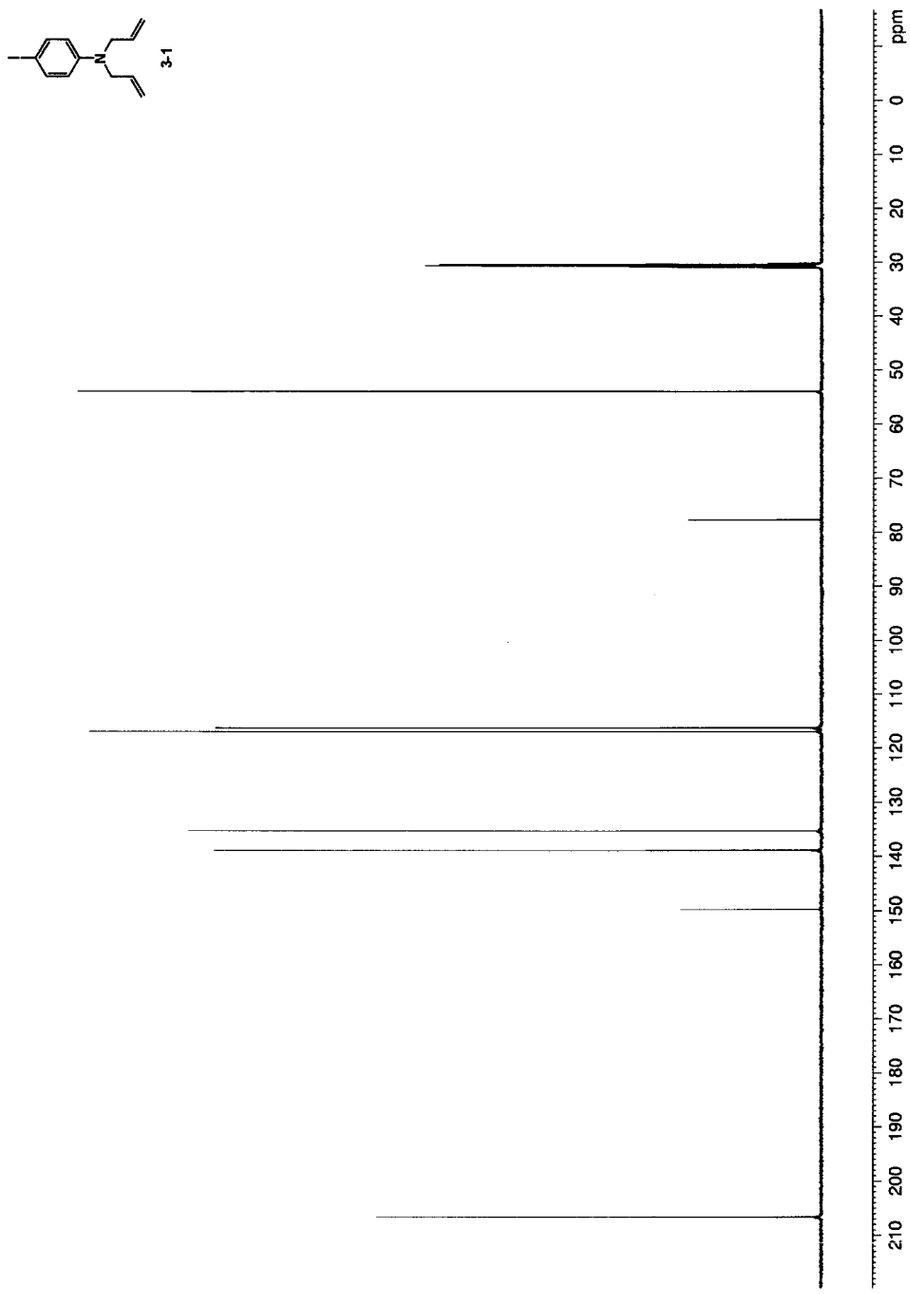

Figure 6-52. The 125 MHz ^{1}H decoupled ^{13}C NMR spectrum of compound **3-1** in acetone-d_6.

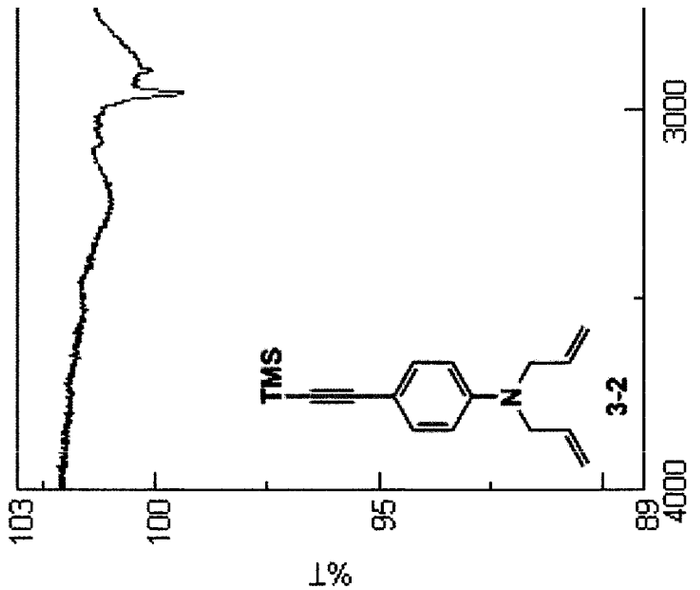

Figure 6-53. The thin film IR spectrum of compound **3-2**.

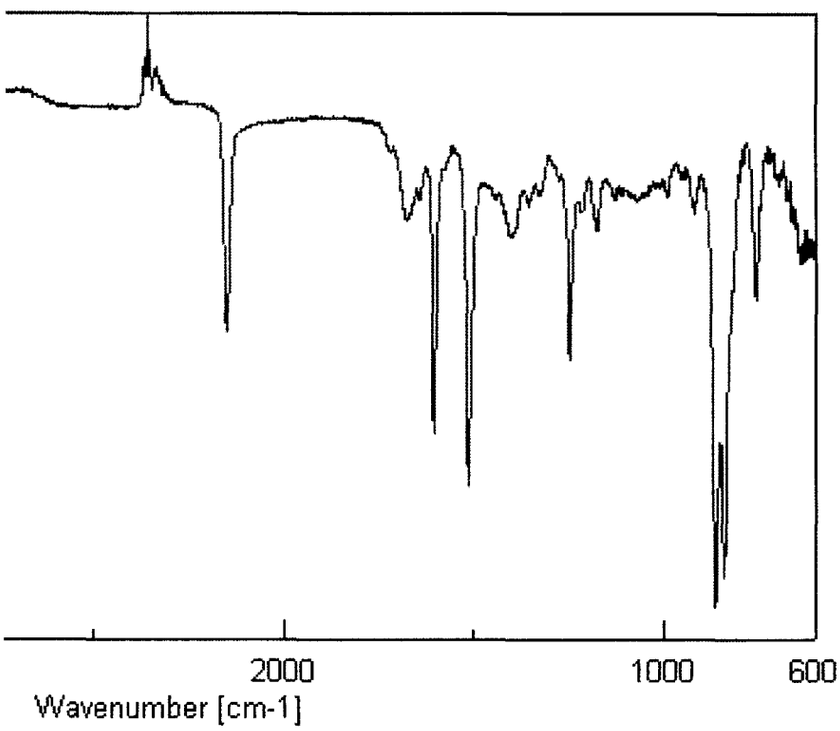
2000
1000
600
Wavenumber [cm-1]

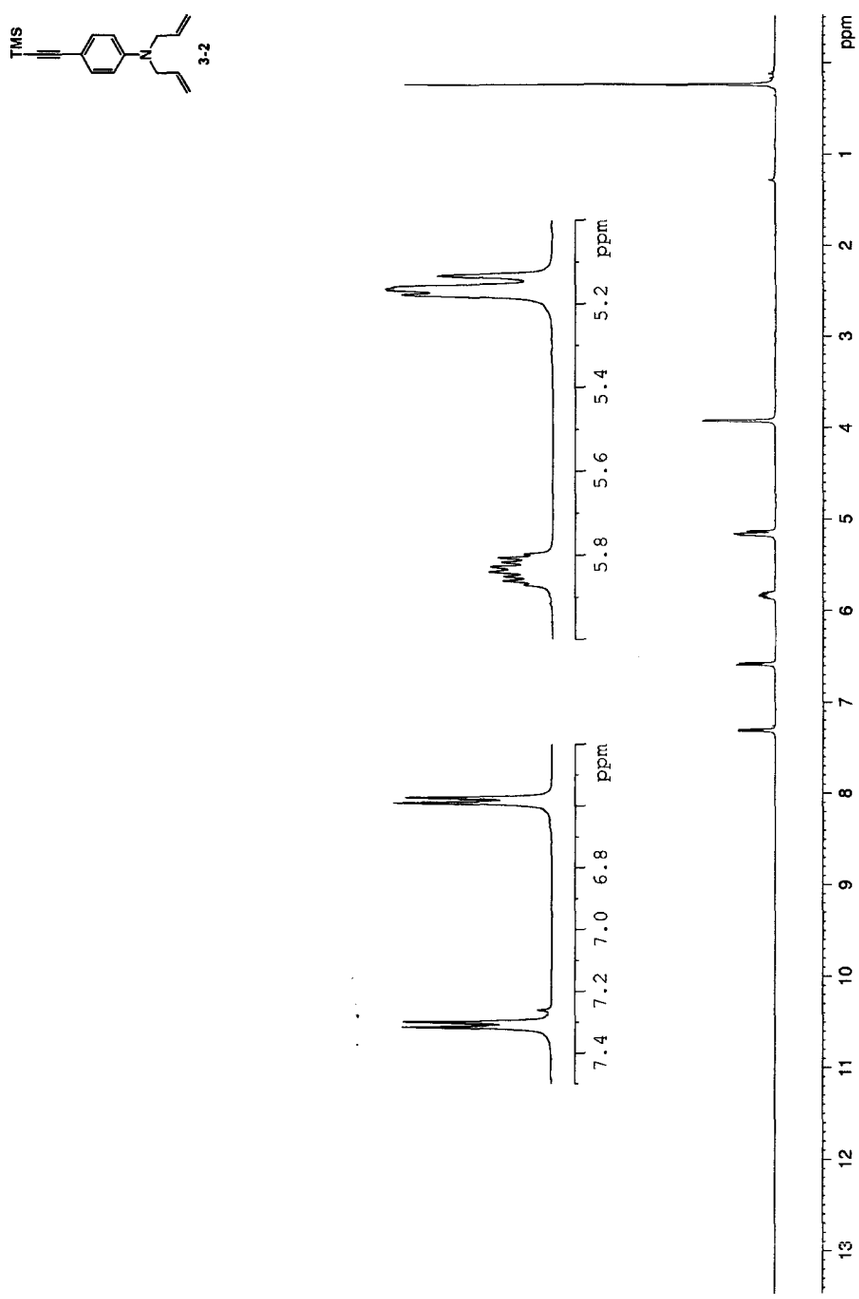

Figure 6-54. The 500 MHz ^{1}H NMR spectrum of compound **3-2** in $CDCl_3$.

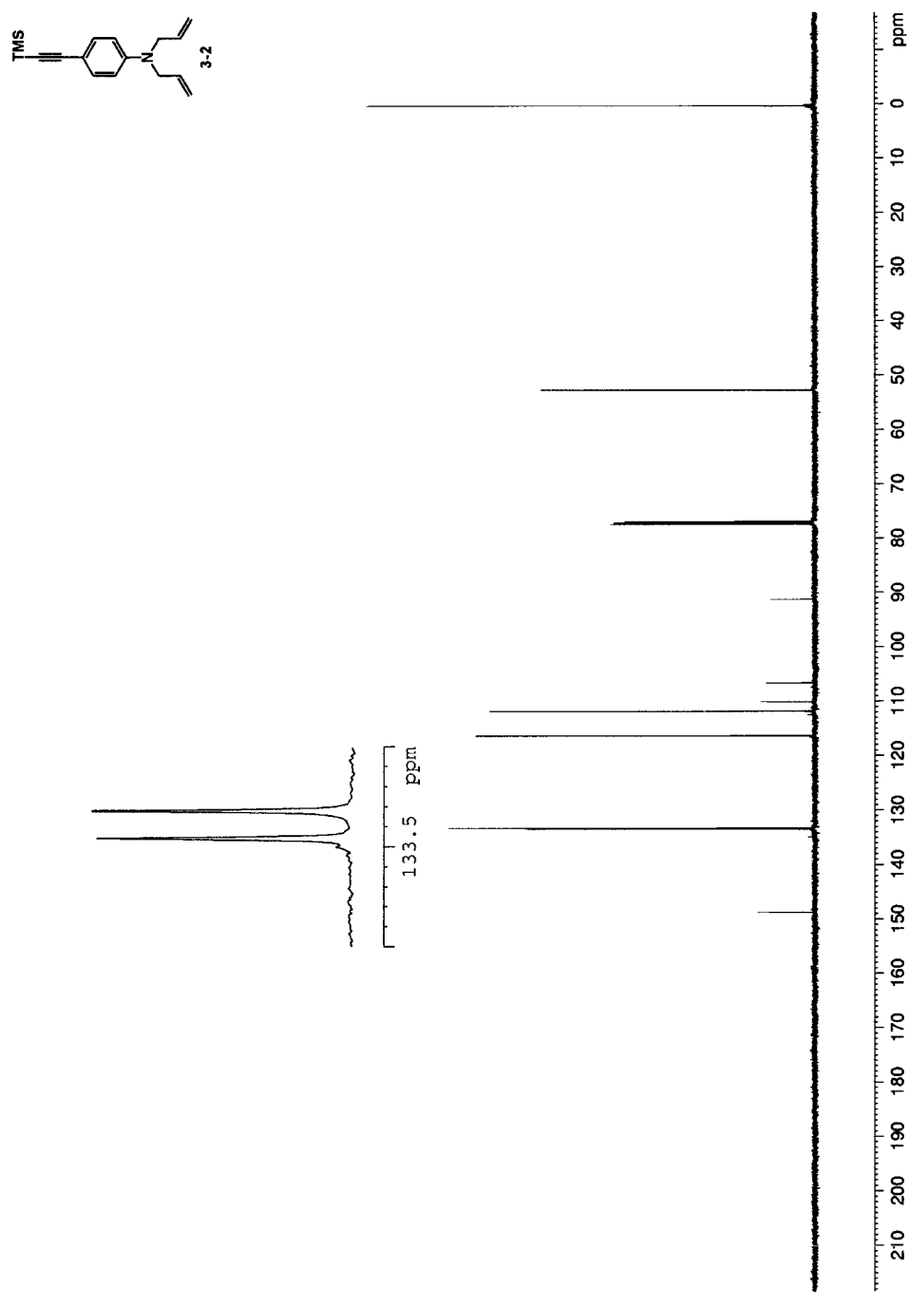

Figure 6-55. The 125 MHz ^{1}H decoupled ^{13}C NMR spectrum of compound **3-2** in $CDCl_3$.

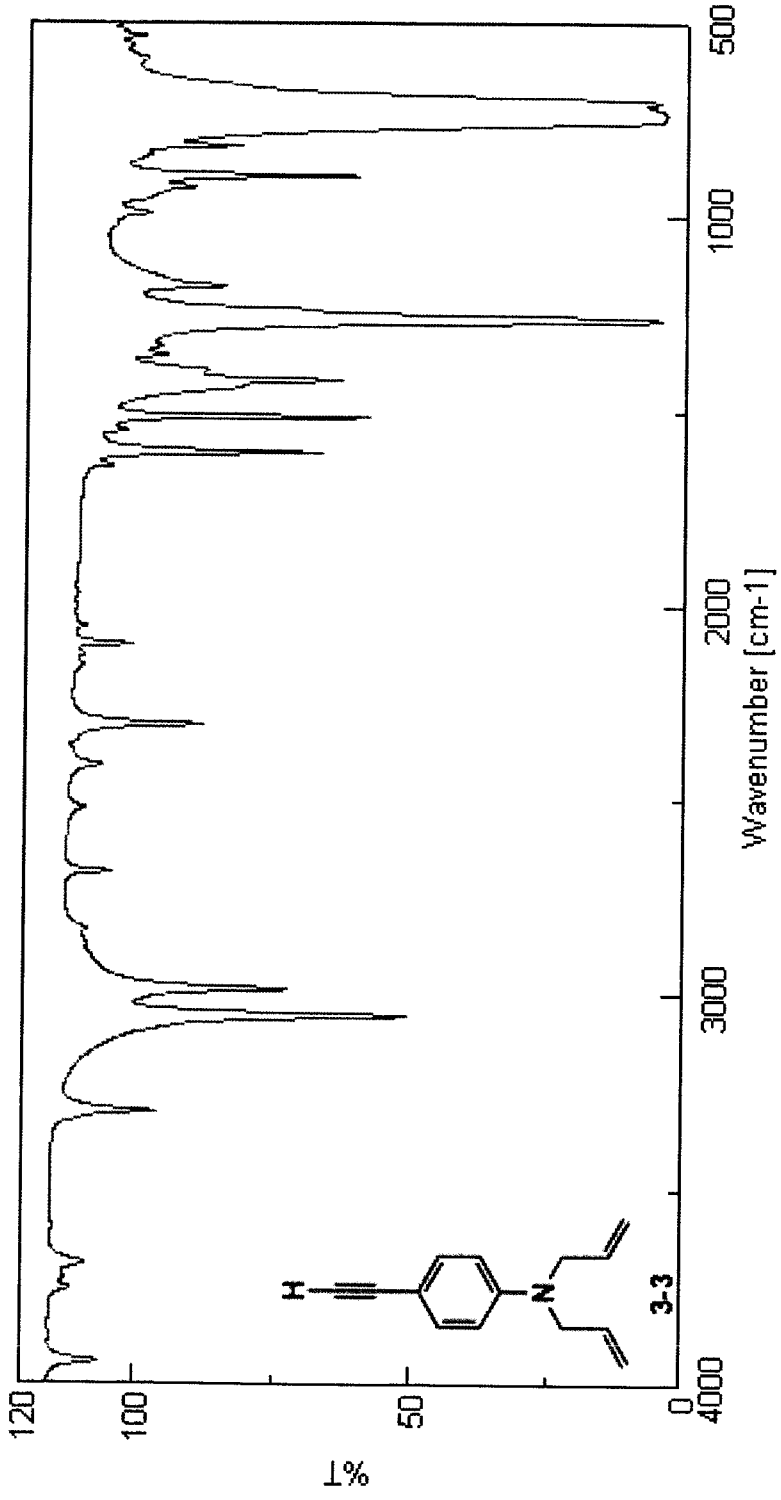

Figure 6-56. The thin film IR spectrum of compound **3-3**.

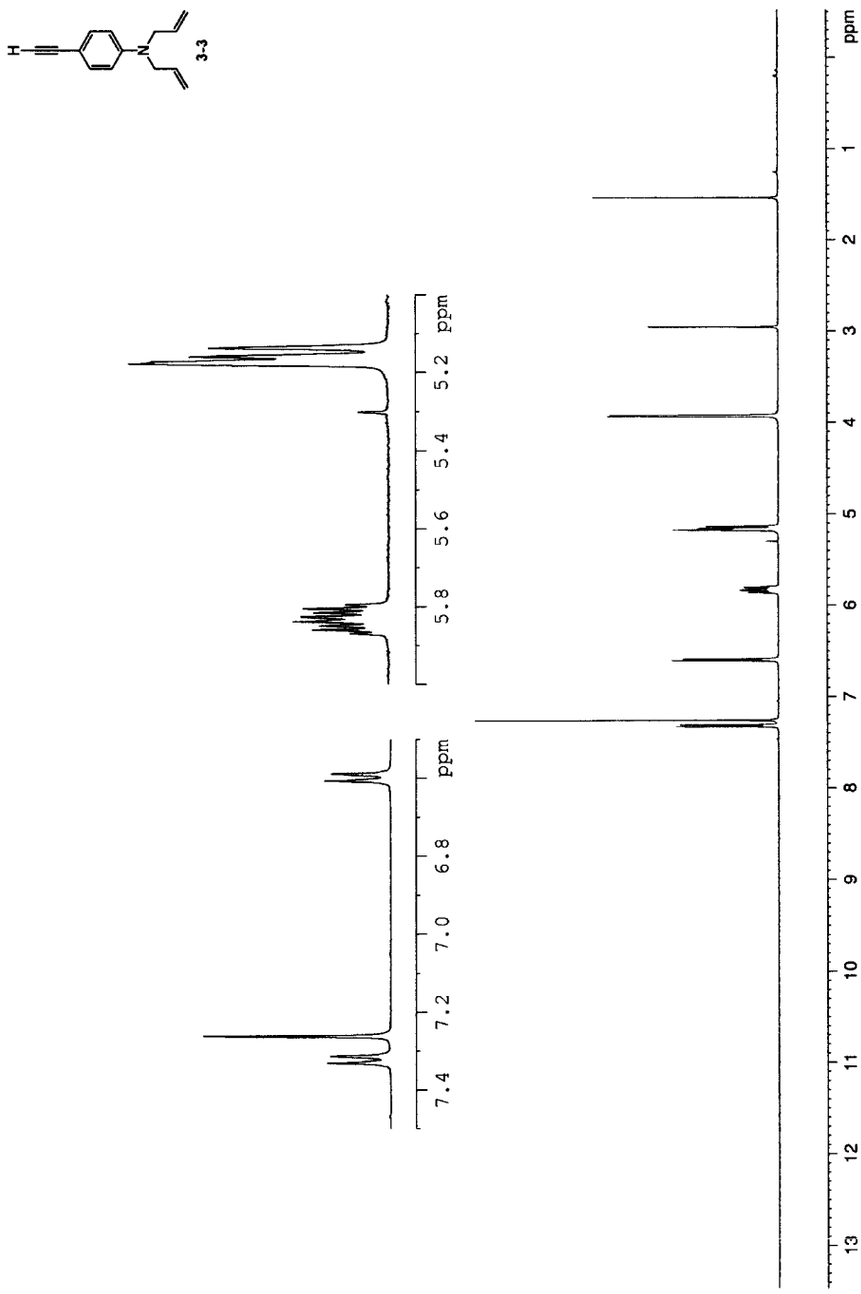

Figure 6-57. The 500 MHz ^{1}H NMR spectrum of compound **3-3** in $CDCl_3$.

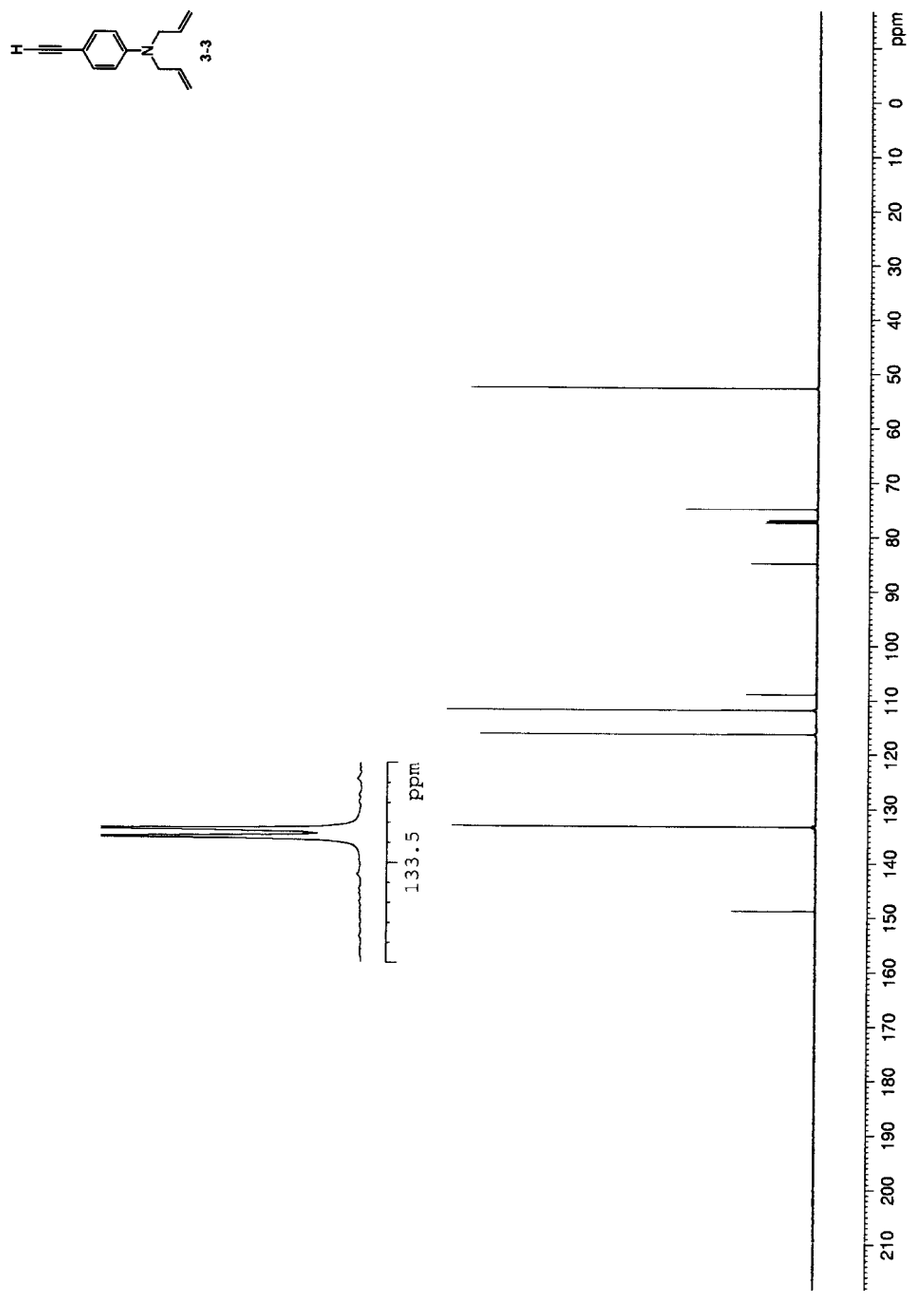

Figure 6-58. The 125 MHz ^{1}H decoupled ^{13}C NMR spectrum of compound **3-3** in $CDCl_3$.

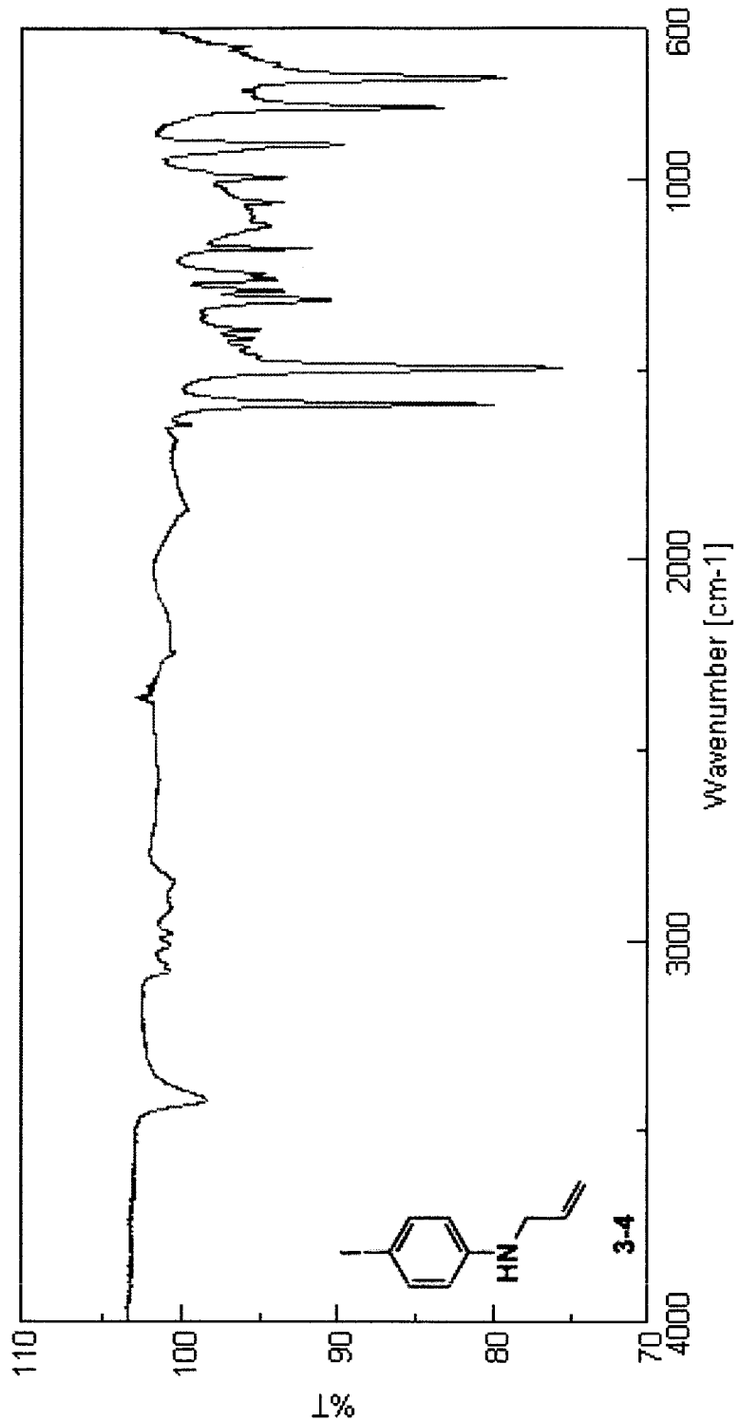

Figure 6-59. The thin film IR spectrum of compound **3-4**.

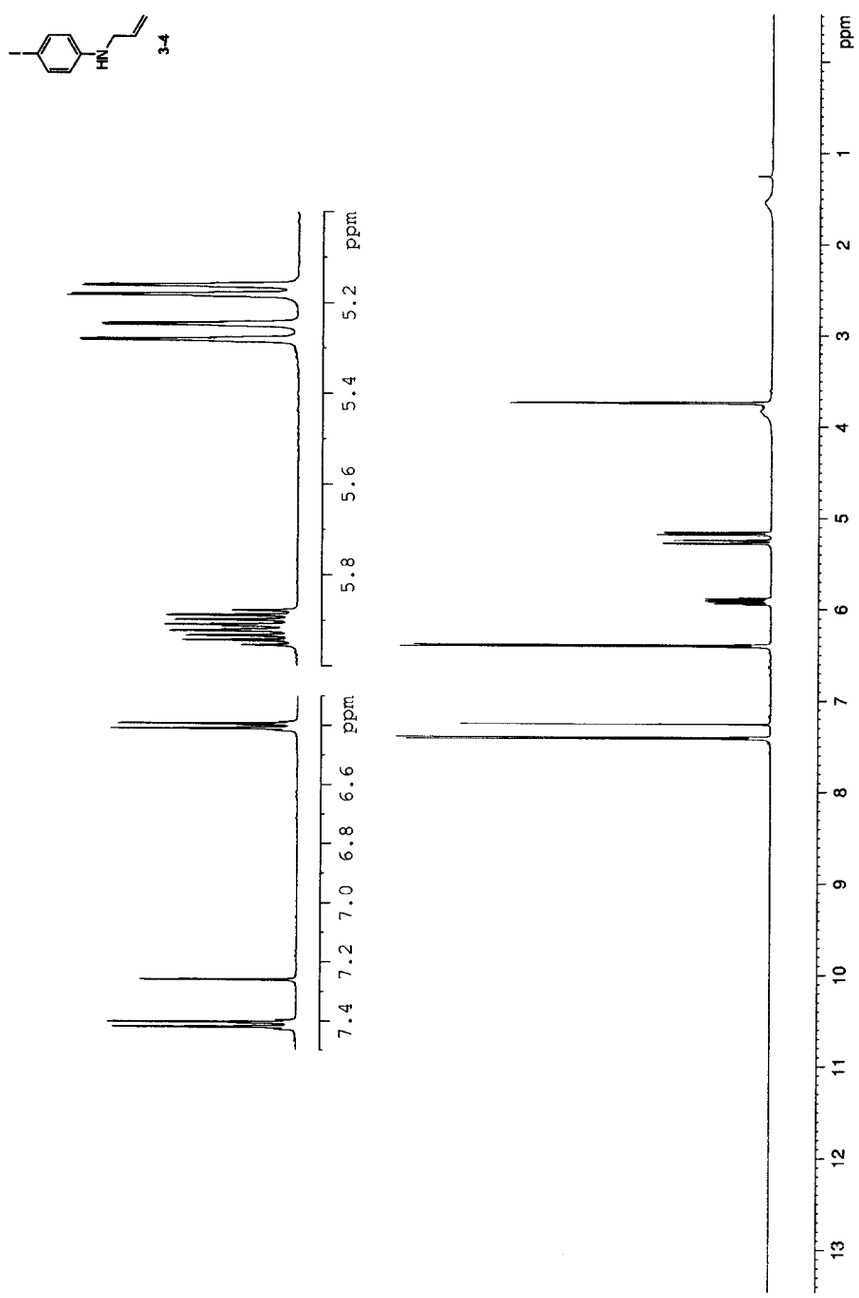

Figure 6-60. The 500 MHz ^{1}H NMR of compound **3-4** in $CDCl_3$.

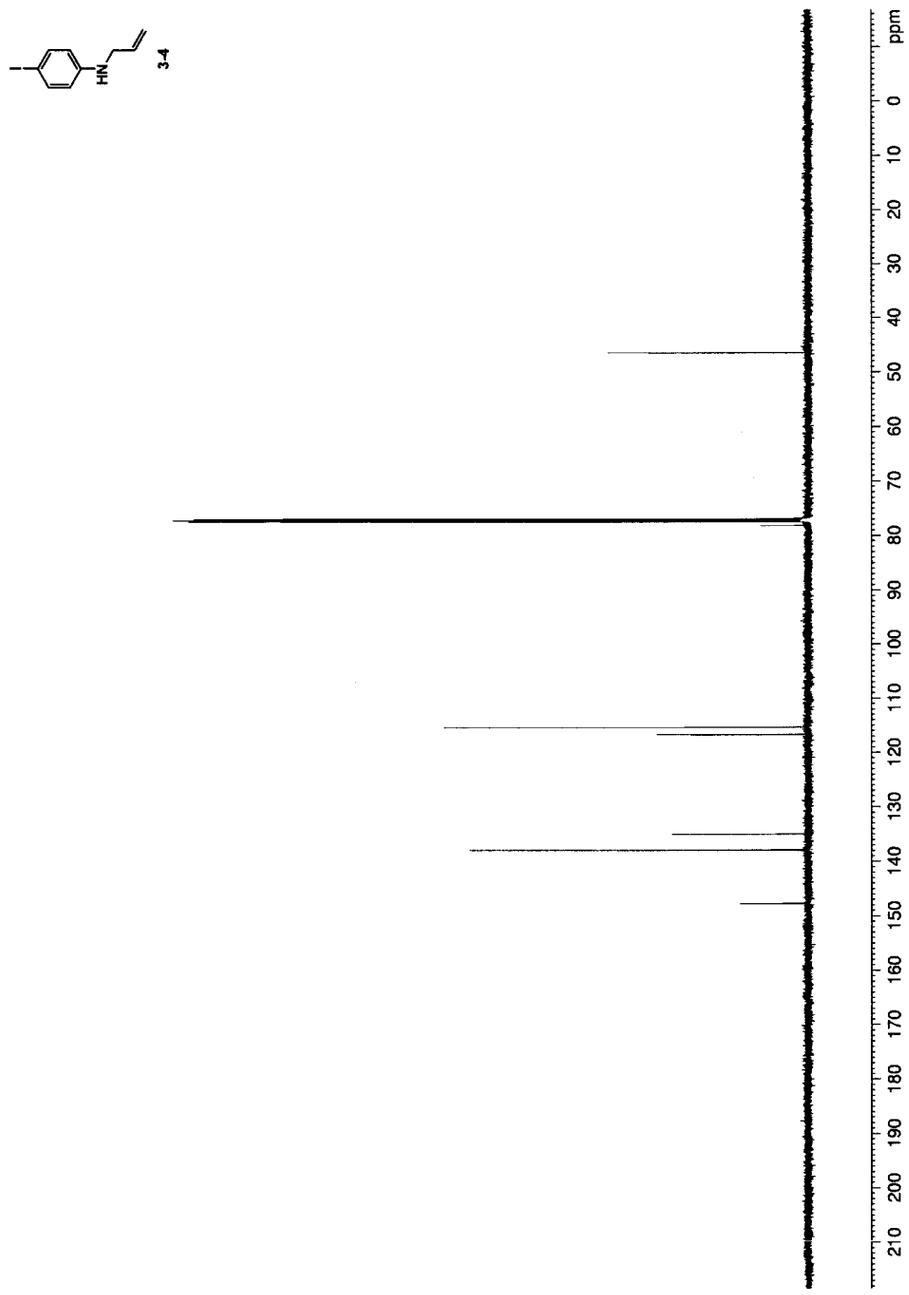

Figure 6-61. The 125 MHz ^{1}H decoupled ^{13}C NMR spectrum of compound **3-4** in $CDCl_3$.

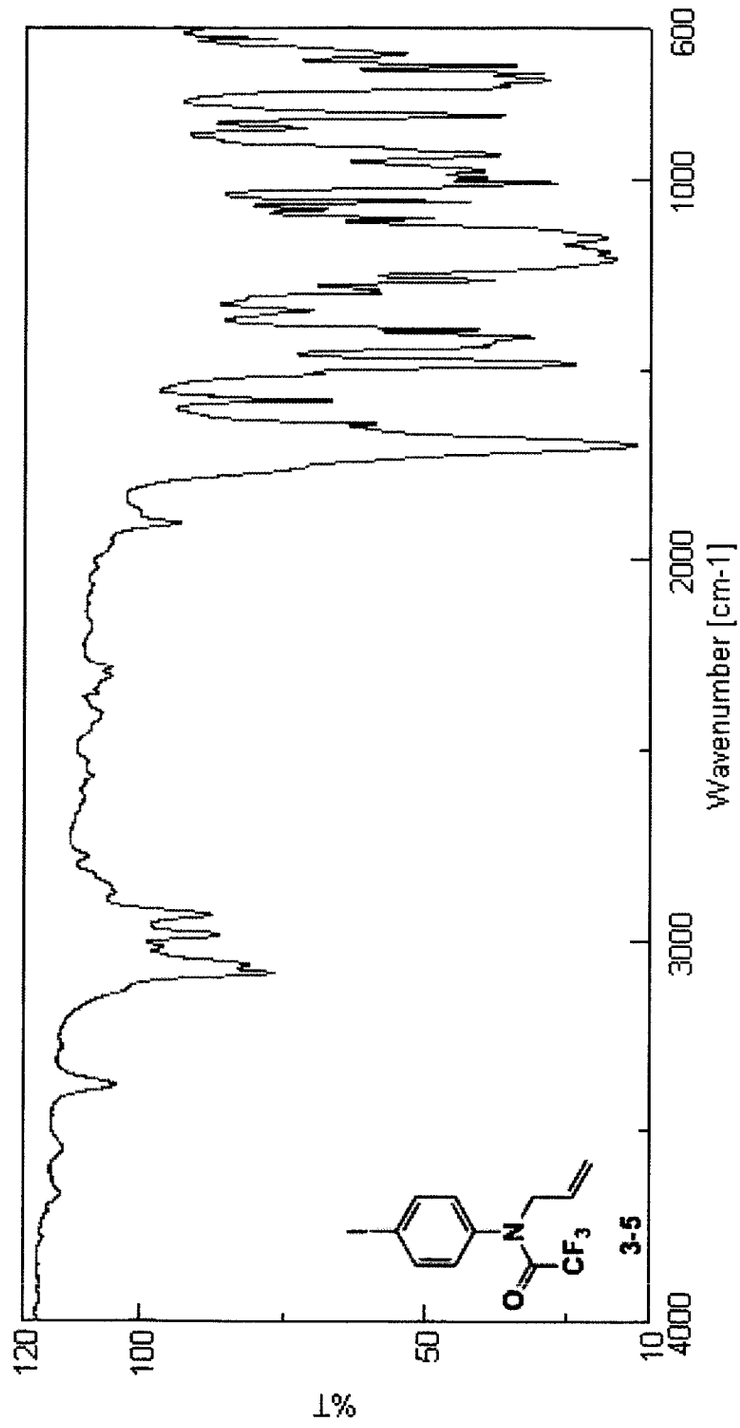

Figure 6-62. The thin film IR spectrum of compound **3-5**.

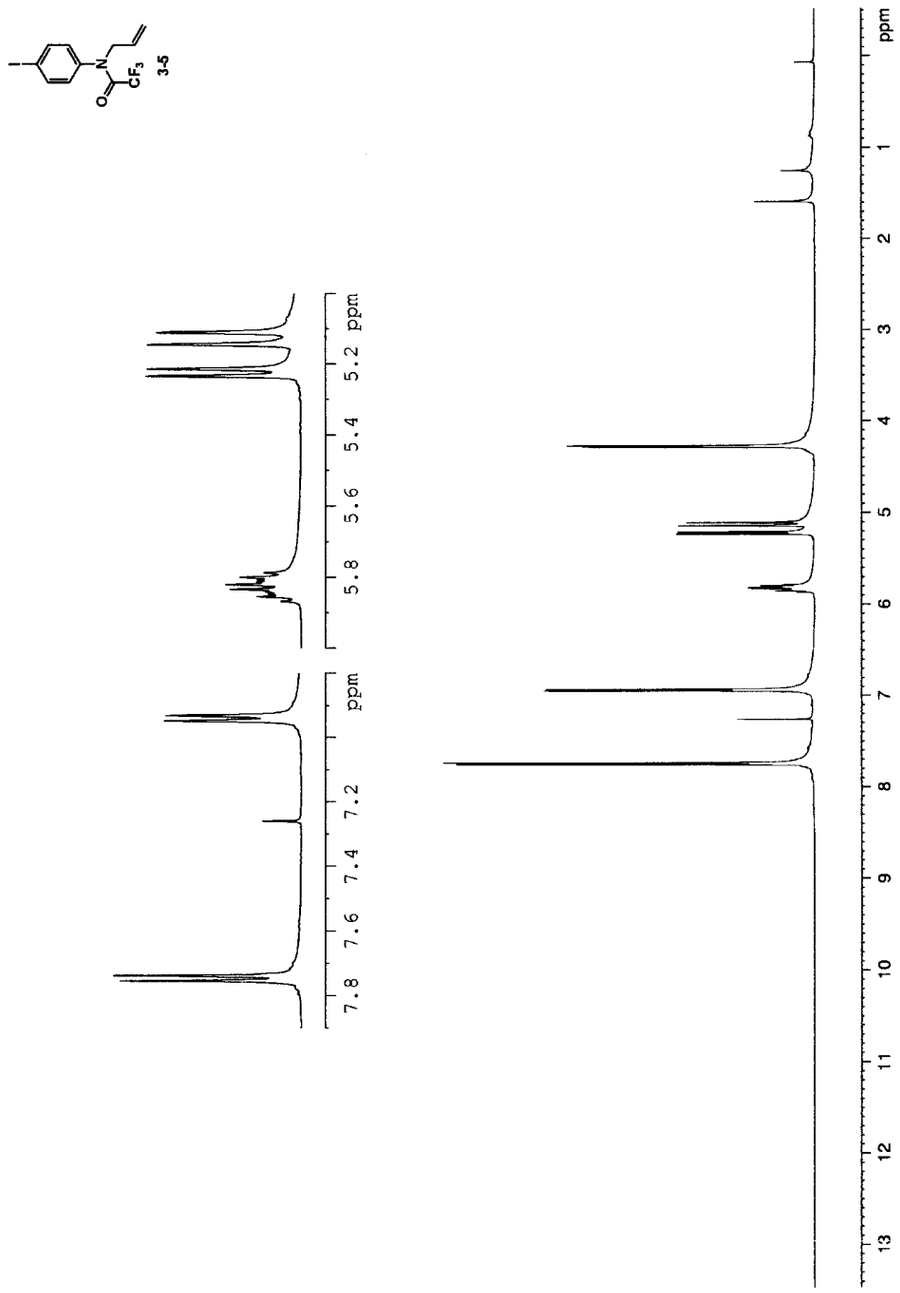

Figure 6-63. The 500 MHz ^{1}H NMR spectrum of compound **3-5** in $CDCl_3$.

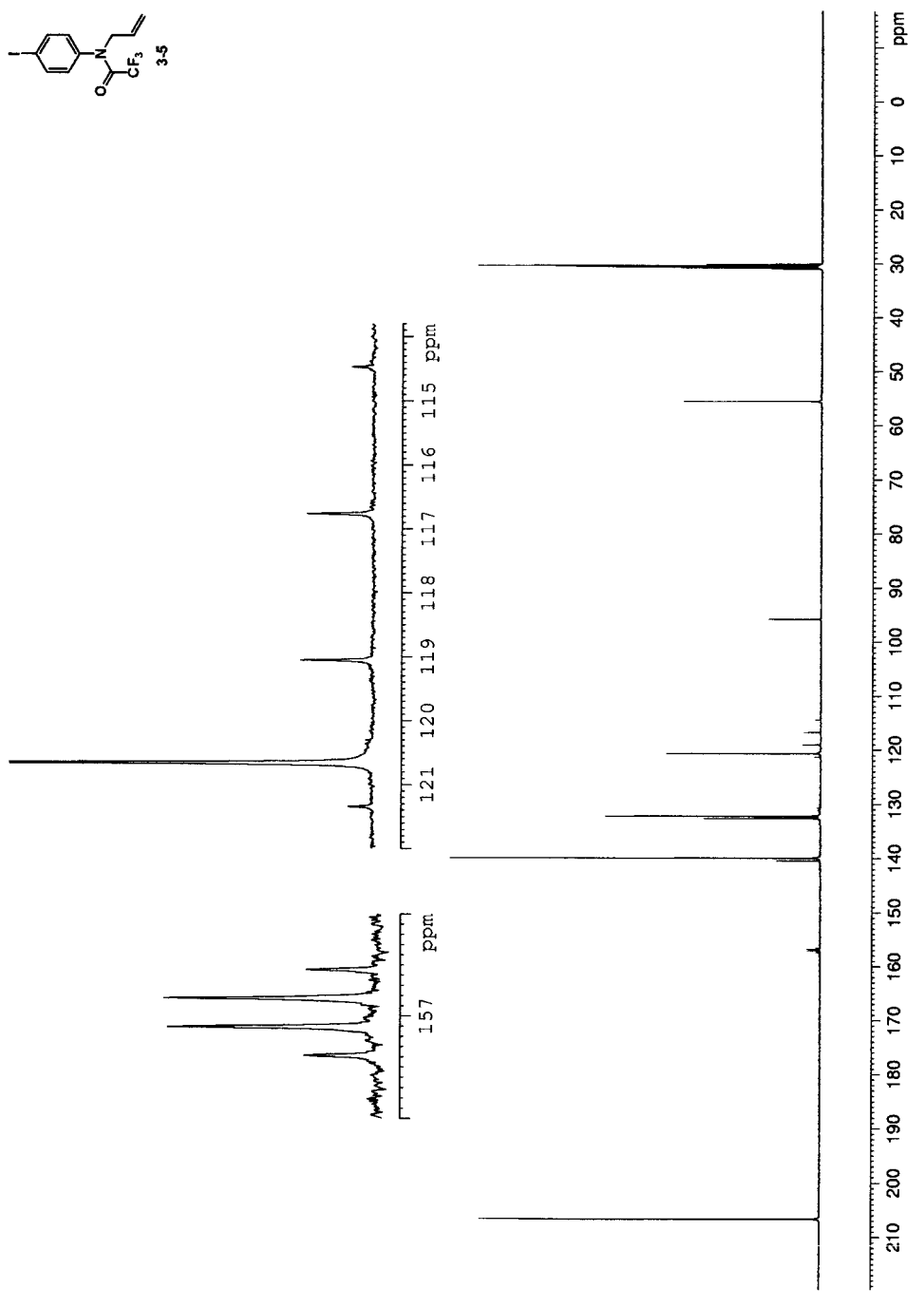

Figure 6-64. The 125 MHz ^{1}H decoupled ^{13}C NMR spectrum of compound **3-5** in acetone-d_6.

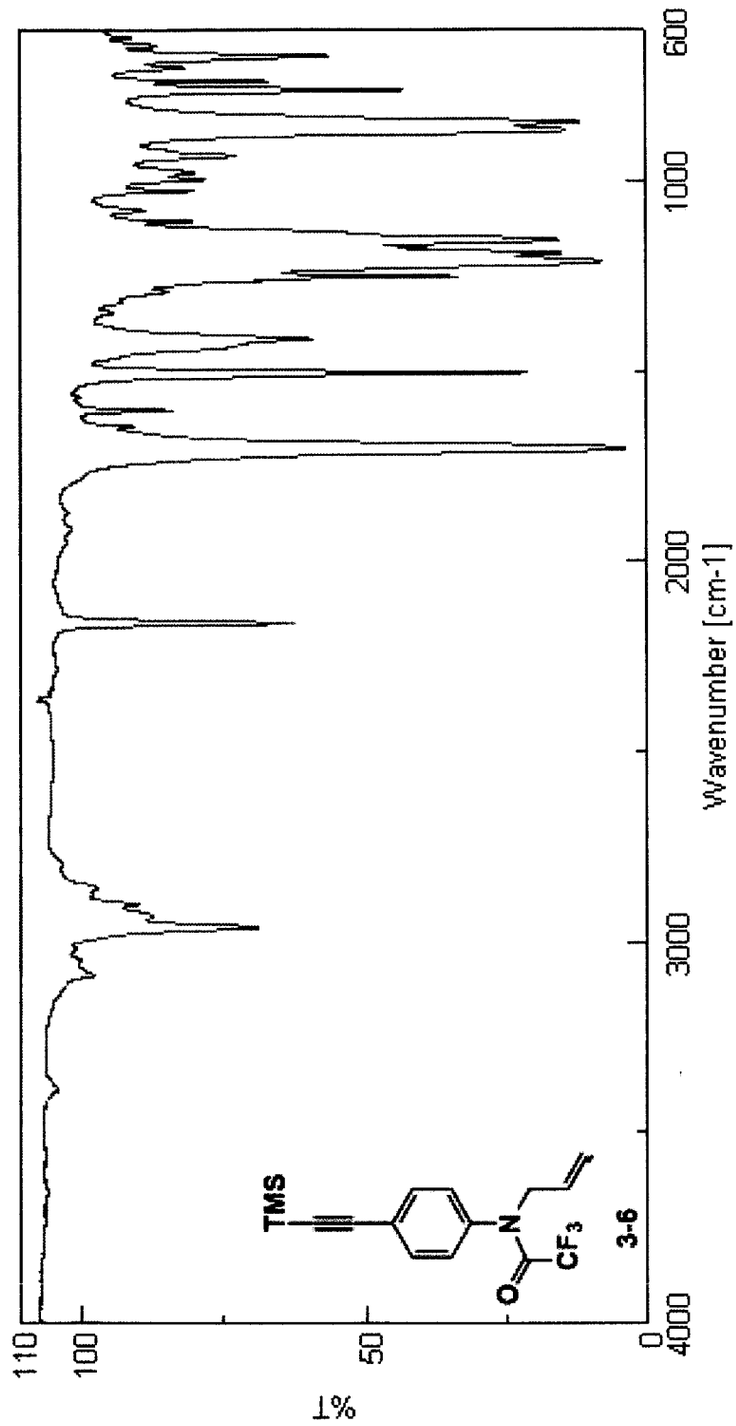

Figure 6-65. The thin film IR spectrum of compound **3-6**.

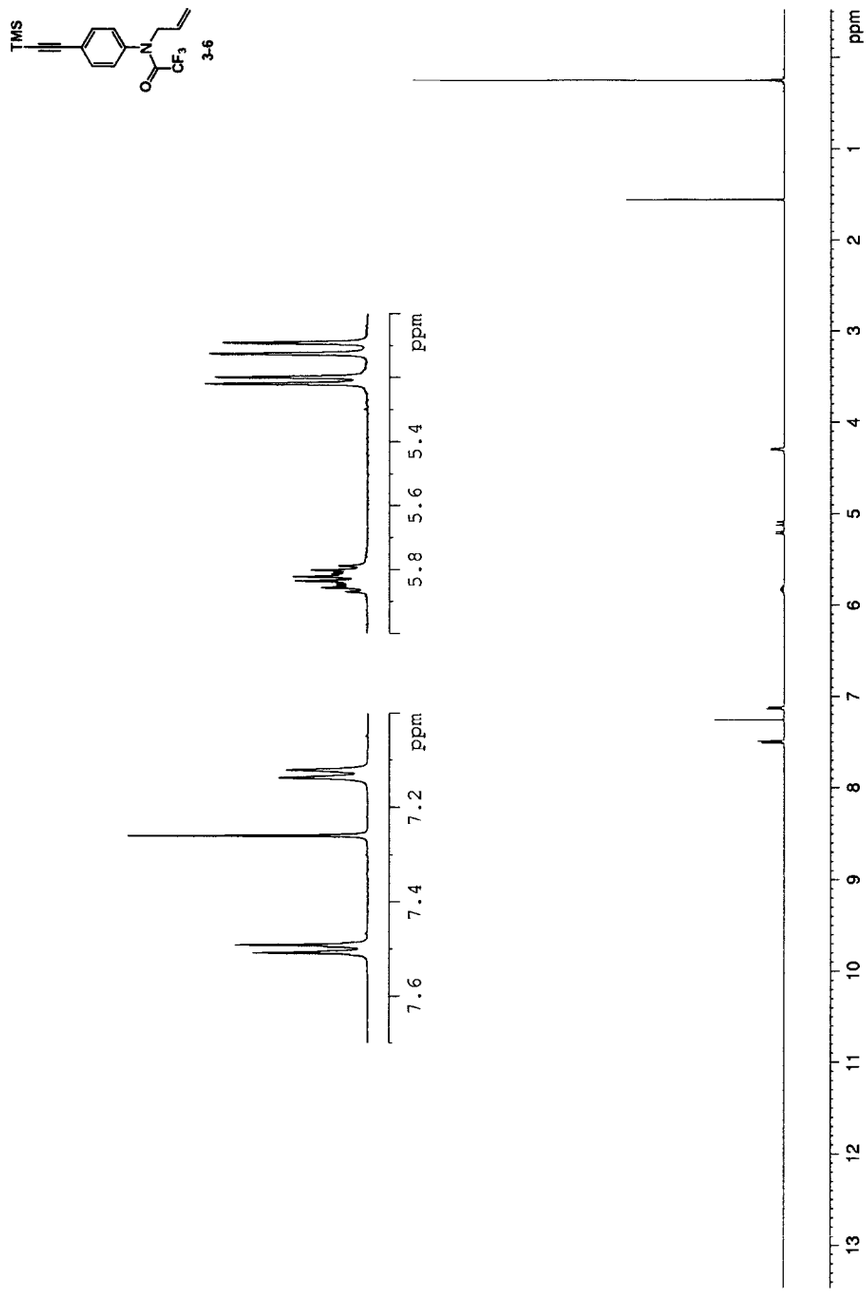

Figure 6-66. The 500 MHz ^{1}H NMR spectrum of compound **3-6** in $CDCl_3$.

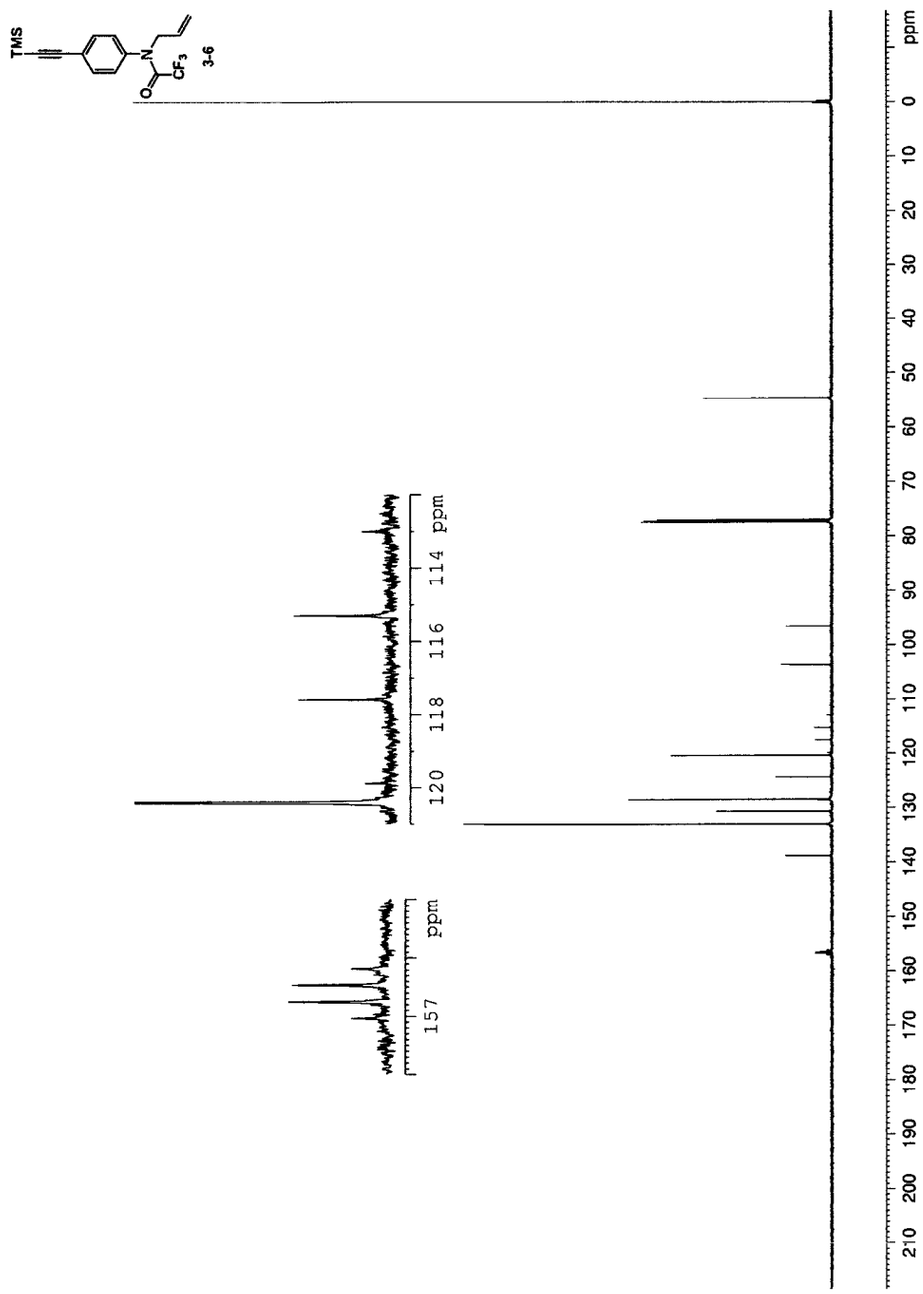

Figure 6-67. The 125 MHz ^{1}H decoupled ^{13}C NMR spectrum of compound **3-6** in $CDCl_3$.

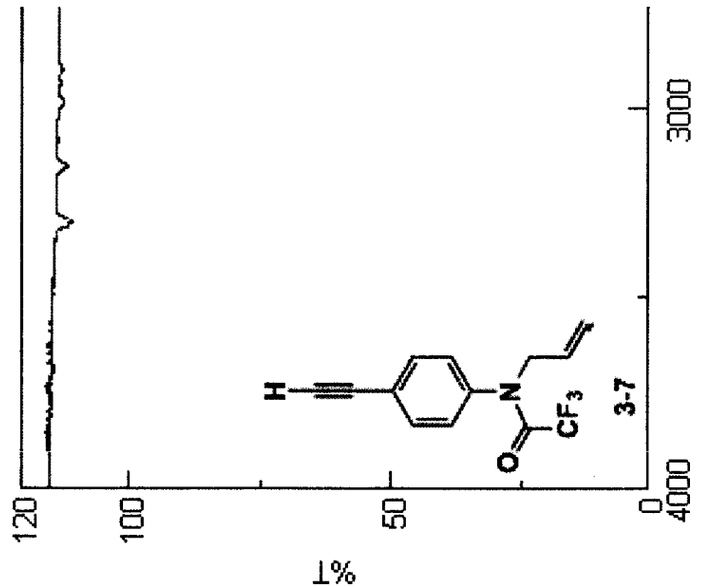

Figure 6-68. The thin film IR spectrum of compound **3-7**.

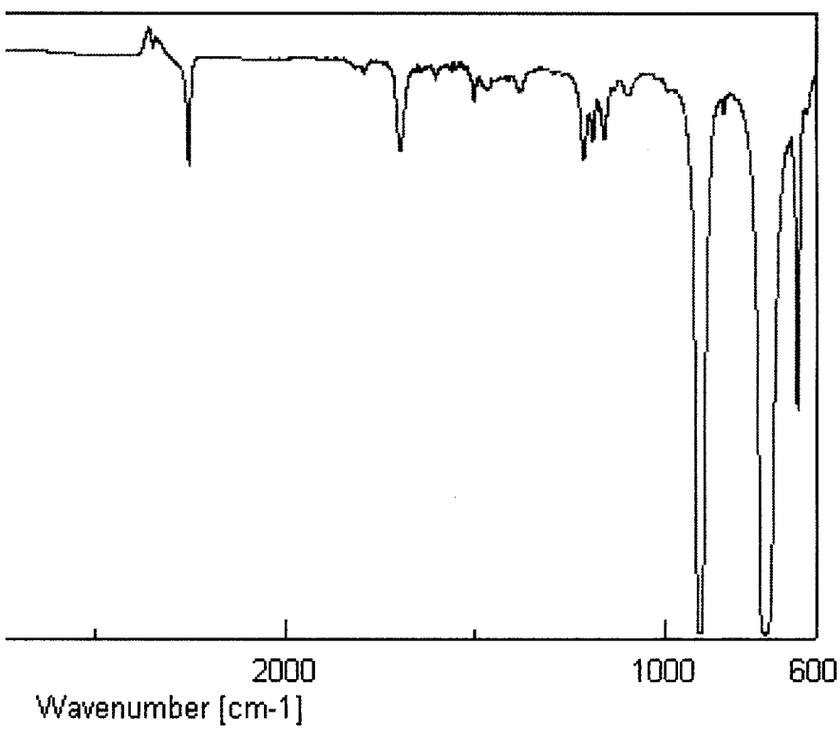
2000
1000
600
Wavenumber [cm-1]

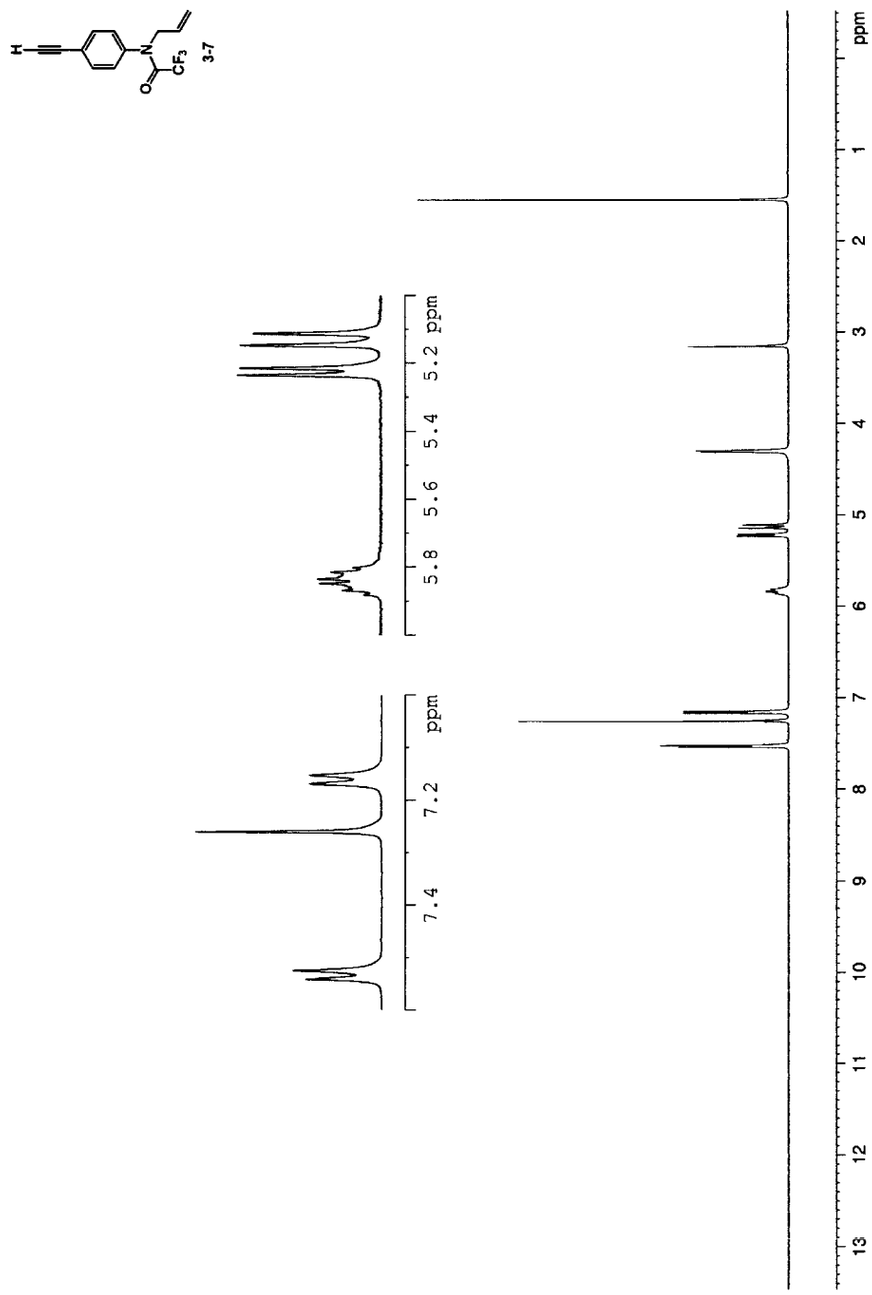

Figure 6-69. The 500 MHz ^{1}H NMR spectrum of compound **3-7** in $CDCl_3$.

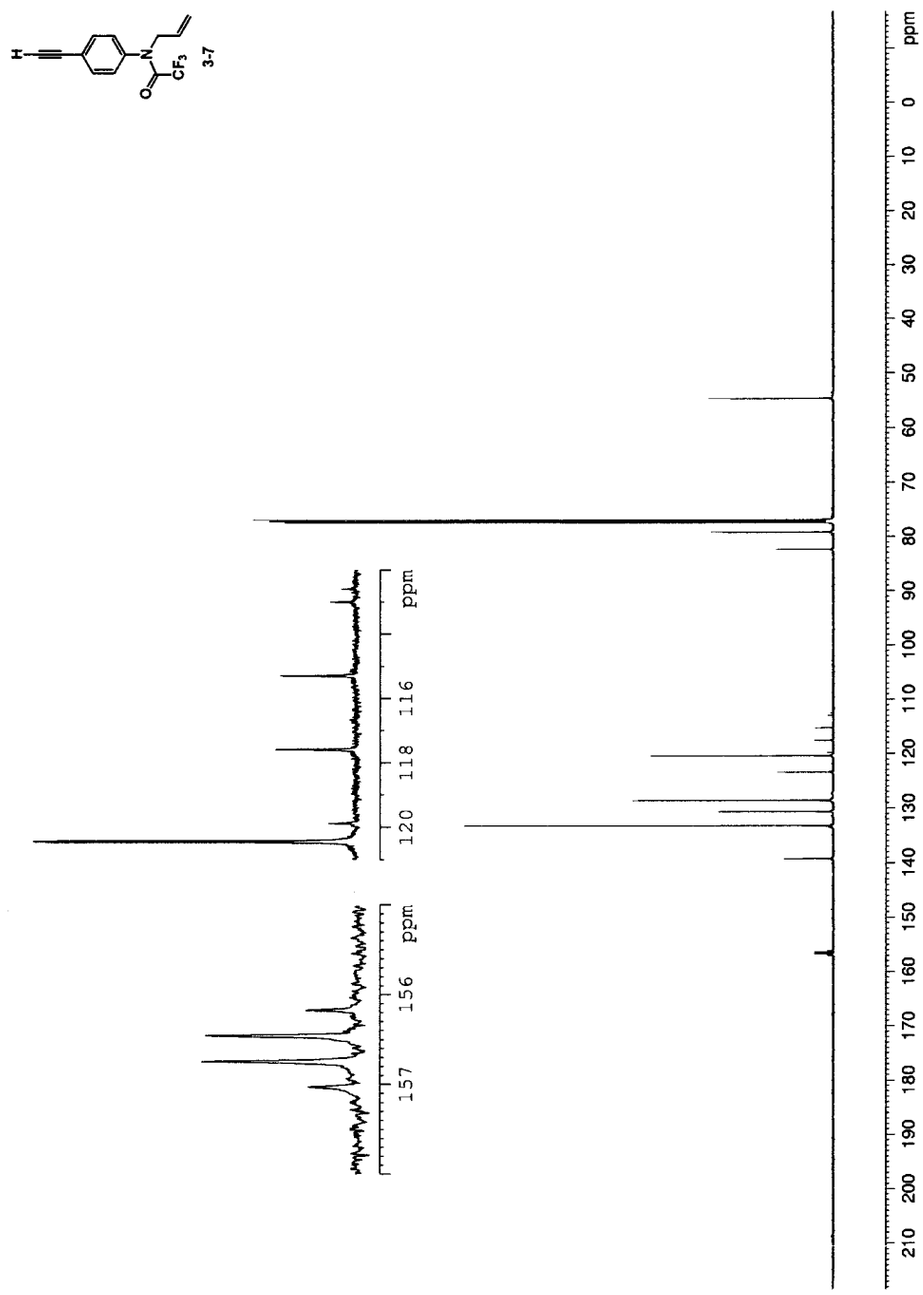

Figure 6-70. The 125 MHz ^{1}H decoupled ^{13}C NMR spectrum of compound **3-7** in $CDCl_3$.

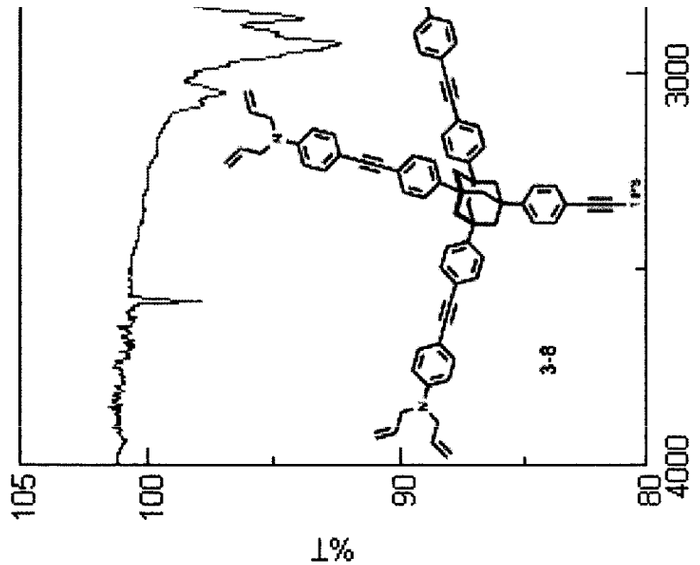

Figure 6-71. The thin film IR spectrum of compound **3-8**.

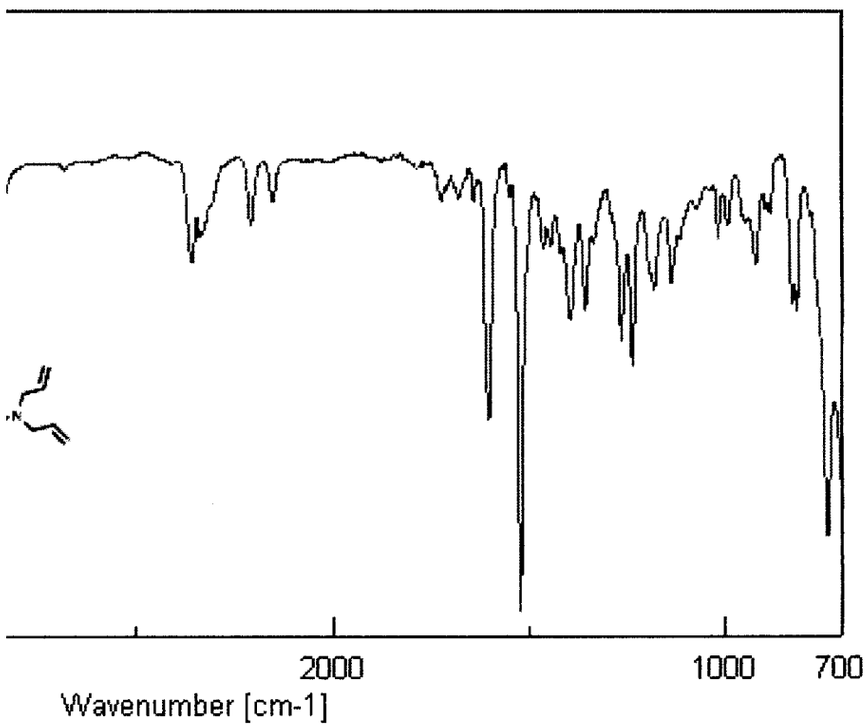
2000
1000
700
Wavenumber [cm-1]

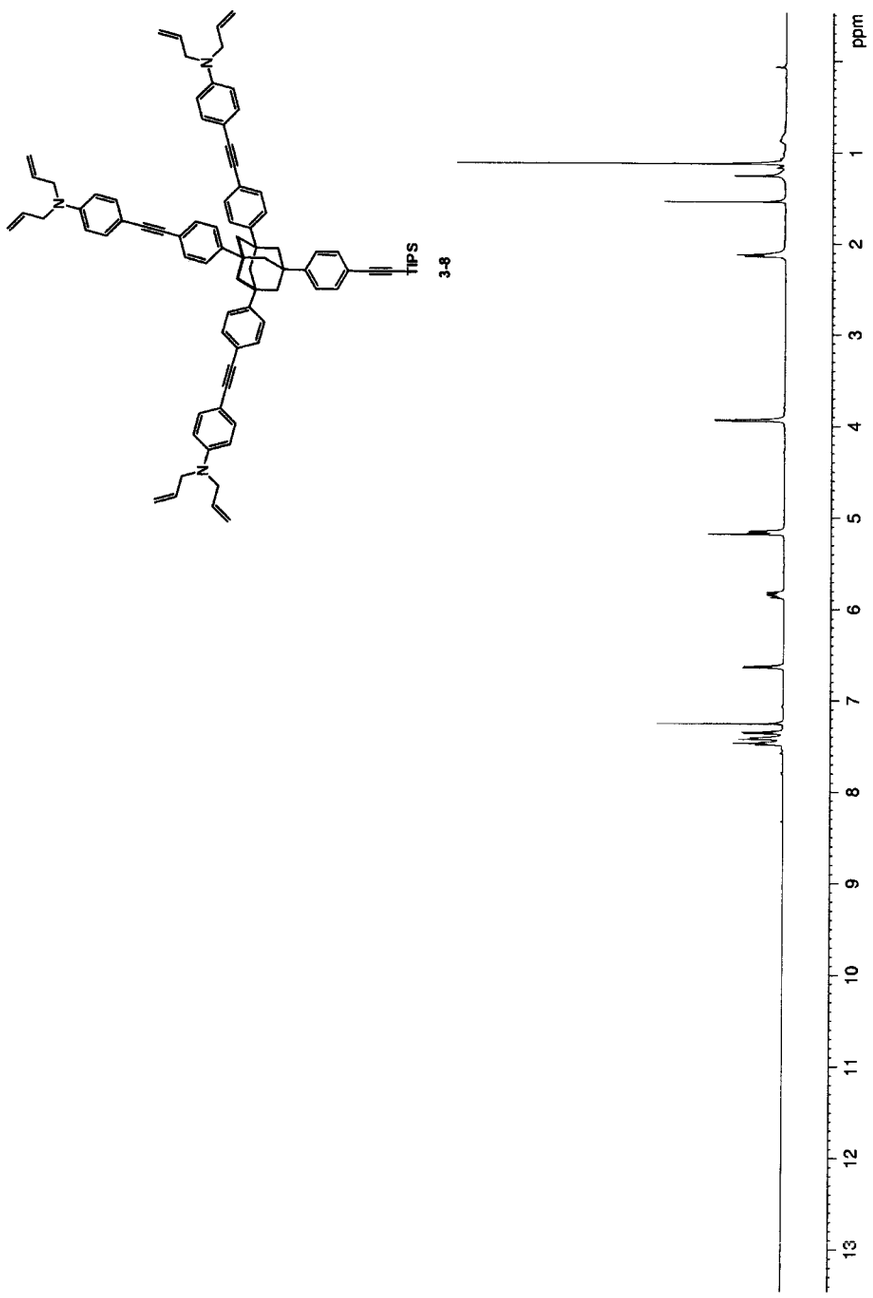

Figure 6-72. The 500 MHz ^{1}H NMR spectrum of compound **3-8** in $CDCl_3$.

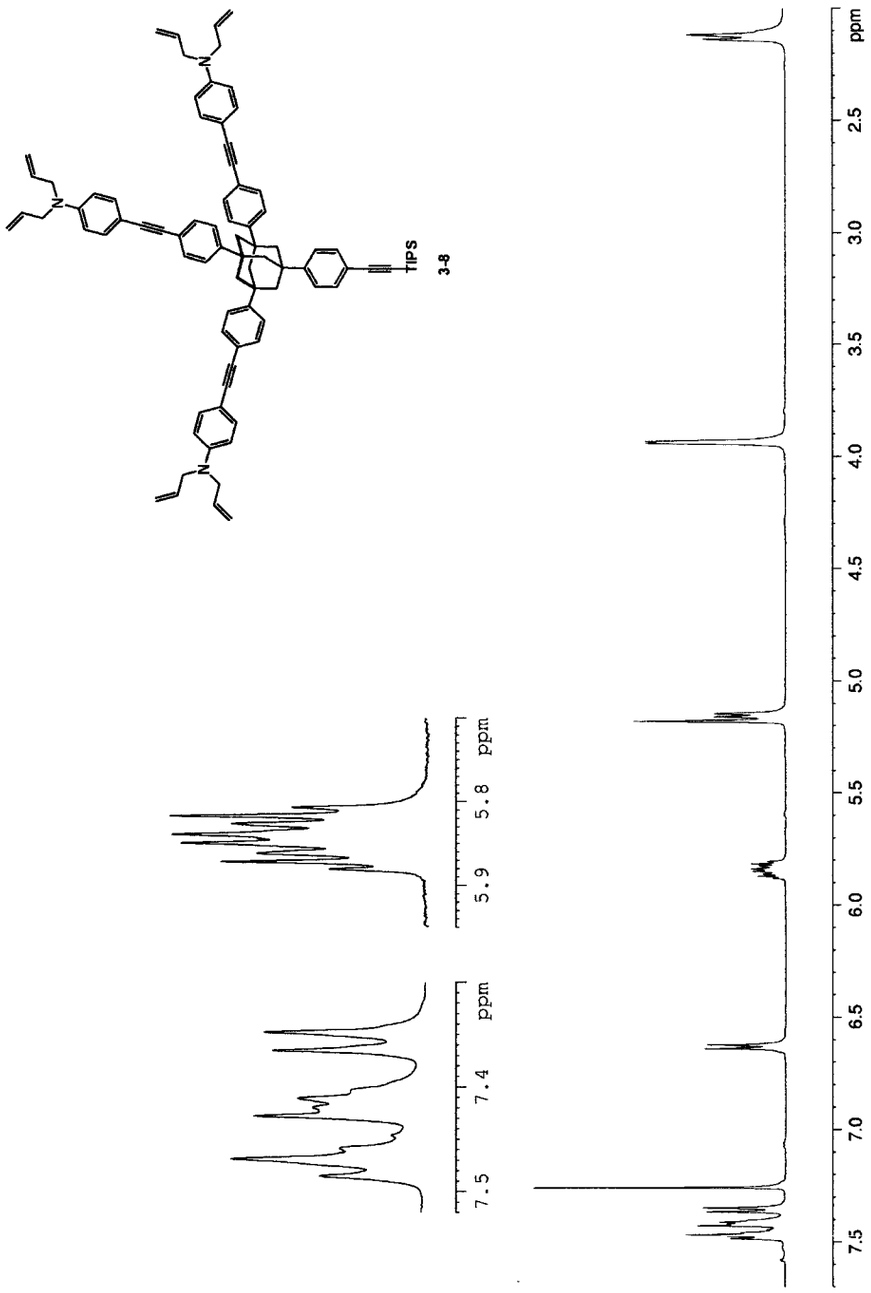

Figure 6-73. The 500 MHz ^{1}H NMR spectrum of compound **3-8** in $CDCl_3$.

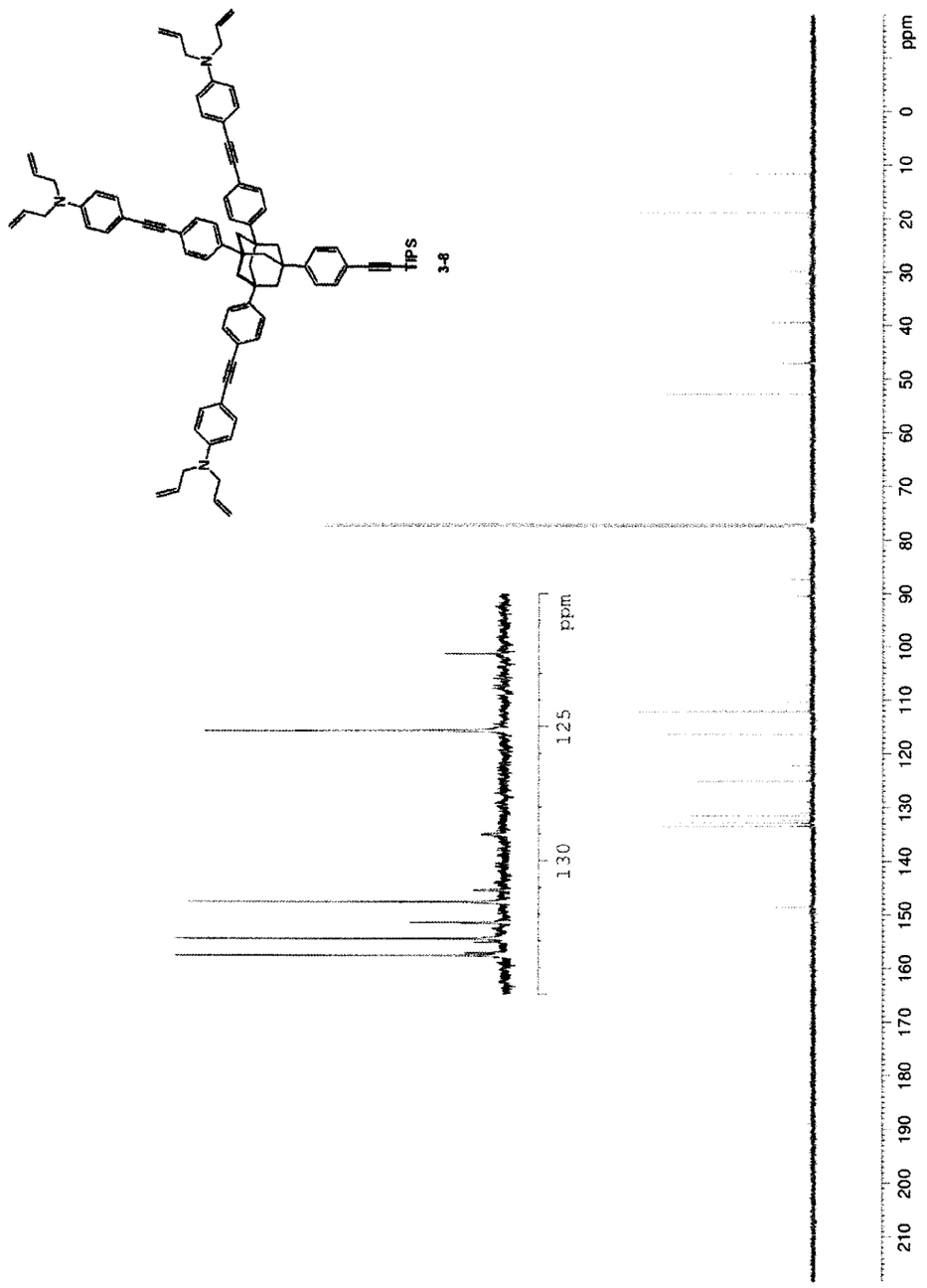

Figure 6-74. The 125 MHz ^{1}H decoupled ^{13}C NMR spectrum of compound **3-8** in $CDCl_3$.

Bibliography:

Abbondanzieri, E. A.; Greenleaf, W. J.; Shaevitz, J. W.; Landick, R.; Block, S. M. "Direct Observation of Base-Pair Stepping by RNA Polymerase" *Nature* **2005**, *438*, 460–465.

Agilent Technologies (Santa Clara, CA). "Hydogen Flame-Annealing"

Albrecht, C.; Blank, K.; Lalic-Multhaler, M.; Hirler, S.; Mai, T.; Gilbert, I.; Schiffmann, S.; Bayer, T.; Clausen-Schaumann, H.; Gaub, H. E. "DNA: A Programmable Force Sensor" *Science* **2003**, *301*, 367–370.

Ali, M. B.; Ondarçuhu, T.; Brust, M.; Joachim, C. "Atomic Force Microscope Tip Nanoprinting of Gold Nanoclusters" *Langmuir* **2002**, *18*, 872–876.

Allen, S.; Chen, X.; Davies, J.; Davies, M. C.; Dawkes, A. C.; Edwards, J. C.; Roberts, C. J.; Sefton, J.; Tendler, S. J.; Williams, P. M. "Detection of Antigen–Antibody Binding Events with the Atomic Force Microscope" *Biochemistry* **1997**, *36*, 7457–7463.

Angus, J. C.; Will, H. A.; Stanko, W. S. "Growth of Diamond Seed Crystals by Vapor Deposition" *J. Appl. Phys.* **1968**, *39*, 2915–2922.

Argoitia, A.; Kovach, C. S.; Angus, J. C. Hot-Filament CVD Methods. In *Handbook of Industrial Diamonds and Diamond Films*; Prelas, M. A., Popovici, G., Bigelow, L. K., Eds.; Marcel Dekker Inc.: New York, 1998; pp. 797–816.

Arnold, R.; Azzam, W.; Terfort, A.; Wöll, C. "Preparation, Modification, and Crystallinity of Aliphatic and Aromatic Carboxylic Acid Terminated Self-Assembled Monolayers" *Langmuir* **2002**, *18*, 3980–3992.

Auletta, R.; de Jong, M. R.; Mulder, A.; van Veggel, F. C. J. M.; Huskens, J.; Reinhoudt, D. N.; Zou, S.; Zapotoczny, S.; Schonherr, H.; Vancso, G. J.; Kuipers, L. " ß-Cyclodextrin Host-Guest Complexes Probed under Thermodynamic Equilibrium: Thermodynamics and AFM Force Spectroscopy" *J. Am. Chem. Soc.* **2004**, *126*, 1577–1584.

Bagus, P.; Weiss, K.; Schertel, A.; Wöll, C.; Braun, W.; Hellwig, C.; Jung, C. "Identification of Transitions into Rydberg States in the X-Ray Absorption Spectra of Condensed Long-Chain Alkanes" *Chem. Phys. Lett.* **1996**, *248*, 129–135.

Bain, C. D.; Troughton, E. B.; Tao, Y.-T.; Evall, J.; Whitesides, G. M.; Nuzzo, R. G. "Formation of Monolayer Films by the Spontaneous Assembly of Organic Thiols from Solution onto Gold" *J. Am. Chem. Soc.* **1989**, *111*, 321–325.

Balgar, T.; Bautista, R.; Hartmann, N.; Hasselbrink, E. "An AFM study of the Growth Kinetics of the Self-Assembled Octadecylsiloxane Monolayer on Oxidized Silicon" *Surf. Sci.* **2003**, *532*, 963–969.

Barrera, N. P.; Ormond, S. J.; Henderson, R. M.; Murrell-Lagnado, R. D.; Edwardson, J. M. "AFM Imaging Demonstrates That $P2X_2$ Receptors Are Trimers, But That $P2X_6$ Receptor Subunits Do Not Oligomerize" *J. Biol. Chem.* **2005**, *180*, 10759–10765.

Bell, G. I. "Models for the Specific Adhesion of Cells to Cells" *Science* **1978**, *200*, 618–627.

Berquand, A.; Xia, N. Castner, D. G.; Clare, B. H.; Abbott, N. L.; Dupres, V.; Adriaensen, Y.; Dufrene, Y. F. "Antigen Binding Forces of Single Antilysozyme Fv Fragments Explored by Atomic Force Microscopy" *Langmuir* **2005**, *21*, 5517–5523.

Bertin, P. A.; Georganopoulou, D.; Liang, T.; Eckermann, A. L.; Wunder, M.; Ahrens, M. J.; Blackburn, G. F.; Meade, T. J. "Electroactive Self-Assembled Monolayers on Gold via Bipodal Dithiazepane Anchoring Groups" *Langmuir* **2008**, *24*, 9096–9101.

Binnig, G.; Despont, M.; Drechsler, U.; Häberle, W.; Lutwyche, M.; Vettiger, P.; Mamin, H. J.; Chui, B. W.; Kenny, T. W. "Ultrahigh-Density Atomic Force Microscopy Data Storage with Erase Capability" *Appl. Phys. Lett.* **1999**, *74*, 1329–1331.

Binnig, G.; Rohrer, H.; Gerber, C.; Weibel, E. "Atomic Force Microscope" *Phys. Rev. Lett.* **1986**, *56*, 930–933.

Birrell, J.; Gerbi, J.E.; Auciello, O.; Gibson, J. M.; Johnson, J.; Carlisle, J. A. "Interpretation of the Raman Spectra of Ultrananocrystalline Diamond" *Diam. Relat. Mater.* **2005**, *14*, 86–92.

Bonaccurso, E.; Gillies, G. "Revealing Contamination on AFM Cantilevers by Microdrops and Microbubbles" *Langmuir* **2004**, *20*, 11824–11827.

Bough, B.; Northrop, B. H.; Schmidt, J. J.; Tseng, H.-R.; Houk, K. N.; Stoddart, J. F.; Ho, C.-M. "Evaluation of Synthetic Linear Motor-Molecule Actuation Energetics" *Proc. Nat. Acad. Sci.* **2006**, *103*, 8583–8588.

Bradford, D. C.; Hutter, E.; Fendler, J. H.; Roy, D. "Surface-Enhanced Infrared Ellipsometry of Self-Assembled Undecane Thiol and Dodecanethiol Monolayers on Disordered Gold Nanoisland Substrates" *J. Phys. Chem. B* **2005**, *109*, 20914–20922.

Bragg, W. H.; Bragg, W. L. "The Structure of the Diamond" *Proc. R. Soc. Lond. A* **1913**, *89*, 277–291.

Brandriss, S.; Margel, S. "Synthesis and Characterization of Self-Assembled Hyddrophobic Monolayer Coatings on Silica Colloids" *Langmuir* **1993**, *9*, 1232–1240.

Brogan, K. L.; Shin, J. H.; Schoenfisch, M. H. "Influence of Surfactants, and Antibody Immobilization Strategy on Reducing Nonspecific Protein Interactions for Molecular Recognition Force Microscopy" *Langmuir* **2004**, *20*, 9729–9735.

Brunner, J. "New Photolabeling and Crosslinking Methods" *Annu. Rev. Biochem.* **1993**, *62*, 483–514.

Bryant, Z.; Stone, M. D.; Gore, J.; Smith, S. B.; Cozzarelli, N. R.; Bustamante, C. "Structural Transitions and Elasticity from Torque Measurements on DNA" *Nature* **2003**, *424,* 338–341.

Burnham, N. A.; Dominguez, D. D.; Mowery, R. L.; Colton, R. J. "Probing the Surface Forces of Monolayer Films with an Atomic-Force Microscope" *Phys. Rev. Lett.* **1990**, *64*, 1931–1934.

Bustamante, C. "*In Singulo* Biochemistry: When Less Is More" *Annu. Rev. Biochem.* **2008**, *77*, 45–50.

Casson, B. D.; Bain, C. D. "Determination of the Optical Properties of Monolayers on Water" *Langmuir* **1997**, *13*, 5465–5469.

Cecconi, C.; Shank, E. A.; Bustamante, C.; Marqusee, S. "Direct Observation of the Three-State Folding of a Single Protein Molecule" *Science* **2005**, *309*, 2057–2060.

Charvin, G.; Allemand, J.-F.; Strick, T. R.; Bensimon, D.; Croquette, V. "Twisting DNA: Single Molecule Studies" *Contemp. Physics* **2004**, *45*, 393–403.

Chen, A.; Moy, M. T. "Cross-linking of Cell Surface Receptors Enhances Cooperativity of Molecular Adhesion" *Biophys. J.* **2000**, *78*, 2814–2820.

Chidsey, C. E. D.; Loiacono, D. N. "Chemical Functionality in Self-Assembled Monolayers: Structural and Electrochemical Properties" *Langmuir* **1990**, *6*, 682–691.

Choudhuri, O.; Parekh, S. H.; Fletcher, D. A. "Reversible Stress Softening of Actin Networks" *Nature* **2007**, *445*, 295–298.

Cicero, R. L.; Chidsey, C. E. D.; Lopinski, G. P.; Wayner, D. D. M.; Wolkow, R. A. "Olefin Additions of H–Si(111): Evidence for a Surface Chain Reaction Initiated at Isolated Dangling Bonds" *Langmuir* **2002**, *18*, 305–307.

Cisneros, D. A.; Muller, D. J.; Daud, S. M.; Lakey, J. H. "An Approach to Prepare Membrane Proteins for Single-Molecule Imaging" *Angew. Chem. Int. Ed.* **2006**, *45*, 3252–3256.

Clausen-Schaumann, H; Seitz, M.; Krautbauer, R.; Gaub, H. E. "Force Spectroscopy with Single Bio-Molecules" *Curr. Opin. Chem. Biol.* **2000**, *4*, 524–530.

Colvita, P. E.; Streifer, J. A.; Sun, B.; Wang, X.; Warf, P.; Hamers, R. J. "Enhancement of Photochemical Grafting of Terminal Alkenes at Surfaces via Molecular Mediators: The Role of Surface-Bound Electron Acceptors" *J. Phys. Chem. C* **2008**, *112*, 5102–5112.

Dammer, U.; Popescu, O.; Wagner, P.; Anselmetti, D.; Guntherodt, H.-J., Misevic, G. N. "Binding Strength Between Cell Adhesion Proteoglycans Measured by Atomic Force Microscopy" *Science* **1995**, *267*, 1173–1175.

Davy, H. *Elements of Chemical Philosophy* Stuart and Murray: London, 1840; pp. 221–232.

Davydov, V. Y.; Kiselev, A. V.; Zhuravlex, L. T. "Study of the Sufarce and Bulk Hydroxyl Groups of Silica by Infra-red Spectra and D_2O-Exchange" *Trans. Faraday Soc.* **1964**, *60*, 2054–2264.

De Boer, B.; Meng, H.; Perepichka, D. F.; Zheng, J.; Frank, M. M.; Chabal, Y. J.; Bao, Z. "Synthesis and Characterization of Conjugated Mono- and Dithiol Oligomers and Characterization of Their Self-Assembled Monolayers" *Langmuir* **2003**, *19*, 4272–4284.

De Carli, P. S.; Jamieson, J. C. "Formation of Diamond by Explosive Shock" *Science* **1961**, *133*, 1821–1822.

Diederich, L.; Küttel, O. M.; Aebi, P.; Maillard-Schaller, E.; Fasel, R.; Schlapbach, L. "Photoelectron Emission from the Negative Electron Affinity Cesiated Natural Diamond (100) Surface" *Diamond Rel. Mater.* **1998**, *7*, 660–665.

Dupres, V.; Menozzi, F. D.; Locht, C.; Clare, B. H.; Abbott, N. L.; Cuenot, S.; Bompard, C.; Raze, D.; Dufrêne, Y. F. "Nanoscale Mapping and Functional Analysis of Individual Adhesins on Living Bacteria" *Nat. Methods* **2005,** *2*, 515–520.

Dürig, U.; Cross, G.; Despont, M.; Drechsler, U.; Häberle, W.; Lutwyche, M. I.; Rothuizen, H.; Stutz, R.; Widmer, R.; Vettiger, P.; Binnig, G. K.; King, W. P.; Goodson, K. E. "'Millipede' – An AFM Data Storage System at the Frontier of Nanotribology" *Tribol. Lett.***2000**, *9*, 25–32.

Duvigneau, J.; Schönherr, H.; Vancso, G. J. "Atomic Force Microscopy Based Thermal Lithography of Poly(*tert*-butylacrylate) Block Copolymer Films for Bioconjugation" *Langmuir* **2008**, *24*, 10825–10832.

Ebner, A.; Wildling, L.; Zhu, R.; Rankl, C.; Haselgrübler, T.; Hinterdorfer, P.; Gruber, H. J. "Functionalization of Probe Tips and Supports for Single-Molecule Recognition Force Microscopy" *Top. Curr. Chem.* **2008**, *285*, 29–76.

Fantner, G.E.; Oroudjev, E.; Schitter, G.; Golde, L. S.; Thurner, P.; Finch, M. M.; Turner, P.; Gutsmann, T.; Morse, D. E.; Hansma, H.; Hansma, P. K. "Sacrificial Bonds and Hidden Length: Unraveling Molecular Mesostructures in Tough Materials" *Biophys. J.* **2006**, *90*, 1411–1418.

Florin, E.-L., Moy, V. T.; Gaub, H. E. "Adhesion Forces Between Individual Ligand–Receptor Pairs" *Science* **1994**, *264*, 415–417.

Fritz, J.; Katopodis, A. G.; Kolbinger, F.; Ansemetti, D. "Force-Mediated Kinetics of Single P-Selectin/Ligand Complexes Observed by Atomic Force Microscopy" *Proc. Nat. Acad. Sci.* **1998**, *95*, 12283–12288.

Fujijira, M.; Okabe, Y.; Tani, Y.; Furugori, M.; Akiba, U. "A Novel Cleaning Method of Gold-Coated Atomic Force Microscope Tips for Their Chemical Modification" *Ultramicroscopy* **2000**, *82*, 181–191.

García, R.; San Paulo, A. "Attractive and Repulsive Tip-Sample Interaction Regimes in Tapping-Mode Atomic Force Microscopy" *Phys. Rev. B* **1999**, *60*, 4961–4967.

Garguilo, J. M.; Davis, B.A.; Buddie, M.; Köck, F. A. M.; Nemanich, R. J. "Fibrinogen Adsorption onto Microwave Plasma Chemical Vapor Deposited Diamond Films" *Diam. Rel. Mat.* **2004**, *13*, 595–599.

Giessibl, F. J. "Atomic Resolution of the Silicon (111)-(7x7) Surface by Atomic Force Microscopy" *Science* **1995**, *267*, 68–71

Giessibl, F. J.; Binnig, G. "Investigation of the (001) Cleavage Plane of Potassium Bromide with an Atomic Force Microscope at 4.2 K in Ultra-High Vacuum" *Ultramicroscopy* **1992**, *42*, 281–289.

Gilbert, Y.; Deghorain, M.; Wang, L.; Xu, B.; Polheimer, P. D.; Gruber, H. J.; Errington, J.; Hallet, B.; Haulot, X.; Verbelen, C.; Hols, P.; Dufrêne, Y. F. "Single-Molecule Force Spectroscopy and Imaging of the Vancomycin/D-Ala-D-Ala Interaction" *Nano Lett.* **2007**, *7*, 796–801.

Ginger, D. S.; Zhang, H.; Mirkin, C. A. "The Evolution of Dip-Pen Nanolithography" *Angew. Chem. Int. Ed.* **2004**, *43*, 30–45.

Goodwin, D. G.; Butler, J. E. Theory of Diamond Chemical Vapor Deposition In *Handbook of Industrial Diamonds and Diamond Films*; Prelas, M. A., Popovici, G., Bigelow, L. K., Eds.; Marcel Dekker Inc.: New York, 1998; pp. 546–586.

Gordon, M. L.; Cooper, G.; Morin, C.; Araki, T.; Turci, C. C.; Kaznatcheev, K.; Hitchcock, A. P. "Inner-Shell Excitation Spectroscopy of the Peptide Bond: Comparison of the C 1s, N 1s, and O 1s Spectra of Glycine, Glycyl-Glycine, and Glycyl-Glycyl-Glycine" *J. Phys. Chem. A* **2003**, *107*, 6144–6159.

Grandbois, M.; Beyer, M.; Rief, M.; Clausen-Schaumann, H.; Gaub, H. E. "How Strong Is a Covalent Bond?" *Science*, **1999**, *283*, 1727–1730.

Grasselli, J. G.; Snavely, M. K.; Bulkin, B. J. The Raman Effect. In *Chemical Applications of Raman Spectroscopy* Wiley New York 1981: 1–11.

Greenleaf, W. J.; Block, S. M. "Single-Molecule, Motion-Based DNA Sequencing Using RNA Polymerase" *Science*, **2006**, *313*, 801.

Gross, A. J.; Yu, S. S. C.; Downard, A. J. "Two-Component Mixed and Patterned Films on Carbon Surfaces Through the Photografting of Arylazides" *Langmuir* **2010** *ASAP*, DOI: 10.1021/la904442u.

Gross, L.; Mohn, F.; Moll, N.; Liljeroth, P.; Meyer, G. "The Chemical Structure of a Molecule Resolved by Atomic Force Microscopy" *Science* **2009**, *325*, 1110–1114.

Gryko, D. T.; Clausen, C.; Roth, K. M.; Dontha, N.; Bocian, D. F.; Kuhr, W. G.; Lindsey, J. S. "Synthesis of 'Porphyrin-Linker-Thiol' Molecules with Diverse Linkers for Studies of Molecular-Based Information Storage" *J. Org. Chem.* **2000**, *65*, 7345–7355.

Guay, D.; Stewart-Ornstein, J.; Zhang, X.; Hitchcock, A. P. "In Situ Spatial and Time-Resolved Studies of Electrochemical Reactions by Scanning Transmission X-Ray Microscopy" *Anal. Chem.* **2005**, *77*, 3479–3487.

Hacker, C. A.; Batteas, J. D.; Garno, J. C.; Marquez, M.; Richter, C. A.; Richter, L. J.; van Zee, R. D.; Zangmeister, C. D. "Sturctural and Chemical Characterization of Monofluoro-Substituted Oligo(phenylene–ethynylene) Thiolate Self-Assembled Monolayers on Gold" *Langmuir* **2004**, *20*, 6195–6205.

Hafner, J. H.; Cheung, C. L.; Woolley, A. T.; Lieber, C. M. "Structural and Functional Imaging with Carbon Nanotube AFM Probes" *Prog. Biophys. Mol. Biol.* **2001**, *77*, 73–110.

Hafner, J. H.; Cheung, C.-L.; Woolley, A. T.; Lieber, C. M. "Structural and Functional Imaging with Carbon Nanotube AFM Probes" *Prog. Biophys. Mol. Biol.* **2001**, *77*, 73–110.

Hansma, H. G.; Hoh, J. H. "Biomolecular Imaging with the Atomic Force Microscope" *Annu. Rev. Biophys. Biomol. Struct.* **1994**, *23*, 115–139.

Harris, A. L.; Chidsey, C. E. D.; Levinos, N. J.; Loiacono, D. N. "Monolayer Vibrational Spectroscopy by Infrared-Visible Sum Generation at Metal and Semiconductor Surfaces" *Chem. Phys. Lett.* **1987**, *141*, 350–356.

Härtl, A.; Schmich, E.; Garrido, J. A.; Hernando, J.; Catharino S. C. R.; Walter, S.; Feulner, P.; Kromka, A.; Steinmüller, D.; Stutzmann, M. "Protein-Modified Nanocrystalline Diamond Thin Films for Biosensor Applications" *Nature Mat.* **2004**, *3*, 736–742.

Haselgrübler, T.; Amerstorfer, A.; Schindler, H.; Gruber, H. J. "Synthesis and Applications of a New Poly(ethylene glycol) Derivative for the Crosslinking of Amines with Thiols" *Bioconj. Chem.* **1995**, *6*, 242–248.

Haubner, R.; Lux, B. "Diamond Growth by Hot-Filament Chemical Vapor Deposition: State of the Art" *Diamond Relat. Mater.* **1993**, *2*, 1277–1294.

Haugland, R. P. Chapter 5 Crosslinking and Photoactivatable Reagents. In *The Handbook: A Guide to Fluorescent Probes and Labeling Technologies*, 10th edition; Spence, M. T. Z.; Invitrogen Corp: USA, 2005, pp. 170–171.

Heister, K.; Zharnikov, M.; Grunze, M. "Characterization of X-Ray Induced Damage in Alkanethiolate Monolayers by High-Resolution Photoelectron Spectroscopy" *Langmuir* **2001**, *17*, 8–11.

Hiller, Y.; Gershoni, J. M.; Bayer, E. A.; Wilchek, M. "Biotin Binding to Avidin. Oligosaccharide Side Chain Not Required for Ligand Association" *Biochem. J.* **1987**, *248*, 167–171.

Himpsel, F. J.; Knapp, J. A.; Van Vechten, J. A.; Eastman, D. E. "Quantum Photoyield of Diamond (111)—A Stable Negative-Affinity Emitter" *Phys. Rev. B* **1979**, *20*, 624–627.

Hinterdorfer, P.; Baumgartner, W.; Gruber, H. J.; Schilcher, K.; Schindler, H. "Detection and Localization of Individual Antibody–Antigen Recognition Events by Atomic Force Microscopy" *Proc. Natl. Acad. Sci.* **1996**, *93*, 3477–3481.

Hinterdorfer, P.; Baumgartner, W.; Gruber, H. J.; Schilcher, K.; Schindler, H. "Detection and Localization of Individual Antibody-Antigen Recognition Events by Atomic Force Microscopy" *Proc. Nat. Acad. Sci.* **1996**, *93*, 3477–3481.

Hinterdorfer, P.; Dufrêne, Y. F. "Detection and Localization of Single Molecular Recognition Events Using Atomic Force Microscopy" *Nat. Methods* **2006**, *3*, 347–355.

Hoh, J. H.; Cleveland, J. P.; Prater, C. B.; Revel, J.-R.; Hansma, P. K. "Quantized Adhesion Detected with the Atomic Force Microscope" *J. Am. Chem. Soc.* **1992**, *114*, 4917–4918.

Hsiao, S. C.; Crow, A. K.; Lam, W. A.; Bertozzi, C. R.; Fletcher, D. A.; Francis, M. B. "DNA-Coated AFM Cantilevers for the Investigation of Cell Adhesion and the Patterning of Live Cells" *Angew. Chem. Int. Ed.* **2008**, *47*, 8473–8477.

Humlícek, J. Polarized Light and Ellipsometry. In *Handbook of Ellipsometry*. Tompkins, H. G.; Irene, E. A., Eds. William Andrew Publishing/Noyes: Norwich, New York, 2005; 1–19.

Huo, F.; Zheng, Z.; Zheng, G.; Giam, L. R.; Zhang, H.; Mirkin, C. A. "Polymer Pen Lithography" *Science*, **2008**, *321*, 1658–1660.

Hutter, J. L.; Bechhoefer, J. "Calibration of Atomic Force Microscope Tips" *Rev. Sci. Instr.* **1993**, *64,* 1868–1873.

IBM The Millipede Project: A Nanomechanical AFM-based Data Storage System. http://www.zurich.ibm.com/st/storage/concept.html (accessed Dec 9, 2009).

Inagaki, M.; Kaneko, K.; Nishizawa, T. "Nanocarbons – recent research in Japan" *Carbon,* **2004**, *42*, 1401.

Ishijima, A.; Yanagida, T. "Single Molecule Nanobioscience" *Trends Biochem. Sci.* **2001**, *26*, 438–444.

Ivanisevic, A.; Im, J.-H.; Lee, K.-B.; Park, S.-J.; Demers, L. M.; Watson, K. J.; Mirkin, C. A. "Redox-Controlled Orthogonal Assembly of Charged Nanostructures" *J. Am. Chem. Soc.* **2001**, *123*, 12424–12425.

Ivanov, V. B.; Behnisch, J.; Hollander, A.; Mehdorn, F.; Zimmermann, H. "Determination of Functional Groups on Polymer Surfaces Using Fluorescence Labeling" *Surf. Interface Anal.* **1996**, *24*, 257–262.

Jackson, F.; Weisstein, E. W. "Tetrahedron" From MathWorld—A Wolfram Web Resource: http://mathworld.wolfram.com/Tetrahedron.html. (accessed Dec 9, 2009)

Jensen, K. F. Fundamental of Chemical Vapor Deposition. In *Chemical Vapor Deposition Principles and Applications*; Hitchman, M. L, Jensen, K. F., Eds.; Academic Press: San Diego, CA, 1993; 31–66.

Jin, Y.; Wang, K.; Tan, W.; Wu, P.; Wang, Q.; Huang, H.; Huang, S.; Tang, Z.; Guo, Q. "Monitoring Molecular Beacon/DNA Interactions Using Atomic Force Microscopy" *Anal. Chem.* **2004**, *76*, 5721–5725.

Joachim, C.; Gimzewski, J. K. "Nanoscience of Single Molecules Using Local Probes" *Science* **1999**, *283*, 1683–1688.

Kang, J. F.; Ulman, A.; Liao, S.; Jordan, R.; Yang, G.; Liu, G. "4'-Substituted-4-mercaptobiphenyls on Gold and Silver Surfaces" *Langmuir* **2001**, *17*, 95–106.

Keana, J. F. W.; Cai, S. X. "New Reagents for Photoaffinity Labeling: Synthesis and Photolysis of Functionalized Perfluorophenyl Azides" *J. Org. Chem.* **1990**, *55*, 3640–3647.

Kedrov, A.; Ziegler, C.; Janovjak, H.; Kühlbrandt, W.; Müller, D. J. "Controlled Unfolding and Refolding of a Single Sodium-Proton Antiporter Using Atomic Force Microscopy" *J. Mol. Biol.* **2004**, *340*, 1143–1152.

Khakh, B. S. "Molecular Physiology of P2X Receptors and ATP Signalling at Synapses" *Nat. Rev. Neurosci.* **2001**, *2*, 165–174.

Khakh, B. S.; North, R. A. "P2X Receptors as Cell-Surface ATP Sensors in Health and Disease" *Nature Rev.* **2006**, *442*, 527–532.

Kim, J.; Shon, H. K.; Jung, D.; Moon, D. W.; Han, S. Y.; Lee, T. G. "Quantitative Chemical Derivatization Technique in Time-Of-Flight Secondary Ion Mass Spectrometry for Surface Amine Groups on Plasma-Polymerized Ethylenediamine Film. *Anal. Chem.* **2005**, *77*, 4137–4141.

Kim, K.-H.; Moldovan, N.; Ke, C.; Espinosa, H. D.; Xiao, X.; Carlisle, J. A.; Auciello, O. "Novel Ultrananocrystalline Diamond for High-Resolution Low-Wear Nanolithographic Techniques" *Small* **2005**, *1*, 866–874.

Knight, D. S.; White, W. B. "Characterization of Diamond Films by Raman Spectroscopy" *J. Mater. Res.* **1989**, *4*, 385–393

Knoll, A.; Bächtold, P.; Bonan, J.; Cherubini, G.; Despont, M.; Dreschsler, U.; Dürig, U.; Gotsmann, B.; Häberle, W.; Hagleitner, C.; Jubin, D.; Lantz, M. A.; Pantazi, A.; Pozidis, H.; Rothuizen, H.; Sebastian, A.; Stutze, R.; Vettiger, P.; Wiesmann, D.; Eleftherious, E. S. "Integrating Nanotechnology into a Working Storage Device" *Microelectron. Eng.* **2006**, *83*, 1692–1697.

Kolb, D. M. "Reconstruction Phenomena at Metal-Electrolyte Interfaces" *Prog. Surf. Sci.* **1996**, *51*, 109–173.

Konicek, A. R.; Grierson, D. S.; Gilbert, P. U. P. A.; Sawyer, W. G.; Sumant, A. V. "Origin of Ultralow Friction and Wear in Ultrananocrystalline Diamond" *Phys. Rev. Lett.* **2008**, *100*, 235502-1–234402-4.

Krauss, A. R.; Auciello, O.; Gruen, D. M.; Jayatissa, A.; Sumant, A.; Tucek, J.; Mancini, D. C.; Moldovan, N.; Erdemir, A.; Ersoy, D.; Gardos, M. N.; Busmann, H. G.; Meyer, E. M.; Ding, M. Q. "Ultrananocrystalline Diamond Thin Films for MEMS and Moving Mechanical Assembly Devices" *Diamond Relat. Mater.* **2001**, *10*, 1952–1961.

Kufer, S. K.; Puchner, E. M.; Gumpp, H.; Liedl, T.; Gaub, H. E. "Single-Molecule Cut-and-Paste Surface Assembly" *Science* **2008**, *319*, 594–596.

Kulisch, W.; Popov, C.; Bliznakov, S.; Ceccone, G.; Gilliland, D.; Sirghi, L.; Rossi, F. "Surface Bioproperties of Nanocrystalline Diamond/Amorphous Carbon Nanocomposite Films" *Thin Solid Films* **2007**, *515*, 8407–8411.

Kulisch, W.; Popov, C.; Gilliland, D.; Ceccone, G.; Sirghi, L.; Ruiz, A.; Rossi, F. "Surface Properties of Differently Prepared Ultrananocrystalline Diamond Surfaces", *Diamond Rel. Mater.* **2009**, *18*, 745–749.

La, Y.-H.; Edwards, E. W.; Park, S.-M.; Nealey, P. F. "Directed Assembly of Cylender-Forming Block Copolymer Films and Thermochemically Induced Cylinder to Sphere Transition: A Hierarchical Route to Linear Arrays of Nanodots" *Nano. Lett.* **2005**, *5*, 1379–1384.

Lahiri, J.; Isaacs, L.; Tien, J.; Whitesides, G. M. "A Strategy for the Generation of Surfaces Presenting Ligands for Studies of Binding Based on an Active Ester as a Common Reactive Intermediate: A Surface Plasmon Resonance Study" *Anal. Chem.* **1999**, *71*, 777–790.

Laibinis, P. E.; Whitesides, G. M.; Allara, D. L.; Tao, Y.-T.; Parikh, A. N.; Nuzzo, R. G. "Comparison of the Stuctures and Wetting Properties of Self-Assembled Monolayers of *n*-Alkanethiols on the Coinage Metal Surfaces, Cu, Ag, Au" *J. Am. Chem. Soc.* **1991**, *113*, 7152–7167.

Lauer, M. E.; Jungmann, R.; Kindt, J. H.; Magonov, S.; Fuhrhop, J.-H.; Oroudjev, E.; Hansma, H. G. "Formation and Healing of Micrometer-Sized Channel Networks on Highly Mobile Au(111) Surfaces" *Langmuir* **2007**, *23*, 5459–5465.

Lavoisier, A. L. "Resultat de quelques experiences faites sur le diamant, par MM. Macquer, Cadet and Lavoisier, lu à la séance publique de l'Académie Royale des Sciences le 29 Avril 1772" Referenced in Siegfried, R. "Lavoisier's View of the Gaseous State and Its Early Application to Pneumatic Chemistry" *Isis*, **1972**, *63*, 59–78.

Lee, K.-B.; Park, S.-J.; Mirkin, C. A.; Smith, J. C.; Mrksich, M. "Protein Nanoarrays Generated By Dip-Pen Nanolithography" *Science* **2002**, *295*, 1702–1705.

Li, Q.; Rukavishnikov, A. V.; Petukhov, P. A.; Zaikova, T. O.; Jin, C.; Keana, J. F. W. "Nanoscale Tripodal 1,3,5,7-Tetrasubstituted Adamantanes for AFM Applications" *J. Org. Chem.* **2003**, *68*, 4862–4869.

Li, Q.; Rukavishnikov, A. V.; Petukhov, P. A.; Zaikova, T. O.; Keana, J. F. W. "Nanoscale 1, 3, 5, 7-Tetrasubstituted Adamantanes and *p*-Substituted Tetraphenylmethanes for AFM Applications" *Org. Lett.* **2002**, *4*, 3631–3634.

Li, Q.; Jin, C.; Petukhov, P. A.; Rukavishnikov, A. V.; Zaikova, T. O.; Phadke, A.; LaMunyon, D. H.; Lee, M. D.; Keana, J. F. W. "Synthesis of Well-Defined Tower-Shaped 1,3,5-Trisubstituted Adamantanes Incorporating a Macrocyclic Trilactam Ring System" *J. Org. Chem.* **2004**, *69,* 1010–1019.

Lin, L.; Wang, H.; Liu, Y.; Yan, H.; Lindsay, S. "Recognition Imaging with a DNA Aptamer" *Biophys. J.* **2006**, *90*, 4236–4238.

Lin, T.;Yu, C. Y.; Wee, A. T. S.; Shen, Z. X.; Loh, K. P. "Compositional Mapping of the Argon–Methane–Hydrogen System for Polycrystalline to Nanocrystalline Diamond Film Growth in a Hot-Filament Chemical Vapor Deposition System" *Appl. Phys. Lett.***2000**, *77,* 2692–2694.

Liphardt, J.; Onoa, B.; Smith, S. B.; Tinoco, Jr., I.; Bustamante, C. "Reversible Unfolding of Single RNA Molecules by Mechanical Force" *Science* **2001**, *292*, 733–736. Onoa, B.; Dumont, S.; Liphardt, J.; Smith, S. B.; Tinoco, Jr., I.; Bustamante, C. "Identifying Kinetic Barriers to Mechanical Unfolding of the *T. thermophila* Ribozyme" *Science* **2003**, *299*, 1892–1895.

Little, R. B.; Roache, J. "Treatise on the Resolution of the Diamond Problem After 200 Years" *Prog. Solid State Chem.* **2008**, *36*, 223–251.

Liu, H.; Dandy, D. S. *Diamond Chemical Vapor Deposition*, Noyes Publications: Park Ridge, New Jersey, 1995.

Liu, X.; Jang, C.-H.; Zheng, F.; Jürgensen, A.; Denlinger, J. D.; Dickson, K. A.; Raines, R. T.; Abbot, N. L.; Himpsel, F. J. "Characterization of Protein Immobilization at Silver Surfaces by Near Edge X-Ray Absorption Fine Spectroscopy" *Langmuir* **2006**, *22*, 7719–7725.

Liu, Y.; Gu, Z.; Margrave, J. L.; Khabashesku, V. N. "Functionalization of Nanoscale Diamond Powder: Fluoro-, Alkyl-, Amino-, and Amino Acid-Nanodiamond Derivatives" *Chem. Mater.* **2004**, *16*, 3924–3930.

Lo, Y.-S.; Heufner, N. D.; Chan, W. S.; Dryden, P.; Hagenhoff, B.; Beebe, T. P. "Organic and Inorganic Contamination on Commercial AFM Cantilevers" *Langmuir*, **1999**, *15*, 6522–6526.

Lo, Y.-S.; Zhu, Y.-J.; Beebe Jr., T. P. "Loading-Rate Dependence of Individual Ligand-Receptor Forces Studied by Atomic Force Microscopy" *Langmuir* **2001**, *17*, 3741–3748.

Love, J. C.; Estroff, L. A.; Kriebel, J. K.; Nuzzo, R. G.; Whitesides, G. M. "Self-Assembled Monolayers of Thiolates on Metals as a Form of Nanotechnology" *Chem. Rev.* **2005**, *105*, 1103–1169.

Maier, F.; Ristein, J.; Ley, L. "Electron Affinity of Plasma-Hydrogenated and Chemically Oxidized Diamond (100) Surfaces" *Phys. Rev. B* **2001**, *64*, 165411-1–165411-7.

Marszalek, P. E.; Li, H.; Fernandez, J. M. "Fingerprinting polysaccharides with Single-Molecule Atomic Force Microscopy" *Nat. Biotech.* **2001**, *19*, 258–262.

Matrab, T.; Chehimi, M. M.; Boudou, J. P.; Benedic, F.; Wang, J.; Naguib, N. N.; Carlisle, J. A. "Surface Functionalization of Ultrananocrystalline Diamond Using Atom Transfer Radical Polymerization (ATRP) Initiated by Electro-Grafted Aryldiazonium Salts" *Diamond Rel. Mater.* **2006**, *15*, 639–644.

Matsumoto, S.; Sato, Y.; Kamo, M.; Setaka, N. "Vapor Deposition of Diamond Particles from Methane" *Jpn. J. Appl. Phys.* **1982**, *21*, L183–L185.

May, P. W. "Diamond Thin Films: a 21st-Century Material" *Phil. Trans. R. Soc. Lond.* A **2000**, *358*, 473–495.

May, P. W.; Ashfold, M. N. R.; Mankelevich, Y. A. "Microcrystalline, Nanocrystalline, and Ultrananocrystalline Diamond, Chemical Vapor Deposition: Experiment and Modeling of the Factors Controlling Growth Rate, Nucleation, and Crystal Size" *J. Appl. Phys.* **2007**, *101*, 053115-1–053115-9.

Mayo, D. W.; Pike, R. M.; Trumper, P. K. Introduction to Infrared Spectroscopy. In *Microscale Techniques for the Organic Laboratory*, 2nd edition; John Wiley and Sons: New York, 2001, pp 151–161.

McConnell, M. D.; Bassani, A. W.; Yang, S.; Composto, R. J. "Tunable Wetting of Nanoparticle-Decorated Polymer Films" *Langmuir* **2009**, *25*, 11014–11020.

McConnell, M. D.; Yang, S.; Composto, R. J. "Covalent Nanoparticle Assembly onto Random Copolymer Films" *Macromolecules* **2009**, *42*, 517–523.

McKendry, R., Theoclitou, M.-E.; Rayment, T.; Abell, C. "Chiral Discrimination by Chemical Force Microscopy" *Nature* **1998**, *391*, 566–568.

Medard, N.; Aouinti, M.; Poncin-Epiallard, F.; Bertrand, P. "ToF-SIMS Ability to Quantify Surface Chemical Groups: Correlation with XPS Analysis and Spectrochemical Titration" *Surf. Interface Anal.* **2001**, *31*, 1042–1047.

Merkel, R.; Nassoy, P.; Leung, A.; Ritchie, K.; Evans, E. "Energy Landscapes of Receptor–Ligand Bonds Explored with Dynamic Force Spectroscopy" *Nature* **1999**, *397*, 50–53.

Mio, K.; Kubo, Y.; Ogura, T.; Yamamoto, T.; Sato, C. "Visualization of the Trimeric $P2X_2$ Receptor with a Crown-capped Extracellular Domain" *Biochem. Biophys. Res. Commun.* **2005**, *337*, 998–1005.

Moy, V. T.; Florin, E.-L.; Gaub, H. E. "Intermolecular Forces and Energies Between Ligands and Receptors" *Science* **1994**, *266*, 257–259.

Moy, V. T.; Florin, E.-L.; Gaub, H. E. "Intermolecular Forces and Energies Between Ligands and Receptors" *Science* **1994**, *266*, 25—259.

Nakazawa, K.; Yamakoshi, Y.; Tsuchiya, T.; Ohno, Y. "Purification and Aqueous Phase Atomic Force Microscopic Observation of Recombinant $P2X_2$ Receptor" *Eur. J. Pharm.* **2005**, *518*, 107–110.

Nakazawa, K.; Yamakoshi, Y.; Tsuchiya, T.; Ohno, Y. "Purification and Aqueous Phase Atomic Force Microscopic Observation of Recombinant P2X2 Receptor" *Eur J. of Pharmacol.* **2005**, *518*, 107–110.

Nassau, K. Synthesis of Bulk Diamond: History and Present Status. In *Diamond Films and Coatings*; Davis, R. F., Ed.; Noyes Publications: Park Ridge, New Jersey, 1993: pp. 40–49.

Naumann, R.; Schiller, S. M.; Giess, F.; Grohe, B.; Hartman, K. B.; Kärcher, I.; Köper, I.; Lübben, J.; Vasilev, K.; Knoll, W. "Tethered Lipid Bilayers on Ultraflat Gold Surfaces" *Langmuir*, **2003**, *19*, 5435–5443.

Nebel, C. E.; Rezek, B.; Shin, D.; Uetsuda, H.; Yang, N. "Diamond for Bio-Sensor Applications" *J. Phys. D: Appl. Phys.* **2007**, *40*, 6443–6466.

Nelson, K. E.; Gamble, L.; Jung, L. S.; Boeckl, M. S.; Naeemi, E.; Golledge, S. L.; Sasaki, T.; Castner, D. G.; Campbell, C. T.; Stayton, P. S. "Surface Characterization of Mixed Self-Assembled Monolayers Designed for Streptavidin Immobilization" *Langmuir*, **2001**, 2807–2816.

Nichols, B. M.; Butler, J. E.; Russell, Jr., J. N.; Hamers, R. J. "Photochemical Functionalization of Hydrogen-Terminated Diamond Surfaces: A Structural and Mechanistic Study" *J. Phys. Chem. B* **2005**, *109*, 20938–20947.

Nikitin, K.; Lestini, E.; Lazzari, M.; Altobello, S.; Fitzmaurice, D. "A Tripodal [2]Rotaxane on the Surface of Gold" *Langmuir* **2007**, *23*, 12147–12153.

Nilsson, D.; Watcharinyanon, S.; Eng, M.; Li, L.; Moons, E.; Johansson, L. S. O.; Zharnikov, M.; Shaporenko, A.; Albinsson, B.; Mårtensson, J. "Characterization of Self-Assembled Monolayers of Oligo(phenyleneethynylene) Derivatives of Varying Shapes on Gold: Effect of Laterally Extended π-Systems" *Langmuir* **2007**, *23*, 6170–6181.

Nishi, N.; Hobara, D.; Yamamoto, M.; Kakiuchi, T. "Chain-Length-Dependent Change in the Structure of Self-Assembled Monolayers of *n*-Alkanethiols on Au(111) Probed by Broad-Bandwidth Sum Frequency Generation Spectroscopy" *J. Chem. Phys.* **2003**, *118*, 1904–1911.

Nistor, L. C.; Van Landuyt, J.; Ralchenko, V. G.; Obraztsova, E. D.; Smolin, A. A. Nanocrystalline Diamond Films: Transmission Electron Microscopy and Raman Spectroscopy Characterization. *Diamond Relat. Mater.* **1997**, *6*, 159–168.

North, R. A. "Molecular Physiology of P2X Receptors" *Physiol. Rev.* **2002**, *82*, 1013–1067.

Noy, A.; Frisbie, C. D.; Rozsnyai, L. F.; Wrighton, M. S.; Lieber, C. M. "Chemical Force Microscopy: Exploiting Chemically-Modified Tips to Quantify Adhesion, Friction, and Functional Group Distributions in Molecular Assemblies" *J. Am. Chem. Soc.* **1995**, *117*, 7943–7951.

Nuzzo, R. G.; Allara, D. L. "Adsorption of Bifunctional Organic Disulfides on Gold Surfaces" *J. Am. Chem. Soc.* **1983**, *105*, 4481–4483.

Oesterhelt, F.; Rief, M.; Gaub, H. E. "Single Molecule Force Spectroscopy by AFM Indicates Helical Structure of Poly(ethylene-glycol) in Water" *New J. Phys.* **1999**, *1*, 6.1–6.11.

Ohnesorge, F.; Binnig, G. "True Atomic Resolution by Atomic Force Microscopy Through Repulsive and Attractive Forces" *Science* **1993**, *260*, 1451–1456.

Overney, R. M.; Meyer, E.; Frommer, J.; Brodbeck, D.; Lüthi, R.; Howald, L.; Güntherodt, H.-J.; Fujihira, M.; Takano, H.; Gotoh, Y. "Friction Measurements on Phase-Separated Thin Films with a Modified Atomic Force Microscope" *Nature* **1992**, *359*, 133–135.

Parikh, A.; Liedberg, B.; Atre, S. V.; Ho, M.; Allara, D. L. "Correlation of Molecular Organization and Substrate Wettability in the Self-Assembly of *n*-Alkylsiloxane Monolayers" *J. Phys. Chem.* **1995**, *99*, 9996–10008.

Paxton, W. F.; Spruell, J. M.; Stoddart, J. F. "Heterogeneous Catalysis of a Copper-Coated Atomic Force Microscopy Tip for Direct-Write Click Chemistry" *J. Am. Chem. Soc.* **2009**, *131*, 6692–6694.

Peng, L.; Lee, H.; Teizer, W.; Liang, H. "Nanowear of Gold and Silver Against Silicon" *Wear* **2009**, *267*, 1177–1180.

Pfister, J. R.; Wymann, W. E. "A Useful Variant of the Curtius Reaction" *Synthesis* **1983**, 38–40.

Piers, A. S.; Rochester, C. H. "Infrared Study of the Adsorption of 1-Aminopropyltrialkoxysilanes on Silica at the Solid/Liquid Interface" *J. Coll. Interface Sci.* **1995**, *174*, 97–103.

Piner, R. D.; Zhu, J.; Xu, F.; Hong, S.; Mirkin, C. A. "'Dip–Pen' Nanolithography" *Science* **1999**, *283*, 661–663.

Porter, M. D.; Bright, T. B.; Allara, D. L.; Chidsey, C. E. D. "Spontaneously Organized Molecular Assemblies. 4. Structural Characterization of *n*-Alkyl Thiol Monolayers on Gold by Optical Ellipsometry, Infrared Spectroscopy, and Elecrochemistry" *J. Am. Chem. Soc.* **1987**, *109*, 3559–3568.

Quéré, D. "Rough Ideas on Wetting" *Physica A* **2002**, *313*, 32–46.

Ralevic, V.; Burnstock, G. "Receptors for Purines and Pyrimidines" *Pharm. Rev.* **1998**, *50*, 415–492.

Reichert, V. R.; Mathias, L. J. "Expanded Tetrahedral Molecules from 1,3,5,7-Tetraphenyladamantane" *Macromolecules* **1994**, *27*, 7015–7023.

Rief, M.; Gautel, M.; Oesterhelt, F. Fernandez, J. M.; Gaub, H. E.. "Reversible Unfolding of Individual Titin Immunoglobulin Domains by AFM" *Science* **1997**, *276*, 1109–1112.

Riener, C. K.; Kienberger, F.; Hahn, C. D.; Buchinger, G. M.; Egwim, I. O. C.; Haselgrübler, T.; Ebner, A.; Romanin, C.; Klampfl, C.; Lackner, B.; Prinz, H.; Blaas, D.; Hinterdorfer, P.; Gruber, H. J. "Heterobifunctional Crosslinkers for Tethering Single Ligand Molecules to Scanning Probes" *Anal. Chim. Acta*, **2003**, *497*, 101–114.

Riener, C. K.; Stroh, C. M.; Ebner, A.; Klampfl, C.; Gall, A. A.; Romanin, C.; Lyubchenko, Y.; Hinterdorfer, P.; Gruber, H. J. "Simple Test System for Single Molecule Recognition Force Microscopy" *Anal. Chim. Acta* **2003**, *479*, 59–75.

Ron, H.; Matlis, S.; Rubinstein, I. "Self-Assembled Monolayers on Oxidized Metals. 2. Gold Surface Oxidative Pretreatment, Monolayer Properties, and Depression Formation" *Langmuir*, **1998**, *14*, 1116–1121.

Ros, R.; Schwesinger, F.; Anselmetti, D.; Kubon, M.; Schafer, R.; Pluckthun, A.; Tiefenauer, L. "Antigen Binding Forces of Individually Addressed Single-chain Fv Antibody Molecules" *Proc. Natl. Acad. Sci.* **1998**, *95*, 7402–7405.

Ros, R.; Schwesinger, F.; Anselmetti, D.; Kubon, M.; Schäfer, R.; Plückthun, A.; Tiefennauer, L. "Antigen Binding Forces of Individually Addressed Single-Chain Fv Antibody Molecules" *Proc. Natl. Acad. Sci.* **1998**, *95*, 7402–7405.

Rostovtsev, V. V.; Green, L. G.; Fokin, V. V.; Sharpless, K. B. "A Stepwise Huisgen Cycloaddition Process: Copper (I)-Catalyzed Regioselective Ligation of Azides and Terminal Alkynes" *Angew. Chem. Int. Ed.* **2002**, *114*, 2708–2711.

S. Szunerits, R. Boukherroub "Different Strategies for Functionalization of Diamond Surfaces" *J. Solid State Electrochem.* **2008**, *12*, 1205–1218.

Sakata, T.; Maruyama, S.; Ueda, A.; Otsuka, H.; Miyahara, Y. "Stable Immobilization of an Oligonucleotide Probe on a Gold Substrate Using Tripodal Thiol Derivatives" *Langmuir* **2007**, *23*, 2269–2272.

Salaita, K.; Wang, Y.; Fragala, J.; Vega, R. A.; Liu, C.; Mirkin, C. A. "Massively Parallel Dip–Pen Nanolithography with 55 000-Pen Two-Dimensional Arrays" *Angew. Chem. Int. Ed.* **2006**, *45*, 7220–7223.

Schlenoff, J. B.; Li, M.; Ly, H. "Stability and Self-Exchange in Alkane Thiol Monolayers" *J. Am. Chem. Soc.* **1995**, *117*, 12528–12536.

Schlierf, M.; Li, H.; Fernandez, J. M. "The Unfolding Kinetics of Ubiquitin Captured with Single-molecule Force-clamp Techniques" *Proc. Nat. Acad. Sci.* **2004**, *101*, 7299–7304.

Schnitzer, M. J.; Visscher, K.; Block, S. M. "Force Production by Single Kinesin Motors" *Nat. Cell Biol.* **2000**, *2*, 718–723.

Schoenfisch, M. H.; Pemberton, J. E. "Air Stability of Alkane Thiol Self-Assembled Monolayers on Silver and Gold Surfaces" *J. Am. Chem. Soc.* **1998**, *120*, 4502–4513.

Schwabacher, A. W.; Lane, J. W.; Schiesher, M. W.; Leigh, K. M.; Johnson, C. W. "Desymmetrization Reactions: Efficient Preparation of Unsymmetrically Substituted Linker Molecules" *J. Org. Chem.* **1998**, *63*, 1727–1729.

Service, R. F. "Optical Lithography Goes To Extremes—And Beyond" *Science* **2001**, *293*, 785–786.

Shenderova, O. A.; Barnard, A. S.; Gruen, D. M. Carbon Family at the Nanoscale. In *Ultrananocrystalline Diamond Synthesis, Properties, and Applications;* Shenderova, O. A., Gruen, D. M.; William Andrew Publishing: Norwich, New York, 2006; pp. 3–12.

Shumaker-Perry, J. S.; Zareie, M. H.; Aebersold, R.; Campbell, C. T. "Microspotting Streptavidin and Double-Stranded DNA Arrays on Gold for High-Throughput Studies of Protein–DNA Interactions by Surface Plasmon Resonance Microscopy" *Anal. Chem.* **2004**, *76*, 918–929.

Sinniah, S. K.; Steel, A. B. Miller, C. J.; Reutt-Robey, J. E. "Solvent Exclusion and Chemical Contrast in Scanning Force Microscopy" *J. Am. Chem. Soc.* **1996**, *118*, 8925–8931

Skokov, S.; Weiner, B.; Frenklach, M. "Elementary Reaction Mechanism of Diamond Growth from Acetylene" *J. Phys. Chem.* **1994**, *98*, 8–11.

Smith, D. P. E. "Limits of Force Microscopy" *Rev. Sci. Instrum.* **1995**, *66*, 3191–3195.

Smith, R. L.; Rohrer, G. S. The Preparation of Tip and Sample Surfaces for Scanning Probe Experiments. In *Scanning Probe Microscopy and Spectroscopy Theory, Techniques, and Applications*, 2nd edition; Bonnell, D. Ed.; Wiley: New York, 2001; 170–178.

Smith, T. "The Hydrophilic Nature of a Clean Gold Surface" *J. Colloid Interface Sci.* **1980**, *75*, 51–55.

Stöhr, J. *NEXAFS Spectroscopy*; Gomer, R., Ed.; Springer Series in Surface Sciences Vol. 25; Springer-Verlag: New York, 1992.

Stöhr, J.; Jaeger, R. "Absorption-Edge Resonances, Core-Hole Screening, and Orientation of Chemisorbed Molecules: CO, NO, and N_2 on Ni (100) *Phys. Rev. B* **1982**, *26*, 4111–4131.

Strick, T. R.; Bensimon, D.; Croquette, V. "Micro-mechanical Measurement of the Torsional Modulus of DNA" *Genetica* **1999**, *106*, 57–62.

Stroh, C.; Wang, H.; Bash, R.; Ashcroft, B.; Nelson, J.; Gruber, H.; Lohr, D.; Lindsay, S. M.; Hinterdorfer, P. "Single-Molecule Recognition Imaging Microscopy" *Proc. Nat. Acad. Sci.* **2004**, *101*, 12503–12507.

Strother, T.; Knickerbocker, T.; Russell, J. N.; Butler, J. E.; Smith, L. M.; Hamers, R. J. "Photochemical Functionalization of Diamond Films" *Langmuir* **2002**, *18*, 968–971.

Strunz, T. Oroszlan, K., Schumakovitch, I., Güntherodt, H.-J., Hegner, M. "Model Energy Landscapes for the Force-Induced Dissociation of Ligand-Receptor Bonds" *Biophys. J.* **2000**, *79*, 1206–1212.

Strunz, T.; Oroszlan, K.; Schäfer, R.; Güntherodt, H.-J. "Dynamic Force Spectroscopy of Single DNA Molecules" *Proc. Nat. Acad. Sci.* **1999**, *96*, 11277–11282.

Su, C.; Huang, L.; Kjoller, K.; Babcock, K. "Studies of Tip Wear Processes in Tapping Mode Atomic Force Microscopy" *Ultramicroscopy*, **2003**, *97*, 135–144.

Sugawara, T.; Matsuda, T. "Photochemical Protein Fixation on Polymer Surfaces via Derivatized Phenyl Azido Group" *Langmuir*, **1995**, *11*, 2272–2276.

Takahashi, Y.; Tadokoro, H. "Structural Studies of Polyethers, $(-(CH_2)_m-O-)_n$. X. Crystal Structure of Poly(ethylene oxide)" *Macromolecules* **1973**, *6*, 672–675.

Takamatsu, D.; Yamakoshi, Y.; Fukui, K. "Photoswitching Behavior of a Novel Single Molecular Tip for Noncontact Atomic Force Microscopy Designed for Chemical Identification" *J. Phys. Chem. B* **2006**, *110*, 1968–1970.

Tang, J.; Ebner, A.; Badelt-Lichtblau, H.; Völlenkle, C.; Rankl, C.; Kraxberger, B.; Leitner, M.; Wildling, L.; Gruber, H. J.; Sleytr, U. B.; Hinterdorfer, P. "Recognition Imaging and Highly Ordered Molecular Templating of Bacterial S-Layer Nanoarrays Containing Affinity-Tags" *Nano Lett.* **2008**, *8*, 4312–4319.

Tennant, S. "On the Nature of the Diamond" *Phil. Trans. R. Soc. Lond.* **1797**, *87*, 123–127. Referenced in May, P. W. "Diamond Thin Films: a 21st-Century Material" *Phil. Trans. R. Soc. Lond.* A **2000**, *358*, 473–495.

Tian, R.; Seitz, O.; Li, M.; Hu, W.; Chabal, Y. J.; Gao, J. "Infrared Characterization of Interfacial Si–O Bond Formation on Silanized Flat SiO_2/Si Surfaces" *Langmuir* **2010** ASAP. DOI: 10.1021/la904597c accessed February 25, 2010.

Tjong, S. C. Properties of Chemical Vapor Deposited Nanocrystalline Diamond and Nanodiamond/Amorphous Carbon Composite Films. In *Nanocomposite Thin Films and Coatings: Processing Properties and Performance*; Zhang, S.; Ali, N.Eds; Imperial College Press: London, 2007; pp 167–206.

Tornoe, C. W.; Christensen, C.; Meldal, M. " Peptidotriazoles on Solid Phase: [1, 2, 3]-Triazoles by Regiospecific Copper (I)-Catalyzed 1, 3-Dipolar Cycloadditions of Terminal Alkynes to Azides" *J. Org. Chem.* **2002**, *67*, 3057–3064.

Touhami, A.; Hoffmann, B.; Vasella, A.; Denis, F.; Dufrêne, Y. F. "Aggregation of Yeast Cells: Direct Measurement of Discrete Lectin–Carbohydrate Interactions" *Microbiology* **2003**, *149*, 2873–2878.

Trau, M.; Murray, B. S.; Grant, K.; Grieser, F. "An Ellipsometric Study of Thin Films on Silica Plates Formed by Alkylchlorosilylation Reagents" *J. Colloid Interface Sci.* **1992**, *148*, 182–189.

Tsubota, T.; Tanii, S.; Ida, S.; Nagata, M.; Matsumoto, Y. "Chemical Modification of Diamond Surface with $CH_3(CH_2)_nCOOH$ Using Benzoyl Peroxide" *Phys. Chem. Chem. Phys.* **2003**, *5*, 1474–1480.

Urquhart, S. G.; Hitchcock, A. P.; Priester, R. D.; Rightor, E. G. "Analysis of Polyurethanes Using Core Excitation Spectroscopy. Part II: Inner Shell Spectra of Ether, Urea, and Carbamate Model Compounds" *J. Polym. Sci., Part B: Polym. Phys.* **1995**, *33*, 1603–1620.

Voicu, R.; Boukherroub, R.; Bartzoka, V.; Ward, T.; Wojtyk, J. T. C.; Wayner, D. D. M. "Formation, Characterization, and Chemistry of Undecanoic Acid-Terminated Silicon Surfaces: Patterning and Immobilization of DNA" *Langmuir* **2004**, *20*, 11713–11720.

Waddell, T. G.; Leyden, D. E.; DeBello, M. T. "The Nature of Organosilane to Silica-Surface Bonding" *J. Am. Chem. Soc.* **1981**, *103*, 5303–5307.

Wallraff, G.; Hutchinson, J.; Hinsberg, W.; Houle, F.; Seidel, P.; Johnson, R.; Oldham, W. "Thermal and Acid-Catalyzed Deprotection Kinetics in Candidate Deep Ultraviolet Resist Materials" *J. Vac. Sci. Technol. B* **1994**, *12*, 3857–3862.

Walsh, J. F.; Dhariwal, H. S.; Gutiérrez-Sosa, A.; Finetti, P.; Muryn, C. A.; Brookes, N. B.; Oldman, R. J.; Thornton, G. "Probing Molecular Orientation in Corrosion Inhibition via a NEXAFS Study of Benzotriazole and Related Molecules on Cu (100)" *Surf. Sci.* **1998**, *415*, 423–432.

Walther, K. A.; Brujic, J.; Li, H.; Fernandez, J. M. "Sub-Angstrom Conformational Changes of a Single Molecule Captured by AFM Variance Analysis" *Biophys. J.* **2006**, *90*, 3806–3812.

Wang, H.; Griffiths, J.-P.; Egdell, R. G.; Moloney, M. G.; Foord, J. S. "Chemical Functionalization of Diamond Surfaces by Reaction with Diaryl Carbenes" *Langmuir* **2008**, *24*, 862–868.

Wang, J.; Carlisle "Covalent Immobilization of Glucose Oxidase on Conducting Ultrananocrystalline Diamond Thin Films" *Diamond Relat. Mater.* **2006**, *15*, 279–284.

Weiss, S. "Measuring Conformational Dynamics of Biomolecules by Single Molecule Fluorescence Spectroscopy" *Nature Struct. Biol.* **2000**, *7*, 724–729.

Wenmackers, S.; Pop, S. D.; Roodenko, K.; Vermeeren, V.; Williams, O. A.; Daenen, M.; Douhéret, O.; D'Haen, J.; Hardy, A.; Van Bael, M. K.; Hinrichs, K.; Cobet, C.; van de Ven, M.; Ameloot, M.; Haenen, K.; Michiels, L.; Esser, N.; Wagner, P. "Structural and Optical Properties of DNA Layers Covalently Attached to Diamond Surfaces" *Langmuir* **2008**, *24*, 7269–7277.

Wilson, D. L.; Martin, R.; Hong, S.; Cronin-Golomb, M.; Mirkin, C. A.; Kaplan, D. L. "Surface Organization and Nanopatterning of Collagen by Dip-Pen Nanolithography" *Proc. Natl. Acad. Sci.* **2001**, *98*, 13660–13664.

Woolley, A. T.; Cheung, C. L.; Hafner, J. H.; Lieber, C. M. "Structural Biology with Carbon Nanotube AFM Probes" *Chem. Biol.* **2000**, *7*, R193–R204.

Wouters, D.; Schubert, U. S. "Nanolithography and Nanochemistry: Probe-Related Patterning Techniques and Chemical Modification for Nanometer-Sized Devices" *Angew. Chem. Int. Ed.* **2004**, *43*, 2480–2495.

Xie, S. Single-Molecule Approach to Enzymology *Single Mol.* **2001**, *2*, 229–236.

Xing, Y.; Borguet, E. "Specificity and Sensitivity of Fluorescence Labeling of Surface Species" *Langmuir*, **2007**, *23*, 684–688.

Xu, C.; Fu, S.; Fryd, M.; Xu, S.; Wayland, B. B.; Winey, K. I.; Composto, R. J. "Reversible Stimuli-Responsive Nanostructures Assembled from Amphiphilic Block Copolymers" *Nano Lett.* **2006**, *6*, 282–287.

Yadavalli, V. K.; Forbes, J. G.; Wang, K. "Functionalized Self-Assembled Monolayers on Ultraflat Gold as Platforms for Single Molecule Force Spectroscopy and Imaging" *Langmuir* **2006**, *22*, 6969–6976.

Yam, C.-M.; Xiao, Z.; Gu, J.; Boutet, S.; Cai, C. "Modification of Silicon AFM Cantilever Tips with an Oligo(ethylene glycol) Derivative for Resisting Proteins and Maintaining a Small Tip Size for High-Resolution Imaging" **2003**, *125*, 7498–7499.

Yan, M.; Cai, S. X.; Wybourne, M. N.; Keana, J. F. W. "*N*-Hydroxysuccinimide Ester Functionalized Perfluorophenyl Azides as Novel Photoactive Heterobifunctional Cross-Linking Reagents. The Covalent Immobilization of Biomolecule to Polymer Surfaces" *Bioconj. Chem.* **1994**, *5*, 151–157.

Yan, M.; Cai, S. X.; Wybourne, M. N.; Keana, J. F. W. "Photochemical Functionalization of Polymer Surfaces and the Production of Biomolecule-Carrying Micrometer-Scale Structures by Deep-UV Lithography Using 4-Substituted Perfluorophenyl Azides" *J. Am. Chem. Soc.* **1993**, *115*, 814–816.

Yang, N.; Uetsuka, H.; Watanabe, H.; Nakamura, R.; Nebel, C. E. "Photochemical Amine Layer Formation on H-Terminated Single-Crystalline CVD Diamond" *Chem. Mater.* **2007**, *19*, 2852–2859

Yang, W.; Auciello, O.; Butler, J.E.; Cai, W.; Carlisle, J. A.; Gerbi, J. E.; Gruen, D. M.; Knickerbocker, T.; Lasseter, T. L.; Russell, Jr., J. N.; Smith, L. M.; Hamers, R. J. "DNA-Modified Nanocrystalline Diamond Thin-Films as Stable, Biologically Active Substrates" *Nature Mat.* **2002**, *1*, 253–257.

Yang, W.; Baker, S. E.; Butler, J. E.; Lee, C.-S.; Russell, Jr., J. N.; Shang, L.; Sun, B.; Hamers, R. J. "Electrically Addressable Biomolecular Functionalization of Conductive Nanocrystalline Diamond Thin Films" *Chem. Mater.* **2005**, *17*, 938–940.

Yang, Z.; Engquist, I. Wirde, M.; Kauffmann, J.-M.; Gelius, U.; Liedberg, B. "Preparation and Characterization of Mixed Monolayer Assemblies Composed of Thiol Analogues of Cholesterol and Fatty Acid" *Langmuir* **1997**, *13*, 3210–3218.

Yao, Y.; Tour, J. M.; "Facile Route to Molecular Caltrops" *J. Org. Chem.* **1999**, *64*, 1968–1971.

Yeap, W. W.; Chen, S.; Loh, K. P. "Detonation Nanodiamond: An Organic Platform for the Suzuki Coupling of Organic Molecules" *Langmuir*, **2009**, *25*, 185–191.

Yoder, M. N. Diamond Properties and Applications. In *Diamond Films and Coatings*; Davis, R. F., Ed.; Noyes Publications: Park Ridge, New Jersey, 1993: pp. 1–15.

Yuan, C.; Chen, A.; Kolb, P.; Moy, V. T. "Energy Landscape of Steptavidin-Biotin Complexes Measured by Atomic Force Microscopy" *Biochemistry* **2000**, *39*, 10219–10223.

Zaborski, M.; Vidal, A.; Ligner, G.; Balard, H.; Papirer, E. "Compoarative Study of the Surface Hydroxyl Groups of Fumed and Precipitated Silicas. 1. Grafting and Chemical Characterization" *Langmuir* **1989**, *5*, 447–451.

Zdyrko, B.; Varshney, S. K.; Luzinov, I. "Effect of Molecular Weight on Synthesis and Surface Morphology of High-Density Poly(ethylene glycol) Grafted Layers" *Langmuir*, **2004**, *20*, 6727–6735.

Zhang, Q.; Lu, Z.; Hu, H.; Yang, W.; Marszalek, P. E. "Direct Detection of the Formation of V-Amylose Helix by Single Molecule Force Spectroscopy" *J. Am. Chem. Soc.* **2006**, *128*, 9387–9393.

Zhong, Y. L.; Chong, K. F.; May, P. W.; Che, Z.-K.; Loh, K. P. "Optimizing Biosensing Properties on Undecylenic Acid-Functionalized Diamond" *Langmuir* **2007**, *23*, 5824–5830.

Zhong, Y. L.; Loh, K. P.; Midya, A.; Chen, Z.-C. "Suzuki Coupling of Aryl Organics on Diamond" *Chem. Mater.* **2008**, *20*, 3137–3144.

Zhong, Y. L.; Midya, A.; Ng, Z.; Chen, Z.-C.; Daenen, M.; Nesladek, M.; Loh, K. P. "Diamond-Based Molecular Platform for Photoelectrochemistry" *J. Am. Chem. Soc.* **2008**, *130*, 17218–17219.

Zhou, D.; McCauley, T. G.; Qin, L. C.; Krauss, A. R.; Gruen, D. M. "Synthesis of Nanocrystalline Diamond Thin Films from an Ar–CH_4 Microwave Plasma" *J. Appl. Phys.* **1998**, *83*, 540–543.

Zou, S.; Schonherr, H.; Vancso, G. J. "Stretching and Rupturing Individual Supramolecular Polymer Chains by AFM" *Angew. Chem. Int. Ed.* **2005**, *44*, 956–959.

Zwahlen, M.; Herrwerth, S.; Eck, W.; Grunze, M.; Hähner, G. "Conformational Order in Oligo(ethylene glycol)-Terminated Self-Assembled Monolayers on Gold Determined by Soft X-Ray Absorption" *Langmuir* **2003**, *19*, 9305–9310.